AGGREGATION/AGGLOMERATION OF TiO_2 NANOPARTICLES IN THE PRESENCE OF NATURAL ORGANIC MATTER

by

Ayşe Hazal Pekcan Çetin

B.Sc. in Chemistry, İstanbul University, 2012

M.Sc. in Chemistry, Boğaziçi University, 2015

Submitted to the Institute of Environmental Sciences in partial fulfillment of
the requirements for the degree of
Doctor of Philosophy
in
Environmental Sciences

Boğaziçi University

2024

AGGREGATION/AGGLOMERATION OF TiO_2 NANOPARTICLES IN THE PRESENCE OF NATURAL ORGANIC MATTER

APPROVED BY:

Prof. Dr. Burak Demirel Dissertation Advisor	. . . . .
Prof. Dr. Miray Bekbölet Co-Advisor	. . . . .
Prof. Dr. İdil Arslan Alaton	. . . . .
Prof. Dr. Nadim Copty	. . . . .
Prof. Dr. Ferhan Çeçen	. . . . .
Assoc. Prof. Dr. Hatice İnan	. . . . .

DATE OF APPROVAL: 12/07/2024

ACKNOWLEDGEMENTS

I want to express my gratitude to my thesis advisors, Prof. Dr. Miray Bekbölet and Prof. Dr. Burak Demirel. I owe them immense appreciation for the infinite patience, support, and leadership they have shown. Throughout our collaboration, their scientific and personal support has been invaluable to me. Particularly, being the last student of Prof. Dr. Miray Bekbölet is both a great pride and a bittersweet experience. I hope to become a valuable scientist like her and take pride in educating future generations. My greatest aspiration is to pass on the scientific perspective and profound life experiences she imparted to us to those who come after me. I will carry the justified honor of being part of the Bekbolet Group throughout my life.

I would also like to express my thanks to the esteemed jury members, Prof. Dr. İdil Arslan Alaton, Prof. Dr. Nadim Copty Prof. Dr. Ferhan Çeçen, Assoc. Prof. Dr. Hatice İnan, and Prof. Dr. Ayşen Erdinçler for their valuable insights, support, and contributions.

Special thanks to my dear mentor, Dr. Ceyda Senem Uyguner Demirel. Her support has always been precious to me. Expressing gratitude for her perspective and valuable contributions, as well as the numerous times she supported me during my doctoral process, feels insufficient.

To my precious colleagues and my greatest supporters during this journey, Dr. Nazmiye Cemre Birben, Dr. Nazlı Türkten, Ezgi Lale, and Didem Sağlık Kanpara, I am very happy to have known and had the honor of working with you. The laboratory adventures we shared were both instructive and enjoyable. I am grateful to have you in my life.

To my best friends, Dr. Duygu Tuncel Turan, Dr. Başak Savun, Güliz Kıvançlı Eren, Elif Gökler Zeytinler, Övgü Özertural Akın and Özlem Ceylan. Thank you for being by my side in my happiness and giving me a shoulder to lean on in my sorrow. Maybe I didn't have a sister, but fate brought me you. I'm so glad you're here. My dearest brothers, Çağdaş Eren, Eren Zeytinler, Berkcan Akın I cannot imagine a world without you guys. Thanks for being a good friend, a great uncle for my son and playmate in the game of life.

To my beloved family, my mother Gülşen Pekcan, and brother Hasan Ali Pekcan. My parents in law Filiz Çetin and Şeref Çetin and little brother Barış Cem Çetin. I am thankful for always encouraging me and standing by me during this process. You are the true architect of my success. I love you so much. I want to extend my thanks especially to my dearest mother and role model Gülşen Pekcan. I am grateful to you for teaching me to be a strong independent woman and to work hard for success in every aspect.

To my dear husband and “partner in crime”, Cafer Çetin, without your unconditional love and support, writing these lines would not have been possible, I believe. We were tired, we faced challenges, but we did not give up. Thank you once again for enabling us to succeed together.

To my beloved son, Ali Kerem Çetin, the biggest thanks go to you for being by my side during sleepless nights, enveloping me with your love, and teaching me a different aspect of life. I hope I can become “the water doctor” you dream of and contribute a piece to a world where all children are happy and play in flower gardens.

Perhaps the hardest part of my work to write could be this paragraph. My dear father, my first and endless love, Merih Pekcan. I wish you could also read these sentences and see the day of my graduation. Maybe I am here today because you instilled honesty, diligence, and determination in me. I wish I had the chance to show you that I embraced the teaching you always said, 'whatever you become, be the best.' Throughout my life, I will experience the pride of being your daughter, and I know that despite not always saying it, you were proud of me too. Until we meet again, we will take good care of ourselves and each other; and you wait for us patiently.

This study is supported by Boğaziçi University Research Fund Grant Number (Project No: 14440).

ABSTRACT

AGGREGATION/AGGLOMERATION OF TiO_2 NANOPARTICLES IN THE PRESENCE OF NATURAL ORGANIC MATTER

Production of nanoparticles has increased extremely in the last decade due to their extended industrial usage. Especially metal oxides, such as TiO_2 awakens big interest on both scientific and industrial areas. However, there is very few information that explains the fate of these nanoparticles following their introduction to water bodies under solar irradiation. The main purpose of this study was to elucidate the aggregation and agglomeration behavior of TiO_2 NPs in sunlit water bodies in the presence of natural organic matter (NOM). Humic acid (HA) has been used as NOM analogue due to its polydispersed chemistry and water solubility. Specific physico-chemical methods were applied to elucidate the interactions between the components of colloidal matter. Aggregation/agglomeration behavior of the NPs as well as organic matter were followed by dynamic light scattering (DLS) technique and sedimentation profiles. All samples were subjected to particle size analyses under both dark and solar light simulator conditions for comparative purposes and prepared samples were defined as mono and binary systems. Mono systems were composed of sole TiO_2, metal doped TiO_2 (Fe-doped TiO_2), non-metal doped TiO_2 (N-doped TiO_2), sole HA and pre-treated HA under solar irradiation. The binary system consisted of the combination of TiO_2 and HA derivatives. All colloidal particles were discussed with respect to their morphological and physicochemical properties. Consequently, aggregation and agglomeration behavior of metal oxide NPs in aquatic media were perceived, interactions between NOM with NPs were explained thereby prediction of the potential effects of metal oxide NPs in aqueous systems could be possible.

ÖZET

TiO_2 NANOPARTİKÜLLERİNİN DOĞAL ORGANİK MADDELER VARLIĞINDA AGGREGASYON/AGGLOMERASYONU

Nanopartiküllerin üretimi, endüstriyel kullanımlarının yaygınlaşması nedeniyle son on yılda oldukça arttı. Özellikle TiO_2 gibi metal oksitler, hem bilimsel hem de endüstriyel alanda büyük ilgi uyandırmaktadır. Ancak bu nanopartiküllerin güneş ışınımı altında su kütlelerine girişinden sonraki akıbetini açıklayan çok az bilgi vardır. Bu çalışmanın temel amacı, doğal organik madde (DOM) varlığında güneş ışığına maruz kalan su kütlelerinde TiO_2 NP'lerin agregasyon ve aglomerasyon davranışını aydınlatmaktır. Hümik asit (HA), polidispers kimyası ve suda çözünürlüğü nedeniyle DOM analoğu olarak kullanılmıştır. Bu kolloidal madde bileşenleri arasındaki etkileşimleri aydınlatmak için özel fiziko-kimyasal yöntemler uygulanmıştır. NP'lerin ve organik maddenin agregasyon/aglomerasyon davranışı, dinamik ışık saçılımı (DLS) tekniği ve sedimantasyon profilleri ile takip edilmiştir. Karşılaştırma amacıyla tüm numuneler hem karanlık hem de güneş ışığı simülatörü koşullarında DLS ölçümüne tabi tutulmuş ve hazırlanan numuneler tekli ve ikili sistemler olarak tanımlanmıştır. Tekli sistemler, TiO_2, metal katkılı TiO_2 (Fe katkılı TiO_2), metal olmayan katkılı TiO_2 (N katkılı TiO_2), HA ve ön işleme tabi tutulmuş HA'dan oluşmuştur. İkili sistem TiO_2 ve HA türevlerinin birleşimleriyle hazırlanmıştır. Tüm koloidal parçacıklar morfolojik ve fizikokimyasal özellikleri göz önünde bulundurularak incelenmiştir. Sonuç olarak, metal oksit NP'lerin su ortamındaki agregasyon ve aglomerasyon davranışları anlaşılmış, DOM'ların NP'ler ile etkileşimleri açıklanmış ve böylece metal oksit NP'lerin sulu sistemlerdeki potansiyel etkilerinin tahmin edilmesi mümkün olabilecektir.

TABLE OF CONTENTS

ACKNOWLEDGEMENTS iii

ABSTRACT v

ÖZET vi

TABLE OF CONTENTS vii

LIST OF FIGURES xi

LIST OF TABLES xxiii

LIST OF SYMBOLS / ABBREVIATIONS xxxi

1. INTRODUCTION 1

1.1. Nanoparticles and Nanocolloids: Definition and Properties 2

1.1.1. Nanoparticles 2

1.1.3.1. Incidental nanoparticles 4

1.1.3.2. Engineered nanoparticles (ENPs) 4

1.2. Fate and Behavior of Nanoparticles in Wastewater and Environmental Systems 8

1.3. Definition of Particle Size and Distribution 12

1.4. Dynamic Light Scattering Methodology 17

1.4.1. Fundamental of Dynamic Light Scattering 17

1.4.2. Monomodal Hydrodynamic Particle Size Distribution 22

1.4.3. Non-monomodal (Multi size) Distribution Methods 22

1.4.4. Size Distribution of Hydrodynamic Radius 23

1.5. Dynamic Light Scattering Analysis of Metal Oxide NPs 25

1.6. Natural Organic Matter 30

1.6.1. Humic Substances Definition and Formation 31

1.6.2. Fulvic Acid 32

1.6.3. Humic Acid 33

1.6.3.1. Micelle Structure 37

1.6.3.2. Pseudo micelle structure 38

1.6.3.3. Core-shell model....39
1.6.3.4. Random coil model....40
1.6.3.5. Train-loops-tail model....41
1.6.4. Humins....43
2. MATERIALS AND METHODS....44
2.1. Materials....44
2.1.1. TiO_2 Nanoparticles, Preparation and Characterization....44
2.1.2. Humic Acid....44
2.2. Instrumentation....45
2.2.1. Solar light simulator....45
2.2.2. Dynamic light scattering instrument....45
2.3. Treatment Conditions and Methodology....45
2.3.1. HA Treatment Conditions....45
2.3.1.1. HA Photolysis....45
2.3.1.2. HA - TiO_2 photocatalysis....45
2.3.2. Nanomaterial Treatment Conditions....46
2.3.2.1. TiO_2 “as-is”....46
2.3.2.2. TiO_2 dispersed under dark condition....46
2.3.2.3. TiO_2 exposed to solar irradiation....46
2.3.3. Treatment Methodology....46
3. RESULTS AND DISCUSSION....48
3.1. Humic Acid - Mono System....48
3.1.1. UV-vis Absorption and Fluorescence Spectroscopic Properties of Humic Acid....48
3.2. Hydrodynamic Size Determination of Humic Acid....50
3.2.1. Assessment of Hydrodynamic Size of $HA_{,as\text{-}is}$....54
3.2.2. Assessment of Hydrodynamic Size of $HA_{,pho}$....61
3.2.3. Assessment of Hydrodynamic Size of $HA_{,photocat}$....69
3.3. TiO_2 Nanoparticles - Mono System....78

3.3.1. TiO_2 78
3.3.2. Metal Doped TiO_2 - Fe-TiO_2 85
3.3.3. Anion Doped TiO_2 – N-TiO_2 87
3.4. Hydrodynamic Size of Undoped and Doped TiO_2 Species 90
3.4.1. Hydrodynamic Size Assessment of $TiO_{2,as\text{-}is}$ 90
3.4.2. Hydrodynamic Size Assessment of $TiO_{2,dark}$ 98
3.4.3. Hydrodynamic Size Assessment of $TiO_{2,irr}$ 107
3.4.4. Hydrodynamic Size Assessment of Fe-$TiO_{2,as\text{-}is}$ 117
3.4.5. Hydrodynamic Size Assessment of Fe-$TiO_{2,dark}$ 126
3.4.6. Hydrodynamic Size Assessment of Fe-$TiO_{2,irr}$ 135
3.4.7. Hydrodynamic Size Assessment of N-$TiO_{2as\text{-}is}$ 144
3.4.8. Hydrodynamic Size Assessment of N-$TiO_{2,dark}$ 153
3.4.9. Hydrodynamic Size Assessment of N-$TiO_{2,irr}$ 163
3.5. HA-TiO_2 – Binary System 172
3.5.1. Hydrodynamic Size Assessment of (HA-TiO_2)$_{,as\text{-}is}$ 172
3.5.2. Hydrodynamic Size Assessment of (HA-TiO_2)$_{,dark}$ 182
3.5.3. Hydrodynamic Size Assessment of (HA$_{,pho}$-TiO_2) 190
3.5.4. Hydrodynamic Size Assessment of (HA-TiO_2)$_{,photocat}$ 198
3.5.5. Hydrodynamic Size Assessment of (HA-Fe-TiO_2)$_{,as\text{-}is}$ 212
3.5.6. Hydrodynamic Size Assessment of (HA-Fe-TiO_2)$_{,dark}$ 222
3.5.7. Hydrodynamic Size Assessment of (HA$_{,pho}$-Fe-TiO_2 231
3.5.8. Hydrodynamic Size Assessment of (HA-Fe-TiO_2)$_{,photocat}$ 240
3.5.9. Hydrodynamic Size Assessment of (HA-N-TiO_2)$_{,as\text{-}is}$ 252
3.5.10. Hydrodynamic Size Assessment of (HA-N-TiO_2)$_{,dark}$ 261
3.5.11. Hydrodynamic Size Assessment of (HA$_{,pho}$-N-TiO_2) 270
3.5.12. Hydrodynamic Size Assessment of (HA-N-TiO_2)$_{,photocat}$ 280
4. CONCLUSION AND RECOMMEDATIONS 292
REFERENCES 294

APPENDIX A: SEDIMENTATION PROFILES AND HDS CORRELATION 321

A.1. Relationship Between Sedimentation Profiles and HDS Variations Over Time:.....321

A.1.1. TiO_2 Mono and Binary Systems.....322

A.1.2. Fe-TiO_2 Mono and Binary Systems.....324

A.1.3. N-TiO_2 Mono and Binary Systems.....326

APPENDIX B: DEFINITIONS 328

LIST OF FIGURES

Figure 1.1. Nanoparticles, aggregates, and agglomerates. 3

Figure 1.2. Size comparison of the nanoparticles and colloids. 3

Figure 1.3. Classification of nanoparticles. 5

Figure 1.4. Transportation of NPs between environmental components. 10

Figure 1.5. General presentation of environmental behavior of NPs. 10

Figure 1.6. Potential exposure routes for NPs in the water column. 11

Figure 1.7. Representation of particle size (measured with TEM) and hydrodynamic size (measured with DLS). a) polymer-like structure adsorbed on to surface, b) aggregated or agglomerated, c) non-spherical. 14

Figure 1.8. Schematic representation of DLS instrument. 18

Figure 1.9. Intensity-, volume- and number-weighted hydrodynamic particle size distributions data for the same sample. 25

Figure 1.10. Postulated structure of FA. 33

Figure 1.11. The postulated structure of the HA. 34

Figure 1.12. The hypothesized configuration of the HA. 35

Figure 1.13. Postulated surface functional groups of HA and FA. 35

Figure 1.14. The computed pseudo-micelle structure of HA. White dots: Hydrogen, Grey dots: Carbon, Black dots: Nitrogen. 39

Figure 1.15. The representation of the deformation process occurring within the glassy chain of HA 40

Figure 1.16. Sorption of HA onto solid matrix in 2-D as train, tail and loop structures. 42

Figure 3.1. Theoretical radius of model HA hydrodynamic structure. R_m; mass radius. R_g; radius of gyration. R_H; hydrodynamic radius. R_r; radius of rotation. 50

Figure 3.2. Intensity-, volume-, surface area- and number-based hydrodynamic size of $HA_{,as\text{-}is}$ at initial time. 55

Figure 3.3. The cumulative ratio comparison and hydrodynamic size of $HA_{,as\text{-}is}$ 30 min intervals as intensity-weighted HDS. 57

Figure 3.4. The cumulative ratio comparison and hydrodynamic size of $HA_{,as\text{-}is}$ 30 min intervals as volume-weighted HDS. 58

Figure 3.5. The cumulative ratio comparison and hydrodynamic size of $HA_{,as\text{-}is}$ 30 min intervals as surface area-weighted HDS. 59

Figure 3.6. The cumulative ratio comparison and hydrodynamic size of $HA_{,as\text{-}is}$ 30 min intervals as number-weighted HDS. 60

Figure 3.7. The cumulative ratio comparison and hydrodynamic size of $HA_{,pho}$ 30 min intervals as intensity-weighted HDS. 65

Figure 3.8. The cumulative ratio comparison and hydrodynamic size of $HA_{,pho}$ 30 min intervals as volume-weighted HDS. 66

Figure 3.9. The cumulative ratio comparison and hydrodynamic size of $HA_{,pho}$ 30 min intervals as surface area-weighted HDS. 67

Figure 3.10. The cumulative ratio comparison and hydrodynamic size of $HA_{,pho}$ 30 min intervals as number-weighted HDS. 68

Figure 3.11. Light excitation mechanism of TiO_2 NPs. 70

Figure 3.12. The cumulative ratio comparison and hydrodynamic size of $HA_{,photocat}$ 30 min intervals as intensity-weighted HDS. 74

Figure 3.13. The cumulative ratio comparison and hydrodynamic size of $HA_{,photocat}$ 30 min intervals as volume-weighted HDS. 75

Figure 3.14. The cumulative ratio comparison and hydrodynamic size of $HA_{,photocat}$ 30 min intervals as surface area-weighted HDS. 76

Figure 3.15. The cumulative ratio comparison and hydrodynamic size of $HA_{,photocat}$ 30 min intervals as number-weighted HDS. 77

Figure 3.16. Attainment of surface charge by colloidal TiO_2 in water. a) Anhydrous TiO_2 consists of two oxygen atom per Ti atom. b) TiO_2 suspended in water as a colloid, it binds to water molecules to form hydrated TiO_2. c) Loss of H^+ from the surface adsorbed H_2O yields a negatively charged colloidal particle. d) Gain of H^+ by surface O atoms yields a positively charged particle. The former process (loss of H^+ ion) predominates for metal oxides. 79

Figure 3.17. SEM image and crystalline structure of TiO_2 NPs. 80

Figure 3.18. Schematic representation of particle Stern layer and electrical double layer formation. 81

Figure 3.19. Illustration of water adsorption onto TiO_2 surface. 82

Figure 3.20. The illustration of the primary particle, aggregate and agglomerate structures, and their interactions of $TiO_{2,as\text{-}is}$ in liquid phase dispersion. 83

Figure 3.21. TEM and SEM images of TiO_2 precipitates. 83

Figure 3.22. SEM image and EDAX data of Fe-doped TiO_2. 87

Figure 3.23. SEM image and theoretical substitutional N doped crystalline structure of TiO_2. 89

Figure 3.24. The cumulative ratio comparison and hydrodynamic size of $TiO_{2,as\text{-}is}$ as intensity-weighted HDS in 30 min intervals. 94

Figure 3.25. The cumulative ratio comparison and hydrodynamic size of $TiO_{2,as\text{-}is}$ as volume-weighted HDS in 30 min intervals. 95

Figure 3.26. The cumulative ratio comparison and hydrodynamic size of $TiO_{2,as\text{-}is}$ as surface area-weighted HDS in 30 min intervals. 96

Figure 3.27. The cumulative ratio comparison and hydrodynamic size of $TiO_{2,as\text{-}is}$ as number-weighted HDS in 30 min intervals. 97

Figure 3.28. The cumulative ratio comparison and hydrodynamic size of $TiO_{2,dark}$ as intensity-weighted HDS in 30 min intervals. 103

Figure 3.29. The cumulative ratio comparison and hydrodynamic size of $TiO_{2,dark}$ as volume-weighted HDS in 30 min intervals. 104

Figure 3.30. The cumulative ratio comparison and hydrodynamic size of $TiO_{2,dark}$ as surface area-weighted HDS in 30 min intervals. 105

Figure 3.31. The cumulative ratio comparison and hydrodynamic size of $TiO_{2,dark}$ as number-weighted HDS in 30 min intervals. 106

Figure 3.32. Schematic representation of hydrophilicity increase, superhydrophilic surface formation, on $TiO_{2,irr}$ surface after solar irradiation. 109

Figure 3.33. Illustration of the aggregation/agglomeration of TiO_2. 110

Figure 3.34. The cumulative ratio comparison and hydrodynamic size of $TiO_{2,irr}$ as intensity-weighted HDS in 30 min intervals. 113

Figure 3.35. The cumulative ratio comparison and hydrodynamic size of $TiO_{2,irr}$ as volume-weighted HDS in 30 min intervals. 114

Figure 3.36. The cumulative ratio comparison and hydrodynamic size of $TiO_{2,irr}$ as surface area-weighted HDS in 30 min intervals. 115

Figure 3.37. The cumulative ratio comparison and hydrodynamic size of $TiO_{2,irr}$ as number-weighted HDS in 30 min intervals. 116

Figure 3.38. Theoretical aggregate and agglomerate shapes of Fe-$TiO_{2,as-is}$.....118

Figure 3.39. The cumulative ratio comparison and hydrodynamic size of Fe-$TiO_{2,as-is}$ as intensity-weighted HDS in 30 min intervals. 122

Figure 3.40. The cumulative ratio comparison and hydrodynamic size of Fe-$TiO_{2,as-is}$ as volume-weighted HDS in 30 min intervals. 123

Figure 3.41. The cumulative ratio comparison and hydrodynamic size of Fe-$TiO_{2,as-is}$ as surface area-weighted HDS in 30 min intervals. 124

Figure 3.42. The cumulative ratio comparison and hydrodynamic size of Fe-$TiO_{2,as-is}$ as number-weighted HDS in 30 min intervals. 125

Figure 3.43. The cumulative ratio comparison and hydrodynamic size of Fe-$TiO_{2,dark}$ as intensity-weighted HDS in 30 min intervals. 131

Figure 3.44. The cumulative ratio comparison and hydrodynamic size of Fe-$TiO_{2,dark}$ as volume-weighted HDS in 30 min intervals. 132

Figure 3.45. The cumulative ratio comparison and hydrodynamic size of Fe-$TiO_{2,dark}$ as surface area-weighted HDS in 30 min intervals. 133

Figure 3.46. The cumulative ratio comparison and hydrodynamic size of Fe-$TiO_{2,dark}$ as number-weighted HDS in 30 min intervals. 134

Figure 3.47. The cumulative ratio comparison and hydrodynamic size of Fe-$TiO_{2,irr}$ as intensity-weighted HDS in 30 min intervals. 140

Figure 3.48. The cumulative ratio comparison and hydrodynamic size of Fe-$TiO_{2,irr}$ as volume-weighted HDS in 30 min intervals. 141

Figure 3.49. The cumulative ratio comparison and hydrodynamic size of Fe-$TiO_{2,irr}$ as surface area-weighted HDS in 30 min intervals. 142

Figure 3.50. The cumulative ratio comparison and hydrodynamic size of Fe-$TiO_{2,irr}$ as number-weighted HDS in 30 min intervals. 143

Figure 3.51. The cumulative ratio comparison and hydrodynamic size of N-$TiO_{2,as-is}$ as intensity-weighted HDS in 30 min intervals. 149

Figure 3.52. The cumulative ratio comparison and hydrodynamic size of N-$TiO_{2,as-is}$ as volume-weighted HDS in 30 min intervals. 150

Figure 3.53. The cumulative ratio comparison and hydrodynamic size of N-$TiO_{2,as-is}$ as surface area-weighted HDS in 30 min intervals. 151

Figure 3.54. The cumulative ratio comparison and hydrodynamic size of N-$TiO_{2,as-is}$ as number-weighted HDS in 30 min intervals. 152

Figure 3.55. The cumulative ratio comparison and hydrodynamic size of N-$TiO_{2,dark}$ as intensity-weighted HDS in 30 min intervals. 159

Figure 3.56. The cumulative ratio comparison and hydrodynamic size of N-$TiO_{2,dark}$ as volume-weighted HDS in 30 min intervals. 160

Figure 3.57. The cumulative ratio comparison and hydrodynamic size of N-$TiO_{2,dark}$ as surface area-weighted HDS in 30 min intervals. 161

Figure 3.58. The cumulative ratio comparison and hydrodynamic size of N-$TiO_{2,dark}$ as number-weighted HDS in 30 min intervals. 162

Figure 3.59. The cumulative ratio comparison and hydrodynamic size of N-$TiO_{2,irr}$ as intensity-weighted HDS in 30 min intervals. 168

Figure 3.60. The cumulative ratio comparison and hydrodynamic size of N-$TiO_{2,irr}$ as volume-weighted HDS in 30 min intervals. 169

Figure 3.61. The cumulative ratio comparison and hydrodynamic size of N-$TiO_{2,irr}$ as surface area-weighted HDS in 30 min intervals. 170

Figure 3.62. The cumulative ratio comparison and hydrodynamic size of N-$TiO_{2,irr}$ as number-weighted HDS in 30 min intervals. 171

Figure 3.63. Representation of HA adsorption onto TiO_2 aggregates/agglomerates. a) "train, tail, and loop" model adsorption of HA onto spherical aggregate/agglomerate of TiO_2, b) "train, tail, and loop" model adsorption of HA onto fractal aggregate/agglomerate of TiO_2, c) Mushroom and pancake model adsorption of HA onto spherical aggregate/agglomerate of TiO_2, d) Mushroom and pancake model adsorption of HA onto fractal aggregate/agglomerate of TiO_2. 176

Figure 3.64. The cumulative ratio comparison and hydrodynamic size of (HA-TiO_2)$_{as\text{-}is}$ as intensity-weighted HDS in 30 min intervals. 178

Figure 3.65. The cumulative ratio comparison and hydrodynamic size of (HA-TiO_2)$_{as\text{-}is}$ as volume-weighted HDS in 30 min intervals. 179

Figure 3.66. The cumulative ratio comparison and hydrodynamic size of (HA-TiO_2)$_{as\text{-}is}$ as surface area-weighted HDS in 30 min intervals. 180

Figure 3.67. The cumulative ratio comparison and hydrodynamic size of (HA-TiO_2)$_{as\text{-}is}$ as number-weighted HDS in 30 min intervals. 181

Figure 3.68. The cumulative ratio comparison and hydrodynamic size of (HA-TiO_2)$_{dark}$ as intensity-weighted HDS in 30 min intervals. 186

Figure 3.69. The cumulative ratio comparison and hydrodynamic size of $(HA\text{-}TiO_2)_{,dark}$ as volume-weighted HDS in 30 min intervals. 187

Figure 3.70. The cumulative ratio comparison and hydrodynamic size of $(HA\text{-}TiO_2)_{,dark}$ as surface area-weighted HDS in 30 min intervals. 188

Figure 3.71. The cumulative ratio comparison and hydrodynamic size of $(HA\text{-}TiO_2)_{,dark}$ as number-weighted HDS in 30 min intervals. 189

Figure 3.72. The cumulative ratio comparison and hydrodynamic size of $(HA_{,pho}\text{-}TiO_2)$ as intensity-weighted HDS in 30 min intervals. 194

Figure 3.73. The cumulative ratio comparison and hydrodynamic size of $(HA_{,pho}\text{-}TiO_2)$ as volume-weighted HDS in 30 min intervals. 195

Figure 3.74. The cumulative ratio comparison and hydrodynamic size of $(HA_{,pho}\text{-}TiO_2)$ as surface area-weighted HDS in 30 min intervals. 196

Figure 3.75. The cumulative ratio comparison and hydrodynamic size of $(HA_{,pho}\text{-}TiO_2)$ as number-weighted HDS in 30 min intervals. 197

Figure 3.76. a) Theoretical representation of surface adsorption of photocatalytically degraded HA onto TiO_2 aggregate, b) Theoretical representation of homo-agglomerates and HA-TiO_2 hetero-aggregates, c) Theoretical representation of HA-TiO_2 hetero-agglomerate. Blue circle: HDS of corresponding system. 200

Figure 3.77. The cumulative ratio comparison and hydrodynamic size of $(HA\text{-}TiO_2)_{,photocat}$ as intensity-weighted HDS in 30 min intervals. 208

Figure 3.78. The cumulative ratio comparison and hydrodynamic size of $(HA\text{-}TiO_2)_{,photocat}$ as volume-weighted HDS in 30 min intervals. 209

Figure 3.79. The cumulative ratio comparison and hydrodynamic size of $(HA\text{-}TiO_2)_{,photocat}$ as surface area-weighted HDS in 30 min intervals. 210

Figure 3.80. The cumulative ratio comparison and hydrodynamic size of $(HA\text{-}TiO_2)_{,photocat}$ as number-weighted HDS in 30 min intervals. 211

Figure 3.81. The cumulative ratio comparison and hydrodynamic size of $(HA\text{-}Fe\text{-}TiO_2)_{,as\text{-}is}$ as intensity-weighted HDS in 30 min intervals. 218

Figure 3.82. The cumulative ratio comparison and hydrodynamic size of $(HA\text{-}Fe\text{-}TiO_2)_{,as\text{-}is}$ as volume-weighted HDS in 30 min intervals. 219

Figure 3.83. The cumulative ratio comparison and hydrodynamic size of $(HA\text{-}Fe\text{-}TiO_2)_{,as\text{-}is}$ as surface area-weighted HDS in 30 min intervals. 220

Figure 3.84. The cumulative ratio comparison and hydrodynamic size of $(HA\text{-}Fe\text{-}TiO_2)_{,as\text{-}is}$ as number-weighted HDS in 30 min intervals. 221

Figure 3.85. The cumulative ratio comparison and hydrodynamic size of $(HA\text{-}Fe\text{-}TiO_2)_{,dark}$ as intensity-weighted HDS in 30 min intervals. 227

Figure 3.86. The cumulative ratio comparison and hydrodynamic size of $(HA\text{-}Fe\text{-}TiO_2)_{,dark}$ as volume-weighted HDS in 30 min intervals. 228

Figure 3.87. The cumulative ratio comparison and hydrodynamic size of $(HA\text{-}Fe\text{-}TiO_2)_{,dark}$ as surface area-weighted HDS in 30 min intervals. 229

Figure 3.88. The cumulative ratio comparison and hydrodynamic size of $(HA\text{-}Fe\text{-}TiO_2)_{,dark}$ as number-weighted HDS in 30 min intervals. 230

Figure 3.89. The cumulative ratio comparison and hydrodynamic size of $(HA_{,pho}\text{-}Fe\text{-}TiO_2)$ as intensity-weighted HDS in 30 min intervals. 236

Figure 3.90. The cumulative ratio comparison and hydrodynamic size of $(HA_{,pho}\text{-}Fe\text{-}TiO_2)$ as volume-weighted HDS in 30 min intervals. 237

Figure 3.91. The cumulative ratio comparison and hydrodynamic size of $(HA_{,pho}\text{-}Fe\text{-}TiO_2)$ as surface area-weighted HDS in 30 min intervals. 238

Figure 3.92. The cumulative ratio comparison and hydrodynamic size of ($HA_{,pho}$-Fe-TiO_2) as number-weighted HDS in 30 min intervals. 239

Figure 3.93. The cumulative ratio comparison and hydrodynamic size of (HA-Fe-TiO_2)$_{,photocat}$ as intensity-weighted HDS in 30 min intervals. 248

Figure 3.94. The cumulative ratio comparison and hydrodynamic size of (HA-Fe-TiO_2)$_{,photocat}$ as volume-weighted HDS in 30 min intervals. 249

Figure 3.95. The cumulative ratio comparison and hydrodynamic size of (HA-Fe-TiO_2)$_{,photocat}$ as surface area-weighted HDS in 30 min intervals. 250

Figure 3.96. The cumulative ratio comparison and hydrodynamic size of (HA-Fe-TiO_2)$_{,photocat}$ as volume-weighted HDS in 30 min intervals. 251

Figure 3.97. The cumulative ratio comparison and hydrodynamic size of (HA-N-TiO_2)$_{,as\text{-}is}$ as intensity-weighted HDS in 30 min intervals. 257

Figure 3.98. The cumulative ratio comparison and hydrodynamic size of (HA-N-TiO_2)$_{,as\text{-}is}$ as volume-weighted HDS in 30 min intervals. 258

Figure 3.99. The cumulative ratio comparison and hydrodynamic size of (HA-N-TiO_2)$_{,as\text{-}is}$ as surface area-weighted HDS in 30 min intervals. 259

Figure 3.100. The cumulative ratio comparison and hydrodynamic size of (HA-N-TiO_2)$_{,as\text{-}is}$ as number-weighted HDS in 30 min intervals. 260

Figure 3.101. The cumulative ratio comparison and hydrodynamic size of (HA-N-TiO_2)$_{,dark}$ as intensity-weighted HDS in 30 min intervals. 266

Figure 3.102. The cumulative ratio comparison and hydrodynamic size of (HA-N-TiO_2)$_{,dark}$ as volume-weighted HDS in 30 min intervals. 267

Figure 3.103. The cumulative ratio comparison and hydrodynamic size of (HA-N-TiO_2)$_{,dark}$ as surface area-weighted HDS in 30 min intervals. 268

Figure 3.104. The cumulative ratio comparison and hydrodynamic size of $(HA\text{-}N\text{-}TiO_2)_{,dark}$ as number-weighted HDS in 30 min intervals. 269

Figure 3.105. The cumulative ratio comparison and hydrodynamic size of $(HA_{,pho}\text{-}N\text{-}TiO_2)$ as intensity-weighted HDS in 30 min intervals. 276

Figure 3.106. The cumulative ratio comparison and hydrodynamic size of $(HA_{,pho}\text{-}N\text{-}TiO_2)$ as volume-weighted HDS in 30 min intervals. 277

Figure 3.107. The cumulative ratio comparison and hydrodynamic size of $(HA_{,pho}\text{-}N\text{-}TiO_2)$ as surface area-weighted HDS in 30 min intervals. 278

Figure 3.108. The cumulative ratio comparison and hydrodynamic size of $(HA_{,pho}\text{-}N\text{-}TiO_2)$ as number-weighted HDS in 30 min intervals. 279

Figure 3.109. The cumulative ratio comparison and hydrodynamic size of $(HA\text{-}N\text{-}TiO_2)_{,photocat}$ as intensity-weighted HDS in 30 min intervals. 288

Figure 3.110. The cumulative ratio comparison and hydrodynamic size of $(HA\text{-}N\text{-}TiO_2)_{,photocat}$ as volume-weighted HDS in 30 min intervals. 289

Figure 3.111. The cumulative ratio comparison and hydrodynamic size of $(HA\text{-}N\text{-}TiO_2)_{,photocat}$ as surface area-weighted HDS in 30 min intervals. 290

Figure 3.112. The cumulative ratio comparison and hydrodynamic size of $(HA\text{-}N\text{-}TiO_2)_{,photocat}$ as number-weighted HDS in 30 min intervals. 291

Figure A.1. Time dependent HDS variation in relation to absorbance changes during sedimentation of TiO_2 under as-is, dark and irradiation conditions. 322

Figure A.2. Time dependent HDS variation in relation to absorbance changes during sedimentation of $HA\text{-}TiO_2$ under as-is, dark and irradiation conditions. 323

Figure A.3. Time dependent HDS variation in relation to absorbance changes during sedimentation of $Fe\text{-}TiO_2$ under as-is, dark and irradiaiton conditions. 324

Figure A.4. Time dependent HDS variation in relation to absorbance changes during sedimentation of HA-Fe-TiO_2 under as-is, dark and irradiaiton conditions. 325

Figure A.5. Time dependent HDS variation in relation to absorbance changes during sedimentation of N-TiO_2 under as-is, dark and irradiaiton conditions. 326

Figure A.6. Time dependent HDS variation in relation to absorbance changes during sedimentation of HA-N-TiO_2 under as-is, dark and irradiaiton conditions. 327

LIST OF TABLES

Table 1.1. Examples of manufactured nanoparticles and their application areas. 7

Table 1.2. Comparison of particle size determination techniques. 15

Table 1.3. Physicochemical properties of TiO_2 NPs sited in literature review, between the years 2009-2023, of DLS measurements. 27

Table 1.4. Literature review of DLS measurements of TiO_2 NPs between the years 2009-2023.....28

Table 1.5. Illustrative depictions of polyelectrolytes at the surface are presented, representing different conditions pertaining to polymer charge density and ionic strength. 43

Table 3.1. Spectroscopic parameters and DOC of HA under the specified conditions. 49

Table 3.2. Intensity-, volume-, surface area- and number-based hydrodynamic size of $HA_{,as\text{-}is}$. 56

Table 3.3. Intensity-, volume-, surface area- and number-weighted HDS of $HA_{,pho}$.....64

Table 3.4. Comparison of intensity-weighted HDS values of $HA_{,as\text{-}is}$ and $HA_{,pho}$. 64

Table 3.5. Intensity-, volume-, surface area- and number-weighted HDS of $HA_{,photocat}$.....72

Table 3.6.Comparison of intensity-weighted HDS values of $HA_{,as\text{-}is}$, $HA_{,pho}$ and $HA_{,photocat}$. 72

Table 3.7. Characterization results of TiO_2. 80

Table 3.8. Table. Physico-chemical properties of metal and anion doped TiO_2 specimens. 89

Table 3.9. Intensity-, volume-, surface area- and number-weighted HDS and cumulative ratios of $TiO_{2,as\text{-}is}$.....93

Table 3.10. Intensity-weighted HDS profile of $TiO_{2,as\text{-}is}$. Time dependent HDS cluster maximas, HDS range and min-max diameter difference with respect to multi-size distribution....93

Table 3.11. Intensity-, volume-, surface area- and number-weighted HDS and cumulative ratios of $TiO_{2,dark}$.....100

Table 3.12. Intensity-weighted HDS profile of $TiO_{2,dark}$. Time dependent HDS cluster maximas, HDS range and min-max diameter difference with respect to multi-size distribution..101

Table 3.13. Comparison of intensity-weighted HDS values of $TiO_{2,as\text{-}is}$ and $TiO_{2,dark}$. 102

Table 3.14. Intensity-, volume-, surface area- and number-weighted HDS and cumulative ratios of $TiO_{2,irr}$. 111

Table 3.15. Intensity-weighted HDS profile of $TiO_{2,irr}$. Time dependent HDS cluster maximas, HDS range and min-max diameter difference with respect to multi-size distribution.....111

Table 3.16. Comparison of intensity-weighted HDS values of $TiO_{2,as\text{-}is}$, $TiO_{2,dark}$ and $TiO_{2,irr}$. 112

Table 3.17. Intensity-, volume-, surface area- and number-weighted HDS and cumulative ratios of Fe-$TiO_{2,as\text{-}is}$. 120

Table 3.18. Intensity-weighted HDS profile of Fe-$TiO_{2,as\text{-}is}$. Time dependent HDS cluster maximas, HDS range and min-max diameter difference with respect to multi-size distribution..121

Table 3.19. Comparison of intensity-weighted HDS values of Fe-$TiO_{2,as\text{-}is}$ and $TiO_{2,as\text{-}is}$.....121

Table 3.20. Intensity-, volume-, surface area- and number-weighted HDS and cumulative ratios of Fe-$TiO_{2,dark}$.....128

Table 3.21. Intensity-weighted HDS profile of Fe-$TiO_{2,dark}$. Time dependent HDS cluster maximas, HDS range and min-max diameter difference with respect to multi-size distribution..128

Table 3.22. Comparison of intensity-weighted HDS values of Fe-$TiO_{2,as\text{-}is}$ and Fe-$TiO_{2,dark}$.....129

Table 3.23. Comparison of intensity-weighted HDS values of $TiO_{2,dark}$ and Fe-$TiO_{2,dark}$ 130

Table 3.24. Intensity-, volume-, surface area- and number-weighted HDS and cumulative ratios of Fe-$TiO_{2,irr}$.....137

Table 3.25. Intensity-weighted HDS profile of Fe-$TiO_{2,irr}$. Time dependent HDS cluster maximas, HDS range and min-max diameter difference with respect to multi-size distribution..137

Table 3.26. Comparison of intensity-weighted HDS values of Fe-$TiO_{2,as-is}$, Fe-$TiO_{2,dark}$ and Fe-$TiO_{2,irr}$. 138

Table 3.27. Comparison of intensity-weighted HDS values of $TiO_{2,irr}$ and Fe-$TiO_{2,irr}$.....139

Table 3.28. Intensity-weighted HDS profile of N-$TiO_{2,as-is}$. Time dependent HDS cluster maximas, HDS range and min-max diameter difference with respect to multi-size distribution..146

Table 3.29. Intensity-, volume-, surface area- and number-weighted HDS and cumulative ratios of N-$TiO_{2,as-is}$. 147

Table 3.30. Comparison of intensity-weighted HDS values of N-$TiO_{2,as-is}$ and Fe-$TiO_{2,as-is}$ and $TiO_{2,as-is}$.....148

Table 3.31. Intensity-, volume-, surface area- and number-weighted HDS and cumulative ratios of N-$TiO_{2,dark}$.....156

Table 3.32. Intensity-weighted HDS profile of N-$TiO_{2,dark}$. Time dependent HDS cluster maximas, HDS range and min-max diameter difference with respect to multi-size distribution..156

Table 3.33. Comparison of intensity-weighted HDS values of N-$TiO_{2,as-is}$ and N-$TiO_{2,dark}$.....157

Table 3.34. Comparison of intensity-weighted HDS values of $TiO_{2,dark}$, Fe-$TiO_{2,dark}$ and N-$TiO_{2,dark}$. 158

Table 3.35. Intensity-, volume-, surface area- and number-weighted HDS and cumulative ratios of N-$TiO_{2,irr}$.....165

Table 3.36. Intensity-weighted HDS profile of N-$TiO_{2,irr}$. Time dependent HDS cluster maximas, HDS range and min-max diameter difference with respect to multi-size distribution..165

Table 3.37. Comparison of intensity-weighted HDS values of N-$TiO_{2,as\text{-}is}$, N-$TiO_{2,dark}$, and N-$TiO_{2,irr}$. 166

Table 3.38. Comparison of intensity-weighted HDS values of $TiO_{2,irr}$, Fe-$TiO_{2,irr}$ and N-$TiO_{2,irr.}$..167

Table 3.39. Intensity-, volume-, surface area- and number-weighted HDS and cumulative ratios of $(HA\text{-}TiO_2)_{as\text{-}is}$.....173

Table 3.40. Comparison of intensity-weighted HDS values of $HA_{,as\text{-}is}$, $TiO_{2,as\text{-}is}$ and $(HA\text{-}TiO_2)_{,as\text{-}is}$. 174

Table 3.41. Intensity-, volume-, surface area- and number-weighted HDS and cumulative ratios of $(HA\text{-}TiO_2)_{,dark}$. 184

Table 3.42. Intensity-weighted HDS profile of $(HA\text{-}TiO_2)_{,dark}$. Time dependent HDS cluster maximas, HDS range and min-max diameter difference with respect to multi-size distribution.....184

Table 3.43. Comparison of intensity-weighted HDS values of $(HA\text{-}TiO_2)_{,as\text{-}is}$ and $(HA\text{-}TiO_2)_{,dark}$.185

Table 3.44. Intensity-, volume-, surface area- and number-weighted HDS and cumulative ratios of $(HA_{,pho}\text{-}TiO_2)$. 192

Table 3.45. Intensity-weighted HDS profile of $(HA_{,pho}\text{-}TiO_2)$. Time dependent HDS cluster maximas, HDS range and min-max diameter difference with respect to multi-size distribution.....193

Table 3.46. Comparison of intensity-weighted HDS values of $HA_{,pho}$, $TiO_{2,as\text{-}is}$, and $(HA_{,pho}\text{-}TiO_2)$. 193

Table 3.47. Intensity-, volume-, surface area- and number-weighted HDS and cumulative ratios of $(HA\text{-}TiO_2)_{,photocat}$.....204

Table 3.48. Intensity-weighted HDS profile of $(HA\text{-}TiO_2)_{,photocat}$. Time dependent HDS cluster maximas, HDS range and min-max diameter difference with respect to multi-size distribution.....205

Table 3.49. Comparison of intensity-weighted HDS values of $HA_{,photocat}$, $TiO_{2,irr}$, and $(HA\text{-}TiO_2)_{,photocat}$. 205

Table 3.50. Comparison of intensity-weighted HDS values of $(HA\text{-}TiO_2)_{,as\text{-}is}$, $(HA\text{-}TiO_2)_{,dark}$, $(HA\text{-}TiO_2)_{,photocat}$ and $(HA_{,pho}\text{-}TiO_2)$. 206

Table 3.51. Intensity-weighted HDS profile of $(HA\text{-}Fe\text{-}TiO_2)_{,as\text{-}is}$. Time dependent HDS cluster maximas, HDS range and min-max diameter difference with respect to multi-size distribution.....214

Table 3.52. Intensity-, volume-, surface area- and number-weighted HDS and cumulative ratios of $(HA\text{-}Fe\text{-}TiO_2)_{,as\text{-}is}$.....215

Table 3.53. Comparison of intensity-weighted HDS values of $HA_{,as\text{-}is}$, $Fe\text{-}TiO_{2,as\text{-}is}$ and $(HA\text{-}Fe\text{-}TiO_2)_{,as\text{-}is}$. 216

Table 3.54. Comparison of intensity-weighted HDS values of $(HA\text{-}TiO_2)_{,as\text{-}is}$ and $(HA\text{-}Fe\text{-}TiO_2)_{,as\text{-}is}$. 217

Table 3.55. Intensity-, volume-, surface area- and number-weighted HDS and cumulative ratios of $(HA\text{-}Fe\text{-}TiO_2)_{,dark}$.....224

Table 3.56. Intensity-weighted HDS profile of $(HA\text{-}Fe\text{-}TiO_2)_{,dark}$. Time dependent HDS cluster maximas, HDS range and min-max diameter difference with respect to multi-size distribution.....224

Table 3.57. Comparison of intensity-weighted HDS values of $(HA\text{-}Fe\text{-}TiO_2)_{,as\text{-}is}$ and $(HA\text{-}Fe\text{-}TiO_2)_{,dark}$.....225

Table 3.58. Comparison of intensity-weighted HDS values of $(HA\text{-}TiO_2)_{,dark}$ and $(HA\text{-}Fe\text{-}TiO_2)_{,dark}$. 226

Table 3.59. Intensity-, volume-, surface area- and number-weighted HDS and cumulative ratios of ($HA_{,pho}$-Fe-TiO_2). 233

Table 3.60. Intensity-weighted HDS profile of ($HA_{,pho}$-Fe-TiO_2). Time dependent HDS cluster maximas, HDS range and min-max diameter difference with respect to multi-size distribution.....234

Table 3.61. Comparison of intensity-weighted HDS values of $HA_{,pho}$, Fe-$TiO_{2,as-is}$, and ($HA_{,pho}$-Fe-TiO_2). 234

Table 3.62. Comparison of intensity-weighted HDS values of ($HA_{,pho}$-TiO_2) and ($HA_{,pho}$-Fe-TiO_2). 235

Table 3.63. Intensity-, volume-, surface area- and number-weighted HDS and cumulative ratios of (HA-Fe-TiO_2)$_{,photocat}$. 243

Table 3.64. Intensity-weighted HDS profile of (HA-Fe-TiO_2)$_{,photocat}$. Time dependent HDS cluster maximas, HDS range and min-max diameter difference with respect to multi-size distribution.....243

Table 3.65. Comparison of intensity-weighted HDS values of $HA_{,photocat}$, $TiO_{2,irr}$, and (HA-TiO_2)$_{,photocat}$. 244

Table 3.66. Comparison of intensity-weighted HDS values of (HA-Fe-TiO_2)$_{,as-is}$, (HA-Fe-TiO_2)$_{,dark}$, ($HA_{,pho}$-Fe-TiO_2) and (HA-Fe-TiO_2)$_{,photocat}$. 245

Table 3.67. Comparison of intensity-weighted HDS values of (HA-TiO_2)$_{,photocat}$ and (HA-Fe-TiO_2)$_{,photocat}$. 247

Table 3.68. Intensity-, volume-, surface area- and number-weighted HDS and cumulative ratios of (HA-N-TiO_2)$_{,as-is}$.....254

Table 3.69. Intensity-weighted HDS profile of (HA-N-TiO_2)$_{,as-is}$. Time dependent HDS cluster maximas, HDS range and min-max diameter difference with respect to multi-size distribution.....255

Table 3.70. Comparison of intensity-weighted HDS values of $HA_{,as\text{-}is}$, $N\text{-}TiO_{2,as\text{-}is}$ and $(HA\text{-}N\text{-}TiO_2)_{,as\text{-}is}$. 255

Table 3.71. Comparison of intensity-weighted HDS values of $(HA\text{-}TiO_2)_{,as\text{-}is}$, $(HA\text{-}Fe\text{-}TiO_2)_{,as\text{-}is}$ and $(HA\text{-}N\text{-}TiO_2)_{,as\text{-}is}$.....256

Table 3.72. Intensity-, volume-, surface area- and number-weighted HDS and cumulative ratios of $(HA\text{-}N\text{-}TiO_2)_{,dark}$.....263

Table 3.73. Intensity-weighted HDS profile of $(HA\text{-}N\text{-}TiO_2)_{,dark}$. Time dependent HDS cluster maximas, HDS range and min-max diameter difference with respect to multi-size distribution.....263

Table 3.74. Comparison of intensity-weighted HDS values of $(HA\text{-}N\text{-}TiO_2)_{,as\text{-}is}$ and $(HA\text{-}N\text{-}TiO_2)_{,dark}$.....264

Table 3.75. Comparison of intensity-weighted HDS values of $(HA\text{-}TiO_2)_{,dark,}$ $(HA\text{-}Fe\text{-}TiO_2)_{,dark}$ and $(HA\text{-}N\text{-}TiO_2)_{,dark}$.....265

Table 3.76. Intensity-weighted HDS profile of $(HA_{,pho}\text{-}N\text{-}TiO_2)$. Time dependent HDS cluster maximas, HDS range and min-max diameter difference with respect to multi-size distribution.....272

Table 3.77. Intensity-, volume-, surface area- and number-weighted HDS and cumulative ratios of $(HA_{,pho}\text{-}N\text{-}TiO_2)$.....273

Table 3.78. Comparison of intensity-weighted HDS values of $HA_{,pho}$, $Fe\text{-}TiO_{2,as\text{-}is}$, and $(HA_{,pho}\text{-}Fe\text{-}TiO_2)$. 274

Table 3.79. Comparison of intensity-weighted HDS values of $(HA_{,pho}\text{-}TiO_2)$, $(HA_{,pho}\text{-}Fe\text{-}TiO_2)$ and $(HA_{,pho}\text{-}N\text{-}TiO_2)$.....275

Table 3.80. Intensity-, volume-, surface area- and number-weighted HDS and cumulative ratios of $(HA\text{-}N\text{-}TiO_2)_{,photocat}$. 283

Table 3.81. Intensity-weighted HDS profile of $(HA\text{-}N\text{-}TiO_2)_{,photocat}$. Time dependent HDS cluster maximas, HDS range and min-max diameter difference with respect to multi-size distribution.....283

Table 3.82. Comparison of intensity-weighted HDS values of $HA_{,photocat}$, $N\text{-}TiO_{2,irr}$ and $(HA\text{-}N\text{-}TiO_2)_{,photocat}$. 284

Table 3.83. Comparison of intensity-weighted HDS values of $(HA\text{-}N\text{-}TiO_2)_{,as\text{-}is}$, $(HA\text{-}N\text{-}TiO_2)_{,dark}$, $(HA_{,pho}\text{-}N\text{-}TiO_2)$ and $(HA\text{-}TiO_2)_{,photocat}$. 285

Table 3.84. Comparison of intensity-weighted HDS values of $(HA\text{-}TiO_2)_{,photocat}$, $(HA\text{-}Fe\text{-}TiO_2)_{,photocat}$, and $(HA\text{-}N\text{-}TiO_2)_{,photocat}$.....287

LIST OF SYMBOLS / ABBREVIATIONS

Symbol	Explanation	Unit
β	Coherence factor	
θ	Detector angle	degree (˚)
π	Pi number	
η	Viscosity of suspension medium	mPa s
τ	Delayed time	s
λ	Wavelength	nm
ρ	Particle density	gcm^{-3}
Γ	Decay constant	
ζ	Zeta potential	eV
D_τ	Translational diffusion coefficient	m^2s^{-1}
$\langle D\tau \rangle$	Average diffusion coefficient	
E	Scattered electric field	
$G_1(\tau)$	Electric field correlation function	
$g_1(\tau)$	Normalized electric field correlation function	
$G_2(\tau)$	Intensity correlation function	
$g_2(\tau)$	Normalized intensity correlation function	
G(Γ)	Distribution of decay rates	
%I	Intensity-weighted hydrodynamic size	
I_o	Light intensity	$\mu Emin^{-1}$
K	Scherrer constant	
k_B	Boltzmann constant	$kgm^2s^{-2}K^{-1}$
M_n	Weight-average molar mass	
M_w	Number-average molar mass	
%N	Number-weighted hydrodynamic size	
P(q,R)	Interparticle interface	
q	Bragg wave vector	
R_h	Hydrodynamic diameter	
r	Radius	
%S	Surface-area weighted hydrodynamic size	
t	Time	

T	Temperature	
%V	Volume-weighted hydrodynamic size	

Abbreviations	**Definition**	**Unit**
AOPs	Advanced oxidation process	
BET	Brunauer-Emmett-Teller	
CB	Conduction band	
$Color_{436}$	Absorbance at 436 nm	
DI	Deionized water	
DLS	Dynamic light scattering	
DLVO	Derjaguin, Landau, Verwey and Overbeek	
DOM	Dissolved organic matter	
DOC	Dissolved organic carbon	mgL^{-1}
E2/E3	Ratio of the absorbances at 254 nm and 436 nm	
ENP	Engineered nanoparticle	
FA	Fulvic acid	
FI	Fluorescence intensity	
FI_{emis}	Fluorescence emission	
HA	Humic acid	
HS	Humic substances	
HDS	Hydrodynamic size	
HDD	Hydrodynamic diameter	
IHSS	International Humic Substance Society	
min	Minute	
MSD	Multi size distribution	
µm	Micrometer	
µs	Microsecond	
nm	Nanometer	
ns	nanosecond	
NOM	Natural organic matter	
NP	Nanoparticle	
NPOC	Non-purgeable organic carbon	$mgOrgCL^{-1}$
NNLS	The non-negative least squares	
PDI	Polydispersity index	

PSD	Particle size distribution	
ROS	Reactive oxygen species	
SEM	Scanning electron microscopy	
SFI_{sync}	Specific fluorescence intensity in synchronous scan mode	
SFI_{emis}	Specific fluorescence intensity in emission scan mode	
$SCoA_{436}$	Specific color absorbance at 436 nm	$Lm^{-1}mg^{-1}$
$SUVA_{254}$	Specific UV Absorbance at 254 nm	$Lm^{-1}mg^{-1}$
$SUVA_{280}$	Specific UV Absorbance at 280 nm	$Lm^{-1}mg^{-1}$
$SUVA_{365}$	Specific UV Absorbance at 365 nm	$Lm^{-1}mg^{-1}$
TEM	Transmission electron microscopy	
TOC	Total organic carbon	
UV	Ultraviolet	
UV_{254}	Absorbance at 254 nm	
UV_{280}	Absorbance at 280 nm	
UV_{365}	Absorbance at 365 nm	
UV-vis	Ultraviolet-visible	
VB	Valence band	

1. INTRODUCTION

In natural waters, prevailing interactions between colloidal particles impart a vital role in colloidal stability. Generally, colloids consisting of nano and micron sized particles are derived from various industrial activities *i.e.*, production of paints, varnishes, inks, cosmetics, etc., food products and bio-medical applications. On the other hand, large-scale colloidal structures (one-, two-, or three-dimensional) are also applied in many areas of modern developments, *e.g.*, infrared-emitting nano crystals, surface coatings, single-nanowire light emitting diodes, single electron transistors, *etc.* Interactions between nano- and micro-sized inorganic colloid particles of various types and organics as surfactants, proteins and/or polymers hold prime importance in field of nanotechnology. The key question arises in terms of stability thereby behavior and fate of nano-colloids deserves to be investigated.

Recently, an accumulation tendency of nano-sized particles (NP) drew the attention of various research groups. Most of the studies reported the presence and possible fate of nanoparticles via various pathways *e.g.*, dispersion and transformation in both aquatic and terrestrial domains. The major attention was devoted to the severe concerns on nano-eco-toxicological assessment of the NPs as the main end-point of fate.

In aquatic environments, nanoparticles as part of colloidal systems would certainly coincide with natural organic matter (NOM). Therefore, the fate of NPs could not be visualized in the absence of NOM thereby binary systems should be considered rather than mono systems. It should be emphasized that all interactions of NPs pertaining in aquatic medium should also address to the contribution of NOM. Since NOM mainly humic matter is recognized as ill-defined, heterogeneous, polydisperse, complex organic matrix with diverse molecular size fractions being < 0.45 mm in size, micro to nano environments govern all the active processes.

From a broader perspective, the main aim of the study is understanding the size dependent stability of nanoparticles in aquatic systems. For this purpose, a specific, widely produced and discharged NP and an omni-present organic matter is to be considered. Following a keen literature survey, TiO_2 is demonstrated as a suitable NP originating from various industrial applications also possessing significant photocatalytic properties. The major drawback of limited UVA light harvesting capacity of TiO_2 could be extended by doping with metals *e.g.* Fe- and anions *e.g.* N. Organic matter

could well be modelled by humic acids. The final consortium would also mimic naturally occurring photocatalysis along with the eco-toxicological concerns. All these interactions could only be understood in actual conditions rather than consideration of well-defined physico-chemical properties of single entities. Therefore, uncertainties in understanding the effective hydrodynamic size (HDS) constitutes prime importance. Since colloidal stability is highly related with aggregation and agglomeration phenomena, behavior of mono- and binary systems under the solar irradiation deserves to be investigated.

Based on this motivation and to fulfill the literature gap in this respect, the following research agenda is developed. Photocatalyst NP specimens are chosen as TiO_2, Fe-TiO_2 and N-TiO_2 and NOM is modeled by humic acids. Specific treatments resembling both natural environment as well as photocatalytic conditions are selected as dark conditions and solar light exposure. As an indicator parameter, the aggregation/agglomeration behavior of mono and binary systems is assessed through HDS variations of all samples that are determined by dynamic light scattering (DLS) technique.

1.1. Nanoparticles and Nanocolloids: Definition and Properties

1.1.1. Nanoparticles

Nanoparticles are basically defined as particulate matter with at least one dimension that is less than 100 nm (SCENIHR, 2005). However, in 2011 European Union specified this definition as "*a natural, incidental or manufactured material containing particles, in an unbound state or as an aggregate or as an agglomerate and where, for 50 % or more of the particles in the number size distribution, one or more external dimensions is in the size range 1 nm-100 nm*" (European Commission, 2011).

Based on the a fore mentioned definition, *particle* is indicated as a minute piece of matter with defined physical boundaries, *agglomerate* as a collection of weakly bound particles or aggregates where the resulting external surface area is similar to the sum of the surface areas of the individual components and *aggregate* as a particle comprising of strongly bound or fused particles (European Commission, 2011). Figure 1.1 shows schematic representation of nanoparticles, aggregates, and agglomerates (Peddieson and Chamka, 2016).

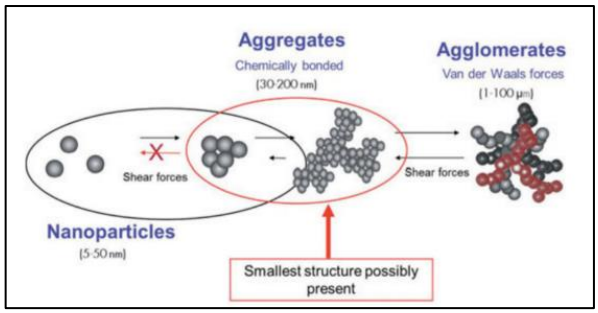


Figure 1.1. Nanoparticles, aggregates, and agglomerates.

However, IUPAC defines nanoparticles as sub-category of the colloidal systems. IUPAC definition of colloid is "*a state of subdivision, implying that the molecules or polymolecular particles dispersed in a medium have at least in one direction a dimension roughly between 1 nm and 1 µm, or that in a system discontinuity are found at distances of that order"* (McNaught and Wilkinson, 1997, pp. 1).

From a general perspective, nanoparticle is defined as "particulate matter with at least one dimension that is less than 100 nm" and this definition is used in literature more frequently. Therefore, components that are present natural waters can be classified according to their size as presented in Figure 1.2 (Christian et al, 2008). Moreover, nanoparticles could be classified as natural nanoparticles and synthetic nanoparticles.

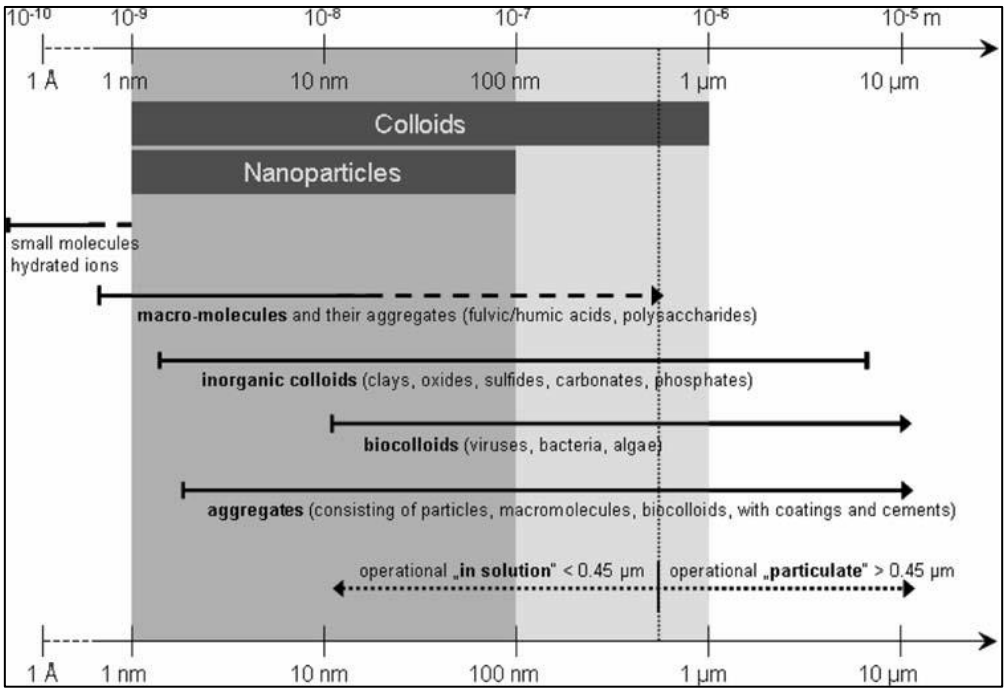


Figure 1.2. Size comparison of the nanoparticles and colloids (Christian et al., 2008).

1.1.2. Natural Nanoparticles

In environmental systems some colloidal particles form natural nanoparticles with a vast number of diverse mechanisms, processes, and conditions; chemical, photochemical, mechanical, thermal, and biological processes separately or in combination (Sharma et al., 2015). Natural nanoparticles mostly comprise of the low molecular weight breakdown products of biological decay (humic matter), various fibrillar and mesh-like organic compounds, and minerals generated during the chemical weathering rocks, principally oxide and oxyhydroxide of iron (Fe), manganese (Mn), aluminum (Al) and aluminosilicates (Hartland et al., 2013). Most common nanoparticles could be visualized in the form of natural organic matter (NOM). From a basic understanding point of view, NOM is composed of particulate organic matter (POM) and dissolved organic matter (DOM). The humic substances (HSs) are functionally defined as chemically extracted fraction of the total natural organic carbon pool and is mostly (not completely) representative of natural organic matter. HSs appear not only as dispersed material at the lower end of the nano size range (<5 nm) but also can aggregate to form larger structures with mineral colloids and at last possibly reaching dimensions outside the nano-range (Stolpe and Hassellöv, 2007; Hartland et al., 2013). Additionally, some examples of bio-colloids, viruses, and some of the bacteria, can also be counted as natural nanoparticles with the consideration of their size range (>10 nm) (Christian et al., 2008). However, most of the biological constituents in natural waters may serve as mediators for the environmental fate of nanoparticles due to their comparatively greater particle sizes.

1.1.3. Synthetic Nanoparticles

Synthetic or anthropogenic nanoparticles are divided into two categories as *i.* incidental and *ii.* engineered nanoparticles.

1.1.3.1. Incidental nanoparticles: The incidental NPs are the consequences of human activities, which are mostly due to daily activities such as running diesel engines, large-scale mining, and even starting fires. Similar to the natural nanoparticles incidental nanoparticles can have irregular or regular shapes (AZoNano, 2016).

1.1.3.2. Engineered nanoparticles (ENPs): ENPs have been specifically designed and purposely synthesized for shape, size and surface properties with special functionalities including behavior, improved strength, enhanced thermal and electrical conductivity, and controlled release of main molecule. The advantage of specifying the properties of ENPs supplies benefits for industrial

applications (Matsoukas et al., 2015). Engineered nanoparticles can be divided into four groups (Christian et al., 2008);

- Standard industrial products: Polymers, surfactants, dyes and pigments.
- NP metals and metal oxides: Metals (Au, Ag, Fe), metal oxides (TiO_2, ZnO, ZrO, …), metal tubes and wires.
- Carbon based NPs: Fullerenes and single and multi-walled nanotubes.
- Hybrid structures: Quantum dots, functionalized materials, and core-shell structures.

Engineered nanoparticles can be classified according to their chemical properties or morphology or size. ENMs classified by means of chemical properties, morphology and size are presented in Figure 1.3 (Bhatia, 2016; Hussainova, 2012; Khan et al., 2017).

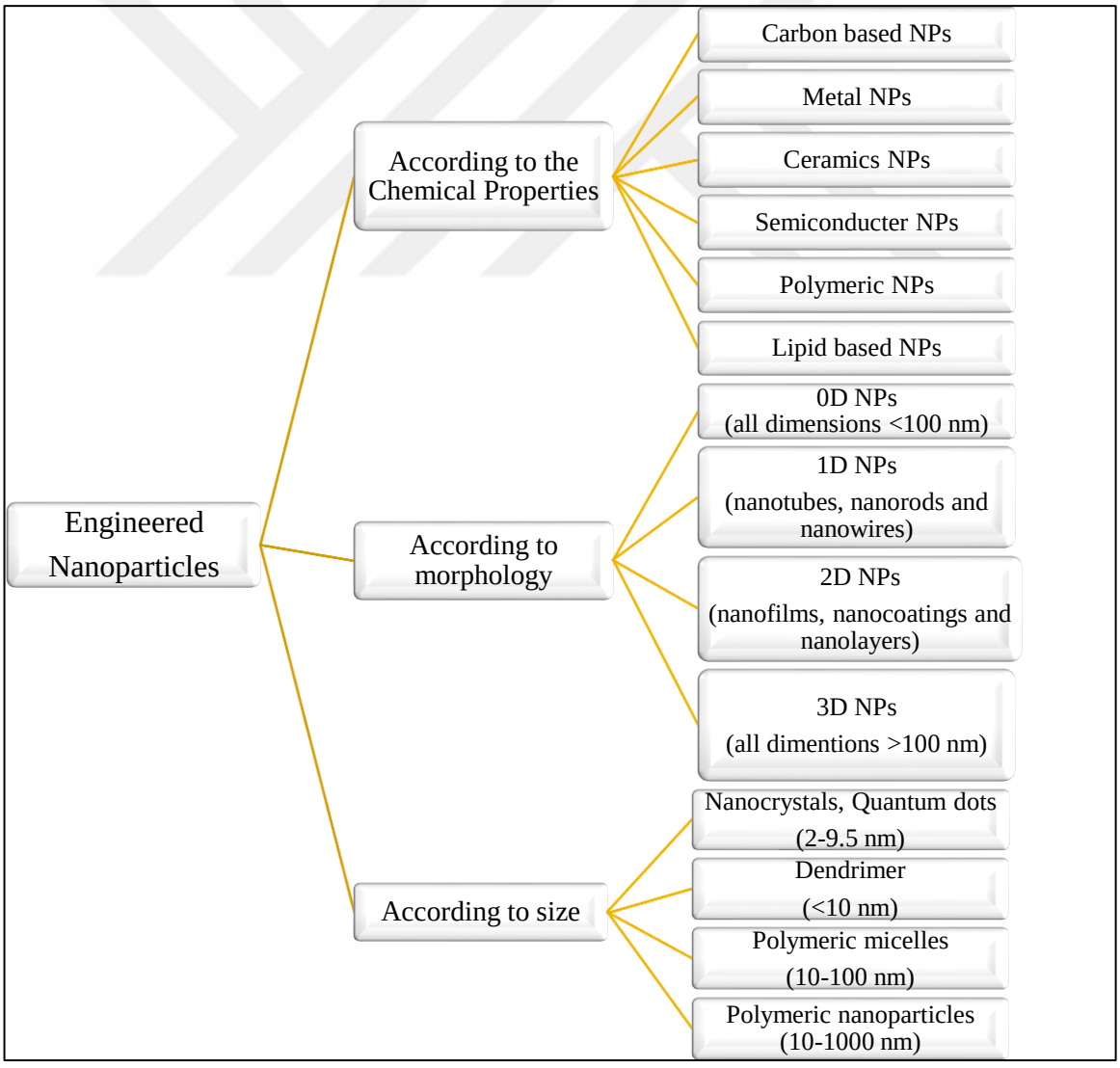


Figure 1.3. Classification of nanoparticles.

Recent research interest in directed to the extensive use of TiO_2 nanoparticles released to environment. Moreover, Ag nanoparticles also constituted the key focus of toxicological studies due to the antimicrobial properties of Ag species. The main features of oxide nanoparticles as TiO_2 could be attributed to their photocatalytic properties leading to degradation of various organic constituents as well as biological consortium of natural waters. Therefore, the presence of TiO_2 holds prime importance in natural waters. TiO_2 NPs has the highest production rate according to the wide usage areas as seen in Table 1.1. However, from scientific view photocatalytic properties of TiO_2 NPs have the top attention (Gupta and Tripathi, 2011). TiO_2 is a transition metal oxide and mostly produced in rutile and anatase crystal structures. According to Zhang and colleagues, anatase structure can be transformed to rutile phase via heat treatment (Zhang et al., 2000). Anatase and rutile structures have a band gap energy, E_{bg}= 3.2 and 3.02 eV, respectively. This band gap energy difference causes high photoactivity for anatase and light reflecting properties for rutile structure. When an electron is excited from valance band to conduction band upon exposure to UV illumination, an electron-hole (e^--h^+) pair as a redox couple is generated. If this e^--h^+ pair recombines photocatalytic efficiency is lost as is in the brookite phase due to its low redox potential. TiO_2 is almost the most ideal photocatalyst because of its decent photocatalytic properties, ease of production and low cost therefore is regarded as a standard photocatalyst.

Doping with transition metal cations adds additional energy levels within the band gap of a semiconductor. Eventually, the energy needed for electron transition from valance band to conduction band has been reduced but this also can cause an increase in the rate of recombination between photogenerated e^--h^+. Photocatalytic effect occurs when the trapped electron and hole are transferred to the surface of the photocatalyst, to prevent this e^--h^+ recombination metal ions must be doped near the surface of NP. As dopant 21 different metal ions can be used among them Fe(III), Mo(V), Ru(III), Os(III), Re(V) and V(V) are most widely used. Doping with anions leads to visible light activation. Doping with anions depends on finding a substitute for oxygen in the TiO_2 lattice. Briefly, the procedure based on the mixing of the p states of the doped anion (N, S or C) with the O2p states shifts the valance band edge upwards, reducing the band gap energy of TiO_2. Different from metal doping in the case of anions there is less chance to form recombination centers and consequently is more efficient in photocatalytic activity (Gupta and Tripathi, 2011). Also, doping with metalloids (such as boron), addition of noble metals (Pt, Ag, Au, Pd, Ni, Rh and Cu) and co-doping is possible and improves photocatalytic activity of TiO_2 in different mechanisms (Gupta and Tripathi, 2011). Therefore, along with bare TiO_2, modified types would also impart significant roles in the environment.

Table 1.1. Examples of manufactured nanoparticles and their application areas.

Nanoparticle	Application/Use	Production Quantities Worldwide (t/year)	Reference
TiO_2	Cosmetics, paints and coatings, filters, consumer electronics, plastics, cleaning agents	3,000	Vance et al., 2015; Piccino et al., 2012; Hendren et al., 2011
ZnO	Cosmetics, paint and coatings, plastics/polymers	550	Vance et al., 2015; Piccino et al., 2012
CeO_2	Fuel Catalyst, chemical planarization, UV-coatings, paints	55	Vance et al., 2015, Piccino et al., 2012; Hendren et al., 2011
SiO_2	Paints, coatings, fireproof glass, UV-protection, ceramics, electronics, food, plastics, sunscreen	5,500	Vance et al., 2015; Piccino et al., 2012
AlO_x	Batteries, grinding, fire protection, metal sorption and biosorption, paints	55	Vance et al., 2015
FeO_x	Concrete additive, biomedical uses, removal of contaminants	55	Vance et al., 2015; Piccino et al., 2012
Mn_2O_3	Catalytic applications	-	Vance et al., 2015
ZrO_2	Biomedical applications as component of bioceramic implants	-	Vance et al., 2015
Ag	Medical applications, paints, coatings and cleaning agents, textiles, consumer electronics and conductivity cosmetics, anti-microbial coatings	55	Trickler et al., 2010; Piccino et al., 2012; Hendren et al., 2011
CNTs	Composites and polymer additives, materials, composites, batteries	300	Piccino et al., 2012; Hendren et al., 2011
Quantum dots	Light conversion for LED/OLED, lab use for imaging	0.6	Piccino et al., 2012

1.2. Fate and Behavior of Nanoparticles in Wastewater and Environmental Systems

According to the report of United Nations Environment Program 2020, production of TiO_2 NPs reached 7.25 million tons per year (McGlade, 2017). Consequently, concerns about the environmental risks have emerged drastically. Eventually a quarter of these amount of product is used and finally released to aquatic systems (Danovaro et al., 2008). Table 1.1 shows the annual production amounts of some nanoparticles and their application areas. Keller and colleagues gathered information about the top 10 ENMs, considering high production estimates for 2010 and high emission assumptions throughout their life cycle (Keller et al., 2010).

Major amount of ENMs (63-91%) end up in landfills, a smaller but still significant fraction goes to soils (8-28%), water (0.4-7%), and the atmosphere (0.2-1.5%). As is seen from Figure 1.3 and Table 1.1 TiO_2 has the largest production, eventually the largest releases into soil, water, and air, pursued by ZnO and iron. Wagner and colleagues reported that predicted environmental concentrations of TiO_2 and ZnO are 0.4-1.4 μg/L and 0.05-0.29 μg/L (Wagner et al., 2014). Due to its low solubility TiO_2 tends to stay as a particle (Keller et al., 2013). Unless it is stabilized, it forms large aggregates in the long term. ZnO NPs, in comparison to TiO_2, dissolve more easily with releasing Zn^{2+}, however at last ZnO NPs re-precipitate as larger particles (Zhou and Keller, 2010; Fairbairn et al., 2011; Lowry et al., 2012).

The interaction routes of ENPs in air, soil and water compartments are presented in Figuıres 1.4-1.6. When ENPs are introduced to the aquatic systems, abiotic and biotic interactions may cause additional alterations to their elemental physicochemical properties, which would create different routes for exposure conditions (Lin et al., 2017). Understanding mobility, bioavailability, and ultimate fate of NPs can be possible with the recognition of NPs advection in and out of the system; diffusive transport; volatilization to air; transformation into other NPs or compounds; aggregation; sedimentation; dissolution; filtration; and sorption to suspended particles and the subsequent deposition to sediment (Quik et al., 2011; Garner and Keller, 2014; Lin et al., 2017). Mueller and Nowack also modelled mechanisms for transition of nanoparticles to environmental systems from manufactured materials. Nanoparticle release depends on some factors such as the particle stock in the material, lifetime of the material, integration way of nanoparticle to the material and material usage (Mueller and Nowack, 2008). Wastewater treatment plants are the last barrier between the release sources of domestic and industrial ENPs and aquatic and terrestrial environments. ENPs can be removed in every step of wastewater treatment systems, such as sorption by activated sludge and

aggregation/settling to activated sludge. The interactions between dense sludge media and NPs increase the flocculation rate of NPs. The negative charges of anionic functional groups of the organic matter used in the medium adsorbed onto the NPs surfaces, transmitting their charge to the NPs, disregarding of the original NPs surface charge. Consequently, major number of NPs are unlikely to pass straight through the bioreactor or continue in the effluent stream due to the adsorption energy barrier in these high ionic strength and organic systems is not sufficient to maintain the NPs in suspension. However, ion solutes and organic species in the media might alter the NPs aggregation behavior. NPs present as solutes in the systems can have toxic effects for the microorganisms in activated sludge processes, but this effect is related with the solubility of metal oxides and respective concentration that the microorganisms can tolerate. Li and co-workers reported that ZnO NPs have toxic effects because of the increment of NP concentration in sludge bed than the effluent, which are responsible for severe inhibition of anaerobic sludge metabolism activities. On the contrary, because it is less soluble than ZnO, TiO_2 NPs are not as toxic as ZnO NPs. Also, under dark conditions, ZnO and TiO_2 metal oxide NPs cannot express photoactivity which do not affect the systems consequently. Nevertheless, NPs can occupy the active cites of the microorganism via surface accumulation. Hence, even effects of ZnO and TiO_2 have different routes they affect the system approximately in same rate (Li et al., 2017). Once released into the environment, ENPs can display various reactivities due to factors such as pH, ionic strength, ionic balance, and organic matter interactions. Environmental processes of ENPs can be itemized as dissolution, deposition, photo transformation, redox-reactions, macromolecular transformations and most specifically aggregation/agglomeration.

The phenomenon of environmental aggregation in natural systems can explained with Derjaguin-Landau-Verwey-Overbeek (DLVO) theory which argues that intermolecular and electrostatic forces are mostly responsible for aggregation. On the contrary, Dwivedi and colleagues proposed a non-DLVO theory which supports that a combination of steric hindrance and magnetic/hydration forces are responsible for NP aggregation (Dwivedi et al., 2015). Both theories required to be assessed in proper understanding of NP homo- and hetero-aggregation mechanism prevailing in the environmental compartments (Goswami et al., 2017).

Once introduced into the environment, due to exposed size variations, ecotoxicological assessment of their presence drew attention. In aqueous medium, toxicity of NPs is dependent on various factors as solar irradiation (UVA-vis), dissolved/particulate organic matter (POC/DOC), physico-chemical properties of water (*e.g.*, hardness, temperature, turbidity, etc.,) as well as the aquatic microbiological systems. Once entered to the environment through partitioning and bioaccumulation processes and via food chain, adverse effects of NPs are realized.

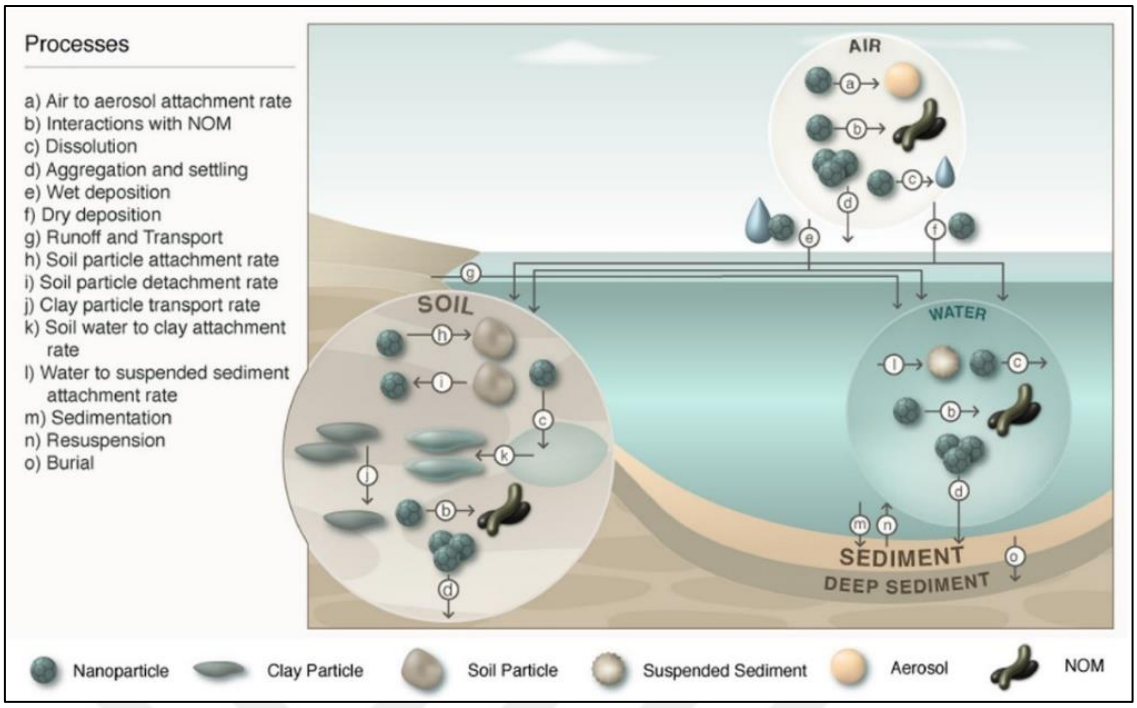


Figure 1.4. Transportation of NPs between environmental components (Garner and Keller, 2014).

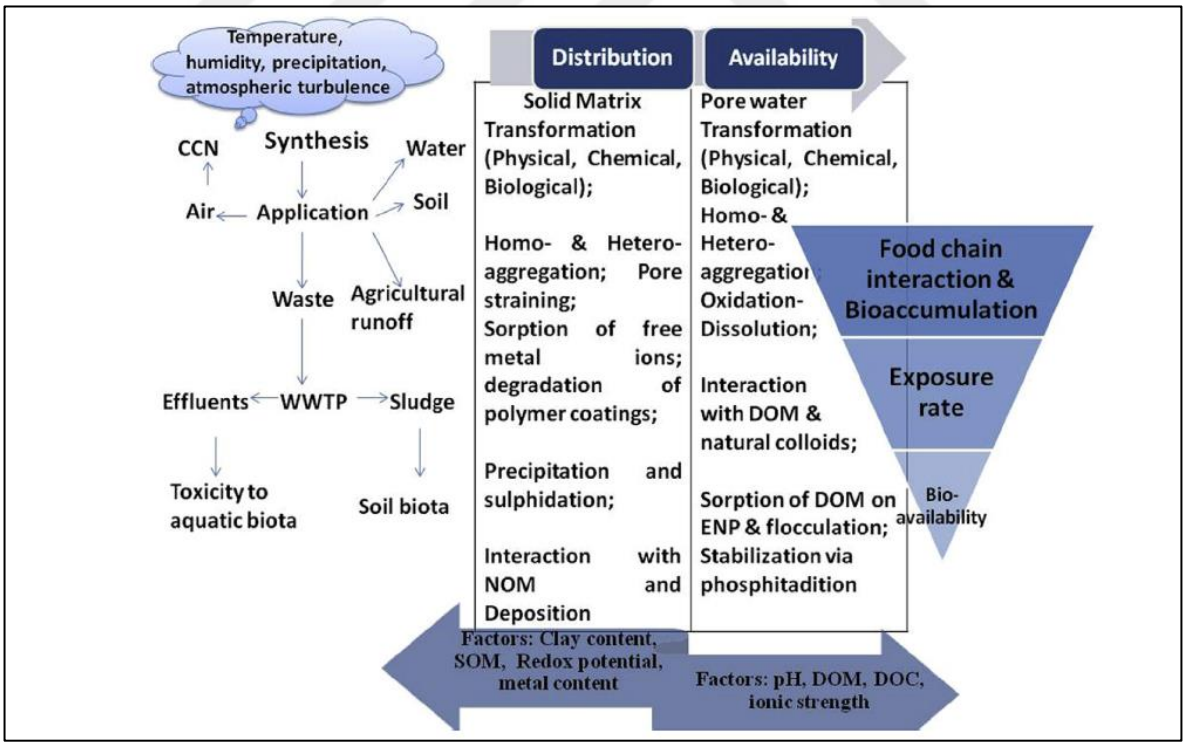


Figure 1.5. General presentation of environmental behavior of NPs (Goswami et al., 2017).

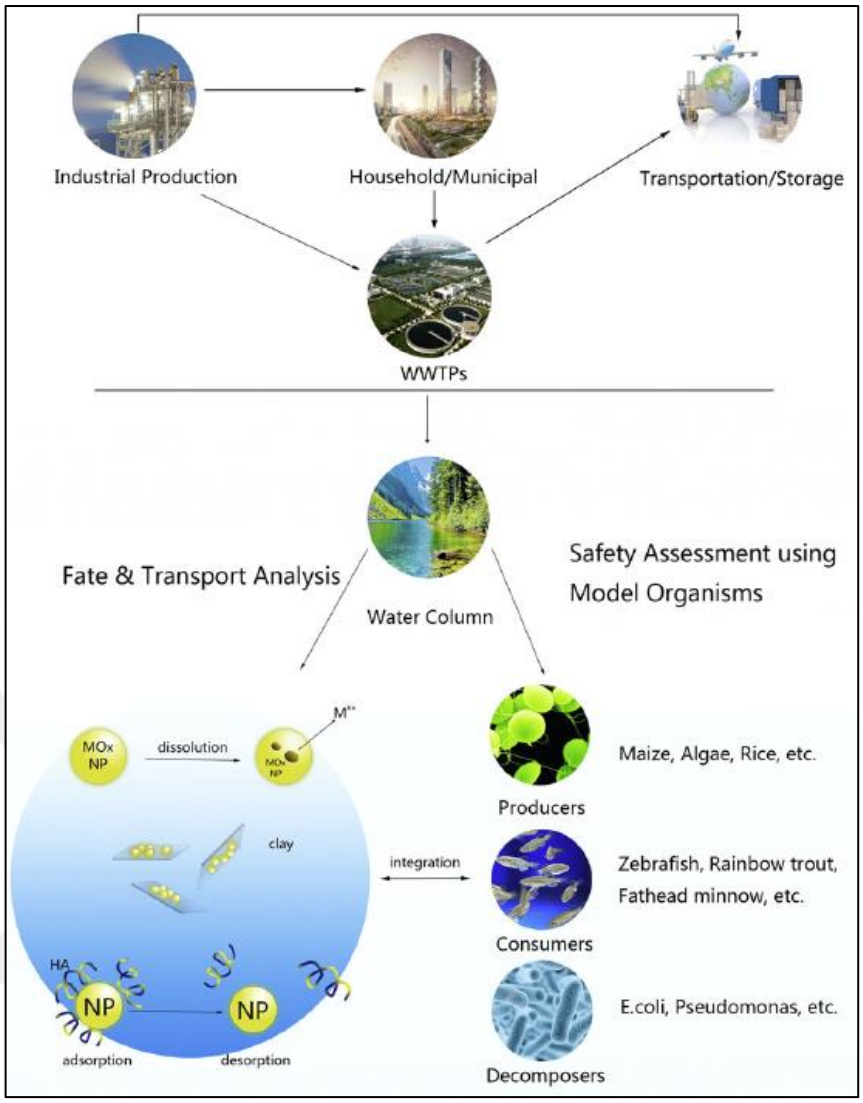


Figure 1.6. Potential exposure routes for NPs in the water column (Lin et al., 2017).

The main concern would be related to the understanding of the relationship between the aggregate/agglomerate size of the NPs and their impact on microbiological consortium. Either direct or indirect exposure mechanisms prevail depending on the medium characteristic properties. The most important pathway is expressed by the photo-toxicity leading to oxidative stress especially in the presence of photo-active NPs *e.g.,* TiO_2. Therefore, as all these interactions are mainly size-dependent, assessment of particle size distribution of NPs holds prime importance. Recently, research interests are directed to the assessment of eco-nano-toxicological behavior of NPs in relation to the environmental risk concerns as well as sustainable development of nanotechnology (Goswami et al., 2017). In this respect, studies on the assessment of environmental fate of NPs mostly rely on modeling techniques through considering the NP particle size as the one of the main contributing parameters (Dale et al., 2015; Garner et al., 2017; Yu et al., 2018).

1.3. Definition of Particle Size and Distribution

As stated, IUPAC defines nanoparticles as sub-category of the colloidal systems. On the other hand, from a general perspective, nanoparticles are defined as "particulate matter with at least one dimension that is less than 100 nm". Therefore, the determination of the size of the NP holds prime importance especially in terms of their presence in aggregated/agglomerated forms. The environmental size strictly deviates from primary crystallite size and is mainly expressed as hydrodynamic size in aqueous medium.

The most widely used methodology is based on dynamic light scattering (DLS) technique that is used to determine the hydrodynamic diameter and polydispersity of the particles in an aqueous media. This technique is based on the measurement of the diffusion coefficient that is related to the hydrodynamic size of the scattering particle by the Stokes-Einstein equation:

$$D = \frac{k_B T}{3\pi\eta d} \tag{1.1}$$

where D is the diffusion coefficient, kB is the Boltzmann constant, T is the temperature, η is the diluent viscosity, and d is the equivalent spherical diameter. This technique also includes the correlation of fluctuations in scattering intensity obtained at different delay times, proceeding from the Brownian motion of the particles (Nobbmann, 2015; Ragheb and Nobbmann, 2020).

There are several other methods for determining the size of the particles such as image analysis (SEM, TEM, optical microscopy), electrical zone determination, light diffraction, and DLS. Table 1.2 shows the characteristics of the measurement techniques and aspects of the particle size analysis techniques. Image analysis techniques such as SEM and optical microscopy supplies information about surface morphology, while TEM, due to its higher resolution, provides information about crystalline structure and inner morphology of the measured structure. One of the most important properties of image analysis is that the size information is related to the precision of operator as well as the instrument. Basically, the size of the sample structure is obtained from a picture of sample in proportion to magnitude scale, so the measured size is approximation of the actual size (Kulkarni and Shawn, 2016; Goldstein et al., 2017; Akhtar et al., 2018). Electrical zone determination, electrical mobility, determines the particle size based on the velocity of the particles in aerosol systems according to their affinity to electrical field (Gensdarmes, 2015; Järvinen et al., 2017). Ultrasound attenuation is a method used to determine grain size by the advantage of ultrasound scattering

attenuation, but it is a slow method and highly effected by external factors such as temperature (Jia et al., 2019; Liu et al., 2021). Moreover, crystalline size and crystalline structure can be determined by XRD measurements. The XRD method also supplies information about the chemical composition, crystal composition, lattice strain, preferred orientation, and layer thickness. However, it does not provide information about the aggregation/agglomeration behavior of the sample (Goldstein et al., 2017). Laser diffraction is another effective method for particle size determination; however, it neglects the particle movement is suspended medium and the measuring limits are higher in comparison to DLS. Hence, laser diffraction is not considered as a proper method for determination of hydrodynamic behavior of the particles. Among the various size determination techniques, DLS is an effective method for determination of both colloidal and non-colloidal structures in solution systems (Babick, 2020). Due to its non-destructive properties the technique gives information according to the light scattering properties of the particles and it is possible to determine the hydrodynamic size of structures from 1 to 10,000 nm. One of the biggest advantages of the DLS is hydrodynamic size measurement could be performed while the sample particles suspended in solution. If the suspension medium is not water, the physicochemical properties of solvent such as viscosity must be known. DLS is a fast methodology that supplies information in a very short period of time *e.g.*, 1 min. It is precise, reproducible, requires very little amount *i.e.*, < 4 mL sample solution, and calibration free. On the contrary the reliability of the measurement can be controlled by measuring particles with a known hydrodynamic size. Also, highly concentrated, and turbid solutions can be measured with DLS since not the transposing or adsorbed light but the scattered light with a specific angle is detected (Jose et al., 2019; Babick, 2020; Caputo et al., 2021). Moreover, DLS technique is applicable to both inorganic and organic samples.

From a better visualization point of view, Figure 1.7 is presented to display the difference between the particle size obtained via TEM images and the hydrodynamic size measured with DLS technique. As mentioned before, image analysis such as TEM pictures, the sample under atmospheric conditions. Even when there is humidity, the water molecules surrounding the particle are not visible and the interaction between water or solvent molecules cannot be obtained through TEM imaging methodology. Additionally, TEM image supplies a 2D image therefore the size evaluation of the structure can only be assessed in two dimensions. On the other hand, when a sample is dispersed in a liquid phase, an electric dipole layer adheres to the surface of the particle. Figure 1.7 also shows the hydrodynamic diameter (R_h) of different shaped or aggregated/agglomerated particle. This electric dipole layer is also included in the R_h. The R_h indicates the diameter of systems are moving via Brownian motion in liquid phase individually or in aggregate/agglomerate form and including their outer shell, *i.e.*, electric double layer (ISO 9276; Babick, 2020). The term aggregate is defined as

"irregular cluster of otherwise individual molecules or particles" and the term aggregation is explained as "The aggregation of oppositely charged free ions into ion pairs or larger, and not necessarily well-defined, clusters of ions held together by electrostatic attraction" by IUPAC (Jones et al., 2012). The term agglomeration is explained by IUPAC as "Process of contact and adhesion whereby dispersed particles are held together by weak physical interactions ultimately leading to phase separation by the formation of precipitates of larger than colloidal size." (Nic et al., 2005). It must be noted that the term particle in Figure 1.7 refers to the structure subjected to measurement. This particle can be homo or hetero aggregated/agglomerated primary particles, or colloidal structures. In Figure 1.7b a representative image of aggregated/agglomerated structure is shown. In TEM measurement it is possible to determine an approximate size of primary spherical particle (grey spherical structure) or approximate aggregate/agglomerate size (the cluster). However, DLS supplies information about the 3D structure of the aggregated/agglomerated structure including the cavities filled with water or solvent and considers the entire cluster as a spherical structure. Another example is the non-spherical structure given in Figure 1.7c. The non-spherical structures in suspensions are also considered spherical in DLS measurements, and an approximate diameter is determined by theoretical comparison with a spherical structure showing similar scattering properties (Jose et al., 2019; Babick, 2020; Caputo et al., 2021). A more detailed explanation of hydrodynamic size determination aspects will be discussed in the next section according to historical background of the DLS theory, data analysis and data interpretation.

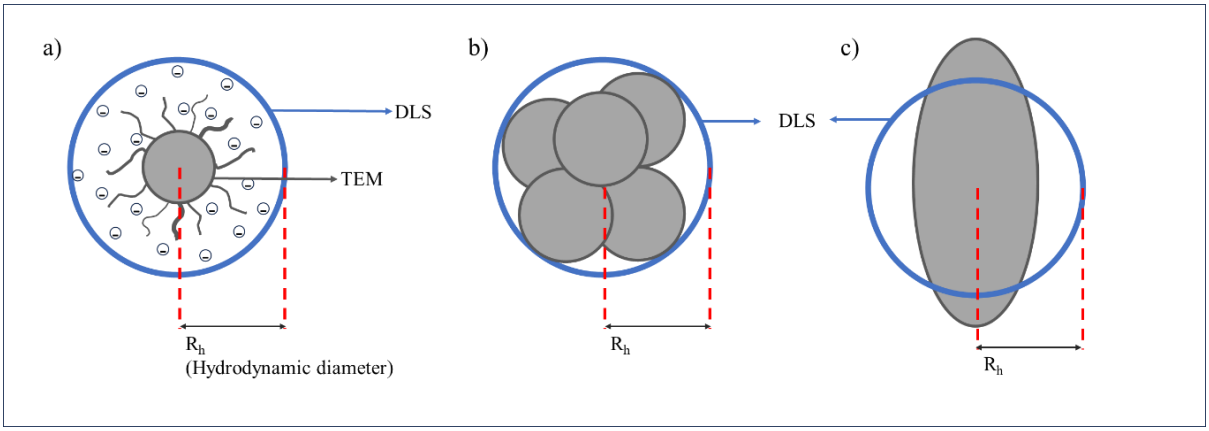


Figure 1.7. Representation of particle size (measured with TEM) and hydrodynamic size (measured with DLS). a) polymer-like structure adsorbed on to surface, b) aggregated or agglomerated, c) non-spherical.

Table 1.2. Comparison of particle size determination techniques.

Technique	Type of Size	Size Range, diameter* *Depending on the instrument	Aspects	Reference
DLS	Hydrodynamic radius	1 nm - 10 µm	Pros: Fast (<1 min), precise, reproducible, requires very little amount (<4 ml sample), calibration free, high concentration and turbid sample measurements Cons: Depended on temperature and solvent viscosity, knowledge of refractive index gives better results.	Jose et al., 2019; Babick, 2020; Caputo et al., 2021
Laser diffraction	Scatter diameter	100 nm – 10^4 µm	Pros: fast, precise, reproducible, can measure highly concentrated samples Cons: Needs several detectors, results depend on refraction method preference.	Fisher et al., 2015
Optical microscopy	Shape/Structure	800 nm - 150 µm	Pros: Supplies visualization, good for semisolid particles, *i.e.,* gels and ointments. Cons: Uses visible light reflection, operator decides the size of the particles or counts, an experienced operator is needed.	Kulkarni and Shawn, 2016
SEM	Shape/Structure	10 nm - 5 µm	Pros: Provides information about surface morphology and structure, sample preparation is easy, electron adsorption measurement, provides 3D images. Cons: Expensive, operator decides the size of the particles or counts, an experienced operator is needed. Non-conductive materials require coating	Goldstein et al., 2017; Akhtar et al., 2018

Table 1.2. Comparison of particle size determination techniques. (Continue)

TEM	Shape/Structure	0.5 nm - 1 µm	Pros: supplies information about crystalline structure, morphology, and magnetic domains. Higher resolution than SEM. Cons: Expensive, non-conductive materials require coating, skilled operator needed for thin sample preparation. Provides 2D black and white image, non-conductive materials require coating	Goldstein et al., 2017; Akhtar et al., 2018
Electrical mobility	Electrical mobility	2 nm - 1µm	Pros: Excellent resolution, effective on high concentration Cons: not reproducible, not effective on dilute ultrafine particles, only detects charged particles	Gensdarmes, 2015; Järvinen et al., 2017
Ultrasound attenuation	Ultrasound attenuation	10 nm - 3000 µm	Pros: Cheap, non-destructive and non-invasive, fast, opaque and high concentration sample measurement. Cons: Effected by temperature change, slow, frequency selection and energy components adjustment of pulse is inflexible.	Jia et al., 2019; Liu et al., 2021
X-ray diffraction	Crystalline size	1 nm - 1 µm	Pros: non-destructive, easy sample preparation, , fast, effective resolution, easy data interpretation, supplies information about chemical composition, crystal structure, crystal composition, crystallite size, lattice strain, preferred orientation, and layer thickness. Cons: Expensive, uses harmful radiation, sample must be in crystal structure.	Goldstein et al., 2017

1.4. Dynamic Light Scattering Methodology

1.4.1. Fundamental of Dynamic Light Scattering

DLS technique depends on two theories: *i.* Rayleigh Scattering, and *ii.* Mie Theory. Rayleigh Scattering explains if the wavelength of the scattered light from the particles is smaller, λ/10, than the wavelength of the light, λ (Tyndall, 1868; Strutt, 1871). On the other hand, Mie Theory identifies the light scattering of light absorbing and non-absorbing particles which are larger than the wavelength of the light considering the shape of the particles and the refractive index differences between the medium and the particles (Mie, 1908). The Fluctuation theory of light scattering was proposed by Smoluchowski that introduces that liquid is a continues medium where inhomogeneities are created by thermal fluctuations (Smoluchowski, 1908; Einstein, 1910). Einstein also explained the molecular motion which is later named Brownian motion. Brownian motion defines the particles in solution moves randomly due to the random forces causing constant collision applied by solvent molecules. The mean square of this displacement of particles is proportional to the time. Einstein and Stokes also proposed the relationship between the diffusion coefficient of particles to their translational friction and the friction is utilized by a moving particle is proportional to its radius and to the viscosity of the solvent surrounding particle (Stokes, 1845; Einstein, 1906). The theory of optically anisotropic scatters and their influence on polarization of scattered light is discussed by various researchers (Cabannes and Rocard, 1929; Gans, 1921, Gans, 1923). After many efforts to explain the interactions between the light scattering and diffusion behavior of particles theory is proved experimentally and light scattering methods are started to be used in hydrodynamic size measurements (Pecora, 1964; Foord et al., 1970).

In the light of the historical background, DLS methodology has been developed so far and application area is expanded from submicron particles to less than a nanometer. Furthermore, DLS not only supplied information about the stability of formulations but also presence of aggregation and/or agglomerations can be detected by DLS measurements (Raval et al., 2019).

DLS is based on the irradiation of a solution containing macromolecules or colloidally suspended particles with monochromatic light at one specific wavelength. This monochromatic light, laser, is coherent and focuses on a very small area, also the monochromatic light must be in a nonionizing wavelength for the sample. Hence, mostly wavelength of the laser light ranges between 405 nm to 1064 nm in DLS instruments and the most widely used wavelengths are 633 nm red laser or 532 nm green laser, due to non-destructive property on the proteins or protein-like structures. According to

the size and shape of particle incoming light scatters in all directions. The intensity of this scattered light is detected as time average intensity, that supplies information about molecular weight and radius of gyration of the particles. However, when the intensity fluctuations is measured, which is related to the Brownian motion, the autocorrelation (Gτ) which is corresponding to hydrodynamic size of the particles in solution, is also obtained. (Jia et al., 2023). Particles move with a random movement in solution systems due to the bombardment from solvent molecules. This movement is stated as Brownian motion and depends on the size and shape of the particles, temperature, and viscosity of the solvent (Harding and Jumel, 1998). Because viscosity is dependent on the temperature, knowledge of accurate temperature during the measurement is a must (Allen, 1997). The smaller particles move faster and their scattered intensity changes more rapidly than big and slow particles and detection of this movement over time supplies the information about the hydrodynamic particle size.

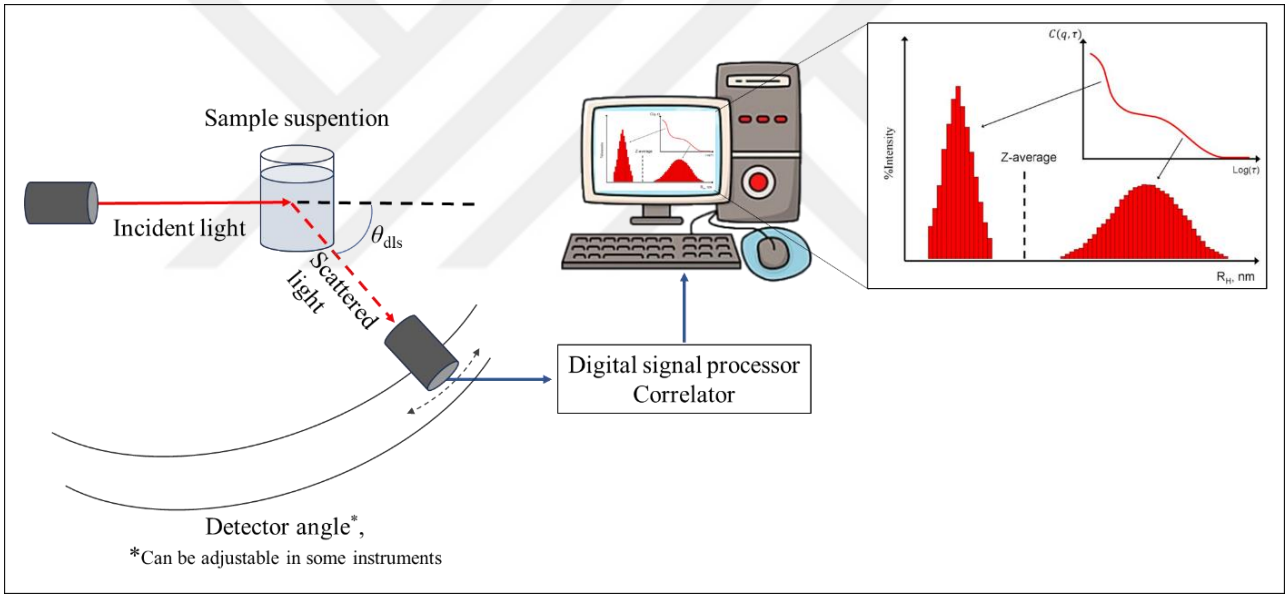


Figure 1.8. Schematic representation of DLS instrument.

DLS instrument is represented in Figure 1.8. The detector of the DLS instrument distinguishes the scattered light intensities of the encountering light with the particle which distributes in all directions. This scattered light can undergo a phenomenon called Doppler broadening and they can either result in mutually destructive phase, cancel each other, or they can produce a detectable signal and the digital autocorrelator compares intensity fluctuations changing by the time in ns to µs. Determination of the rate of fluctuation in change depends on the diffusion behavior of the suspended particles in solution system (Stetefeld et al., 2016). DLS is based on the detection of motion of

particles by measuring the intensity correlation function which is expressed as an integral of over the product of intensities at time, t, and delayed time, t + τ, (Berne and Pecora, 1976; Stetefeld et al., 2016):

$$G_2(\tau) = \langle I(t)I(t + \tau)\rangle \quad (1.2)$$

Where $G_2(\tau)$ is the intensity correlation function, or second order correlation function, τ is the lag time between the two time-points. Normalization of $G_2(\tau)$ can be done as:

$$g_2(\tau) = \frac{\langle I(t)I(t+\tau)\rangle}{\langle I(t)\rangle^2} \quad (1.3)$$

The averaging of properties over the duration of the experiment (time, t) is represented by the braces in both equations.

Even it is not possible to precise the random motion of the particles in solution, this motion is correlated by means of an electric field correlation function, and it can be defined as:

$$G_1(\tau) = \langle E(t)E(t + \tau)\rangle \quad (1.4)$$

Where $G_1(\tau)$ is the electric field correlation function, E(t) and E(t + τ) is the scattered electric fields at times (t) and (t + τ). The equation can be normalized as:

$$g_1(\tau) = \frac{\langle E(t)E(t+\tau)\rangle}{\langle E(t)\rangle^2} \quad (1.5)$$

According to the Siegert relation $g_1(\tau)$ and $g_2(\tau)$ can be coupled to each other which is based on the scattering can only be detected by photodetector also called as homodyne, and this is basically random Gaussian process by counting photon;

$$g_1(\tau) = B + \beta|g_1(\tau)|^2 \quad (1.6)$$

B is the baseline (~1) and β is the coherence factor that rely on the detector area, optical alignment, and scattering properties of the suspended particles.

If the hydrodynamic size of the particles is monodispersed, hydrodynamic size of the particles approximately same, the electric field correlation factor, $g_1(\tau)$, declines exponentially and is correlated with decay constant, Γ, for the structures moving with Brownian motion and it can be illustrated as:

$$g_1(\tau) = e^{-\Gamma\tau} \quad (1.7)$$

hence the normalized equation of intensity correlation function, $g_2(\tau)$, can be defined as:

$$g_2(\tau) = 1 + \beta e^{-2\Gamma\tau} \quad (1.8)$$

On the other hand, if the system is polydispersed (Appendix B), composed of different sized structures, hydrodynamic size of the particles varies within a range, $g_1(\tau)$ do not give a single exponential decay, however it can be shown as an intensity-weighted integral over a distribution of decay rates G(Γ):

$$g_1(\tau) = \int_0^\infty G(\Gamma) e^{-\Gamma\tau d\Gamma} \quad (1.9)$$

Because the Γ is directly associated to the diffusion behavior of the particles, D_τ, it is expressed as:

$$\Gamma = - D_\tau q^2 \quad (1.10)$$

q represents the Bragg wave vector which is proportional to solvent refractive index n (Harding, 1999).

$$q = \frac{4\pi n}{\lambda} \sin\left(\frac{\theta}{2}\right) \quad (1.11)$$

λ is the wavelength of incident light and, θ is the detector angle.

Accordingly, particle motion and measured fluctuations can be linked as (Burchard, 1983):

$$g_2(\tau) = 1 + \beta e^{-2D\tau q^2 \tau} \quad (1.12)$$

The detector of DLS instrument can be placed in every angle most widely used angles are 173˚, back scattering best for large particles and highly concentrated solutions, 90˚, side scattering is useful for small particles and transparent samples, and 15˚, forward scattering is preferred for small particles with few large particles. When the sample solution contains particles with different sizes, multiple light scattering occurs, and this affects the accuracy of the obtained hydrodynamic particle size distribution. Diluting the sample solution or shortening the light path methods can be used to eliminate this effect, however also selecting a larger detection angle, or using higher laser power also reduce the influence of multiple scattering effect on the hydrodynamic particle size range detection (Stetefeld, 2016; Jose et al.; 2019; Jia et al., 2023).

The diffusion coefficient, Dτ, is depended on the solution concentration, for a proper particle size determination there should be multiple concentration and extrapolated to infinite dilution (D^0_τ) in practice. However, Dτ can be adapted to the standard solution properties, viscosity, and temperature of solvent, so the hydrodynamic radius (R_h), which is estimating the measured particle as a hypothetical sphere that diffuses the same rate as the investigated particle, can be obtained (Pusey, 1972; Stetefeld et al., 2016).

$$D\tau = \frac{k_B T}{6\pi\eta R_h} \qquad (1.13)$$

k_B is Boltzmann constant, 1.380 x 10^{-23} $kgm^2s^{-2}K^{-1}$, T is the absolute temperature and η is the viscosity of the sample solute.

Because the R_h value is a hypothetical value, the PSD of the sample is more practical to use. The DLS measurement supplies PSD in intensity-, volume-, surface area-, and number-weighted data. The volume-, surface area-, and number-weighted hydrodynamic size values are converted from the intensity-weighted (fundamental size) distribution (Stetefeld et al., 2016; Jia et al., 2023).

The Z-average value is one of the most used terminologies that represents the intensity-weighted mean hydrodynamic size. For the mono dispersed samples, Z-average can be representative for all sample, however for the polydispersed sample containing diverse size of particles, because intensity-weighted data would give at least two or more peaks with specific mean and width, Z-mean value cannot represent the true distribution of the actual composition and in such conditions rather than reporting an average value, describing the system as range is more applicable (Stetefeld et al., 2016; Jia et al., 2023).

1.4.2. Monomodal Hydrodynamic Particle Size Distribution

The monomodal distribution corresponds to only one maximum and it supplies the mean values of the diffusion coefficient but not the distribution of diffusion coefficient, so it is only proper for the Gaussian-like distributions around the mean values. The monomodal distribution is also associated with cumulant analysis. The cumulant analysis was proposed in 1972 by Koppel (Koppel, 1972) and in 1996 and 2008 the method is accepted by the International Standards Organization (ISO). Koppel suggested the experimentally measured $g_2(\tau)$ (Eq, 12) can be plotted against τ that gives the Gaussian distribution of hydrodynamic size:

$$\ln(g_2(\tau)\text{-}B) = \ln\beta + 2\left(-\bar{\Gamma}^2\tau + \frac{k_2}{2!}\tau^2 - \frac{k_3}{3!}\tau^3 + \frac{k_4}{4!}\tau^4 \ldots\right) \quad (1.14)$$

where, $\bar{\Gamma}$ (k_1), k_2, k_3 and k_4 show the average variance, skewness, and kurtosis of measured distributions respectively for decrease rate of the Gaussian distribution. Also, by using $k_2/\bar{\Gamma}^2$ ratio, the polydispersity index (PDI) of the composition can be calculated (Stetefeld et al., 2016).

1.4.3. Non-monomodal (Multi size) Distribution Methods

Differing from cumulant analysis by excluding certain type of distribution of diffusion properties, non-monomodel is more proper for polydisperse systems. The non-negative least squares (NNLS) method is applicable for broad monomodal or multimodal distributed systems that include non-negativity constraints and the geometrical spacing of the distribution established from the Laplace transform of Eq. 8 (Morrison et al., 1985). By employing NNLS method Γ_i and b_i, representing zero or positive values of linear or logarithmic form over a chosen range in means of geometrical spacing, to the following equation (Stetefeld, 2016):

$$\chi^2 = \sum_{j=1}^{N}\left[g_1(\tau_j) - \sum_{i=1}^{M} b_i e^{(-\Gamma_i\tau_j)}\right]^2 \quad (1.15)$$

where, N is the data points and M is the number of decay constant with the constraint Γ_i and b_i (Hassan and Kulshreshtha, 2006).

In cumulant analysis PDI is defined as $k_2/\bar{\Gamma}^2$, however this definition should not be compared with the ratio of weight-average molar mass to number-average molar mass, M_w/M_n, which is essential for the static light-scattering method (Cabaniss et al., 2000; Stetefeld, 2016). The PDI in

DLS ranging between 0 to 1, 0 represents the monodispersed system, on the other hand for the monodispersed systems M_w/M_n value will be approximately 1.

For monodispersed systems, PDI ~ 0.1, the cumulant method is more appropriate, however, PDI ranging between 0.1 to 0.7 illustrates the nearly monodispersed samples and PDI > 0.7 represents broad distribution of particle sizes in solution so the non-monomodal distribution method is more proper for data analysis (Stetefeld, 2016, Nobbmann, 2017). Also, it should be considered that PDI of natural organics is rarely smaller than 0.1 (Chin et al., 1994).

1.4.4. Size Distribution of Hydrodynamic Radius

Previously described methods and equations explained the distribution of diffusion behavior of the particles in solution systems, hence the distribution of R_h. The average diffusion coefficient, ($\langle D\tau \rangle$), in a solution system can be represented as:

$$\langle D\tau \rangle = \frac{\sum_i N_i M_{w,i}^2 P(q,R) D_{\tau i}}{\sum_i N_i M_{w,i}^2 P(q,R)} \quad (1.16)$$

M_w shows the molecular weight of N number of particles and P(q,R) is the interparticle interface. The diffusion coefficient depends on M_w^2, as indicated from the equation which shows the DLS technique is naturally having tendency for the particles with higher molecular weight. The refractive index also effective in DLS measurements, so the term P(q,R) approximated to 1 for the particles smaller than the wavelength of irradiated light, hence Dτ gets closer to the Z-average. Considering the intensity fluctuation of particles is measured in DLS technique, Z-average value is based on intensity-weighted hydrodynamic size definition. Z-averaged R_h value also depends on refractive index and solvent viscosity and according to Rayleigh approximation, the relation between the intensity of the particle size equals to the $(size)^6$ for small particles (Barnett, 1942). If the average hydrodynamic size is reported as Z-average this value is only comparable with R_h from other methods if the particle under investigation is spherical in shape, monodispersed and showing monomodal distribution and solubilized in suitable buffer system (Stetefeld et al., 2016).

Intensity-weighted hydrodynamic diameter of particles N_a and N_b with size a and b can be described as:

$$\%I_a = \frac{a^6 N_a 100}{N_a a^6 + N_b b^6} \quad (1.17)$$

Where $\%I_a$ represents the relative amount of intensity of particles with a size "a" and gives the intensity-weighted hydrodynamic size of particle "a" (Stetefeld et al., 2016; Jia et al., 2023).

If the density of the system is homogeneous by using Rayleigh approximation, the mass of a spherical particle is proportional to $(size)^3$, the intensity-weighted hydrodynamic size can be converted to volume-weighted hydrodynamic size, relative proportion of multiple sizes based on their volume or size but not their intensity. Because the intensity is dependent on the $(size)^6$ and volume is dependent on $(size)^3$, the R_h value obtained from volume-weighted hydrodynamic size distribution will be smaller than the R_h value obtained from intensity-weighted hydrodynamic size distribution.

$$\%V_a = \frac{a^3 N_a 100}{N_a a^3 + N_b b^3} \quad (1.18)$$

The $\%V_a$ illustrates the relative amount of volume of particles with a size "a" and thereby volume-weighted hydrodynamic size of particle "a". However, volume-weighted hydrodynamic distribution states that there are no errors originating from intensity-weighted distribution and the investigated particles are homogenously spherical (Stetefeld et al., 2016; Jia et al., 2023).

Surface area-weighted hydrodynamic diameter of the particles is proportional the $(size)^2$. Hence, the equation can be shown as:

$$\%S_a = \frac{a^2 N_a 100}{N_a a^2 + N_b b^2} \quad (1.19)$$

where, $\%S_a$ is the corresponding amount of surface area of particles with a size "a" and supplies the surface-area weighted hydrodynamic distribution. Similar with the volume-weighted hydrodynamic distribution accepts the particle as homogenous spheres and excludes the errors can be originated from the intensity-weighted hydrodynamic distribution (Sauter, 1928; Lefebvre, 1989; Scala, 2013).

The intensity-weighted distribution can be converted to number-weighted distribution which indicates the abundance of each particle that is giving histogram. The number-weighted distribution of two particles can be described as:

$$\%N_a = \frac{N_a 100}{N_a + N_b} \quad (1.20)$$

where the $\%N_a$ represents the number-weighted hydrodynamic distribution based on the number abundance of particles that have size "a". Number-weighted hydrodynamic size distribution is related to the count of particles that have the same intensity. Figure 1.9 shows the relation between intensity-, weight- and number-weighted hydrodynamic size distributions.

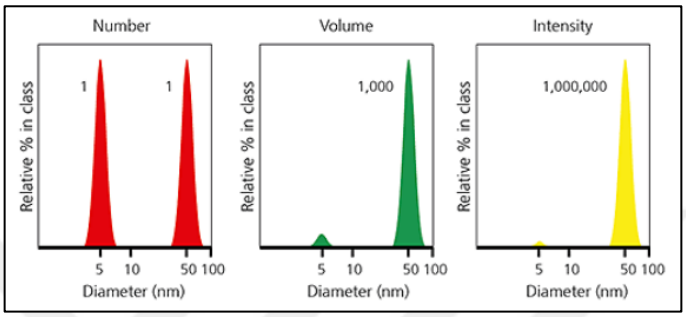


Figure 1.9. Intensity-, volume- and number-weighted hydrodynamic particle size distributions data for the same sample.

1.5. Dynamic Light Scattering Analysis of Metal Oxide NPs

The aggregation and agglomeration behavior of industrial metal oxide NPs recently awakened attention due to their high production rate and many usage areas. Through several pathways these nanomaterials reach to surface waters and interact with natural systems. The application areas and environmental fate of nanoparticles is illustrated in Figure 1.6 (Park and Yeo, 2016; Lin et al., 2017). Investigation of aggregation and agglomeration behavior or NPs provides convenience for understanding environmental impacts, especially the interactions in water bodies.

The metal oxide NPs can interact with natural organic material depending on the ionic strength, pH, cation composition and salinity and can led to not only NOM flocculation or NOM stabilization, but also photoactive metal oxide NPs such as TiO_2 can cause the degradation of NOM (Abbas et al., 2020) in sunlit surface waters. Figure 1.5 shows not only homo-interactions of metal oxide particles but also hetero-interactions that metal oxide NPs go through in surface waters. Therefore, understanding the hydrodynamic behavior of metal oxide NPs has a great importance. Not only surface interactions between TiO_2 NP and NOM, but also photocatalytic properties of TiO_2 depend on hydrodynamic size of TiO_2 NPS. As indicated in Table 1.2 DLS is an effective method to investigate the hydrodynamic size (HDS) of suspended structures, also with time depending on

investigation aggregation/agglomeration of NPS can be followed. Table 1.3 shows the physicochemical properties of cited literatures and Table 1.4 compiles the literature examples of hydrodynamic size measurements of TiO_2 NPs.

The volume-, surface area- and number- weighted HDS is calculated from intensity-weighted HDS so if data from these would be published some exceptions must be accepted. For example, volume-weighted HDS accepts the particles as spheres, homogenous (having same primary particle), refractive index of particle is known and there is no error in the intensity-weighted distribution. However, if the obtained data is compared between intensity-, volume-, surface area-, or number-weighted DLS, not between the literature examples, all exclusions can be negligible. Since the DLS system depends on the temperature, concentration and preparation methodology, different results can be obtained from different preparation methods (Tantra et al., 2014). Emphasizing the importance of nano-eco-toxicological investigations, the necessity in standardization of particle size determination methods were considered by Tantra and colleagues. The researchers focused on the dispersion step as one of the most influencing steps in sample preparation for providing a sound baseline for comparison especially for screening tests. Repeatability of DLS measurements is also discussed by Nickel and her colleagues. They conclude that there was approximately 11% difference between commercial TiO_2 NP measurements and 5% difference between synthesized TiO_2 NPs, while commercial standard was giving <1% coefficient of variance (Nickel et al., 2014). Therefore, literature data should only be directly compared in case the conditions were expressed in detail.

As an example, Suttiponparnit and colleagues reported that the intensity-weighted average hydrodynamic diameter of TiO_2 (Degussa/Evonik), 80% anatase, 20% rutile and aqueous suspension concentration is 25 mgL^{-1}) is 756 nm (Suttiponparnit et al., 2011). However, hydrodynamic particle size distribution was not presented and discussed. The study covered a comprehensive number of TiO_2 specimens prepared by various methods and solution properties were varied according to the IS effects, surface area variations and zeta potential conditions. The outcome of this study could be considered as intra-calibrated system results open to closed system comparison.

Another study published by Carbajo and colleagues for HDS of TiO_2 (P-25, Aeroxide, 86% anatase, 14% rutile, aqueous suspension concentration is 250 mgL^{-1}) reported the volume-weighted HDS range in monomodal distribution as 500 nm - 10000 nm. Sonication for 1 h was applied prior to the DLS measurements, (Carbajo et al., 2018). Moreover, polydispersity of the system was not considered as an important parameter in determination of particle size via aforementioned DLS methodology.

Table 1.3. Physicochemical properties of TiO_2 NPs sited in literature review, between the years 2009-2023, of DLS measurements.

Nanoparticle	Crystalline Size, nm	Surface Area, BET, m^2g^{-1}	SEM/TEM	Reference
TiO_2 P25 Aeroxide, Evonik 86% anatase, 14% rutile	-	-	-	Budarz et al., 2017
TiO_2 P25 Aeroxide, Evonik 86% anatase, 14% rutile	Anatase, 21, XRD Rutile, 33, XRD	55.00	1-2 μm aggregate size, SEM	Carbajo et al., 2018
TiO_2, Sigma-Aldrich, 99.7% anatase	Anatase:<25, TEM	45.00-55.0	14 – 28 nm, TEM	De Silva and Pathiratne, 2023
TiO_2, US Research Nanomaterials Inc., 99% anatase	Anatase: 20, TEM	-	20 nm, TEM	Frazier et al., 2023
TiO_2 P25, Degussa, 80% anatase, 20% rutile	25, XRD	57.40	-	Jiang et al., 2009
TiO_2 P25, Degussa, 80% anatase, 20% rutile	27, XRD	57.40	-	Suttiponparnit et al., 2011
TiO_2 P25 Aeroxide, Evonik 86% anatase, 14% rutile	Anatase, 21, XRD Rutile, 33, XRD	54.00	-	Tolosana-Moranchel et al., 2021
TiO_2, sol-gel synthesized, 82% anatase, 18% rutile	Anatase, 25.74, XRD Rutile 31.52, XRD	30.32	150-220 nm cluster size, SEM	Wang et al., 2017
TiO_2 P25, Evonik Degussa 70% anatase, 30% rutile	28.2, XRD	53.8	-	Wu and Choi, 2016
TiO_2, Ishihara Sangyo Kaisha, Ltd., 100% anatase	7, XRD	290	10±2 nm, TEM	Wu et al., 2017

Table 1.4. Literature review of DLS measurements of TiO_2 NPs between the years 2009-2023.

Nanoparticle	Hydrodynamic Particle Size	Instrument	Experimental conditions	Reference
TiO_2 P25 Aeroxide, Evonik 86% anatase, 14% rutile	Number-weighted HDS range, monomodal distribution, 50 – 150 nm Voume-weighted HDS range, multi size distribution, 50-150 nm and 200-1000 nm	Mastersizer 3000, Malvern Instruments	Conc: 40 mgL^{-1} Solvent: DI water	Budarz et al., 2017
TiO_2 P25 Aeroxide, Evonik 86% anatase, 14% rutile	Volume-weighted HDS range, monomodal distribution 500 nm – 10000 nm	Mastersizer S, Malvern Instruments	Conc: 250 mgL^{-1} Solvent: Milli-Q water Pretreatment: Sonication, 1h	Carbajo et al., 2018
TiO_2, Sigma-Aldrich, 99.7% anatase	Intensity-weighted average HDS, 0.1 mgL^{-1}, 478 nm 0.5 mgL^{-1}, 825 nm 1.0 mgL^{-1}, 1718 nm	ZetaSizer Nano ZS, Malvern Instrument	Conc: 0.1, 0.5, and 1.0 mgL^{-1} Solvent: DI water	De Silva and Pathiratne, 2023
TiO_2, US Research Nanomaterials Inc. 99% anatase	Intensity-weighted HDS range, monomodal distribution, 180-600 nm Intensity-weighted average HDS, monomodal distribution, 290 nm	N5 Submicron ParticleSize Analyzer, Beckman Coulter	Conc: 25 ppm Solvent: Milli-Q water pH: 8.12	Frazier et al., 2023
TiO_2 P25, Degussa, 80% anatase, 20% rutile	Intensity-weighted average HDS, monomodal distribution, 90 nm Intensity-weighted HDS range, monomodal distribution, 30-500 nm	ZetaSizer Nano ZS, Malvern Instrument	Conc: 50 – 200 μgml^{-1} Solvent: DI water + 0.005 $Na_4P_2O_7$	Jiang et al., 2009

Table 1.4. Literature review of DLS measurements of TiO_2 NPs between the years 2009-2023. (Continue).

TiO_2 P25, Degussa, 80% anatase, 20% rutile	Intensity-weighted average hydrodynamic diameter, 756 nm	ZetaSizer Nano ZS, Malvern Instrument	Conc: 25 mgL^{-1} Solvent: DI water	Suttiponparnit et al., 2011
TiO_2 P25 Aeroxide, Evonik 86% anatase, 14% rutile	Volume-weighted HDS distribution, 100 – 1000 nm	Mastersizer 3000, Malvern Instruments	Conc: 1.6 mgL^{-1} Solvent Milli-Q water	Tolosana-Moranchel et al., 2021
TiO_2, sol-gel synthesized, 82% anatase, 18% rutile	Number-weighted average HDS, monomodal distribution, 215.4 nm Number-weighted HDS range, monomodal distribution, 150-600 nm	ZetaSizer Nano ZS, Malvern Instrument	Conc: - Solvent: Milli-Q water	Wang et al., 2017
TiO_2 P25 Degussa, Evonik 70% anatase, 30% rutile	Intensity-weighted average hydrodynamic diameter, 633 nm	Horiba SZ-100, Horiba	Conc: 50 mgL^{-1} Pretreatment: Sonication, 30 mins. Solvent: DI water	Wu and Choi, 2016
TiO_2, Ishihara Sangyo Kaisha, Ltd., 100% anatase	Intensity-weighted average hydrodynamic diameter, 820 nm Intensity-weighted hydrodynamic range, 80-150nm, 800-1200 nm, 8000-9000 nm	Zetasizer Nano ZS	Conc: 15 mgL^{-1} Pretreatment: Sonication, 40 min. Solvent: DI water	Wu et al., 2017

1.6. Natural Organic Matter

Withering plant and animal material as well as byproducts of their deterioration are considered to be a part of the content of naturally occurring organic material in terrestrial habitats and aquatic systems and are named as natural organic matter (NOM). NOM can be divided into two categories by their production pathways *i.* aquagenic and *ii.* Pedogenic or terrestrial (Buffle, 1988). Aquagenic is the term used to define the decomposition product of aquatic organisms forming NOM and pedogenic refers to terrestrial sources. Due to the fact that most of the decomposition process occurs within soils and most biomass is contained in plant materials, pedogenic sources are considered to dominate the aquatic NOM. On the other hand, in eutrophic freshwater environments and marine water bodies, due to excessive biological production aquagenic NOM is generated over time. According to their transformation pathways NOM, is defined as *i.* allochthonous, materials transferred from the surrounding watershed, and *ii.* autochthonous, produced within the water body (Leenheer, 1981; Filella, 2009).

The most general approach in quantification of NOM that is present in both aquatic and as well as terrestrial systems is determination of the total organic carbon (TOC) content. TOC encompassed all organic matter excluding living organisms and synthetic compounds, and comprehensive elucidations were provided concerning the characteristics of various classes and their interconnection with chemically fractionated NOM (Buffle, 1984; Buffle,1988). The split of TOC into operationally defined fractions like dissolved organic carbon (DOC) and particulate organic matter (POC) can serve as the foundation for the most basic description of NOM.

POC denotes the portion of TOC retained on a 0.45 μm porosity membrane, whereas DOC denotes organic carbon with a diameter less than 0.45 μm (Thurman and Malcolm, 1981; APHA, 1998). Particles smaller than 0.45 μm are considered dissolved in aqueous suspensions. (Suffet and MacCarthy, 1989). DOC is further named as recalcitrant and/or refractory organic matter (RfOM) due to its physicochemical properties expressing resistivity to various degradation processes including microbiological pathways (Frimmel et al., 2008). The main component of NOM/DOC is defined as humic substances (HS). Imparting yellow color in aquatic environment, HSs are also known as Gelbstoff as well as chromophoric organic matter (CDOM) (Gjessing, 1976; Sonnenberg et al, 1988).

1.6.1. Humic Substances Definition and Formation

HS is a constituent of soils, sediments, and natural waters with its complex, polyelectrolytic structure and dark color. Depending on their origin heteropolycondense structure of HSs may contain carbohydrates, proteins, fatty acids lignins, tannins and many other materials (Gjessing, 1976) that forms the structure containing aromatic structures, carboxylic acids, phenols, quinones, and aliphatic chains (Gerke, 2018; Sonnenberg et al., 1988). Source of HSs are compiled in four different concepts:

1. Degradation and/or fraction of dead organic matter, mainly sourcing from plants and soil microorganisms (Suffet and MacCarthy, 1989; Leenheer, 1981; Leenheer et al., 1989; Thurman and Malcolm, 1981).
2. Formation of medium to higher molecular weight of organic substances but mainly humic framework by polymerization, reaction and polycondensation of residual organic molecules *i.e.,* phenols, phenylpropene units, amino acids, peptides, amino sugars, and sugars, partly catalyzed by soil oxidoreductases or mineral surfaces (Stevenson, 1994).
3. The complex formation of humic substances with inorganic soil components, clays, di- or trivalent cations (Ca^{2+}, Cu(II), Fe(III) or Al(III)), during and/or after formation of humic network (Boudot, 1992; Jones and Edwards, 1998; Gerke, 2010; Gerke, 2015). These structures are highly resistance to microbial degradation (Haider, 1992).
4. Structural model formation of HS by formation of inter and/or intra molecular bonding (Stevenson, 1994; Schnitzer, 1978; Schulten and Schnitzer, 1993; Engebretson and von Wandruszka, 1994; Engebretson et al., 1996).

HSs encompass a broad spectrum of organic compounds representing high-molecular-mass with molecular weights ranging from thousands to hundreds of Daltons and polyelectrolytic macromolecules (Gaffney et al., 1996). HSs also possess a carbon framework exhibiting a substantial degree of aromatic character, with a considerable proportion of their molecular mass attributed to functional groups, predominantly containing oxygen. The elemental composition of most HS falls within the following ranges: C, 45–55%; O, 30–45%; H, 3–6%; N, 1–5%; and S, 0–1% (Suffet and MacCarthy, 1989).

HSs demonstrate hydrophilic characteristics thereby displaying an affinity for water. HSs have the capacity to form colloidal suspensions and possess a propensity for self-association and aggregation, resulting in the creation of supramolecular structures (von Wandruszka et al., 1996). Furthermore, HSs are known to interact with a range of inorganic and organic compounds, including

metal ions, pesticides, and pharmaceuticals, through processes like adsorption and complexation (Schnitzer and Khan, 1972; Buffle, 1988; Stevenson, 1994; Hofrichter and Steinbüchel, 2001). Phenolic groups within HSs can undergo oxidation, leading to the formation of quinones. These quinones play pivotal roles in redox reactions, integral to the transformation and degradation of organic matter within natural systems (Leenheer, 1981; Thurman and Malcolm, 1981; Suffet and MacCarthy, 1989). HS can also react with several inorganic and organic pollutants in water bodies and sometimes reduce their toxicity. On the other hand, it can form harmful disinfection by products (DBP) during drinking water treatment with chlorination. HS, form trihalomethane (THM) and haloacetic acids, haloacetonitriles, haloketones, chloropicrin by reacting chlorine or bromine which are carcinogenic DBPs (Rook, 1974; Krasner et al., 1989; Reckhow et al., 1990; Nieuwenhuijsen, 2000). Besides chlorinated-, and brominated DBPs, recent studies showed that iodo-DBP's may also form which is also considered as carcinogenic compounds (Becalski et al., 2006; Dong et al., 2023). Furthermore, during soil digestion, HA may form dioxin derivatives which are also highly harmful to human health (Xie, 2023). For these reasons, removal of dissolved HS species from drinking water sources prior to disinfection is important. Several methodologies, *i.e.*, membrane filtration, enhanced coagulation (Liu et al., 2005), activated carbon adsorption, catalytic ozonation, ozone enhanced coagulation or ozonation (Singer et al., 2003; Bekbolet et al., 2005), photo(electro)catalysis (Selcuk, et al., 2003; Selcuk et al., 2004), are used for improvement of the water quality (Selcuk et al., 2011).

HSs are commonly classified according to their solubility. Upon extraction of a substance containing HSs using a strong base, the resulting solution is then acidified, ending up with the formation of three distinct products: *i*. fulvic acid (FA), an organic material that remains dissolved in the acidified solution *ii.* Humic acid (HA), a precipitate that separates from the acidified extract; and *iii.* Humin, a fraction of HS is not soluble in both alkali and acidic conditions; (Suffet and MacCarthy, 1989).

1.6.2. Fulvic Acid

FA is a crucial component of HSs with distinct properties and roles in various environmental contexts. Figure 1.10 illustrates the proposed model structure of FA and Figure 1.13 shows the postulated surface functional groups of FA (Buffle, 1988; Yang, 2003). FA, demonstrates solubility across a broad pH range, making it more readily soluble compared to other fractions of HSs. FA forms stable complexes with metal ions and plays a vital role in metal mobility and transport. Furthermore, FA is known for its ability to chelate and bind to organic and inorganic compounds,

affecting the bioavailability and fate of various substances in the environment (Rook, 1977; Reckhow et al., 1990).

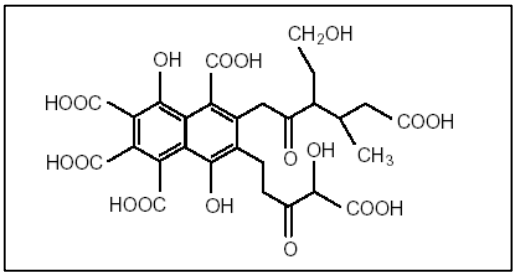


Figure 1.10. Postulated structure of FA (Buffle, 1988).

1.6.3. Humic Acid

HA, the acid-insoluble (pH<2) component of HS, is composed of several different structures depending on the medium pH with a polymeric nature and possesses a high molecular weight and is characterized by its dark color and colloidal nature. Solubility properties of HA in alkaline solutions serve as a distinguishing characteristic from FA. It exhibits various properties that contribute to its significance in environmental and agricultural contexts such as a natural soil conditioner, promoted soil fertility, nutrient retention, and high water-holding capacity so, it enhances the cation exchange capacity of soils, facilitating nutrient uptake by plants and reducing nutrient leaching. Additionally, HA influences the soil structure by improving microbial activity, and carbon sequestration, thereby impacting overall soil health and sustainability (Suffet and MacCarthy, 1989).

Figure 1.11 and Figure 1.12 show the postulated structure of model HA in water bodies and Figure 1.13 gives surface humic functional groups (Stevenson, 1994; Fetsch et al., 1998; Yang, 2003). HA represents a diverse group of negatively charged large structures with varying molecular weights, encompassing aromatic and aliphatic constituents that possess carboxylic and phenolic functional groups. In HA structure, oxygen is the main heteroatom, and it primarily appears in the functional groups as carboxylic phenolic and alcoholic OH, ketonic and quinoid C=O, and as ester/ether -OCH_3 groups. Functional groups in humic structures are either dissociated or protonated depending on the pH of the solution. HA has a fundamental structure characterized by aromatic rings, which can be di- or tri-hydroxy phenols, connected by various groups like −O−, −CH_2−, −NR−, −N=, −S−, and others. Additionally, they contain both free −OR groups and double bonds in the form of quinones. HA structure under neutral conditions is deprotonated, following in the order, strong acidic -COOH, pK_a

= 1.8; salicylic acid type-COOH, pK_a = 3.2; weak acidic COOH, pK_a = 4.2; and acidic alcoholic OH (enol) group pK_a = 5.7 (Stevenson, 1994). These carboxylic groups (pK_a ~4) and phenolic groups (pK_a ~10) may undergo deprotonation generating negatively charged sites resulting in substantial changes in macromolecular properties of HA. When the phenolic and/or carboxylic groups are deprotonated, HA structure stretches due to electrostatic repulsions between nearby negatively charged regions. Consequently, HA structure alters from having a big, flexible, linear shape at high pH, low ionic strength, and low humic concentration to having a small, rigid, and sphero-colloidal conformation at low pH, high ionic strength, and high concentration (Ghosh and Schnitzer, 1980). Additionally, factors like ionic strength, and existence of cationic species, are also effective on electrostatic forces. The reactivity of HA toward components within natural aquatic systems is primarily influenced by the chemistry of these functional groups and the microstructure of HA (Suffet and MacCarthy, 1989).

Humic matter cannot be regarded as single chemical entities described by unique, chemically defined molecular structures. HA displays polydisperse character due to the presence of diverse molecular size fractions. Based on the definition of DOC composed of organics passing from 0.4 mm membrane filter, further size fractionations are in the range from several kDa unites to even smaller fractions < 500 Da. With respect to the complex polymeric structure composed of various discrete molecular size fractions, heterogeneity of HA poses as significant effect in all environmetally important processes.

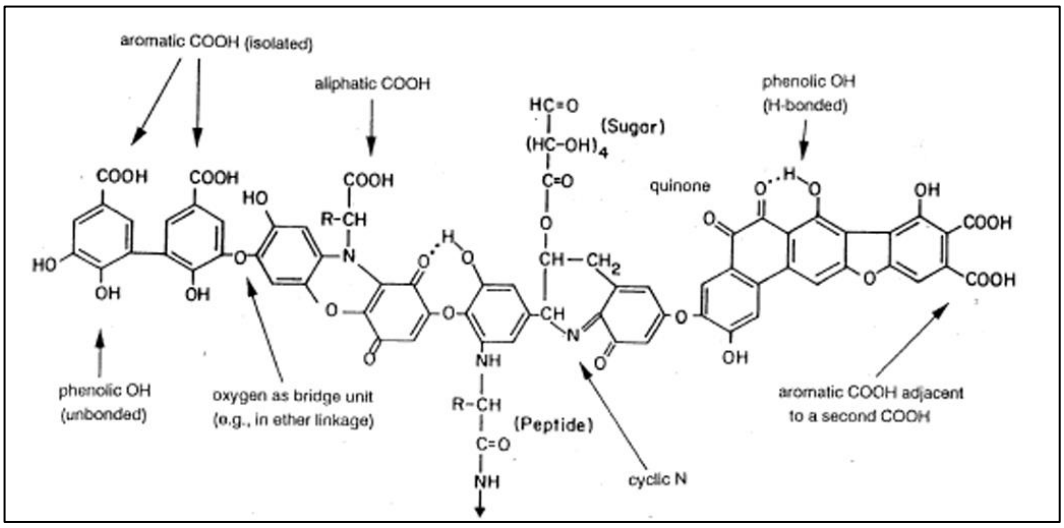


Figure 1.11. The postulated structure of the HA (Stevenson, 1994).

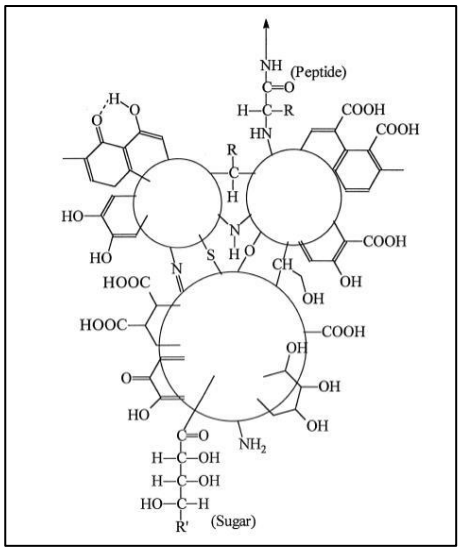


Figure 1.12. The hypothesized configuration of the HA (Fetsch et al., 1998).

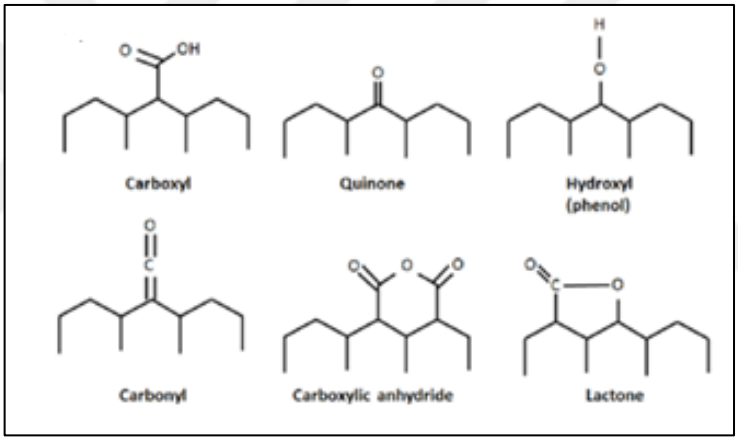


Figure 1.13. Postulated surface functional groups of HA and FA (Yang, 2003).

The degree of molecular weight distribution and hydrophobic/hydrophilic fraction ratio also affects the interaction of HA with surrounding moieties. Determination of molecular weight distribution by high performance size exclusion chromatography (HPSEC) is a widely used method. The methodology is based on the affinity of HA subfractions to mobile phase and stationary phase. While larger particles move with the mobile phase, smaller particles penetrate the pores of the gel that performs as stationary phase. Results of HPSEC also give information about the charge, molecular structure, stearic effects, and hydrophobicity of HA structure (Uyguner et al., 2007). Considering that HA is an ill-natured complex organic matter composed of various molecular size fractions, the “polydispersity” term is widely used to emphasize its diverse range of molecular sizes and structural heterogeneity.

Various model structures have been proposed to represent the potential arrangements of functional groups and chemical moieties within HA. Although structural study of humic material is challenging due to its complex polymeric nature and interactions between component chains, compositional information can be achieved via elemental and functional group analysis. Multiple structural models for HA have been posited to facilitate a more profound comprehension of interactions within aquatic environments. These models are predominantly based on variables encompassing the source of HA, prevailing environmental conditions, and the pH of the solution medium. Due to the heterogeneity of surface groups, *i.e.*, -COOH, -OH, -C=O and -NH_2, and hydrophobic groups such as long alkyl chains and fatty acid residues, uniform behavior of HA structure cannot be expected. However, theoretical structures are purposed to explain the homo- and hetero-interactions of HA in aquatic media. Solubility properties of HA in aqueous media also have great importance to postulate HA structure and understand the interaction between HA and other solutes. At low pH values *i.e.,* pH ≈ 4, H^+-exchanged HA structure shows the physicochemical properties of neural polymers such as having significant amount of hydrogen bonding. Upon raising the pH to alkaline levels, the acidic groups undergo dissociation, thereby resulting in the emergence of polyelectrolytic properties. These properties encompass superior water solubility, enhanced capacity for swelling and binding significant volumes of water, and increased tendency to engage in robust interactions with surfaces and macromolecules with opposite charges (Aiken et al., 1985). Natural aqueous media comprises not only the dissolved organics such as HA and FA, but also dispersed particles *e.g.*, clays, metals and metal oxides. In aqueous systems metal oxide particles are in hydrated form and their surface is covered with Metal-OH (Me-OH) groups. This hydrous metal-oxide shows amphoteric character, and the Me-OH surface can react with H^+ and OH^- ions from dissolved acids of bases (Cornell and Schwertmann, 1996; Tombácz, 2002). This mechanism is also effective on HA adsorption onto metal/metal oxide surfaces. The capacity of HA to create complexes with metal ions is based on their abundant presence of oxygen-containing functional groups, such as COOH, phenolic-alcoholic, enolic-OH, and diverse C=O structures as well as amino groups (aniline derivatives are deprotonated between the pK_a 4.9 and 12.1) (Busschaert et al., 2014). At acidic pH conditions a reduction in proton adsorption occurs and this reduction leads to deviation from the combined adsorptive effects attributed to a decrease in available proton-binding sites on HA, thus adsorption onto metal/metal oxide surface decreases. Conversely, at relatively alkali pH levels, proton adsorption transpires at the metal/metal oxide surface increases. This is a consequence of the adsorbed HA effectively shielding the positive electric field of the metal oxide (Vermeer and Koopal, 1999; Vermeer et al., 1999). Consequently, discussion on HA structure should be made by considering the pH of the surrounding medium, the presence of electrolytes, and the various other structures present within the medium. It is important to note that these models represent simplified representations of

the complex and heterogeneous and polydisperse nature of HA. The actual HA structure is likely to be a combination of these model and the structures fluctuating to adapt to the media.

1.6.3.1. Micelle Structure: suggests that HA can form micellar structures in aqueous solutions. These micelles are formed through the association of hydrophobic regions, such as aromatic rings and aliphatic chains, which are enclosed by hydrophilic groups on the surface (Sposito et al., 1982). The micellar model of HA is developed as a result of research into the ionic exclusion and specific adsorption effect interactions that also encourage supramolecular associations. The HA structure comprises elongated hydrophobic fraction with one or more anionic *i.e.*, carboxylate groups attached at the end. In acidic aqueous conditions this structures coalescence to surfactant resembling moieties combined with supramolecular interactions such as van der Waals forces, π-π stacking, hydrogen bonding, metal-ligand coordination, electrostatic forces, and host-guest relations (Wershaw, 1986). High quantities of HA cover the whole surface of the interface, replacing the water surface layer with a hydrocarbon monolayer and creating a "Langmuir stockade". The Langmuir structures exhibit a spiral morphology, wherein their axes frequently orientate towards the surface of the material during adsorption onto another surface in acidic conditions (Hesselink, 1969). The arrangement and folding of HA results in structures resembling surfactants. The aggregation of these structures leads to the formation of micelles. Micelle structure formation also explains the detergent properties of HA (von Wandruszka, 1998). Macromolecular micelles are created as a result when the concentration of HA in the system reaches a critical point. These micellar structures loss the surface activity and do not contribute to a further lowering of the surface tension of the solvents at the phase boundary and this interaction is independent from the source of HA (Dmitrieva et al., 2015). It is proposed that NOM has glassy and rubbery domains, analogous to the polymer theory. While glassy domains are made up of fairly stiff and unyielding strands that are restricted in their mobility by closely spaced side chains, rubbery domains are characterized by highly flexible polymer chains. Slow desorption, linear sorption, and sorption/desorption hysteresis are thought to be caused by glassy domains, whereas higher diffusion rates, linear sorption, partitioning-like processes and non-Fickian diffusion may be caused by rubbery domains (Huang and Weber, 1997). In aquatic systems, diffusion of HA can be explained as linearly advancing sharp boundaries of dispersed swollen and un-swollen regions. This sharp front, indicative of non-Fickian diffusion, steadily progresses into the polymer like structure at a constant velocity, resulting in a linear increase in the absorbed fluid amount over time (Rehage et al., 1970). These interactions form the basis of micelle formation of HA. Under neutral to acidic pH conditions, HA tends to form micellar structures more frequently than under basic circumstances, and FA forms the micellar structures more quickly than HA (Sutton and Sposito, 2005). Dispersion of HA micelle structure increases in aquatic medium in alkali solutions due to the ionization of more

acidic groups. This ionization increases the surface charge and disrupts the surface interactions which leads to formation of smaller micelle-like structures. Increasing the dispersion of HA through a rise in pH levels facilitates the extraction of humic materials from aquatic environments employing alkaline solutions (Wershaw, 1986).

1.6.3.2. Pseudo micelle structure: Intramolecular aggregates are expressed by pseudo micelle structure structures (Rochus and Sipos, 1974; Wershaw, 1986). The formation of micelles depends on critical micelle concentration (CMC), the concentration spontaneous aggregation occurs to form micellar assemblies. The reported CMC of Aldrich HA (12.3 gL^{-1}, dissolved in NaOH, pH: 12.3±0.2) is approximately 7.4 gL^{-1} (Guetzloff and Rice, 1994). However, in dilute solutions of HA regardless of CMC, micelle-like formations can be formed that called pseudo micelle structure (Engebretson and von Wandruszka, 1994; Engebretson et al., 1996). HA pseudo micelle structure arises through self-assembly of its constituent molecules. The presence of an aromatic carbon framework in HA promotes the development of hydrophobic regions, while the incorporation of polar functional groups facilitates the formation of hydrophilic regions. Consequently, these distinct hydrophobic and hydrophilic domains within HA molecules enable their assembly into micelle-like accumulation. This accumulation is made feasible by the long and flexible *i.e.*, hydrocarbon chains of humic polymers and enable them to fold and coil in a way that keeps more hydrophobic, aromatic hydrocarbons, moieties isolated in the core and directs hydrophilic groups, carboxy and hydroxy, outward. This structure could be carried out with a single polymer chain, resulting in an object that functions similarly to a typical micelle but is more restricted structurally (von Wandruszka, 2000). Figure 1.14 illustrates the computed structure of the proposed pseudo-micelle structure of HA (Schulten, 1995). The pseudo-micelle structure of HA not only affects its solubility and interactions with other molecules but also influences its behavior and function within various environmental processes (von Wandruszka et al., 1996).

The white dots presented in Figure 1.14 representing the Hydrogen (H) atoms, the grey dots were carbon (C) atoms, and the black dots were the nitrogen (N) atoms. The computed pseudo micelle structure (Schulten, 1995) showed in the Figure 1.14 was mostly composed of a non-spherical structure with a dense aromatic core and aliphatic tails on the surface. The presence of these aliphatic tails actively played role during the surface adsorption onto other structures,

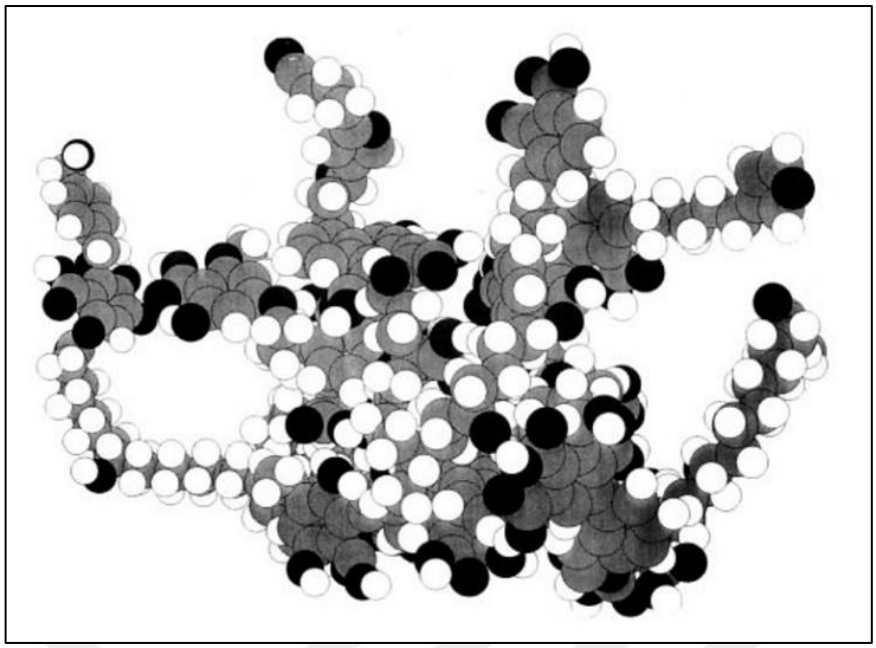


Figure 1.14. The computed pseudo-micelle structure of HA. White dots: Hydrogen, Grey dots: Carbon, Black dots: Nitrogen (Schulten, 1995).

The pseudo-micelle arrangement provides the best isolation for HA structures, according to fluorescence measurements of hydrophobic probes trapped by the pseudo-micelles (Engebretson and von Wandruszka, 1994). Also, it has been stated that when HA treated (*e.g.*, photocatalysis), formed short humic sub-fractions are found to be insufficient to create efficient pseudo-micelles as evidence by fluorescence spectroscopic methods (Engebretson and von Wandruszka, 1997).

1.6.3.3. Core-shell model: Another proposed model is the "core-shel" structure, which posits that HA consists of a hydrophobic core surrounded by a hydrophilic shell. The core is believed to contain aromatic structures and aliphatic chains, while the shell is enriched with polar functional groups such as carboxylic acids and phenols (Guggenberger et al., 1994). Also, HA/FA adsorption onto metal oxide surfaces is explained with the core-shell model (Yang et al., 2012; Mendez and Hiemstra, 2020). The metal oxide aggregate constitutes the central core, enveloped by the outer shell comprised of HA and/or FA. The physicochemical characteristics and sorption behaviors of metal oxides can be increased by the relatively high binding of HA and/or FA to such materials (Illés and Tombácz, 2003). In addition, under physiological conditions, the humic shell provides essential colloidal stability and creates active sites for core particles (Tóth et al., 2014). HA structure consists of rubbery, flexible, chains and glassy, rigid, parts depending on the physico-chemical structure, the sorbing molecule concentration and the temperature of the media. It has been postulated that within terrestrial-based

HA, the proportion of glassy chains diminishes concomitantly with the enhancement of rubbery chains, spanning the temperature range from ambient conditions to temperatures exceeding 70°C (Schaumann and Antelmann, 2000; DeLapp and LeBoeuf, 2004). The concept of the glassy state can be simplified by envisioning it as characterized by two distinct sorptive regions. A 'hole-filling' domain, composed of molecular-scale pores (resembling tiny holes), dispersed within a surrounding ''dissolution'' domain, which constitutes a more fluid-like matrix and constitutes the predominant portion of the solid phase. The existence of these voids signifies a lasting state of imbalance within the solid, resulting from the matrix resistance to attaining full thermodynamic relaxation due to the rigidity of its macromolecules. Glassy solid sorption is frequently modeled using the dual-mode model (DMM). The DMM encompasses a nonlinear component to characterize hole-filling and a linear component to elucidate the dissolution of the solid phase. Nonlinear, competitive, and irreversible sorption phenomena are linked to the hole-filled domain. This glassy structure composes the walls of cavity, however rubbery regions still exist in the HA framework. Considering that there is no compelling evidence to suggest a significant chemical distinction between the composition of the hole walls and that of the overall solid-like structure, the pronounced affinity for hole locations stems from the preexisting presence of an empty space within the nonpolar HA moieties, ready to accommodate the incoming sorbent. Conversely, the formation of a cavity for dissolution sites necessitates the separation of HA chains, incurring a free energy consumption in natural pH conditions. Figure 1.15 shows the proposed theory of deformation occurring within the glassy chain of HA. This deformation leaves an irreversible volume in HA structure by the incoming sorbate. This sorbate can be another humic structure, metal oxide aggregate, clay or any other resembling structures in aquatic media (Lu and Pignatello, 2004).

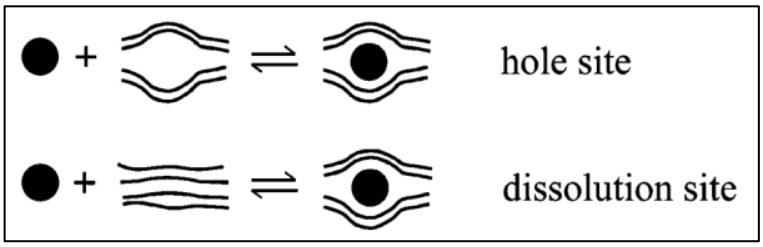


Figure 1.15. The representation of the deformation process occurring within the glassy chain of HA (Lu and Pignatello, 2004).

1.6.3.4. Random coil model: One commonly used model is the "random coil" or "stochastic assembly" model, which suggests that HA is an amorphous polymer formed through the random association of different organic components. This model emphasizes the flexible and disordered

nature of HA, with interactions between functional groups occurring in a stochastic manner (Wershaw, 1993; Swift, 1996). Humic coil structures are bound together by weak H-bonds and hydrophobic interactions that explain unsuccessful attempts to extract monodisperse fractions from humic solution (Piccolo and Conte, 2000). The vast variety of molecular weight fractions will be accompanied by a corresponding variance in molecular size, but this will also rely on the conformational state of the molecules. It has been argued that the random coil shape is the most suitable model for macromolecular conformation for HSs. The random coil model also takes into account the disordered chemical structure of HA, solubility and solution characteristics, and charge characteristics (Swift, 1989).

1.6.3.5. Train-loops-tail model: In the environmental systems, HA has a strong affinity for the soil mineral surfaces and soil clays. Mostly with the Al-OH and Fe-OH, that formed on the metal (hydr)-oxide surfaces, the exterior part of clay mineral and deprotonated functional groups for example carboxyl and phenolic hydroxyls of HA forms interactions at the mineral water interface. These aquatic systems form the heterogeneous mixtures of polyelectrolytes and the “train-loops-tail model” or “umbrella effect” explains the sorption of HA onto these heterogeneous mixtures of polyelectrolytes. The sections in direct proximity to the surface are denoted as "*train”* while “*loop”* refers to segments not directly linked to the surface but connected at their extremities to the trains. Lastly, the term “*tail”* designates segments linked to a train at one end but devoid of direct surface connection. Figure 1.16 illustrates the possible sorption formations onto a solid matrix. Even the (hydr)-oxide surface is also heterogeneous, it is negligible in comparison to the HA active site heterogeneity therefore, the model excepts the solid matrix as a reactive surface with a surface having one type of sorption site that can adsorbed by different molecules (Fleer et al., 1993). Considering the more rigid structure of lower molecular weight structures, occupied sites on the solid matrix are limited, however, higher molecular weight structures can bind to the solid matrix in several ways and form structures resembling loops and tails. Due to the electrostatic interactions between the disparately charged segments, “trains-loops-tail” can account for the adsorption of HA on the metal oxide surface. Owing to intra-molecular electrostatic repulsive interactions, charged HA macrostructures are thought to have relatively stretched morphologies (and a large hydrodynamic radius) in neutral pH circumstances (Fendorf et al., 1997; Jardine et al., 1999). The occupied sites by larger molecular weight structures can vary in time and might be one or more than one. On the other hand, because of the stearic hindrance additional sites may be occupied in addition to those used for direct binding.

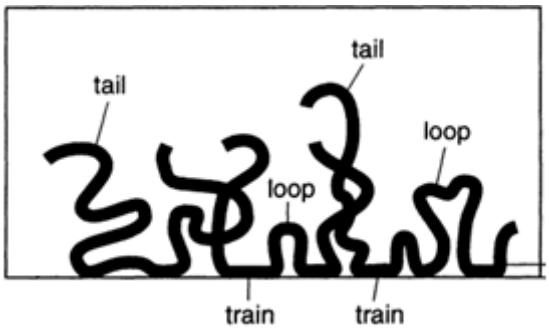


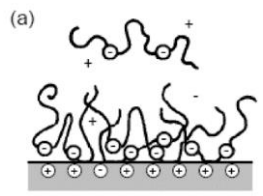
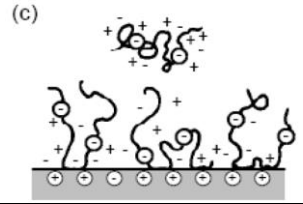
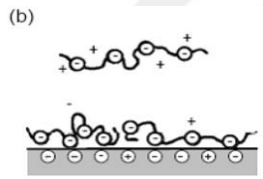
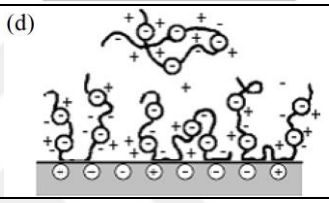
Figure 1.16. Sorption of HA onto solid matrix in 2-D as train, tail and loop structures (Fleer et al., 1993).

Natural water composition contains various inorganic compounds *i.e.*, CO_2, CO_3^{2-}, HCO_3^-, SO_4^{2-}, Cl^-, Ca^{2+}, Mg^{2+}, Na^+, K^+, metal (hydro)-oxides, and clays. An illustrative depiction of the HA adsorbed layer under different circumstances with the interaction of this inorganic compounds can be observed in Table 1.5. The polyelectrolyte is considered to possess a negative charge, while the surface charge density of the adsorbent remains constant. In the images (a) and (b) (Table 1.5. (a) and (b)), the scenarios are observed that with low ionic strength solutions the electrostatic forces predominantly govern adsorption. Within the acidic pH region (indicative of a low polymer dissociation degree), the polymer-like HA structure undergoes slight ionization, displaying minimal intrapolymer-chain electrostatic repulsion and adopting a coiled conformation. Notably, increase in adsorption is commonly witnessed in this pH range, attributed to the smaller size of the adsorbate due to the coiled conformation (Table 1.5. (a)). Conversely, at a basic pH range, the adsorbed quantity diminishes due to polyelectrolyte ionization, resulting in negative charges within the polymer chain and reduced coiling. Consequently, a smaller portion of the polymer-like HA structure is required for complete surface coverage (Table 1.5. (b)). Figures (c) and (d) in Table 1.5. showing the adsorption corresponding to high ionic strength, both the adsorbed amounts and the polymer-like HA structure conformations remain consistent. This uniformity arises from the screening of charges associated with the polyelectrolytes by the electrolyte ions, causing the polyelectrolyte molecules to adopt a tightly coiled and compact conformation in the solution (Fleer et al., 1993).

Considering all the information presented above, proposed structural models also must be elucidated with respect to the molecular size distribution of HA. As indicated in pseudo micelle and core-shell models, there are distinct hydrophilic and hydrophobic sections within HA. These structural models suggest that internal aggregation is essential for the formation of HA structure. However, the random coil, micelle, and train-loop-tail models propose that intra-structural aggregation/agglomeration also occurs. Notably, the random coil model posits that

aggregation/agglomeration results in a unique structure. Nevertheless, this model does not provide a comprehensive explanation for the interactions between metal ions or other potential molecular interactions involving HA and the surrounding media.

Table 1.5. Illustrative depictions of polyelectrolytes at the surface are presented, representing different conditions pertaining to polymer charge density and ionic strength (Fleer et al., 1993).

	Low ionic strength	High ionic strength
Low pH value		
High pH value		

1.6.3. Humins

Humins are typically insoluble in both acidic and alkaline conditions, displaying a higher molecular weight and more resistant nature compared to HA and FA (Thurman and Malcolm, 1981; Stevenson, 1994). Because of their more stable and persistent nature, humins contribute to the long-term retention of carbon in soils and sediments. Due to their insolubility, humins can serve as depot for organic carbon, storing it over extended periods. Their presence in natural environments impacts soil fertility, nutrient cycling, and the overall carbon equilibrium. Comprehending the composition and behavior of humins is vital for unraveling the intricate dynamics of HSs and their implications in ecosystem processes (Stevenson, 1994; Suffet and MacCarthy, 1989).

2. MATERIALS AND METHODS

2.1. Materials

2.1.1. TiO_2 Nanoparticles, Preparation and Characterization

TiO_2, P25 was purchased from Evonik. Fe-doped TiO_2 (Fe-TiO_2) nanoparticles were synthesized using $Fe(NO_3)_3.9H_2O$ as the Fe^{3+} source according to the procedure presented by Yalçın and colleagues (Yalçın et al., 2010). An incipient wet impregnation method was applied to prepare N-doped TiO_2 (N-TiO_2) using appropriate amount urea as the N source (Gurkan et al, 2012). Morphological properties were characterized by X-ray diffraction (XRD), scanning electron microscopy (SEM) with subsequent elemental analysis (EDX) and atomic force microscopy (AFM) techniques whereas specific surface area, pore size and pore volume of nanoparticles were determined by BET (Brunauer, Emmet and Teller) measurements. Band gap energies of bare and doped nanoparticles were calculated from UV-Vis DRS analysis (Yalçın et al., 2010; Birben et al., 2017). Detailed information on the preparation methodologies as well as characterization techniques were presented in the Results and Discussion Section under related sub-sections to provide a comprehensive basis for comparison.

2.1.2. Humic Acid

HA was supplied form Aldrich. Humic acid solution was prepared by dissolving1.0 g HA into 1 L of ultra-pure water and mixed with magnetic stirrer to obtain a homogeneous 1000 mg/L stock solution followed by filtration through 0.45 μm Millipore cellulose acetate membrane filters. Working 50 mgL^{-1} HA solution was prepared by dilution (Birben et al., 2015). Total dissolved organic contents (DOC, mgL^{-1}) of all HA solutions were determined with a TOC analyzer (Shimadzu VWP Total Organic Carbon analyzer). UV-vis absorption and fluorescence techniques were employed for the elucidation of spectroscopic properties of HA. Detailed information on humic acid properties determined under all conditions were presented in Section .3.1.

Ultrapure water *i.e*. Milli-Q water was used for preparation of all solutions.

2.2. Instrumentation

2.2.1. Solar light simulator:

Solar light-initiated experiments were performed according to the procedure reported by Birben and colleagues (Birben et al., 2015). Solar photocatalytic degradation experiments were carried out in an Atlas-Suntest CPS+ SolarBox solar simulator using the light source is an air-cooled Xenon lamp (wavelength range, λ= 290 to 800 nm, light intensity, I_o=250 W/m^2 and I_o = 1.67 μE/min). The solar simulator was equipped with quartz and UV special glass filters to simulate typical outdoor sunlight irradiation time (0-120 min with 10 min intervals).

2.2.2. Dynamic light scattering instrument:

Hydrodynamic particle size analysis was performed by a Brookhaven 90Plus Particle Size Analyzer equipped with a 633 nm laser source using a 5 mL polystyrene cuvette. The detection angle was set as 90^o and all measurements were taken at room temperature. The refractive index value was adjusted as 1.0.

General laboratory equipment *i.e.,* magnetic stirrer and ultrasound instrument as well as all other apparatuses were utilized where necessary.

2.3. Treatment Conditions and Methodology

2.3.1. HA Treatment Conditions

HA solution was subjected to the following procedures;

2.3.1.1. HA Photolysis; HA solution was subjected to solar irradiation using Solar Box ATLAS Suntest CPS+ instrument for 60 minutes.

2.3.1.2. HA - TiO_2 photocatalysis: HA was subjected to TiO_2 photocatalysis for 30 minutes under simulated solar irradiation using Solar Box ATLAS Suntest CPS+ instrument and filtered through 0.45 μm Millipore cellulose acetate membrane filter to separate photocatalytically degraded HA.

2.3.2. Nanomaterial Treatment Conditions

2.3.2.1. TiO_2 "as-is": Aqueous solution of 0.25 $mgmL^{-1}$ TiO_2 in Milli-Q water was sonicated 1 minute, followed by 4 minutes mixing with a magnetic stirrer.

2.3.2.2. TiO_2 dispersed under dark condition: 0.25 mg/mL solution of TiO_2 in ultra-pure water was sonicated for 1 minute to obtain a homogeneous mixture and mixed for 4 min with a magnetic stirrer as indicated for the $TiO_{2,as\text{-}is}$ preparation. The sample was kept mixing with a magnetic stirrer under dark condition in solar simulator for 60 minutes to provide the same conditions with solar light irradiated samples.

2.3.2.3. TiO_2 exposed to solar irradiation: Aqueous solution of 0.25 mg/mL TiO_2 in ultra-pure water was sonicated for 1 minute to achieve a homogeneous mixture and mixed for 4 min with a magnetic stirrer as in the $TiO_{2,as\text{-}is}$ preparation The obtained solution was exposed to simulated solar irradiation for 60 min.

Thus, obtained samples were defined as follows:

Mono system:

1. $TiO_{2,as\text{-}is}$; as prepared.
2. $TiO_{2,dark}$: mixing 60 minutes in Solar Box under dark conditions.
3. $TiO_{2,irr}$; mixing 60 minutes in Solar Box under similar photocatalytic treatment conditions.
4. $HA_{,as\text{-}is}$; as prepared.
5. $HA_{,pho}$; HA exposed to solar irradiation in Solar Box for 60 minutes.

Binary system: TiO_2 nanoparticles were directly dispersed in HA solution.

1. $(HA\text{-}TiO_2)_{as\text{-}is}$; as prepared.
2. $(HA_{pho}\text{-}TiO_2)$; HA photolytically treated in Solar Box for 30 minutes, then mixed with TiO_2.
3. $(HA - TiO_2)_{photocat}$; HA photocatalytically treated with TiO_2 in Solar Box for 30 minutes.

The above given systems were also applied to Fe-TiO_2 and N-TiO_2.

2.3.3. Treatment Methodology

Hydrodynamic size measurements of all defined samples (Section 2.3.2.1., 2.3.2.2 and 2.3.2.3) were performed using the dynamic light scattering instrument as indicated in Section 2.2.2.

Complementary to HDS measurements, sedimentation profiles of all samples were also considered. Sedimentation experiments were performed by time resolved optical absorbance measurements under specified experimental conditions. Aqueous nanoparticle suspensions of mono- and binary systems were sonicated for 1 minute and stirred for 4 minutes using a magnetic stirrer. UV-vis absorbance scan was recorded in the wavelength of 200-600 nm using quartz UV-vis cuvette with optimal path length of 1.0 cm every 30 min for a total duration of 2 h. Shimadzu UV-100 instrument was used. All sedimentation data were derived from a previously conducted MSc thesis (Sağlık, 2022).

3. RESULTS AND DISCUSSION

3.1. Humic Acid – Mono System

3.1.1. UV-vis Absorption and Fluorescence Spectroscopic Properties of Humic Acid

Under all conditions, UV-vis absorption and fluorescence spectral features of HA solutions were elucidated for comparative characterization of the organic matrix in relation to the expected hydrodynamic size variations. UV-vis spectroscopic parameters were $Color_{436}$, UV_{365}, UV_{280} and UV_{254}, regarding the absorbance recordings at 436, 365, 280 and 254 nm respectively as recorded by UV–vis spectrophotometry (Perkin Elmer lambda 35). UV-vis absorbance at 436 nm represented color forming moieties of organic matter; UV_{365} was related to the conjugated systems and related components, whereas UV_{280} was designated to the core aromatic UV absorbing centers (Korshin et al., 1997; Zhang et al., 2016). UV_{254} parameter was accepted as a surrogate parameter to dissolved organic carbon (DOC, mgL^{-1}). Synchronous scan fluorescence spectra were measured in the excitation wavelength range of 200-600 nm with the bandwidth of $\Delta\lambda$=18 nm between the excitation and emission monochromators (FI_{syn}) using Perkin Elmer LS 55 Luminescence Spectrometer. Specific UV absorbance parameters were described as SUVA ($Lm^{-1}mg^{-1}$) was a representative of DOC normalized aromatic or color forming moieties. $SUVA_{254}$ and $SUVA_{280}$, were indicators of total aromaticity due to π-π* transitions in the 270-280 nm region attributed to the presence of phenolic arenes, benzoic acids, aniline derivatives, polyenes and polycyclic aromatic hydrocarbons with two or more rings. $SUVA_{365}$ was related to the molecular size heterogeneity and $sCoA_{436}$ signified the DOC normalized color forming moieties (Traina et al., 1990, Chin et al., 1994; Langhals et al., 2000; Johnson et al., 2002; Hua et al., 2020). Moreover, a ratio of A_{254}/A_{365} displayed molecular size dependent aromatic moiety distributions (Peuravuori and Pihlaja, 1996).

Besides mono-humic condition, since hydrodynamic size variations of the specified binary systems would mostly be dependent on the humic properties, understanding of indicative parameters would hold prime importance. Under all conditions, all mentioned humic parameters were determined and presented in Table 3.1.

Table 3.1 shows the UV-vis and fluorescence spectral parameters as well as DOC of bare HA ($HA_{,as\text{-}is}$), photolytically treated (HA_{pho}) and photocatalytically treated humic acid ($HA_{photocat}$).

Table 3.1. Spectroscopic parameters and DOC of HA under the specified conditions.

	Specified UV-vis parameters				DOC, mgL^{-1}
HA	$Color_{436}$	UV_{365}	UV_{280}	UV_{254}	
Initial	0.080	0.166	0.388	0.451	4.80
Photolysis	0.069	0.146	0.353	0.416	4.53
Photocatalysis	0.001	0.002	0.011	0.013	1.12

	Specific UV-vis parameters, $Lm^{-1}mg^{-1}$				A_{254}/A_{365}	SFI_{syn}
HA	$SCoA_{436}$	$SUVA_{365}$	$SUVA_{280}$	$SUVA_{254}$		
Initial	1.670	3.450	8.080	9.41	2.71	1.17
Photolysis	1.520	3.220	7.790	9.18	2.85	1.08
Photocatalysis	0.089	0.179	0.981	1.16	6.50	1.25

Photolytic treatment led to minor removal (<5%) of DOC of HA, on the other hand DOC removal efficiency of photocatalytically treated HA was approximately 87%. Photocatalytic treatment removed all color forming moieties and conjugated systems, and mostly deteriorated core aromatic UV absorbing centers, while photolytic treatment slightly decreased of these parameters due to the charge localization effect. Photocatalytical treatment also caused a decrease of molecular size distribution of $HA_{,photocat}$ (Birben et al., 2017). Birben and colleagues reported that higher molecular size fractions (*i.e.,* 100 kDa, 30 kDa and 3 kDa) were degraded and/or transformed to lower molecular as 3 kDa sub-fraction. The decrease of $SUVA_{280}$ and $SUVA_{254}$ after photolytic treatment implied degradation of core aromatic groups via excitation of the conjugated bond systems upon UVA light region. Visible light absorbing moieties, functional groups with quinoid structures and keto-enol systems, are responsible for the alteration of $SUVA_{365}$ and $SCoA_{436}$. (Li et al., 2020). A_{254}/A_{365} ratio was used to elucidate the changes in aromaticity and molecular size (Peuravuori and Pihlaja, 1997). Increasing trend of A_{254}/A_{365} ratio indicated a decreasing trend of aromaticity per molecular size of HA as expressed by the following order: $A_{254}/A_{365,photocat} > A_{254}/A_{365,pho} > A_{254}/A_{365,initial}$. On the other hand, increase of A_{254}/A_{365} ratio of $HA_{,pho}$ in comparison to the $HA_{,as\text{-}is}$ showed that while molecular size nearly remained stable, charge localization caused increase of aromaticity. These results were also evidenced by the results of SFI_{syn} which was an indicator of changes in low molecular size fractions. Slight decrease in SFI_{syn} of HA_{pho} showed the changes in chemical structure excluding degradation, although photocatalytic treatment caused a remarkable shift lower molecular size region in fluorescence intensity (Table 3.1). By comparing $SUVA_{254}$ and SFI_{syn} results it could be deduced that HA chemical structure was altered by photolytic treatment, on the other hand photocatalytic treatment increased the number of lower molecular size fractions in the aqueous medium (Uyguner-Demirel et al., 2013).

3.2. Hydrodynamic Size Determination of Humic Acid

As stated previously, HA constitutes the major fraction of DOC (50-90 %) in natural waters (Rook, 1976; Bond et al, 2009). Almost all environmentally significant reactions take place due to the interactions of HA with other materials *i.e.*, clays, metals, metal oxides, microbial organisms, etc. Due to the ill-defined structural properties and molecular size dependent polydisperse nature of HA, hydrodynamic size of humic sub-fractions plays a crucial role in all interactions. Principally, the structural formation of any substance in aqueous phase is defined as hydrodynamic structure and the theoretical spheric radius of this structure is accepted as hydrodynamic size (Dahneke, 1983). Based on the previous investigations on the structural diversity of HA, and molecular size descriptive models of humic sub-fractions could be regarded as possessing a non-spherical structure (Figure 3.1).

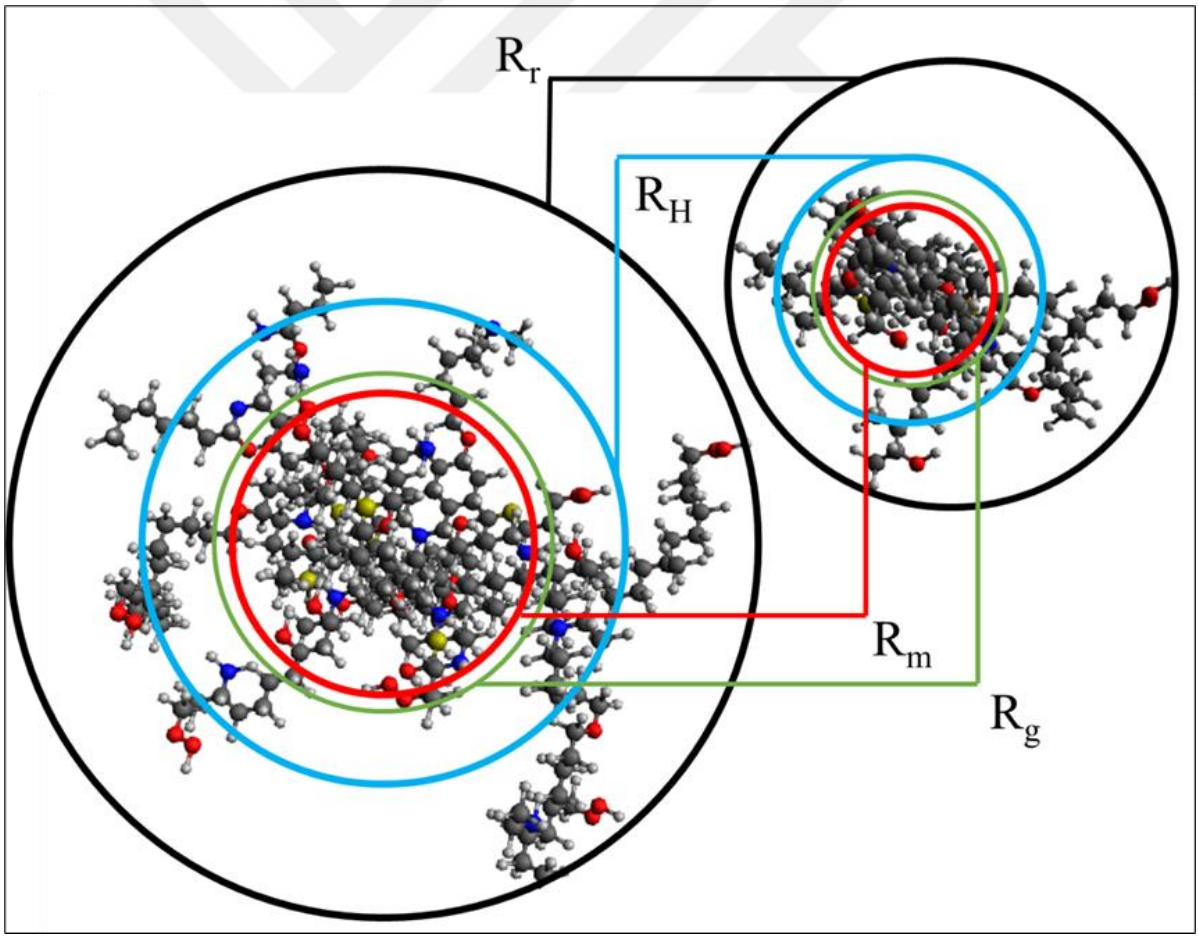


Figure 3.1. Theoretical radius of model HA hydrodynamic structure. R_m; mass radius. R_g; radius of gyration. R_H; hydrodynamic radius. R_r; radius of rotation.

The mass radius (R_m) is the radius off sphere with the same partial specific volume as the sample structure. It also refers to the densest core of the structure. The radius of gyration (R_g) is the mathematically defined dimension description of distribution of mass centers in the structure. The hydrodynamic radius (R_H) is the observable property of the structure, and the radius of the rotation (R_r) is describing the radius of the sphere that can fully cover the structure (Van Saarlos, 1987).

HA structural model definition is an essential tool in interpretation of the hydrodynamic size in aqueous medium. Although it does not have a constant shape, the molecular structure of HA depends on the pH of the surrounding medium, the presence of electrolytes, and the various other structures present within the medium (Ghosh and Schnitzer, 1980; Klučáková, 2018). Humic hydrodynamic structure is mainly affected by the non-specific van der Waals forces, *i.e.,* London dispersive forces, Debye energies and Keesom energies and specific polar interactions such as, hydrogen bonding, electron donor-acceptor (Schwarzenbach et al, 2017; Wells and Stretz, 2019). Due to these interactions, HA colloidal aggregations may occur and not only molecular discrete structures but also homo or hetero aggregation/agglomeration of the individual hydrodynamic structures would be suspended in aqueous solution of HA. The hydrodynamic size definition may also be expressed by the selected fractional model structure.

As indicated in Section 1.6., HA structure changes form according to the condition of its presented medium according to pH and/or concentration. From basic to acidic conditions HA structure tends to form micellar structure due to coalescence of aromatic parts to the center and hydrophilic parts of HA oriented to the surface (Sposito et al., 1982). This model was used to explain the detergent effect of HA (von Wandruszka, 1997), however in neutral pH conditions micellar model was not sufficient to explain the overall structural configuration in aqueous media. Furthermore, micelle formation was dependent on the HA concentration thereby CMC which was reported as 7.4 gL^{-1} under basic pH conditions (12.3±0.2) (Guetzloff and Rice, 1994). Similarly, pseudo micelle structure purposes that intramolecular aggregates forms micelle like structure by coming together. Resembling the micelle structures more hydrophobic portions of the different HA structures interact with each other and form the center of pseudo micelle structure regardless of the HA concentration. On the contrary this model cannot explain the smaller molecular size fractions, <100 kDa, which are mostly composed of hydrophilic fragments (Engebretson and von Wandruszka, 1997). The most accepted model to explain HA structure is the random coil as a stochastic assembly model. The stochastic assembly model explains the flexible and disordered nature of HA, with the mutual effect of functional groups existing in a stochastic manner (Wershaw, 1993; Swift, 1996). This model also

is more suitable to explain the variance in molecular size, solubility and solution characteristics, and charge characteristics (Swift, 1989).

Based on the expected conformational changes during adsorptive interactions, humic acid could well be expressed by various models. Among these models, core-shell model proposes that there are glassy and rubbery sections of HA. This model explains HA scaffolds as linear oriented and harmony of glassy and rubbery parts forming a hole that can absorb other materials such as smaller HA structures, metal oxide aggregates, clays, *etc.* (Figure 1.15) (Lu and Pignatello, 2004). Another model that is used to explain the adsorption of HA onto other materials, mostly Me-OH structures, is the "train-loops-tail" model (Figure 1.16). This model accepts the Me-OH surface as homogeneous in case of active sites and explains the HA affinity towards these reactive surfaces (Fleer et al., 1993). According to the model HA structure can attached to the surface to form "trains" which are the HA section directly proximate to the surface or "loops" that are not connected directly but their extremities to the trains and "tails" are the segments that are attached to the tail but not in relation with the active surface. Because in neutral pH conditions HA structure is more elongated due to the intra-molecular electro repulsive interactions formation of "trains", "tails" and "loops" are more possible towards an active surface (Fendorf et al., 1997; Jardine et al., 1999). Therefore, polydispersity and heterogenous nature of humics should be considered in accordance with the selected descriptive parameter described as intensity-, number-, surface area and volume-weighted HDS.

For instance, it is easier to define hydrodynamic radius of the micelle like structure, denser in the core and with fringes on the surface, of HA. However, the supramolecular assembly (net like structure) of HA covers more volume in comparison to the similar molecular weighted micelle structure and its hydrodynamic size will be bigger. Also, supramolecular structure can link relatively smaller HA structures therefore a shadowing effect during hydrodynamic size analysis should be encountered (Wells and Stretz, 2019). In this respect, description of the media and time dependent measurements should be done for better understanding of the structural heterogeneity.

At neutral pH conditions, humic carboxylate groups are mostly deprotonated (pKa= ±2.5) creating very strong negatively charge assisted H-bonding between both homo-molecular and hetero-molecular structures thereby structures called metachemical hydrogels are formed. Metachemical hydrogels also provide strong resonance-assisted H-bond (π-bond cooperative H-bond), moderate polarization-assisted H-bond (σ-bond cooperative H-bond) and weak (<4–5 kcal mol^{-1}) ordinary H-bond (Gilli and Gilli, 2013; Wells and Stretz, 2019). The range of H-bonds changes from <1 to 45

kcal mol^{-1} for weak, moderate, strong and very strong H-bonds and the energy of very strong H-bonds are close to near-covalent bonds crosslinks (Gilli and Gilli, 2013). Due to these attractive forces, humic structures are held together strongly and H-bonded aggregates of stochastic assemblies of HA would be present (Wershaw, 1993; Swift, 1996; Wells and Stretz, 2019). At neutral pH, HA scaffolds can also form physical hydrogels which are bigger than 1 μm. These hydrogel scaffolds are reversible abiotic self-assembled structures that can dissipate or reform via turbulence-inducing pouring, filtering, or shaking (Esfahani et al, 2015; Wells and Stretz, 2019).

Recently hydrodynamic size analysis of humic structure with DLS technique has attracted attention to investigate the hydrodynamic structure and aggregation behavior of HA (Esfahani, 2015; Klucakova and Veznikova, 2017; Wells and Stretz, 2019). Due to the polydisperse and heterogeneous properties, water-based dissolution of humic acid (Aldrich) was attained revealing various fractions (Swiech et al., 2017). The sub-fractions were composed of non-covalently bonded species of diverse chemical properties and were considered as anionic colloids. Topological features indicated the presence of aggregates expressing a radii of gyration (R_g) as ≥ 50 nm. It should also be noted that radius of gyration could only refer to the inner core of the species whereas hydrodynamic size would display the hydrated size in aqueous medium. Therefore, HDS would be larger than the R_g. Moreover, HA was shown to be present as supramolecular structures composed of macromolecular aggregates.

The presence of both small spheres (10-50 nm) and “sponge-like ring structures” and aggregates of spheres (heights of ca. 9.5 nm) had been previously reported for fulvic acids composed of relatively dense aromatic moieties and functional groups (Namjesnik-Dejanovic and Maurice, 1997). Later, Balnois and co-workers reported relative height variations of IHSS humic acids as a function of pH and ionic strength through AFM measurements (Balnois et al., 1999). Colombo and colleagues expressed that under slightly acidic conditions, HA were composed of supramolecular particles with a conic shape and a hole in the center exhibiting a pseudo-amphiphilic nature, with secluded hydrophobic domains (Colombo et al., 2015). These conical structural entities possessed diameters of 50-280 nm and uniform height of 2 nm. Moreover, the presence of spherical ring-like structures bearing a shallow depression in the middle, with apparent colloidal diameters < 500 nm and vertical size of 3-4 nm were also reported (Angelico et al., 2023; Cid-Samamed et al., 2022).

AFM data expressed lateral dimensions in lieu of approximations in 3-D conformational variations including several layers of hydration water as expressed by HDS. Moreover, the origin of humic acid would also exert a crucial role disabling a direct comparison of hydrodynamic size measurements.

3.2.1. Assessment of Hydrodynamic Size of $HA_{,as\text{-}is}$

$HA_{,as\text{-}is}$ was prepared according to procedure outlined in Section 2.1.2. HDS data of $HA_{as\text{-}is}$ expressed in terms of intensity-, volume-, surface area- and number-weighted size parameters were illustrated in Figure 3.2 and Table 3.2.

Under initial conditions, the most abounded cluster was observed in the size range of 106.5 nm-197.8 nm as intensity- (73%), volume- (61%) and surface size (49%)-based HDS. Number-based HDS showed that the particles around 106.5 nm and 130.9 nm expressed a CR% as 35% and 34% respectively. There are also larger particles with sizes up to 3561.7 nm and 6617.0, being only CR 1% as intensity based-HDS. The particles around 3561.7 nm also covering 7% of the volume-based HDS. On the other hand, these particles are negligible in comparison to the smaller particles according to surface area-based HDS and number-based HDS. Peaks detected around 3561 nm and 6617 nm could be related to previously mentioned physicochemical hydrogel structures which are formed during filtration through 0.45 μm filter, and/or after pouring prepared $HA_{,as\text{-}is}$ solution to the instrument cuvette. Otherwise, detection of almost ten times larger particles from filter pores (diameter 0.45 μm) wouldn't be possible (Esfahani et al, 2015; Wells and Stretz, 2019). Slightly smaller metachemical hydrogels are also visualized in the range of 106.5-299.0 nm. The physical hydrogels form a net-like structure that holds metachemical hydrogels and these metachemical hydrogels provide colloidal suspension of physicochemical hydrogels rather than aggregation (Wells and Stretz, 2019).

Hydrodynamic size changes during 210 mins with 30 min intervals were also presented in Figures 3-6. While the physical hydrogel structure disappeared after initial measurement, metachemical structures remained stable for 210 minutes. On the other hand, at 90 min, 150 min and 210 min periods, a new cluster around 47 nm to 61 nm was observed. This new cluster was high in number at 90 min, 150 min and 210 min, however, disappeared upon periods of120 min and 180 min. Since there was no external intervention during measurements and laser light was not absorbed by HA at 633 nm, a drastic change in pertaining forces was not expected. Due to lack of external disturbance, these smaller particles might initially be present in the media under the shadowing effect of the larger particles masking their detection. This relatively smaller particles could move to water faster due to HA affinity to water and intrude through the larger particles expressing shielding effect. When the particles move and/or rotate in water, smaller particles could also reflect the laser light therefore peak intensification could be monitored (Aranson, 2013; Ziepke et al, 2022).

Klučáková reported HDS parameters of humic matter (IHSS) in terms of intensity, volume, and number particle size distribution (Klučáková, 2018). Mainly two or three different size fractions comprised of large macroparticles (> 1μm), medium fractions as sub-microparticles of fulvic acids (average diameters, 500-1,200 nm) and in humic acids (300-600 nm). The study covered a diverse range of humic acids derived from various aquatic and terrestrial sources (*e.g.*, Nordic Lake humic acids, Elliot soil humic acids, Suwannee River humic acids, Pahokee peat humic acids, Leonardite humic acids, and Nordic Lake fulvic acids) therefore a sound comparison basis could be visualized. All samples expressed considerably high polydispersity index as ~0.4-0.6 emphasizing the significance of the definition of "polydispersity" in simple NPs and polymeric, multi sized, molecularly sub-fractionated organic matter.

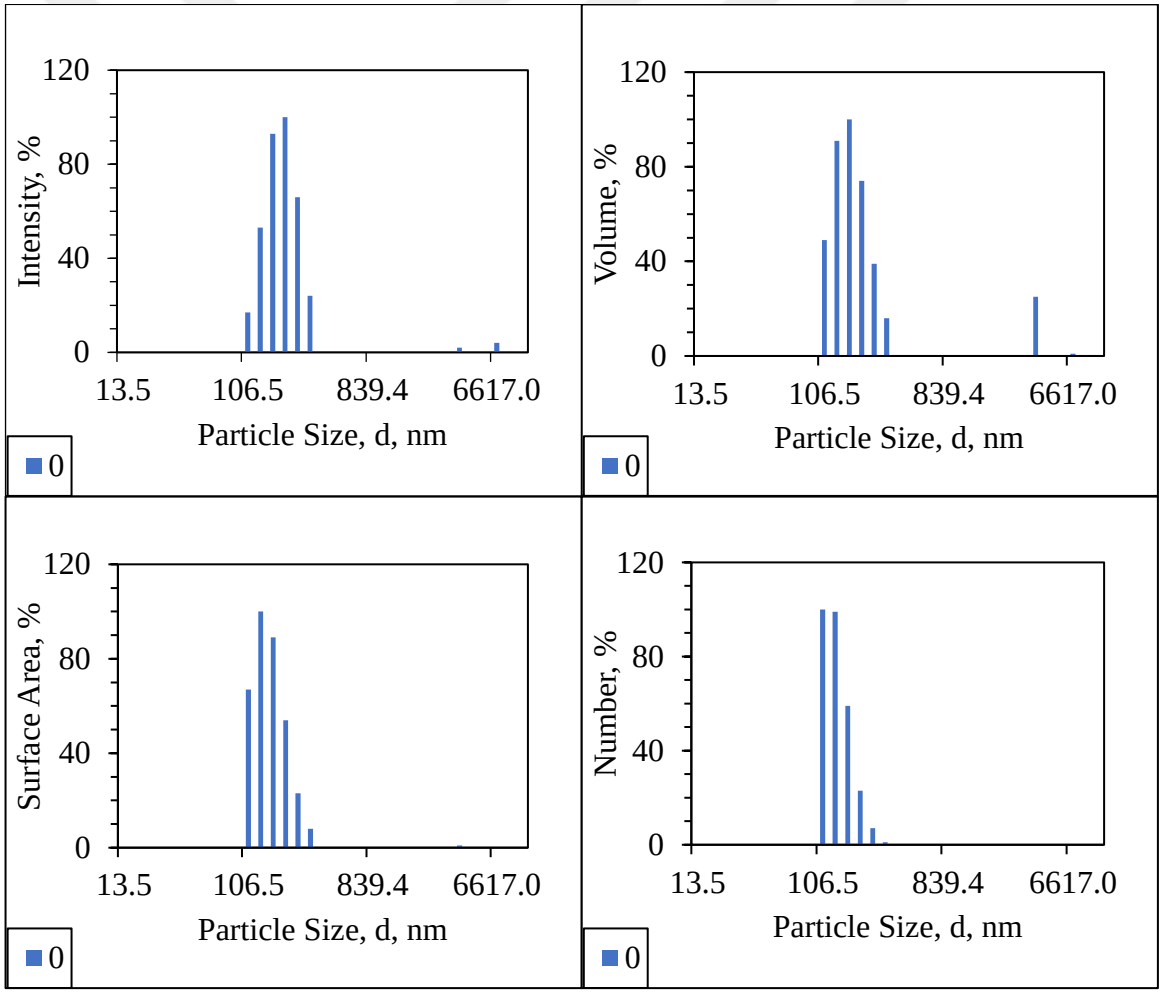


Figure 3.2. Intensity-, volume-, surface area- and number-based hydrodynamic size of $HA_{,as\text{-}is}$ at initial time.

Table 3.2. Intensity-, volume-, surface area- and number-based hydrodynamic size of $HA_{,as\text{-}is}$.

	HDS, nm	Cumulative Ratio, %			
		Intensity	Volume	Surface Area	Number
Initial	106.5-197.8	73%	61%	49%	35%
	243.2-299.0	25%	32%	51%	34%
	3561.7	1%	7%	-	31%
	6617.0	1%	-	-	-
60 min	155.4-182.0	72%	75%	76%	65%
	185.3-188.5	28%	25%	24%	35%
90 min	47.7-61.1	4%	41%	64%	32%
	164.4-186.3	62%	11%	15%	51%
	198.2-224.3	34%	33%	21%	15%
	-	-	15%	-	2%
120 min	167.8-169.9	62%	63%	63%	64%
	171.0-173.2	38%	37%	37%	36%
150 min	47.0-55.6	4%	31%	48%	64%
	160.1-178.9	50%	22%	32%	34%
	189.2-211.4	46%	27%	12%	2%
	-	-	20%	8%	-
180 min	168.5-174.0	74%	75%	75%	76%
	175.9-177.8	26%	25%	25%	24%
210 min	49.0-58.8	5%	47%	71%	59%
	165.4-186.8	55%	7%	10%	39%
	198.6-224.3	40%	29%	12%	2%
	-	-	17%	2%	-

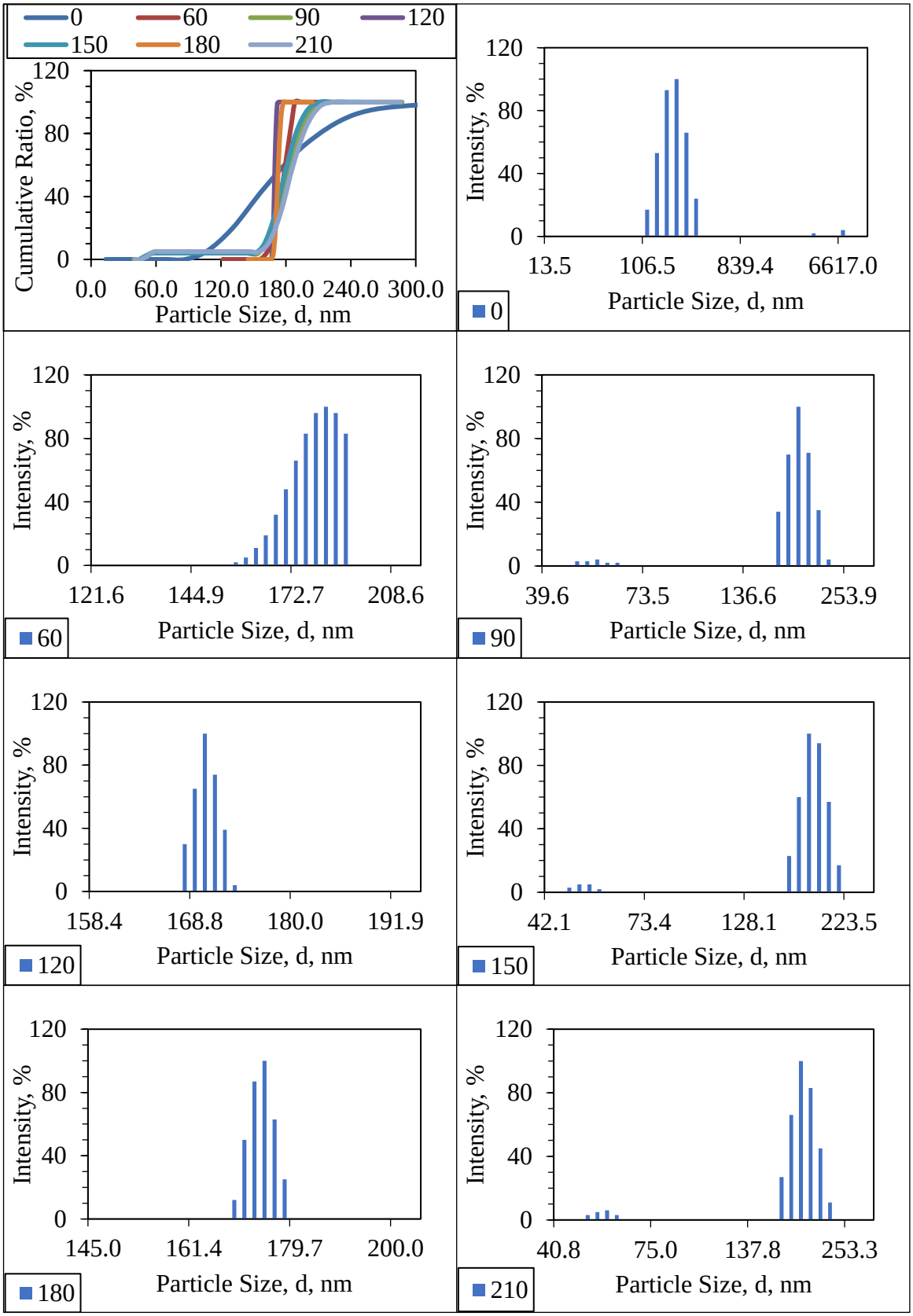


Figure 3.3. The cumulative ratio comparison and hydrodynamic size of $HA_{,as\text{-}is}$ 30 min intervals as intensity-weighted HDS.

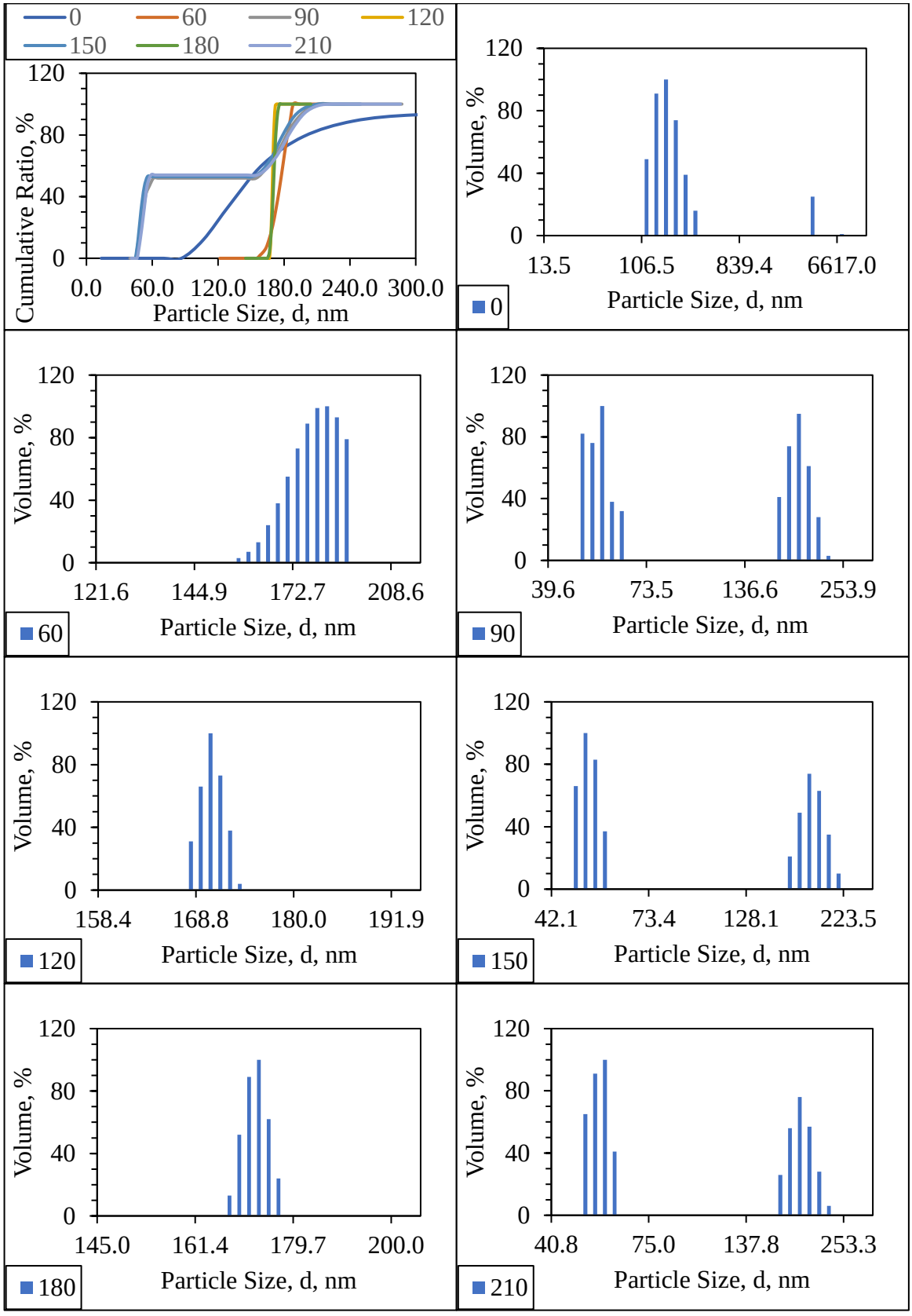


Figure 3.4. The cumulative ratio comparison and hydrodynamic size of $HA_{,as\text{-}is}$ 30 min intervals as volume-weighted HDS.

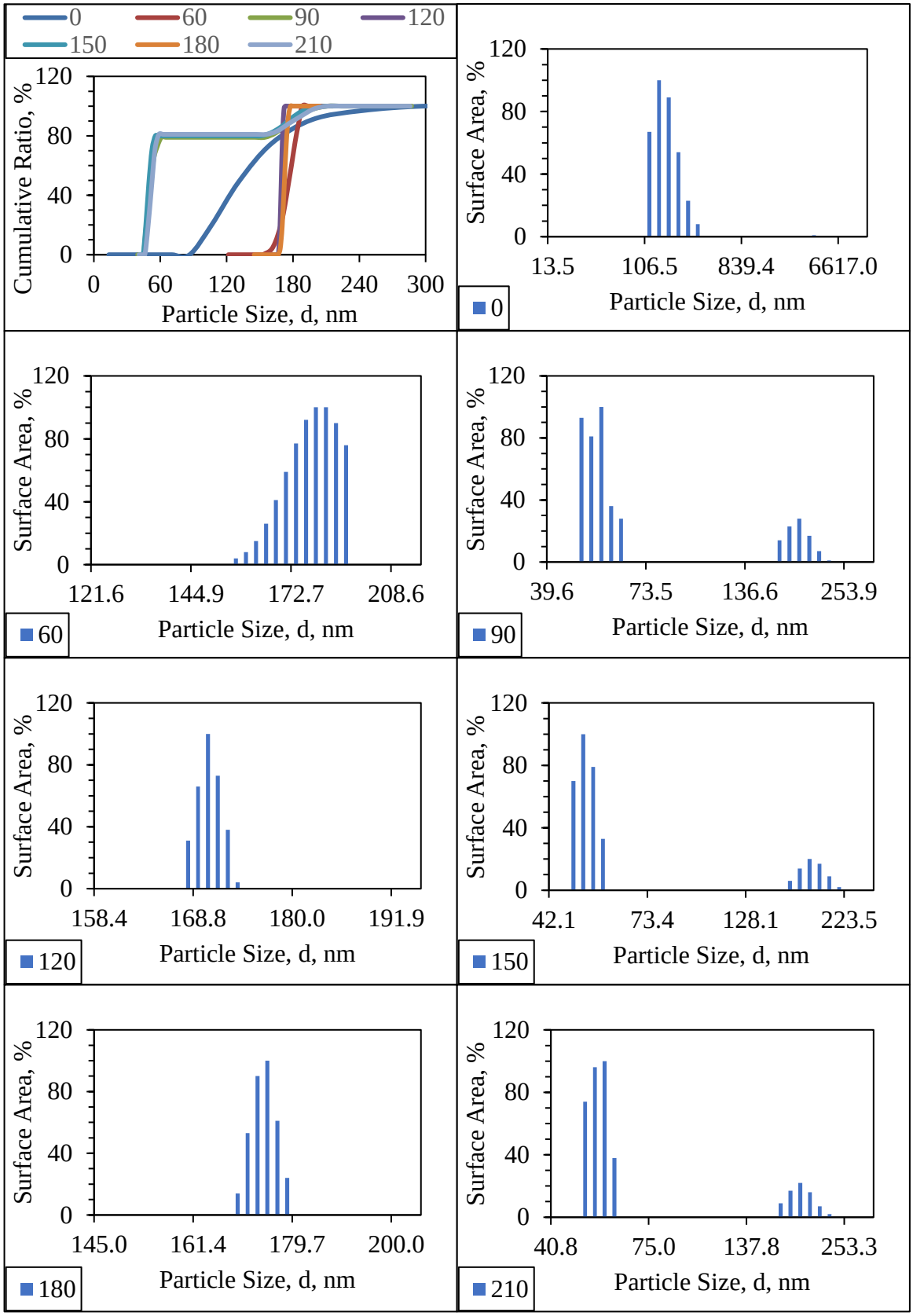


Figure 3.5. The cumulative ratio comparison and hydrodynamic size of $HA_{,as\text{-}is}$ 30 min intervals as surface area-weighted HDS.

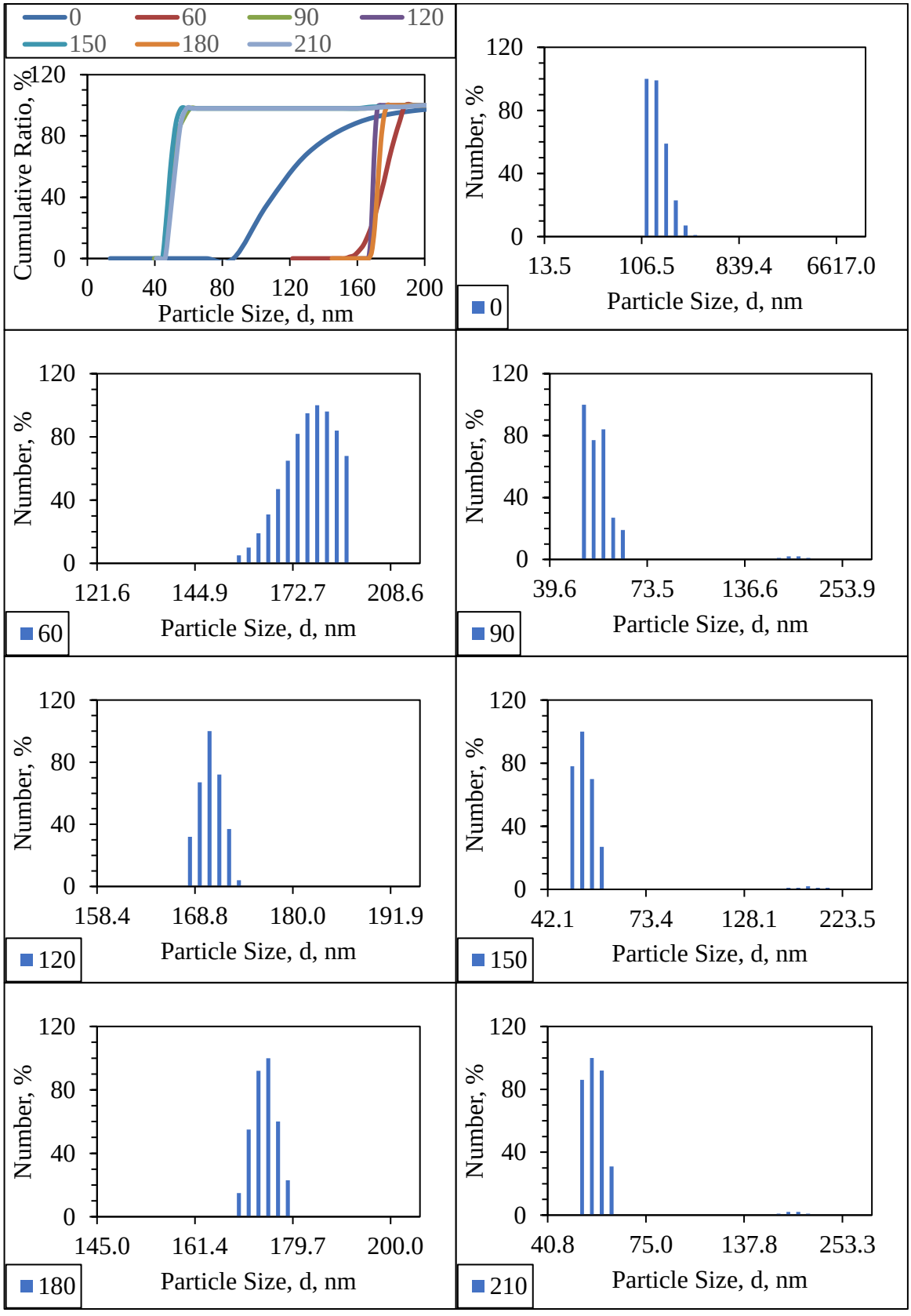


Figure 3.6. The cumulative ratio comparison and hydrodynamic size of $HA_{,as\text{-}is}$ 30 min intervals as number-weighted HDS.

3.2.2. Assessment of Hydrodynamic Size of HA_{pho}

In natural surface water systems, HA is directly subjected to solar light irradiation that causes physicochemical changes in HA structure via absorbing light in the visible as well as in ultraviolet spectral domain. Upon solar irradiation of aquatic systems, HA expresses properties both as a photosensitizer and a quencher. HA excited states shown as $^3HA^*$ and $^1HA^*$, and reactive oxygen species (ROS) *i.e.*, $O_2^{\bullet-}$, $HO^\bullet$ and H_2O_2, constitute the main components of light-initiated active species (Dalrymple et al, 2010). Pertaining photolytic interactions of HA, with ROS (Uyguner-Demirel et al, 2023) are presented as in the following reactions 1-19.

$$^1HA + h\nu \rightarrow {}^1HA^* \rightarrow \text{intersystem crossing} \rightarrow {}^3HA^* \quad (3.1)$$

$$^3HA^* + O_2 \rightarrow {}^1HA + {}^1O_2 \quad (3.2)$$

$$^1HA + h\nu \rightarrow HA^{\bullet+/\bullet-} \quad (3.3)$$

$$^1HA^* \rightarrow HA^{\bullet+/\bullet-} \quad (3.4)$$

$$^3HA^* \rightarrow HA^{\bullet+/\bullet-} \quad (3.5)$$

$$HA^{\bullet+/\bullet-} \rightarrow O_2 \rightarrow {}^\bullet HA^+ + O_2^- \quad (3.6)$$

$$^3HA^* + O_2 \rightarrow {}^\bullet HA^+ + O_2^- \quad (3.7)$$

$$^1HA + {}^1O_2 \rightarrow O_2^- + {}^\bullet HA^+ \rightarrow \text{products} \quad (3.8)$$

$$^3HA^* + H_2O \rightarrow HA\text{-}H^\bullet + HO^\bullet \quad (3.9)$$

$$^3HA^* + O_2 \rightarrow (HA)_{deg} + O_2^{\bullet-}/HO_2^\bullet \quad (3.10)$$

$$^3HA^* + O_2 \rightarrow {}^1HA + {}^1O_2 \quad (3.11)$$

Following formation of oxygen radicals, radical termination reactions and other successive reactions may also take place concomitantly as expressed by the following reactions 12-19.

$$O_2^{\bullet-}/HO_2^\bullet \rightarrow H_2O_2 \quad (3.12)$$

$$2O_2^{\bullet-} + 2H^+ \rightarrow H_2O_2 + O_2 \quad (3.13)$$

$$H_2O_2 \leftrightarrow H^+ + HO_2^- \qquad pK_a = 11.6 \quad (3.14)$$

$$2O_2^{\bullet-} + H_2O_2 \rightarrow O_2 + HO^\bullet + OH^- \quad (3.15)$$

$$O_2^{\bullet-} + H^+ \rightarrow HO_2^\bullet \quad (3.16)$$

$$O_2^{\bullet-} + HO_2^\bullet \rightarrow HO_2^- + O_2 \quad (3.17)$$

$$HO_2^\bullet + HO_2^\bullet \rightarrow O_2 + H_2O_2 \quad (3.18)$$

$$HO^\bullet + HO_2^\bullet \rightarrow H_2O + O_2 \quad (3.19)$$

^{1}HA and ^{3}HA express the single and triple states of HA respectively, hν is the photon energy of the incident radiation, $^{1}HA^{*}$ and $^{3}HA^{*}$ is the excited singlet and triplet HA structure, k is the reaction rate constant.

The excited state may also follow relaxation by fluorescence or subsequent sensitization reactions. Formed radicals can react through a non-selective route or with a selective reaction pathway with nearly located compounds in close vicinity (Uyguner-Demirel et al, 2023). Additionally, radicals tend to react with electron-rich species, *e.g.,* phenolic groups and/or activated aromatic domains (Lee and von Gunten, 2010). Solar irradiation onto HA in aqueous medium leads to formation of $^{1}O_2$ and O_2^{-} that contribute to the oxidizing reaction medium (Garg et al, 2011). The overall photolytic reactions of HA end up with minimal (< 5%) self-degradation as indicated in characteristic analysis of HA (Table 3.1). The electrons obtained during photolytic treatment have low quantum yield and low energy that is not enough for direct homogeneous reduction process and excited triplet state transition occurs through fluorescence and phosphorescence decays (Zepp et al, 1987; Vinodgopal and Kamat, 1992; Frimmel, 1994). Considering that the visible light energy would be insufficient to initiate photoionization of HA, photosensitization capacity of HA prevails and are responsible for further reactions *i.e.,* production of transient intermediates, such as ROS, or to the formation of relatively stable, light-induced free radicals (Zepp et al, 1985; Haag and Hoigne, 1986; Frimmel and Christman, 1988; Blough and Zepp, 1995; Aguer et al, 2002; Polewski et al, 2005). Solar irradiation generates primary and secondary radicals on HA, besides auto-oxidation. Radicals cause several decomposition and formation of chemical bonds within the humic structure and consequently hydrodynamic molecular size of HA would be reshaped that could be visualized by minor decreases in $SUVA_{280}$ and $SUVA_{254}$ (Table 3.1) (Polewski et al, 2005). These obtained radicals cause charge shifts and π-bond disruption (inter-system crossing) on HA structure which is leading to hydrodynamic size changes via changing non-specific van der Waals interactions (London dispersive forces, Debye energies and/or Keesom energies) (Schwarzenbach et al, 2017). Following photolysis, spectroscopic properties of HA showed a substantial increase in HA structure in accordance with molecular size decrease (Uyguner-Demirel et al., 2022).

Effect of solar light irradiation on hydrodynamic size of $HA_{,pho}$, was shown as multi size distribution profiles in Figures 3.7-3.10 in terms of intensity-, volume-, surface area-, and number-weighted HDS respectively and Table 3.3 compiled the cumulative HDS values. Table 3.4 compared the intensity-weighted HDS values of $HA_{,as\text{-}is}$ and $HA_{,pho}$. Intensity weighted HDS of the HA_{pho} showed that similar to $HA_{,as\text{-}is}$ metachemical hydrogel formation may take place in similar and relatively larger sizes due to π-bond disruption which increases van der Waals interactions

(Schwarzenbach et al, 2017). These larger metachemical hydrogel structures were few in number such that in number-weighted HDS their peak height decreases.

Similar with $HA_{,as\text{-}is}$, hydrodynamic size of $HA_{,pho}$ was mainly composed of particles around 100-200 nm which was evidenced by intensity-weighted HDS. These structures were stable for 120 min duration. Photolytic treatment could cause π bond disruption which also caused internal e^- localization thereby heterostructural interactions increased due to increases of van der Waals interactions between smaller particles (Schwarzenbach et al, 2017). Since HA structure was re-organized during solar irradiation, recombination of smaller structures could occur in time that could also attributed to homoaggregation formation. During irradiation, partially oxidized HA fractions could interact with non-oxidized HA moieties and this interaction could create structural changes and aggregation behavior differing from $HA_{,as\text{-}is}$. Photolysis also increased the probability of H-bonding due to the hydroxyl group deformation. The hydrophilic carboxyl groups present on outer branches of HA were the most effected group in HA structure upon photolysis. Aside from carboxyl groups, the second most effected structures were aromatic moieties *i.e.*, phenol, hydroquinone, benzoic acid, and benzoquinones. The Mulliken charges of oxygen, local electron density, in aromatic compounds were relatively higher in phenols and hydroquinones resulting in faster structure deformation than benzoic acid and benzoquinone structures (Yang et al, 2022). All these light-initiated interactions might result in diverse aggregate/agglomerate formation tendencies in comparison to non-irradiated HA. During 120 min, $HA_{,pho}$ structures around 100 nm - 200 nm remained more stable than $HA_{,as\text{-}is}$ structures. On the other hand, relatively bigger metachemical hydrogel structures continued their heteroaggregation trend and consequently, their size increased in a sequence from 300 nm - 400 nm to 600 nm - 800 nm. As followed by the characteristic analysis of $HA_{,pho}$, increased aromaticity caused the increase of specific van der Waals interactions between heterostructures. Increased aromaticity may also lead to formation of weak H-bonds and hydrophobic interactions explaining the formation of non-uniform hydrodynamic size fractions (Table 3.1) (Bekbolet et al., 2017). The structures displaying HDS variations in between 300 nm - 400 nm could combine creating bulkier structures. This interaction was evidenced by the decrease in cumulative ratio of structures around 300 nm to 400 nm. However, upon prolonged duration, cumulative ratio of structures between 600 nm to 800 nm increased. During these interactions, the percentage of smaller particles remained nearly stable. Since larger particles would carry more charge than smaller ones, their inter-attractive forces would be higher, and they would tend to aggregate/agglomerate easier. Also, these higher structures were still in colloidal form in aqueous medium which exhibiting more H-bonding interactions in comparison to the $HA_{,as\text{-}is}$. Since photolytic irradiation affected π bonds mainly, the influence of light might be less on the structure of smaller particles which were mostly composed of non-aromatic

structures. While higher molecular size fractions, 450 kDa, 100 kDa, 30 kDa, 10 kDa of HA were affected by solar light irradiation, smaller size fractions such as 3 kDa were not affected (Bekbolet et al, 2017).

Table 3.3. Intensity-, volume-, surface area- and number-weighted HDS of $HA_{,pho}$.

	HDS, nm	Cumulative Ratio, %			
		Intensity	Volume	Surface Area	Number
Initial	121.8-139.5	25%	27%	47%	64%
	149.3-170.9	29%	22%	34%	35%
	539.8-757.1	46%	51%	-	1%
30 min	133.8-142.6	22%	24%	38%	51%
	152.1	21%	21%	26%	30%
	162.2-173.0	19%	14%	19%	18%
	483.9-667.3	38%	43%	17%	1%
60 min	100.0-177.8	45%	42%	65%	92%
	237.1	28%	12%	11%	4%
	316.2-421.7	27%	46%	24%	4%
90 min	135.0-150.4	27%	8%	19%	48%
	158.8	19%	5%	10%	22%
	167.6-177.0	16%	3%	7%	14%
	398.8-444.4	13%	41%	33%	9%
	469.1-522.8	25%	43%	31%	16%
120 min	131.1-151.3	27%	18%	36%	54%
	162.5	24%	12%	24%	28%
	174.5-187.5	22%	10%	16%	17%
	633.2-843.2	27%	58%	24%	1%

Table 3.4. Comparison of intensity-weighted HDS values of $HA_{,as\text{-}is}$ and $HA_{,pho}$.

	$HA_{,as\text{-}is}$		$HA_{,pho}$	
Initial	106.5-197.8	73%	121.8-139.5	25%
	243.2-299.0	25%	149.3-170.9	29%
	3561.7	1%	539.8-757.1	46%
	6617.0	1%	-	-
60 min	155.4-182.0	72%	100.0-177.8	45%
	185.3-188.5	28%	237.1	28%
	-	-	316.2-421.7	27%
90 min	47.7-61.1	4%	135.0-150.4	27%
	164.4-186.3	62%	158.8	19%
	198.2-224.3	34%	167.6-177.0	16%
	-	-	398.8-444.4	13%
			469.1-522.8	25%
120 min	167.8-169.9	62%	131.1-151.3	27%
	171.0-173.2	38%	162.5	24%
	-	-	174.5-187.5	22%
	-	-	633.2-843.2	27%

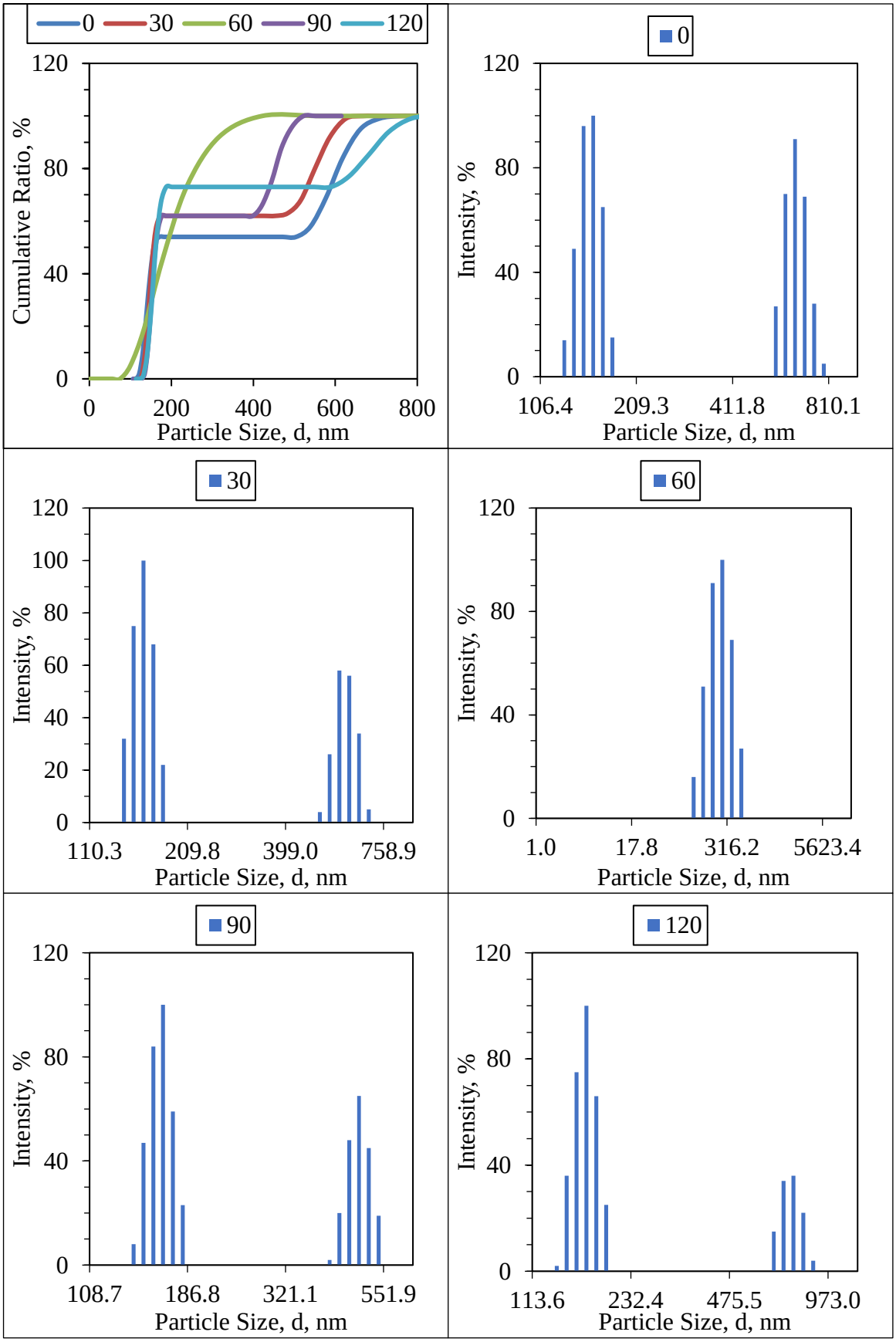


Figure 3.7. The cumulative ratio comparison and hydrodynamic size of $HA_{,pho}$ 30 min intervals as intensity-weighted HDS.

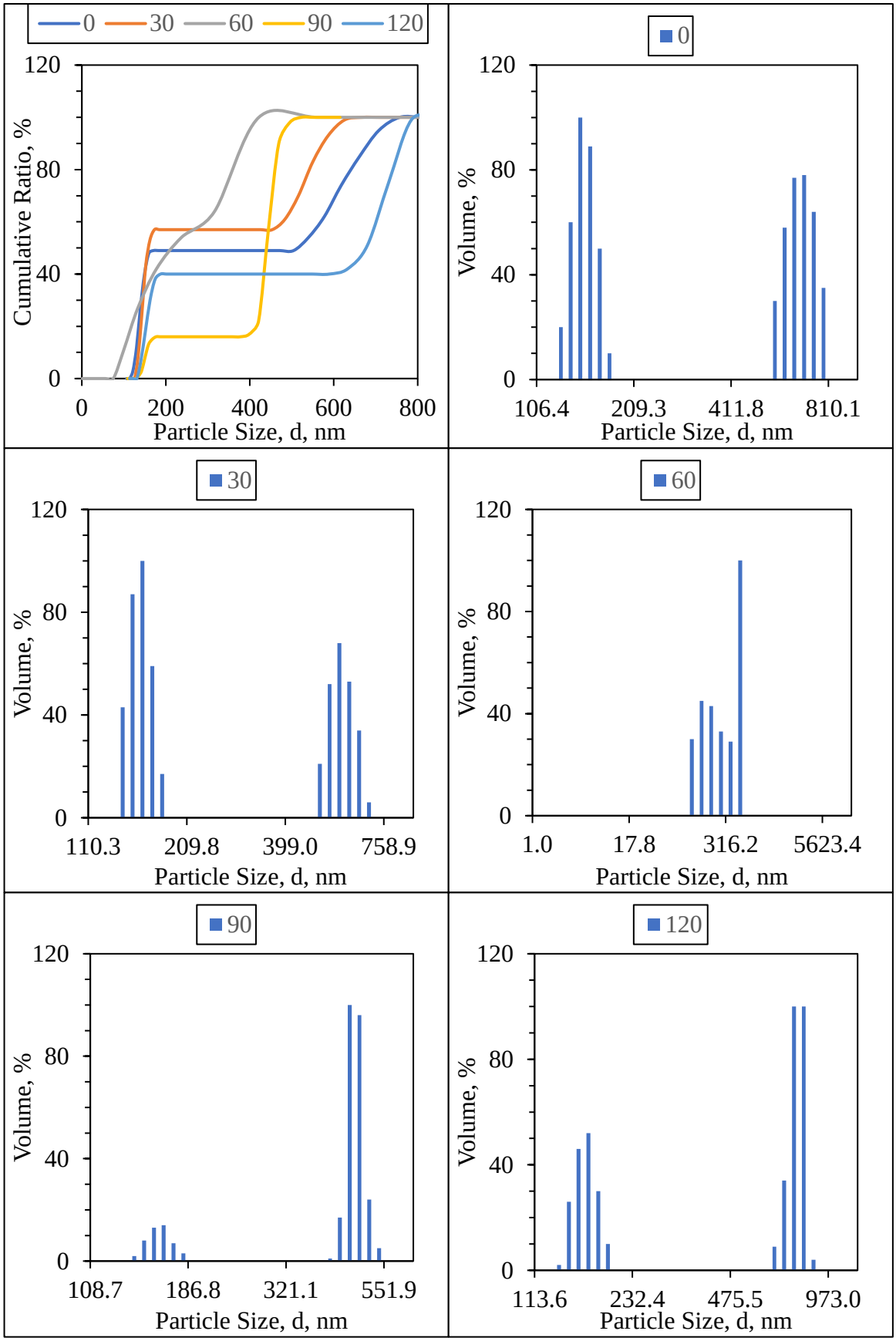


Figure 3.8. The cumulative ratio comparison and hydrodynamic size of $HA_{,pho}$ 30 min intervals as volume-weighted HDS.

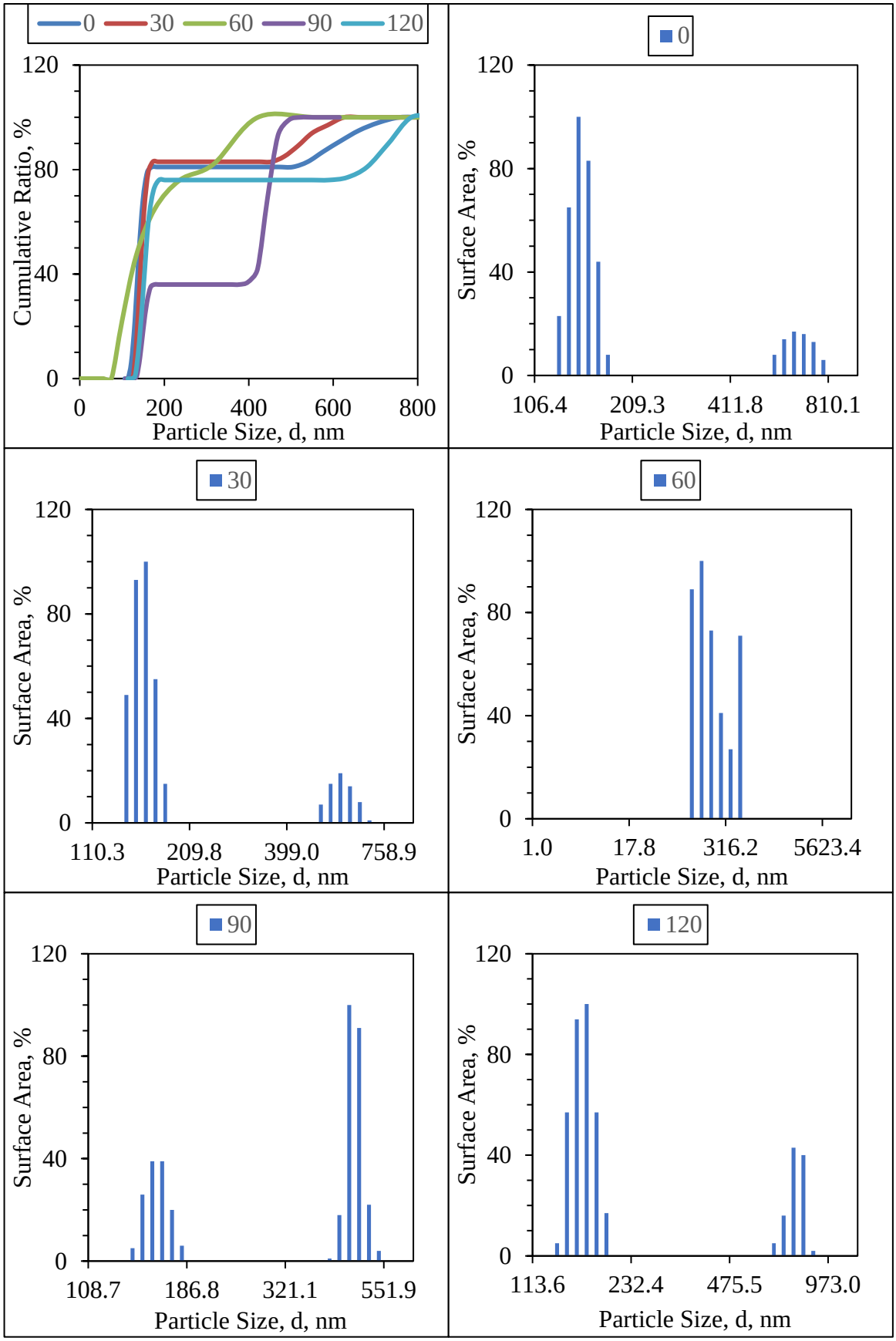


Figure 3.9. The cumulative ratio comparison and hydrodynamic size of $HA_{,pho}$ 30 min intervals as surface area-weighted HDS.

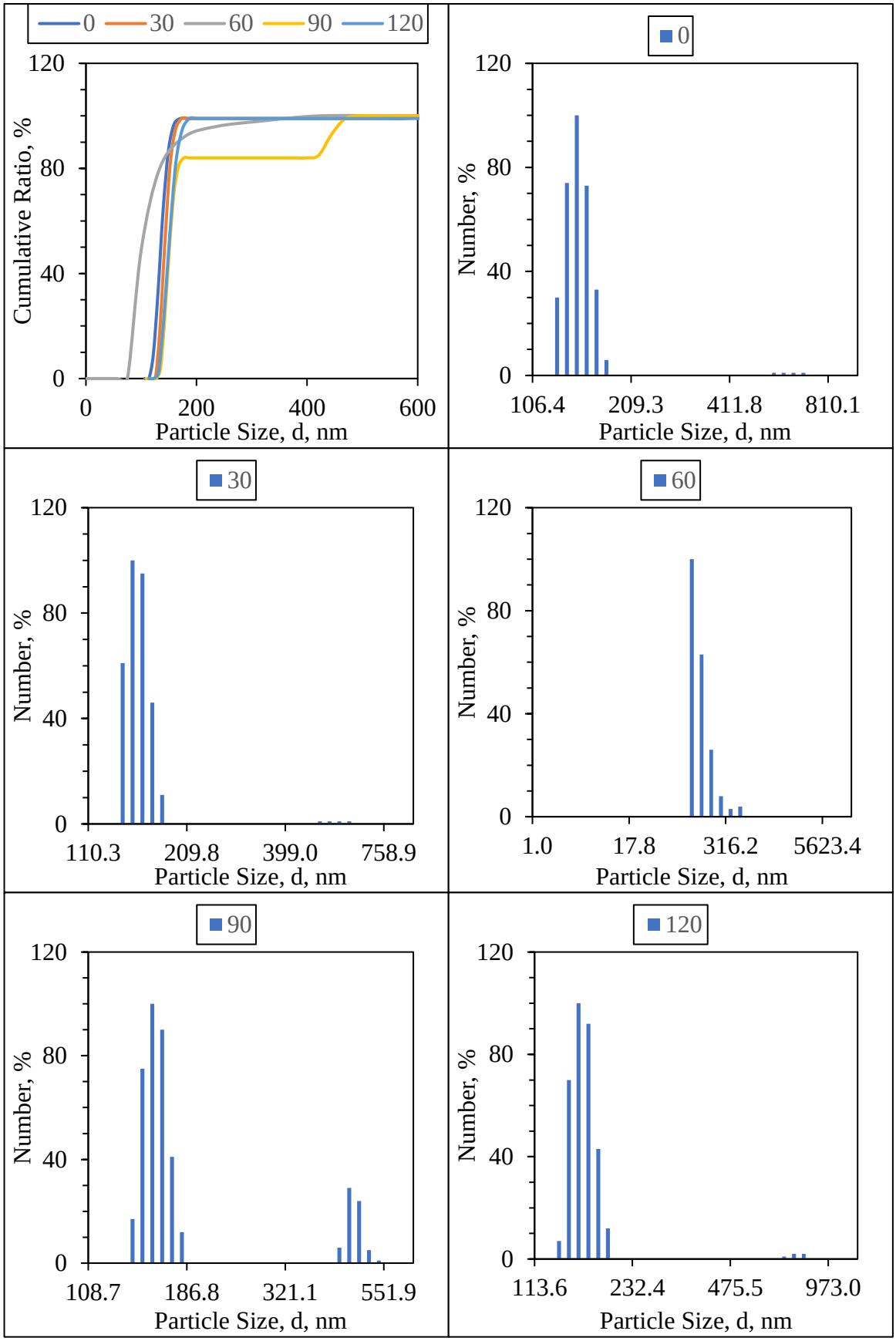


Figure 3.10. The cumulative ratio comparison and hydrodynamic size of $HA_{,pho}$ 30 min intervals as number-weighted HDS.

3.2.3. Assessment of Hydrodynamic Size of $HA_{,photocat}$

As previously introduced in Section 1.6 HAs been color forming compounds present in drinking water, which are not desirable and causing several problems in the industrial applications such as, textile, food, and the paper industries. Their adverse effects are not only limited to aesthetic concerns, but also bacterial growth in water distribution systems that causes the deterioration of the membrane and ion exchange resins. HAs also react with the oxidizing agents that are used for disinfection purposes, *i.e*. chlorination, and forms toxic disinfection by-products such as trihalomethanes. Eventually, removal of HAs during wastewater treatment has a great importance for the prevention of health and environmental problems. As stated before, HA (pH>2) and FA (in all pH values) are the water-soluble fractions of humic matter so their adequately elimination during wastewater treatment with conventional treatment procedures is not quite possible. Therefore, several HA and FA removal methods are published in the literature such as advanced oxidation process (AOPs) (Bekbolet and Balcioglu, 1996; Bekbolet and Özkösemen, 1996; Wenzel et al, 1999; Wang et al, 2000). One of the most effective processes among AOPs is the heterogeneous photocatalysis which is based on photocatalytic treatment with the presence of metal oxide NPs *e.g.*, TiO_2 (Espinoza and Frimmel, 2009; Matilainen and Sillanpää, 2010).

UV light could excite an electron to conduction band (CB) on the TiO_2 surface, leaving a hole in the valance band (VB) (Dordevic et al, 2017; Romanias et al, 2012; Uyguner-Demirel et al, 2023). Overall photochemical reactions in the presence of organic matter could be explained by the following expressions;

Upon excitation;

$$TiO_2 + h\nu\ (E \geq E_{bg}) \rightarrow TiO_{2,VB}h^+ + TiO_{2,CB}e^- \quad (3.20)$$

$TiO_{2,CB}e^-$ reactions;

$$TiO_{2,CB}e^- + O_2 \rightarrow TiO_2 + O_2^{\bullet-} \quad (3.21)$$

$$TiO_{2,CB}e^- + O_2^{\bullet-} + 2H^+ \rightarrow TiO_2 + H_2O_2 \quad (3.22)$$

$$TiO_{2,CB}e^- + H_2O_2 \rightarrow TiO_2 + HO^{\bullet} + OH^- \quad (3.23)$$

$$2O_2^{\bullet-} + H_2O_2 \rightarrow HO^{\bullet} + OH^- + O_2 \quad (3.24)$$

$$O_2^{\bullet-} + H^+ \rightarrow HO_2^{\bullet} \quad (3.25)$$

$$TiO_{2,CB}e^- + HO_2^{\bullet} \rightarrow TiO_2 + HO_2^- \quad (3.26)$$

$$HO_2^- + H+ \rightarrow H_2O_2 \quad (3.27)$$

$$HO_2^{\bullet} + HO_2^{\bullet} \rightarrow O_2 + H_2O_2 \quad (3.18)$$

The $TiO_{2,VB}h^+$ reactions,

$$TiO_{2,VB}h^+ + H_2O_{ads} \rightarrow TiO_2 + HO^{\bullet}_{ads} + H^+ \quad (3.28)$$

$$TiO_{2,VB}h^+ + H_2O_{ads} \rightarrow TiO_2 + H_2O_2 + H^+ \quad (3.29)$$

$$TiO_{2,VB}h^+ + OH^- \rightarrow TiO_2 + HO^{\bullet}_{ads} \quad (3.30)$$

The above presented primary and secondary reactions could lead to surface charge development via adsorption of species leading to further various electrostatic attractions (Figure 3.11). Also, radical termination reactions could also take place as;

$$O_2^{\bullet-} + HO_2^{\bullet} \rightarrow HO_2^- + O_2 \quad (3.17)$$

$$HO_2^{\bullet} + HO_2^{\bullet} \rightarrow O_2 + H_2O_2 \quad (3.18)$$

$$HO^{\bullet} + HO_2^{\bullet} \rightarrow H_2O + O_2 \quad (3.19)$$

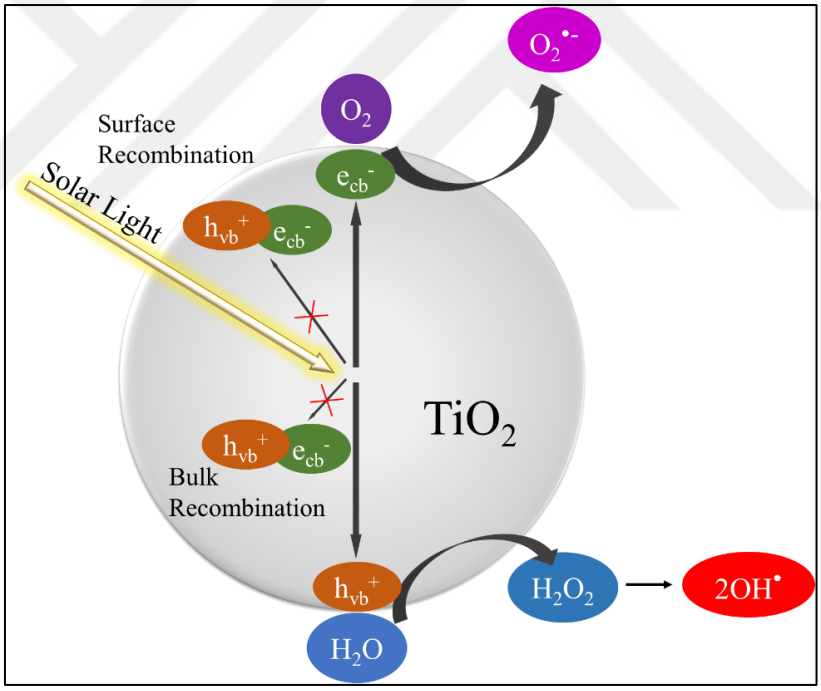


Figure 0.11. Light excitation mechanism of TiO_2 NPs.

The point-of-zero-charge of commercially available TiO_2 Degussa P-25 is reported as pH_{pcz} = 3.5-6.7 (Jaffrezic-Renault et al., 1986; Bahnemann, 1991; Hoffmann et al., 1995; O'Shea and Cardona, 1995).

In the presence of organic matrix, produced radicals could directly attack the organic matter and degradation could be achieved, however when sole TiO_2 was exposed to solar light particle hindrance of the TiO_2 NPs would decrease. Upon irradiation, due to the presence of chromophoric/fluorophoric groups and dense aromatic skeleton, photosensitization reactions occur within humic sub-fractions leading to various intra- and inter rearrangements and conformational transformations as given below reactions;

$$HA/DOM + h^+ \rightarrow DOM/HA^* \quad (3.31)$$

$$DOM/HA^* \rightarrow DOM/HA\text{-}H^{\bullet} + {}^{\bullet}OH \quad (3.32)$$

Moreover, radical species could also react within the bulk humic matrix leading to slight variations in humic descriptive parameters;

$$TiO_2 + h\nu\ (\lambda<388\ nm) \rightarrow TiO_2(h^+_{VB} + e^-_{CB}) \rightarrow \ldots \rightarrow ROS\ \{HO^{\bullet}/HO_2^{\bullet}/O_2^{\bullet-}\} \rightarrow \ldots$$
$$\rightarrow HO\bullet + HA_{ads} \rightarrow \bullet A + H_2O \rightarrow \text{via radical reactions} \rightarrow \ldots$$
$$\rightarrow HA_{ox} \rightarrow \ldots CO_2 + H_2O \quad (3.33)$$

These main reaction conditions could lead to sequential photocatalytic degradation of HA, expressed by their removal efficiencies or reaction kinetics. The main functional feature would be the selection of the descriptive parameter for the characterization of HA (Uyguner-Demirel and Bekbolet, 2011).

Under these conditions, hydrodynamic size variations of photocatalytically treated HA designated as $HA_{photocat}$ was also investigated to maintain a basis for further assessments.

Intensity-, volume-, surface area-, and number-weighted hydrodynamic size data of $HA_{photocat}$ are shown in Figures 3.12-3.15, respectively. Time dependent HDS variations of $HA_{,photocat}$ is compiled on Table 3.5 and HDS comparison of $HA_{,as\text{-}is}$, $HA_{,pho}$ and $HA_{,photocat}$ was given in Table 3.6. Three main pathways that affect HA during photocatalytic treatment were as follows; *i.* solar light irradiation on HA and auto-oxidation/degradation, *ii.* solar light irradiation on HA and radical formation, *iii.* pH depended HA adsorption on TiO_2 surface and degradation of HA with the activation of irradiation ($\lambda<388$ nm) (Uyguner-Demirel and Bekbolet, 2011). The first and second pathways were interpreted by investigating the hydrodynamic size of HA_{pho}. Third pathway, which includes degradation of HA through photocatalytic reactions was evaluated in this section.

Table 3.5. Intensity-, volume-, surface area- and number-weighted HDS of $HA_{,photocat}$.

	HDS, nm	Cumulative Ratio, %			
		Intensity	Volume	Surface Area	Number
Initial	52.3-62.7	24%	36%	45%	57%
	75.2-90.1	19%	56%	55%	43%
	6961.0-10000	57%	8%	-	-
30 min	45.8-51.7	9%	75%	36%	43%
	155.0-175.1	50%	15%	55%	56%
	186.1-210.2	41%	10%	9%	1%
60 min	88.3-106.2	30%	38%	61%	75%
	116.4-139.8	29%	22%	30%	25%
	554.8-666.7	29%	31%	7%	-
	730.8-801.1	12%	9%	2%	-
90 min	21.3-26.0	2%	32%	44%	53%
	86.8-106.2	20%	42%	50%	47%
	117.4-129.8	12%	13%	5%	-
	175.4-237.0	52%	5%	1%	-
	262.0-289.7	14%	8%	-	-
120 min	99.0-113.4	37%	23%	50%	48%
	121.3-129.8	19%	9%	17%	29%
	438.7-502.2	33%	53%	31%	20%
	537.4-575.0	11%	15%	2%	3%

Table 3.6. Comparison of intensity-weighted HDS values of $HA_{,as\text{-}is}$, $HA_{,pho}$ and $HA_{,photocat}$.

	$HA_{,as\text{-}is}$		$HA_{,pho}$		$HA_{,photocat}$	
Initial	106.5-197.8	73%	121.8-139.5	25%	52.3-62.7	24%
	243.2-299.0	25%	149.3-170.9	29%	75.2-90.1	19%
	3561.7	1%	539.8-757.1	46%	6961.0-10000	57%
	6617.0	1%	-	-	-	-
60 min	155.4-182.0	72%	100.0-177.8	45%	88.3-106.2	30%
	185.3-188.5	28%	237.1	28%	116.4-139.8	29%
	-	-	316.2-421.7	27%	554.8-666.7	29%
	-	-	135.0-150.4	27%	730.8-801.1	12%
90 min	47.7-61.1	4%	158.8	19%	21.3-26.0	2%
	164.4-186.3	62%	167.6-177.0	16%	86.8-106.2	20%
	198.2-224.3	34%	398.8-444.4	13%	117.4-129.8	12%
	-	-	469.1-522.8	25%	175.4-237.0	52%
	-	-	-	-	262.0-289.7	14%
120 min	167.8-169.9	62%	131.1-151.3	27%	99.0-113.4	37%
	171.0-173.2	38%	162.5	24%	121.3-129.8	19%
	-	-	174.5-187.5	22%	438.7-502.2	33%
	-	-	633.2-843.2	27%	537.4-575.0	11%

Initial hydrodynamic size of $HA_{,photocat}$ was mainly composed of particles ranging around 50 nm - 100 nm, and around 6 μm - 10 μm formed by decomposition of metachemical hydrogel, and physical hydrogel structures (Wells and Stretz, 2019; Zavarzina et al, 2021; de Aguiar et al, 2022). The

physical hydrogels were mainly agglomeration of metachemical hydrogels which were connected with weak hydrogen bonds and these structures vanished after the solution settles and did not form again due to their nature (Wells and Stretz, 2019; Zavarzina et al, 2021). Birben and colleagues investigated the molecular size distribution of photocatalytically degraded HA structure in the presence of TiO_2. Following photocatalytic treatment, via degradation, humic sub-fractions transformed from 450 kDa to less than 30 kDa molecular size fractions and the most abundant molecular size fraction was the 3 kDa. It should be mentioned that kDa is a weight unit and hydrodynamic size, nm, is a unit of diameter length. Therefore, any conversion data would be meaningless provided that both parameters were determined simultaneously. HA structures that have the same molecular weight cut off, could have different hydrodynamic structures depending on the descriptive DLS parameter. Erickson explained the conversation of kDa to nm of protein structures (Ericson, 2009). He stated that the minimum hydrodynamic radius of 10 kDa protein structure is 1.42 nm and minimum hydrodynamic radius of 500 kDa is 5.21 nm. However, direct determination of maximum value of the hydrodynamic radius was not reported to be quite possible (Ericson, 2009). According to data compiled in Table 3.5, decomposition of HA structure was achieved to smaller size fractions and these smaller fractions form smaller metachemical hydrogel structures in comparison to the $HA_{,as\text{-}is}$, $HA_{,photocat}$. On the contrary, colloidal stability of these smaller metachemical structures were less than non-treated, $HA_{,as\text{-}is}$, and heteroaggregation developed in time. Heteroaggregation was evidenced with the cumulative ratio increase of structures. Photocatalytic degradation decomposed not only aromatic structures but also σ bonds which caused formation of more hydrophilic string-like structures as was evidenced by the decrease in aromaticity (Table 3.1). These hydrophilic structures were mostly affected by H-bonds that increased colloidal stability. On the other hand, in some structures, charge localization increased, and these structures were more prone to form colloidal hetero-aggregates via van der Waals interactions (Wells and Stretz, 2019). The hydrodynamic size of these hetero-aggregates increased from 200 nm to 600 nm - 800 nm upon duration of 120 min. Also, numerical amount of these bigger metachemical hydrogels increased in number-weighted HDS measurement in time. Even though these structures were large enough to precipitate due to H-bonding and their hydrophilic nature upon 120 min, they remained stable as colloidal particles in the solution. It was also evidenced via number-weighted HDS data that cumulative number of structures around 50 nm to 90 nm decreased with formation of bigger structures at the end of 90 min. The increase in structures around 20 nm-30 nm in number-weighted HSD was presumably due to the aggregation of structures in the vicinity of approximately 90 nm, resulting in the formation of fewer but larger structures. Therefore, this phenomenon led to the increased visibility of structures around 20-30 nm that were already present in the medium. Consequently, at the end of 120 min, in comparison to $HA_{,as\text{-}}$

$_{is}$, following photocatalytic treatment, metachemical hydrogel structures having approximately five times larger hydrodynamic sized structures were obtained.

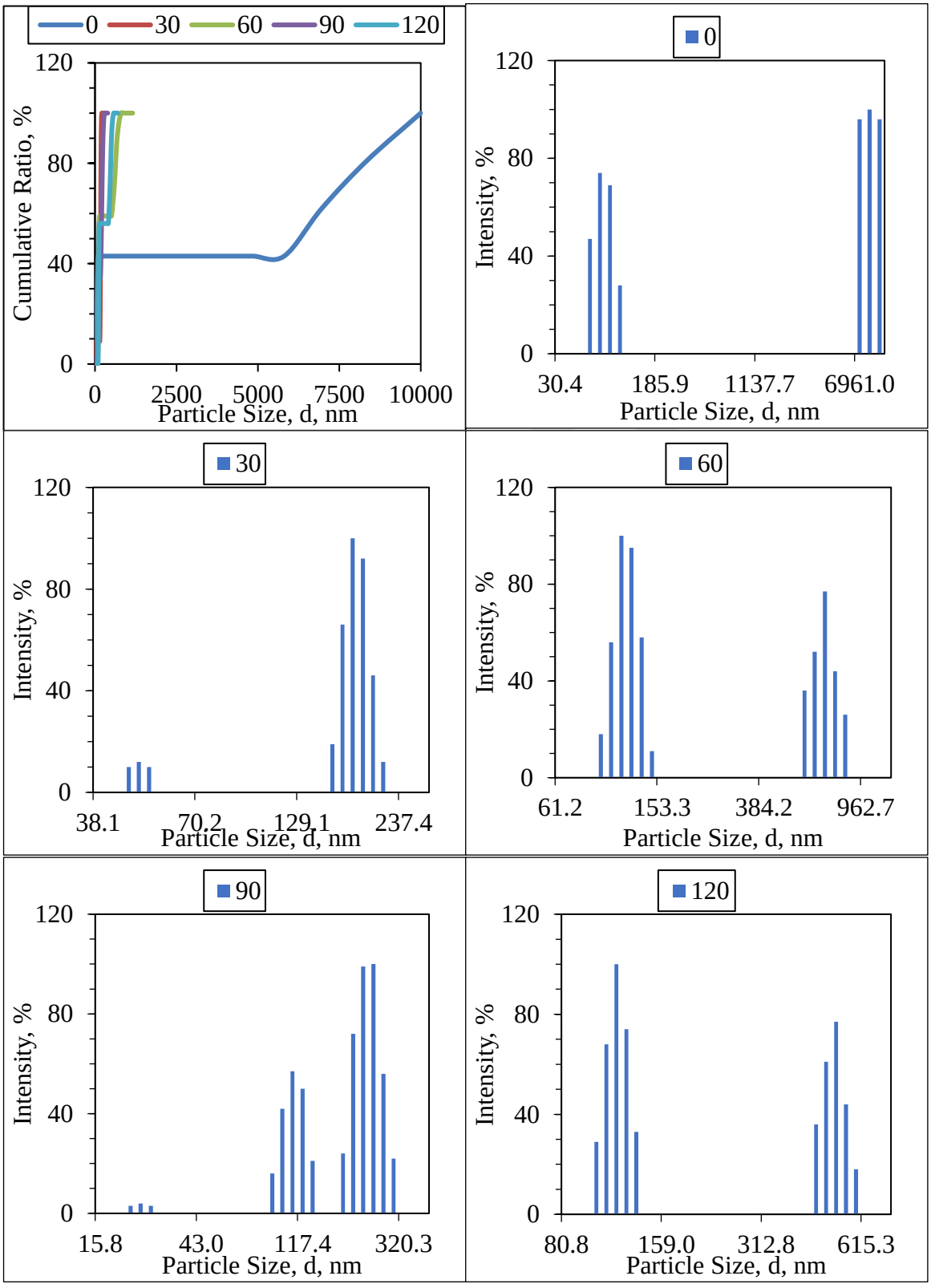


Figure 3.12. The cumulative ratio comparison and hydrodynamic size of $HA_{,photocat}$ 30 min intervals as intensity-weighted HDS.

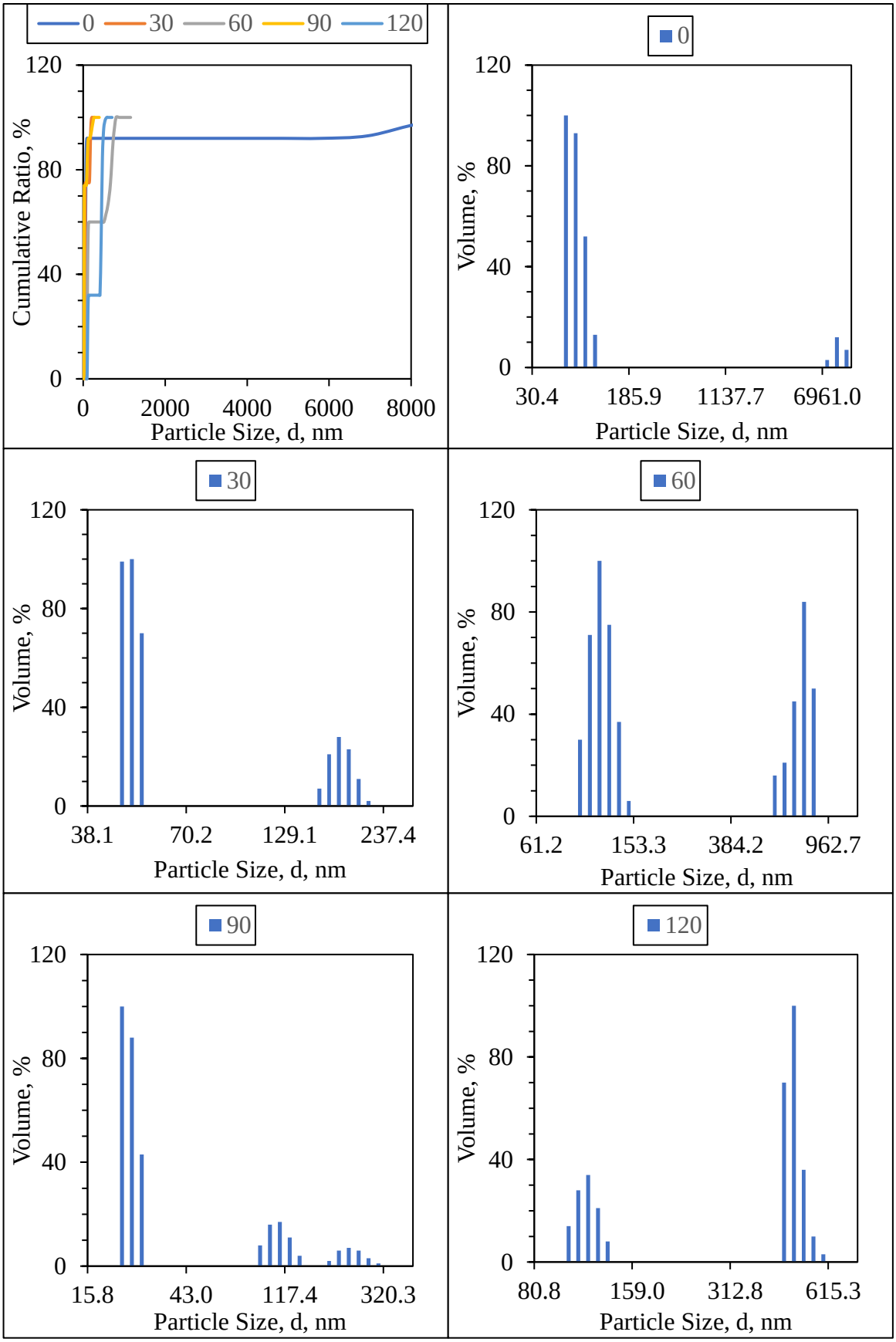


Figure 3.13. The cumulative ratio comparison and hydrodynamic size of $HA_{,photocat}$ 30 min intervals as volume-weighted HDS.

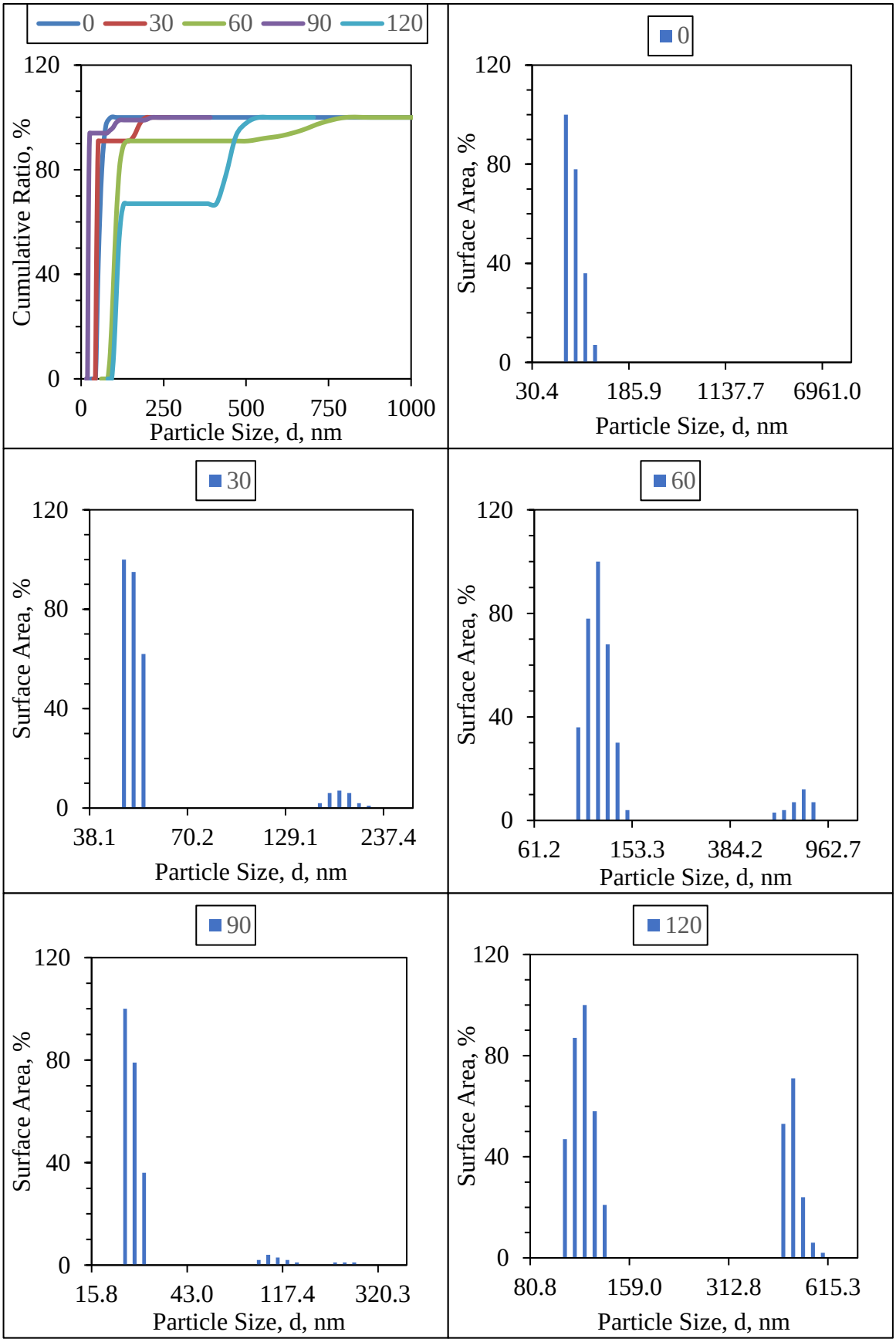


Figure 3.14. The cumulative ratio comparison and hydrodynamic size of $HA_{,photocat}$ 30 min intervals as surface area-weighted HDS.

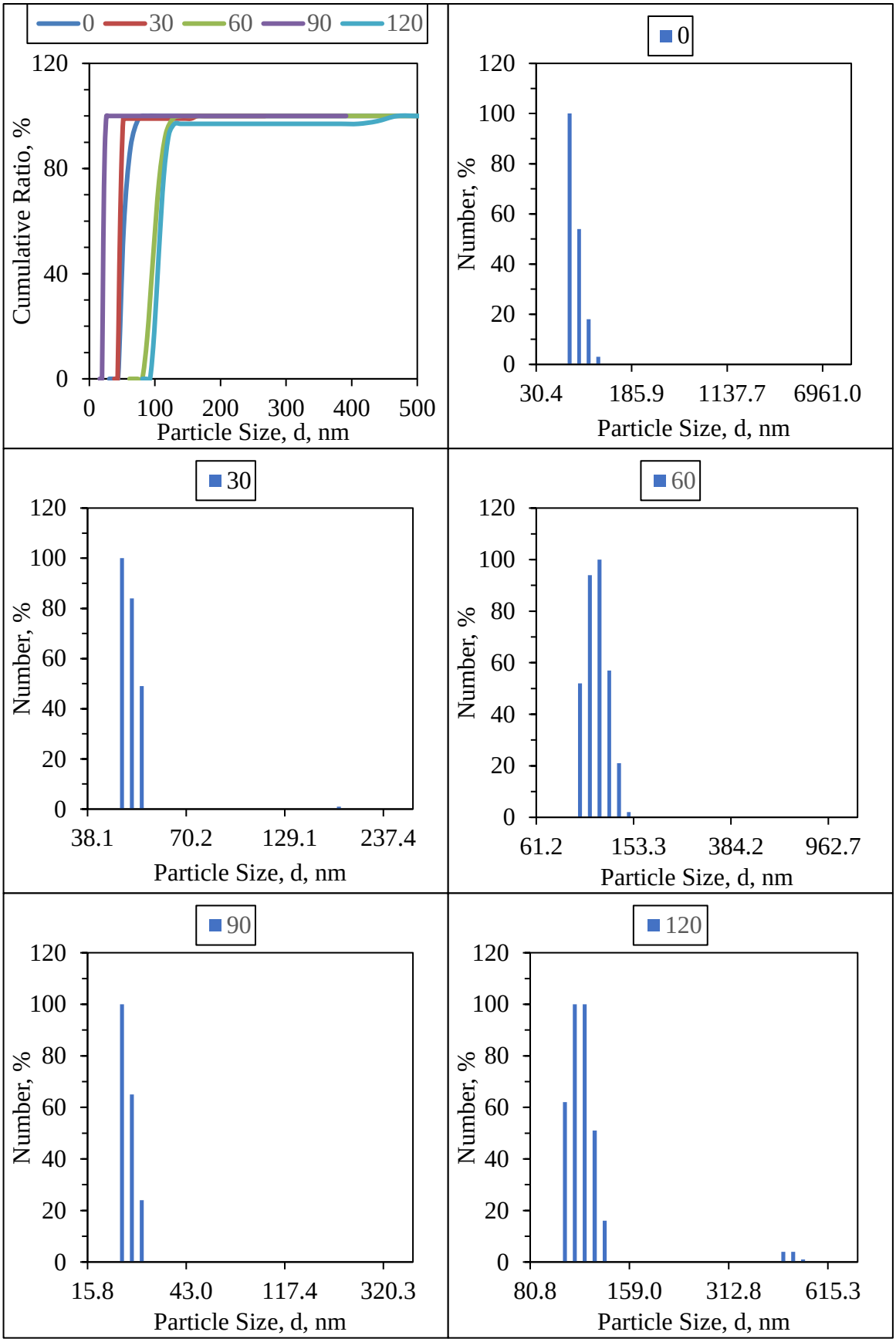


Figure 3.15. The cumulative ratio comparison and hydrodynamic size of $HA_{,photocat}$ 30 min intervals as number-weighted HDS.

3.3. TiO_2 Nanoparticles - Mono System

3.3.1. TiO_2

The importance and significance of TiO_2 particles should also be assessed through its environmental behavior and fate. TiO_2 has the highest production rate as 3000 ton per year, according to the wide usage areas such as cosmetics, paints, coatings, filters, consumer electronics, plastics, cleaning agents, and pharmaceutical industry (Hendren et al., 2011; Piccino et al., 2012; Nakata and Fujishima, 2012; Vance et al., 2015). However, in scientific view photocatalytic properties of TiO_2 deserved the top attention (Gupta and Tripathi, 2011; Nakata and Fujisima; 2012; Schneider et al, 2014; Guo et al, 2019). TiO_2 is also one of the most widely used photocatalyst in the literature more specifically for NOM/humic degradation (Bekbolet et al., 2002; Uyguner and Bekbolet, 2004; Kavurmaci and Bekbolet, 2008; Selcuk and Bekbolet, 2008; Uyguner and Bekbolet, 2010; Birben et al., 2015; Birben et al., 2017; Turkten and Bekbolet, 2020), however it was also cited that aggregation of TiO_2 decreased the photo-efficiency (Maira et al., 2000; Lin et al., 2006; Tseng et al., 2006; Siedl et al., 2009). Since the colloidal stability of the photocatalytic particles had a great importance on photocatalytic degradation efficiency, the main characteristics of colloid properties such as rheology, surface area, and packing density were directly affected by not only particle size distribution of particles but also the hydrodynamic size of the particles. Consequently, hydrodynamic size measurement would be a suitable method for understanding both aggregation/agglomeration behavior of TiO_2 particles.

Basic physicochemical properties of TiO_2 P-25 were compiled and presented in Table 3.1 (Birben et al., 2015). Primary crystal size of TiO_2 particles was 22.3 nm and specific surface area was 57.55 m^2g^{-1}. The band gap energy of TiO_2 was reported as 3.2 eV/ 3.02 eV for anatase and rutile phases respectively. This band gap energy difference causes high photoactivity for anatase and light reflecting properties for rutile structure. The electron-hole recombination would be faster in rutile phase in comparison to anatase, therefore radical formation rate of anatase structures would be higher than rutile structures. However, the overall band gap energy of the TiO_2 could vary according to the anatase/rutile ratio. The point of zero charge value was pH_{zpc}= 6.25 which indicated that under $pH=pH_{zpc}$ condition, the surface of TiO_2 was equally composed of positively and negatively charged sites thereby the overall surface charge of a particle would be practically zero. Figure 3.16 illustrates the pertaining surface reactions due to the deprotonation and protonation of surface adsorbed H_2O molecules and detailed surface reactions were presented in Section.3.4.3. equations 3.41.

Where, $pH_{zpc}=(pK_{a1}$ and $pK_{a2})/2$ (3.41)

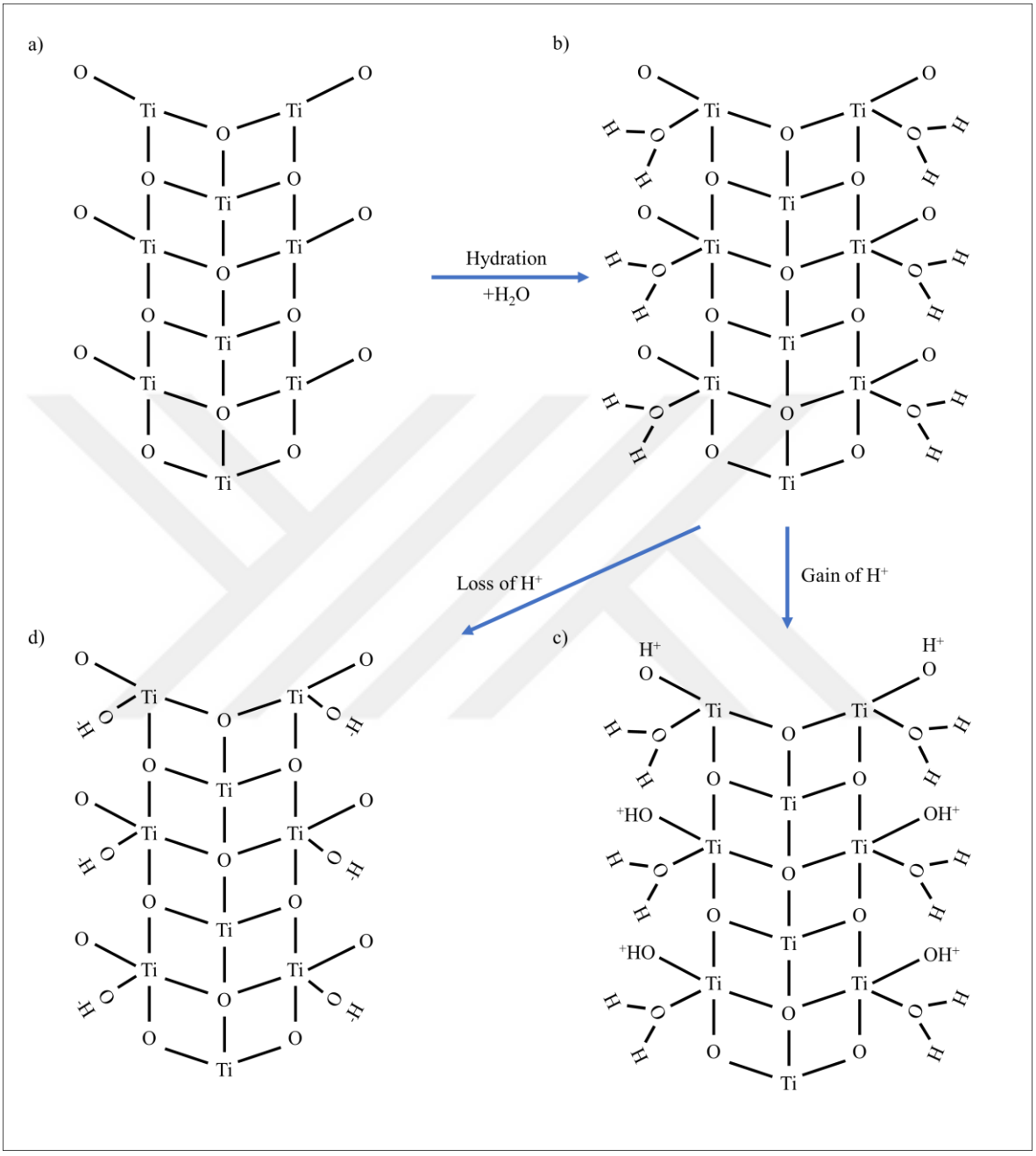


Figure 3.16. Attainment of surface charge by colloidal TiO_2 in water. a) Anhydrous TiO_2 consists of two oxygen atom per Ti atom. b) TiO_2 suspended in water as a colloid, it binds to water molecules to form hydrated TiO_2. c) Loss of H^+ from the surface adsorbed H_2O yields a negatively charged colloidal particle. d) Gain of H^+ by surface O atoms yields a positively charged particle. The former process (loss of H^+ ion) predominates for metal oxides. (Adapted from Manahan, 2022).

Table 3.7. Characterization results of TiO_2. * Measured during the study.

Nanoparticle	Band Gap Energy, eV	λ, nm	pH_{zpc}	Zeta Potential*, eV	Crystallite Size, nm	BET Surface Area, m^2g^{-1}	Reference
TiO_2	3.01	411	6.25	16.06	22.3	57.55	Birben et al., 2015

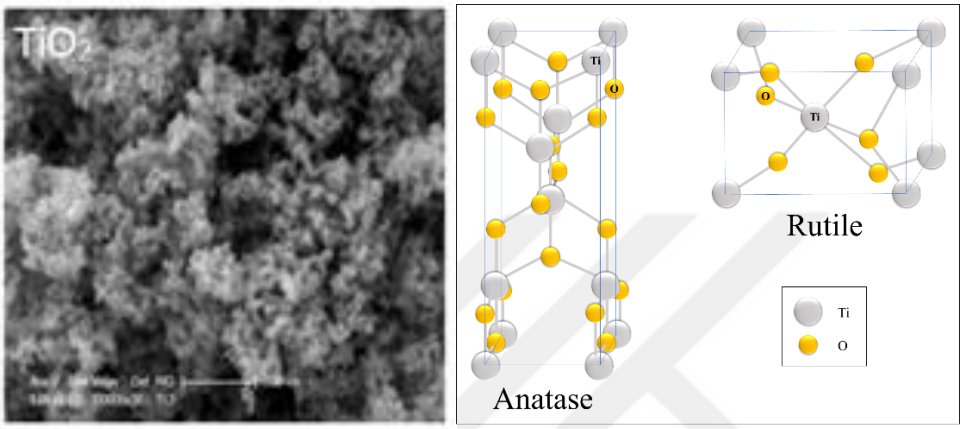


Figure 3.17. SEM image and crystalline structure of TiO_2 NPs.

Figure 3.17 displayed the SEM image and crystalline structure of TiO_2 particles. TiO_2 expressed a bean like shape and even in atmospheric conditions and would be in agglomerated and/or aggregated state due to the humidity in room conditions as could also be visualized by SEM image. TiO_2 particles were covered by hydroxide groups supplied by atmospheric humidity that created changes in surface potential and electrostatic repulsions between the particles (Kaegi et al., 2008; Thio et al., 2011). This behavior could be explained by Derjaguin-Landau-Verwey-Overbeek (DLVO) theory (Derjaguin and Landau 1941; Verwey and Overbeek 1948), which argued that the sum of attractive, van der Waals forces, and repulsive, electrostatic, forces could determine the agglomeration/aggregation and stability of the primary particles in liquid suspensions. Zeta potential and thickness of electrical double layer were the main properties determining the strength of electrostatic repulsive forces (Morrison and Ross, 2002; Pate and Safier, 2016). The surface ionization, thereby zeta potential, could depend on several mechanisms such as ion adsorption and lattice ion dissolution (Stumm and Mogan, 1996). The thickness of electrical double layer was related to the ionic strength of the solution (Figure 3.18). On the contrary, DLVO theory was not very descriptive in cases of low ionic strength (Widegren and Bergstrom, 2002). Dwivedi and his colleagues proposed a non-DLVO theory which supported that a combination of steric hindrance and magnetic/hydration forces are responsible for

particle aggregation (Dwivedi et al., 2015). In case of low ionic strength conditions both theories could be effective during aggregation/agglomeration of TiO_2 particles, however since ionic strength would be constant during sole TiO_2 particle size analysis the stability of the electrical double layer thickness could be expected.

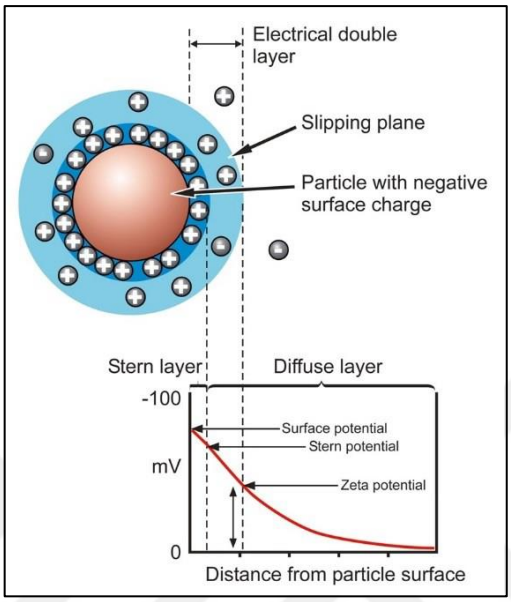


Figure 3.18. Schematic representation of particle Stern layer and electrical double layer formation (Hendricks, 2006).

The TiO_2 surface would be covered with surface-adsorbed water layer as illustrated in Figure 3.19. This surface-adsorbed water layer was comprised of two different hydration layers *i.* chemisorbed water, *ii.* physisorbed water. The chemisorbed water, the water-particle surface phase, was formed by more ordered water molecules. The chemisorbed water layer was stable up to 300-500˚C. Over 300˚C two contiguous OH groups would condense and evolve into a water molecule (Wu et al., 2017). However, in the second hydration layer as physisorbed water, no orientation preferences would be observed. The physisorbed water layer consisted of three layers as stabilized water, relatively mobile water, and mobile water. The stabilized water layer was the closest one to the chemisorbed water and this layer was stable up to 100-160˚C. The relatively mobile water layer was removable at 80-100˚C and the mobile water layer was stable up to 50˚C. The structural uniformity of adsorbed water could deteriorate by the order of stabilized water, relatively mobile water and mobile water (Figure 3.19). The chemisorbed water could create strong hydration forces that form aggregates smaller than 100 nm. For the structures sizing over 100 nm on the other hand van der Waals interactions, capillary forces and electrostatic forces were directly proportional with the particle size so, van der Waals interactions could dominate the structures smaller than 1µ (Laube

et al., 2017). Also, the forces developed by chemisorbed water layer could weaken on bigger particles. On the other hand, the physisorbed water could not affect the particle-particle or particle-water interactions. (Koparde and Cummings, 2007; Jiang et al., 2009; Wu et al., 2017).

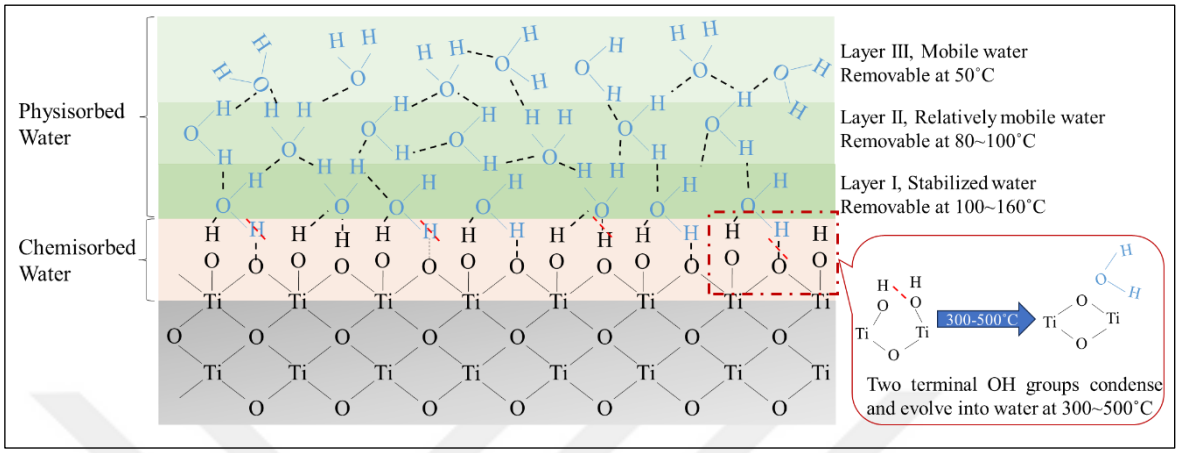


Figure 3.19. Illustration of water adsorption onto TiO_2 surface.

Figure 3.20 illustrated the primary particle, aggregate and agglomerate structures, and their interactions of $TiO_{2,as\text{-}is}$ in liquid phase dispersion (Jiang et al, 2009). Colloidal stabilization of primary particle, $TiO_{2,as\text{-}is}$ crystals, were dependent on IS as previously mentioned, also aggregated structures could act as primary particles due to their high surface charge, ticker double layer and stearic forces which is leading to domination of repulsive forces and supplies the colloidal stability of these structures. On the other hand, in the case of low IS condition surface charge decreases, double layer would be thinner, and no steric forces would be observed. This condition would result in agglomeration of both primary particles and already aggregated structures. The agglomerated structures could be separated by simple physical interference such as mixing and/or shaking. However, when the interference was removed, separated particles would again tend to agglomerate. Under the specified experimental conditions where absence of any IS was under consideration, aggregation/agglomeration of TiO_2 particles would experience solely electrostatic interactions governed by point of zero charge (pH_{zpc}) conditions. pH_{pzc} of TiO_2 was reported as 6.25 which was consistent with formerly reported data by various research groups (Kosmulski, 2002; Jiang et al., 2009; Birben et al., 2015) and zeta potential of $TiO_{2,as\text{-}is}$ was measured as +16.06 eV. The positive value of zeta potential indicated that surface of $TiO_{2,as\text{-}is}$ agglomerates would be protonated and surface structure of protonated TiO_2 (He et al., 2017) could be shown as,

$$Ti\text{-}OH + H^+ \leftrightarrow TiOH_2^+ \qquad (3.42)$$

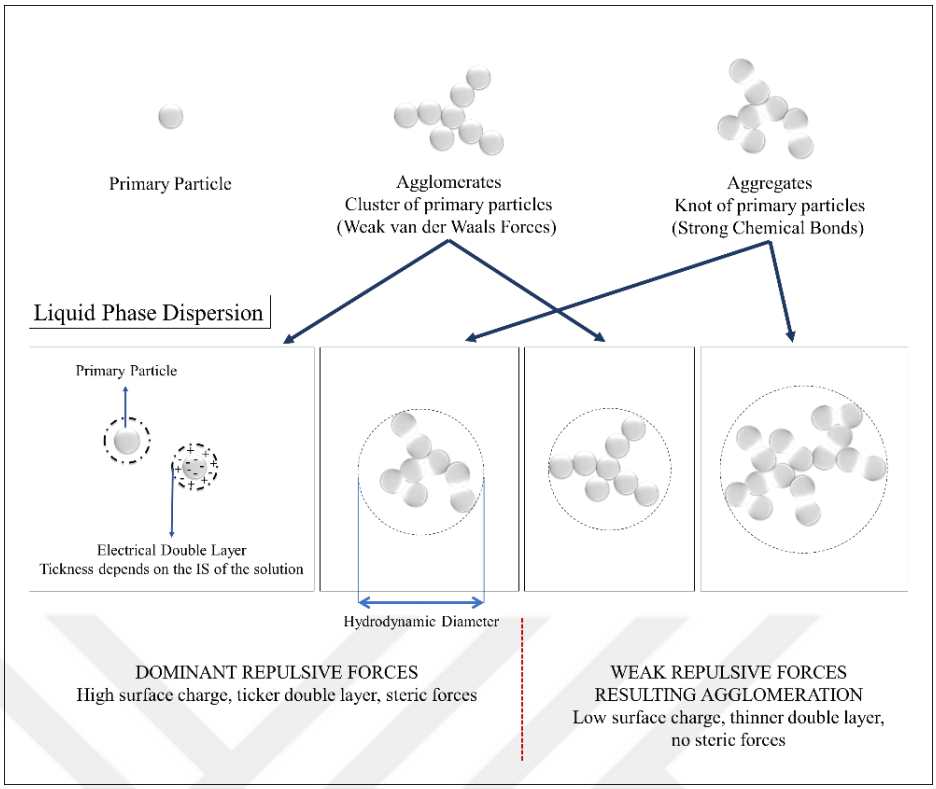


Figure 3.20. The illustration of the primary particle, aggregate and agglomerate structures, and their interactions of $TiO_{2,as\text{-}is}$ in liquid phase dispersion.

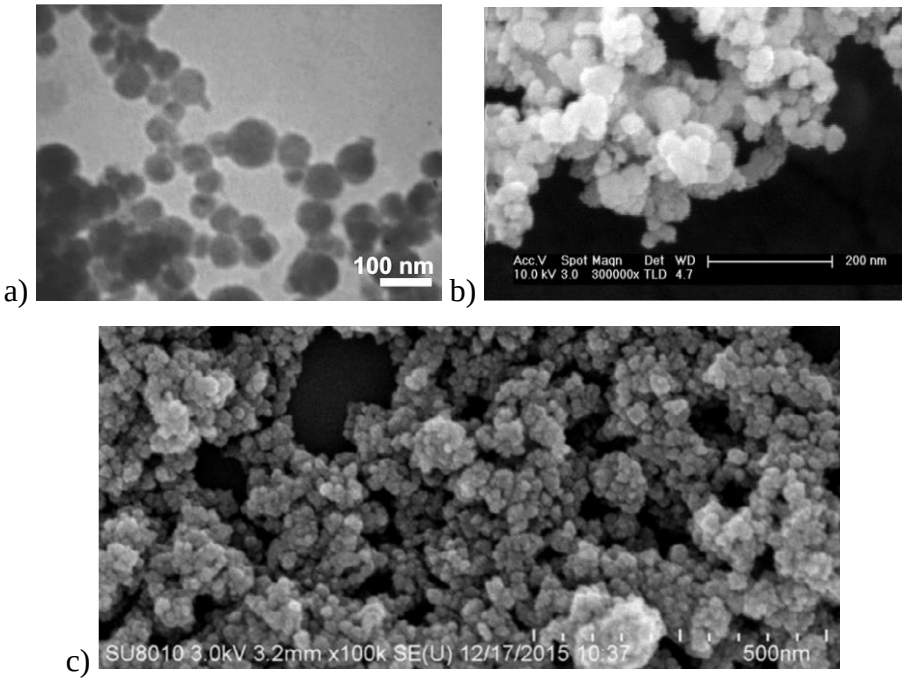


Figure 3.21. TEM and SEM images of TiO_2 precipitates. a) Adapted from Usenko et al., 2023. b) Adapted from Carbajo et al., 2018 and c) Adapted from Wang et al., 2017.

Figure 3.21 showed the literature examples of TEM and SEM images of aggregated/agglomerated structure of sole TiO_2. The particle size determined from TEM/SEM images were definitely operator dependent. For instance, Figure 3.21 a was adapted from the work of Usenko and colleagues. The aggregate size obtained in TEM image was around 50 to 100 nm and agglomerate size was ranging between 300-600 nm). Spherical aggregate structures were visualized, and the structure was formed by gathering of these sapphires as agglomerates (Usenko et al., 2023). Another example was given in Figure 3.21 b which was adapted from the work of Carbajo and colleagues (Carbajo et al., 2018). Aggregate size was reported as 1-2 μm as deduced from the SEM image excluding any verification of aggregate structure. Figure 5 c was adapted from the work of Wang and colleagues (Wang et al., 2017). Aggregate size of sol-gel synthesized TiO_2 (86% anatase, 18% rutile) was reported as 150-220 nm via SEM image. Apart from being based on interpretation, size measurements obtained from TEM/SEM images would not include the surface adsorbed structures. Even if there would be no humidity adsorption onto TiO_2 surface during TEM measurements, hydration forces were not effective as would be in water suspension. Consequently, aggregate and agglomerate size of TiO_2 particles would express different pictorial presentation in TEM/SEM and DLS.

As stated previously, TiO_2 is one of the most widely used photocatalyst due to its superior properties such as, high stability, non-solubility in water media, low-cost, ease to produce, chemically inert structure, low toxicity and being a highly oxidative semi-conductor (Suib, 2013; Parrino and Palmisano, 2021). The detailed photocatalytic degradation mechanism of TiO_2 in the presence of HA under solar light irradiation has been explained in section ($TiO_{2,irr}$ info). Basically, in the presence of air and water, UV/visible light excites an electron to conduction band that located in the surface of the TiO_2 semiconductor and leaving a hole between the valance band (Parrino and Palmisano, 2021; Uyguner-Demirel et al., 2023). The pertaining fundamental reactions were presented in section 3.2.3 Overall mechanism continues until all organic/inorganic substrate degraded into simple organic materials, inorganic species and even to CO_2 and H_2O. On the other hand, beside the advantages of TiO_2 as a photocatalyst, there were some specific properties that should be improved for instance, the wide bad gap energy (3.2 eV) thereby the weak visible light adsorption (~5%, corresponding UV light content). Some methods have been proposed to overcome these disadvantages *i.e.* doping with metal (Fe, Ag, Cu, Cr, Pt, etc.) or non-metal (N, B, C, S, F, etc.) or co-doped (Zn/Fe, C/N, Fe/Co, W/N, N/Fe, etc.) compounds to enhance activity under solar light (Zaleska, 2008; Lee et al., 2013; Valetin and Pacchioni, 2013; Basavarajappa et al., 2020; Parrino and Palmisano, 2021; Hasanuzzaman et al., 2023; Eldoma et al., 2024).

3.3.2. Metal Doped TiO_2 - Fe-TiO_2

Doping with metal ions could improve the efficiency of photocatalysis by reducing the recombination rate of electron-hole pairs. Transition metal ions were commonly used to decrease the energy barrier, extending the time before electron-hole pairs recombine, thus making TiO_2 more active under solar light. By substituting metal ions into the crystal structure of TiO_2 (Ti^{4+}), additional electrons were introduced, making it responsive to visible light region (λ= 400-800 nm). Metal ions also slowed down the rate at which charged particles recombine on the surface by acting as traps for electrons and holes, thereby the reaction catalyzation ability of TiO_2 was enhanced under visible light. Among the several metal ions Fe(III) was a good substitute due to its low band gap energy (2.6 eV) and having similar elemental radius with Ti^{4+} (Adan et al., 2007; Khaleel and Al-Nayli, 2008; Tsoncheva et al., 2016; Cheng et al., 2020). Also, Fe(III) could be analogous of Ti^{4+} because of the similar energy level of Fe^{2+}/Fe^{3+} and Ti^{3+}/Ti^{4+} transitions so, according to following reactions Fe(III) could trap both e^- and h^+;

$$Fe^{3+} + e^- \rightarrow Fe^{2+} \quad (3.43)$$

$$Fe^{2+} + O_{2(ads)} \rightarrow Fe^{3+} + O_2^- \quad (3.44)$$

$$Fe^{2+} + Ti^{4+} \rightarrow Fe^{3+} + Ti^{3+} \quad (3.45)$$

$$Fe^{3+} + h_{vb}^+ \rightarrow Fe^{4+} \quad (3.46)$$

The existence of O_2 is essential for the photocatalytic reaction due to retardation effect of O_2 over the e^--h^+ recombination. Also, O_2^- is involved in several reactions during photocatalytic degradation reactions. On the other hand, doped Fe(III) in the TiO_2 lattices could act as recombination centers for e^--h^+ pairs in case of high iron concentration as in the following reactions;

$$Fe^{3+} + e^- \rightarrow Fe^{2+} \quad (3.47)$$

$$Fe^{2+} + h_{vb}^+ \rightarrow Fe^{3+} \quad (3.48)$$

$$Fe^{3+} + h_{vb}^+ \rightarrow Fe^{4+} \quad (3.49)$$

$$Fe^{4+} + e^- \rightarrow Fe^{3+} \quad (3.50)$$

Therefore Fe(III) doping concentration was also an important parameter in the case of improving photocatalytic efficiency. As another aspect, photocatalytic activity was directly related to surface area of TiO_2 (Zhang et al., 1998; Araña et al., 2003; Zhu et al., 2004). There are several methodologies to synthesize Fe-TiO_2 such as, sol-gel (Ranjit and Viswanathan, 1997; Akpan and Hameed, 2010), hydrothermal (Li et al., 2008; Nguyen et al., 2011), thermal hydrolysis (Ambrus et al, 2008; Tongs et

al., 2008), solvothermal (Wang et al., 2011; Sood et al., 2015), and wet impregnation (Navio et al., 1998; Yalçın et al., 2010; Birben et al., 2017) methods. Among these methods wet impregnation technique was used to avoid the dopant cations penetrating the bulk TiO_2, so the recombination rate increases by bulk doping inhibited (Jiang, 2006; Yalçın et al., 2010).Fe-$TiO_{2,as\text{-}is}$ was synthesized by wet-impregnation method by following the procedure published by Yalçın and colleagues (Yalçın et al., 2010). 8 g TiO_2 P25 (Evonik) was suspended in distilled water and 0.25 wt% $Fe(NO_3)_3.9H_2O$ was added to suspension and mixed for 1h at room temperature. The Fe(III) doping on $TiO_{2,as\text{-}is}$ was evidence with the color change from white to light brownish beige at the end of 1 h period. After mixing obtained Fe-$TiO_{2,as\text{-}is}$ was washed with distilled water three times and following to washing dried at 373 K for 24h. Finally obtained Fe-$TiO_{2,as\text{-}is}$ calcinated at 773 K for 4 h, grounded and sieved.

Physico-chemical properties of the prepared doped TiO_2 specimens could be determined by well-defined characterization methods. The band gap energy of Fe-TiO_2 was calculated according to the UV-visible diffuse reflectance data by using the relation between adsorption coefficient and α and incident photon energy *hν*;

$$\alpha = \frac{B_d(h\nu - E_g)^{1/2}}{h\nu} \qquad (3.51)$$

B_d stands for the absorption constant, and the $(\alpha h\nu)^{1/2}$ vs hν were plated from the spectral data. The specific band gap energy was implied from the intersection of the linear part of the extrapolation with the axis of photon energy (Yalçın et al., 2010). According to plotted data after doping with Fe, the band gap energy decreased from 3.01 eV (E_{bg} of bare TiO_2) to 2.55 eV. The interaction between VB electrons and the localized d electrons of Fe(III) was responsible for the narrowing of band gap value. Doping with Fe(III) created a mid-gap with its 3d orbital electrons between the CB and VB of TiO_2 (Birben et al., 2017). Doping with Fe(III) also decreased the pH_{zpc} from 6.25 to 4.80 (pH_{zpc} of Fe-TiO_2) so at neutral pH conditions the surface of Fe-TiO_2 was negatively charged (Kosmulski, 1997). Crystalline size changes were followed by XRD results of Fe-$TiO_{2,as\text{-}is}$. Doping with Fe(III) decreased the primary crystalline size in comparison to the undoped-TiO_2. The primary particle size of Fe-TiO_2 (doped with 0.25 wt% Fe(III)) was found to be 16.4 nm by using Scherrer equation, which shows the slow decrease in comparison to the undoped TiO_2 (22.3 nm). The decrease of primary particle size demonstrates that doping caused a slight deformation in the crystal structure. Hence substitutional doping of Fe(III) obtained rather than interstitial doping (Yalçın et al., 2010). This structural change might be related to the charge accumulations occurred after doping with Fe(III) that creating electrostatic interactions between different edges and corners of the structures (Birben et al.,

2017). The change of crystal structure and formation of electrostatic interactions also affects the hydrodynamic size of Fe-doped TiO_2 in comparison to the undoped-TiO_2. Although the primary crystalline size decreased, the SEM image showed that the aggregate/agglomerate size was larger in Fe-$TiO_{2,as\text{-}is}$ than in $TiO_{2,as\text{-}is}$, due to the formation of While undoped-TiO_2 ($TiO_{2,as\text{-}is}$) comprised of homogenous bean like shape, Fe-doped TiO_2 (Fe-$TiO_{2,as\text{-}is}$) showed a more heterogeneous structures in case of shape and dimension. In comparison to the $TiO_{2,as\text{-}is}$, aggregates of Fe-$TiO_{2,as\text{-}is}$ demonstrated more straight edges and sharp corners which generated to a high degree of porosity. Despite shape and size, Fe(III) distribution was homogeneous in anatase phase, according to EDX results of Fe-$TiO_{2,as\text{-}is}$ (Yalçın et al., 2010; Ali et al., 2017; Kruanetr and Wanchanthuek, 2017).

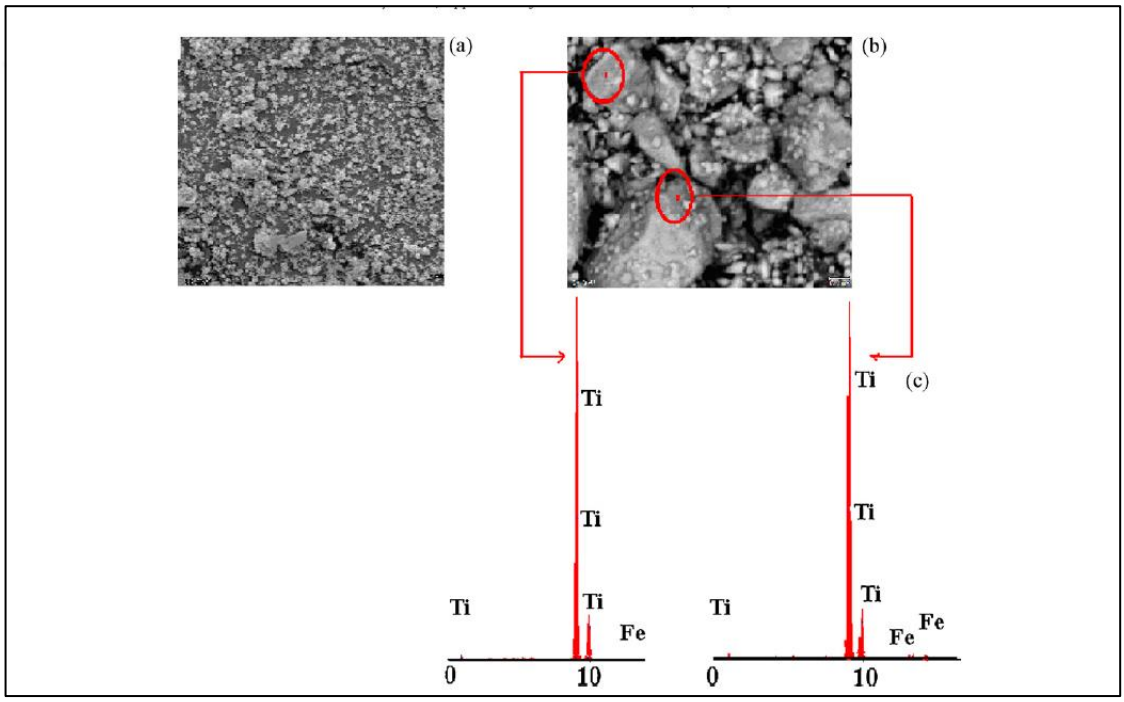


Figure 3.22. SEM image and EDAX data of Fe-doped TiO_2 (Yalçın et al., 2010).

3.3.3. Anion Doped TiO_2 – N-TiO_2

Beside the metal doping, non-metal doping was used as an alternative method in several studies and among these several non-metal doping materials *e.g.*, nitrogen (N) was a good substitution for oxygen due to its suitable size, small ionization energy and stability (Khataee et al., 2013; Moosavi et al., 2016; Vaiano et al., 2017; Ferrara et a., 2023; Kassalia et al., 2023a; Kassalia et al., 2023b). There were several methodologies to achieve N-TiO_2 such as nitrogen or oxygen treatment, chemical vapor deposition, ball milling, hydrothermal, solvothermal, micro-emulsion, sol-gel, precipitation, sputtering, atomic layer deposition and wet impregnation methods (Du et al., 2022). Doping

methodologies differentiate according to obtaining substitutional N doped TiO_2 or interstitial N-doped TiO_2. The wet impregnation method was chosen as proper methodology to obtain substitutional N doped TiO_2 due to its ease to application, cost-efficiency, wide applicability, and scientific familiarity (Yalçın et al., 2010b; Birben et al., 2015). Also, the substitutional doping was reported as the most efficient due to p state of N interaction with 2p states of O leading to band-gap narrowing (Asahi et al., 2001). After pioneering work of Asahi and their colleagues, several theories were proposed to explain band gap narrowing effect of N. The substitutional doping was based on substitution of two N atom with the two O atom located in TiO_2 crystalline structure by a leaving oxygen vacancy. Irie and their colleagues reported that N doping created an isolated and localized mid-gap state above the VB, by increasing concentration of N and this state was (Irie et al., 2003). Another theory advocated that the decreased band gap energy was a result of a synergetic effect of defected energy states including Ti^{3+} and oxygen vacancies (OVs) and mid gap state of N 2p and by this way N caused the formation of a mid-gap under the CB by Ti^{3+} and OVs (Yalçın et al., 2010b; Powell et al., 2014; Nakada et al., 2017). Although there were other theories proposed for explaining band-gap narrowing effect of N still no consensus was achieved (Du et al., 2022).

An incipient wet impregnation method could be a practical technique to prepare N-doped TiO_2. Certain amount of TiO_2 (Evonik, 8 g) was mixed with 10 mL of aqueous solution of urea and stirred at room temperature for 1 h. Depending on the urea concentration, color change was attained as yellowish white. Doping concentration was selected as 0.5 wt % N to prepare N-doped TiO_2 due to better performance during photocatalysis. Finally, prepared N-doped TiO_2 was dried at 100˚C after that calcinated at 500˚C and stored in dark conditions (Gurkan et al, 2012; Birben et al., 2015).

Characterization of N-TiO_2 was realized according to the methodology described for Fe-TiO_2. The band gap energy of prepared N-TiO_2 was calculated by using the relation between UV-DRS adsorption coefficient and α and incident photon energy *hv* as indicated above. Similar to the Fe-TiO_2, the intersection of the linear part of the extrapolation with the axis of photon energy was plotted and band gap energy was determined. The band gap energy of N-TiO_2, was calculated as 2.79 eV that was quite lower than the E_{bg}=3.01 of TiO_2. N-doping was reported as substitutional contrary to the interstitial doping of Fe (Du et al., 2022). Anion doping also caused a lowering effect on the point of zero charge value from 6.25 (TiO_2) to 5.15 (N-TiO_2). The octahedral TiO_2 crystalline structure was formed with coordination of Ti^{4+} atoms with six O^{2-} atoms. Figure 3.23 illustrated the octahedral structure in anatase and rutile forms of N-TiO_2. While the anatase structure came up together via corner sharing, the rutile structures were formed by edge sharing, hence the dopant N atom could be located at different position in the octahedral crystal structure. This location differences might cause

various redistribution of local charges on the surface atoms of TiO_2 due to the different electronegativities depending on the position of dopant atom in the crystalline lattice. Consequently, due to the two different crystalline shapes (anatase and rutile), positioning of dopant atoms might cause fluctuations on zero charge value (Birben et al., 2015). Both crystalline size (18.8 nm) and surface area (55.35 m^2g^{-1}) of N-TiO_2 were slightly decreased in comparison to the TiO_2 (CS: 22.3 nm, SA: 57.55 m^2g^{-1}). Even the N doping caused charge localizations, the crystalline structure was not distorted. This trend was evidenced with the SEM images showed in Figure 3.23. Similar with the TiO_2, N-TiO_2 illustrated a homogeneous distribution and uniform structures. On the other hand, the XRD peak of (101) plane of anatase a marginal shift from its normal position was observed. This shift indicated that the crystal was distorted by the substitution of N atoms with O atoms and compressive stress resulting from the change in the electronic structure of N-TiO_2, corresponding with a slight decrease in the d value (Yalçın et al., 2010b). The physico-chemical properties of TiO_2, Fe-TiO_2, and N-TiO_2 were presented in Table 3.8.

Table 3.8. Table. Physico-chemical properties of metal and anion doped TiO_2 specimens.

Nanoparticle	Band Gap Energy, eV	λ, nm	pH_{zpc}	Zeta Potential*, eV	Crystallite Size, nm	BET Surface Area, m^2g^{-1}	Reference
N-TiO_2	2.79	479	5.15	-	18.8	55.35	Birben et al., 2015
Fe-TiO_2	2.55	486	4.80	-	16.4	33.00	Birben et al., 2017

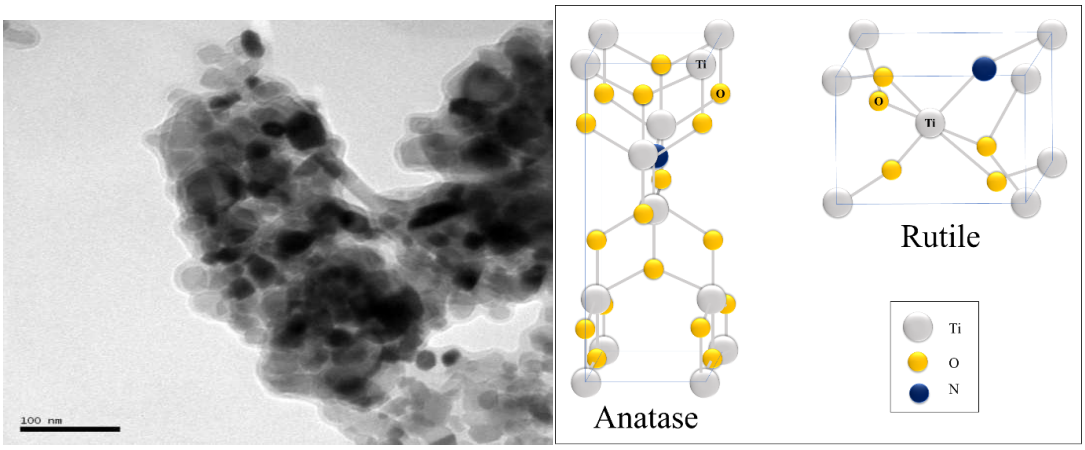


Figure 3.23. SEM image and theoretical substitutional N doped crystalline structure of TiO_2 (Yalçın et al., 2010)

3.4. Hydrodynamic Size of Undoped and Doped TiO_2 Species

3.4.1. Hydrodynamic Size Assessment of $TiO_{2,as\text{-}is}$

Hydrodynamic particle size distribution of TiO_2 particles under "as-is" condition was determined by preparing 0.25 $mgmL^{-1}$ TiO_2 suspension in Milli-Q water that was sonicated for 1 min and magnetically stirred for 4 minutes to ensure complete homogenization. Time depended HDS measurements were followed for 180 min under steady conditions within the DLS instrument. Figures 3.24-3.27 displayed the intensity-, volume-, surface area- and number-weighted HDS graphs and Table 3.9 compiled the time dependent HDS cluster maxima, HDS range and min-max diameter difference with respect to multi-size distribution data. Table 3.10 gathered the cumulative distribution ratios of $TiO_{2,as\text{-}is}$ aggregates and agglomerates during 180 min.

The Polydispersity index of $TiO_{2,as\text{-}is}$ were 0.323, 0.322, 0.318, 0.310, 0.314 0.297 and 0.301 for initial, 30 min, 60 min, 90 min 120 min, 150 min and 180 min respectively. An average value of 0.312 would signify the presence of continuous nearly mono dispersed medium during DLS measurements. This trend implies that both aggregation/agglomeration and dissaglomeretion of TiO_2 was continuous for 180 min. At the end of 180 min a slight decrease of PDI (from 323 to 0.301) was observed which might be related to sedimentation of the bigger structures, however the TiO_2 suspension was still containing aggregates/agglomerates in several sizes. In the following paragraph this phenomenon will be explained.

Because the nearly monodispersed size distribution of TiO_2 was evidenced by PDI, MSD had been used to illustrate HDS distribution of $TiO_{2,as\text{-}is}$. The intensity-weighted HDS showed mainly two clusters except for in 150 min which demonstrated 3 clusters. Initial measurement revealed two clusters as 98.6-380.3 nm and 498.3-1467.5 nm. The volume-weighted HDS range of TiO_2 was reported as two clusters, 50-150 nm and 200-1000 nm, which was in agreement with the results of Budarz and colleagues (Table 3.9) (Budarz et al., 2017). Carbajo and colleagues reported the average volume-weighted HDS of TiO_2 (250 mgL^{-1}) as 3 μm. On the other hand, they stated that the aggregation/agglomeration formation of TiO_2 was concentration and pretreatment condition depended and for lower concentration of TiO_2 lower aggregate size could be obtained (Carbajo et al., 2018). The primary crystalline particle size of $TiO_{2,as\text{-}is}$ was 22.3 nm, on the other hand lowest measured particle size of $TiO_{2,as\text{-}is}$ solution was 66.6 nm (Figure 3.24, in 150 min), which could be interpreted as the minimal TiO_2 aggregate size composed of almost 2-3 particles due to the effective intramolecular hydration forces on the particles less than 100 nm (Koparde and Cummings, 2007;

Laube et al, 2017). These aggregated structures could further form not only larger aggregates, but also agglomerates in solution through grouping as well as disaggregation phenomena (Jiang et al, 2009; Jassby et al, 2012). Sol gel synthesized TiO_2 displayed a pH dependent profile of DLS diameters in between 10 nm-140 nm being higher under acidic conditions (French et al., 2009: Dunphy Guzman et al., 2006; Kignelman et al., 2021). TiO_2 P-25 expressed hydrodynamic size variations such as 350 nm (Suttiponparnit et al., 2011), 10-1000 nm (Jassby et al., 2012), 220 nm (Nickel et al., 2014), 252 nm (Sun et al., 2014), 653 nm (Brunelli et al., 2022), 633±103 nm (Wu and Choi, 2016) and 150 nm (Tan et al., 2021).

Differing from number-weighted HDS, intensity-, volume-, and surface area-weighted HDS data showed an intense peak around 855.1-1467.5 nm range which was evidence for agglomeration due to attractive forces domination over repulsive forces (Jiang et al, 2009). The positive value of zeta potential (16.06 eV, Table 3.7) indicated that the surface of $TiO_{2,as\text{-}is}$ agglomerates were protonated and leading to deterioration of repulsive forces and increase in van der Waals interactions (He et al., 2017). The domination of van der Waals forces were mainly responsible from instability thereby agglomerated dispersion of $TiO_{2,as\text{-}is}$ (Jiang et al., 2009; Wyrwoll et al., 2016; He et al., 2017). This trend was evidenced by increased HDS values upon duration of 180 min. During the first 90 min while the intensity-, volume- and surface area-weighted HDS clusters ranging around 600 nm to 1500 nm were remaining stable, their number-weighted HDS were increasing cumulatively. The settlement of these bigger clusters to the bottom of the cuvette was not only visible to eye but also could be followed with the cumulative amount changes in 120 min and after. Data taken at 120 min HDS expressed similarity to initial condition except for the largest cluster in the range 855.1-1467.5 nm. Cumulative rate of detectable smaller clusters approximately 90 to 150 nm, which were present however dominated over by the larger clusters, expressed an increasing trend. Sedimentation kinetic results evidenced this trend. During 60 min in respected to specified wavelength (λ= 550 nm) approximately 10% of TiO_2 precipitated and the final ratio of settlement was approximately 20%.

The cumulative ratio of volume-weighted HDS data indicated the volume covered by the hydrodynamic structure. This ratio was also related to the number abundance of particles in the medium. For instance, under initial conditions, the particle size ranging in between 498.3-652.7 nm were occupying more space in comparison to the other clusters. This situation could be explained by the comparison of number-weighted HDS and volume-weighted HDS. The particles around 100 nm were the most abundant structures in number-weighted HDS measurements and the particles around 500-650 nm were only representing 3% of the system. Even the structures around 500-650 nm were less in number since they covered more volume than smaller particles, therefore the peak intensity of

the volume fraction increases. Aggregates around 800 nm-1500 nm reflected a small ratio in volume-weighted HDS, due to their numerical minority under initial conditions (Figure 3.25 and Table 3.9).

Conversely, since the surface area of small particles of uniform properties would cover more area in the liquid medium therefore, cumulative ratio of numerous smaller particles had the highest ratio in surface area-weighted HDS. However, formation of agglomerates by combination of relatively smaller aggregates could create non-spherical structures which could possess relatively higher surface area than the spherical structures. For instance, following 150 min, hydrodynamic structures between 218.6-237.8 nm exhibited a very small surface area ratio in comparison to the clusters 587.9-710.4 nm and 780.9-943.7 nm. This phenomenon could be explained as the cluster around 218.6-237.8 nm in the form of spherical aggregates and the clusters 587.9-710.4 nm and 780.9-943.7 nm were in the form of non-spherical agglomerates. The aggregate formation was also evidenced by the disappearance of the cluster, 218.6-237.8 nm, and by the increase of agglomerates around 550 nm following 180 min duration time (Figure 3.26 and Table 3.9).

Budarz and colleagues reported volume and number weighted hydrodynamic aggregate sizes extending beyond the nanoparticle range as 1000-2000 nm (Budarz et al., 2017). However, Teulon and colleagues indicated that the number weighted hydrodynamic size of TiO_2 P-25 would display 5-65 nm range whereas Turella and co-workers reported as 114 ± 0.5 nm (Teulon et al., 2018; Turella et al., 2015).

On the other hand, volume-weighted average hydrodynamic size was shown to be in between 100-1000 nm by Song and co-workers as well as by Tolosana-Moranchel and co-workers (Song et al., 2016; Tolosana-Moranchel et al, 2021). Sole anatase TiO_2 expressed number-weighted average hydrodynamic diameter as 105±64 nm at pH=8 (Domingos et al., 2009). Based on the reported data as presented in Table 3.9., the reason of hydrodynamic size variations could be attributed to the selected indicative parameter as well as to the instrumentation. Moreover, pH induced surface potential could affect the aggregate size due to dominating particle-particle interactions (Dunphy Guzman et al., 2006). Considering the neutral pH of the experimental conditions, TiO_2 P-25 expressing a pH_{zpc}= 6.3, the surface of the particles would express almost equal number of positively and negatively charged sites resulting in both attractive and repulsive forces most probably leading to enhanced aggregation (Dunphy Guzman et al., 2006).

Table 3.9. Intensity-, volume-, surface area- and number-weighted HDS and cumulative ratios of $TiO_{2,as\text{-}is}$.

	HDS, nm	Cumulative Ratio, %			
		Intensity	Volume	Surface Area	Number
Initial	98.6-129.1	10%	11%	41%	88%
	169.2-380.3	14%	6%	13%	9%
	498.3-652.7	34%	37%	28%	3%
	855.1	23%	19%	9%	-
	1120.2	14%	23%	8%	-
	1467.5	5%	4%	1%	-
30 min	140.7-164.0	16%	6%	21%	64%
	177.1-206.6	15%	4%	12%	28%
	706.5-763.0	19%	55%	44%	6%
	823.9	22%	21%	14%	1%
	889.7-1037.6	28%	14%	9%	1%
60 min	144.3-184.4	26%	11%	34%	80%
	200.1-217.1	11%	3%	10%	15%
	739.9-802.9	19%	49%	35%	3%
	871.2	20%	13%	8%	2%
	945.4	15%	9%	5%	-
	1080.9-1214.3	9%	15%	8%	-
90 min	739.9-802.9	19%	32%	20%	60%
	871.2	20%	42%	15%	33%
	945.4	15%	13%	11%	1%
	1025.9-1113.3	9%	5%	25%	6%
120 min	96.8-146.1	20%	21%	61%	98%
	501.7-544.7	16%	14%	8%	1%
	591.4-642.2	45%	25%	14%	1%
	697.2-757.0	19%	40%	17%	-
150 min	66.6-143.6	7%	6%	26%	84%
	156.2-201.0	19%	5%	16%	12%
	218.6-237.8	8%	2%	3%	2%
	587.9-710.4	42%	32%	22%	1%
	780.9-943.7	24%	55%	33%	1%
180 min	117.0-158.5	24%	21%	56%	97%
	534.6-576.7	23%	16%	11%	2%
	622.3-671.4	42%	33%	18%	1%
	724.4-781.6	11%	30%	15%	-

Table 3.10. Intensity-weighted HDS profile of $TiO_{2,as\text{-}is}$. Time dependent HDS cluster maximas, HDS range and min-max diameter difference with respect to multi-size distribution.

	Cluster				
Time, min	Max 1, nm	Max 2, nm	Max 3, nm	Range, nm	Difference, nm
Initial	169.2	855.1	-	1.0-5662.2	5661.2
30	164.0	823.9	-	111.7-1306.6	1194.9
60	184.4	871.2	-	112.9-1543.8	1430.9
90	160.9	733.7	-	102.1-1156.5	1054.4
120	114.1	642.2	-	75.6-1052.0	976.4
150	66.6	184.8	710.4	55.2-1140.4	1085.2
180	136.2	622.3	-	93.1-1059.1	966.0

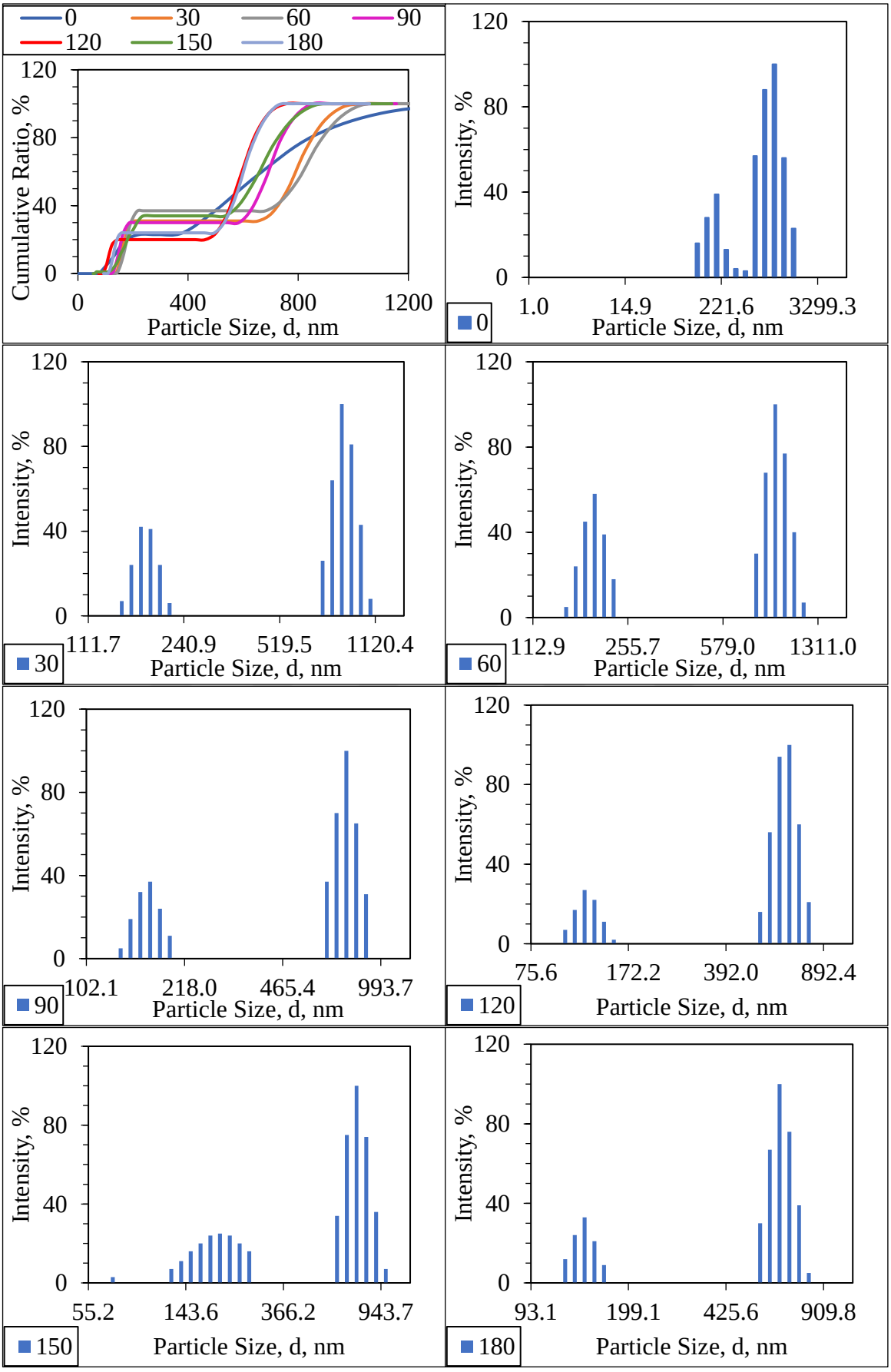


Figure 3.24. The cumulative ratio comparison and hydrodynamic size of $TiO_{2,as\text{-}is}$ as intensity-weighted HDS in 30 min intervals.

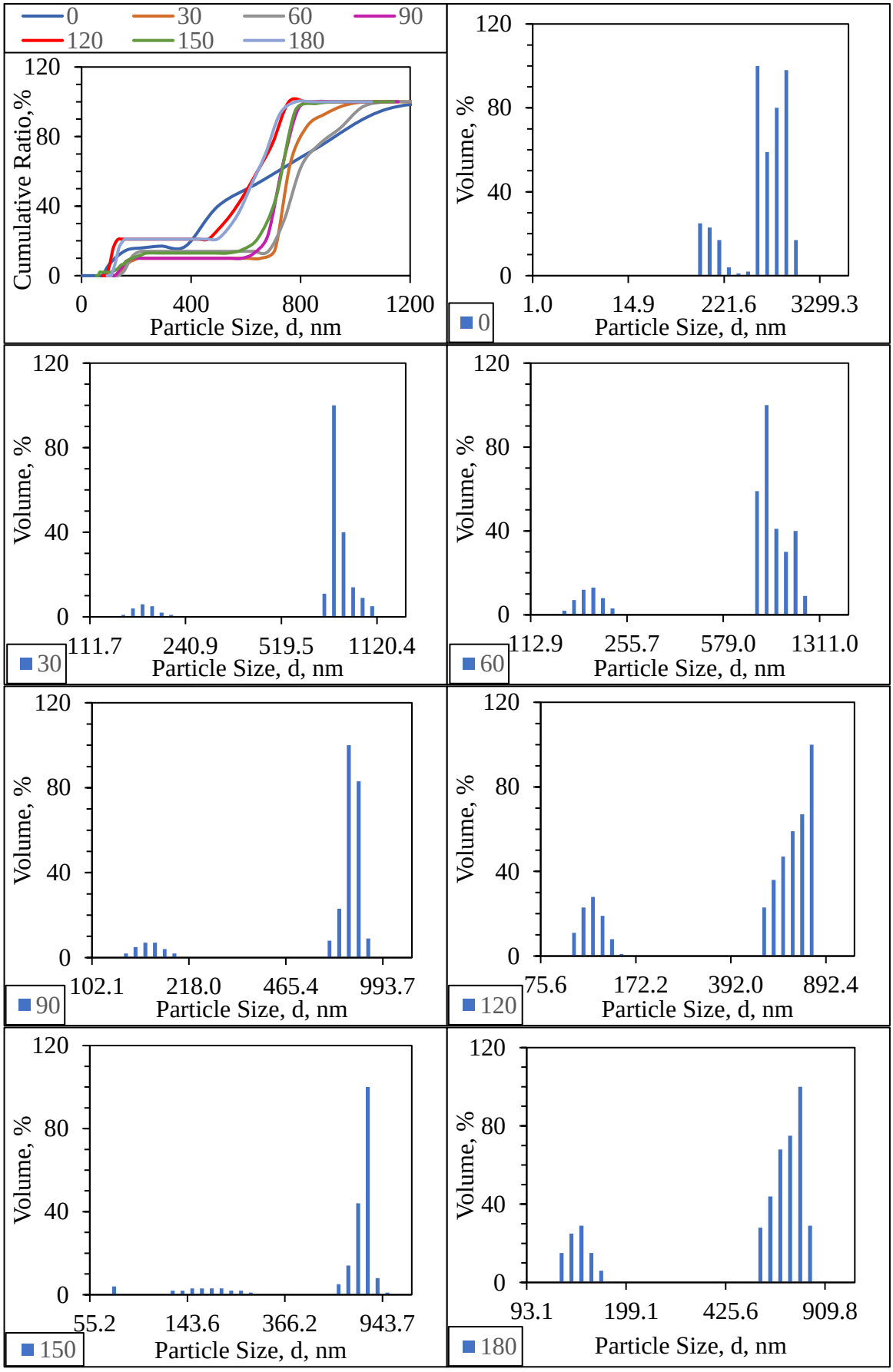


Figure 3.25. The cumulative ratio comparison and hydrodynamic size of $TiO_{2,as\text{-}is}$ as volume-weighted HDS in 30 min intervals.

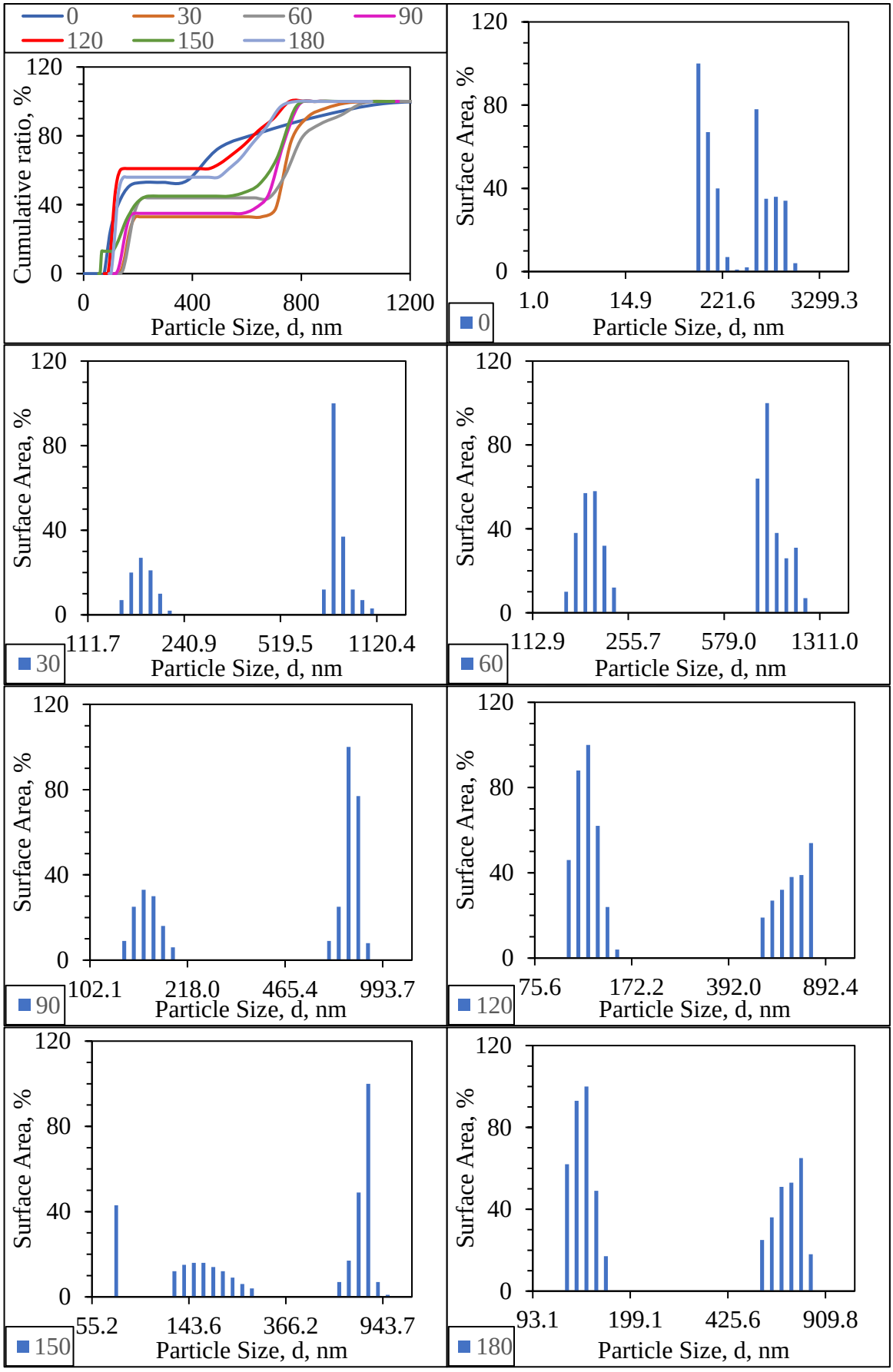


Figure 3.26. The cumulative ratio comparison and hydrodynamic size of $TiO_{2,as\text{-}is}$ as surface area-weighted HDS in 30 min intervals.

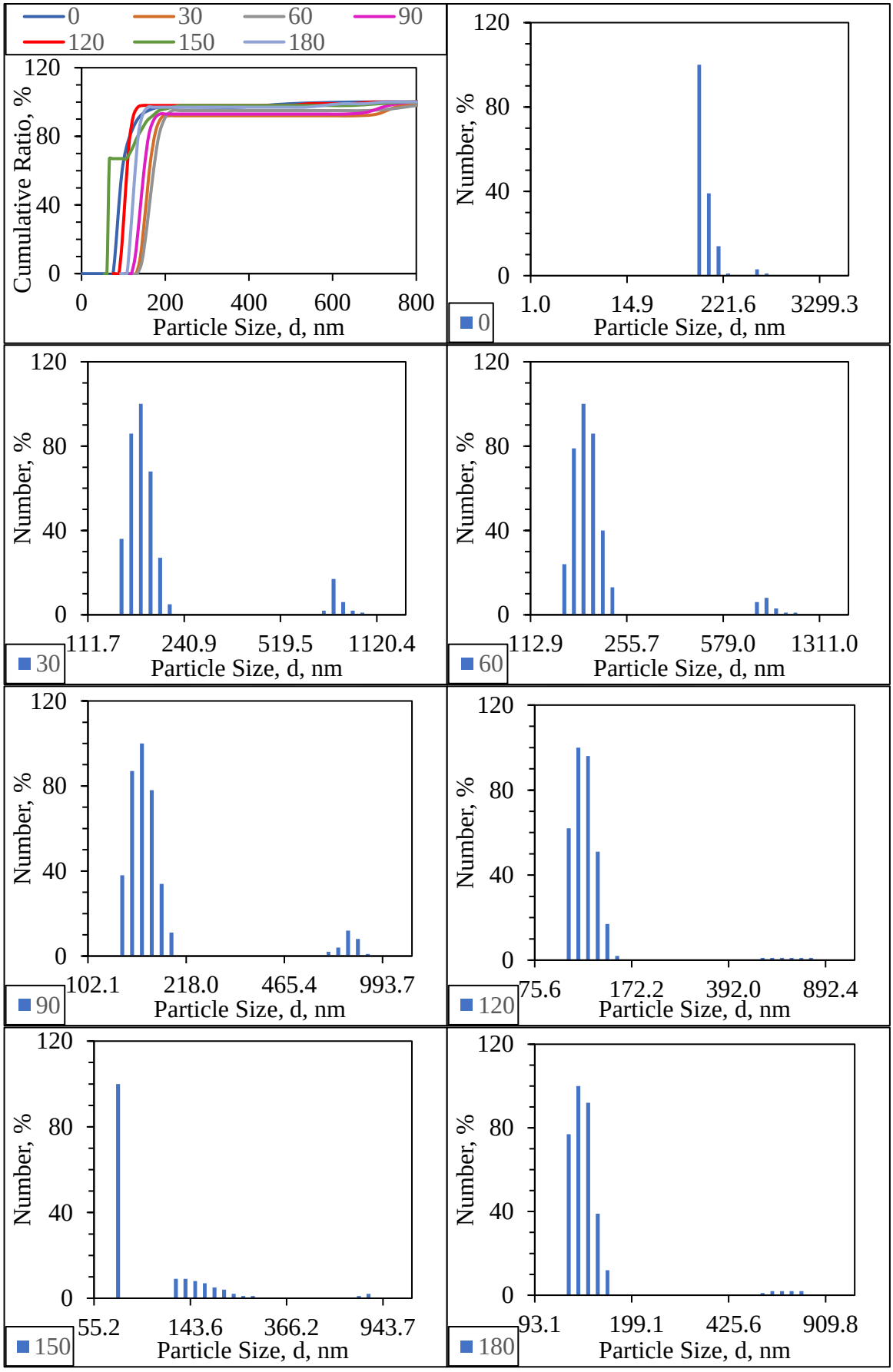


Figure 3.27. The cumulative ratio comparison and hydrodynamic size of $TiO_{2,as\text{-}is}$ as number-weighted HDS in 30 min intervals.

3.4.2. Hydrodynamic Size Assessment of $TiO_{2,dark}$

The effect of mixing over aggregation/agglomeration behavior is investigated by mixing TiO_2 particles in Solar simulator under dark conditions. In a similar fashion to $TiO_{2as\text{-}is}$ preparation, TiO_2 powders (0.25 $mgmL^{-1}$) were suspended in Milli-Q water and sonicated for 1 min followed by mixing with magnetic stirrer for 4 min to ensure a homogeneous suspension. Later the suspension was placed in solar simulator and mixed for 60 min thus obtained slurry is termed as $TiO_{2,dark}$. The sample was subjected to HDS analysis for 120 min with 30 min intervals. HDS measurements of $TiO_{2,dark}$ as intensity-, volume-, surface area- and number-weighted HDS are illustrated in Figure 3.28, Figure 3.29, Figure 3.30, Figure 3.31, and Table 3.11.

The PI (polydispersity index) of $TiO_{2,dark}$ was 0.306, 0.317, 0.314, 0.307 and 0.290 for initial, 30 min, 60 min, 90 min, and 120 min, respectively, and no significant difference was noticed in comparison to the PI of $TiO_{2,as\text{-}is}$ (initial, 0.323; 30 min, 0.322; 60 min, 0.318; 90 min, 0.310; 120 min, 0.314; 150 min, 0.297; and 180 min, 0.301).

It should also be noted that “initial” term referred to the first DLS measurement of the solution system. A comparison could be made between $TiO_{2,as\text{-}is}$ upon 60 min duration and $TiO_{2,dark}$ mixed in dark for 60 min in solar light simulator. According to polydispersity data, HDS of $TiO_{2,dark}$ showed nearly monodispersed configuration similar with the $TiO_{2,as\text{-}is}$, therefore, MSD has been chosen to represent hydrodynamic size distribution. At initial condition, intensity-weighted HDS distribution displayed two main clusters ranging between 153.6 nm – 292 nm and 652 nm – 1455.5 nm with cumulative ratio of 37% and 65% respectively. However, the cumulative ratio of the first cluster was 8% and the cumulative ratio of second cluster is 92% in number-weighted HDS, which was indicative of abundance of the larger agglomerates in the media. During 120 min both the size range and the cumulative ratio of the second cluster decreased due to the precipitation of agglomerates in accordance with the increase of visibility. As indicated before (Section 1.4 Dynamic Light Scattering Methodology) existence of larger particles could obscure the visibility of smaller particles, however after precipitation of larger particles the visibility of smaller clusters increases. Also, the agglomerates around 150 nm - 180 nm remained nearly stable and did not form further agglomerates which could be evidenced by increased cumulative ratio of first cluster during 120 min (Table 3.11). The comparison of cumulative ratios as intensity-, volume- surface area- and number-weighted HDS confirmed the precipitation of agglomerates by the recorded shift to lower sizes over time. Moreover, the plateau formation between the clusters decreased, which was indicative of the disappearance of

larger particles as agglomerates from the measurement area and increased abundance of smaller particles.

Basically, TiO_2 morphology was composed of 80% anatase and 20% rutile crystal structures (Ref). The water binding capabilities of these two crystalline phases would be different, which affected the hydration of TiO_2 and accordingly aggregation/agglomeration performance of the NPs. The water molecules absorbed in rutile phase of TiO_2 formed intermolecular hydrogen bonds resulting in more spherical aggregates (Guo et al., 2019). This formation was also evidenced by comparison of the volume-weighted and surface area-weighted hydrodynamic size of TiO_2. For instance, initially present 652.0-765.6 nm cluster showed higher volume (52%) then surface area (20%). Since the spherical structure would be stiffer, pore formation could be observed less, and higher volume ratio exhibited than surface area ratio. Also, the cumulative ratio of number-weighted HDS of the cluster 652.0-765.6 nm was very high (50%) Volume>Surface area relation evidence the spherical structure. Similar trend could also be seen in the clusters 734.8-794.4 nm in 30 min and 712.7-769.0 nm in 60 min which were probably the same cluster of 652.0-765.6 nm displaying a small change. After precipitation with time, the cumulative ratio decreased from 50% to <6% in number-weighted HDS, indicating that a small amount of this structure remained stable in the medium. These more spherical structures showed less tendency to agglomerate due to two possibilities: *i.* the hindrance effect of surface adsorbed water and *ii.* their smooth surface could not tangle with other structures therefore agglomeration was prohibited. During 120 min, this cluster stayed steady even cumulatively. However, the structures around 899.0 nm (Table 3.11) shows higher surface area than volume and their number-weighted cumulative ratio was low. This trend showed that structures around 899.0 nm comprise non spherical agglomerates.

On the other hand, the water adsorbed onto anatase phase of TiO_2 created a saturation coverage on the surface by long term exposure to water (Guo et al., 2019). The surface adsorbed H_2O adhered onto Ti atoms of TiO_2 in anatase structure and metastable clusters of H_2O were observed which increased intermolecular H-bonding. Later OH bonds created by H_2O adsorption onto TiO_2 surface established a decrease of H-bonding between water and surface adsorbed OH sites that further stabilized smaller structures and prevented agglomeration (Dahal and Dohnalek, 2017; Dette et al., 2018; Guo et al., 2019). Furthermore, considering the anatase/rutile ratio as 80/20, anatase interactions would dominate over rutile in overall aggregate formation tendency through hydration in aqueous medium.

Table 3.11. Intensity-, volume-, surface area- and number-weighted HDS and cumulative ratios of $TiO_{2,dark}$.

	HDS, nm	Cumulative Distribution, %			
		Intensity	Volume	Surface Area	Number
Initial	153.6-211.8	23%	6%	25%	8%
	248.8-292.1	12%	2%	12%	6%
	652.0-765.6	20%	52%	20%	50%
	899.0	21%	8%	19%	6%
	1055.6-1455.5	24%	32%	24%	30%
30 min	154.8-180.9	17%	7%	25%	65%
	195.6-228.5	18%	6%	16%	10%
	734.8-794.4	10%	31%	24%	3%
	858.7	17%	12%	9%	1%
	928.2	20%	22%	8%	1%
	1003.4-1084.6	18%	32%	18%	1%
60 min	155.9-181.5	23%	8%	27%	75%
	195.8-211.3	12%	3%	9%	17%
	712.7-769.0	14%	50%	39%	5%
	829.7	18%	18%	12%	2%
	895.2	19%	8%	6%	1%
	965.9-1042.2	14%	13%	7%	-
90 min	134.3-156.1	18%	6%	23%	77%
	168.3-181.4	7%	2%	6%	14%
	605.0-652.3	17%	6%	5%	1%
	703.3	21%	15%	13%	2%
	758.3	19%	59%	45%	6%
	817.6-881.5	16%	12%	8%	1%
120 min	130.1-172.5	21%	14%	42%	94%
	532.0-570.8	15%	9%	8%	1%
	612.4	21%	12%	8%	1%
	657.1	23%	17%	12%	1%
	705.0-756.5	20%	48%	30%	3%

Table 3.12 compiled the comparison data in terms of intensity-weighted HDS of $TiO_{2,as\text{-}is}$ vs $TiO_{2,dark}$. The cumulative ratio of the smaller structure of $TiO_{2,as\text{-}is}$, decreased or remained stable due to the formation of new agglomerates following the precipitation of larger structures, conversely this trend was not observable for $TiO_{2,dark}$. This phenomenon could be explained with the combination of hydration forces and steric effects resulting from saturation coverage of the adsorbed water. Even the collusion probability of the TiO_2 aggregates/agglomerates increased with mixing, due to the low concentration (0.25 $mgmL^{-1}$) of TiO_2 suspension, only the structures around 1 μm could collide with each other and smaller structures < 200 nm were suspended more evenly (Heine and Pratsinis, 2007; Zhang et al., 2017; Sharma et al., 2019; Suresh et al., 2022). This phenomenon could be also explained by the formation of hydration chains between hydrated TiO_2 aggregates. Mixing increased the collision probability of these larger structures and by the formation of longer hydration chains agglomeration occurred. These agglomerates are less stable due to the weak hydration forces between two hydrodynamic structure and upon prolonged mixing deagglomeration could also take place (Dahal and Dohnalek, 2017).

Table 3.12. Intensity-weighted HDS profile of $TiO_{2,dark}$. Time dependent HDS cluster maximas, HDS range and min-max diameter difference with respect to multi-size distribution.

	Cluster				
Time, min	Max 1, nm	Max 2, nm	Max 3, nm	Range, nm	Difference, nm
Initial	211.8	899.0	-	58.6-10000.0	9941.4
30	180.9	195.6	928.2	113.4-1370.0	1256.6
60	181.5	895.2	-	115.0-1309.0	1194.0
90	156.1	703.3	-	107.1-1191.2	1084.1
120	149.8	657.1	-	105.4-1002.5	897.1

Table 3.13. Comparison of intensity-weighted HDS values of $TiO_{2,as\text{-}is}$ and $TiO_{2,dark}$.

	$TiO_{2,as\text{-}is}$		$TiO_{2,dark}$		
Initial	98.6-129.1	10%	Dark Mixing		
	169.2-380.3	14%			
	498.3-652.7	34%			
	855.1	23%			
	1120.2	14%			
	1467.5	5%			
30 min	140.7-164.0	16%			
	177.1-206.6	15%			
	706.5-763.0	19%			
	823.9	22%			
	889.7-1037.6	28%			
	-	-			
60 min	144.3-184.4	26%	153.6-211.8	25%	Initial
	200.1-217.1	11%	248.8-292.1	12%	
	739.9-802.9	19%	652.0-765.6	20%	
	871.2	20%	899.0	19%	
	945.4	15%	1055.6	15%	
	1025.9-1113.3	9%	1239.5-1455.5	9%	
90 min	128.2-149.2	13%	154.8-180.9	17%	30 min
	160.9-187-3	10%	195.6-228.5	18%	
	630.4-680.1	25%	734.8-794.4	10%	
	733.7-853.9	45%	858.7	17%	
	-	-	928.2	20%	
	-	-	1003.4-1084.6	18%	
120 min	96.8-146.1	20%	155.9-181.5	23%	60 min
	501.7-544.7	16%	195.8-211.3	12%	
	591.4-642.2	45%	712.7-769.0	14%	
	697.2-757.0	19%	829.7	18%	
	-	-	895.2	19%	
			965.9-1042.2	14%	
150 min	66.6-143.6	7%	134.3-156.1	18%	90 min
	156.2-201.0	19%	168.3-181.4	7%	
	218.6-237.8	8%	605.0-652.3	17%	
	587.9-710.4	42%	703.3	21%	
	780.9-943.7	24%	758.3	19%	
	-	-	817.6-881.5	16%	
180 min	117.0-158.5	24%	130.1-172.5	21%	120 min
	534.6-576.7	23%	532.0-570.8	15%	
	622.3-671.4	42%	612.4	21%	
	724.4-781.6	11%	657.1	23%	
	-	-	705.0-756.5	20%	

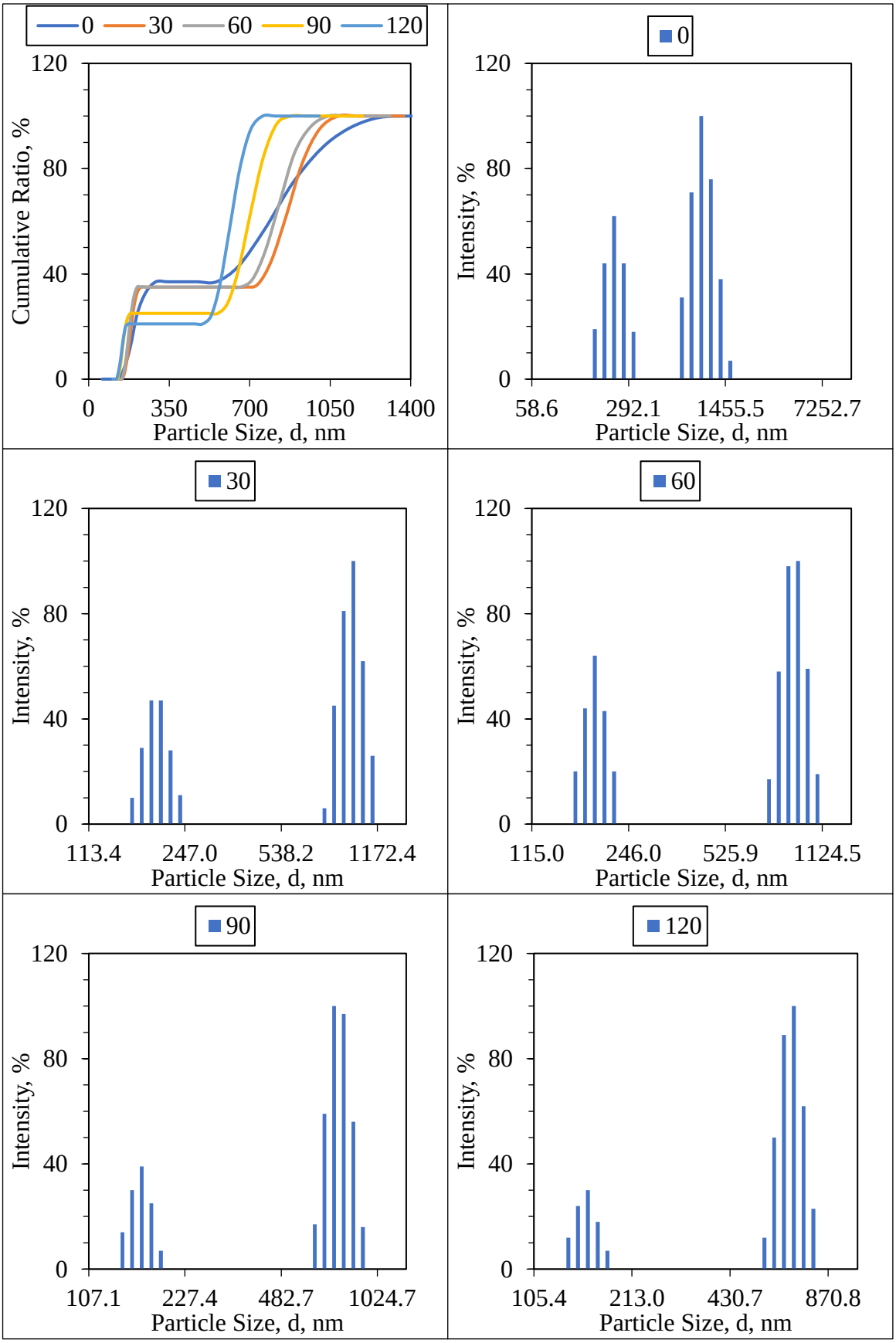


Figure 3.28. The cumulative ratio comparison and hydrodynamic size of $TiO_{2,dark}$ as intensity-weighted HDS in 30 min intervals.

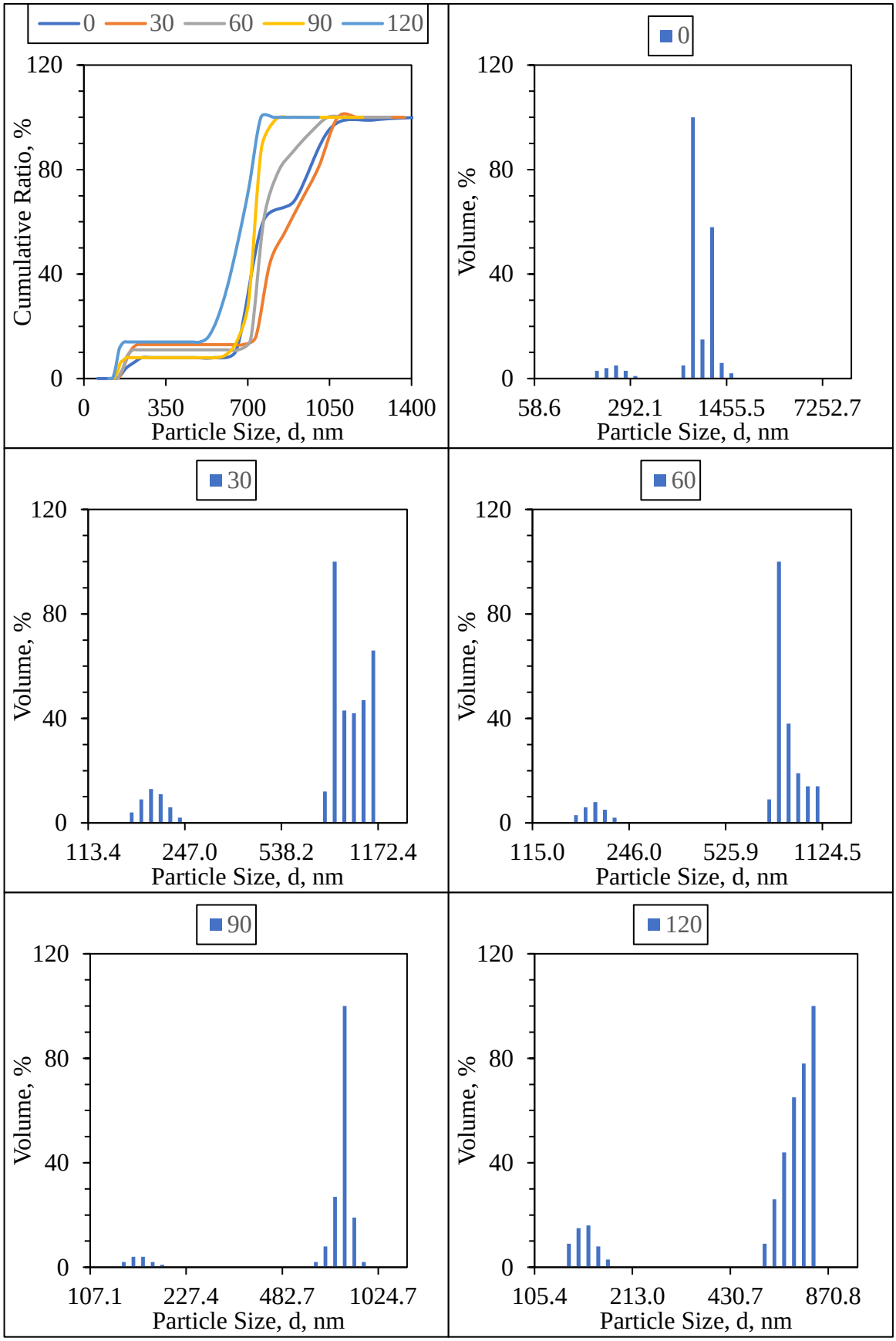


Figure 3.29. The cumulative ratio comparison and hydrodynamic size of $TiO_{2,dark}$ as volume-weighted HDS in 30 min intervals.

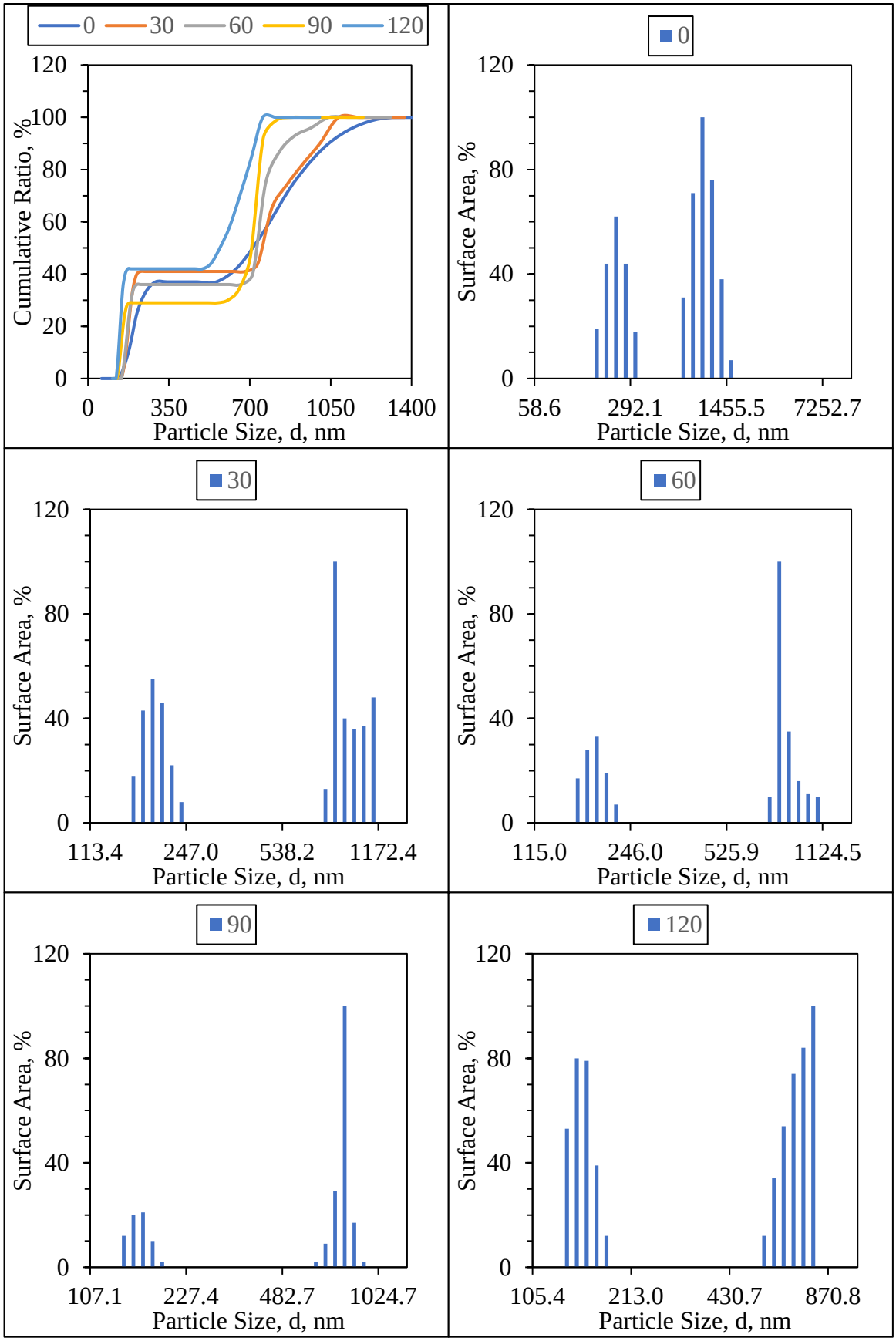


Figure 3.30. The cumulative ratio comparison and hydrodynamic size of $TiO_{2,dark}$ as surface area-weighted HDS in 30 min intervals.

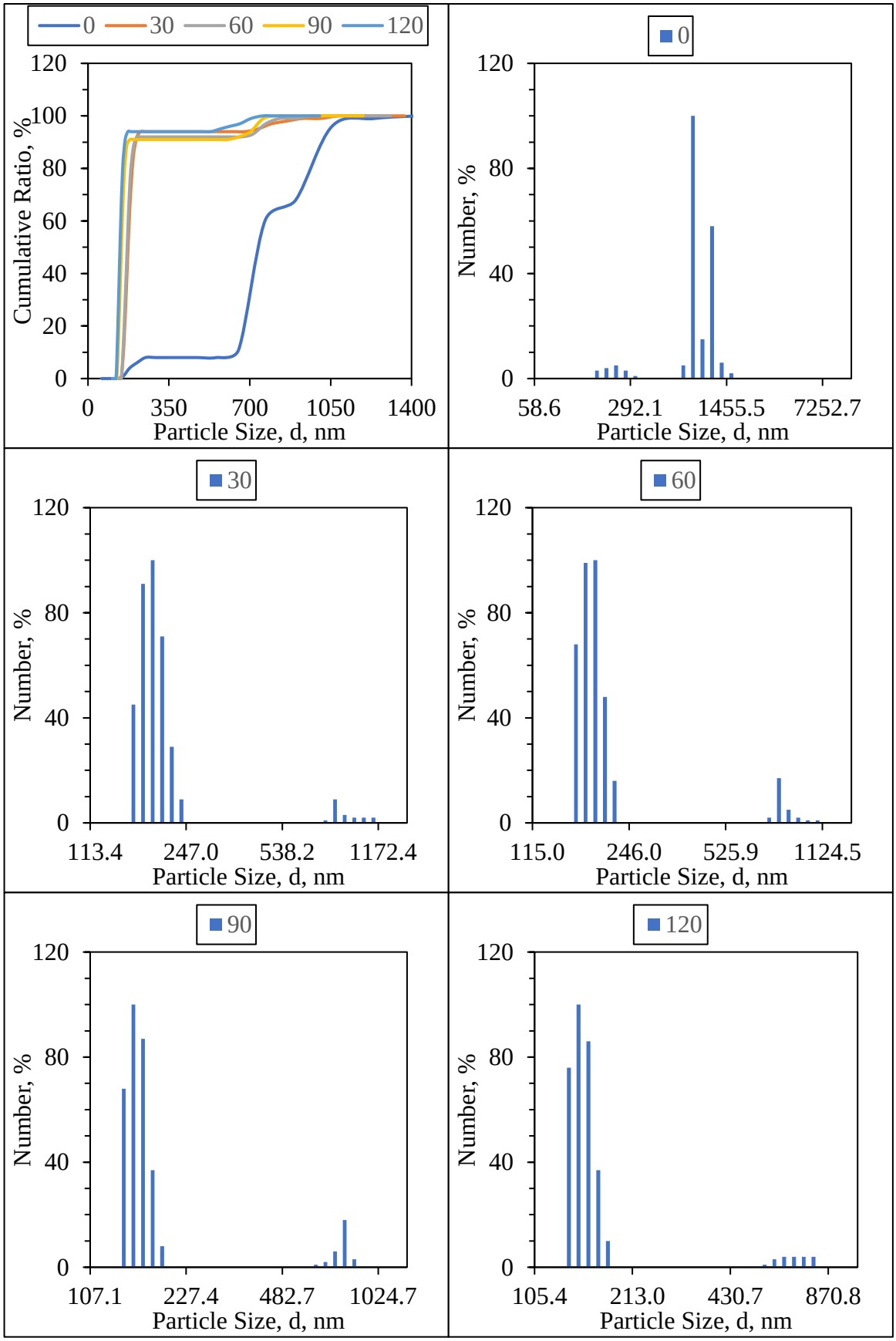


Figure 3.31. The cumulative ratio comparison and hydrodynamic size of $TiO_{2,dark}$ as number-weighted HDS in 30 min intervals.

3.4.3. Hydrodynamic Size Assessment of $TiO_{2,irr}$

From fundamental point of view, solar irradiation onto TiO_2 particles could create a redox couple as e_{CB}^- - h_{VB}^+ pair by adsorption of the light energy of which should be equivalent or greater than the band gap energy of TiO_2 ($E_{irr} \geq E_{bg}$) reported as E_{bg}:3.2 eV for anatase phase and E_{bg}:3.03 eV for rutile phase. The photogenerated h^+ in the valance band could react with the water molecules absorbed onto TiO_2 surface and could further lead to the formation of ROS in oxygenated aqueous solutions. The photogenerated e_{CB}^- on the other hand could also react with the molecular oxygen (Section 3.2.3). Respective surface changes during solar irradiation as well as under dark conditions were illustrated in Figure 3.32. However, some of the photogenerated h_{VB}^+ could be trapped as h_t^+, at the lattice oxygen sites and could also attack back to the TiO_2 itself (Figure 3.32 B). This attack could weaken the Ti-O bond and the water molecules adsorbed on the TiO_2 surface could interrupt these weakened bonds leading to formation of new hydroxyl groups (Figure 3.32 C) (Nakata and Fujishima, 2012). This newly produced surface adsorbed OH groups expressed high surface energy, and were thermodynamically less stable, which conducted the development of superhydrophilic TiO_2 surface. This superhydrophilic surface had a contact angle less than 5˚ (Wang et al., 1997) which created ticker electric dipole layer in comparison to the $TiO_{2,as\text{-}is}$. On the contrary, the photogenerated e_{VB}^- might create conductive regions by moving through the TiO_2 surface producing interstitial hydrogen atoms that could act as a second electron released through the conductive region. This phenomenon depended on the electron density for the bulk trapped electron. Also, in case that the electrons could target to the same point, electron flow occurred thereby electron repulsion would be inhibited, preventing the electron dispersion, and localization of electrons hindered the recombination. This additional hydrogen intake could increase the volume of the crystalline size of TiO_2 particles simultaneously affecting the tensile stress and roughness (Koudriachova et al., 2004; Fujishima et al., 2008).

The intensity-, volume-, surface-area and number-weighted HDS of $TiO_{2,irr}$, were illustrated in Figures 3.34-3.37 respectively. Intensity-weighted HDS range of $TiO_{2,irr}$ consisted of two clusters as shown in Figure 3.34. The first cluster range was in between 169.6 nm - 245.6 nm and the second was in between 745.9 nm - 1080.2 nm with cumulative abundancies of 39% and 61% respectively. The cumulative ratios of these two clusters in number-weighted HDS are 94% for the first cluster and 6% for the second cluster. During 90 min, the hydrodynamic size and the cumulative ratio of the clusters did not change significantly. However, at 120 min the size of second cluster decreased to 486.9 nm - 737.8 nm and the cumulative ratio increased to 78% while the first cluster decreased to 100.3 nm -139.9 nm with a cumulative ratio of 22% as intensity-weighted HDS. This dramatic change

could be explained by the deformation of thermodynamically unstable superhydrophilic surface of $TiO_{2,irr}$. Figure 3.32 C expressed the deformation of superhydrophilic surface under dark conditions (Nakata and Fujishima, 2012). Upon irradiation, the dissociated surface adsorbed water interacted with anatase and rutile structures in different pathways. The dissociated H atom from adsorbed water interacted with the oxygen of R-TiO_2 and formed single intermolecular bond which was leading to long water chain formation on the TiO_2 surface and excessive water adsorption eventually that also decreased the photo-efficiency because of the inhibition of water dissociation. On the contrary, water adsorbed into anatase phase could dissociate independently thereby the thickness of adsorbed water layer after irradiation and the superhydrophilic surface formation was mainly originated from the water adsorbed into anatase phase (Nakata and Fujishima, 2012; Guo et al., 2019). After loss of irradiation effect, staying in the dark for a while, superhydrophilicity deteriorated which accelerated the agglomeration of TiO_2 due to decrease on electric doble layer thickness. This situation could also be explained by DLVO theory (Morrison and Ross, 2002; Hendricks, 2006). Because the van der Waals forces could increase by the decrease of hydrogen forces, agglomeration of TiO_2 could occur which could be followed by size changes of the first and second clusters.

The effect of solar light irradiation on TiO_2 aggregation/agglomeration behavior was investigated by preparing TiO_2 solution as previously described in methodology section (2.3.2). TiO_2 particles were suspended in Milli-Q water (0.25 $mgmL^{-1}$) followed by one min sonication and 4 min magnetic stirring. As stated for $TiO_{2,dark}$, the prepared solution was placed in solar light simulator and exposed to solar irradiation for 60 min followed by incremental increases at every 30 min up to 120 min while continuously mixing. Thus obtained TiO_2 suspension was referred to as $TiO_{2,irr}$. Figures 3.34-3.37 displayed the intensity-, volume-, surface area- and number-weighted HDS graphs and Table 3.14 compiled the time dependent HDS cluster maxima, HDS range and min-max diameter difference with respect to multi-size distribution data. Table 3.15 gathered the cumulative distribution ratios of $TiO_{2,irr}$ aggregates and agglomerates during 180 min. Similar with the $TiO_{2,dark,}$ HDS data were compared with 60 min results of $TiO_{2,as\text{-}is}$ for a more reliable comparison. Hydrodynamic size changes during 120 min with the cumulative abundance ratios and Table 3.16 represented the difference between $TiO_{2,as\text{-}is}$ and $TiO_{2,irr}$ (Table 3.16).

The HDS data of $TiO_{2,dark}$ supported the loss of extended stability of bigger structures of $TiO_{2,irr}$. Due to the simultaneous exposure to irradiation and mixing effect on $TiO_{2,irr}$, stability increase effect of irradiation could later be diminished and surface structure transformed to similar arrangement as $TiO_{2,dark}$ (Nakata and Fujisima, 2012) (Figure 3.32). Following the auto-transformation of the surface,

the structures losing its stability, particles were inclined to precipitate colliding with other particles thereby creating bigger agglomerates which was evidenced by the hydrodynamic size trend of $TiO_{2,irr}$.

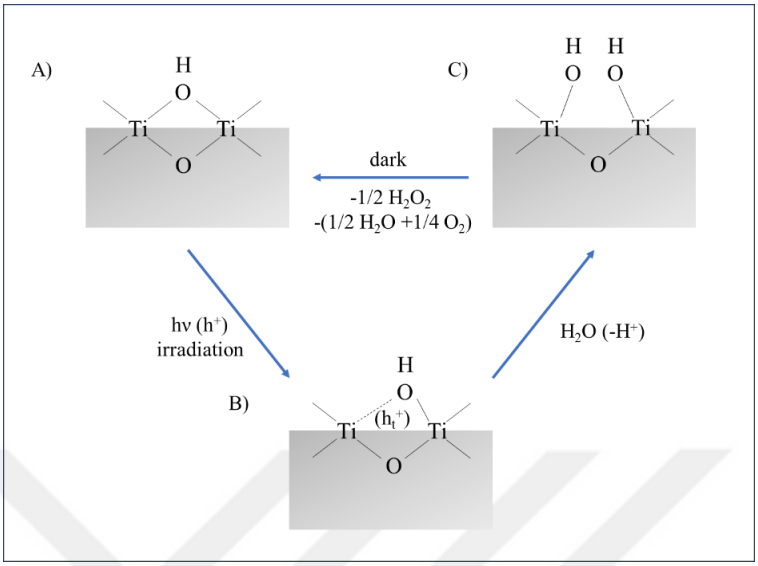


Figure 3.32. Schematic representation of hydrophilicity increase, superhydrophilic surface formation, on $TiO_{2,irr}$ surface after solar irradiation.

The intensity-weighted HDS comparison of $TiO_{2,as\text{-}is}$ $TiO_{2,dark}$ and $TiO_{2,irr}$ was compiled in Table 3.15. The reproducibility of TiO_2 HDS measurements could show11% deviation for commercial TiO_2 P-25 particles (Nickel et al., 2014). However, aside from slight HDS differences between $TiO_{2,as\text{-}is}$, $TiO_{2,dark}$ and $TiO_{2,irr}$, their agglomeration behavior was also different upon duration of 120 min. This phenomenon could be explained by the theory explained formerly in this section,

i. the HDS of $TiO_{2,irr}$ was more stable than $TiO_{2,as\text{-}is}$ upon 90 min duration which could be ascribed to the development of superhydrophilic surface upon solar light irradiance and through strong van der Waal interactions leading to stabilization of the bigger TiO_2 agglomerates in aqueous media (Nakata and Fujishima, 2012),

ii. Crystalline volume increased due to the entrapped hydrogen by photogenerated e_{CB}^-, which also increased the hydrodynamic size of TiO_2 during irradiation (Koudriachova et al., 2004; Fujishima et al., 2008). This effect later disappeared upon exposure to dark conditions during DLS measurements (Nakata and Fujishima, 2012).

The comparison of cumulative ratio distribution also proved the occurrence of more stable structure during 90 min by showing the similar order (Figures 3.34-3.37). Upon prolonged duration of 120 min, HDS data of $TiO_{2,dark}$ and $TiO_{2,irr}$ expressed almost similar results in both HDS measurements and cumulative ratio (Table 3.16). This also showed that following dark conditions for a while (*i.e.*, 90 min), particles exhibited similar aggregation/agglomeration properties. However, after removal of irradiation source, aggregates and agglomerates could maintain the effect (~90 min) of irradiation more than irradiation duration (60 min).

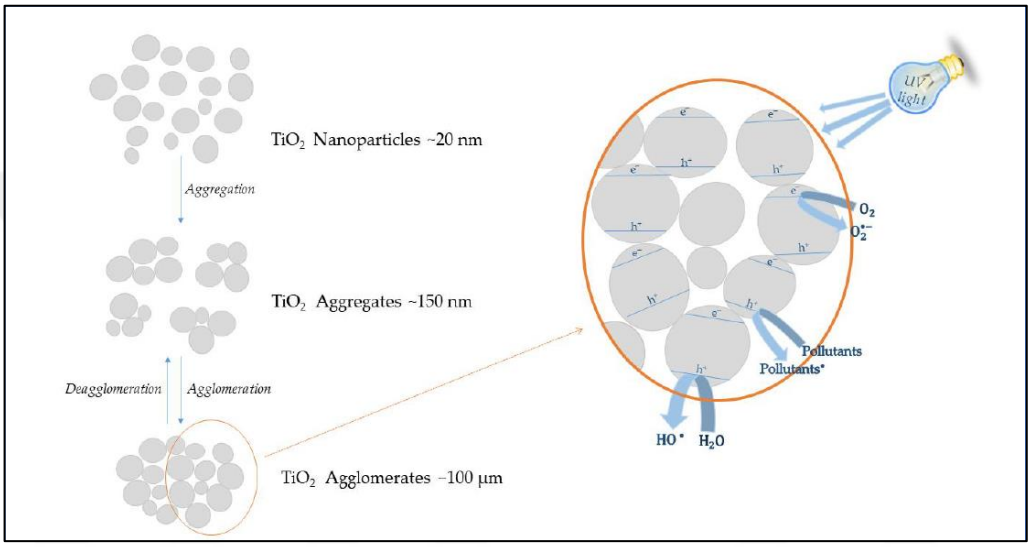


Figure 3.33. Illustration of the aggregation/agglomeration of TiO_2 (Armaković et al., 2023).

Under continuous irradiation, noticeable changes in surface properties of TiO_2 particles would occur leading to variations in aggregation trend (Tan et al., 2021). Upon incremental increase of irradiation period (40 h), HDS of TiO_2 determined as ~2000 nm substantially increased to 2800 nm at pH conditions similar to pH_{zpc} (pH_{zpc} = 6.3) contrary to the observed insignificant changes recorded under dark conditions.

From photocatalysis point of view, the aggregate size of TiO_2 is an important factor in terms of photocatalytic degradation performance. Considering the light harvesting efficiency of TiO_2, assessment of effective dose is highly dependent on the aggregate size of the particles. Aggregate size directly affects the light penetration depth leading to limitations in the volume fraction of the irradiated aggregates. Under the specified conditions at which the TiO_2 aggregates possessed similar 3D networks, photon energy transfer between the particles would be possible, thereby enhanced degradation efficiency could be achieved (Armaković et al., 2023; Tolosana-Moranchel et al., 2021).

Table 3.14. Intensity-, volume-, surface area- and number-weighted HDS and cumulative ratios of $TiO_{2,irr}$.

	HDS, nm	Cumulative Ratio, %			
		Intensity	Volume	Surface Area	Number
Initial	169.6-196.7	19%	8%	25%	63%
	211.8-245.6	20%	6%	17%	31%
	745.9-803.3	9%	26%	20%	2%
	865.0	15%	11%	8%	1%
	931.5	20%	13%	9%	1%
	1003.1-1080.2	17%	36%	21%	2%
30 min	149.7-174.9	17%	7%	24%	64%
	189.0-220.9	18%	5%	15%	30%
	767.8-829.9	25%	56%	42%	3%
	897.1	21%	10%	7%	2%
	969.8-1048.3	19%	22%	12%	1%
60 min	137.8-162.9	17%	8%	29%	66%
	177.1-209.4	18%	7%	19%	30%
	735.3-799.5	16%	42%	28%	2%
	869.3	19%	12%	8%	1%
	945.2-1117.5	30%	31%	16%	1%
90 min	155.2-180.0	16%	6%	19%	53%
	193.8-224.8	24%	7%	19%	39%
	735.1-791.6	23%	62%	46%	6%
	852.4	19%	14%	10%	1%
	917.9-988.5	18%	11%	6%	1%
120 min	100.3-139.9	22%	23%	59%	97%
	486.9-529.1	19%	27%	17%	2%
	574.9	23%	13%	7%	1%
	624.8	21%	13%	7%	-
	678.9-737.8	15%	24%	10%	-

Table 3.15. Intensity-weighted HDS profile of $TiO_{2,irr}$. Time dependent HDS cluster maximas, HDS range and min-max diameter difference with respect to multi-size distribution.

	Cluster				
Time, min	Max 1, nm	Max 2, nm	Max 3, nm	Range, nm	Difference, nm
Initial	196.7	931.5	-	126.1-1348.9	1222.8
30	174.9	189.0	897.1	109.6-1324.1	1214.5
60	177.1	869.3	-	107.2-1562.1	1454.9
90	193.8	852.4	-	115.4-1234.4	1119.0
120	118.5	574.9	-	71.9-1028.8	956.9

Table 3.16. Comparison of intensity-weighted HDS values of $TiO_{2,as\text{-}is}$, $TiO_{2,dark}$ and $TiO_{2,irr}$.

	$TiO_{2,as\text{-}is}$		$TiO_{2,dark}$		$TiO_{2,irr}$		
Initial	98.6-129.1	10%	Dark Mixing		Solar Irradiation and Mixing		
	169.2-380.3	14%					
	498.3-652.7	34%					
	855.1	23%					
	1120.2	14%					
	1467.5	5%					
30 min	140.7-164.0	16%					
	177.1-206.6	15%					
	706.5-763.0	19%					
	823.9	22%					
	889.7-1037.6	28%					
	-	-					
60 min	144.3-184.4	26%	153.6-211.8	25%	169.6-196.7	19%	Initial
	200.1-217.1	11%	248.8-292.1	12%	211.8-245.6	20%	
	739.9-802.9	19%	652.0-765.6	20%	745.9-803.3	9%	
	871.2	20%	899.0	19%	865.0	15%	
	945.4	15%	1055.6	15%	931.5	20%	
	1025.9-1113.3	9%	1239.5-1455.5	9%	1003.1-1080.2	17%	
90 min	128.2-149.2	13%	154.8-180.9	17%	149.7-174.9	17%	30 min
	160.9-187-3	10%	195.6-228.5	18%	189.0-220.9	18%	
	630.4-680.1	25%	734.8-794.4	10%	767.8-829.9	25%	
	733.7-853.9	45%	858.7	17%	897.1	21%	
	-	-	928.2	20%	969.8-1048.3	19%	
	-	-	1003.4-1084.6	18%	-	-	
120 min	96.8-146.1	20%	155.9-181.5	23%	137.8-162.9	17%	60 min
	501.7-544.7	16%	195.8-211.3	12%	177.1-209.4	18%	
	591.4-642.2	45%	712.7-769.0	14%	735.3-799.5	16%	
	697.2-757.0	19%	829.7	18%	869.3	19%	
	-	-	895.2	19%	945.2-1117.5	30%	
			965.9-1042.2	14%	-	-	
150 min	66.6-143.6	7%	134.3-156.1	18%	155.2-180.0	16%	90 min
	156.2-201.0	19%	168.3-181.4	7%	193.8-224.8	24%	
	218.6-237.8	8%	605.0-652.3	17%	735.1-791.6	23%	
	587.9-710.4	42%	703.3	21%	852.4	19%	
	780.9-943.7	24%	758.3	19%	917.9-988.5	18%	
	-	-	817.6-881.5	16%	-	-	
180 min	117.0-158.5	24%	130.1-172.5	21%	100.3-139.9	22%	120 min
	534.6-576.7	23%	532.0-570.8	15%	486.9-529.1	19%	
	622.3-671.4	42%	612.4	21%	574.9	23%	
	724.4-781.6	11%	657.1	23%	624.8	21%	
	-	-	705.0-756.5	20%	678.9-737.8	15%	

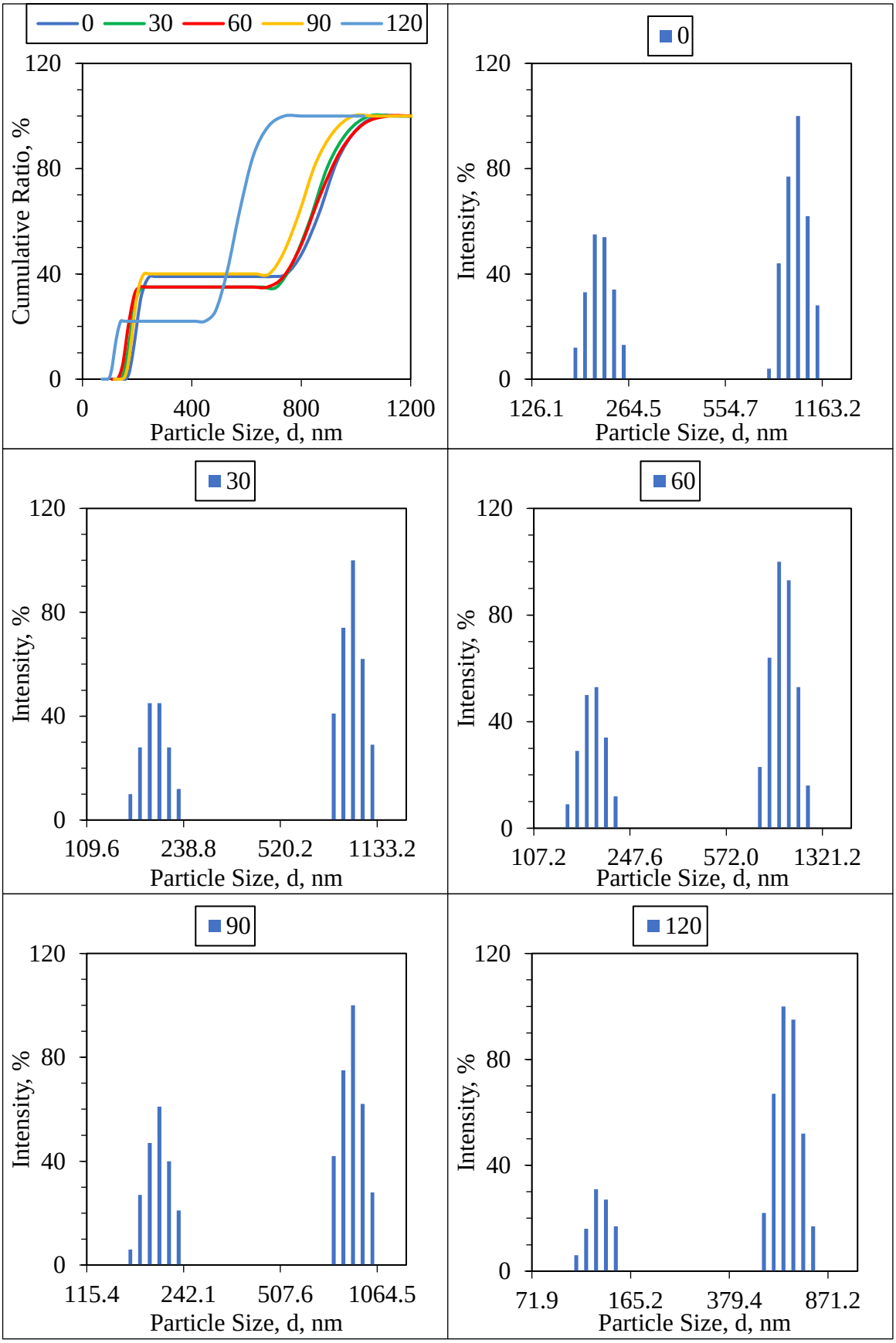


Figure 3.34. The cumulative ratio comparison and hydrodynamic size of $TiO_{2,irr}$ as intensity-weighted HDS in 30 min intervals.

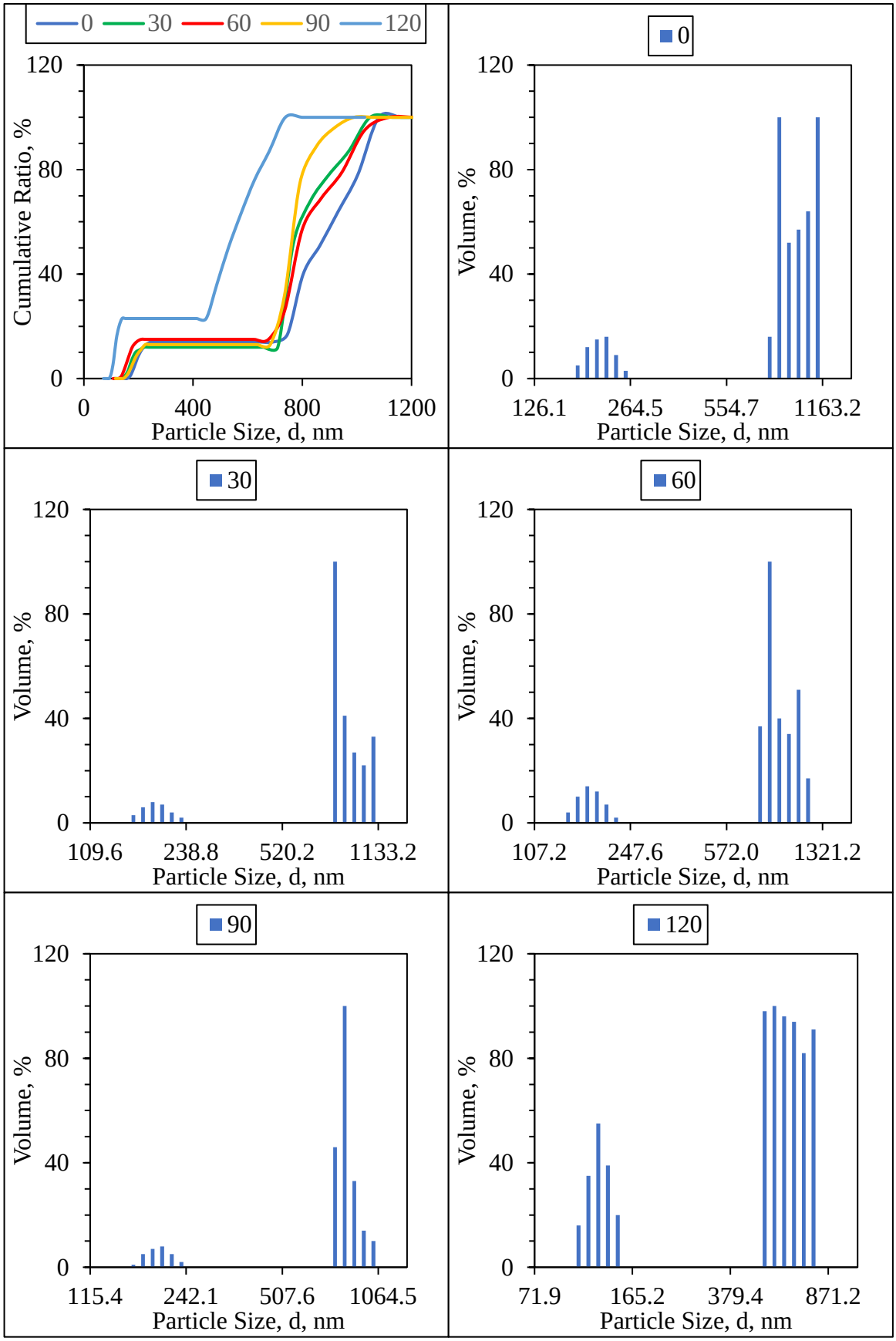


Figure 3.35. The cumulative ratio comparison and hydrodynamic size of $TiO_{2,irr}$ as volume-weighted HDS in 30 min intervals.

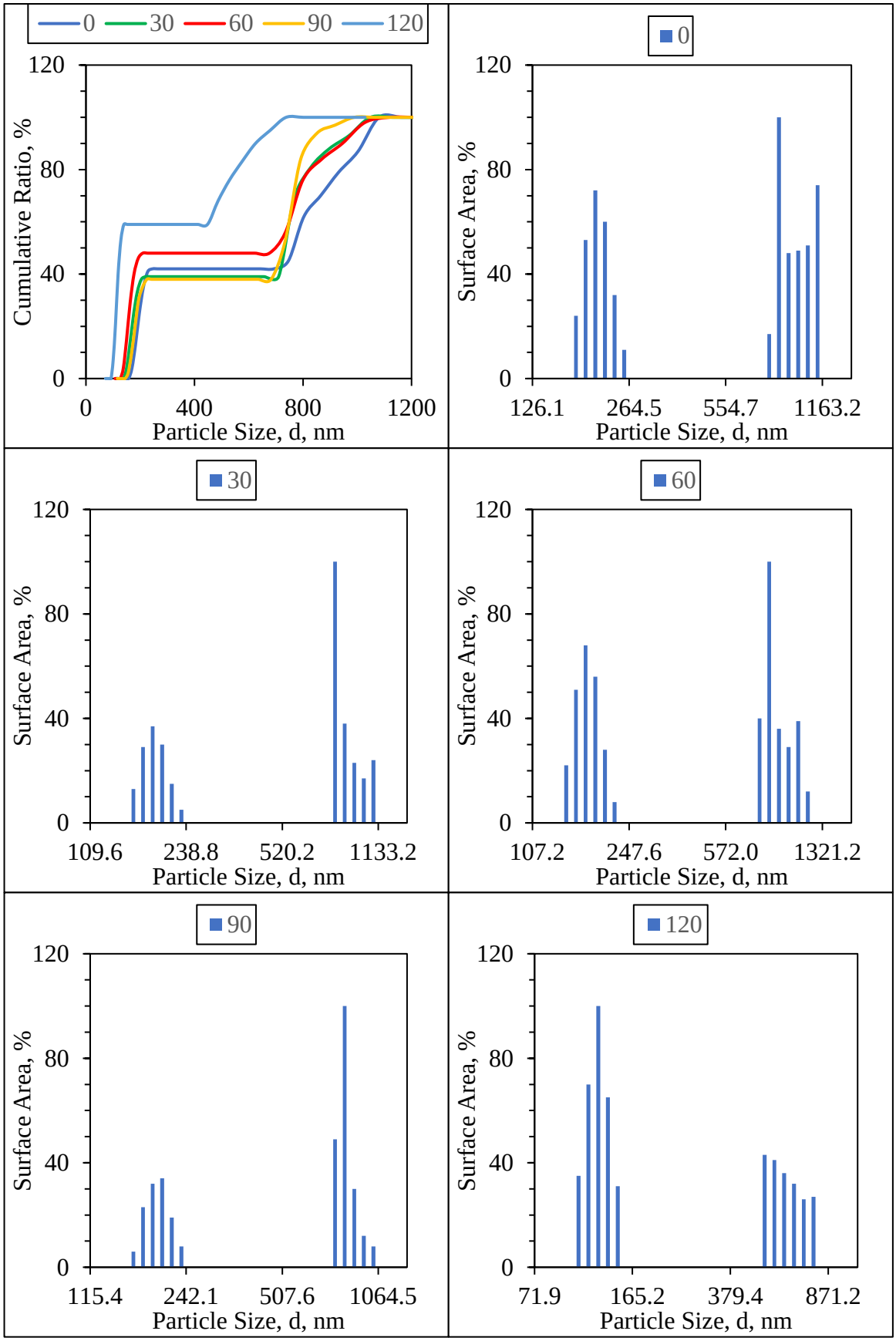


Figure 3.36. The cumulative ratio comparison and hydrodynamic size of $TiO_{2,irr}$ as surface area-weighted HDS in 30 min intervals.

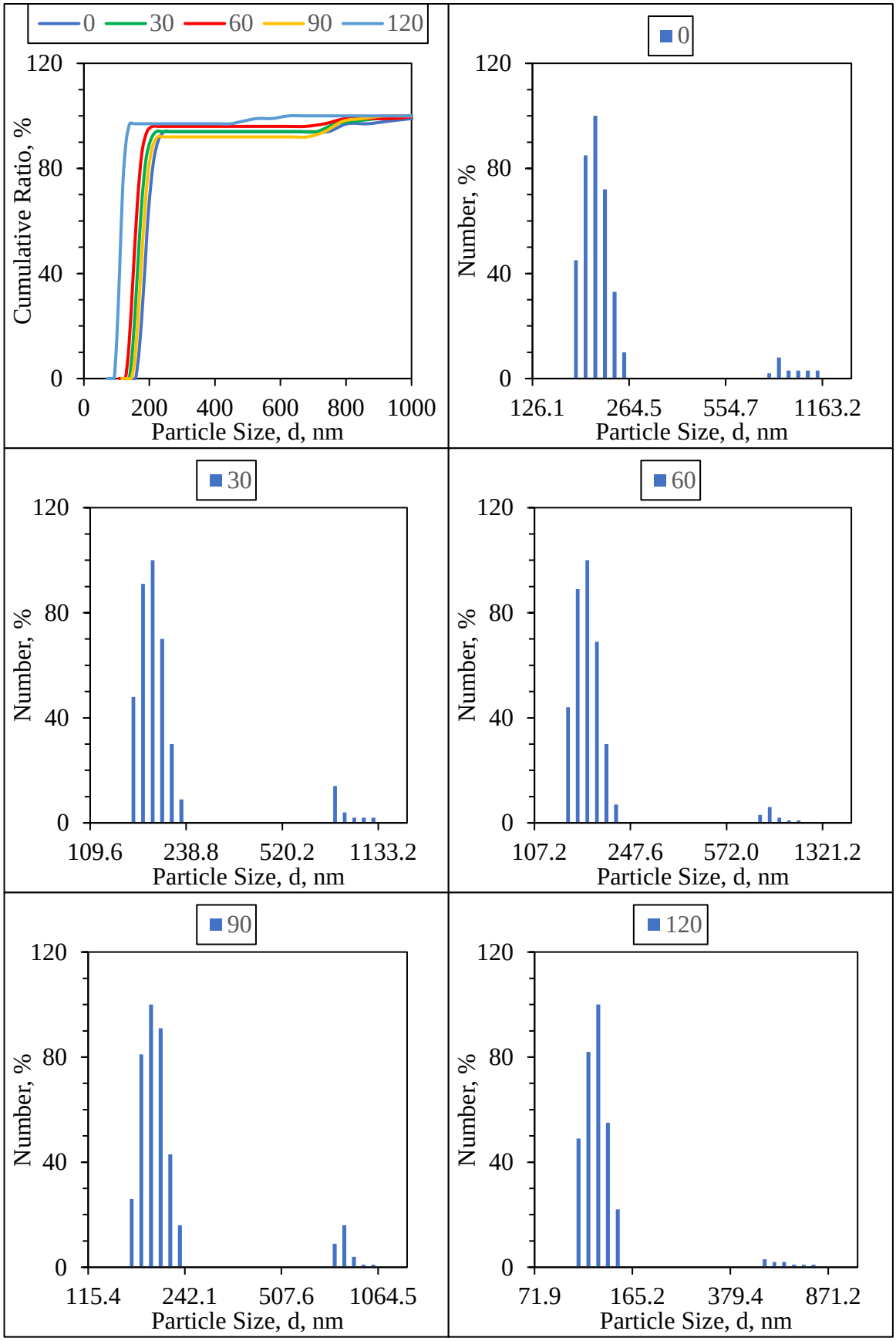


Figure 3.37. The cumulative ratio comparison and hydrodynamic size of $TiO_{2,irr}$ as number-weighted HDS in 30 min intervals.

3.4.4. Hydrodynamic Size Assessment of Fe-$TiO_{2,as\text{-}is}$

Hydrodynamic size changes of Fe-$TiO_{2,as\text{-}is}$ were followed with the same procedure of $TiO_{2,as\text{-}is}$. 0.25 gL^{-1} Fe-TiO_2 was suspended in Milli-Q water and sonicated for 1 min, followed by 4 min mixing with magnetic stirrer. After mixing, the obtained suspension was directly transferred to polystyrene cuvette of hydrodynamic size analyzer and HDS was followed for every 30 mins for 180 mins without removing the cuvette. Hydrodynamic size changes of Fe-$TiO_{2,as\text{-}is}$ was elucidated by following intensity-, volume-, surface area, and number-weighted HDS data. The effect of doping on hydrodynamic size variations was investigated by comparing intensity-weighted HDS of $TiO_{2,as\text{-}is}$ and Fe-$TiO_{2,as\text{-}is}$. Table 3.17 showed the HDS changes during 180 min in terms of intensity-, volume-, surface area-, and number-weighted HDS with the specific cumulative ratios (CR%). peak maxima and HDS range differences of Fe-$TiO_{2,as\text{-}is}$ and the intensity-weighted HDS of $TiO_{2,as\text{-}is}$ and Fe-$TiO_{2,as\text{-}is}$ were presented in Tables 3.18. Figure 3.39, Figure 3.40, Figure 3.41, and Figure 3.42 demonstrated the graphical abstracts of intensity-, volume-, surface area-, and number-weighted HDS and CR% during 180 mins. The PDI of the Fe-TiO_2 was observed as 0.381, 0.303, 0.250, 0.271, 0.275, 0.226, and 0.268 for initial, 30 min, 60 min, 90 min, 120 min, 150 min and 180 min, respectively. The average PDI of the system during the 180 min was calculated as 0.282 which was an indicator of nearly monodispersed system. Hence MSD approximation was used to investigate HDS of Fe-$TiO_{2,as\text{-}is}$.

The initial intensity-weighted HDS of Fe-TiO_2 showed two main peaks around 209.5 nm and 1915.9 nm. On the other hand, the first maxima shifted to slightly lower number-weighted HDS as 189.5 nm and the second maxima almost disappeared. Disappearance of the second cluster around 1915.9 nm in number-weighted HDS implied that these structures were only few in number and these structures could be related with agglomeration of Fe-TiO_2 structures. Similar results were published by Gupta and colleagues (Gupta et al., 2015). HDS of Fe-TiO_2 was reported as around 181 nm in comparison to TEM images. It was stated that aggregate size determined by TEM images (115±10 nm) was slightly smaller than HDS due to the ability of DLS to include a hydration layer covering Fe-TiO_2 aggregates, which was also responsible for the Brownian motion and the transmission of gravitational forces (Gupta et al., 2015; Ma et al., 2015). Hence formation of not only aggregation but also agglomeration could also be observed by DLS technique. The second maxima around 1915.9 nm of intensity-weighted HDS (cluster range 1416.8-2342.8 nm) disappeared after 30 min and this cluster shifted to lower size domain as a new cluster (711.0 nm to 982.3 nm). Differing from the cluster around 1416.8-2342.8 nm, this new cluster was also observable in number-weighted HDS data so, this new cluster might have resulted from dissaglomeration or sedimentation of the structures

around 1416.8-2342.8 nm. The reason of dissagglomeration might be the decrease of hydration forces affecting Fe-$TiO_{2,as\text{-}is}$ due to *i.* existence of less hydroxyl groups on the Fe-$TiO_{2,as\text{-}is}$ surface in comparison to the $TiO_{2,as\text{-}is}$, *ii.* change of surface oxygen orientation in comparison to $TiO_{2,as\text{-}is}$. In a model structure of Fe-$TiO_{2,as\text{-}is}$, the OH group were positioned at the apex of the photocatalyst at an angle of 90.5° with respect to the surface oxygen atom, while simultaneously guiding the hydrogen atom towards the oxygen atom within the lattice structure (Yalçın et al., 2010). Also, sedimentation profiles of Fe-$TiO_{2,as\text{-}is}$ showed 35% removal at the end of first 60 min and the percentage of removal increased to 45% at the end of 180 min duration. The structures formed after 60 min around 600-800 nm were stable during 180 min according to number-weighted HDS (Table 3.17, Figure 3.42). However, relatively smaller structures around 150-200 nm could be related to both agglomerated and disagglomerated structures, which was evidenced by simultaneous appearance/disappearance of structures approximately 500 nm. The number-weighted CR% of the smaller cluster (150-200 nm) decreases by the increase of the CR% of the middle size cluster (~500 nm). This trend might be the effect of magnetic forces affecting Fe-$TiO_{2,as\text{-}is}$ due to the presence of Fe atoms (Kalan et al., 2016).

Initially, volume-weighted HDS data expressed the presence of agglomerates around 1732.5 nm covering the highest volume (37%) (Table 3.17). Following disaggregation and/or sedimentation of larger structures around 1500-2000 nm following 30 min duration, CR% of agglomerates around 700-800 nm increased to 65%. Also, this cluster around 700-800 nm was the second (6%) most abundant formation in number-weighted HDS. Since the cluster around 700-800 nm slightly disappeared (shifted to 680-750 nm) as most volume covering cluster (37%) in volume-weighted HDS, it can be concluded that structures around 1732.5 nm firstly disaggregated to structures around 700-800 nm then these slightly smaller structures sedimented. Agglomeration and sedimentation of these structures continued at 90 min by formation of 800-900 nm structures. Even though the CR% of these structures was 5% in volume-weighted HDS, their CR% in number-weighted HDS was 2%, which showed that agglomeration formation continued. After disappearance of the structures >700 nm at 120 min, volume ratio of the structures was almost homogeneous. This trend was also evidenced with sedimentation profile results (Jiang et al, 2009). Most of the suspended structures were sedimented at first 60 min (35%) and remaining 10% was sedimented at following 120 min (at the end of 180 min).

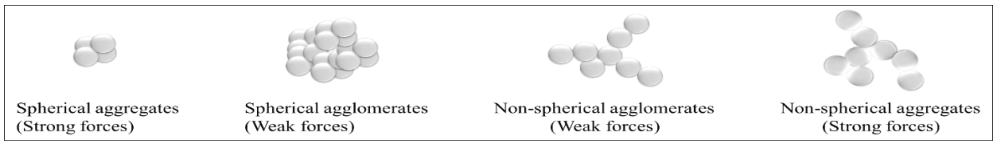


Figure 3.38. Theoretical aggregate and agglomerate shapes of Fe-$TiO_{2,as\text{-}is}$.

The surface area of the spherical structures would be inversely related to their size. Hence the smaller the particle the bigger the surface area of the agglomerates. On the other hand, hydrodynamic agglomerates of Fe-$TiO_{2,as\text{-}is}$ might be in non-spherical shapes in aquatic environments due to the magnetic forces effecting Fe-TiO_2 (Kalan et al., 2016). These magnetic forces might create different oriented agglomerates differing from $TiO_{2,as\text{-}is}$. Because the crystal structure of Fe-$TiO_{2,as\text{-}is}$ (Figure 3.20, altered with substitution of Ti^{4+} with Fe^{3+}, primary particles affinity towards each other during hydrodynamic aggregation/agglomeration differentiates from $TiO_{2,as\text{-}is}$ (Yalçın et al., 2010). Figure 3.38 illustrated the theoretical aggregate and agglomerate shapes of Fe-$TiO_{2,as\text{-}is}$ structures. The CR% of structures around 150-250 nm was 73% as surface area-weighted HDS at initial time, which might be related to spherical aggregates of Fe-TiO_2 structures. However, the CR% of the structures 1732.5 nm was 13%, while the CR% of 1915.9 nm was 5% as surface area-weighted HDS. The structures around 1732.5 might be non-spherical agglomerates and the structures around 1915.9 nm might be spherical agglomerates in this manner. A similar trend was also observed for the structures expressed by surface area-weighted HDS sized as 710-770 nm at time 30 min. These structures were also agglomerates formed before dissaglomeretion or sedimentation according to trend followed in number-weighted HDS. This might be concluded as non-spherical aggregates were more prone to sedimentation and non-spherical agglomerates were more prone to disagglomerate.

The comparison of HDSs of $TiO_{2,as\text{-}is}$ with Fe-$TiO_{2,as\text{-}is}$ was illustrated in Table 3. 17. The initial HDS of $TiO_{2,as\text{-}is}$ was relatively smaller than Fe-$TiO_{2,as\text{-}is}$. The removal ratio observed in sedimentation profiles of $TiO_{2,as\text{-}is}$ was 10% at the end of 60 min, on the other hand, the removal ratio of Fe-$TiO_{2,as\text{-}is}$ was 35%. This trend showed that the agglomerated structures of Fe-$TiO_{2,as\text{-}is}$ were more prone to sedimentation in comparison to agglomerates of $TiO_{2,as\text{-}is}$. The reason of sudden sedimentation of Fe-$TiO_{2,as\text{-}is}$ in comparison to the $TiO_{2,as\text{-}is}$ might be attributed to the atomic weight differences. The atomic weight of Ti was 48 Da and the atomic mass unit of Fe(III) was 56 Da (Petrucci et al., 1997), therefore, Fe(III) substitution would increase the molecular weight of the doped crystalline structure. However, the remaining Fe-$TiO_{2,as\text{-}is}$ structures were colloidally more stable than $TiO_{2,as\text{-}is}$ structures. Due to the surface structure differences between $TiO_{2,as\text{-}is}$ and Fe-$TiO_{2,as\text{-}is}$, hydration forces were more dominant on $TiO_{2,as\text{-}is}$ (Koparde and Cummings, 2007; Laube et al., 2017), on the contrary, van der Waals and magnetic interactions were more effective on Fe-$TiO_{2,as\text{-}is}$ stability (Gupta et al., 2015; Paramo et al., 2023). Hence, the HDS of Fe-$TiO_{2,as\text{-}is}$ did not change during 180 min due to low interactions of colloidal structures while $TiO_{2,as\text{-}is}$ was continuing its agglomeration.

Table 3.17. Intensity-, volume-, surface area- and number-weighted HDS and cumulative ratios of Fe-$TiO_{2,as\text{-}is}$.

	HDS, nm	Cumulative Ratio, %			
		Intensity	Volume	Surface Area	Number
Initial	155.0-189.5	16%	12%	43%	68%
	209.5-256.2	20%	11%	30%	32%
	1416.8-1566.7	10%	11%	5%	-
	1732.5	16%	37%	13%	-
	1915.9	21%	15%	5%	-
	2118.6-2342.8	17%	14%	4%	-
30 min	141.2-166.0	17%	6%	20%	83%
	180.0	14%	4%	12%	8%
	195.1-211.5	13%	3%	9%	1%
	711.0-770.8	23%	65%	46%	6%
	835.7	18%	15%	9%	1%
	906.0-982.3	15%	7%	4%	1%
60 min	144.5-165.5	21%	15%	34%	88%
	177.2	14%	9%	17%	6%
	189.6-203.0	12%	6%	11%	-
	562.3-601.8	21%	17%	11%	6%
	644.1	18%	16%	9%	-
	689.4-737.8	15%	37%	18%	-
90 min	158.1-170.3	11%	4%	12%	26%
	183.3	15%	5%	14%	30%
	197.4-228.9	25%	6%	16%	39%
	644.7-694.2	12%	10%	8%	1%
	747.5	13%	53%	30%	1%
	804.9	15%	26%	17%	1%
	866.7-933.3	9%	5%	3%	2%
120 min	128.5-147.0	17%	17%	37%	87%
	157.1-179.6	19%	16%	29%	5%
	524.3-560.6	22%	25%	14%	3%
	599.4	21%	18%	9%	2%
	640.9-685.3	21%	24%	11%	3%
150 min	165.9-175.5	13%	10%	21%	39%
	185.6	17%	12%	21%	31%
	196.3-207.7	21%	13%	23%	15%
	570.4-603.4	19%	19%	11%	3%
	638.2	16%	19%	10%	1%
	675.1-714.0	14%	27%	14%	-
180 min	126.6-146.1	19%	19%	39%	38%
	156.9-181.1	21%	16%	28%	52%
	492.0-528.4	16%	24%	14%	1%
	567.5	16%	14%	7%	3%
	609.6	17%	13%	6%	3%
	654.7-703.2	11%	14%	6%	4%

Table 3.18. Intensity-weighted HDS profile of Fe-$TiO_{2,as\text{-}is}$. Time dependent HDS cluster maximas, HDS range and min-max diameter difference with respect to multi-size distribution.

	Cluster				
Time, min	Max 1, nm	Max 2, nm	Max 3, nm	Range, nm	Difference, nm
Initial	209.5	1915.9	-	126.7-3168.1	3041.4
30	180.0	835.7	-	102.2-1357.1	1254.9
60	177.2	644.1	-	110.1-968.2	858.1
90	183.3	804.9	-	117.6-1254.6	1137.0
120	157.1	599.4	-	98.3-837.7	739.4
150	185.6	638.2	-	140.2-845.0	704.8
180	146.1	567.5	609.6	95.1-935.8	840.7

Table 3.19. Comparison of intensity-weighted HDS values of Fe-$TiO_{2,as\text{-}is}$ and $TiO_{2,as\text{-}is}$.

	Fe-$TiO_{2,as\text{-}is}$		$TiO_{2,as\text{-}is}$	
	HDS, nm	CR, %	HDS, nm	CR, %
Initial	155.0-189.5	16%	98.6-129.1	10%
	209.5-256.2	20%	169.2-380.3	14%
	1416.8-1566.7	10%	498.3-652.7	34%
	1732.5	16%	855.1	23%
	1915.9	21%	1120.2	14%
	2118.6-2342.8	17%	1467.5	5%
30 min	141.2-166.0	17%	140.7-164.0	16%
	180.0	14%	177.1-206.6	15%
	195.1-211.5	13%	706.5-763.0	19%
	711.0-770.8	23%	823.9	22%
	835.7	18%	889.7-1037.6	28%
	906.0-982.3	15%	-	-
60 min	144.5-165.5	21%	144.3-184.4	26%
	177.2	14%	200.1-217.1	11%
	189.6-203.0	12%	739.9-802.9	19%
	562.3-601.8	21%	871.2	20%
	644.1	18%	945.4	15%
	689.4-737.8	15%	1025.9-1113.3	9%
90 min	158.1-170.3	11%	739.9-802.9	19%
	183.3	15%	871.2	20%
	197.4-228.9	25%	945.4	15%
	644.7-694.2	12%	1025.9-1113.3	9%
	747.5	13%	-	-
	804.9	15%	-	-
	866.7-933.3	9%	-	-
120 min	128.5-147.0	17%	96.8-146.1	20%
	157.1-179.6	19%	501.7-544.7	16%
	524.3-560.6	22%	591.4-642.2	45%
	599.4	21%	697.2-757.0	19%
	640.9-685.3	21%	-	-
150 min	165.9-175.5	13%	66.6-143.6	7%
	185.6	17%	156.2-201.0	19%
	196.3-207.7	21%	218.6-237.8	8%
	570.4-603.4	19%	587.9-710.4	42%
	638.2	16%	780.9-943.7	24%
	675.1-714.0	14%	-	-
180 min	126.6-146.1	19%	117.0-158.5	24%
	156.9-181.1	21%	534.6-576.7	23%
	492.0-528.4	16%	622.3-671.4	42%
	567.5	16%	724.4-781.6	11%
	609.6-703.2	28%	-	-

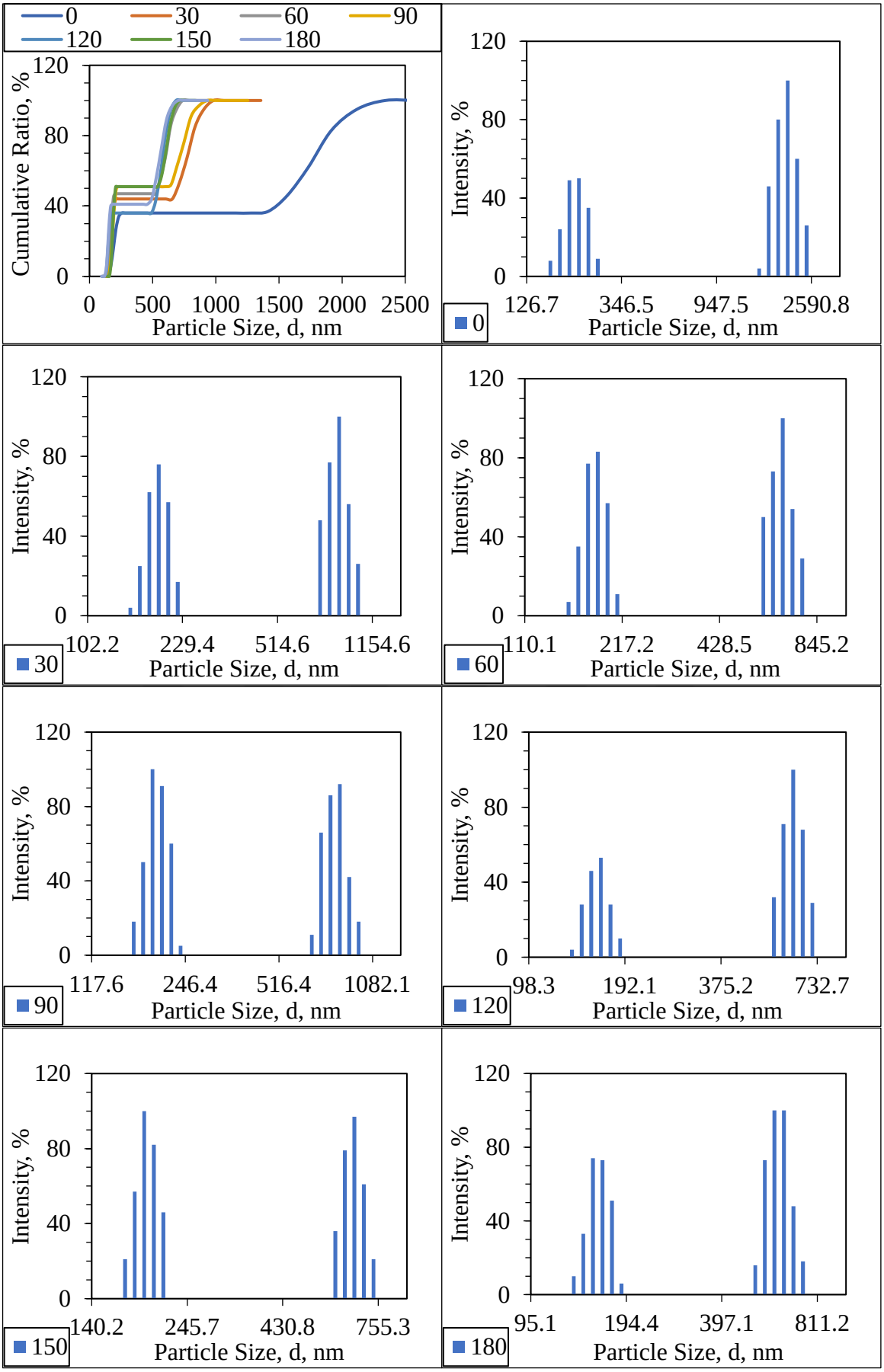


Figure 3.39. The cumulative ratio comparison and hydrodynamic size of Fe-$TiO_{2,as\text{-}is}$ as intensity-weighted HDS in 30 min intervals.

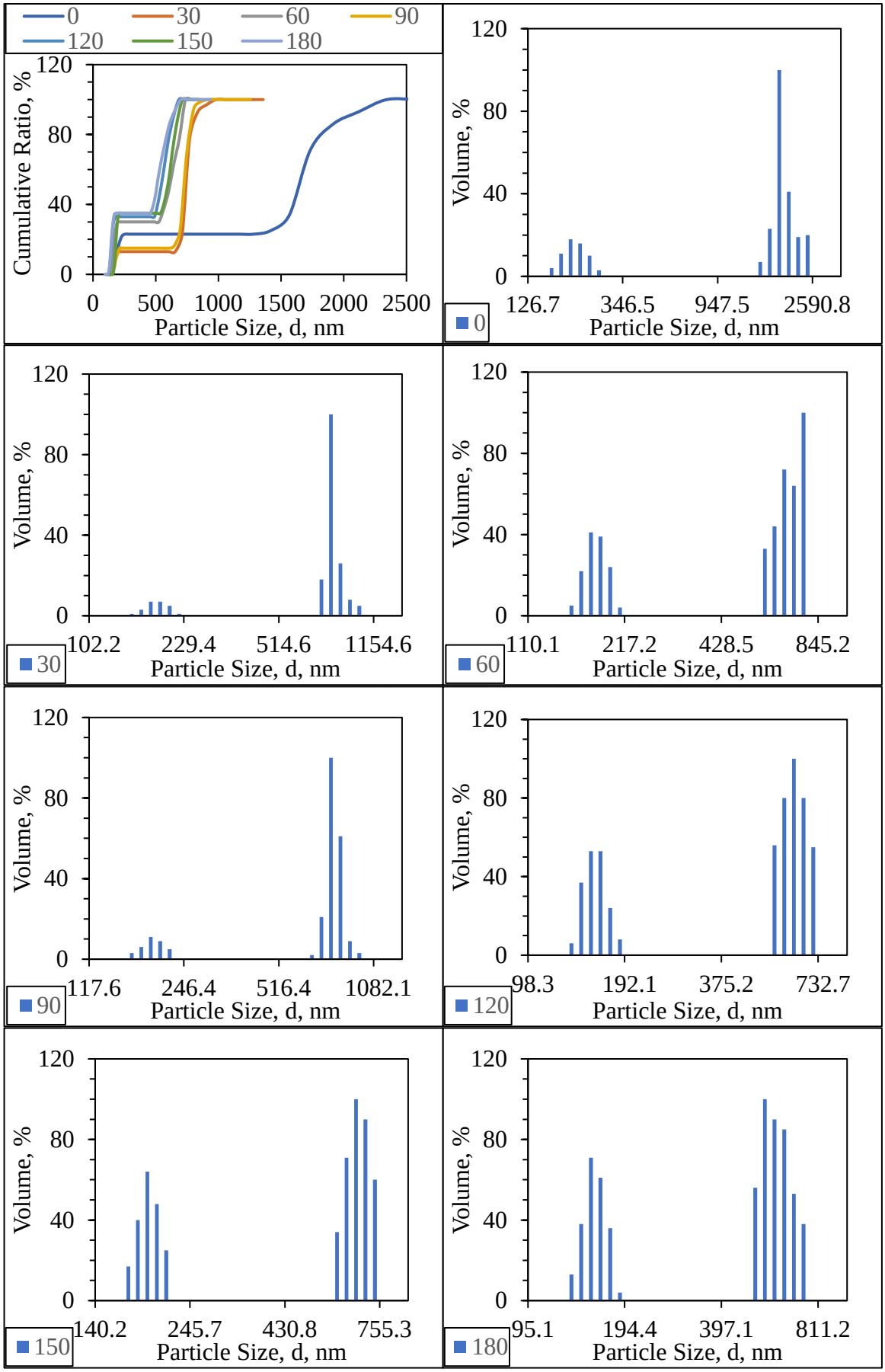


Figure 3.40. The cumulative ratio comparison and hydrodynamic size of Fe-$TiO_{2,as\text{-}is}$ as volume-weighted HDS in 30 min intervals.

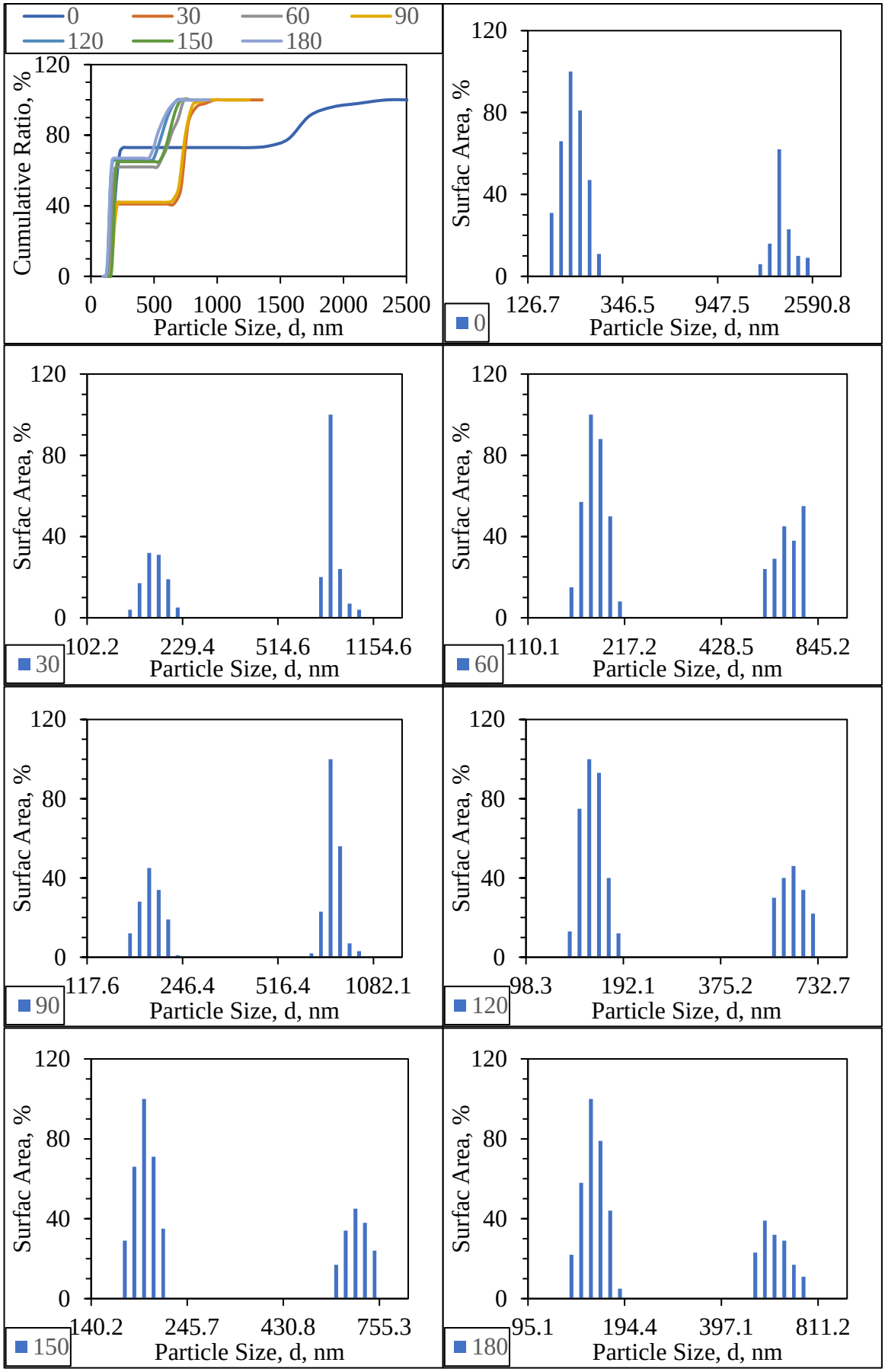


Figure 3.41. The cumulative ratio comparison and hydrodynamic size of Fe-$TiO_{2,as\text{-}is}$ as surface area-weighted HDS in 30 min intervals.

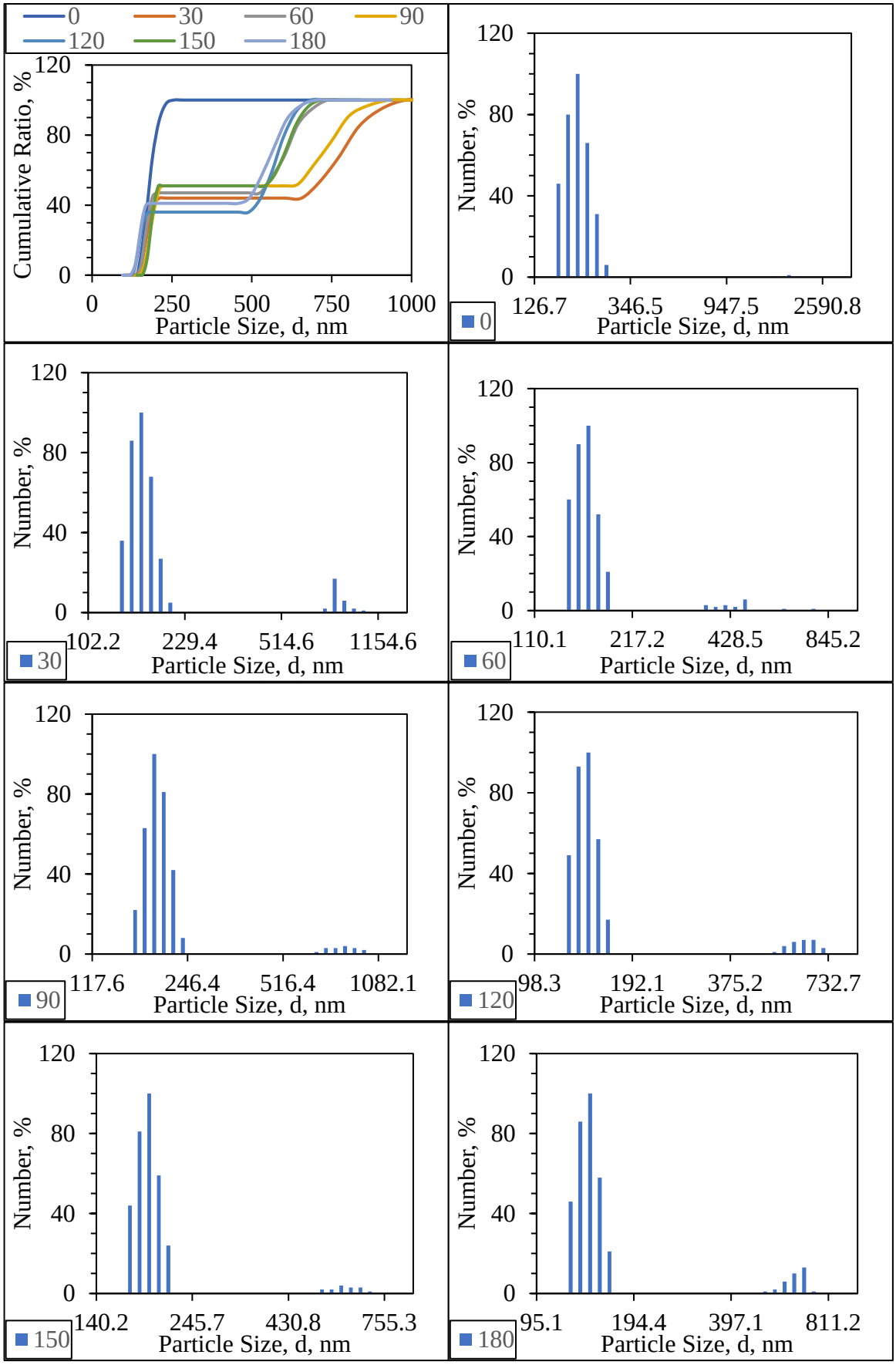


Figure 3.42. The cumulative ratio comparison and hydrodynamic size of Fe-$TiO_{2,as\text{-}is}$ as number-weighted HDS in 30 min intervals.

3.4.5. Hydrodynamic Size Assessment of Fe-$TiO_{2,dark}$

The aggregation/agglomeration behavior of Fe-TiO_2 was evaluated under dark conditions by following DLS measurements. 0.25 mgL^{-1} Fe-TiO_2 was suspended in Milli-Q water and ultrasonicated for 1 min then magnetically stirred for 4 min and placed into solar light simulator in the absence of irradiation for 60 min, and continuously mixed with a magnetic stirrer to maintain similar conditions as $TiO_{2,dark}$. The slurry was directly transferred to polystyrene cuvette and subjected to HDS measurements for 120 min without removing the cuvette. The obtained system was named Fe-$TiO_{2,dark}$. The HDS results were compiled in Table 3.20 as intensity-, volume-, surface area-, and number-weighted HDS with their corresponding cumulative ratios. Also, graphical abstracts were illustrated in Figure 3.43, Figure 3.44, Figure 3.45, and Figure 4.45. Detailed information on time depended changes of HDS range and min max changes was compiled in Table 3.21. Finally, HDS results of Fe-$TiO_{2,dark}$ was compared with Fe-$TiO_{2,as-is}$ in Table 3.22 and $TiO_{2,dark}$ in Table 3.23 as intensity-weighted HDS.

The polydispersity index values of Fe-$TiO_{2,dark}$ was found as 0.313, 0.256, 0.281, 0.239 and 0.229 for initial, 30 min, 60 min, 90 min, and 120 min respectively. The average polydispersity index was 0.264 implying that the system was nearly monodispersed during 120 min and MSD was found to be applicable.

The MSD of Fe-$TiO_{2,dark}$ showed three main peaks at 177.8 nm, 624.6 nm and 1401.4 nm as intensity, volume-, surface area-, and number-weighted HDS respectively (Table 3.20, Figure 3.43, Figure 3.44, Figure 3.45 and Figure 3.46). The average HDS of 1 $mgmL^{-1}$ Fe-TiO_2 was reported as 1125±48.22 nm by Paramo and colleagues (Paramo et al., 2023). They applied 15 min sonication as pretreatment and measured the HDS in DI water. They also reported the PDI of Fe-TiO_2 as 0.227. The initial polydispersity of Fe-$TiO_{2,dark}$ was 0.313 as indicated above. These results were in line with our results; however, it must be noted that sonication and magnetically stirring would affect HDS differently. The difference between PDI reported by Paramo and colleagues and results obtained from this work might be related with the pre-treatment methodology. While magnetic stirrer could increase the collision probability, sonication enhanced the dispersion of dense structures. After 30 min, the bigger cluster around 1401.4 nm disappeared, however the other two maxima remained almost stable (Table 3.20). The magnetic forces created by Fe doping might cause disagglomeration of this cluster (1401.4 nm), as well as sedimentation of agglomerates could be possible (Kalan et al., 2016). Dissaglomeration of the cluster around 1401.4 nm might be evidenced with the increase of the structures around 600-700 nm and smaller structures following 30 min of duration. Especially the

CR% of number-weighted HDS of 600-700 nm structures increased to 3% from 1%. Also, sedimentation results showed that the removal ratio of Fe-$TiO_{2,dark}$ at the end of 30 min was 6%, which supported the approach that dissaglomeration probability was more than sedimentation probability. A similar relation was visualized between the decrease of CR% of structures approximately 900-1200 nm at time initial and increase of CR% of structures around 500-600 nm at 30 min (Table 3.20-3.21) as number-weighted HDS. These structures (1401.4 nm and 900-1200 nm) were nearly spherical according to volume-weighted HDS to surface area-weighted HDS comparison (Table 1). The spherical structure of the agglomerates might be related to mixing effect. Due to the mixing Fe-TiO_2 aggregates might be combined through partially positive and partially negative sites created by van der Waals forces. On the other hand, external magnetic forces formed by other colloidal Fe-$TiO_{2,dark}$ structures overcame the van der Waals forces and caused the dissaglomeretion of bigger structures (Gupta et al., 2015; Paramo et al., 2023). After 60 min the structures around 500-700 nm were continued sedimentation and dissaglomeretion by following the change of CR% of number-weighted HDS. At the same time smaller aggregates (100-200 nm) continued to form new agglomerates around 500-600 nm. Hence the appearance of the Fe-$TiO_{2,dark}$ sizing around 600-800 nm was continued for 120 min. The removal efficiency obtained with sedimentation results were 15% at the end of 120 min. These results also supported that the sedimentation probability was higher for the structures around 700-800 nm than the structures around 1400 nm.

Table 3.22 compiled the comparison of HDS of Fe-$TiO_{2,as\text{-}is}$ and Fe-$TiO_{2,dark}$ as intensity-weighted HDS. Because 60 min pre-treatment applied to Fe-$TiO_{2,dark}$, the initial of Fe-$TiO_{2,dark}$ was compared to 60 min of Fe-$TiO_{2,as\text{-}is}$. Mixing effect led to better suspension agglomerates around 500-1400 nm of Fe-$TiO_{2,dark}$ however after 30 min these bigger structures disagglomerated/sedimented and conditions of Fe-$TiO_{2,as\text{-}is}$ and Fe-$TiO_{2,dark}$ became equal. Besides HDS of the structures mixing slightly increased the CR% of the structures around 700-800 nm as intensity-weighted HDS. Sedimentation profile results also supported these results. While 45% removal was achieved for Fe-$TiO_{2,as\text{-}is}$, 15% removal was achieved for Fe-$TiO_{2,dark}$ at the end of sedimentation experiments. HDS of $TiO_{2,dark}$ and Fe-$TiO_{2,dark}$ was also compared in Table 3.23 as intensity-weighted CR%. According to the intensity-weighted CR% during 120 min $TiO_{2,dark}$ showed more suspended agglomerates > 500 nm compared to Fe-$TiO_{2,dark}$. TiO_2 agglomerates were mostly effected by hydration and van der Waals forces, however aggregation/agglomeration of Fe-TiO_2 not only effected by hydration and van der Waals forces but also effected by magnetic forces both internally and externally. Consequently, dissaglomeretion of Fe-TiO_2 was higher than TiO_2, which led to slightly smaller HDS of Fe-$TiO_{2,dark}$. Additionally, the CR% ratios of structures > 600 nm was higher on $TiO_{2,dark}$ in comparison to the Fe-$TiO_{2,as\text{-}is}$ at the end of 120 min.

Table 3.20. Intensity-, volume-, surface area- and number-weighted HDS and cumulative ratios of Fe-$TiO_{2,dark}$.

	HDS, nm	Cumulative Ratio, %			
		Intensity	Volume	Surface Area	Number
Initial	148.6-177.8	22%	10%	33%	73%
	194.5-212.7	15%	5%	14%	21%
	522.0-624.6	19%	12%	12%	3%
	683.3-747.4	12%	33%	21%	2%
	978.4-1280.7	17%	18%	10%	1%
	1401.0-1676.5	15%	27%	20%	-
30 min	144.8-166.5	18%	12%	29%	56%
	178.5	13%	7%	16%	24%
	191.4-205.2	12%	6%	12%	15%
	544.5-583.9	16%	12%	8%	16%
	626.0	16%	13%	8%	1%
	671.2-771.6	9%	34%	27%	3%
60 min	170.0-180.2	14%	7%	19%	41%
	191.1	14%	7%	15%	31%
	202.5-214.7	15%	5%	13%	21%
	578.6-613.4	15%	11%	8%	2%
	650.2	18%	14%	10%	1%
	689.3-774.6	24%	56%	35%	5%
90 min	161.5-171.8	14%	10%	21%	39%
	182.8	16%	9%	20%	31%
	194.6-207.1	19%	11%	20%	25%
	559.9-595.8	16%	14%	8%	2%
	634.0	16%	14%	9%	1%
	674.7	12%	16%	9%	1%
	718.0-764.0	7%	26%	13%	1%
120 min	179.0-190.2	16%	6%	15%	38%
	202.1	18%	5%	14%	30%
	214.8-228.3	20%	5%	12%	22%
	604.6-642.5	10%	6%	5%	1%
	682.9	13%	11%	9%	2%
	725.7	13%	25%	17%	3%
	771.3-819.7	10%	42%	28%	4%

Table 3.21. Intensity-weighted HDS profile of Fe-$TiO_{2,dark}$. Time dependent HDS cluster maximas, HDS range and min-max diameter difference with respect to multi-size distribution.

	Cluster				
Time, min	Max 1, nm	Max 2, nm	Max 3, nm	Range, nm	Difference, nm
Initial	177.8	624.6	1401.0	113.5-2006.1	1892.6
30	178.5	626.0	-	109.6-1019.8	910.2
60	191.1	650.2	-	142.7-922.7	780.0
90	182.8	634.0	-	134.0-979.8	845.8
120	202.1	682.9	-	149.1-1045.6	896.5

Table 3.22. Comparison of intensity-weighted HDS values of Fe-$TiO_{2,as\text{-}is}$ and Fe-$TiO_{2,dark}$.

	Fe-$TiO_{2,as\text{-}is}$		Fe-$TiO_{2,dark}$		
	HDS, nm	CR, %	HDS, nm	CR, %	
Initial	155.0-189.5	16%	Dark Mixing		
	209.5-256.2	20%			
	1416.8-1566.7	10%			
	1732.5	16%			
	1915.9	21%			
	2118.6-2342.8	17%			
30 min	141.2-166.0	17%			
	180.0	14%			
	195.1-211.5	13%			
	711.0-770.8	23%			
	835.7	18%			
	906.0-982.3	15%			
60 min	144.5-165.5	21%	148.6-177.8	22%	Initial
	177.2	14%	194.5-212.7	15%	
	189.6-203.0	12%	522.0-624.6	19%	
	562.3-601.8	21%	683.3-747.4	12%	
	644.1	18%	978.4-1280.7	17%	
	689.4-737.8	15%	1401.0-1676.5	15%	
90 min	158.1-170.3	11%	144.8-166.5	18%	30 min
	183.3	15%	178.5	13%	
	197.4-228.9	25%	191.4-205.2	12%	
	644.7-694.2	12%	544.5-583.9	16%	
	747.5	13%	626.0	16%	
	804.9	15%	671.2-771.6	9%	
	866.7-933.3	9%	-	-	
120 min	128.5-147.0	17%	170.0-180.2	14%	60 min
	157.1-179.6	19%	191.1	14%	
	524.3-560.6	22%	202.5-214.7	15%	
	599.4	21%	578.6-613.4	15%	
	640.9-685.3	21%	650.2	18%	
	-	-	689.3-774.6	24%	
150 min	165.9-175.5	13%	161.5-171.8	14%	90 min
	185.6	17%	182.8	16%	
	196.3-207.7	21%	194.6-207.1	19%	
	570.4-603.4	19%	559.9-595.8	16%	
	638.2	16%	634.0	16%	
	675.1-714.0	14%	674.7	12%	
	-	-	718.0-764.0	7%	
180 min	126.6-146.1	19%	179.0-190.2	16%	120 min
	156.9-181.1	21%	202.1	18%	
	492.0-528.4	16%	214.8-228.3	20%	
	567.5	16%	604.6-642.5	10%	
	609.6	17%	682.9	13%	
	654.7-703.2	11%	725.7	13%	
	-	-	771.3-819.7	10%	

Table 3.23. Comparison of intensity-weighted HDS values of $TiO_{2,dark}$ and Fe-$TiO_{2,dark}$

	$TiO_{2,dark}$		Fe-$TiO_{2,dark}$	
Initial	153.6-211.8	25%	148.6-177.8	22%
	248.8-292.1	12%	194.5-212.7	15%
	652.0-765.6	20%	522.0-624.6	19%
	899.0	21%	683.3-747.4	12%
	1055.6-1455.5	24%	978.4-1280.7	17%
	-	-	1401.0-1676.5	15%
30 min	154.8-180.9	17%	144.8-166.5	18%
	195.6-228.5	18%	178.5	13%
	734.8-794.4	10%	191.4-205.2	12%
	858.7	17%	544.5-583.9	16%
	928.2	20%	626.0	16%
	1003.4-1084.6	18%	671.2-771.6	9%
60 min	155.9-181.5	23%	170.0-180.2	14%
	195.8-211.3	12%	191.1	14%
	712.7-769.0	14%	202.5-214.7	15%
	829.7	18%	578.6-613.4	15%
	895.2	19%	650.2	18%
	965.9-1042.2	14%	689.3-774.6	24%
90 min	134.3-156.1	18%	161.5-171.8	14%
	168.3-181.4	7%	182.8	16%
	605.0-652.3	17%	194.6-207.1	19%
	703.3	21%	559.9-595.8	16%
	758.3	19%	634.0	16%
	817.6-881.5	16%	674.7	12%
	-	-	718.0-764.0	7%
120 min	130.1-172.5	21%	179.0-190.2	16%
	532.0-570.8	15%	202.1	18%
	612.4	21%	214.8-228.3	20%
	657.1	23%	604.6-642.5	10%
	705.0-756.5	20%	682.9	13%
	-	-	725.7	13%
	-	-	771.3-819.7	10%

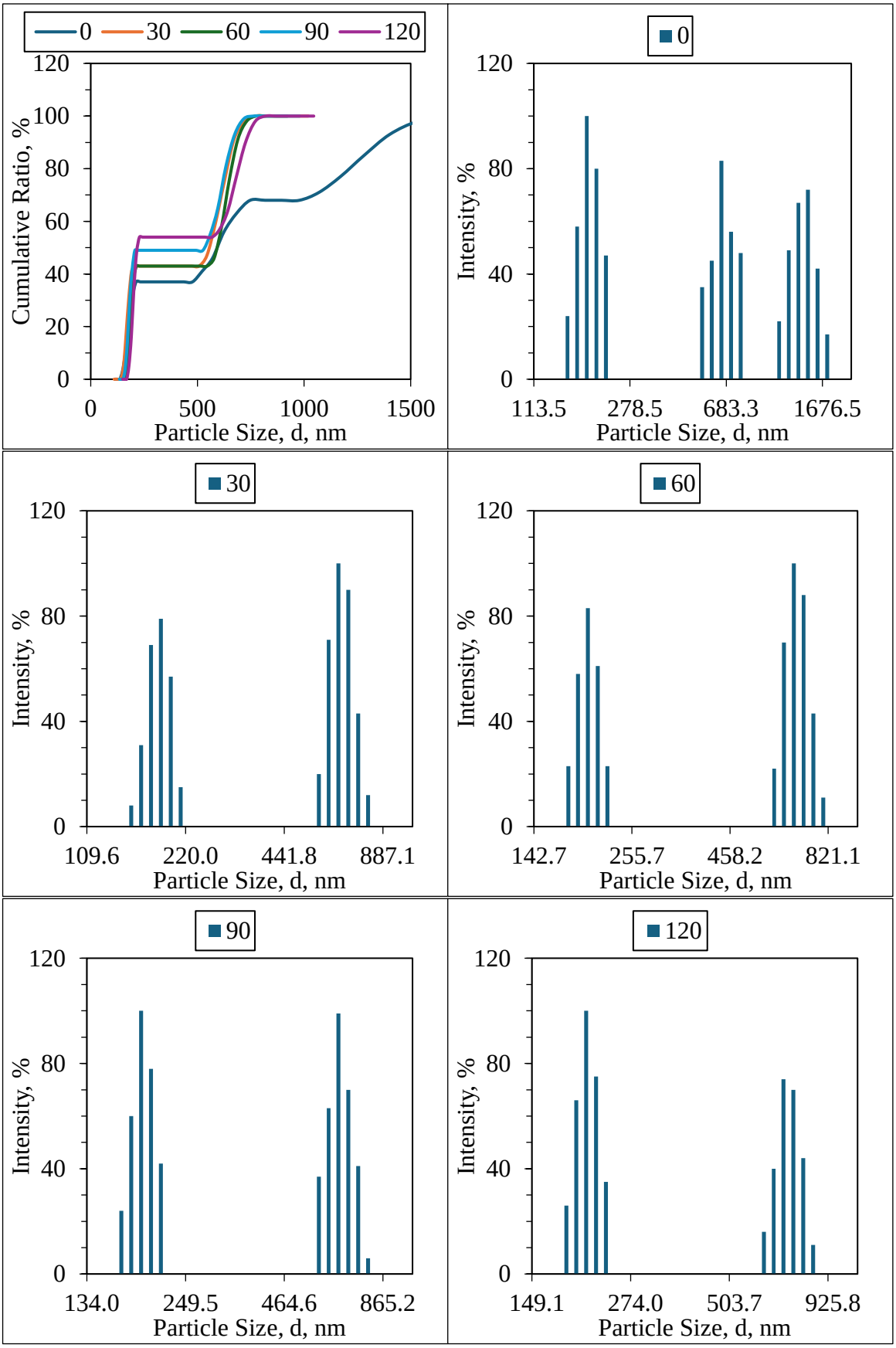


Figure 3.43. The cumulative ratio comparison and hydrodynamic size of Fe-$TiO_{2,dark}$ as intensity-weighted HDS in 30 min intervals.

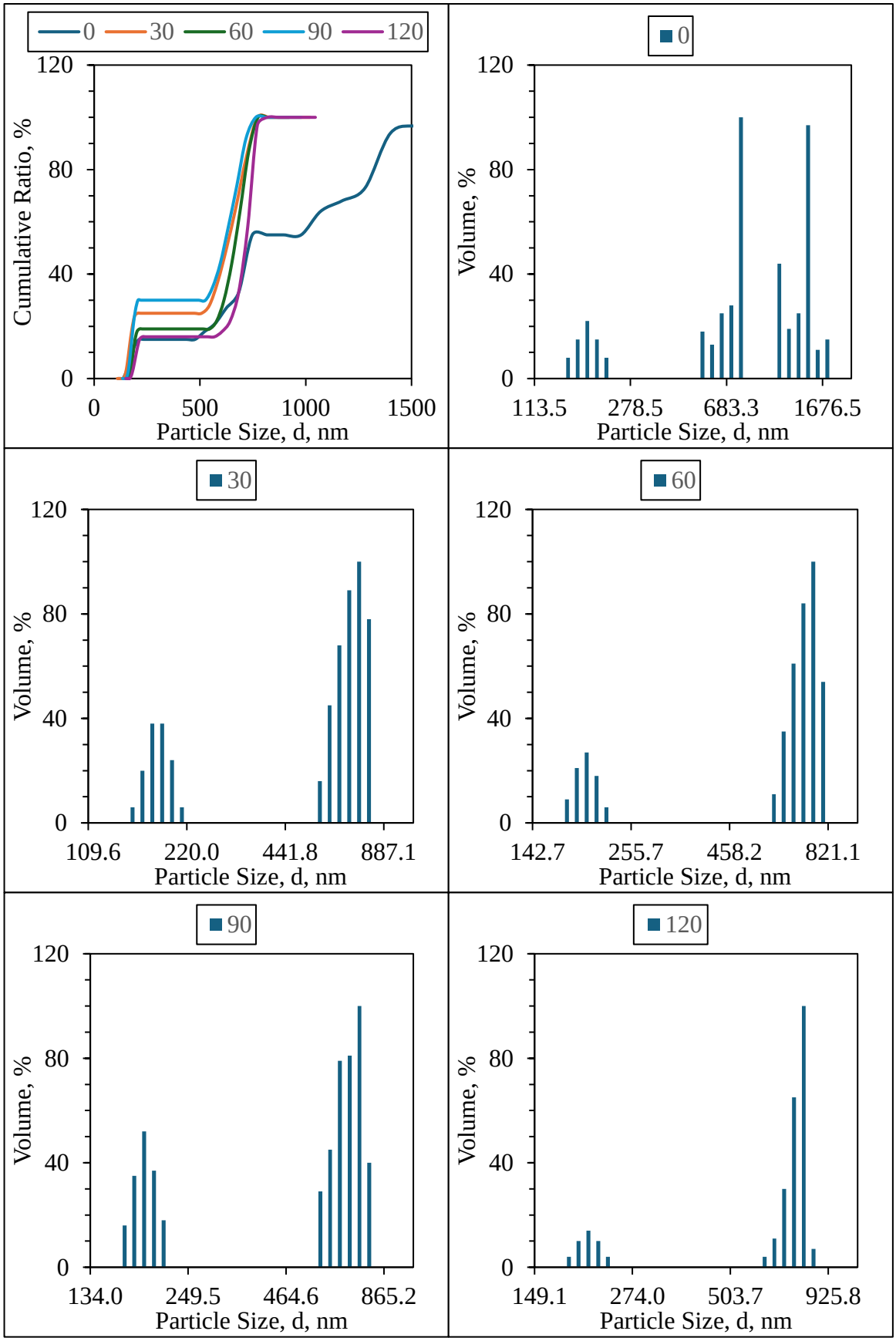


Figure 3.44. The cumulative ratio comparison and hydrodynamic size of Fe-$TiO_{2,dark}$ as volume-weighted HDS in 30 min intervals.

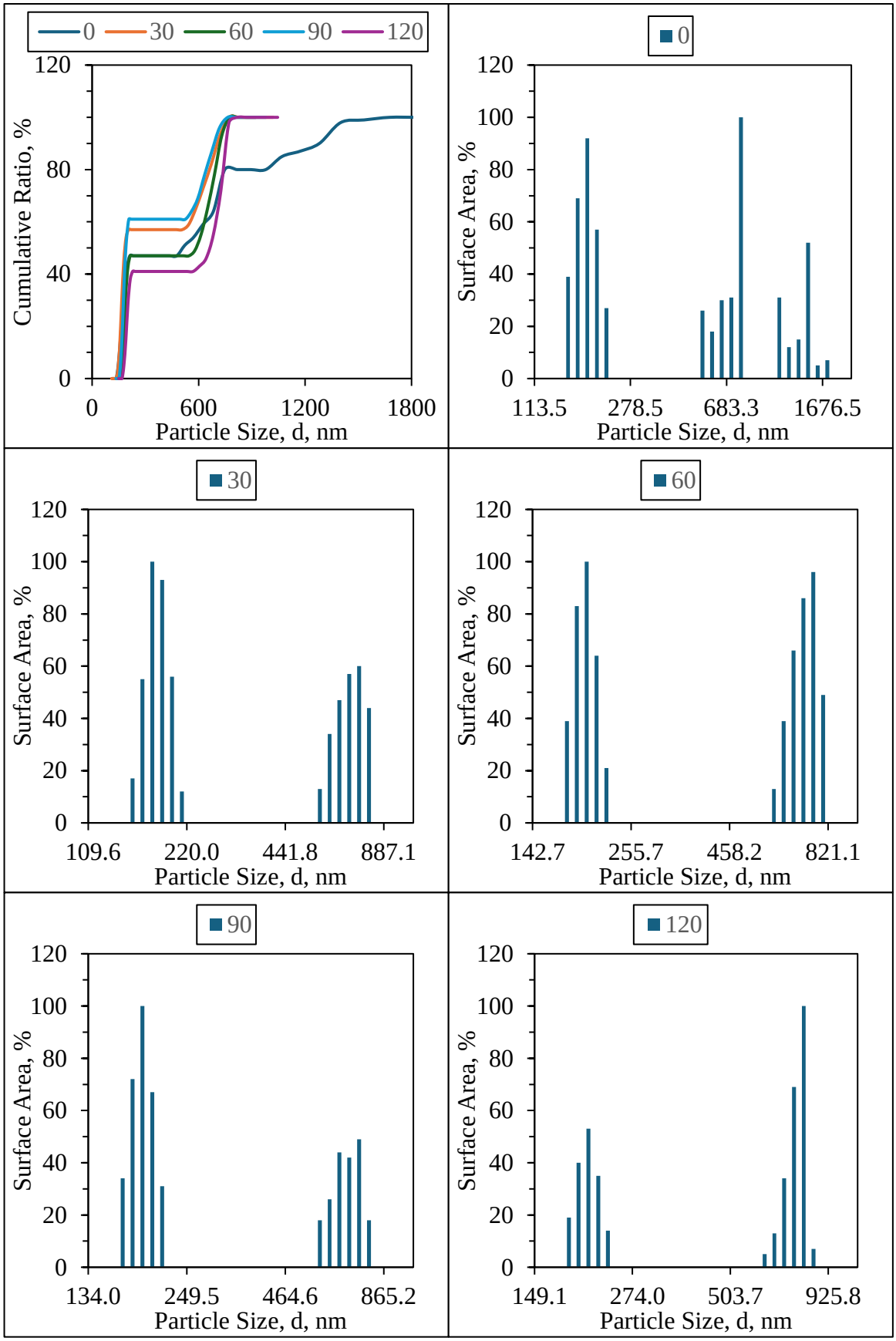


Figure 3.45. The cumulative ratio comparison and hydrodynamic size of Fe-$TiO_{2,dark}$ as surface area-weighted HDS in 30 min intervals.

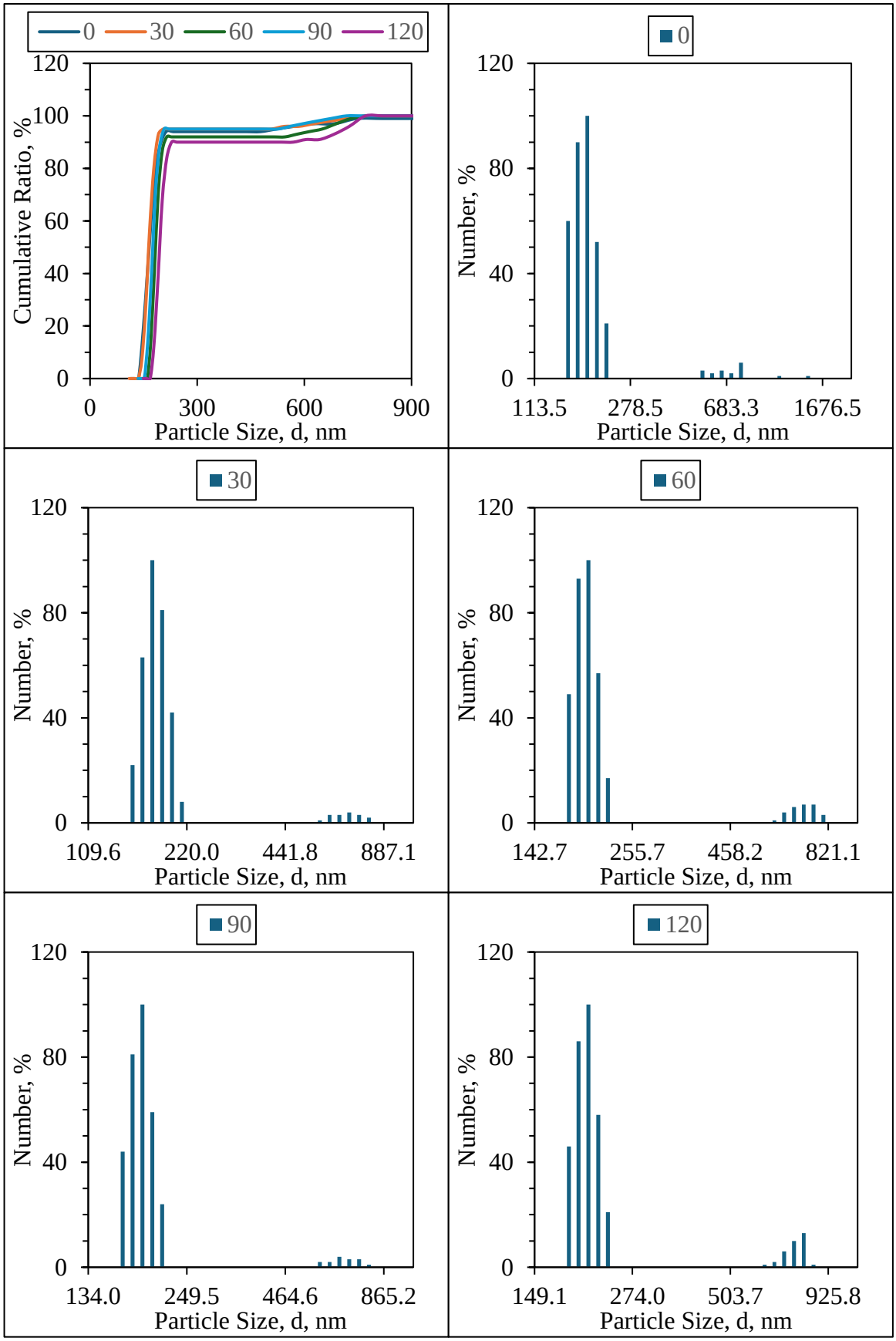


Figure 3.46. The cumulative ratio comparison and hydrodynamic size of Fe-$TiO_{2,dark}$ as number-weighted HDS in 30 min intervals.

3.4.6. Hydrodynamic Size Assessment of Fe-$TiO_{2,irr}$

The effect of solar irradiation on aggregation/agglomeration behavior of visible light active Fe-TiO_2 was investigated by following the DLS measurements. A 0.25 mgL^{-1} solution (suspended in Milli-Q water) of Fe-TiO_2 was ultrasonicated for 1 min and magnetically stirred for 4 min. The prepared solution was placed in the Solar Box and mixed for 60 min under solar irradiation. Following irradiation and mixing the obtained slurry was transferred to polystyrene cuvette and subjected to HDS measurements for 120 min without removing the cuvette. The system was named Fe-$TiO_{2,irr}$. HDS results of Fe-$TiO_{2,irr}$ was compiled in Table 3.24 as intensity-, volume-, surface area-, and number-weighted HDS and their corresponding CR%. Figure 3.47, Figure 3.48, Figure 3.49 and Figure 3.50 shows the graphical abstract of HDS and the CR% in multi size distribution as intensity-, volume-, surface area-, and number-weighted HDS. The time depended results of HDS as min-max difference, HDS range and the max HDS of Fe-$TiO_{2,irr}$ was gathered in Table 3.25. Comparative results of Fe-$TiO_{2,irr}$ with Fe-$TiO_{2,as\text{-}is}$ and Fe-$TiO_{2,dark}$ was shown in Table 3.26. Also, HDS results of Fe-$TiO_{2,irr}$ was compared with $TiO_{2,irr}$ in Table 3.27.

The PDI of Fe-$TiO_{2,irr}$ was 0.445, 0.334, 0.299, 0.258 and 0.288 for initial, 30 min, 60 min, 90 min, and 120 min respectively. The average PDI of Fe-$TiO_{2,irr}$ during 120 min was 0.325 which indicates nearly monodispersed distribution, so MSD was applied to determine HDS of Fe-$TiO_{2,irr}$.

The HDS distribution of Fe-$TiO_{2,irr}$ showed two main peaks around 197.9 nm and 2871.2 nm as intensity-, volume-, and surface area-weighted HDS. The larger cluster near the 2871.2 nm was not visible in number-weighted HDS due to the negligible quantity of this cluster in comparison to the smaller cluster (197.9 nm). Ambati and Gogate reported that the average intensity-weighted HDS of Fe-TiO_2 exposed to UV irradiation for 60 min was 325 nm (PDI: 0.246). They also mentioned that there was another peak around 1000 nm which was related to the presence of any impurity or agglomerated structures, (Ambati and Gogate, 2018). Fe-TiO_2 (0.4 mol% Fe) was synthesized following a different ultrasound assisted methodology and the sample was prepared in an organic solvent. Therefore, no direct comparison would be meaningful. Shuaibu and colleagues synthesized Fe-TiO_2 with a modified sol-gel method and treated Fe-TiO_2 (5 wt%) with UV light for 2 h. They reported the average HDS of Fe-TiO_2 as 527 nm without mentioning PDI or the evaluation criteria (Shuaibu et al., 2024).

Table 3.24 illustrated the detailed CR% changes by time as intensity-, volume-, surface area- and number-weighted HDS. The bigger cluster around 2871.2 nm was disagglomerated or sedimented

after 30 min. Sedimentation results indicated that removal efficiency at the end of 60 min was 40% so, disappearance of the structures>2000 nm was related with sedimentation. After disappearance of the structures>2000 nm new cluster around 500-800 nm was detected in all weighted HDS parameters (Table 3.24). The appearance of this new cluster might be related to the disappearance of bigger clusters. These structures (500-800 nm) could be present in the medium under initial conditions however their low signals could have been masked by bigger clusters. Another possibility could be that a small portion of disagglomerated clusters could form these middle-sized structures. On the other hand, HDS range and difference data (compiled in Table 3.25) indicated that the middle-size structures were already present at time initial. Also, time depended data showed that the middle-size class was very stable during the whole duration and only a small fluctuation was observed in cumulative ratios of intensity-, volume, surface area- and number-weighted HDS. Especially, the CR% of number-weighted HDS was still evident after 60 min. Sedimentation profiles supported these approximation. After the first 60 min only 10% removal was achieved which could be related to slight precipitation of the structures around 800 nm.

The effect of irradiation and mixing on aggregation/agglomeration of Fe-TiO_2 was evaluated by comparing Fe-$TiO_{2,as\text{-}is}$, Fe-$TiO_{2,dark}$ and Fe-$TiO_{2,irr}$. The CR% of HDS in all three experiments were compared as intensity-weighted HDS. Although the solar irradiation formed bigger structures in comparison to Fe-$TiO_{2,as\text{-}is}$, and Fe-$TiO_{2,dark}$, after 60 min the effect of irradiation diminished and the size of both aggregated and agglomerated structures were similar to Fe-$TiO_{2,dark}$ (Nakata and Fujishima, 2012). The solar irradiation also created more hole traps on Fe-$TiO_{2,irr}$ which created adsorption sites for water molecules (Chang and Liu, 2014), so the hydration layer on the Fe-$TiO_{2,irr}$ should be thicker than Fe-$TiO_{2,as\text{-}is}$ and Fe-$TiO_{2,dark}$ during 90 min.

The effect of Fe doping under irradiation was investigated by analyzing $TiO_{2,irr}$ and Fe-$TiO_{2,irr}$ in Table 3.27 as intensity-weighted CR%. As indicated in the previous paragraph, doping with Fe created more adsorption sites which created a thicker chemisorbed hydration layer (Figure 3.21). Also doping with Fe formed magnetic forces that might create bigger agglomerates in comparison to the $TiO_{2,irr}$. The combination of these two forces created almost three times bigger hydrodynamic structures of Fe-$TiO_{2,irr}$. Despite the thicker hydration layer, Fe doping increased the weight of Fe-TiO_2 structures in comparison to TiO_2 which could lead to a faster sedimentation rate (Petrucci et al., 1997). While the removal efficiency of $TiO_{2,irr}$ was approximately 15%, 40% of Fe-$TiO_{2,irr}$ was precipitated at the end of 60 min. HDS results of $TiO_{2,irr}$ and Fe-$TiO_{2,irr}$ supported these results (Table 3.27). Hence it can be concluded that Fe-$TiO_{2,irr}$ was less colloidally stable than $TiO_{2,irr}$ (Koparde and Cummings, 2007; Laube et al., 2017).

Table 3.24. Intensity-, volume-, surface area- and number-weighted HDS and cumulative ratios of Fe-$TiO_{2,irr}$.

	HDS, nm	Cumulative Ratio, %			
		Intensity	Volume	Surface Area	Number
Initial	153.4-197.9	17%	18%	63%	84%
	224.8-255.3	10%	8%	22%	16%
	2225.5	7%	5%	1%	-
	2527.8	17%	5%	1%	-
	2871.2	25%	9%	2%	-
	3261.2-3704.2	24%	55%	11%	-
30 min	148.5-176.0	16%	7%	26%	61%
	191.6	10%	4%	13%	22%
	208.6-227.1	9%	3%	10%	14%
	811.1-882.9	11%	9%	6%	-
	961.1	16%	12%	8%	1%
	1046.2	19%	48%	28%	2%
	1138.9-1239.8	17%	17%	9%	-
60 min	134.9-145.1	13%	7%	23%	50%
	156.1	13%	6%	16%	28%
	168.0-180.7	13%	5%	12%	17%
	582.1-626.2	18%	8%	6%	1%
	673.7	19%	14%	9%	1%
	724.8	15%	28%	16%	1%
	779.8-838.9	9%	32%	18%	2%
90 min	132.1-150.1	17%	16%	34%	57%
	160.0	12%	10%	18%	24%
	170.5-181.7	11%	7%	12%	15%
	504.1-537.3	22%	34%	19%	2%
	572.7	20%	17%	9%	1%
	610.4-650.6	18%	16%	8%	1%
120 min	142.5-164.5	20%	8%	26%	61%
	176.8	13%	4%	11%	21%
	190.0-204.2	10%	3%	7%	12%
	601.4-646.3	15%	7%	5%	1%
	694.5	16%	15%	11%	1%
	746.4	15%	45%	29%	3%
	802.1-862.0	11%	18%	11%	1%

Table 3.25. Intensity-weighted HDS profile of Fe-$TiO_{2,irr}$. Time dependent HDS cluster maximas, HDS range and min-max diameter difference with respect to multi-size distribution.

	Cluster			
Time, min	Max 1, nm	Max 2, nm	Range, nm	Difference, nm
Initial	197.9	2871.2	92.1-5428.1	5336.0
30	191.6	1046.2	115.2-1741.0	1625.8
60	156.1	673.7	100.7-1044.7	944.0
90	160.0	572.7	102.4-787.7	685.3
120	176.8	694.5	106.8-1069.8	963.0

Table 3.26. Comparison of intensity-weighted HDS values of Fe-$TiO_{2,as\text{-}is}$, Fe-$TiO_{2,dark}$ and Fe-$TiO_{2,irr}$.

	Fe-$TiO_{2,as\text{-}is}$		Fe-$TiO_{2,dark}$		Fe-$TiO_{2,irr}$		
	HDS, nm	CR, %	HDS, nm	CR, %	HDS, nm	CR, %	
Initial	155.0-189.5	16%	Dark Mixing		Solar Irradiation and Mixing		
	209.5-256.2	20%					
	1416.8-1566.7	10%					
	1732.5	16%					
	1915.9	21%					
	2118.6-2342.8	17%					
30 min	141.2-166.0	17%					
	180.0	14%					
	195.1-211.5	13%					
	711.0-770.8	23%					
	835.7	18%					
	906.0-982.3	15%					
60 min	144.5-165.5	21%	148.6-177.8	22%	153.4-197.9	17%	Initial
	177.2	14%	194.5-212.7	15%	224.8-255.3	10%	
	189.6-203.0	12%	522.0-624.6	19%	2225.5	7%	
	562.3-601.8	21%	683.3-747.4	12%	2527.8	17%	
	644.1	18%	978.4-1280.7	17%	2871.2	25%	
	689.4-737.8	15%	1401.0-1676.5	15%	3261.2-3704.2	24%	
	-	-	-	-	-	-	
90 min	158.1-170.3	11%	144.8-166.5	18%	148.5-176.0	16%	30 min
	183.3	15%	178.5	13%	191.6	10%	
	197.4-228.9	25%	191.4-205.2	12%	208.6-227.1	9%	
	644.7-694.2	12%	544.5-583.9	16%	811.1-882.9	11%	
	747.5	13%	626.0	16%	961.1	16%	
	804.9	15%	671.2-771.6	9%	1046.2	19%	
	866.7-933.3	9%	-	-	1138.9-1239.8	17%	
120 min	128.5-147.0	17%	170.0-180.2	14%	134.9-145.1	13%	60 min
	157.1-179.6	19%	191.1	14%	156.1	13%	
	524.3-560.6	22%	202.5-214.7	15%	168.0-180.7	13%	
	599.4	21%	578.6-613.4	15%	582.1-626.2	18%	
	640.9-685.3	21%	650.2	18%	673.7	19%	
	-	-	689.3-774.6	24%	724.8	15%	
	-	-	-	-	779.8-838.9	9%	
150 min	165.9-175.5	13%	161.5-171.8	14%	132.1-150.1	17%	90 min
	185.6	17%	182.8	16%	160.0	12%	
	196.3-207.7	21%	194.6-207.1	19%	170.5-181.7	11%	
	570.4-603.4	19%	559.9-595.8	16%	504.1-537.3	22%	
	638.2	16%	634.0	16%	572.7	20%	
	675.1-714.0	14%	674.7	12%	610.4-650.6	18%	
	-	-	718.0-764.0	7%			
180 min	126.6-146.1	19%	179.0-190.2	16%	142.5-164.5	20%	120 min
	156.9-181.1	21%	202.1	18%	176.8	13%	
	492.0-528.4	16%	214.8-228.3	20%	190.0-204.2	10%	
	567.5	16%	604.6-642.5	10%	601.4-646.3	15%	
	609.6	17%	682.9	13%	694.5	16%	
	654.7-703.2	11%	725.7	13%	746.4	15%	
	-	-	771.3-819.7	10%	802.1-862.0	11%	

Table 3.27. Comparison of intensity-weighted HDS values of $TiO_{2,irr}$ and Fe-$TiO_{2,irr}$.

	$TiO_{2,irr}$		Fe-$TiO_{2,irr}$	
	HDS, nm	CR, %	HDS, nm	CR, %
Initial	169.6-196.7	19%	153.4-197.9	17%
	211.8-245.6	20%	224.8-255.3	10%
	745.9-803.3	9%	2225.5	7%
	865.0	15%	2527.8	17%
	931.5	20%	2871.2	25%
	1003.1-1080.2	17%	3261.2-3704.2	24%
30 min	149.7-174.9	17%	148.5-176.0	16%
	189.0-220.9	18%	191.6	10%
	767.8-829.9	25%	208.6-227.1	9%
	897.1	21%	811.1-882.9	11%
	969.8-1048.3	19%	961.1	16%
	-	-	1046.2	19%
	-	-	1138.9-1239.8	17%
60 min	137.8-162.9	17%	134.9-145.1	13%
	177.1-209.4	18%	156.1	13%
	735.3-799.5	16%	168.0-180.7	13%
	869.3	19%	582.1-626.2	18%
	945.2-1117.5	30%	673.7	19%
	-	-	724.8	15%
	-	-	779.8-838.9	9%
90 min	155.2-180.0	16%	132.1-150.1	17%
	193.8-224.8	24%	160.0	12%
	735.1-791.6	23%	170.5-181.7	11%
	852.4	19%	504.1-537.3	22%
	917.9-988.5	18%	572.7	20%
	-	-	610.4-650.6	18%
120 min	100.3-139.9	22%	142.5-164.5	20%
	486.9-529.1	19%	176.8	13%
	574.9	23%	190.0-204.2	10%
	624.8	21%	601.4-646.3	15%
	-	-	694.5	16%
	-	-	746.4	15%
	-	-	802.1-862.0	11%

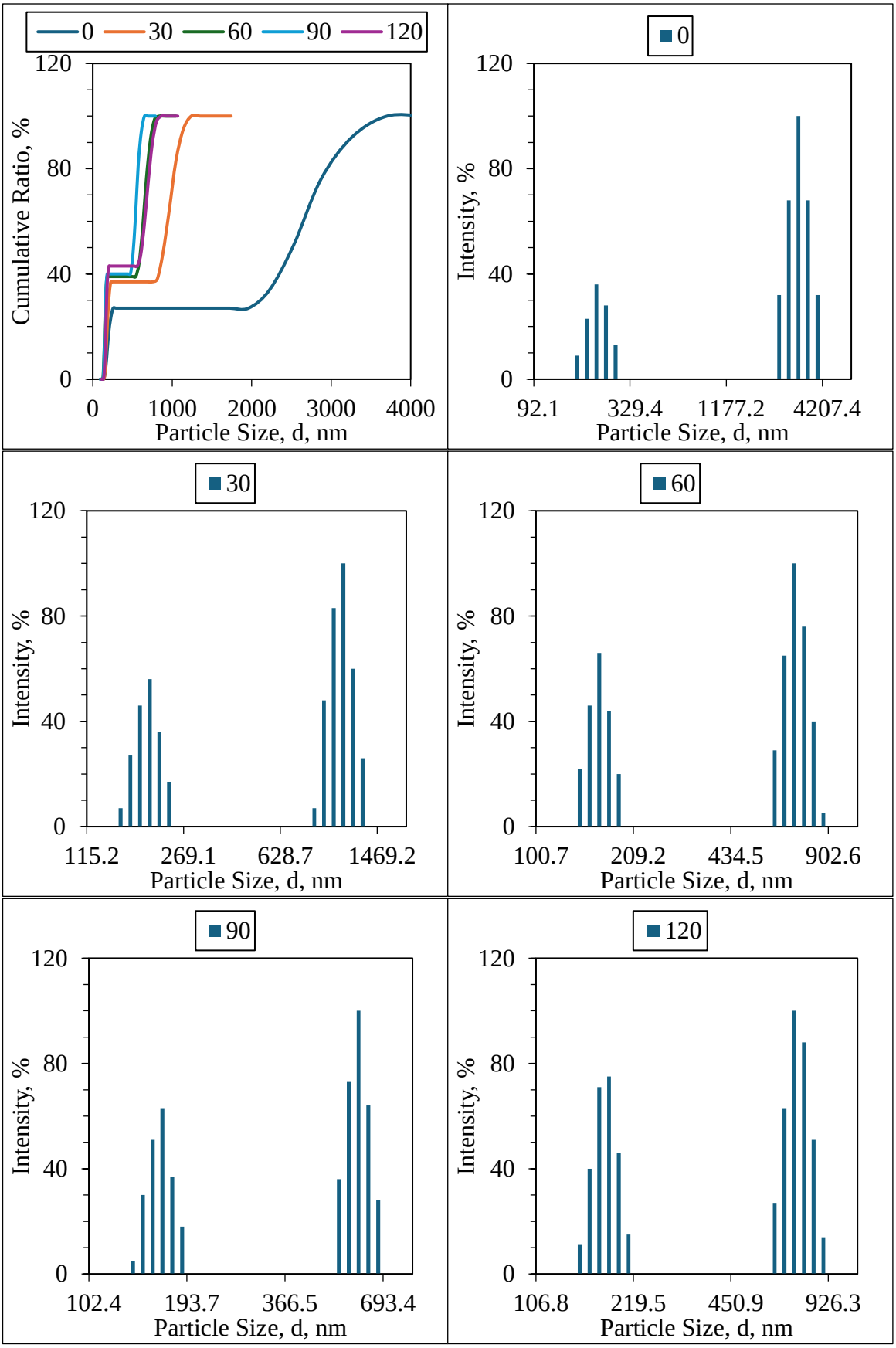


Figure 3.47. The cumulative ratio comparison and hydrodynamic size of Fe-$TiO_{2,irr}$ as intensity-weighted HDS in 30 min intervals.

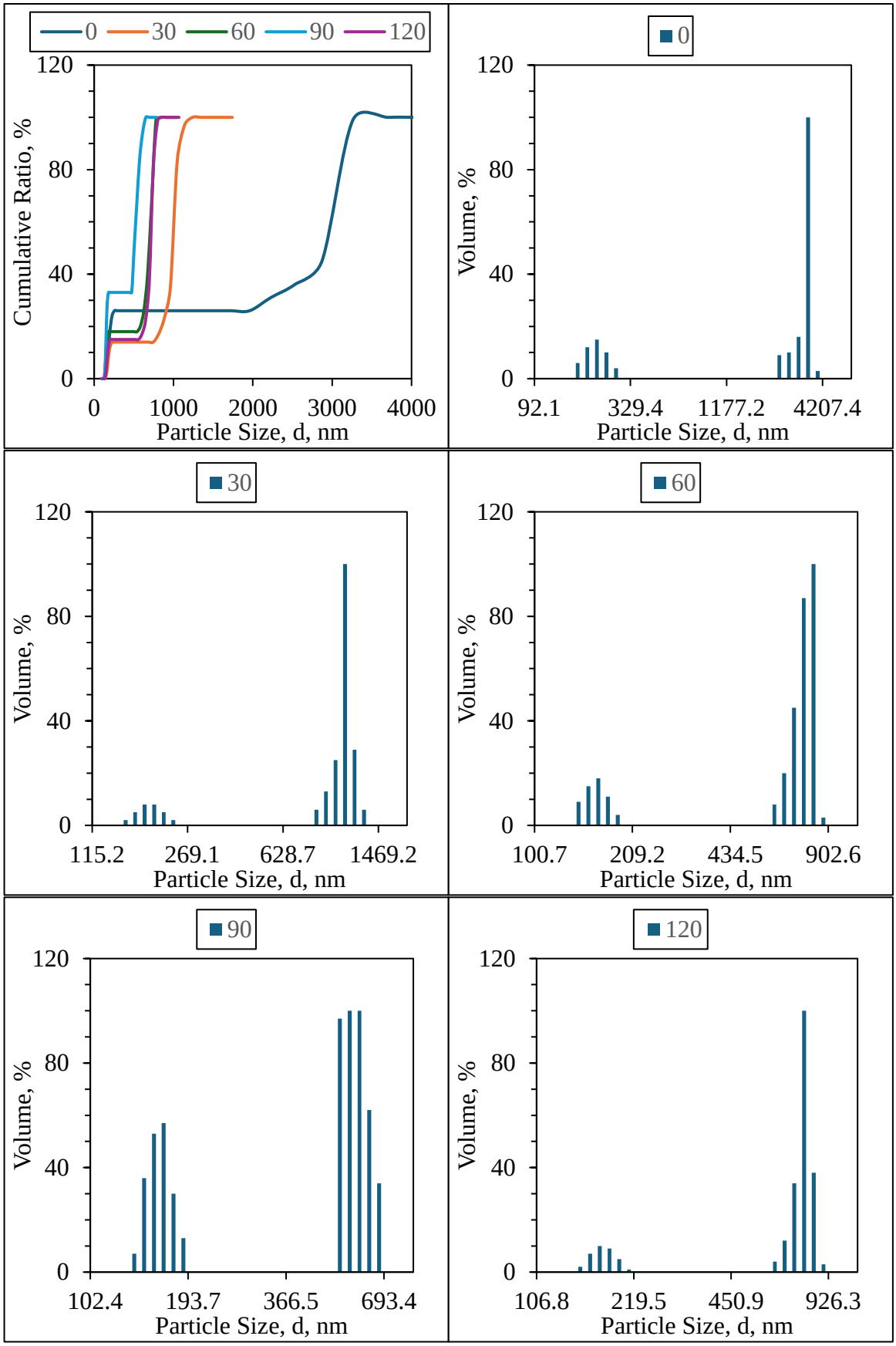


Figure 3.48. The cumulative ratio comparison and hydrodynamic size of Fe-$TiO_{2,irr}$ as volume-weighted HDS in 30 min intervals.

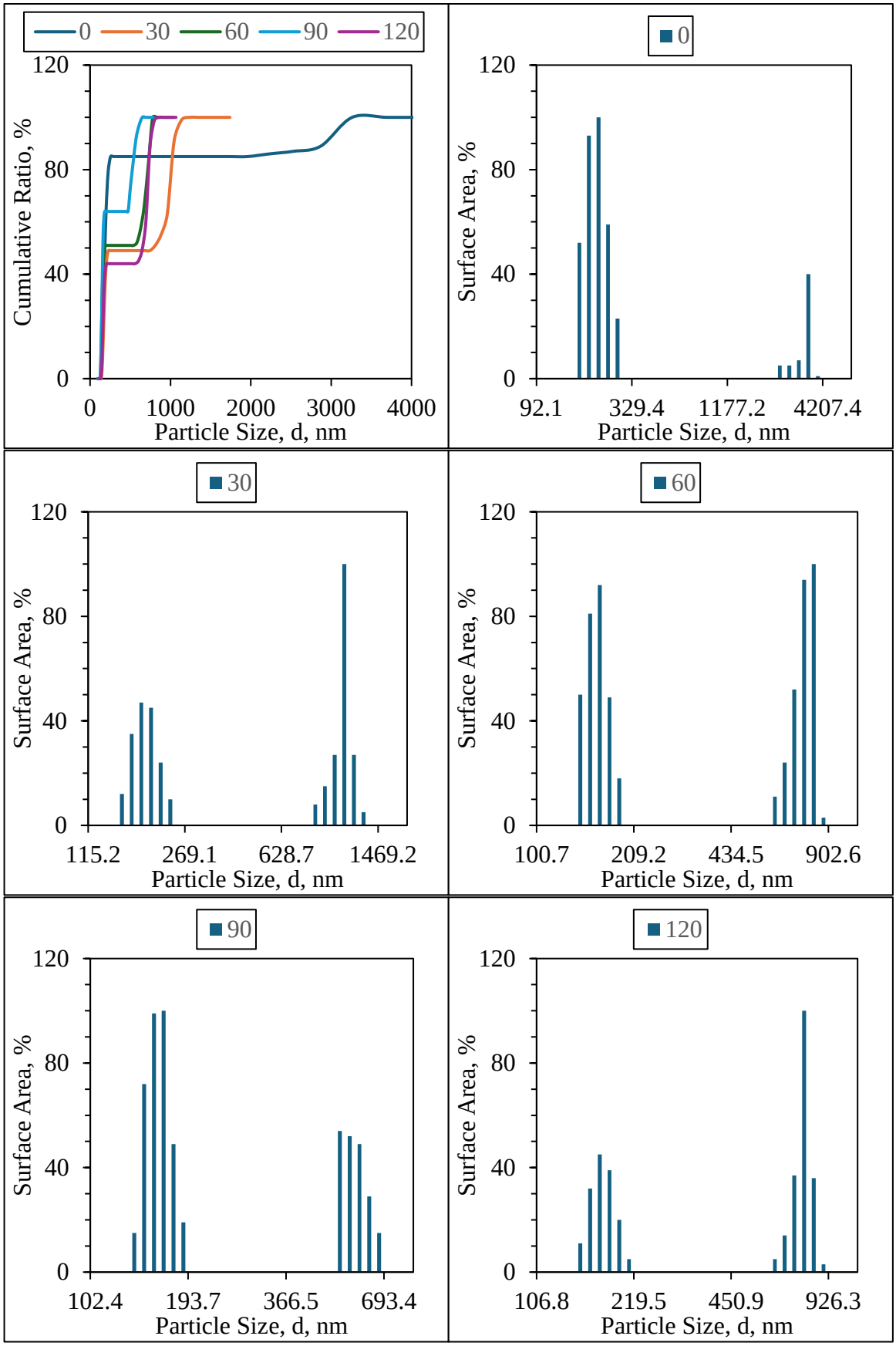


Figure 3.49. The cumulative ratio comparison and hydrodynamic size of Fe-$TiO_{2,irr}$ as surface area-weighted HDS in 30 min intervals.

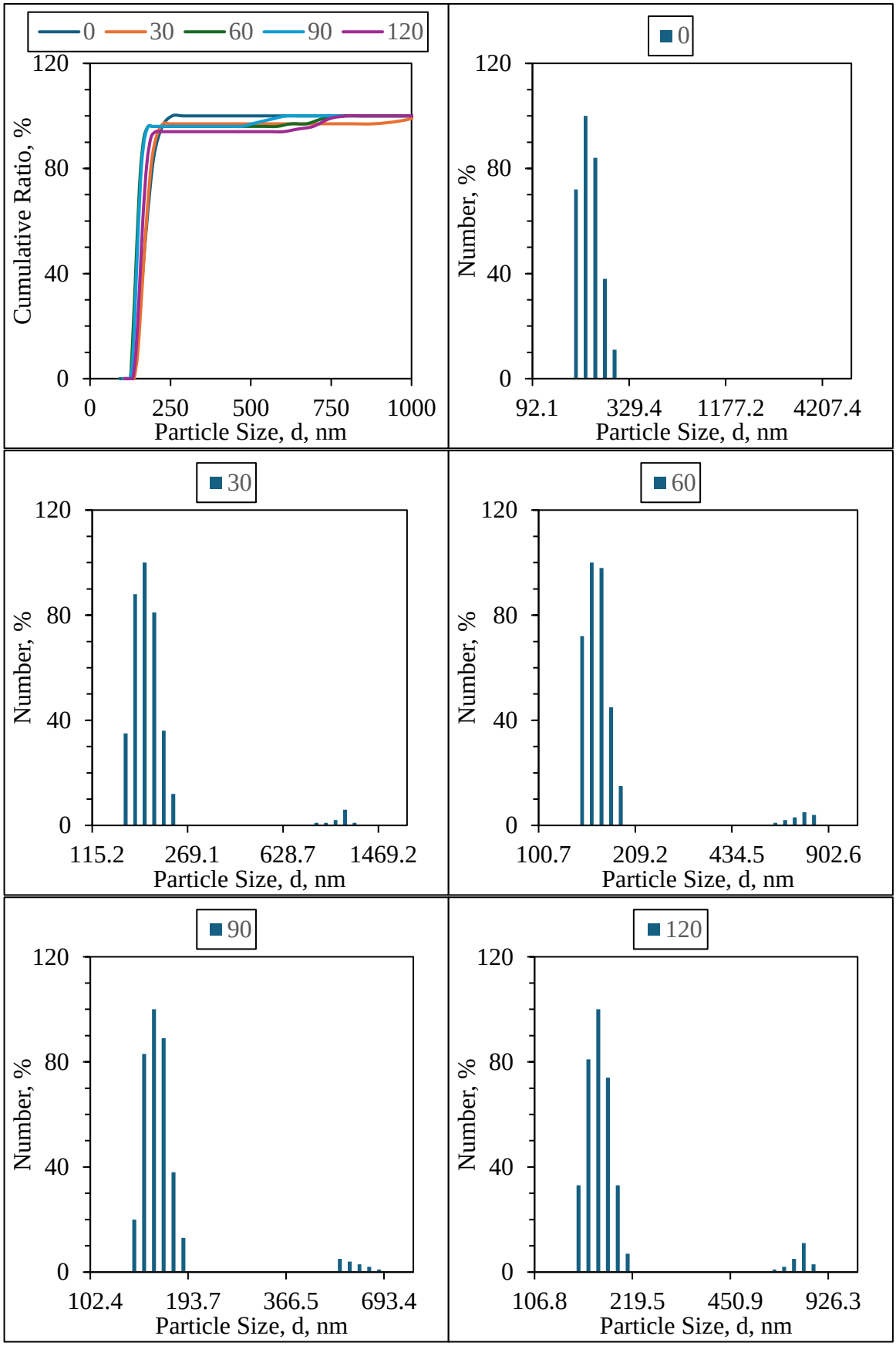


Figure 3.50. The cumulative ratio comparison and hydrodynamic size of Fe-$TiO_{2,irr}$ as number-weighted HDS in 30 min intervals.

3.4.7. Hydrodynamic Size Assessment of N-TiO_{2as-is}

Anion doped visible light active N-TiO_2 was subjected to HDS measurements by using dynamic light scattering technique. The same procedure was applied to N-TiO_2 as in the case of TiO_2 and Fe-TiO_2 HDS measurements. 0.25 gL^{-1} N-TiO_2 was suspended in Milli-Q water and sonicated for 1 min later mixed with magnetic stirrer for 4 min. Approximately 4 mL aliquot solution was transferred to polystyrene cuvette and the cuvette placed into DLS instrument. HDS was followed for 180 min with 30 min intervals without removing the cuvette. Aggregation/agglomeration profiles of N-TiO_2 specimen were investigated by DLS data reported in terms of intensity-, volume, surface area-, and number-weighted parameters. The HDS data of N-$TiO_{2,as-is}$ was compared with $TiO_{2,as-is}$ and Fe-$TiO_{2,as-is}$ by using intensity-weighted HDS.

Table 3.29 compiled the data of corresponding to cumulative ratios of intensity-, volume-, surface area-, and number-weighted HDS and Figure 3.51, Figure 3.52, Figure 3.53 and Figure 3.54 illustrated the graphical abstracts of HDS measurements respectively. Table 3.30 displayed the peak maxima of graphical abstracts and the corresponding size range measured with the difference between the biggest and smallest clusters.

The PDI of N-$TiO_{2,as-is}$ was 0.445, 0.334, 0.299, 0.258 and 0.288 for initial, 30 min, 60 min, 90 min, and 120 min respectively. The average PDI of N-$TiO_{2,as-is}$ during 120 min was 0.325 which indicates nearly monodispersed distribution, so MSD was applied to determine HDS of N-$TiO_{2,as-is}$. The N-$TiO_{2,as-is}$ suspension consisted of two main clusters sizing 187.8 nm and 1717.2 nm as intensity-weighted HDS. On the other hand, the cluster maximizing around 1717.2 nm was numerically negligible according to number-weighted HDS. These values were compared with the literature examples, although experimental conditions were not clearly stated. For achieving a proper comparison, the doping method, suspension media (Milli Q water, DI water or solution type, *etc.*) and pH conditions should be similar. For instance, Vaiano and colleagues reported the intensity-weighted HDS of N-TiO_2 synthesized by hydrolysis reaction, in three size ranges of 1480-3000 nm, 300-553 μm and 553-3000 μm. However, pretreatment procedures (sonication or mixing, duration, *etc.*) used in preparation of N-TiO_2 for HDS were not mentioned (Vaiano et al., 2017).

In another example, suspension concentration was 1 $mgmL^{-1}$ and N-TiO_2 was prepared by mechanical mixing method. The reported average intensity-weighted HDS of N-TiO_2 (1 $mgmL^{-1}$) was reported as 773±24 nm. Since the polydispersity index was not indicated, no direct comparison could be assessed (Moosavi et al., 2016). Ferrera and their group also reported the HDS size of N-

TiO_2, at pH 2 to obtain more colloidal structures and reported the average hydrodynamic size as 200 nm with the polydispersity index 0.093 (Ferrera et al., 2023). Moreover, Yalçın and colleagues presented an approximate dense aggregate size of N-TiO_2 as 100 nm in comparison to rather branched pattern <100 nm of TiO_2 by visual examination of SEM images (Yalçın et al., 2010).

The aggregation/agglomeration behavior of N-$TiO_{2,as\text{-}is}$ was evaluated by comparing HDS variations recorded during 180 min. While the maxima around 187.8 nm could refer aggregation of N-$TiO_{2,as\text{-}is}$, the cluster represented with the maxima at 1717.2 nm could be attributed to agglomeration. The hydration forces responsible for the aggregation formation were not strong enough to form structures bigger than 1000 nm (Laube et al., 2017). This cluster covered the most volume and the surface area according to volume- and surface area-weighted HDS. The surface area of the aggregated structures around 1717.2 nm was cumulatively 4 times larger in comparison to the structures around 2000 according to surface area-weighted HDS. There might be two reasons;

i. while the cluster around 2000 nm forming a more tangled structure, the cluster of 1717.2 nm was connected in a more branched structure,

ii. the agglomeration shapes were similar for both clusters but the presence of the structures around 2000 nm was way less than the structures 1717.2 nm so the CR%s of volume- and surface area-weighted HDS.

The second probability was not evidenced from number-weighted HDS because of the lack of signal for both clusters as number-weighted HDS (Table 1). On the contrary, intensity-weighted HDS of 2000 nm size was less than of 1717.2 nm so it could be concluded as fewer formation tendency of the cluster around 2000 nm in comparison with the structures of 1717.2 nm. The initial maxima on 1717.2 nm shifted to smaller size ranges and decreased to 1100.8 nm after 30 min (Table 1). Although the cluster around 1717.2 nm disappeared the cumulative ratio of 1100.8 nm increased to 2% and smaller clusters appeared around 277 nm. This trend might be the result of dissaglomeration, however, HDS profile at 60 min showed that the clusters >1000 nm totally disappeared. Also, sedimentation profile results indicated that after 60 min 20% removal was achieved. It must be noted that there was no relation between sedimentation percentages and CR% of HDS.

After 60 min, agglomeration formation slowed down and clusters around 600-800 nm was highly stable in contrast with smaller structures according to CR% of both intensity- and number-weighted HDS. Even the CR% of the intensity-weighted HDS of clusters around 600-800 nm was nearly stable

the CR% of volume- and surface area-weighted HDS decreased which showed that the structure of agglomerate was gyrated.

The agglomeration trend was continued by the affiliation of the structures around 200 nm leading to formation of agglomerates sizing ~500-600 nm according to intensity- and number-weighted HDS. By comparing the volume- and surface area-weighted HDS of these clusters it could be concluded as the agglomerate structure was more spherical rather than branched. The overall removal of N-$TiO_{2,as-is}$ was ~35% at the end of 180 min. So even though the CR% of HDS was almost stable, sedimentation of N-$TiO_{2,as-is}$ continued after 60 min.

The obtained HDS results of N-$TiO_{2,as-is}$ was also compared with Fe-$TiO_{2,as-is}$ and $TiO_{2,as-is}$ as intensity-weighted HDS which was summarized in Table 3. Rather than $TiO_{2,as-is}$, hydrodynamic size fluctuations of N-$TiO_{2,as-is}$ were more similar to Fe-$TiO_{2,as-is}$. Both N-$TiO_{2,as-is}$ and Fe-$TiO_{2,as-is}$ formed bigger clusters in comparison to $TiO_{2,as-is}$. However, the settling velocity of Fe-$TiO_{2,as-is}$ was faster than N-$TiO_{2,as-is}$. The CR% of particles >600 nm was higher than both Fe-$TiO_{2,as-is}$ and $TiO_{2,as-is}$ after 60 min which showed that anion doping formed colloidally more stable structures. This might be related to the formation of stronger hydrogen bonds due to the presence of N.

Table 3.28. Intensity-weighted HDS profile of N-$TiO_{2,as-is}$. Time dependent HDS cluster maximas, HDS range and min-max diameter difference with respect to multi-size distribution.

	Cluster				
Time, min	Max 1, nm	Max 2, nm	Max 3, nm	Range, nm	Difference, nm
Initial	187.8	1717.2	-	113.6-2839.6	2726.0
30	217.4	235.7	1100.8	133.6-1790.8	1657.2
60	171.0	699.0		112.1-1066.3	954.2
90	175.7	189.2	771.5	112.7-1202.5	1089.8
120	200.8	211.8	584.7	145.7-805.8	660.1
150	180.8	670.6		132.3-975.2	842.9
180	195.4	209.7	862.9	147.3-1415.8	1268.5

Table 3.29. Intensity-, volume-, surface area- and number-weighted HDS and cumulative ratios of N-$TiO_{2,as\text{-}is}$.

	HDS, nm	Cumulative Ratio, %			
		Intensity	Volume	Surface Area	Number
Initial	153.6-187.8	23%	11%	46%	80%
	207.7-229.7	15%	6%	16%	19%
	1269.9-1404.3	10%	27%	14%	1%
	1552.9	17%	9%	4%	-
	1717.2	19%	39%	16%	-
	1898.9-2099.9	17%	8%	4%	-
30 min	184.8-200.4	13%	6%	16%	33%
	217.4	17%	7%	18%	30%
	235.7	18%	6%	16%	22%
	255.6-277.2	14%	5%	11%	12%
	935.9-1015.0	12%	17%	10%	1%
	1100.8	12%	46%	23%	2%
	1193.8-1294.6	14%	13%	6%	-
60 min	148.6-159.4	13%	5%	16%	41%
	171.0	14%	5%	14%	30%
	183.5-196.9	17%	5%	13%	23%
	607.2-651.5	15%	7%	6%	-
	699.0	17%	17%	11%	2%
	749.9	14%	45%	30%	3%
	804.6-863.6	10%	16%	10%	1%
90 min	151.6-175.7	22%	7%	21%	55%
	189.2	16%	4%	12%	23%
	203.7-219.4	14%	3%	8%	14%
	665.4-716.5	20%	18%	13%	2%
	771.5	15%	59%	40%	5%
	830.7-894.5	13%	9%	6%	1%
120 min	180.4-190.3	13%	11%	19%	30%
	200.8	17%	13%	20%	29%
	211.8	16%	11%	17%	22%
	223.4-235.7	14%	9%	13%	14%
	525.4-554.3	14%	22%	13%	2%
	584.7	12%	15%	8%	2%
	616.8-686.4	14%	19%	10%	1%
150 min	159.6-169.9	14%	10%	21%	39%
	180.8	16%	9%	20%	31%
	192.5-204.9	21%	11%	20%	25%
	556.1-591.9	14%	12%	8%	2%
	630.0	15%	13%	7%	1%
	670.6-759.8	20%	45%	24%	2%
180 min	169.6	27%	1%	3%	7%
	182.1	18%	4%	11%	22%
	195.4-209.7	15%	14%	31%	52%
	698.0-749.1	16%	32%	28%	16%
	804.0	12%	28%	16%	2%
	862.9-926.2	12%	21%	11%	1%

Table 3.30. Comparison of intensity-weighted HDS values of N-$TiO_{2,as\text{-}is}$ and Fe-$TiO_{2,as\text{-}is}$ and $TiO_{2,as\text{-}is}$.

	N-$TiO_{2,as\text{-}is}$		Fe-$TiO_{2,as\text{-}is}$		$TiO_{2,as\text{-}is}$	
	HDS, nm	CR, %	HDS, nm	CR, %	HDS, nm	CR, %
Initial	153.6-187.8	23%	155.0-189.5	16%	98.6-129.1	10%
	207.7-229.7	15%	209.5-256.2	20%	169.2-380.3	14%
	1269.9-1404.3	10%	1416.8-1566.7	10%	498.3-652.7	34%
	1552.9	17%	1732.5	16%	855.1	23%
	1717.2	19%	1915.9	21%	1120.2	14%
	1898.9-2099.9	17%	2118.6-2342.8	17%	1467.5	5%
30 min	184.8-200.4	13%	141.2-166.0	17%	140.7-164.0	16%
	217.4	17%	180.0	14%	177.1-206.6	15%
	235.7	18%	195.1-211.5	13%	706.5-763.0	19%
	255.6-277.2	14%	711.0-770.8	23%	823.9	22%
	935.9-1015.0	12%	835.7	18%	889.7-1037.6	28%
	1100.8	12%	906.0-982.3	15%	-	-
	1193.8-1294.6	14%	-	-	-	-
60 min	148.6-159.4	13%	144.5-165.5	21%	144.3-184.4	26%
	171.0	14%	177.2	14%	200.1-217.1	11%
	183.5-196.9	17%	189.6-203.0	12%	739.9-802.9	19%
	607.2-651.5	15%	562.3-601.8	21%	871.2	20%
	699.0	17%	644.1	18%	945.4	15%
	749.9	14%	689.4-737.8	15%	1025.9-1113.3	9%
	804.6-863.6	10%				
90 min	151.6-175.7	22%	158.1-170.3	11%	739.9-802.9	19%
	189.2	16%	183.3	15%	871.2	20%
	203.7-219.4	14%	197.4-228.9	25%	945.4	15%
	665.4-716.5	20%	644.7-694.2	12%	1025.9-1113.3	9%
	771.5	15%	747.5	13%	-	-
	830.7-894.5	13%	804.9	15%	-	-
	-	-	866.7-933.3	9%	-	-
120 min	180.4-190.3	13%	128.5-147.0	17%	96.8-146.1	20%
	200.8	17%	157.1-179.6	19%	501.7-544.7	16%
	211.8	16%	524.3-560.6	22%	591.4-642.2	45%
	223.4-235.7	14%	599.4	21%	697.2-757.0	19%
	525.4-554.3	14%	640.9-685.3	21%	-	-
	584.7	12%	-	-	-	-
	616.8-686.4	14%	-	-	-	-
150 min	159.6-169.9	14%	165.9-175.5	13%	66.6-143.6	7%
	180.8	16%	185.6	17%	156.2-201.0	19%
	192.5-204.9	21%	196.3-207.7	21%	218.6-237.8	8%
	556.1-591.9	14%	570.4-603.4	19%	587.9-710.4	42%
	630.0	15%	638.2	16%	780.9-943.7	24%
	670.6-759.8	20%	675.1-714.0	14%	-	-
180 min	169.6	27%	126.6-146.1	19%	117.0-158.5	24%
	182.1	18%	156.9-181.1	21%	534.6-576.7	23%
	195.4-209.7	15%	492.0-528.4	16%	622.3-671.4	42%
	698.0-749.1	16%	567.5	16%	724.4-781.6	11%
	804.0	12%	609.6	17%	-	-
	862.9-926.2	12%	654.7-703.2	11%	-	-

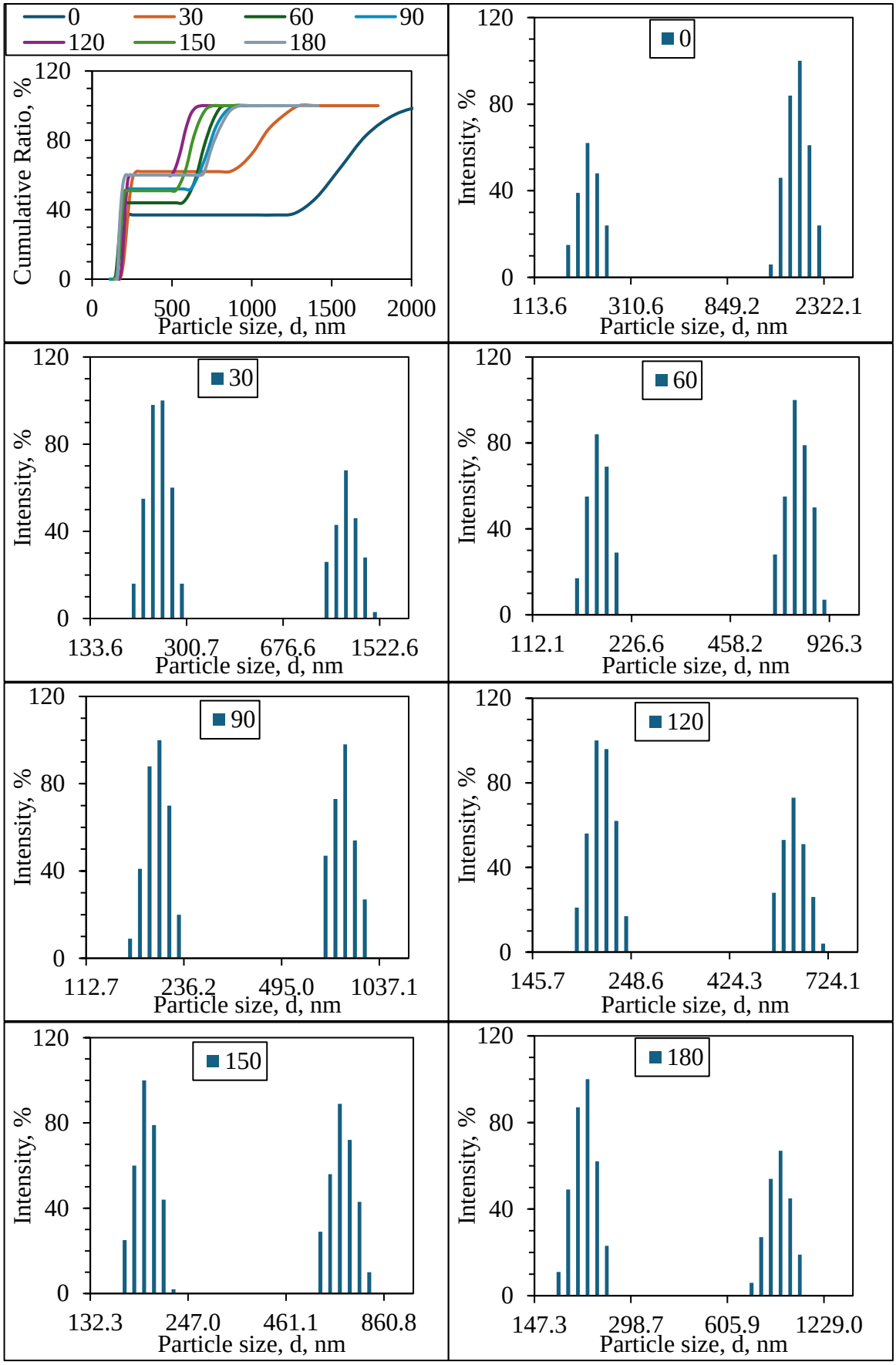


Figure 3.51. The cumulative ratio comparison and hydrodynamic size of N-$TiO_{2,as\text{-}is}$ as intensity-weighted HDS in 30 min intervals.

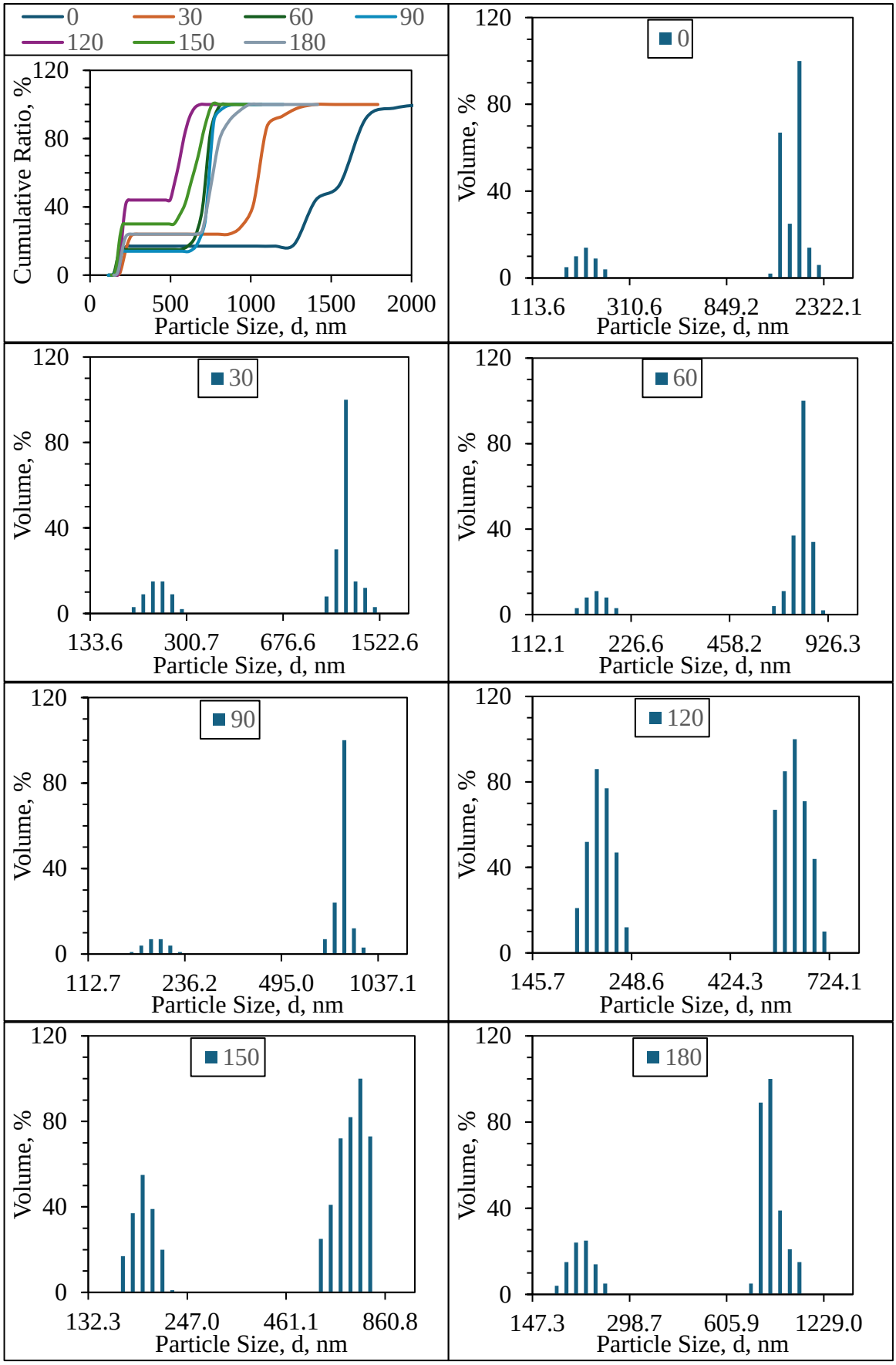


Figure 3.52. The cumulative ratio comparison and hydrodynamic size of N-$TiO_{2,as\text{-}is}$ as volume-weighted HDS in 30 min intervals.

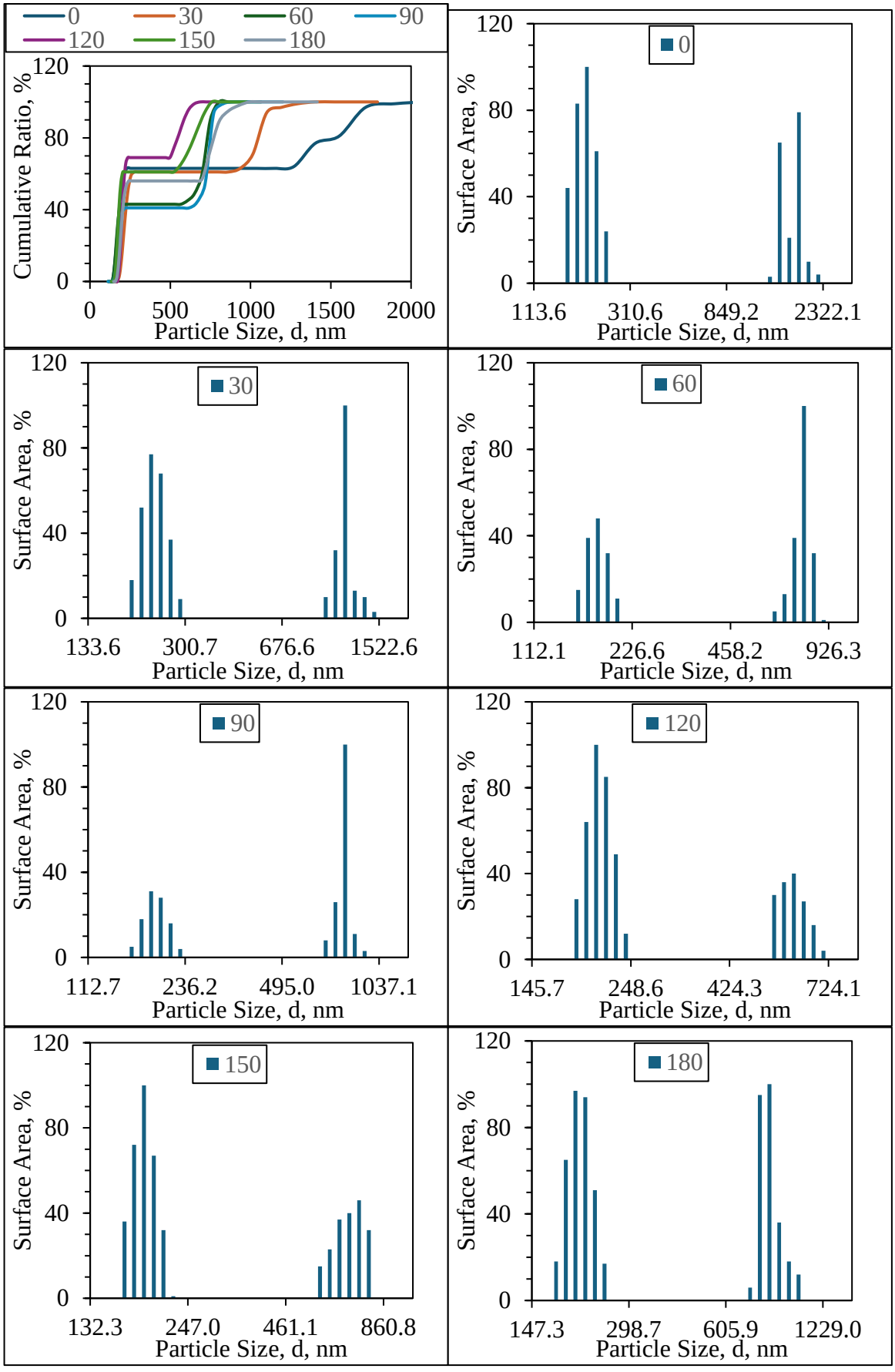


Figure 3.53. The cumulative ratio comparison and hydrodynamic size of N-$TiO_{2,as\text{-}is}$ as surface area-weighted HDS in 30 min intervals.

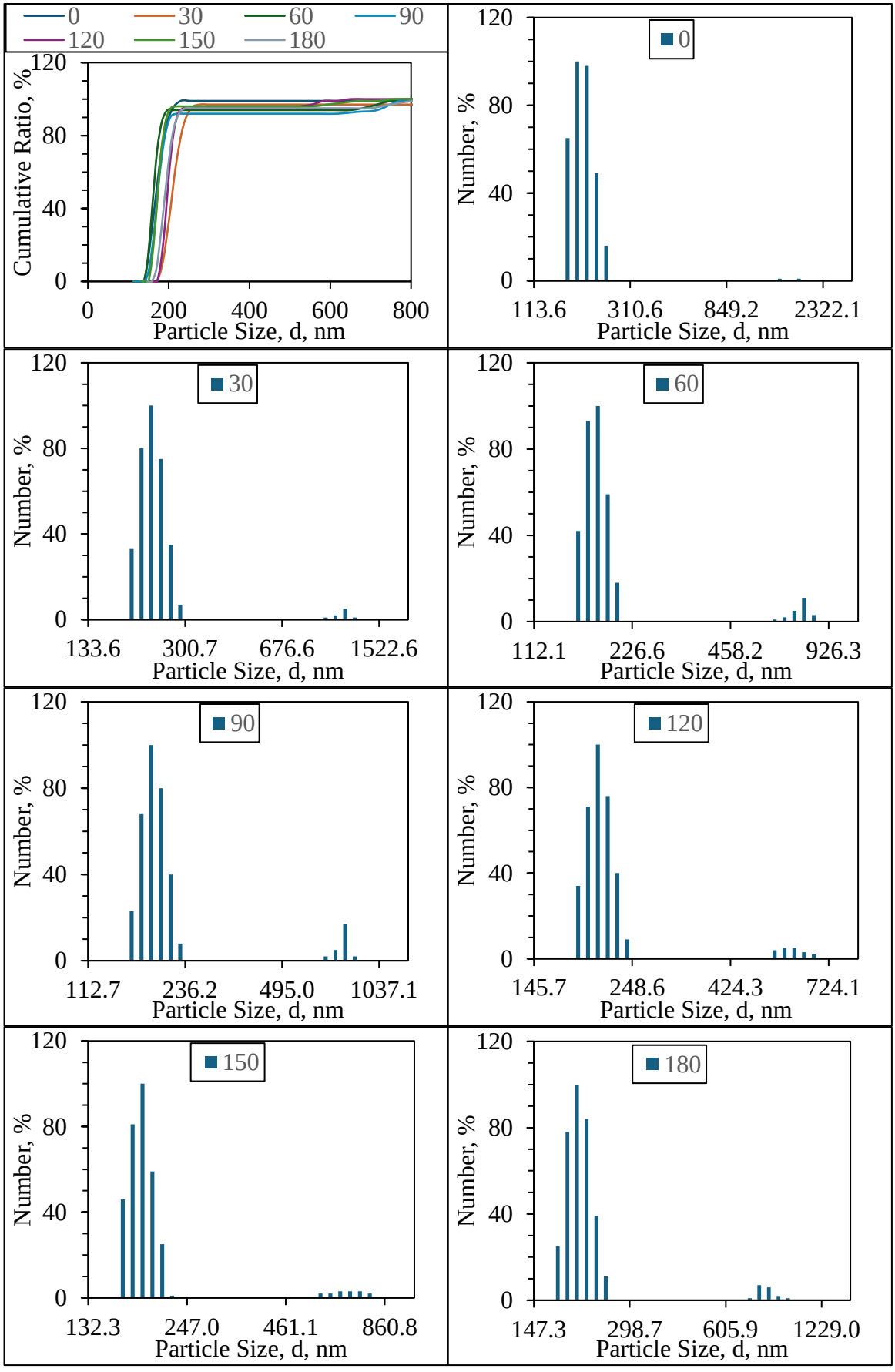


Figure 3.54. The cumulative ratio comparison and hydrodynamic size of N-$TiO_{2,as\text{-}is}$ as number-weighted HDS in 30 min intervals.

3.4.8. Hydrodynamic Size Assessment of N-$TiO_{2,dark}$

The effect of anion doping on the aggregation/agglomeration behavior of TiO_2 in dark condition was investigated by following the HDS data of N doped TiO_2. 0.25 mgL^{-1} N doped TiO_2 was added in Milli-Q water and ultrasonicated for 1 min and later magnetically stirred for 4 min, the obtained solution was continued magnetically mixing in solar light simulator while the lights were closed to supply similar conditions with $TiO_{2,dark}$. The slurry was named N-$TiO_{2,dark}$. After 60 min, 4 mL of N-TiO_2 solution was transferred to polystyrene cuvette and placed into DLS instrument and the HDS was followed for 120 min in 30 min intervals without removing the cuvette. Table 3.31 compiled the HDS results and their corresponding CR% as intensity-, volume, surface area-, and number-weighted HDS parameters and their graphical abstracts were illustrated in Figure 3.55-3.58. Time depended changes of HDS were summarized in detail in Table 3.33 as maxima, range and corresponding size difference. Also, comparative results in terms of intensity-weighted HDS were outlined in Table 3.33 and Table 3.34 for as N-$TiO_{2,as\text{-}is}$ vs N-$TiO_{2,dark}$ and $TiO_{2,dark}$ vs Fe-$TiO_{2,dark}$ vs N-$TiO_{2,dark}$.

The PDI values of N-$TiO_{2,dark}$ was found as 0.343, 0.293, 0.258, 0.234 and 0.199 for initial, 30 min, 60 min, 90 min and 120 min, respectively. The average PDI was calculated as 0.265 which was an indicator of nearly monodispersed system therefore MSD approximation was applied to define HDS of N-$TiO_{2,dark}$.

Initially, MSD of N-$TiO_{2,dark}$ illustrated three main peaks around 161.3 nm, 175.4 nm and 1013.4 nm for intensity-, volume-, and surface area-weighted HDS (Table 3.31, Figure 3.55, Figure . 3.56, and Figure 3.57). However, the largest cluster (1013.4 nm) was not visible in number-weighted HDS. Table 3.31 showed that structures larger than 1013.4 nm (1101.7 nm-1197.7 nm) constituted 1% of the overall system which evidenced that the presence of largest cluster could be regarded as negligible. The HDS of sol-gel synthesized N-TiO_2 was reported as 275.7 nm and 5076.0 nm with two main peaks and the average intensity-weighted HDS was calculated as 237 nm by Kassalini and colleagues (Kassalini et al., 2023). The system was previously mixed under dark conditions and the PDI of the system was found to be 0.327. The average size measured from TEM images was reported approximately as 5 nm to 15 nm and HDS was larger due to the hydration layer covering the N-TiO_2 structures and colloidally suspended aggregates. The aggregates and agglomerates of N-TiO_2 via HDS measurements could also be differentiated. The structures around 275.7 nm were denoted as aggregates and the structures around 5076.0 nm were denoted as agglomerates. The aggregate size (275.7 nm) reported by Kassalini and colleagues were in line with the results attained for N-$TiO_{2,dark}$ as 161.3-175.4 nm, on the other hand the reported agglomerate size as 5076.0 nm was almost five

times bigger than size attained for N-$TiO_{2,dark}$ as 1013.4 nm. This size difference might be related to pretreatment procedures applied by Kassalini and co-workers in comparison to the methodology reported herein. Upon 1 min sonication applied prior to the magnetically mixing resulted in colloidally more dispersed structures of N-$TiO_{2,dark}$ however, Kassalini and colleagues applied only magnetically mixing leading to formation of larger agglomerates due to the collusion of N-TiO_2 aggregates.

The cluster greater than 1000 nm disappeared after 30 min (Table 3.31). These structures disagglomerated due to the van der Waals forces that created partially charged sites (Natarajan et al., 2021). The van der Waal forces was a function of DLVO theory however there were other forces affecting the aggregation agglomeration of N-TiO_2 such as hydration forces, magnetic and hydrophobic forces (Dwivedi et al., 2015; Sendra et al., 2017a). The shape of ~1000 nm agglomerates could be considered as spherical with respect to their volume- and surface area-weighted CR%. The spherical shape decreased the same charged points and edges and accelerated the dissaglomeretion. Because doping with N increased the probability of hydrogen bonding by extra lone pair electrons supplied by N, N-$TiO_{2,dark}$ more tended to be colloidally stable (Gomes et al. 2019). This trend was also evidenced through the sedimentation profiles. The removal efficiency attained at the end of 30 min was less than 10% which showed that only a small portion of N-$TiO_{2,dark}$ precipitated. Upon visual inspection of the polystyrene cuvette following 120 min at which < 20% removal was attained, only a thin sediment layer was detected. Another evidence for dissaglomeretion of N-$TiO_{2,dark}$ was the appearance of structures around 500-600 nm at 30 min. These structures were mostly comprised of spherical agglomerates of the 100-200 nm size as deduced from their volume- and surface area-weighted HDS parameters. However, these were mostly stable agglomerates formed during 120 min. The number-weighted CR% of the agglomerates around 500-600 nm was 1% that showed their quantity in the medium would be stable. On the other hand, the number-weighted CR% of the smallest fraction (100-200 nm) fluctuated during 120 min that was mostly related with the Brownian motion of the aggregated structures. When the laser beam of DLS hits from different directions of the structures, the measured size might change thereby the number-weighted CR% of these structures would be differentiated. The structure around 1800 nm appeared at the end of 120 min with a very small fraction might be related to an agglomerated form of two or three middle-sized agglomerates. It must be noted that this appearance was very few in number, but it was enough to mask the middle size agglomerates (Table 1). Because the size range (641.6-1884.3) was broad, placement of agglomeration could not be specified by comparing volume- and surface size-weighted HDS (Table 3.31 and Table 3.32).

Comparison of N-$TiO_{2,as\text{-}is}$ and N-$TiO_{2,dark}$ was aligned with the 60 min of N-$TiO_{2,as\text{-}is}$ and initial of N-$TiO_{2,dark}$ due to the pretreatment conditions applied as 60 min dark mixing (Table 3.33). Due to the mixing collusion of N-TiO_2 structures collided and larger agglomerates obtained in N-$TiO_{2,dark}$ on the other hand after 30 min, 90 min for N-$TiO_{2,as\text{-}is}$, no distinct difference between N-$TiO_{2,as\text{-}is}$ and N-$TiO_{2,dark}$ was observed in terms of intensity-weighted HDS. However, the removal efficiencies of N-$TiO_{2,as\text{-}is}$ (35%) and N-$TiO_{2,dark}$ (20%) evidenced that magnetically mixing supplied colloidally more stable aggregates as well as agglomerates.

The effect of doping under dark conditions was evaluated by comparing $TiO_{2,dark}$, Fe-$TiO_{2,dark}$ and N-$TiO_{2,dark}$ in terms of intensity-weighted HDS (Table 3.34). The hydration and van der Waals forces would be effective not only for $TiO_{2,dark}$ but also Fe-$TiO_{2,dark}$ and N-$TiO_{2,dark}$. Apart from hydration and van der Waals forces F-$TiO_{2,dark}$ was affected from magnetic forces and N-$TiO_{2,dark}$ had more H-bonding sites in comparison to the $TiO_{2,dark}$ and Fe-$TiO_{2,dark}$. Due to the magnetic forces, larger agglomerates were formed in Fe-$TiO_{2,dark}$, however, these agglomerates were not colloidally stable due to the high atomic weight of iron and approximately 60% of the agglomerates precipitated at the end of the 120 min period. The removal efficiencies for $TiO_{2,dark}$ and N-$TiO_{2,dark}$ was determined as15% and 20%, respectively. It must be considered that the removal of N-$TiO_{2,dark}$ was actually related with the dissaglomeration of N-TiO_2 structures. Because the UV-Vis spectroscopy measured the passing light efficiency during sedimentation experiment smaller colloids supplied more room for to light pass therefore dissaglomeration could also lead to reduction in light absorption efficiency. Therefore N-$TiO_{2,dark}$ was colloidally equal or more stable than $TiO_{2,dark}$. After 30 min, differing from Fe-$TiO_{2,dark}$ and N-$TiO_{2,dark}$, $TiO_{2,dark}$ continued to agglomerate during 120 min, however aggregates and middle-size agglomerates of Fe-$TiO_{2,dark}$ and N-$TiO_{2,dark}$ was colloidally more stable. This phenomena might be related to thicker hydration layer covering N-TiO_2 aggregates due to the more H-bonding sites of N-TiO_2, and magnetic repulsive forces created by Fe onto Fe-$TiO_{2,dark}$. Agglomerate formation was dependent on the collision of structures therefore prevented continues agglomeration of Fe-$TiO_{2,dark}$ and N-$TiO_{2,dark}$ during the time duration. Also, the high precipitation ratio of Fe-$TiO_{2,dark}$ decreased the quantity of colloids in the suspension and probability of collusion was less if the quantity of structures were few in number.

Table 3.31. Intensity-, volume-, surface area- and number-weighted HDS and cumulative ratios of N-$TiO_{2,dark}$.

	HDS, nm	Cumulative Ratio, %			
		Intensity	Volume	Surface Area	Number
Initial	136.5-161.3	20%	11%	37%	68%
	175.4-207.3	21%	9%	24%	30%
	857.5-932.2	23%	16%	9%	1%
	1013.4	19%	26%	13%	-%
	1101.7-1197.7	17%	38%	17%	1%
30 min	136.0-146.3	13%	8%	23%	49%
	157.4	12%	6%	16%	29%
	169.3-182.2	13%	11%	13%	21%
	586.8-631.3	23%	12%	8%	1%
	679.1	21%	17%	11%	1%
	730.6-786.1	18%	52%	29%	1%
60 min	139.8-160.1	18%	14%	31%	54%
	171.1	15%	9%	19%	26%
	183.3-196.2	15%	8%	14%	17%
	542.3-580.4	14%	12%	8%	1%
	621.1	16%	13%	6%	-
	664.7-761.2	22%	44%	22%	2%
90 min	166.0-176.4	13%	7%	17%	34%
	187.4	16%	8%	17%	29%
	199.2-225.0	26%	11%	23%	32%
	560.7-633.3	19%	14%	9%	1%
	673.0	14%	16%	9%	1%
	715.3-760.1	12%	44%	25%	3%
120 min	97.4-166.9	18%	14%	34%	77%
	218.5	19%	8%	12%	10%
	286.0	22%	16%	22%	5%
	374.4	18%	19%	17%	4%
	490.1	10%	28%	19%	4%
	641.6-1884.3	19%	23%	8%	-

Table 3.32. Intensity-weighted HDS profile of N-$TiO_{2,dark}$. Time dependent HDS cluster maximas, HDS range and min-max diameter difference with respect to multi-size distribution.

	Cluster					
Time, min	Max 1, nm	Max 2, nm	Max 3, nm	Max 4, nm	Range, nm	Difference, nm
Initial	161.3	175.4	1013.4	-	106.3-1538.7	1432.4
30	157.4	730.6	-	-	101.5-1053.1	951.6
60	171.3	711.3	-	-	106.6-932.9	826.3
90	187.4	760.1	-	-	132.3-969.7	831.4
120	218.5	286.0	490.1	1099.5	1.0-5533.9	5532.9

Table 3.33. Comparison of intensity-weighted HDS values of N-$TiO_{2,as\text{-}is}$ and N-$TiO_{2,dark}$.

	N-$TiO_{2,as\text{-}is}$		N-$TiO_{2,dark}$		
	HDS, nm	CR, %	HDS, nm	CR, %	
Initial	153.6-187.8	23%			
	207.7-229.7	15%			
	1269.9-1404.3	10%			
	1552.9	17%			
	1717.2	19%			
	1898.9-2099.9	17%			
30 min	184.8-200.4	13%	Dark Mixing		
	217.4	17%			
	235.7	18%			
	255.6-277.2	14%			
	935.9-1015.0	12%			
	1100.8	12%			
	1193.8-1294.6	14%			
60 min	148.6-159.4	13%	136.5-161.3	20%	Initial
	171.0	14%	175.4-207.3	21%	
	183.5-196.9	17%	857.5-932.2	23%	
	607.2-651.5	15%	1013.4	19%	
	699.0	17%	1101.7-1197.7	17%	
	749.9	14%	-	-	
	804.6-863.6	10%	-	-	
90 min	151.6-175.7	22%	136.0-146.3	13%	30 min
	189.2	16%	157.4	12%	
	203.7-219.4	14%	169.3-182.2	13%	
	665.4-716.5	20%	586.8-631.3	23%	
	771.5	15%	679.1	21%	
	830.7-894.5	13%	730.6-786.1	18%	
120 min	180.4-190.3	13%	139.8-160.1	18%	60 min
	200.8	17%	171.1	15%	
	211.8	16%	183.3-196.2	15%	
	223.4-235.7	14%	542.3-580.4	14%	
	525.4-554.3	14%	621.1	16%	
	584.7	12%	664.7-761.2	22%	
	616.8-686.4	14%	-	-	
150 min	159.6-169.9	14%	166.0-176.4	13%	90 min
	180.8	16%	187.4	16%	
	192.5-204.9	21%	199.2-225.0	26%	
	556.1-591.9	14%	560.7-633.3	19%	
	630.0	15%	673.0	14%	
	670.6-759.8	20%	715.3-760.1	12%	
180 min	169.6	27%	97.4-166.9	18%	120 min
	182.1	18%	218.5	19%	
	195.4-209.7	15%	286.0	22%	
	698.0-749.1	16%	374.4	18%	
	804.0	12%	490.1	10%	
	862.9-926.2	12%	641.6-1884.3	19%	

Table 3.34. Comparison of intensity-weighted HDS values of $TiO_{2,dark}$, Fe-$TiO_{2,dark}$ and N-$TiO_{2,dark}$.

	$TiO_{2,dark}$		Fe-$TiO_{2,dark}$		N-$TiO_{2,dark}$	
Initial	153.6-211.8	25%	148.6-177.8	22%	136.5-161.3	20%
	248.8-292.1	12%	194.5-212.7	15%	175.4-207.3	21%
	652.0-765.6	20%	522.0-624.6	19%	857.5-932.2	23%
	899.0	21%	683.3-747.4	12%	1013.4	19%
	1055.6-1455.5	24%	978.4-1280.7	17%	1101.7-1197.7	17%
	-	-	1401.0-1676.5	15%	-	-
30 min	154.8-180.9	17%	144.8-166.5	18%	136.0-146.3	13%
	195.6-228.5	18%	178.5	13%	157.4	12%
	734.8-794.4	10%	191.4-205.2	12%	169.3-182.2	13%
	858.7	17%	544.5-583.9	16%	586.8-631.3	23%
	928.2	20%	626.0	16%	679.1	21%
	1003.4-1084.6	18%	671.2-771.6	9%	730.6-786.1	18%
60 min	155.9-181.5	23%	170.0-180.2	14%	139.8-160.1	18%
	195.8-211.3	12%	191.1	14%	171.1	15%
	712.7-769.0	14%	202.5-214.7	15%	183.3-196.2	15%
	829.7	18%	578.6-613.4	15%	542.3-580.4	14%
	895.2	19%	650.2	18%	621.1	16%
	965.9-1042.2	14%	689.3-774.6	24%	664.7-761.2	22%
90 min	134.3-156.1	18%	161.5-171.8	14%	166.0-176.4	13%
	168.3-181.4	7%	182.8	16%	187.4	16%
	605.0-652.3	17%	194.6-207.1	19%	199.2-225.0	26%
	703.3	21%	559.9-595.8	16%	560.7-633.3	19%
	758.3	19%	634.0	16%	673.0	14%
	817.6-881.5	16%	674.7	12%	715.3-760.1	12%
	-	-	718.0-764.0	7%	-	-
120 min	130.1-172.5	21%	179.0-190.2	16%	97.4-166.9	18%
	532.0-570.8	15%	202.1	18%	218.5	19%
	612.4	21%	214.8-228.3	20%	286.0	22%
	657.1	23%	604.6-642.5	10%	374.4	18%
	705.0-756.5	20%	682.9	13%	490.1	10%
	-	-	725.7	13%	641.6-1884.3	19%
	-	-	771.3-819.7	10%	-	-

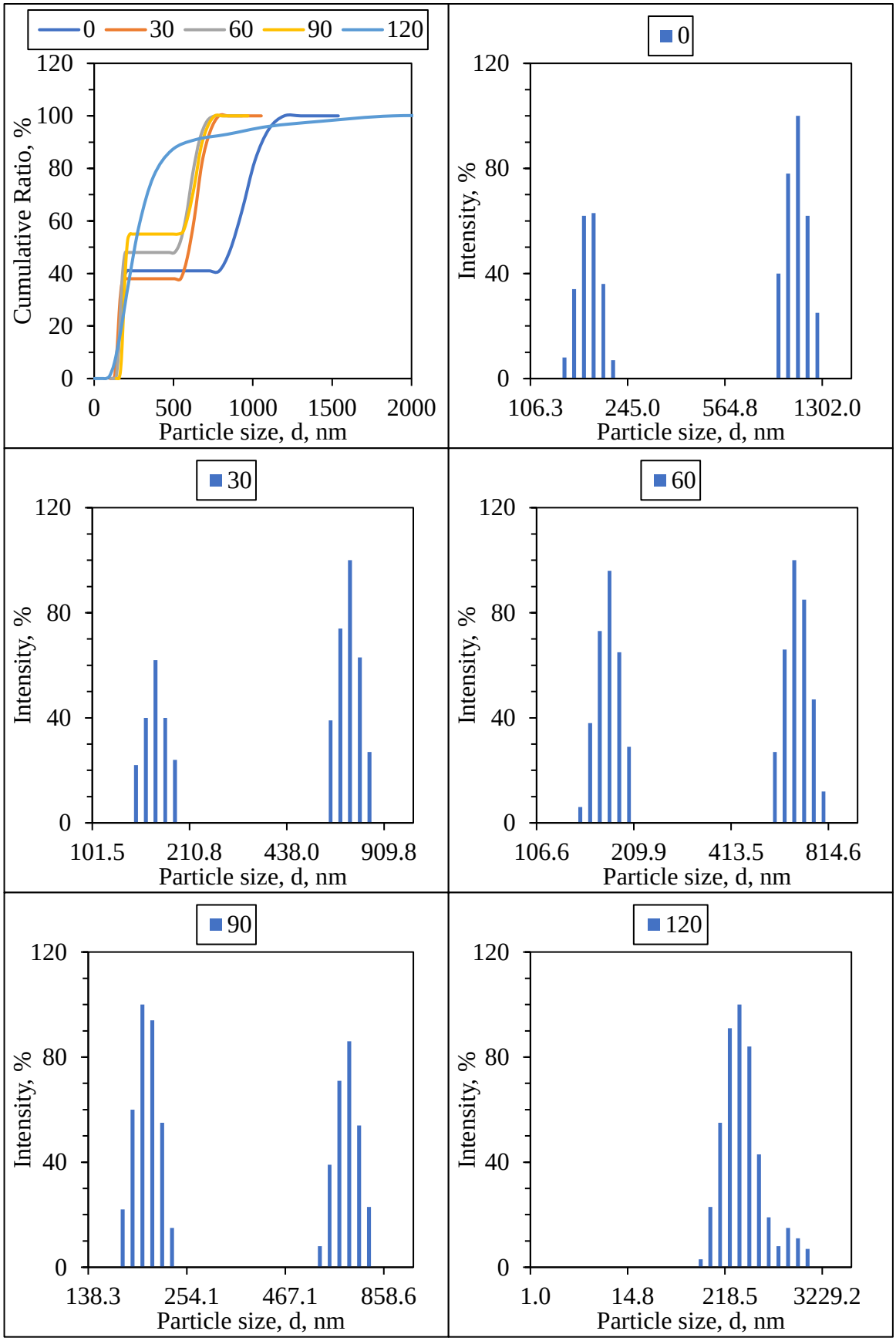


Figure 3.55. The cumulative ratio comparison and hydrodynamic size of N-$TiO_{2,dark}$ as intensity-weighted HDS in 30 min intervals.

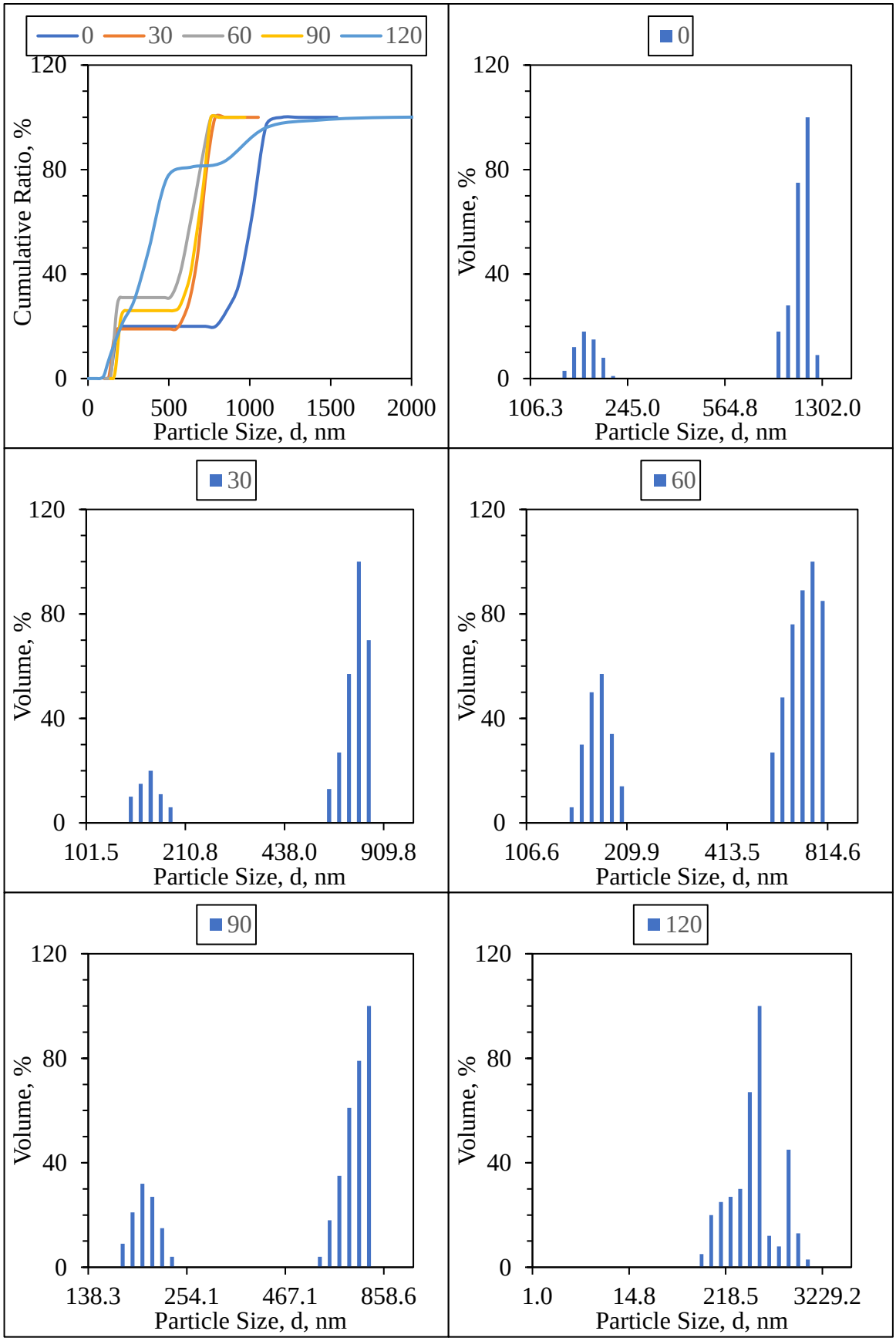


Figure 3.56. The cumulative ratio comparison and hydrodynamic size of N-$TiO_{2,dark}$ as volume-weighted HDS in 30 min intervals.

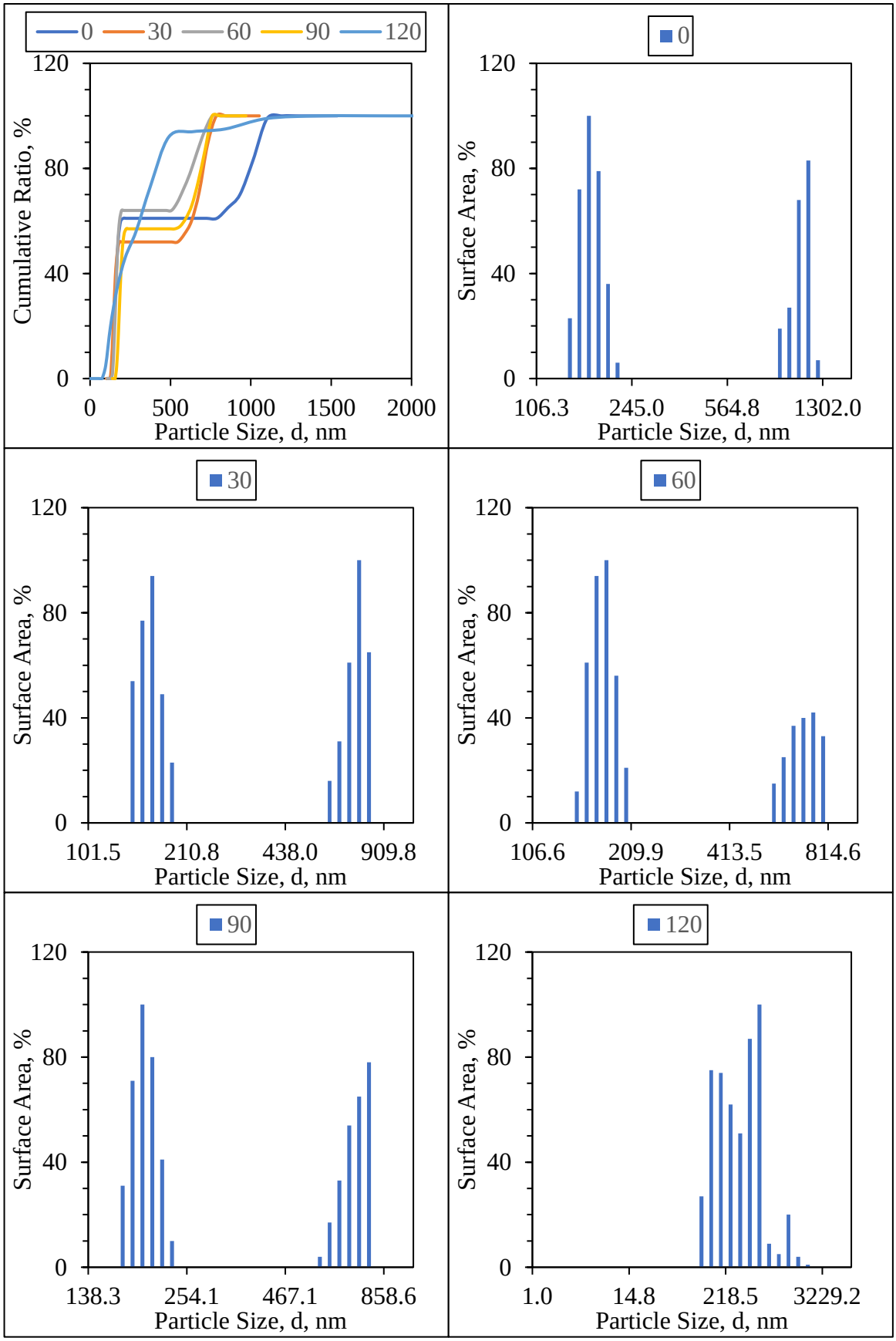


Figure 3.57. The cumulative ratio comparison and hydrodynamic size of N-$TiO_{2,dark}$ as surface area-weighted HDS in 30 min intervals.

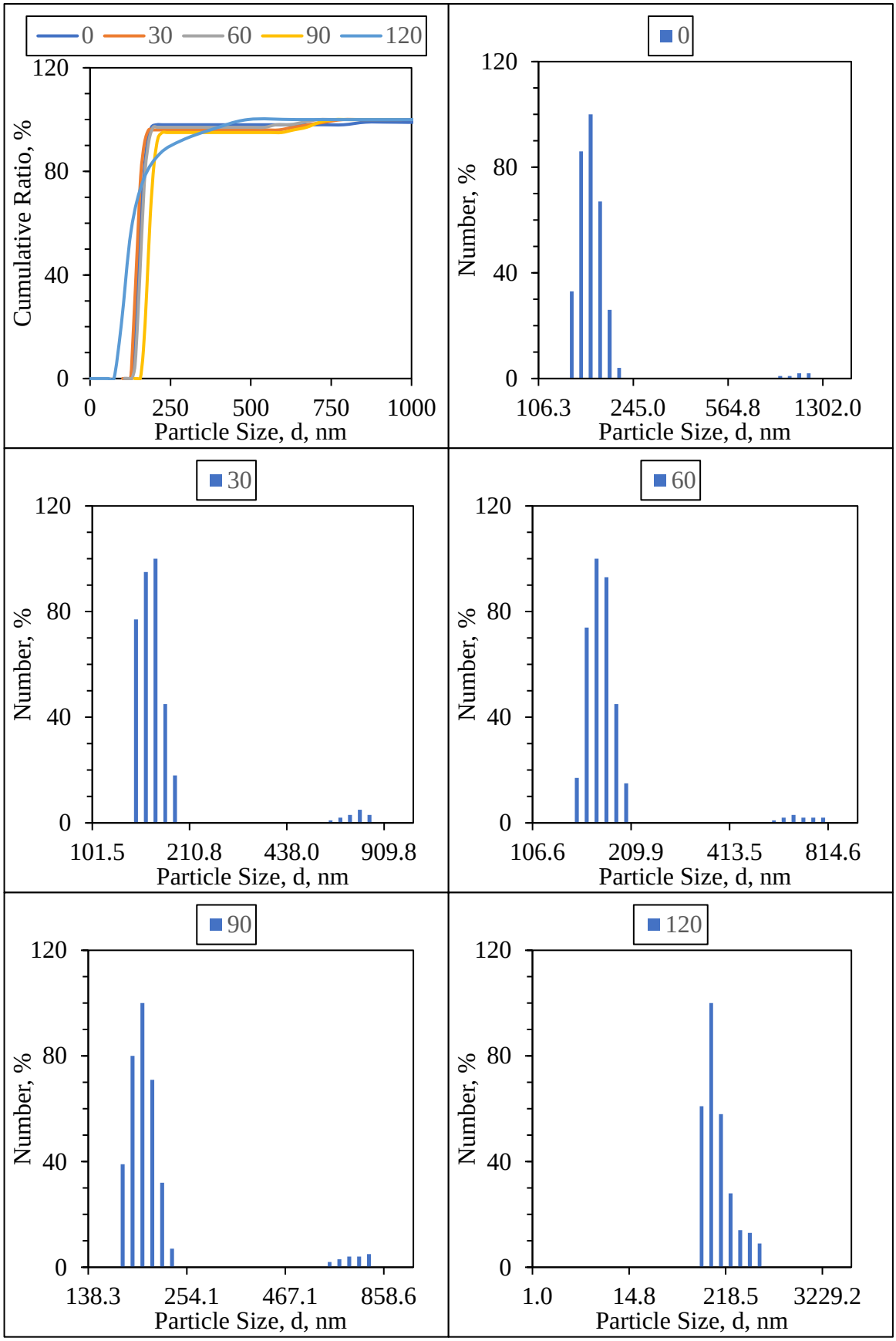


Figure 3.58. The cumulative ratio comparison and hydrodynamic size of N-$TiO_{2,dark}$ as number-weighted HDS in 30 min intervals.

3.4.9. Hydrodynamic Size Assessment of N-$TiO_{2,irr}$

The aggregation/agglomeration behavior of solar light irradiated anion doped TiO_2 was investigated by following the DLS measurements. N-TiO_2 was used as an anion doped visible light active TiO_2 representative. N-TiO_2 was weighted as 0.25 mgL^{-1} and suspended in Milli-Q water by sonicating for 1 min to disperse N-TiO_2 more evenly and magnetically stirred for 4 min. The obtained solution was placed in solar light simulator and exposed to solar light for 60 min while continuously mixing with a magnetic stirrer. After 60 min irradiation, the system was named N-$TiO_{2,irr}$ and 4 mL of the solution directly placed in DLS instrument with a polystyrene cuvette. Results of DLS measurements were compiled in Table 3.35 as intensity-, volume, surface area-, and number-weighted HDS and their corresponding CR%. The graphical illustrations of HDS and corresponding CR% were showed in Figure 3.60, Figure 3.61, Figure 3.62, and Figure 3.63. Detailed information on HDS min-max, HDS range and HDS difference were listed in Table 3.36. The comparative evaluation of N-$TiO_{2,as\text{-}is}$, N-$TiO_{2,dark}$ and N-$TiO_{2,irr}$ were compiled in Table 3.37 as intensity-weighted HDS and corresponding CR%. Finally, the intensity-weighted HDS of N-$TiO_{2,irr}$ was compared to HDS of TiO_2 and Fe-TiO_2.

PDI of N-$TiO_{2,irr}$ was found as 0.348 for initial, 0.292 for 30 min, 0.295 for 60 min, 0.260 for 90 min and 0.274 for 120 min. The average PDI during 120 min was calculated as 0.294 which was the indicator of nearly monodispersed HDS distribution. Consequently, MSD approximation was used to evaluate the time depended HDS alteration for 120 min. Under initial conditions, intensity-weighted HDS of N-$TiO_{2,irr}$ expressed three main peaks around 180.6 nm, 511.3 nm and 5517.4 nm (Table 3.35 and Table 3.36). However, the biggest cluster around 5517.4 was not visible in number-weighted HDS which indicated there were only few agglomerates bigger than 4000 nm (Table 3.35). The primary crystallite size of N-TiO_2 was calculated as 18.8 nm by using Scherrer equation from the XRD results (Table 3.8). The cluster around 100-250 nm corresponding to aggregate formation by the combination of approximately 5 to 10 N-TiO_2 crystals with the effect of electrostatic interactions and van der Waals forces (Fujishima et al., 2008). The structures above 5000 nm were formed by the combination of the agglomerates around 100-250 nm. This trend was evidenced by the disappearance of this structures at 30 min which might be attributed with the rapid sedimentation which was also evidenced by the sedimentation results. The removal efficiency of N-$TiO_{2,irr}$ at the end of 30 min was approximately 25%. Following the precipitation of the agglomerated structures, visibility of the smallest aggregates increased and the CR% of both intensity-, and number weighted HDS of the structures around 90 nm- 175 nm were increased to 21% and 89%, respectively (Table 3.35). The aggregate and agglomerate structures of N-$TiO_{2,irr}$ mostly showed spherical structures by

comparing the volume-, and surface area-weighted HDS except from the 4755.2 nm sized structures detected at time initial. These agglomerates were also visible at 30 min as 4679.9 nm, which showed that the structure was more stable than other agglomerates. Formation of these stable agglomerates might be related to formation of superhydrophilic surface after exposition to solar light (Nakata and Fujishima, 2012). However, after 60 min the agglomerates > 1000 nm totally disappeared and the number-weighted CR% of smaller structures increased almost 98% (Table 3.35). The substitutional N-doping decreases the band gap energy by forming a transition step between 3d orbital of Ti and 2p orbital of O as π^* state by replacing with the O located in anatase structure if the N-TiO_2 calcinated at 500-550˚C (Irie et al., 2003; Thompson and Yates, 2006; Petela et al., 2014). Due to the formation of the extra π^* transition states, lower energy was needed to move electron from CB to VB, on the other hand re-combination probability of e^--h^+ pair also increased. Consequently, N-$TiO_{2,irr}$ could form superhydrophilic surface after solar irradiation but it would be expected that superhydrophilic surface would last less after removal of light source in comparison to the $TiO_{2,irr}$ (Wojtaszek et al., 2019).

The formation of superhydrophilic surface might be evidenced by comparing the intensity-weighted HDS of N-$TiO_{2,as\text{-}is}$, N-$TiO_{2,dark}$ and N-$TiO_{2,irr}$ (Table 3.37). The agglomerate size of N-$TiO_{2,irr}$ was almost 8 times bigger than N-$TiO_{2,as\text{-}is}$ and N-$TiO_{2,dark}$ at initial time. The effect of solar irradiation would last almost 90 min and after that similar HDS trends were observed for N-$TiO_{2,as\text{-}is}$, N-$TiO_{2,dark}$ and N-$TiO_{2,irr}$. Even though the HDS of the remained structures were similar, a visible precipitation at the bottom of the cuvette was evidenced. The removal efficiencies at the end of the DLS measurements for N-$TiO_{2,as\text{-}is}$, N-$TiO_{2,dark}$ and N-$TiO_{2,irr}$ were 35%, 20% and 30% respectively. It could be concluded that solar light exposure thickened the surface adsorbed water layer and increased the HDS thereby forming more stable agglomerates in comparison to N-$TiO_{2,dark}$. Because the agglomerates were more stable and surface charge was neutralized by water molecules N-$TiO_{2,irr}$ would tend to precipitate rather than disagglomerate. Similar results were obtained by comparing intensity-weighted HDS of $TiO_{2,irr}$, Fe-$TiO_{2,irr}$ and N-$TiO_{2,irr}$. The intensity-weighted HDS of agglomerated structures could be ordered as N-$TiO_{2,irr}$ > Fe-$TiO_{2,irr}$ > $TiO_{2,irr}$. The narrowed band gap energy after cation and/or anion doping increased the surface adsorbed water and increased the aggregate-aggregate tension in comparison to the undoped TiO_2. However, the HDS of N-$TiO_{2,irr}$ was 2-2.5 times larger than Fe-$TiO_{2,irr}$. The trend might be related to the formation of stronger H bonding formed by the lone pair electrons of N atom that located in N-O state in N-TiO_2 crystal. It must be noted that the dopant N substituted of O, however there was also formation of N-O localization that supplies extra H-bonding sites (Petela et al., 2014; Fernandes et al., 2020).

Table 3.35. Intensity-, volume-, surface area- and number-weighted HDS and cumulative ratios of N-$TiO_{2,irr}$.

	HDS, nm	Cumulative Ratio, %			
		Intensity	Volume	Surface Area	Number
Initial	134.2-209.6	19%	5%	27%	75%
	243.1-511.3	18%	30%	60%	24%
	593.3-4098.3	11%	5%	5%	1%
	4755.2	12%	1%	1%	-
	5517.4	16%	10%	1%	-
	6401.8	14%	7%	1%	-
	7427.9-8618.9	10%	42%	5%	-
30 min	89.5-173.1	21%	9%	30%	89%
	334.7-394.6	12%	6%	7%	2%
	465.3	16%	52%	44%	7%
	548.7	20%	6%	5%	1%
	647.1	16%	6%	3%	-
	763.0-4676.9	15%	21%	11%	1%
60 min	115.7-132.4	19%	23%	48%	73%
	141.7-151.6	14%	12%	22%	25%
	511.5	7%	13%	7%	-
	547.2	16%	16%	7%	1%
	585.5	23%	17%	8%	1%
	626.4-670.2	21%	36%	8%	-
90 min	49.1-210.5	18%	27%	78%	99%
	240.3	21%	6%	5%	1%
	274.3	17%	5%	3%	-
	313.1-790.6	17%	29%	8%	-
	902.5-1030.2	18%	23%	5%	-
	1175.9-1342.2	8%	10%	1%	-
120 min	144.9-155.2	10%	9%	21%	39%
	166.3	14%	9%	20%	41%
	178.1-190.7	17%	10%	19%	26%
	534.3-572.3	18%	18%	11%	1%
	613.0	18%	15%	9%	1%
	656.5-753.2	23%	39%	20%	2%

Table 3.36. Intensity-weighted HDS profile of N-$TiO_{2,irr}$. Time dependent HDS cluster maximas, HDS range and min-max diameter difference with respect to multi-size distribution.

	Cluster					
Time, min	Max 1, nm	Max 2, nm	Max 3, nm	Max 4, nm	Range, nm	Difference, nm
Initial	180.6	511.3	5517.4		85.9-10000.0	9914.1
30	124.5	548.7	2418.9	4676.9	46.3-9042.5	8996.2
60	132.4	585.5			94.5-820.7	726.2
90	56.1	240.3	1030.3		33.0-2278.7	2245.7
120	166.3	613.0			110.1-991.3	881.2

Table 3.37. Comparison of intensity-weighted HDS values of N-$TiO_{2,as\text{-}is}$, N-$TiO_{2,dark}$, and N-$TiO_{2,irr}$.

	N-$TiO_{2,as\text{-}is}$		N-$TiO_{2,dark}$		N-$TiO_{2,irr}$		
	HDS, nm	CR, %	HDS, nm	CR, %	HDS, nm	CR, %	
Initial	153.6-187.8	23%	Dark Mixing		Solar Irradiation and Mixing		
	207.7-229.7	15%					
	1269.9-1404.3	10%					
	1552.9	17%					
	1717.2	19%					
	1898.9-2099.9	17%					
30 min	184.8-200.4	13%					
	217.4	17%					
	235.7	18%					
	255.6-277.2	14%					
	935.9-1015.0	12%					
	1100.8	12%					
	1193.8-1294.6	14%					
60 min	148.6-159.4	13%	136.5-161.3	20%	134.2-209.6	19%	Initial
	171.0	14%	175.4-207.3	21%	243.1-511.3	18%	
	183.5-196.9	17%	857.5-932.2	23%	593.3-4098.3	11%	
	607.2-651.5	15%	1013.4	19%	4755.2	12%	
	699.0	17%	1101.7-1197.7	17%	5517.4	16%	
	749.9	14%	-	-	6401.8	14%	
	804.6-863.6	10%	-	-	7427.9-8618.9	10%	
90 min	151.6-175.7	22%	136.0-146.3	13%	89.5-173.1	21%	30 min
	189.2	16%	157.4	12%	334.7-394.6	12%	
	203.7-219.4	14%	169.3-182.2	13%	465.3	16%	
	665.4-716.5	20%	586.8-631.3	23%	548.7	20%	
	771.5	15%	679.1	21%	647.1	16%	
	830.7-894.5	13%	730.6-786.1	18%	763.0-4676.9	15%	
120 min	180.4-190.3	13%	139.8-160.1	18%	115.7-132.4	19%	60 min
	200.8	17%	171.1	15%	141.7-151.6	14%	
	211.8	16%	183.3-196.2	15%	511.5	7%	
	223.4-235.7	14%	542.3-580.4	14%	547.2	16%	
	525.4-554.3	14%	621.1	16%	585.5	23%	
	584.7	12%	664.7-761.2	22%	626.4-670.2	21%	
	616.8-686.4	14%	-	-			
150 min	159.6-169.9	14%	166.0-176.4	13%	49.1-210.5	18%	90 min
	180.8	16%	187.4	16%	240.3	21%	
	192.5-204.9	21%	199.2-225.0	26%	274.3	17%	
	556.1-591.9	14%	560.7-633.3	19%	313.1-790.6	17%	
	630.0	15%	673.0	14%	902.5-1030.2	18%	
	670.6-759.8	20%	715.3-760.1	12%	1175.9-1342.2	8%	
180 min	169.6	27%	97.4-166.9	18%	144.9-155.2	10%	120 min
	182.1	18%	218.5	19%	166.3	14%	
	195.4-209.7	15%	286.0	22%	178.1-190.7	17%	
	698.0-749.1	16%	374.4	18%	534.3-572.3	18%	
	804.0	12%	490.1	10%	613.0	18%	
	862.9-926.2	12%	641.6-1884.3	19%	656.5-753.2	23%	

Table 3.38. Comparison of intensity-weighted HDS values of $TiO_{2,irr}$, Fe-$TiO_{2,irr}$ and N-$TiO_{2,irr}$.

	$TiO_{2,irr}$		Fe-$TiO_{2,irr}$		N-$TiO_{2,irr}$	
	HDS, nm	CR, %	HDS, nm	CR, %	HDS, nm	CR, %
Initial	169.6-196.7	19%	153.4-197.9	17%	134.2-209.6	19%
	211.8-245.6	20%	224.8-255.3	10%	243.1-511.3	18%
	745.9-803.3	9%	2225.5	7%	593.3-4098.3	11%
	865.0	15%	2527.8	17%	4755.2	12%
	931.5	20%	2871.2	25%	5517.4	16%
	1003.1-1080.2	17%	3261.2-3704.2	24%	6401.8	14%
					7427.9-8618.9	10%
30 min	149.7-174.9	17%	148.5-176.0	16%	89.5-173.1	21%
	189.0-220.9	18%	191.6	10%	334.7-394.6	12%
	767.8-829.9	25%	208.6-227.1	9%	465.3	16%
	897.1	21%	811.1-882.9	11%	548.7	20%
	969.8-1048.3	19%	961.1	16%	647.1	16%
	-	-	1046.2	19%	763.0-4676.9	15%
	-	-	1138.9-1239.8	17%	-	-
60 min	137.8-162.9	17%	134.9-145.1	13%	115.7-132.4	19%
	177.1-209.4	18%	156.1	13%	141.7-151.6	14%
	735.3-799.5	16%	168.0-180.7	13%	511.5	7%
	869.3	19%	582.1-626.2	18%	547.2	16%
	945.2-1117.5	30%	673.7	19%	585.5	23%
	-	-	724.8	15%	626.4-670.2	21%
	-	-	779.8-838.9	9%	-	-
90 min	155.2-180.0	16%	132.1-150.1	17%	49.1-210.5	18%
	193.8-224.8	24%	160.0	12%	240.3	21%
	735.1-791.6	23%	170.5-181.7	11%	274.3	17%
	852.4	19%	504.1-537.3	22%	313.1-790.6	17%
	917.9-988.5	18%	572.7	20%	902.5-1030.2	18%
	-	-	610.4-650.6	18%	1175.9-1342.2	8%
120 min	100.3-139.9	22%	142.5-164.5	20%	144.9-155.2	10%
	486.9-529.1	19%	176.8	13%	166.3	14%
	574.9	23%	190.0-204.2	10%	178.1-190.7	17%
	624.8	21%	601.4-646.3	15%	534.3-572.3	18%
	-	-	694.5	16%	613.0	18%
	-	-	746.4	15%	656.5-753.2	23%
	-	-	802.1-862.0	11%	-	-

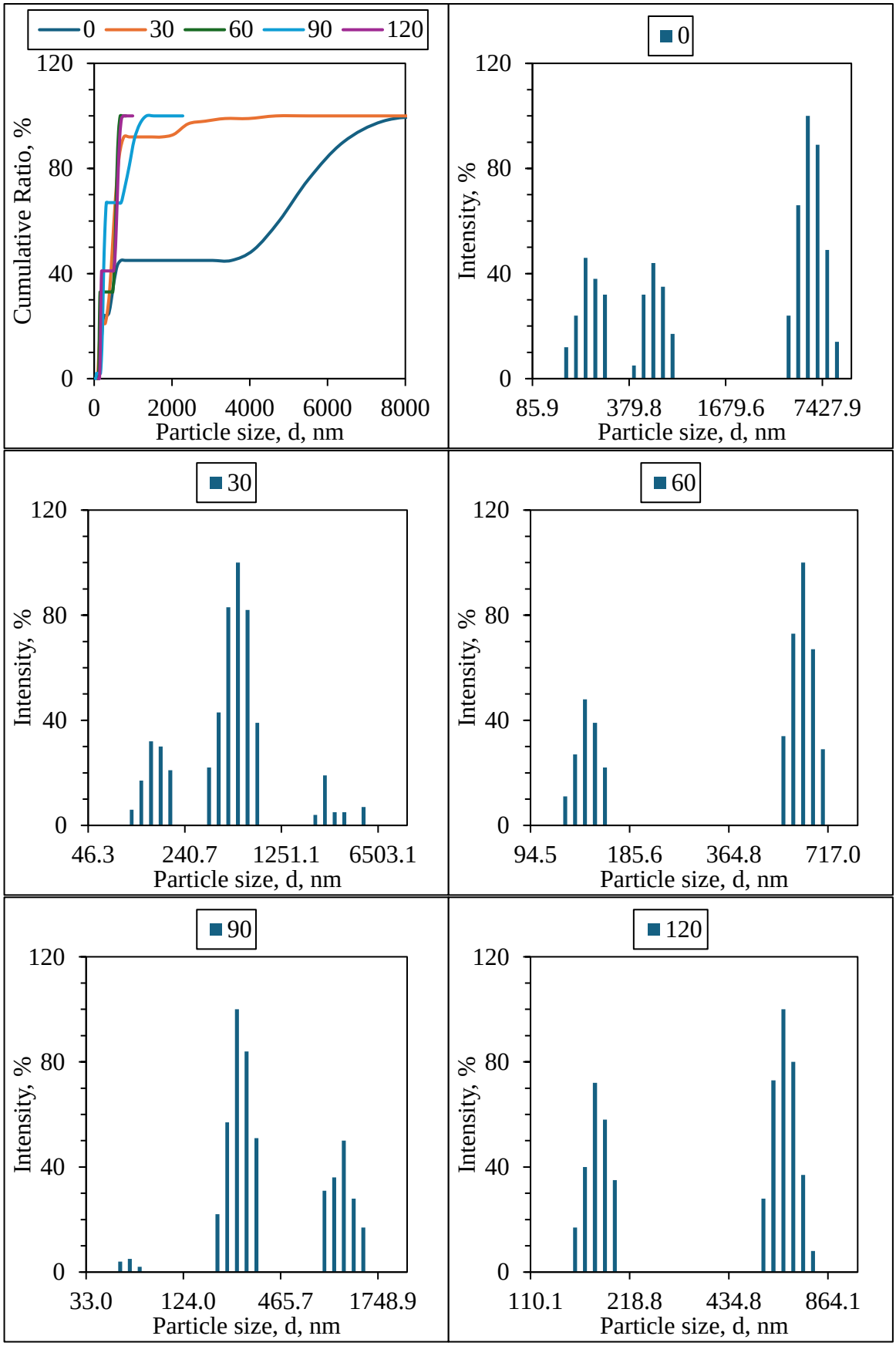


Figure 3.59. The cumulative ratio comparison and hydrodynamic size of N-$TiO_{2,irr}$ as intensity-weighted HDS in 30 min intervals.

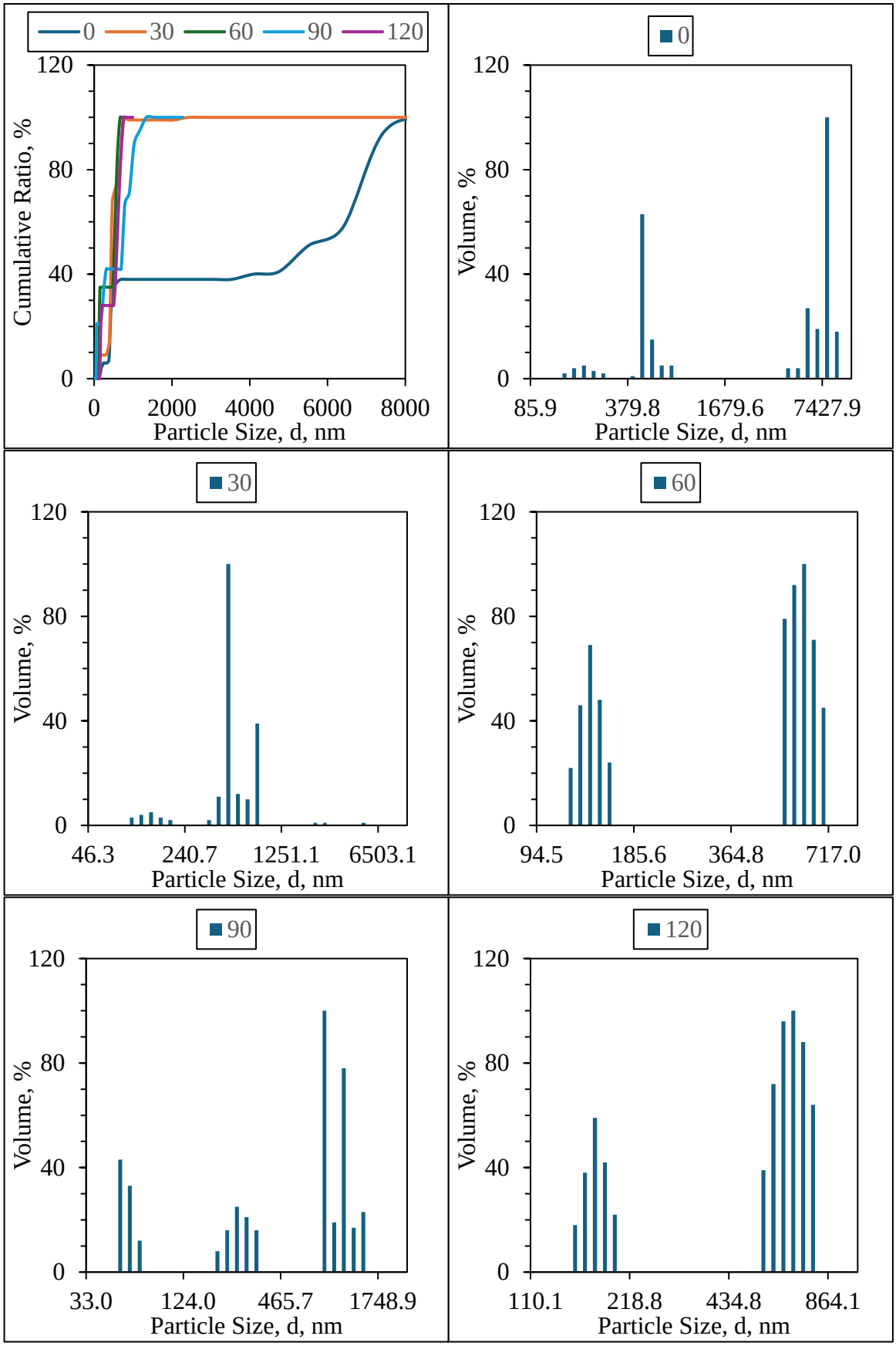


Figure 3.60. The cumulative ratio comparison and hydrodynamic size of N-$TiO_{2,irr}$ as volume-weighted HDS in 30 min intervals.

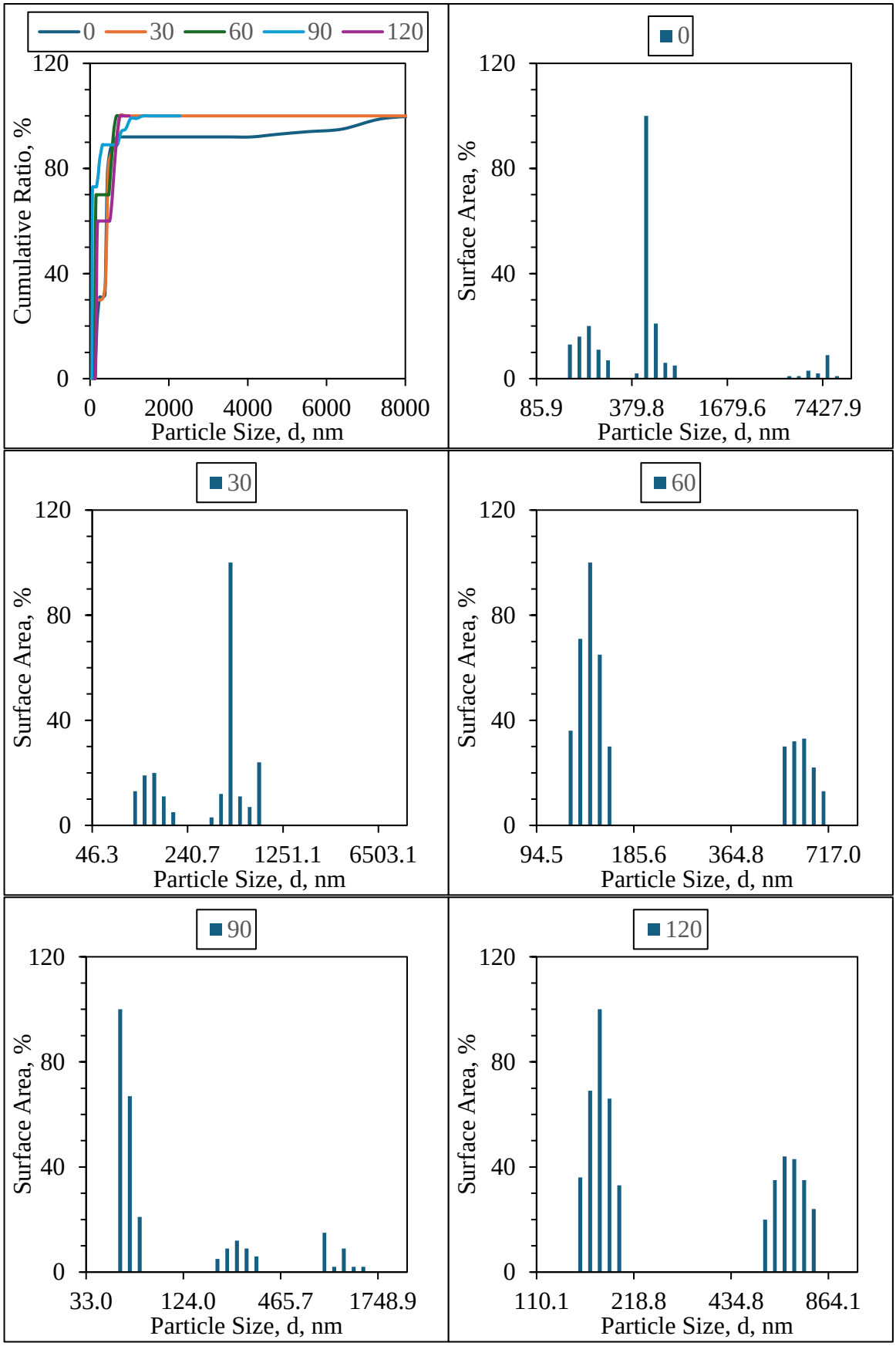


Figure 3.61. The cumulative ratio comparison and hydrodynamic size of N-$TiO_{2,irr}$ as surface area-weighted HDS in 30 min intervals.

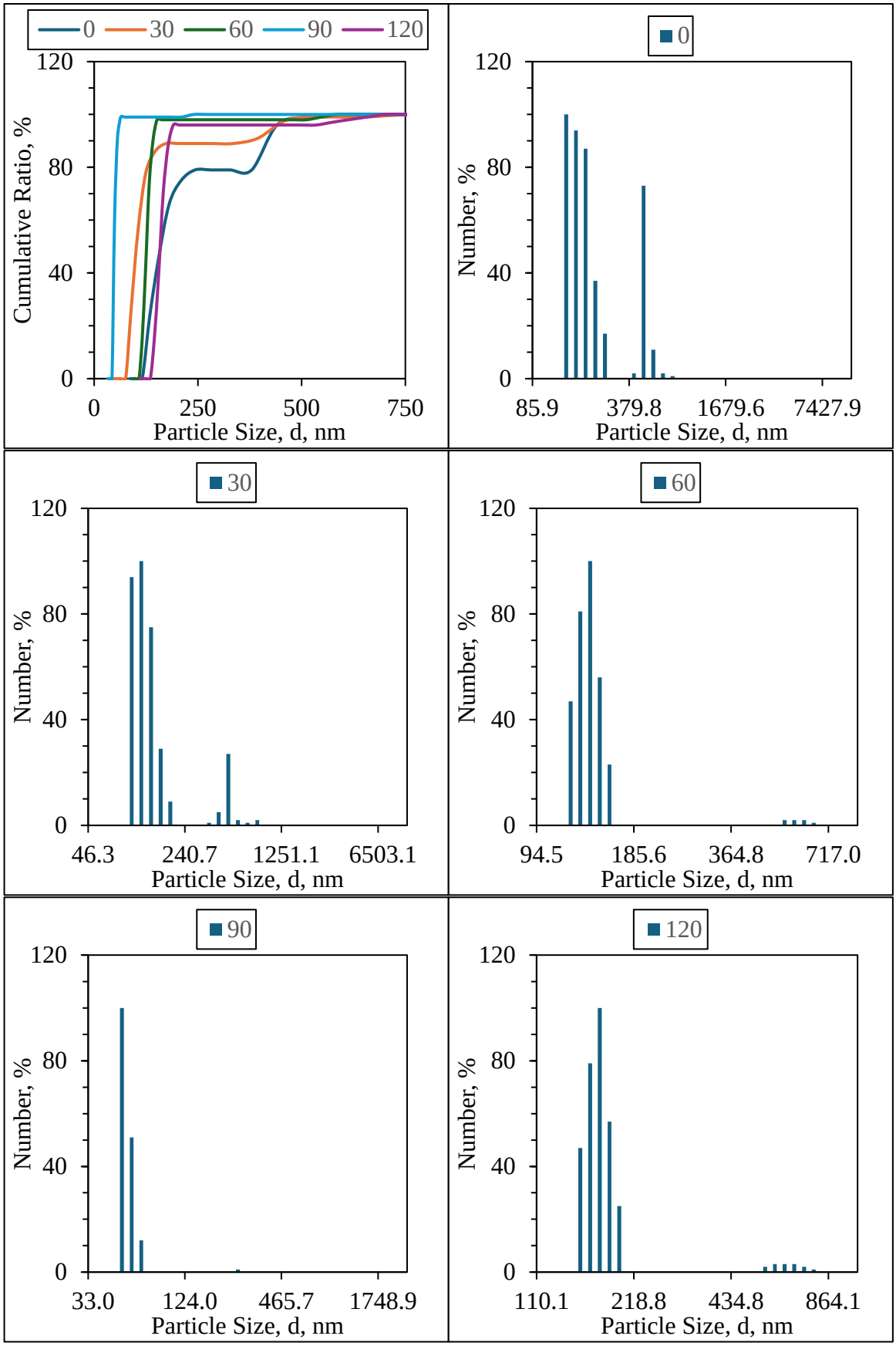


Figure 3.62. The cumulative ratio comparison and hydrodynamic size of N-$TiO_{2,irr}$ as number-weighted HDS in 30 min intervals.

3.5. HA-TiO_2 – Binary System

Due to the extreme complexity of TiO_2 and humic matter co-presence, multiple interaction mechanisms covering adsorption should be considered (Yu et al., 2018). As stated previously, (Section 1.6.3. Humic Acid), these interactions could well be described as; primarily electrostatic interactions, ligand exchange mechanism, hydrophobic interactions, p-p interactions and hydrogen bonding Aggregation behavior of the binary system may be explained through understanding of the physico-chemical properties of both counterparts *i.e.*, intrinsic properties of surface of TiO_2 and ill-defined nature of organic matter (Danielsson et al., 2018; Gallego-Urrea et al., 2014; Holmes et al., 2018; Li et al., 2020; Tang and Cheng, 2018). Regarding the stability of the formed aggregates, selection of humic descriptive model may also direct the possible explanatory route in aggregation/disaggregation phenomena during binary system formation.

HA can influence the stability of TiO_2 (rutile) NPs through charge neutralization, steric hindrance and bridging effects. In the absence of IS, aggregation was promoted by adding HA only when the pH (pH = 4) is less than the point of zero charge for the TiO_2 ($pH_{PZC} \approx 6$) because HA reduces the zeta potential of the TiO_2 via charge neutralization. At pH = 4 and when the concentration of HA is 94.5 μgL^{-1}, the zeta potential of TiO_2 is close to zero, and they reach an aggregation maximum

3.5.1. Hydrodynamic Size Assessment of $(HA\text{-}TiO_2)_{as\text{-}is}$

Aggregation and agglomeration behavior in the co-presence of "TiO_2 and HA" was investigated by suspending TiO_2 (0.25 mgL^{-1}) into HA solution as mentioned in Materials and Methods section. The prepared suspension was magnetically stirred for 30 min and then subjected to DLS measurement for 180 min without removing DLS cuvette. The sample was named as $(HA\text{-}TiO_2)_{as\text{-}is}$.

Table 3.39 compiled the hydrodynamic size data and cumulative ratios of $(HA\text{-}TiO_2)_{as\text{-}is}$ and Figure 3.64, Figure 3.65, Figure 3.66, and Figure 3.67 illustrated the graphical abstract of cumulative ratio comparison and hydrodynamic size range as intensity-, volume-, surface area-, and number-weighted HDS.

Table 3.39. Intensity-, volume-, surface area- and number-weighted HDS and cumulative ratios of $(HA\text{-}TiO_2)_{as\text{-}is}$.

	HDS, nm	Cumulative Ratio, %			
		Intensity	Volume	Surface Area	Number
Initial	156.1-184.7	9%	3%	14%	52%
	200.9-237.3	16%	4%	15%	40%
	840.8	9%	8%	8%	1%
	914.7	18%	9%	7%	1%
	995.1	25%	22%	17%	2%
	1082.5-1177.6	23%	54%	39%	4%
30 min	157.0-172.2	8%	3%	14%	46%
	188.9-227.3	21%	6%	22%	49%
	911.1-999.5	21%	16%	13%	4%
	1096.4	22%	58%	40%	4%
	1202.7-1447.3	28%	17%	11%	1%
60 min	193.0-208.8	15%	4%	16%	57%
	225.8-264.3	16%	4%	14%	35%
	1005.2	13%	10%	9%	1%
	1087.4	18%	54%	42%	5%
	1176.3	21%	9%	8%	1%
	1272.5-1376.5	17%	17%	11%	1%
90 min	164.6-192.0	18%	6%	23%	72%
	207.3-223.9	9%	3%	8%	19%
	766.9-828.2	18%	39%	34%	5%
	894.5	21%	12%	8%	1%
	966.0	20%	13%	10%	1%
	1043.3-1126.7	14%	27%	17%	2%
120 min	143.8-156.6	9%	5%	19%	54%
	170.5-202.2	15%	5%	20%	41%
	789.6	8%	29%	19%	2%
	859.8	16%	12%	8%	1%
	936.2	25%	13%	10%	1%
	1019.4	17%	23%	14%	1%
	1110.0-1208.7	10%	18%	24%	-
150 min	138.7-164.4	14%	5%	22%	71%
	179.0-194.9	11%	3%	10%	22%
	761.3-829.0	25%	47%	39%	5%
	902.7	24%	11%	8%	1%
	982.9	17%	19%	8%	1%
	1070.2-1165.4	9%	24%	14%	-
180 min	39.8-175.3	12%	10%	65%	99%
	200.6-262.6	20%	8%	11%	1%
	674.9-772.4	18%	51%	16%	-
	883.9	20%	8%	3%	-
	1011.5	17%	15%	3%	-
	1157.5-1324.5	13%	8%	2%	-

Table 3.40. Comparison of intensity-weighted HDS values of $HA_{,as\text{-}is}$, $TiO_{2,as\text{-}is}$ and $(HA\text{-}TiO_2)_{,as\text{-}is}$.

	$HA_{,as\text{-}is}$		$TiO_{2,as\text{-}is}$		$(HA\text{-}TiO_2)_{as\text{-}is}$	
Initial	106.5-197.8	73%	98.6-129.1	10%	156.1-184.7	9%
	243.2-299.0	25%	169.2-380.3	14%	200.9-237.3	16%
	3561.7	1%	498.3-652.7	34%	840.8	9%
	6617.0	1%	855.1	23%	914.7	18%
			1120.2	14%	995.1	25%
			1467.5	5%	1082.5-1177.6	23%
60 min	155.4-182.0	72%	144.3-184.4	26%	193.0-208.8	15%
	185.3-188.5	28%	200.1-217.1	11%	225.8-264.3	16%
			739.9-802.9	19%	1005.2	13%
			871.2-1113.3	34%	1087.4	18%
			-	-	1176.3	21%
			-	-	1272.5-1376.5	17%
90 min	47.7-61.1	4%	128.2-149.2	13%	164.6-192.0	18%
	164.4-186.3	62%	160.9-187-3	10%	207.3-223.9	9%
	198.2-224.3	34%	630.4-680.1	25%	766.9-828.2	18%
	-	-	733.7-853.9	45%	894.5	21%
			-	-	966.0	20%
			-	-	1043.3-1126.7	14%
120 min	167.8-169.9	62%	96.8-146.1	20%	143.8-156.6	9%
	171.0-173.2	38%	501.7-544.7	16%	170.5-202.2	15%
			591.4-642.2	45%	789.6	8%
			697.2-757.0	19%	859.8	16%
			-	-	936.2	25%
					1019.4	17%
					1110.0-1208.7	10%

$(HA\text{-}TiO_2)_{,as\text{-}is}$ system would contain not only structures formed by HA adsorption onto TiO_2 surface, but also sole TiO_2 aggregates and suspended HA. Therefore, a comparison of $HA_{,as\text{-}is}$, $TiO_{2,as\text{-}is}$ and $(HA\text{-}TiO_2)_{,as\text{-}is}$ was compiled in Table 3.40. At neutral pH and low IS surface of $TiO_2$was mostly positive as evidenced by zeta potential measurement (+16.06 eV). HA structure could also resume an elongated form due to repulsive forces (Fleer et al, 1993). Consequently, train, tail, and loop model (Figure 1.6) might be the most suitable adsorption model expressing $(HA\text{-}TiO_2)_{,as\text{-}is}$.

$HA_{,as\text{-}is}$ might form metachemical hydrogel structures (Gilli and Gilli, 2013; Wells and Stretz, 2019), which was similar to aggregate of $TiO_{2,as\text{-}is}$ by means of structural stability. Also, physical hydrogel formation of $HA_{,as\text{-}is}$ might transform to an agglomerate like structure. Suspending TiO_2 into HA solution might end up to more stable structures. Only a small portion of sub-fractions might be present as bigger structures prone to precipitation during 180 min. This trend can be evidenced by following cumulative ratio of number-weighted HDS structures around 1000-1200 nm. The disappearance of bigger clusters increased the visibility of smaller clusters that might be evidenced by sedimentation kinetics.

Keesom forces provided by metachemical hydrogel of HA might form near-covalent bonds with TiO_2 aggregates. These forces also transform to strong H-bonds which might be a plausible reason for more stabilized aggregates (Wershaw, 1993; Swift, 1996; Gilli and Gilli, 2013; Wells and Stretz, 2019). HA adsorption onto TiO_2 aggregates could be evidenced by increase of cumulatively higher ratio (13%) of structures around 1100-1300 nm in comparison to the $TiO_{2,as\text{-}is}$ as intensity-weighted HDS.

TiO_2 and HA binary system primarily expresses an adsorption phenomenon prevailing through electrostatic interactions originating from pH dependent charge development. More specifically, HA adsorption onto TiO_2 might be reversible and aggregate structures express dynamic behavior (Philippe and Schaumann, 2014). Depending on the representative schematic models, humic sub-fractions would be located on the oxide particles protruding from the surface in shapes resembling “train, tail and loops”, “mushroom”, “brush” or “pancake” type conformational rearrangements as a result of various interactions (Louie, 2014; Louie et al., 2015). Therefore, each species could resemble different shapes prone to aggregation or agglomeration. It should also be mentioned that each hypothetical shape could be expressed by the defined DLS parameters depending on the selected assumptions. Figure 3.63 shows the HA adsorption onto TiO_2 aggregates/agglomerates in different shapes. Figure 3.63a and b illustrates the theoretical representation of “train, tail, loop” resembling

adsorption onto spherical or fractal aggregate/agglomerate of TiO_2. Similarly, "mushroom", "pancake" and "brush" resembling adsorption shapes represented in Figure 3.63c and d.

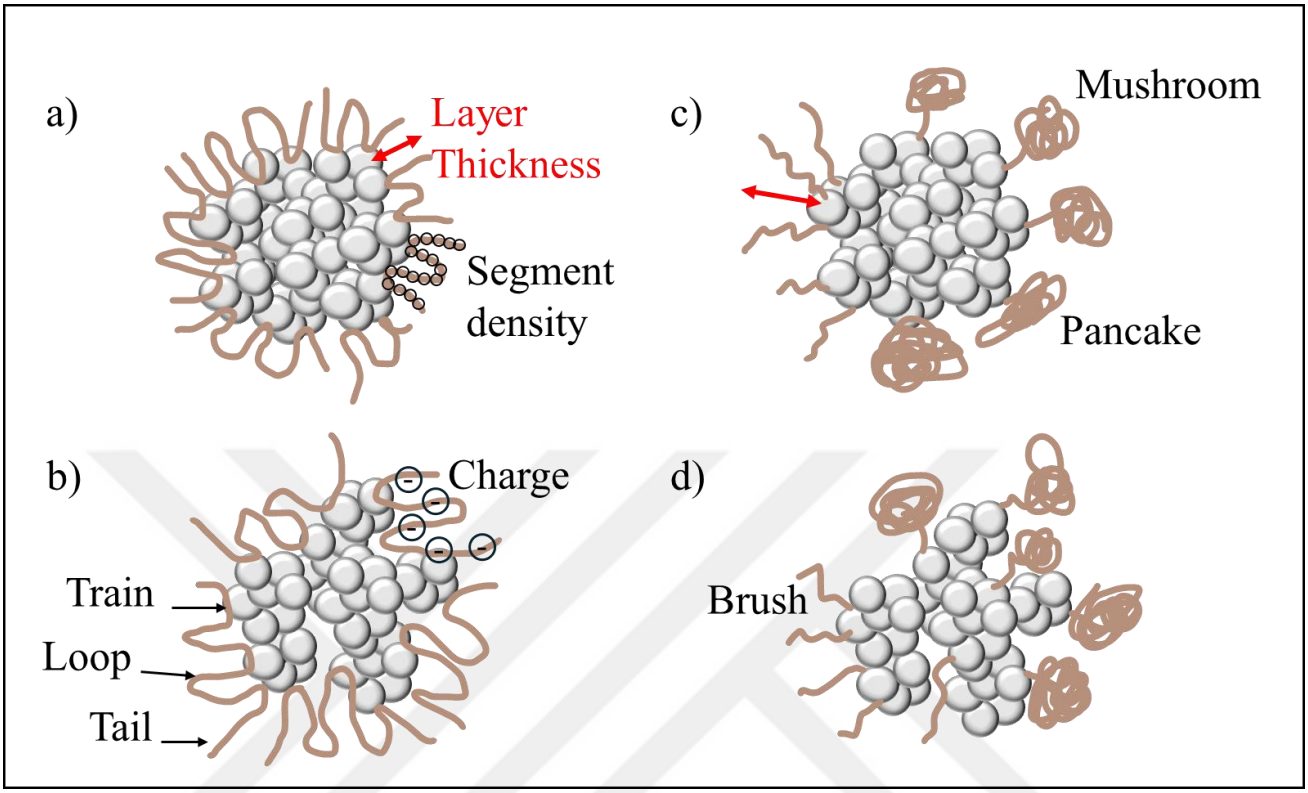


Figure 3.63. Representation of HA adsorption onto TiO_2 aggregates/agglomerates. a) "train, tail, and loop" model adsorption of HA onto spherical aggregate/agglomerate of TiO_2, b) "train, tail, and loop" model adsorption of HA onto fractal aggregate/agglomerate of TiO_2, c) Mushroom and pancake model adsorption of HA onto spherical aggregate/agglomerate of TiO_2, d) Mushroom and pancake model adsorption of HA onto fractal aggregate/agglomerate of TiO_2.

Adsorption effect may also lead to molecular size fractionation. Under initial conditions, the aqueous medium is composed of homo- and hetero aggregated mono and binary entities. The system can be expressed as;

i. homoaggregation of TiO_2, *ii.* homoaggregation of HA is found to be very ambiguous since each molecular size fraction may also be regarded as a different entity thereby heteroaggregation term may also be relevant, *iii.* heteroaggregation of HA sub-fractions and TiO_2 aggregates resulting in agglomeration. The resultant solution may undergo dynamic transformations via disintegration/disaggregation through formation/deformation of bridges between the components.

Aggregation and disaggregation capacity of anatase TiO_2 (commercial) in the presence of HA (SRHA, IHSS) was investigated by DLS measurements accompanied by zeta potential measurements (Loosli et al., 2014). Under neutral pH conditions at around pH_{zpc}, TiO_2 HDS was reported as 1400 nm. HDS of HA was shown as 379±19 nm irrespective of zeta potential variation. HDS of TiO_2 and HA aggregates was 250 nm. Aggregation and disaggregation were followed under varying pH conditions indicating that disaggregation was more noticeable under alkaline conditions.

Chen and colleagues reported aggregate size variations of TiO_2 (commercial) under slightly acidic conditions (pH 4.30) as 400-420 nm for rutile and 200 nm for anatase crystal forms. The effect of ultrasonication as applied as a pre-preparation step in the presence of HA was expressed by agglomeration, deagglomeration and re-agglomeration phenomena (Chen et al., 2018). Raza and co-workers reported an intensity based hydrodynamic size of TiO_2 (sol-gel prepared) and fulvic acid (IHSS) binary system as ~100 nm expressing a spherical shape whereas ~90 nm in ellipsoidal shape as visualized by TEM imaging technique (Raza et al., 2016). Ren and colleagues reported a HDS of TiO_2 (P-25) (20 mgL^{-1}) as ~1200 nm in the absence of synthetically prepared DOM (TOC=10.67 mgL^{-1}) being comparatively higher under pH conditions at around $pH=pH_{zpc}$ (Ren et al., 2018). Moreover, in the presence of various DOM substances, a remarkable variation in between 100-1000 nm of HDS was recorded. The average HDS of TiO_2 was reported as approximately 800 nm, 150 nm, 200 nm, 150 nm, and 160 nm in the presence of sodium dodecylbenzene sulfonate, FA, alginate, bovine serum albumin and amylase respectively at neutral pH conditions.

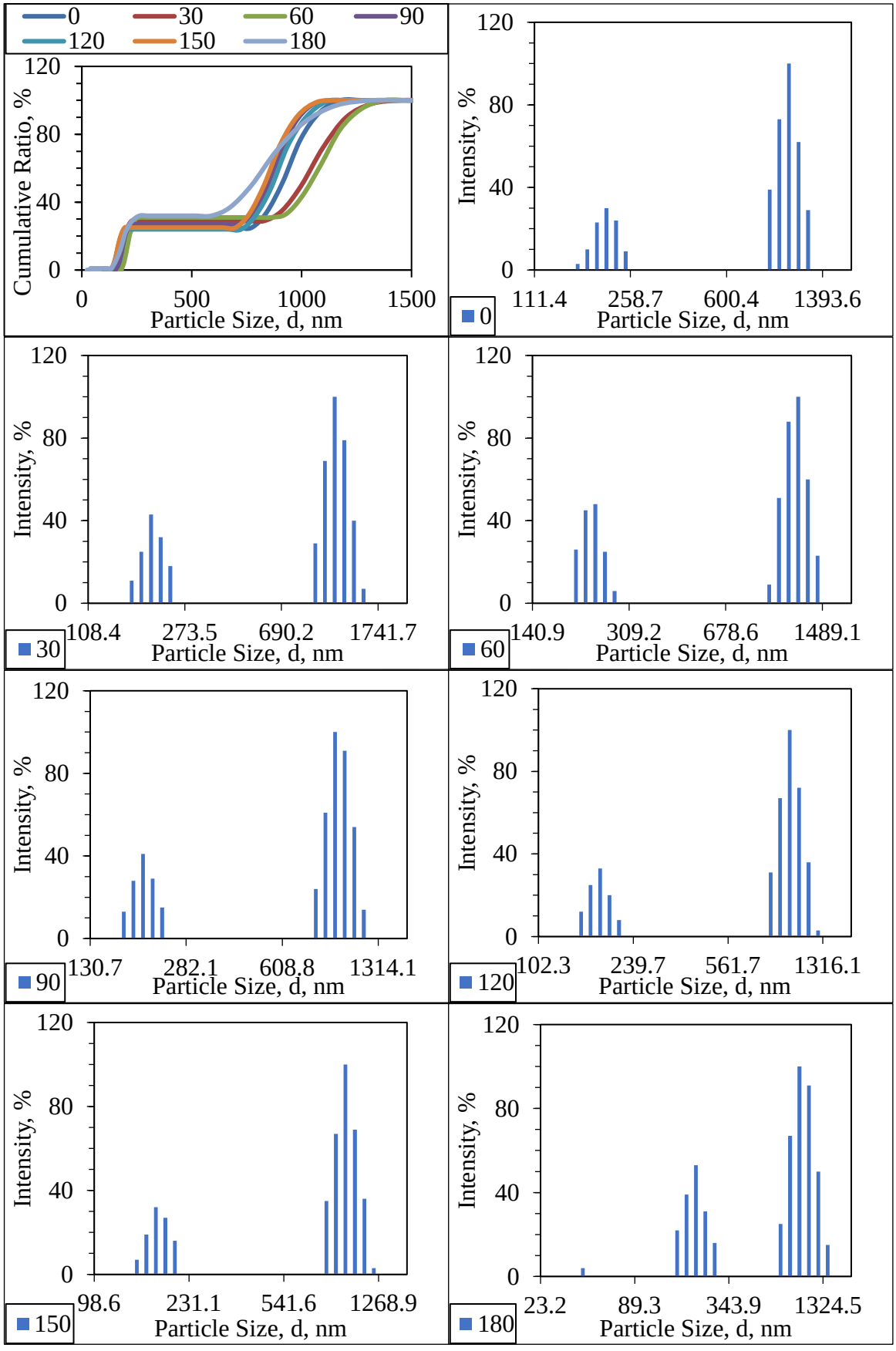


Figure 3.64. The cumulative ratio comparison and hydrodynamic size of $(HA\text{-}TiO_2)_{,as\text{-}is}$ as intensity-weighted HDS in 30 min intervals.

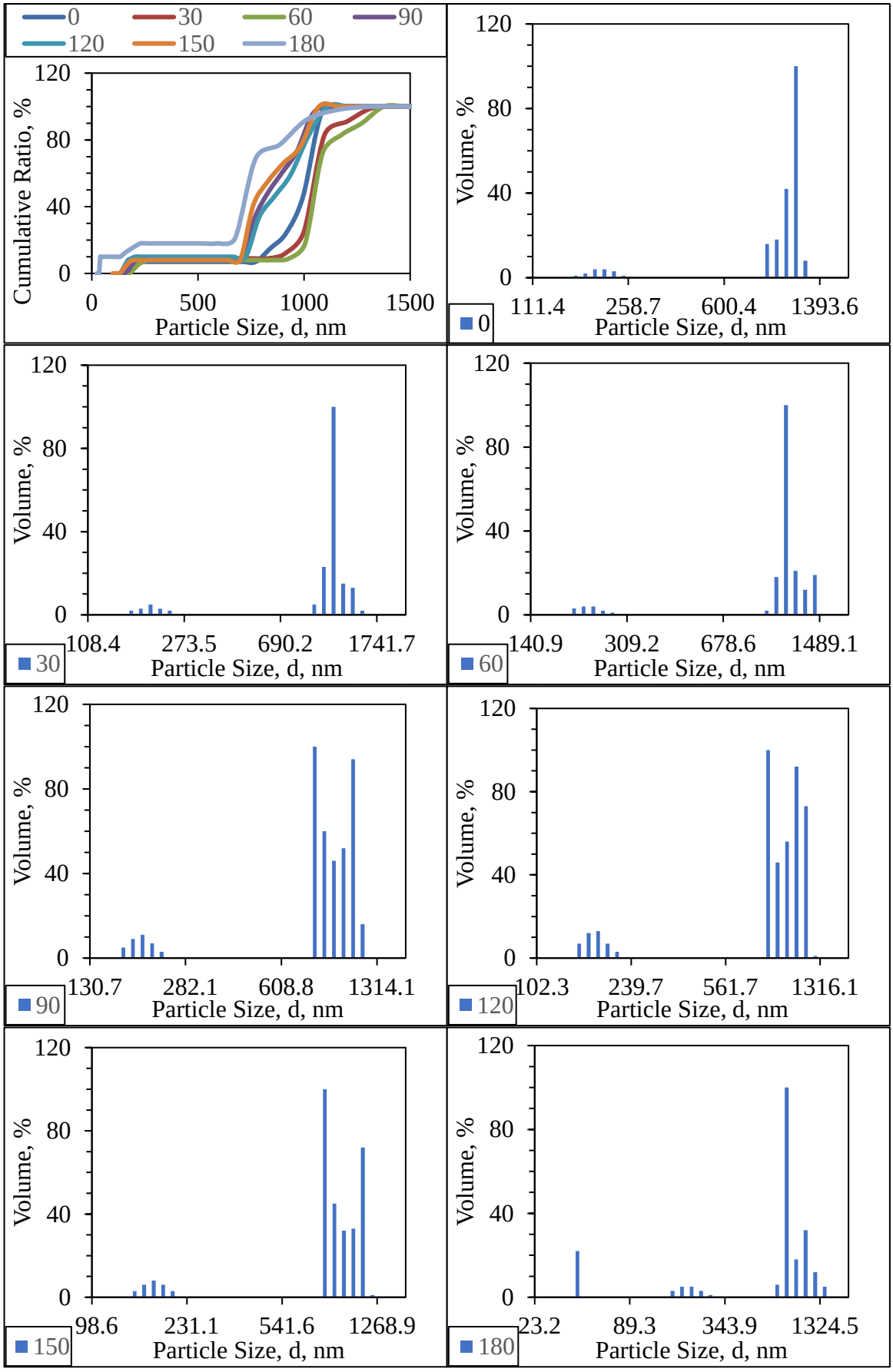


Figure 3.65. The cumulative ratio comparison and hydrodynamic size of $(HA\text{-}TiO_2)_{,as\text{-}is}$ as volume-weighted HDS in 30 min intervals.

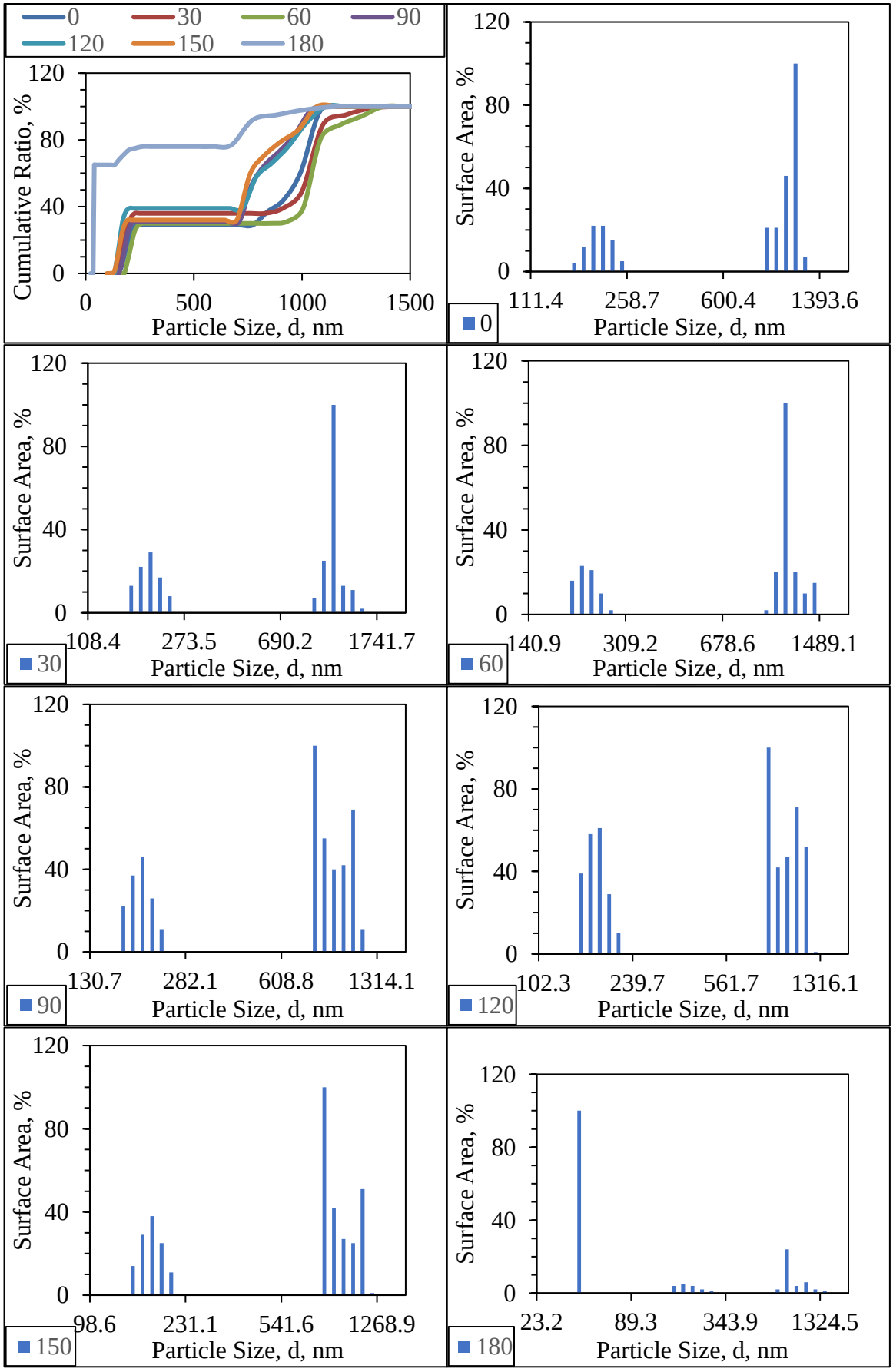


Figure 3.66. The cumulative ratio comparison and hydrodynamic size of $(HA\text{-}TiO_2)_{,as\text{-}is}$ as surface area-weighted HDS in 30 min intervals.

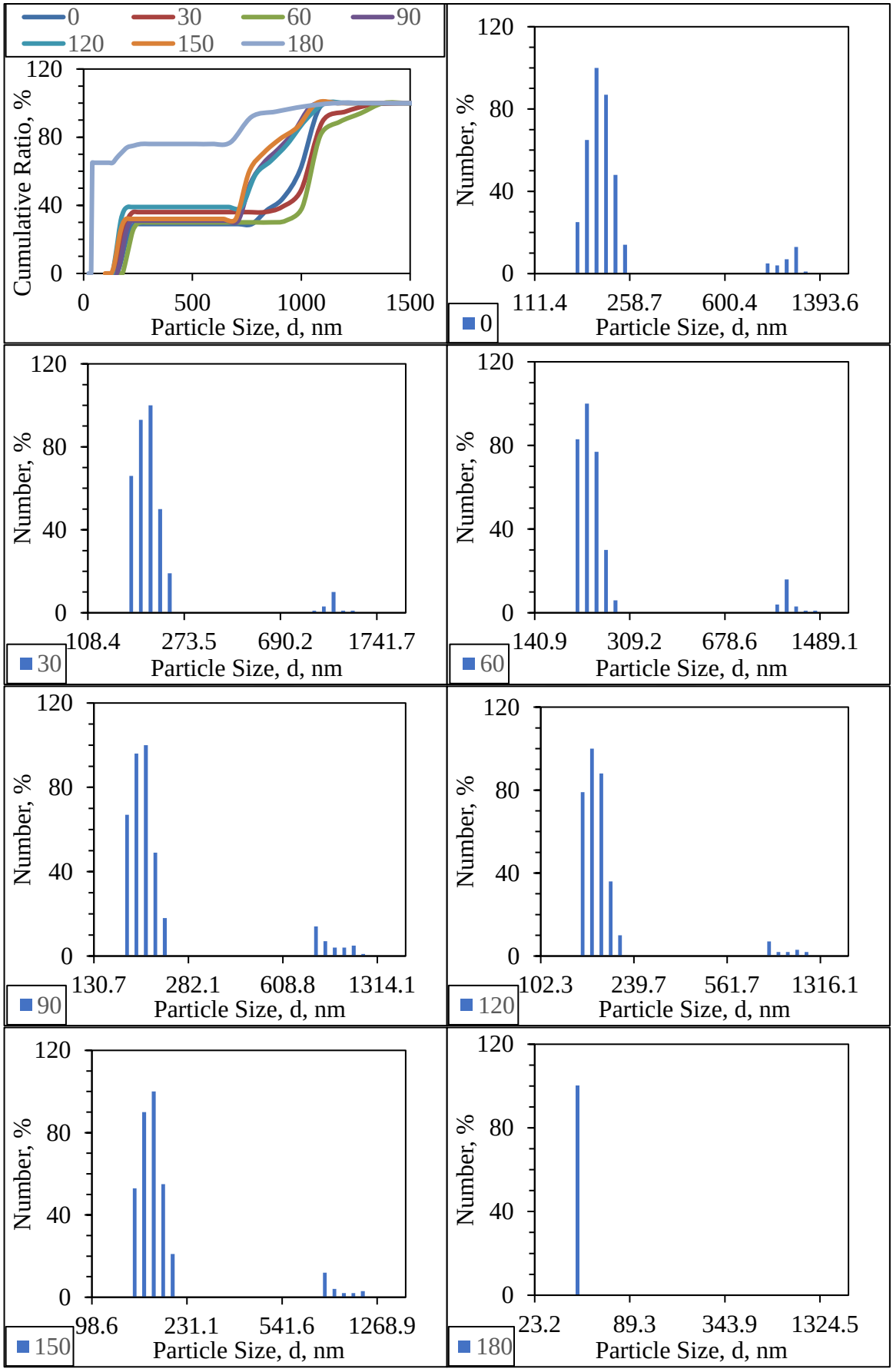


Figure 3.67. The cumulative ratio comparison and hydrodynamic size of $(HA\text{-}TiO_2)_{,as\text{-}is}$ as number-weighted HDS in 30 min intervals.

3.5.2. Hydrodynamic Size Assessment of $(HA\text{-}TiO_2)_{,dark}$

The hindrance effect of solar irradiation on $(HA\text{-}TiO_2)_{,dark}$ was investigated with the dark condition experiments. As indicated in methodology section, 0.25 mgL^{-1} TiO_2 was mixed with HA solution in dark as in the same conditions with $(HA\text{-}TiO_2)_{,as\text{-}is}$ to compare solar irradiation effect, and influence of mixing on aggregation as well as surface adsorption. Hydrodynamic size measurements of $(HA\text{-}TiO_2)_{,dark}$ as intensity-, volume-, surface area- and number-weighted HDS and their cumulative ratios were presented in Figure 3.68, Figure 3.69, Figure 3.70, Figure 3.71, and Table 3.41. Also, HDS ranges and maximas were compiled in Table 3.42.

As mentioned before there are several mechanisms undergo during the suspension of TiO_2 in HA solution such as;

i. TiO_2 aggregation/agglomeration (Dahal and Dohnalek, 2017; Dette et al., 2018; Guo et al., 2019).

ii. Disruption of physico hydrogel structure of HA (Wells and Stretz, 2019).

iii. Dissaglomeretion of TiO_2 by continuous mixing (Heine and Pratsinis, 2007; Zhang et al., 2017; Sharma et al., 2019; Suresh et al., 2022)

iv. Disaggregation of TiO_2 structures by HA (Zhang et al., 2009; Zhao et al., 2019)

v. Colloidal stabilization of TiO_2 by HA adsorption onto aggregated or disaggregated TiO_2 structures (Bekbolet et al., 2002; Chen and Elimelech, 2007; Hyung et al., 2007; Zhang et al., 2009; Keller et al., 2010; Li et al., 2015).

vi. Formation of bridges between TiO_2 structures by adsorption of two edges of elongated HA structures onto two different TiO_2 surfaces (Hajdú et al., 2009; Keller et al., 2010; Turkten and Bekbolet, 2020).

The initial measurement taken right after 60 min mixing in the dark conditions, HDS range of $(HA\text{-}TiO_2)_{,dark}$ was obtained as 56.0-3007.5 nm which includes both sole-TiO_2 and sole-HA and structures formed as a result of HA adsorption onto TiO_2 surface. When the clusters in solution were examined in detail, three main size clusters were observed in the intensity-, volume-, surface area- and number-weighted hydrodynamic size definitions that maximas located at 92.1 nm, 362.3 nm and 1258.2 nm. Intensity- and volume-weighted hydrodynamic size definitions gave almost similar graphs with slight changes in 104.3-118.2 nm, 282.5-464.7 nm, and 980.9-1827.9 nm. The cluster between 282.5-464.7 nm is dominantly spherical according to surface area-weighted hydrodynamic size measurement. Even if the other two clusters showed a similar trend due to the decrease on the percentage of the particle size range between 980.9-1827.9 nm, exhibiting that this cluster tends to

deviate from the spherical structure. The 980.9-1827.9 nm cluster might be derived from the HA absorbed onto the TiO_2 aggregate surface, so its radius was large however differing from sole TiO_2 and HA, structure aberrated from the spherical framework. However, in the number-weighted hydrodynamic size definition the cluster between 980.9-1827.9 nm was not observed. This cluster might have been formed via HA adsorption onto TiO_2 surface, so structure was less in number. At neutral pH conditions HA adsorption onto TiO_2 surface is approximately 10-15% (Zhao et al, 2019), so clusters between 92.1-118.2 nm and 282.5-464.7 nm might be corresponding from TiO_2-TiO_2 homo-aggregation and segregated HA. On the other hand, by the passing time the cumulative ratio of bigger clusters increased. The surface of TiO_2 at neutral pH is equally positive and negative (Bekbolet et al., 2002; Zhou et al., 2019) and at all pH values surface charge of HA is negative due to deprotonation of carboxylic groups (Bekbolet et al., 2002). Through the ligand exchange mechanism, the $-OH_2^+$ and -OH groups of TiO_2 might exchange with the anionic groups of HA which later causes chelating of HA by removal of surface adsorbed water. This relatively strong structure might form van der Waals forces and TiO_2-HA-TiO_2 agglomerations can form. This trend can be evidenced by the formation of structures 1500 nm to 2000 nm. This relation is different from basic agglomeration mechanism. During agglomeration, by increasing cluster size cumulative ratio decreases and first cumulative ratio of moderate structures increases, on the other hand sudden formation of bigger clusters occurred by interactions of TiO_2-HA structures with each other.

Table 3.43 shows the hydrodynamic size and cumulative ratio comparison of $(HA\text{-}TiO_2)_{,as\text{-}is}$ and $(HA\text{-}TiO_2)_{,dark}$. As stated in methodology section $(HA\text{-}TiO_2)_{,dark}$ was prepared as $(HA\text{-}TiO_2)_{,as\text{-}is}$ and subjected to dark mixing during 60 min in SolarBox while lights were close, so the initial HDS measurement of $(HA\text{-}TiO_2)_{,dark}$ corresponding to 60 min of $(HA\text{-}TiO_2)_{,as\text{-}is.}$ Dissaglomeretion of TiO_2 structure in solution by mixing created smaller TiO_2 structures in solution and also increased the surface area of TiO_2 that HA can be adsorbed. Although stabilization of these relatively smaller TiO_2 structure was easier because of higher available adsorption sites. By decrease of hydrodynamic size of TiO_2, van der Waals interactions may also increase which was creating homoaggregation of HA-TiO_2 structures. These structures might form net like formations which was also preventing aggregation/agglomeration of sole TiO_2 structures. This trend was evidenced with the range differences in Table 3.43. In the results section of $TiO_{2,\ dark}$ it was stated that the hydrodynamic size increases by time via formation of agglomeration and this bigger structures precipitates by time. However, this trend cannot be followed in the presence of HA. On the contrary, cumulative ratio of structures above 1 µm increases and after 60 min structures around 1500 nm remain stable. This might be because of the stabilization effect of HA and balanced var der Waals forces.

Table 3.41. Intensity-, volume-, surface area- and number-weighted HDS and cumulative ratios of $(HA\text{-}TiO_2)_{,dark}$.

	HDS, nm	Cumulative Ratio, %			
		Intensity	Volume	Surface Area	Number
Initial	92.1-319.9	13%	4%	13%	70%
	362.3	14%	6%	10%	6%
	410.3-464.7	16%	41%	54%	23%
	980.9-1110.9	20%	25%	13%	1%
	1258.2	17%	7%	3%	-
	1425.0	13%	14%	6%	-
	1613.9-1827.9	7%	3%	1%	-
30 min	209.4-230.0	12%	5%	22%	49%
	252.6-304.7	10%	9%	31%	49%
	1364.5-1498.6	16%	24%	15%	1%
	1645.8	20%	20%	17%	1%
	1807.5	18%	13%	6%	-
	1985.1-2180.1	14%	19%	9%	-
60 min	212.8-291.0	18%	9%	40%	98%
	340.2	14%	6%	8%	1%
	397.8-465.2	15%	45%	42%	1%
	1390.4-1625.8	20%	29%	8%	-
	1901.1	18%	6%	1%	-
	2229.9-2599.3	15%	5%	1%	-
90 min	155.0-186.5	15%	6%	27%	69%
	204.6-246.2	14%	5%	17%	28%
	1082.6	11%	33%	23%	2%
	1187.6	17%	10%	7%	-
	1302.8	23%	21%	12%	-
	1429.1-1567.7	22%	25%	14%	1%
120 min	172.5-207.6	11%	4%	18%	51%
	227.8-274.1	21%	7%	23%	45%
	1098.7	9%	32%	24%	2%
	1205.2	17%	11%	7%	-
	1322.1	22%	28%	18%	1%
	1450.3-1590.9	20%	18%	10%	1%

Table 3.42. Intensity-weighted HDS profile of $(HA\text{-}TiO_2)_{,dark}$. Time dependent HDS cluster maximas, HDS range and min-max diameter difference with respect to multi-size distribution.

	Cluster				
Time, min	Max 1, nm	Max 2, nm	Max 3, nm	Range, nm	Difference, nm
Initial	92.1	362.3	1258.2	56.0-3007.5	2951.5
30	252.6	1645.8	-	144.0-2887.8	2743.8
60	52.1	340.2	1901.1	23.8-3553.9	3530.1
90	204.6	1302.8	-	117.4-2270.2	2152.8
120	227.8	1322.1	-	119.2-2303.8	2184.6

Table 3.43. Comparison of intensity-weighted HDS values of $(HA\text{-}TiO_2)_{,as\text{-}is}$ and $(HA\text{-}TiO_2)_{,dark}$.

	$(HA\text{-}TiO_2)_{,as\text{-}is}$		$(HA\text{-}TiO_2)_{,dark}$		
	HDS, nm	CR, %	HDS, nm	CR, %	
Initial	156.1-184.7	9%	Dark Mixing		
	200.9-237.3	16%			
	840.8	9%			
	914.7	18%			
	995.1	25%			
	1082.5-1177.6	23%			
30 min	157.0-172.2	8%			
	188.9-227.3	21%			
	911.1-999.5	21%			
	1096.4	22%			
	1202.7-1447.3	28%			
60 min	193.0-208.8	15%	92.1-319.9	13%	Initial
	225.8-264.3	16%	362.3	14%	
	1005.2	13%	410.3-464.7	16%	
	1087.4	18%	980.9-1110.9	20%	
	1176.3	21%	1258.2	17%	
	1272.5-1376.5	17%	1425.0	13%	
	-	-	1613.9-1827.9	7%	
90 min	164.6-192.0	18%	209.4-230.0	12%	30 min
	207.3-223.9	9%	252.6-304.7	10%	
	766.9-828.2	18%	1364.5-1498.6	16%	
	894.5	21%	1645.8	20%	
	966.0	20%	1807.5	18%	
	1043.3-1126.7	14%	1985.1-2180.1	14%	
120 min	143.8-156.6	9%	212.8-291.0	18%	60 min
	170.5-202.2	15%	340.2	14%	
	789.6	8%	397.8-465.2	15%	
	859.8	16%	1390.4-1625.8	20%	
	936.2	25%	1901.1	18%	
	1019.4	17%	2229.9-2599.3	15%	
	1110.0-1208.7	10%	-	-	
150 min	138.7-164.4	14%	155.0-186.5	15%	90 min
	179.0-194.9	11%	204.6-246.2	14%	
	761.3-829.0	25%	1082.6	11%	
	902.7	24%	1187.6	17%	
	982.9	17%	1302.8	23%	
	1070.2-1165.4	9%	1429.1-1567.7	22%	
180 min	39.8-175.3	12%	172.5-207.6	11%	120 min
	200.6-262.6	20%	227.8-274.1	21%	
	674.9-772.4	18%	1098.7	9%	
	883.9	20%	1205.2	17%	
	1011.5	17%	1322.1	22%	
	1157.5-1324.5	13%	1450.3-1590.9	20%	

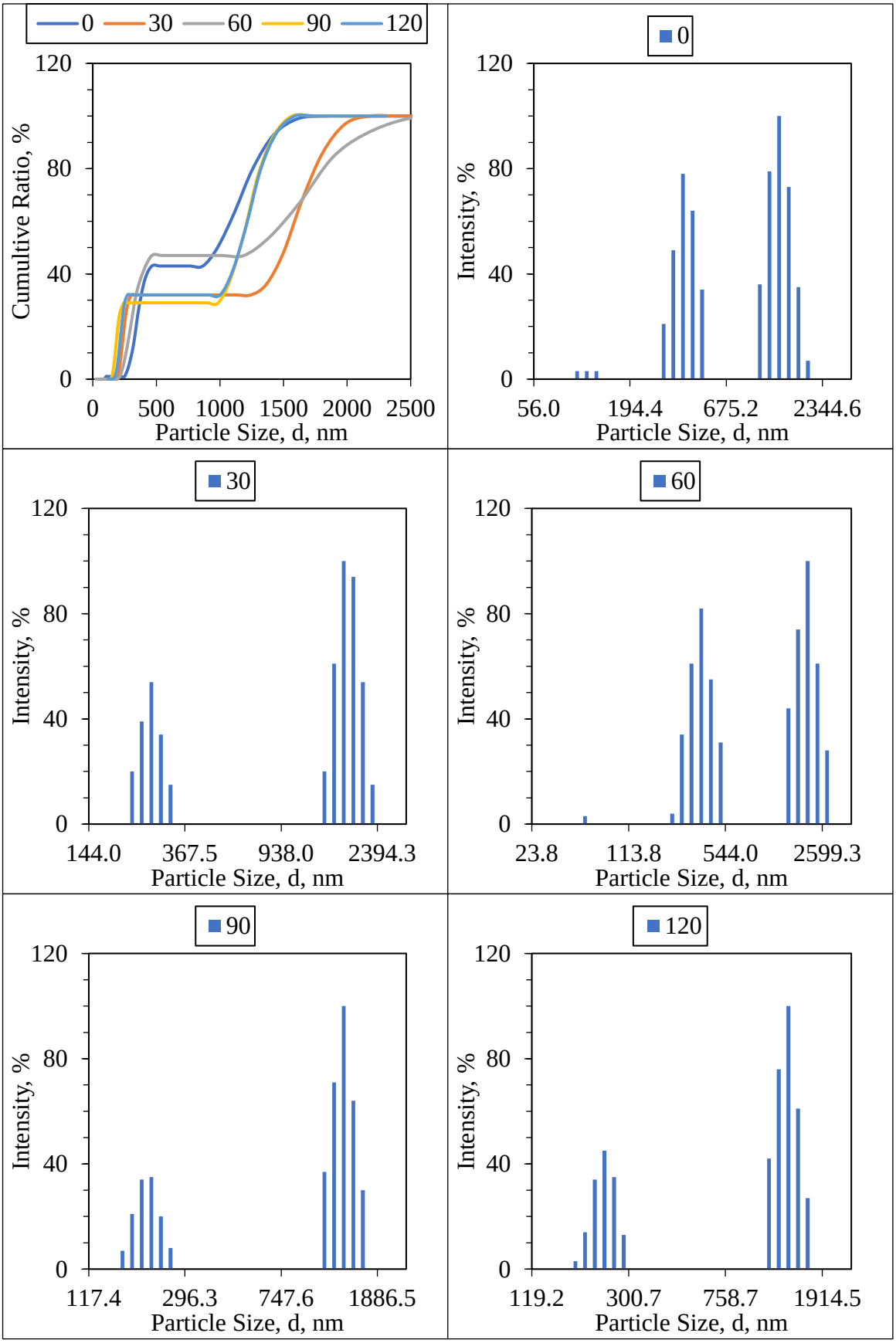


Figure 3.68. The cumulative ratio comparison and hydrodynamic size of $(HA\text{-}TiO_2)_{,dark}$ as intensity-weighted HDS in 30 min intervals.

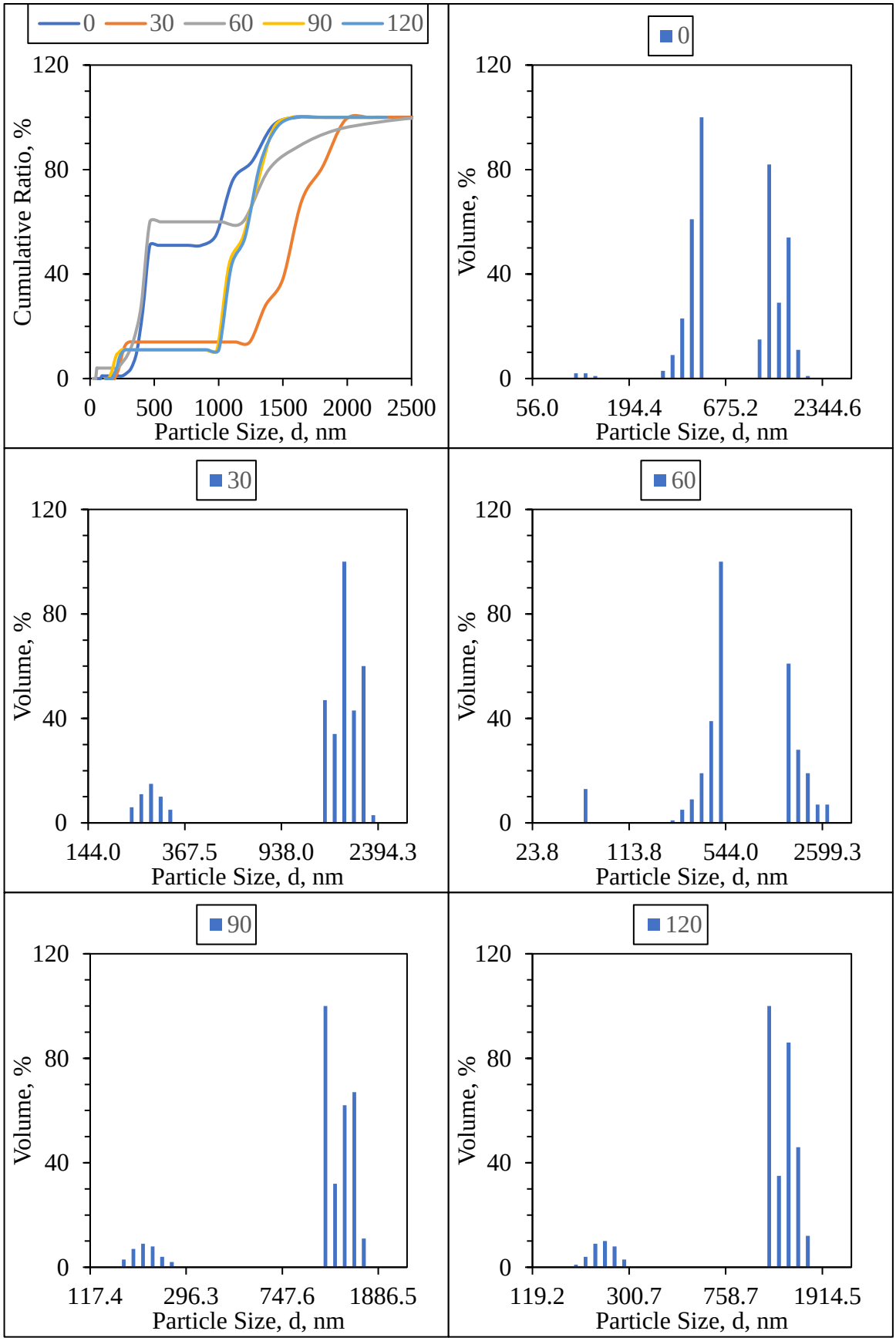


Figure 3.69. The cumulative ratio comparison and hydrodynamic size of $(HA\text{-}TiO_2)_{,dark}$ as volume-weighted HDS in 30 min intervals.

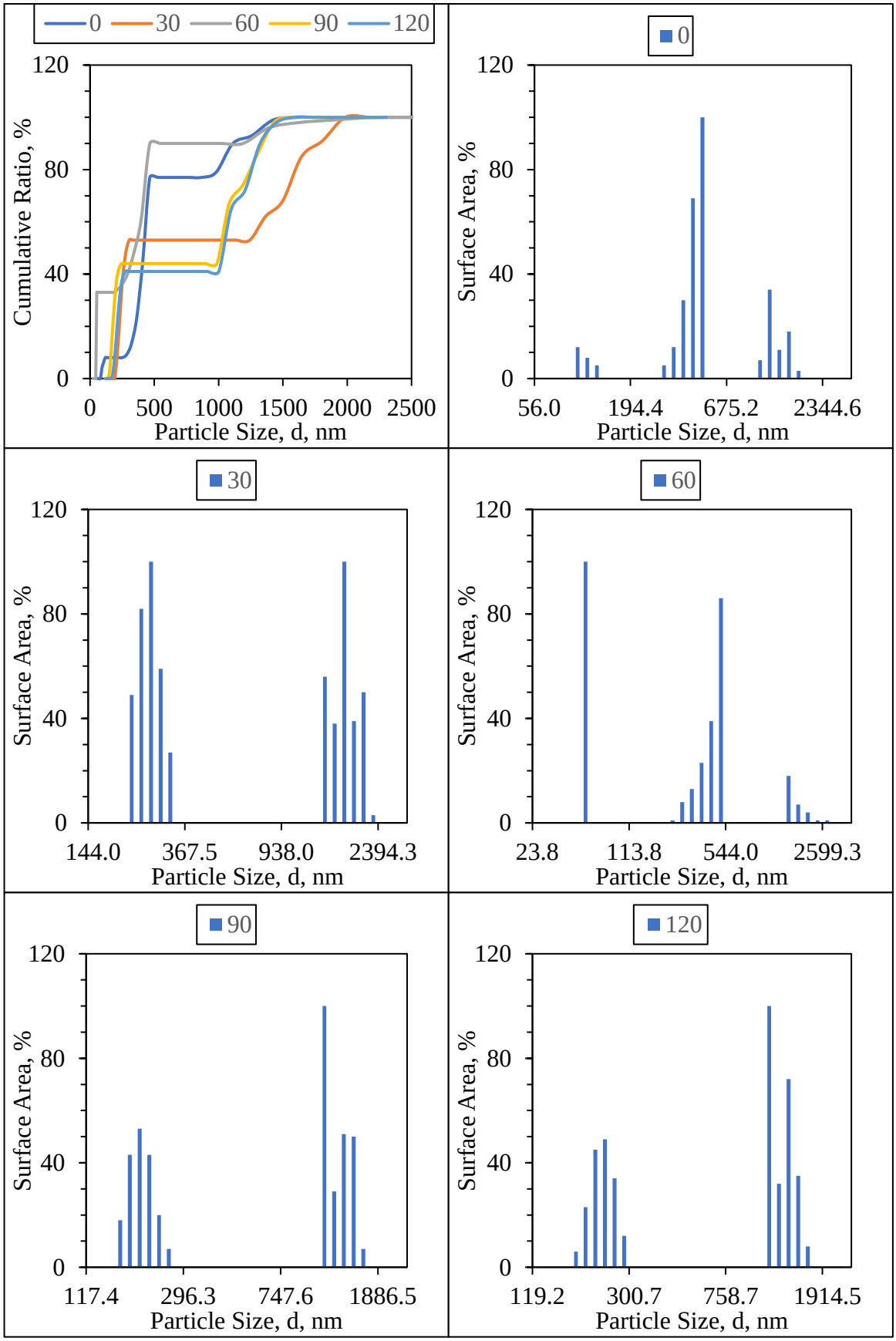


Figure 3.70. The cumulative ratio comparison and hydrodynamic size of $(HA\text{-}TiO_2)_{,dark}$ as surface area-weighted HDS in 30 min intervals.

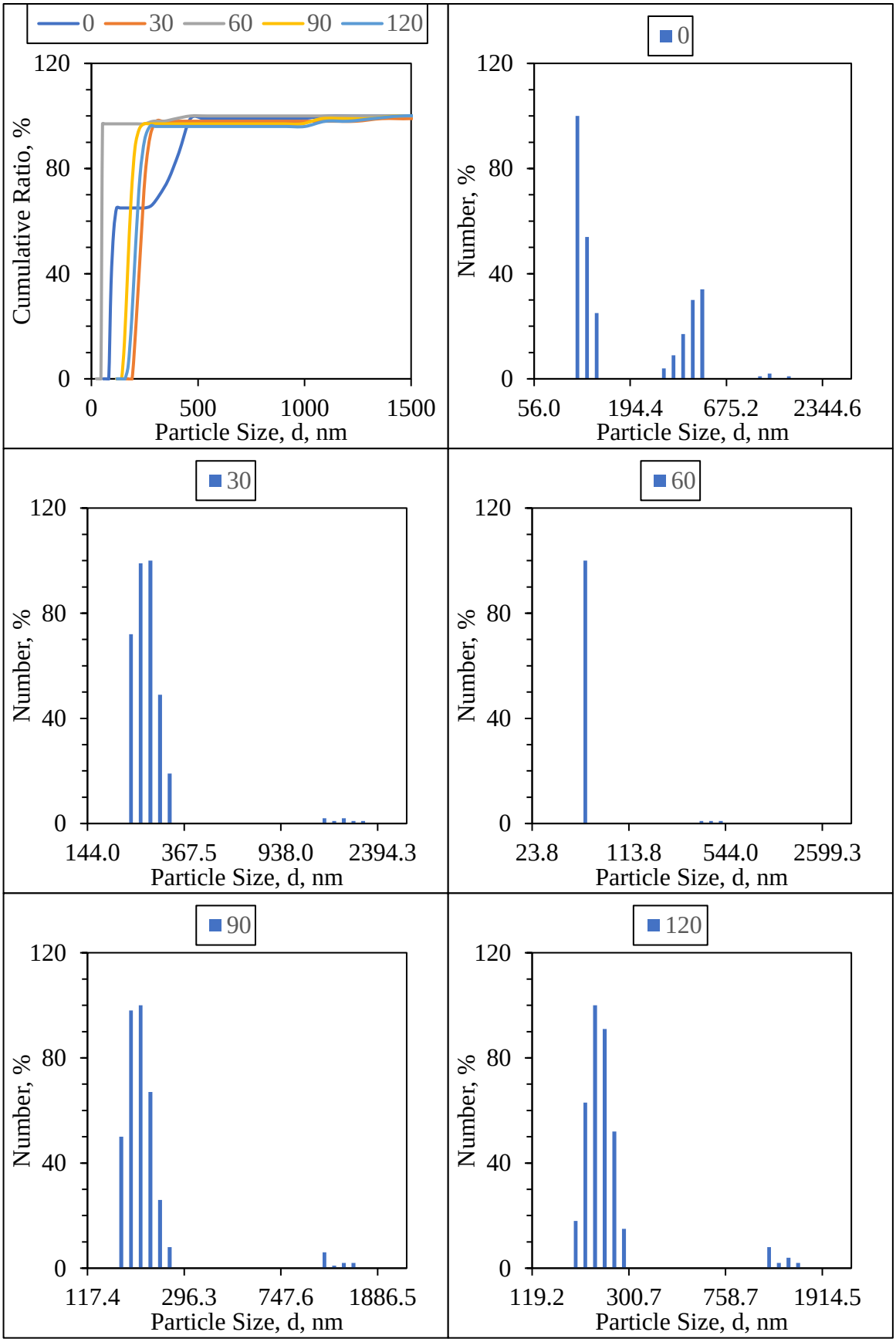


Figure 3.71. The cumulative ratio comparison and hydrodynamic size of $(HA\text{-}TiO_2)_{,dark}$ as number-weighted HDS in 30 min intervals.

3.5.3. Hydrodynamic Size Assessment of ($HA_{,pho}$-TiO_2)

Organic matter effect on hydrodynamic size of TiO_2 was investigated by suspending TiO_2 into the previously photolytically treated HA solution under solar light (wavelength range, λ= 290 to 800 nm and light intensity, I_o=250 W/m^2). HA solution (50 mgL^{-1}, DOC: 4.80 mgL^{-1}) was subjected to solar light for 60 min. After solar photolytic treatment 0.25 mgL^{-1} TiO_2 was suspended in obtained $HA_{,pho}$ solution by mixing by a magnetic stirrer (Materials and Methods Section 2.3.2). The obtained binary system was named as ($HA_{,pho}$-TiO_2).

Under photolytic conditions, HDS data of sole $HA_{,pho}$ was explained (Section 3.2.2.; Uyguner-Demirel et al., 2023). Through the solar irradiation, photosensitizer properties of HA were activated by production of triplet HA and reactive oxygen species ($O_2^{\bullet-}$, $HO^{\bullet}$ and H_2O_2) (Dalrymple et al., 2010). Self-degradation of HA (<5%) was accomplished by attack of primary and secondary radicals towards electron-rich species with a non-selective route or with a selective reaction pathway according to nearly located compounds. This results were evidenced by comparing initial 50 mgL^{-1} HA solution ($DOC_{,initial}$= 4.80 $mgL^{-1)}$ to photolytically treated $HA_{,pho}$ ($DOC_{,pho}$=4.53 mgL^{-1}) (Table 3.1). The radical attacks also caused chemical bond decomposition and new bond formation via intra-system crossing and re-conformational changes (Polewski et al., 2005) which can be followed by a minor decrease in $SUVA_{280}$ and $SUVA_{254}$ (Section 3.1.1. (Physicochemical Characterization Results of HA) Table 3.1). $SUVA_{254}$ and $SUVA_{280}$ are indicators of total aromaticity due to the π-π* transition in the 270-280 nm. The initial ($HA_{,as\text{-}is}$ conditions) value of $SUVA_{254}$ slightly decreased from 9.41 $Lm^{-1}mg^{-1}$ to 9.18 $Lm^{-1}mg^{-1}$ and similarly $SUVA_{280}$ slightly decreased from 8.08 $Lm^{-1}mg^{-1}$ to 7.79 $Lm^{-1}mg^{-1}$ that showed the decrease of total aromaticity in the present structures. On the other hand, the A_{254}/A_{365} ratio, which is an indicator of aromaticity per molecular size, also slightly increased from 2.71 to 2.85. In the case of solar photolytic treatment, only <5% degradation occurred as indicated above so the charge localization caused the formation of aromatic structures that causes increase of A_{254}/A_{365}. According to the results obtained by Uyguner-Demirel and her colleagues after photolysis the $SFI_{syn,470}$ results showed that higher molecular size fractions disaggregated or bond cleavage occurred in HA structures following to photolysis (Hansen et al., 2016; Uyguner-Demirel et al., 2022). The increase of aromaticity, and hence increase of hydrophobic behavior and decreased surface adsorption onto TiO_2 (Bekbolet et al., 2002). This trend was evidenced by the DOC normalized FI_{syn}, SFI_{syn}, an indicator of changes in low molecular size fractions (Uyguner and Bekbolet, 2005b), supported the conformational changes in HA structure after photolysis (Table 3.1). Decrease of SFI_{syn} implies that decrease of conjugated systems with e^- withdrawing groups (Uyguner

and Bekbolet, 2010; Uyguner-Demirel et al., 2013). The overall structural changes on HA after photolytic oxidation may cause the formation of supramolecular structures capacity that having tendency to self-assemble and aggregate (von Wandruszka et al., 1997; Uyguner-Demirel and Bekbolet, 2011; Vione et al, 2014). Graphical abstract of the HDS measurements were shown in Figure 3.72, Figure 3.73, Figure 3.74, and Figure 3.75 as intensity-, volume-, surface area- and number-weighted HDS. Table 3.44 compiles the HDS and corresponding cumulative ratios as intensity-, volume-, surface area-, and number-weighted hydrodynamic size definitions and Table 3.45 shows the HDS maximas corresponding the graphical abstracts as intensity-weighted HDS. Table 3.46 gathers the comparative HDS and corresponding cumulative ratio results of $HA_{,pho}$, $TiO_{2,as-is}$ and ($HA_{,pho}$-TiO_2) as intensity-weighted HDS data. These results also proved that hetero-aggregation formation was barely accomplished. HDS comparison of mono, $HA_{,pho}$, $TiO_{2,as-is}$, and binary systems ($HA_{,pho}$-TiO_2) displayed that most of the hydrodynamic structures were originating from homo-aggregate or homo-agglomerate of mono systems.

Also, the stabilizing effect of HA onto TiO_2 aggregates was not observed in time dependent HDS measurements. The surface of supramolecular $HA_{,pho}$ was negatively charged under neutral pH due to the deprotonation of surface carboxyl groups. On the other hand, surface charge of TiO_2 aggregates was neutral due to the pH_{pzc} (6.5) value of TiO_2. Consequently, in comparison to the $TiO_{2,as-is}$ homo-agglomerates, $HA_{,pho}$ hetero-agglomerates were more stable in aquatic environment, due to the non-specific van der Waals forces (Schwarzenbach et al., 2017). HA adsorption onto TiO_2 surface were governed by surface complexation mechanisms that take place via coulombic electrostatic interactions and van der Waals forces (Sen-Kavurmaci and Bekbolet, 2013; Wang et al., 2016). Since HA was bonded to the Ti-OH sites, ionization of the carboxylic groups of HA cause negatively charged TiO_2 surface (Sun and Lee, 2012; Wang et al., 2016). However, due to the conformational changes during solar photolytic treatment of $HA_{,pho}$ these complexation might not take place (Bekbolet et al., 2002). Hence, disappearance of the structures around 1 μm might be related to the precipitation of homo-agglomerated TiO_2 structures that were not interacted with $HA_{,pho}$. This trend can be evidenced by the increase of both cumulative ratios and HDS values of lower sized structures during 120 min. Volume- and surface area-weighted hydrodynamic size definitions proved that clusters consisted of spherical structures covering most of the solution volume. The TiO_2-TiO_2 homoaggregation and segregated $HA_{,pho}$ framework was numerically superior to (HA_{pho}-TiO_2) which was evidenced with number-weighted hydrodynamic size measurement. This propensity is also similar with the $(HA\text{-}TiO_2)_{,as-is}$ hydrodynamic size measurement of TiO_2-HA heteroaggregation that comprises a minor part of the solution.

Table 3.44. Intensity-, volume-, surface area- and number-weighted HDS and cumulative ratios of ($HA_{,pho}$-TiO_2).

	HDS, nm	Cumulative Ratio, %			
		Intensity	Volume	Surface Area	Number
Initial	148.5-175.3	14%	5%	21%	73%
	190.5-207.0	8%	2%	8%	18%
	783.0	11%	36%	31%	5%
	850.9	19%	12%	10%	1%
	924.6	25%	12%	9%	1%
	1004.8-1091.9	23%	33%	21%	2%
30 min	165.4-188.9	14%	3%	11%	51%
	201.9-230.5	9%	2%	7%	27%
	623.1-665.8	12%	5%	5%	1%
	711.5	19%	16%	15%	5%
	760.2	22%	59%	50%	7%
	812.3-868.0	18%	15%	12%	3%
60 min	113.4-154.9	20%	14%	46%	95%
	538.2-581.8	22%	14%	11%	2%
	628.9	23%	13%	19%	1%
	679.9	21%	18%	11%	1%
	734.9-794.4	13%	41%	23%	1%
90 min	204.4-234.5	19%	5%	15%	48%
	251.2-288.1	22%	7%	16%	35%
	753.8-807.2	20%	59%	48%	13%
	864.5	19%	13%	11%	2%
	926.0	13%	8%	5%	1%
	991.8-1062.3	7%	8%	5%	1%
120 min	225.9-239.9	13%	4%	10%	29%
	254.7	15%	5%	11%	26%
	270.5-304.9	20%	6%	15%	30%
	749.8-796.1	14%	53%	41%	11%
	845.4	15%	15%	12%	2%
	897.6-1012.0	23%	17%	11%	2%

Table 3.45. Intensity-weighted HDS profile of ($HA_{,pho}$-TiO_2). Time dependent HDS cluster maximas, HDS range and min-max diameter difference with respect to multi-size distribution.

	Cluster				
Time, min	Max 1, nm	Max 2, nm	Max 3, nm	Range, nm	Difference, nm
Initial	92.1	362.3	1258.2	56.0-3007.5	2951.5
30	252.6	1645.8	-	144.0-2887.8	2743.8
60	52.1	340.2	1901.1	23.8-3553.9	3530.1
90	204.6	1302.8	-	117.4-2270.2	2152.8
120	227.8	1322.1	-	119.2-2303.8	2184.6

Table 3.46. Comparison of intensity-weighted HDS values of $HA_{,pho}$, $TiO_{2,as-is}$, and ($HA_{,pho}$-TiO_2).

	$HA_{,pho}$		$TiO_{2,as-is}$		($HA_{,pho}$-TiO_2)	
	HDS, nm	CR, %	HDS, nm	CR, %	HDS, nm	CR, %
Initial	121.8-139.5	25%	144.3-184.4	26%	148.5-175.3	14%
	149.3-170.9	29%	200.1-217.1	11%	190.5-207.0	8%
	539.8-757.1	46%	739.9-802.9	19%	783.0	11%
	-	-	871.2	20%	850.9	19%
	-	-	945.4	15%	924.6	25%
	-	-	-	-	1004.8-1091.9	23%
30 min	133.8-142.6	22%	739.9-802.9	19%	165.4-188.9	14%
	152.1	21%	871.2	20%	201.9-230.5	9%
	162.2-173.0	19%	945.4	15%	623.1-665.8	12%
	483.9-667.3	38%	1025.9-1113.3	9%	711.5	19%
	-	-	-	-	760.2	22%
			-	-	812.3-868.0	18%
60 min	100.0-177.8	45%	96.8-146.1	20%	113.4-154.9	20%
	237.1	28%	501.7-544.7	16%	538.2-581.8	22%
	316.2-421.7	27%	591.4-642.2	45%	628.9	23%
			697.2-757.0	19%	679.9	21%
	-	-	-	-	734.9-794.4	13%
90 min	135.0-150.4	27%	66.6-143.6	7%	204.4-234.5	19%
	158.8	19%	156.2-201.0	19%	251.2-288.1	22%
	167.6-177.0	16%	218.6-237.8	8%	753.8-807.2	20%
	398.8-444.4	13%	587.9-710.4	42%	864.5	19%
	469.1-522.8	25%	780.9-943.7	24%	926.0	13%
	-	-	-	-	991.8-1062.3	7%
120 min	131.1-151.3	27%	117.0-158.5	24%	225.9-239.9	13%
	162.5	24%	534.6-576.7	23%	254.7	15%
	174.5-187.5	22%	622.3-671.4	42%	270.5-304.9	20%
	633.2-843.2	27%	724.4-781.6	11%	749.8-796.1	14%
	-	-	-	-	845.4	15%
	-	-	-	-	897.6-1012.0	23%

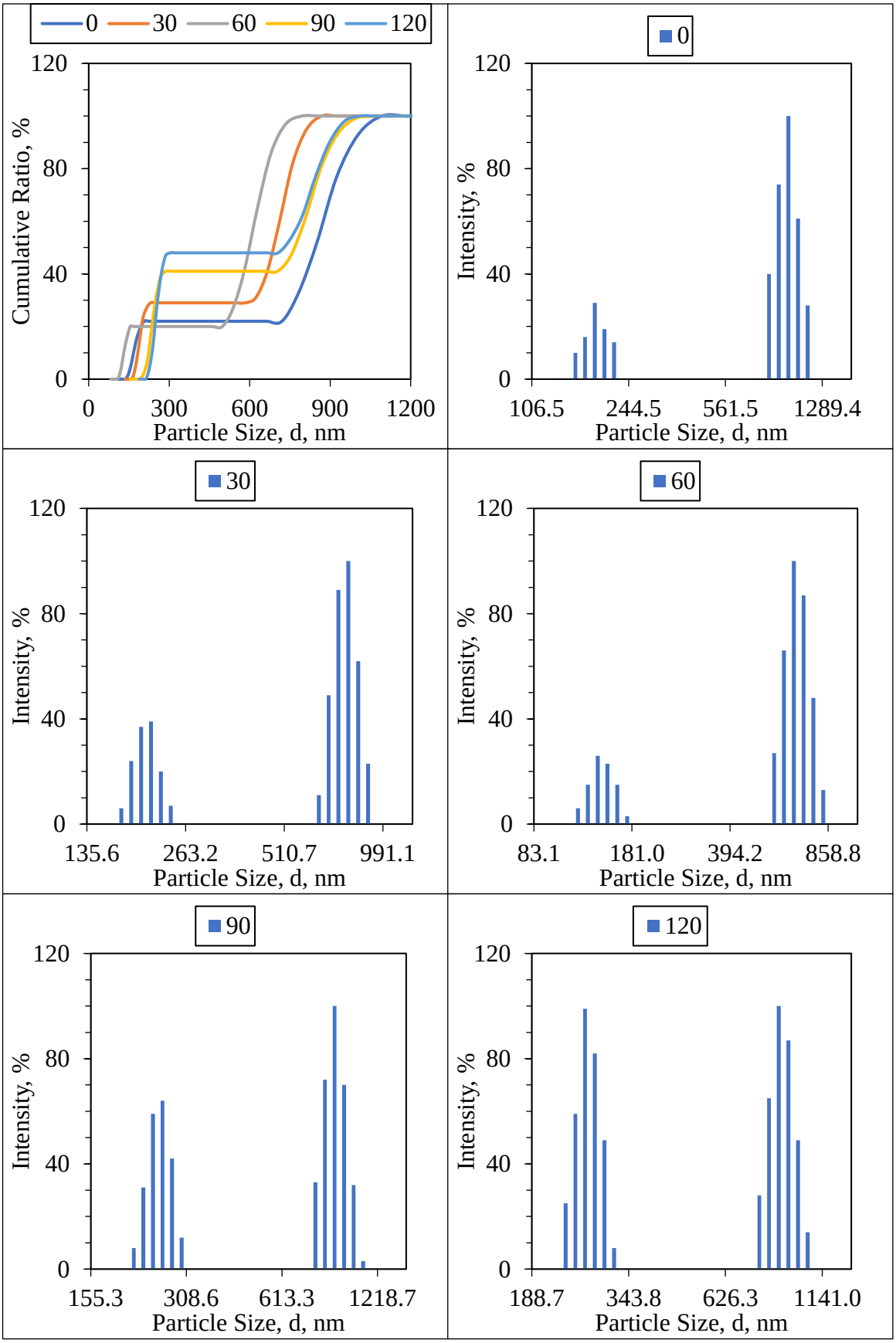


Figure 3.72. The cumulative ratio comparison and hydrodynamic size of ($HA_{,pho}$-TiO_2) as intensity-weighted HDS in 30 min intervals.

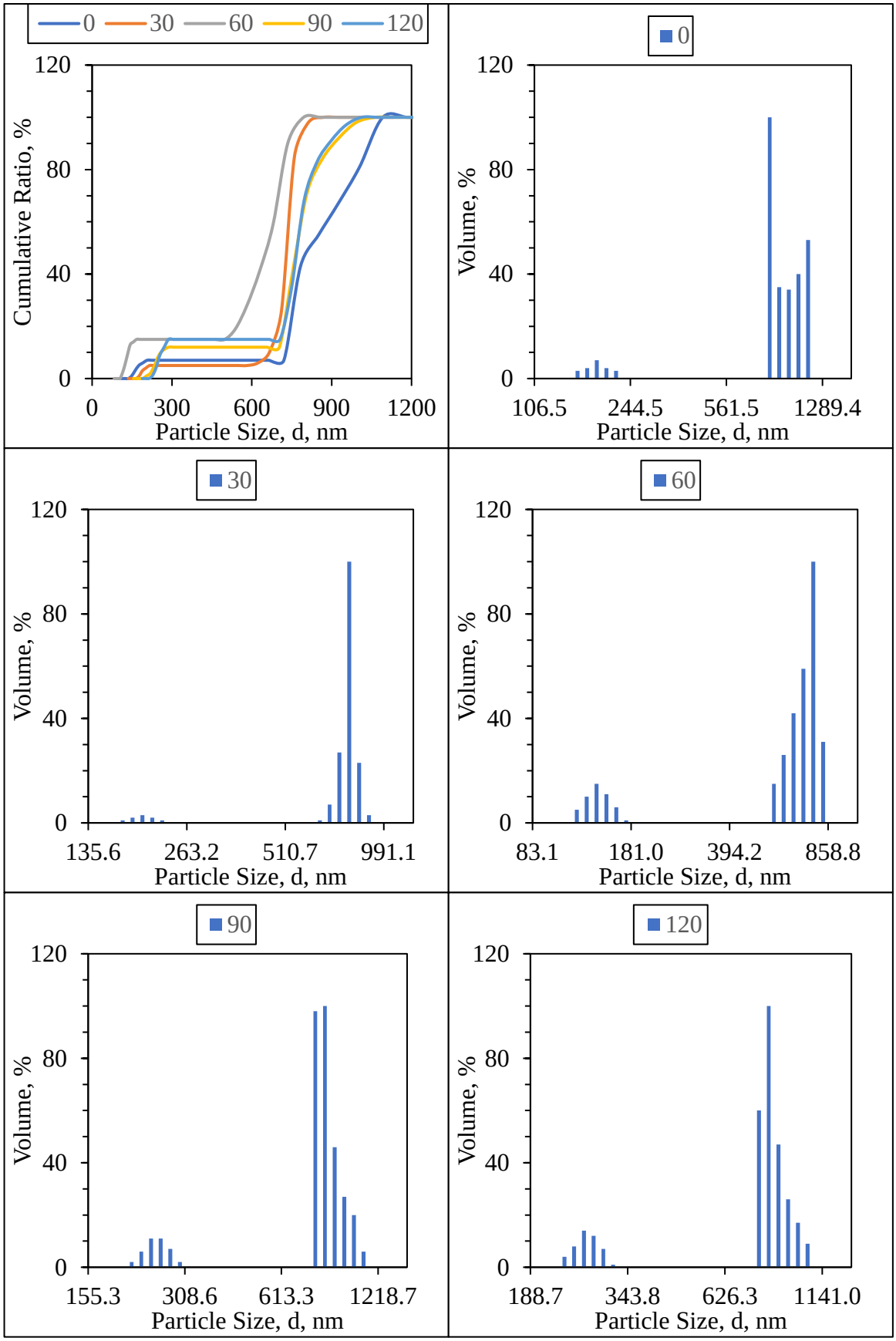


Figure 3.73. The cumulative ratio comparison and hydrodynamic size of ($HA_{,pho}$-TiO_2) as volume-weighted HDS in 30 min intervals.

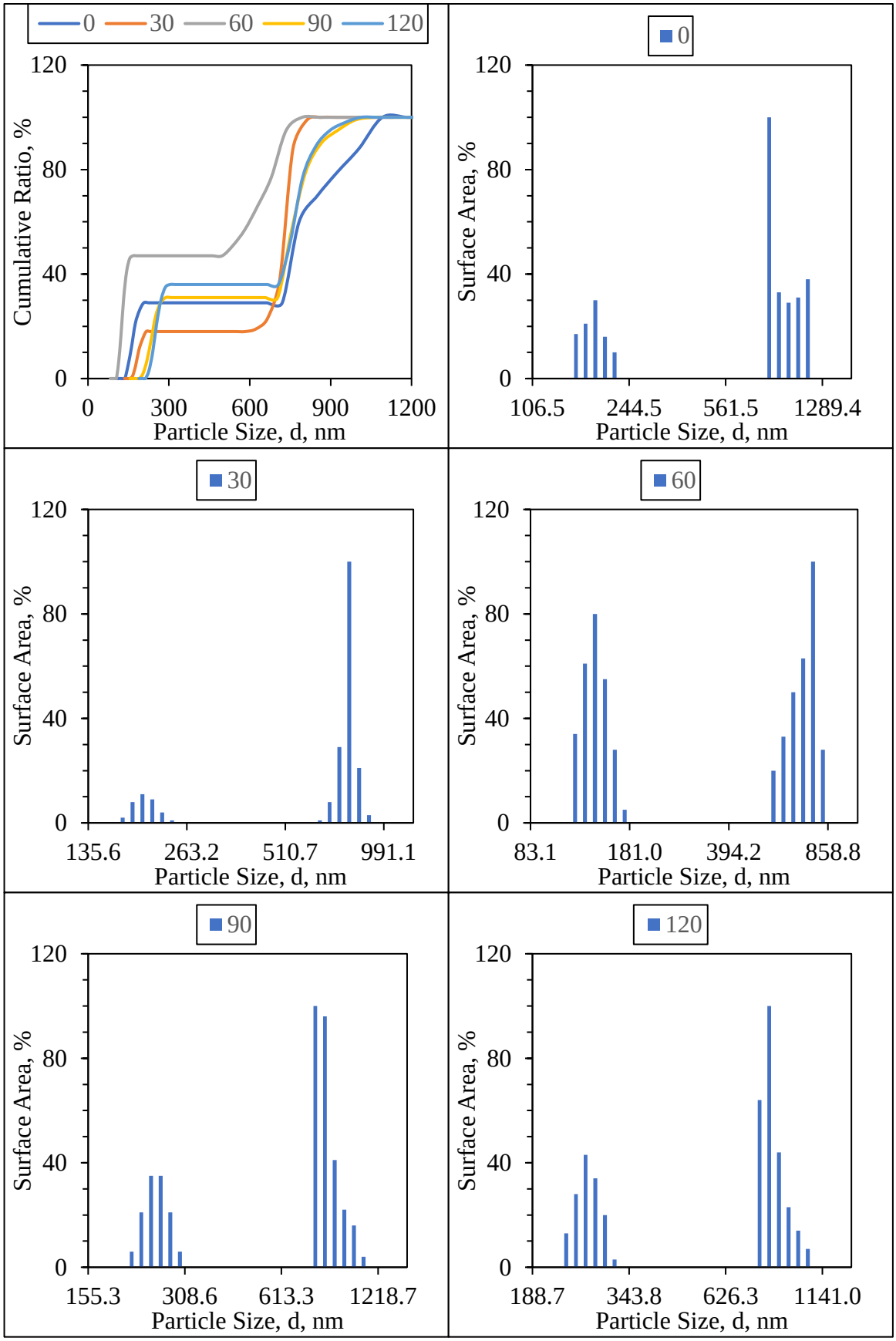


Figure 3.74. The cumulative ratio comparison and hydrodynamic size of ($HA_{,pho}$-TiO_2) as surface area-weighted HDS in 30 min intervals.

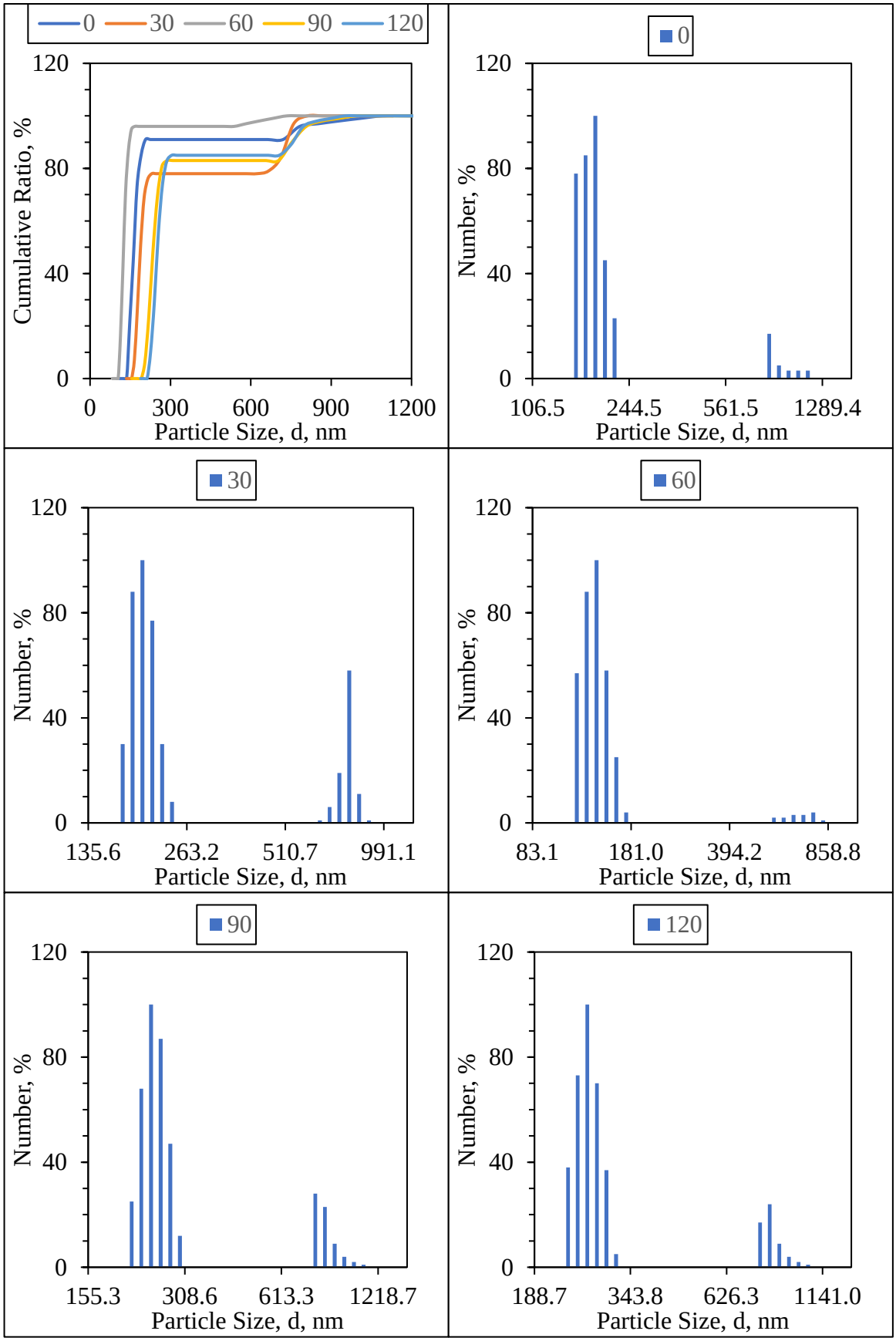


Figure 3.75. The cumulative ratio comparison and hydrodynamic size of ($HA_{,pho}$-TiO_2) as number-weighted HDS in 30 min intervals.

3.5.4. Hydrodynamic Size Assessment of $(HA\text{-}TiO_2)_{,photocat}$

Hydrodynamic size changes during photocatalytical conditions were investigated by measuring $(HA\text{-}TiO_2)_{,photocat}$ binary system. 0.25 mgL^{-1} TiO_2 was suspended in 50 mgL^{-1} HA (DOC: 4.80 mgL^{-1}) solution as and subjected to solar irradiation for 60 min (Materials and Methods Section 2.3.1). Following photocatalysis, sample was named as **(**$HA\text{-}TiO_2)_{,photocat}$ and subjected to HDS measurement for 120 min without removing the cuvette. Residual solution was filtered from 0.45 μm cellulose membrane filter to remove TiO_2 from the media and photocatalytically degraded HA solution was subjected to physicochemical characterization by measuring designed UV-vis parameters such as UV_{254}, UV_{280}, UV_{365} and $Color_{436}$.

The characterization results were presented in Table 3.1 in section 3.1.1 (Physicochemical Characterization Results of Humic Acid). In addition, DOC normalized UV-vis parameters were calculated as $SUVA_{254}$, $SUVA_{280}$, $SUVA_{365}$, and $SCoA_{436}$ and compiled in Table 3.1. Aromaticity per molecular size were calculated by using A_{254}/A_{365} ratio and changes in molecular size fractions were followed by DOC normalized FI_{syn}, SFI_{syn}, data (Table 3.1). DOC decrease ($DOC_{,photocat}$ 1.12 mgL^{-1}) in comparison to $DOC_{,initial}$ (4.80 mgL^{-1}) was indicated that degradation of HA structure took place during 60 min and smaller size fractions were observed. As mentioned in the physicochemical characterization results of HA, after solar photocatalytic treatment in the presence of TiO_2, DOC of HA decreased 87% ($DOC_{,photocat}$= 1.12 mgL^{-1}). The indicators of total aromaticity, $SUVA_{254}$ and $SUVA_{280}$ values, were investigated to understand confirmational changes after photocatalytic degradation of HA. Similarly, physicochemical characterization results of $HA_{,photocat}$ showed that $SUVA_{254}$ and $SUVA_{280}$ values decreased to 1.16 $Lm^{-1}mg^{-1}$ and 0.981 $Lm^{-1}mg^{-1}$ that show decrease in total aromaticity. The change on molecular size heterogeneity after solar photocatalytic degradation was investigated by monitoring the changes in $SUVA_{365}$. The initial HA solution (filtered from 0.45 μm) comprises molecular size fractions corresponding approximately smaller than 450 kDa (Uyguner and Bekbolet, 2005a). In comparison to the initial HA solution ($SUVA_{365,as\text{-}is}$= 3.450 $Lm^{-1}mg^{-1}$), solar photocatalytic treatment decreased the molecular size heterogeneity ($SUVA_{365,photocat}$=0.179 $Lm^{-1}mg^{-1}$). This trend showed the formation of smaller molecular size fractions by degradation of bigger molecular size fractions. Several literature examples were reported according to changes on molecular size fractionations of HA after solar photocatalytic degradation that $HA_{,photocat}$ showed similar properties withs 3 kDa structures which were comprised of mostly hydrophilic structures according to SUVA<2 values (Uyguner-Demirel and Bekbolet, 2009; Uyguner-Demirel et al., 2013; Birben et al., 2017). The characterization results of $HA_{,photocat}$ were in line with these examples. The decrease in $SCoA_{436}$, indicator of color forming moieties, from 1.670 $Lm^{-1}mg^{-1}$ to 0.089 $Lm^{-1}mg^{-1}$ evidenced

the degradation of these structures. Following the $SCoA_{436}$, and $SUVA_{365}$, results also showed that degraded structures were mostly core aromatic groups and UV absorbing centers due to the deterioration of primarily π and later σ bonds (Li et al., 2020). Alteration of molecular size fractions were also followed by increase of A_{254}/A_{365} (6.50) ratio and the DOC normalized FI_{syn} (SFI_{syn}) (1.25) values. Because of the formation of smaller size molecular size fractions absorbance value at 365 nm (0.002) decreases and similarly DOC indicator value at 254 nm (0.013) decreases (Table 3.1), this trend leads to increase of A_{254}/A_{365}. Similarly, formation of smaller size fractions after solar photocatalytic treatment slightly increased the SFI_{syn} ratio due to decrease of both $FI_{syn,photocat}$ (1.4) and $DOC_{,photocat}$ (1.12) values. Consequently, $SFI_{syn,photocat}>SFI_{,as-is}$ relation was observed.

A more specific characterization of Aldrich HA after 60 min solar photocatalysis was published by Uyguner-Demirel and colleagues (Uyguner-Demirel et al., 2022). They investigated the chemical structure of HA molecular size fractions after solar photocatalysis after being treated by TiO_2 via FTIR measurements. They suggested the deformation of oxygenated groups such as carboxylic acids, phenols, and aromatic or unsaturated ethers by following the peak change around 1260-1200 cm^{-1}. This peak was associated with these chemical groups by several researchers (Kim and Yu, 2005; Kim et al., 2006), however others proposed that peak around 1260-1200 cm^{-1} could be related to C-O stretching and O-H deformation of COOH groups (Chen et al., 2002; Sillanpää et al., 2014; Uyguner-Demirel et al., 2022). Uyguner-Demirel and colleagues reported to disappearance of this peak after photocatalytic degradation and formation of a new peak in the 1170-1120 cm^{-1} region may be related with the formation of new organic structures that have aliphatic character (Uyguner-Demirel et al., 2022). Also, after solar photocatalysis FTIR peaks around formation of aliphatic esters were reported. During photocatalytic treatment in the presence of TiO_2 alteration or removal of alcohols and ethers were identified by diminish of corresponding C-O stretching peak. Disappearance of peak around 1630-1650 cm^{-1} was reported that could be in relation with decomposition of aromatic structures after photocatalysis (Uyguner-Demirel et al., 2022). Similar relation was found to decrease of $SUVA_{280}$ (Table 3.1). Also increase of A_{254}/A_{365} ratio (initial: 2.71, photocatalysis: 6.50) showed that aromaticity per molecular size was decreased after photocatalytic degradation (Table 3.1). Decomposition of polysaccharide or similar structures, stretching of alcohols and aliphatic ethers also noticed after photocatalytic treatment (Uyguner-Demirel et al., 2022). On the other hand, during 60 min organic moieties in HA solution was not totally degraded and these non-degraded structures were mainly composed of aliphatic structures by following the change of $SUVA_{254}$ (initial: 9.41, photocatalytic: 1.16) and $SCoA_{436}$ (initial: 1.670, photocatalytic: 0.089) (Table 3.1).

According to physicochemical characterization results, surface adsorption of photocatalytically degraded HA structures onto TiO_2 could be represented with “train, tail, loops” model (Figure 1.16). Table 1.5 shows the interaction between organic moieties and TiO_2 structure under low ionic strength conditions at low and high pH conditions. At neutral pH conditions surface charge of TiO_2 aggregates were also neutral and degraded HA structures were negatively charged. Hence these organic moieties forms structures as represented in Figure 3.76. Figure 3.76 a shows the HDS of HA-TiO_2 binary system which includes stern layer covering the aggregate. Differing from TEM and SEM, DLS system allows the measuring organic moieties absorbed onto bulk aggregates. On the contrary TEM and SEM only show the bulk TiO_2 aggregates or agglomerates (Tan et al., 2021).

Table 1.2 also compared the disadvantages of other size determination techniques against dynamic light scattering. The main struggle was measuring HDS of binary systems because there were two different structures in the media (TiO_2 crystals and polymer-like HA) refractive index was set to 1.0, so it would be possible to measure HDS of all possible structures formed in the $(HA\text{-}TiO_2)_{,photocat}$ composition (Stetefeld et al., 2016). Table 1.3 compiled the size and HDS values determined by TEM/SEM and DLS measurements taken for TiO_2 in HA solution. While size measurements taken with TEM/SEM showing bulk TiO_2 aggregates and agglomerates, DLS measurements showed the overall size of hydrodynamic structures in the media including surface absorbed organic moieties and homo-aggregates/homo agglomerates.

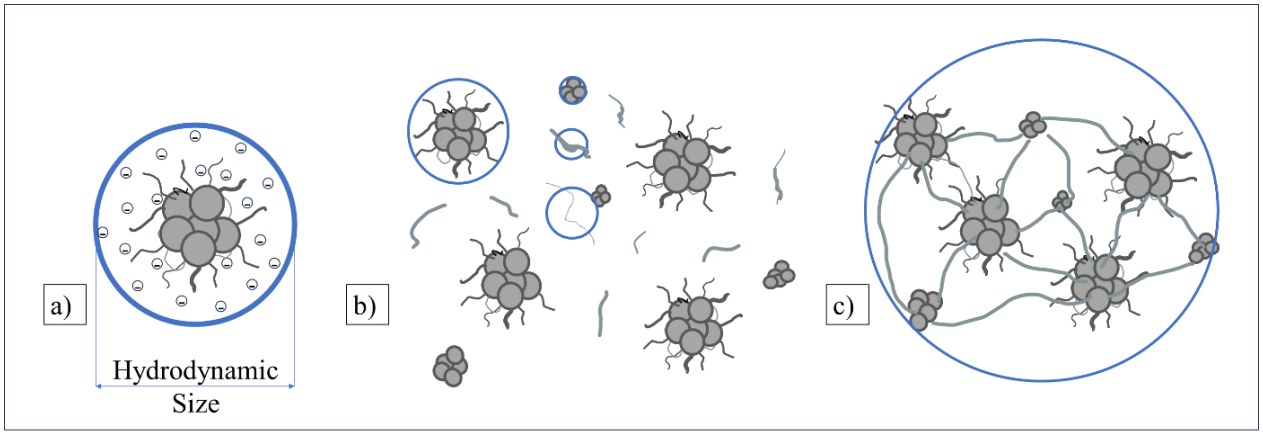


Figure 3.76. a) Theoretical representation of surface adsorption of photocatalytically degraded HA onto TiO_2 aggregate, b) Theoretical representation of homo-agglomerates and HA-TiO_2 hetero-aggregates, c) Theoretical representation of HA-TiO_2 hetero-agglomerate. Blue circle: HDS of corresponding system.

Detailed explanation on HDS parameters were already given in section 1.4.4 (Size definitions of hydrodynamic radius). As seen in Figure 3.76 a and Figure 3.76 c the most suitable HDS definition could be chosen as volume-weighted HDS because the hetero-aggregates and hetero-agglomerates cover a volume rather than a bulk structure. However, comparison with other mono and binary systems could be dubious if volume-weighted HDS was chosen as representative. Because composition of other systems such as $(HA\text{-}TiO_2)_{,as\text{-}is}$ and $(HA\text{-}TiO_2)_{,dark}$ cover more homo-aggregate/agglomerates intensity- or number-weighted HDS data was more proper for evaluation. Furthermore, the European commission suggests that for defining HDS of TiO_2 number-weighted HDS definition is more appropriate (Usenko et al., 2023). For preventing the conflict rising from "polydispersed" size variations and structures comparison, tables were prepared by using intensity-weighted HDS data and corresponding system was evaluated by considering all HDS definitions (intensity, volume, surface area and number).

Figure 3.77, Figure 3.78, Figure 3.79, and Figure 3.80 demonstrated the intensity-, volume, surface area- and number-weighted hydrodynamic size definitions of the $(HA\text{-}TiO_2)_{,photocat}$ binary system. HDS of $(HA - TiO_2)_{,photocat}$ with cumulative ratios were listed in Table 3.47. Table 3.48 compiled the time depended HDS measurement data with the maxima and range values. Intensity- and volume-weighted hydrodynamic size definitions were showed three maxima as 120.8 nm, 253.2-414.8 nm and 1822.5-3376.9 nm. Due to the formation of radicals in the presence of solar irradiation surface interaction of TiO_2 and HA residues increased, which created relatively bigger clusters comparing to the $(HA\text{-}TiO_2)_{,as\text{-}is}$ and $(HA\text{-}TiO_2)_{,dark}$. These bigger clusters were evidenced in the intensity- and volume-weighted hydrodynamic size definitions. Nonetheless, the cluster between 1822.5-3376.9 nm is still few in number as indicated from the number-weighted hydrodynamic measurement. The clusters, 120.8 nm, 253.2-414.8 nm, formed more spherical structures by comparing volume-weighted HDS and surface area-weighted HDS (Figure 3.76 b). On the other hand, the biggest cluster 1822.5-3376.9 nm, was presumably less spherical in comparison to the small clusters, 120.8 nm, and 253.2-414.8 nm due to the net-like agglomerate structures formed by photocatalytically degraded HA structures and hetero-agglomerate formation by $HA\text{-}TiO_2$. Figure 3.76 c shows a theoretical representation of these net like non-spherical hetero-agglomerates. This trend was also evidenced by comparing volume- and surface area weighted HDS values.

$HA\text{-}TiO_2$ binary system interactions would take place in several mechanisms such as coulombic electrostatic interactions and Van der Waal forces, via surface complexation reactions (Sen Kavurmaci and Bekbolet, 2013; Wang et al., 2016). Under solar irradiation conditions, the surface adsorbed HA photocatalytically degraded by TiO_2 catalyzed hydroxyl radicals. These degraded

organic structures properties of which were previously explained prevented TiO_2 agglomeration regardless of pH. Due to the occupation of active sites by HA, surface charge differences of TiO_2 were eliminated agglomeration of TiO_2 was prohibited (Wang et al., 2016). Also, the pH change during photocatalytic reactions were reported by several researchers (Liu et al., 2008; Wang et al., 2016). The hydroxyl radicals formed under solar irradiation were consumed during degradation of HA and no pH change was observed during the process according to work of Wang and colleagues (Wang et al., 2016).

The effect of solar irradiation on hydrodynamic size of TiO_2 was explained in the results section, in $TiO_{2,irr}$ part (Section 3.4.3. Hydrodynamic Size Results of TiO2,irr). During solar irradiation the surface of TiO_2 changes and this change would result in formation of bigger agglomerates due to the formation of superhydrophilic surface structure (Koudriachova et al., 2004; Fujishima et al., 2008). The affinity of photocatalytically degraded HA structures increased towards the superhydrophilic TiO_2 surface due to their more hydrophilic structure. The van der Waals forces were also weakened after photocatalytically degradation of HA structure and these phenomena causes inhibition of agglomeration of currently aggregated TiO_2 structures by $HA_{,photocat}$ adsorption onto $TiO_{2,irr}$ surface. Consequently, colloidally more stable structures in comparison to the $(HA\text{-}TiO_2)_{,as\text{-}is}$ and $(HA\text{-}TiO_2)_{,dark}$ was accomplished. Similar results were obtained with HDS measurements of $(HA\text{-}TiO_2)_{,photocat}$. Table 3.49 gathers the comparative HDS data of $HA_{,photocat}$, $TiO_{2,irr}$, and $(HA\text{-}TiO_2)_{,photocat}$ and Table 3.50 compiles the comparative HDS data of $(HA\text{-}TiO_2)_{,as\text{-}is}$, $(HA\text{-}TiO_2)_{,photocat}$, and $(HA - TiO_2)_{,dark}$.

The hydrodynamic size of $(HA\text{-}TiO_2)_{,photocat}$ sample comprised not only $HA\text{-}TiO_2$ heteroaggregates but also homo-aggregates of TiO_2 and hetero-aggregates/agglomerates of $HA_{,photocat}$. It must be noted that HA was composed of degraded smaller organic structures so the heteroaggregates would be a mixture of all these entities *i.e.*, $TiO_{2,irr}$ and $HA_{,photocat}$. Also, the term "hetero-aggregate/agglomerate" was used for $HA_{,photocat}$ agglomeration/aggregation due to the polydispersed structures comprising HA. In Table 3.49 the HDS data of $(HA\text{-}TiO_2)_{,photocat}$ was compared with both $HA_{,photocat}$ and $TiO_{2,irr}$ to identify the corresponding aggregates and agglomerates of the binary system. HDS results of $TiO_{2,irr}$ showed that larger aggregates formed after solar irradiation, however these structures were not colloidally stable and precipitated during DLS measurements.

HDS of TiO_2 in colloidal systems was reported as reproducible in aqueous suspensions and the agglomerate size range was reported as 200-400 nm (Cardot et al., 2001). These results were

consistent with the $TiO_{2,as\text{-}is}$ and $TiO_{2,irr}$ results. According to the information, 98% of number-weighted HDS could be regarded as homo-aggregation of TiO_2 (Table 3.47, initial). On the other hand, it must be considered that HA homo-aggregates and smaller hetero-aggregates also could be in this range. However, remaining 2% could be a mixture of web-like $HA_{,photocat}$ hetero-aggregates and $TiO_{2,irr}$-$HA_{,photocat}$ hetero-aggregates structures sizing approximately 1.7-2.5 µm. The structures over 3 microns that form over time might be the hetero-agglomerates formed by photocatalytically degraded HA structures. Agglomeration formation can be signified by dissaglomeretion of these structures during the time dependent DLS measurement, on the other hand, aggregated structures remain stable for 120 min.

HDS data of $HA_{,photocat}$ supported the formation larger structures by degraded organic moieties via hetero-aggregation, even the HA degradation evidenced with drastic decrease of DOC and increase of lower molecular size fraction. This aggregate formation might also be attributed to the development of peptide linkages by photocatalytically degraded HA structures. These results were in line with the characterization results reported by Bekbolet and Sen-Kavurmaci (Bekbolet and Sen-Kavurmaci, 2015). Also, these highly reactive organic moieties could easily interact with TiO_2 surface via electric repulsion and stearic hindrance and might form $HA_{,photocat}$-$TiO_{2,irr}$- $HA_{,photocat}$ structures as shown in Figure 3.76 c. These structures might show net like framework that has non-polar nature. Therefore, even TiO_2 agglomeration occurs surface adsorbed organic moieties stabilizes the hetero-agglomerate structures (Wang et al., 2016).

Table 3.50 compiles the comparison results of HDS and cumulative ratio results of intensity-weighted HDS values of $(HA\text{-}TiO_2)_{,as\text{-}is}$, $(HA\text{-}TiO_2)_{,dark}$, and $(HA\text{-}TiO_2)_{,photocat}$. Effect of solar light and mixing over "as-is" conditions were followed by HDS of $(HA\text{-}TiO_2)_{,photocat}$, also sole effect of solar irradiation over HDS can be observed by comparing "dark" and "photocat" binary systems. Both $HA_{,photocat}$ hetero-aggregates and $TiO_{2,irr}$ homo-aggregates created bigger aggregates/agglomerates in the presence of solar irradiation. As indicated above in comparison to the "as-is" and "dark" conditions of binary systems $(HA\text{-}TiO_2)_{,photocat}$ binary system exhibits stabilized structures around 2 µm during 120 min. Degraded HA structures might increase the stearic hindrance and electric repulsion which stabilizes $TiO_{2,irr}$ structures which probably creates linkages between $TiO_{2,irr}$ aggregates and forms more stable hetero-agglomerates in comparison to the "dark" condition (Gilli and Gilli, 2013; Wells and Stretz, 2019).

Table 3.47. Intensity-, volume-, surface area- and number-weighted HDS and cumulative ratios of $(HA\text{-}TiO_2)_{,photocat}$.

	HDS, nm	Cumulative Ratio, %			
		Intensity	Volume	Surface Area	Number
Initial	253.2-286.5	8%	4%	17%	58%
	324.1-414.8	18%	25%	56%	40%
	1822.5	7%	3%	2%	1%
	2061.8	15%	15%	6%	1%
	2332.4	21%	29%	11%	-
	2638.7	19%	19%	7%	-
	2985.1-3376.9	13%	5%	1%	-
30 min	218.5-242.3	10%	6%	24%	49%
	268.6-330.2	17%	11%	37%	50%
	1721.5-1908.6	19%	28%	16%	1%
	2116.2	22%	15%	17%	-
	2346.2	19%	28%	9%	-
	2603.1-2884.1	13%	12%	5%	-
60 min	261.8-306.6	8%	5%	19%	86%
	359.1	12%	7%	12%	3%
	420.6-576.9	17%	52%	74%	11%
	2042.5	8%	8%	2%	-
	2392.1	16%	6%	2%	-
	2801.6	21%	1%	-	-
	3281.3-3843.0	18%	21%	3%	-
90 min	228.9-253.1	12%	6%	24%	47%
	279.9-342.4	20%	13%	39%	52%
	1711.6-1892.7	20%	31%	16%	1%
	2093.0	21%	17%	8%	-
	2314.5	17%	30%	12%	-
	2559.5-2830.3	10%	3%	1%	-
120 min	224.9-302.4	17%	11%	38%	96%
	350.5-471.2	23%	50%	54%	4%
	1538.4-1783.6	14%	11%	3%	-
	2068.0	17%	15%	3%	-
	2397.6	17%	8%	1%	-
	2779.8-3222.8	12%	5%	1%	-

Table 3.48. Intensity-weighted HDS profile of $(HA\text{-}TiO_2)_{,photocat}$. Time dependent HDS cluster maximas, HDS range and min-max diameter difference with respect to multi-size distribution.

	Cluster				
Time, min	Max 1, nm	Max 2, nm	Max 3, nm	Range, nm	Difference, nm
Initial	120.8	324.1	2332.4	94.4-4889.2	4794.8
30	268.6	2116.2	-	160.3-4358.2	4197.9
60	74.0	359.1	2801.6	46.0-7230.7	7184.7
90	279.9	2093.0	-	169.3-4232.2	4063.0
120	59.4	350.5	2068.0	38.1-4332.2	4294.1

Table 3.49. Comparison of intensity-weighted HDS values of $HA_{,photocat}$, $TiO_{2,irr}$, and $(HA\text{-}TiO_2)_{,photocat}$.

	$HA_{,photocat}$		$TiO_{2,irr}$		$(HA\text{-}TiO_2)_{,photocat}$	
	HDS, nm	CR, %	HDS, nm	CR, %	HDS, nm	CR, %
Initial	52.3-62.7	24%	169.6-196.7	19%	253.2-286.5	8%
	75.2-90.1	19%	211.8-245.6	20%	324.1-414.8	18%
	6961.0-10000	57%	745.9-803.3	9%	1822.5	7%
	-	-	865.0	15%	2061.8	15%
	-	-	931.5	20%	2332.4	21%
	-	-	1003.1-1080.2	17%	2638.7	19%
			-	-	2985.1-3376.9	13%
30 min	45.8-51.7	9%	149.7-174.9	17%	218.5-242.3	10%
	155.0-175.1	50%	189.0-220.9	18%	268.6-330.2	17%
	186.1-210.2	41%	767.8-829.9	25%	1721.5-1908.6	19%
	-	-	897.1	21%	2116.2	22%
	-	-	969.8-1048.3	19%	2346.2	19%
			-	-	2603.1-2884.1	13%
60 min	88.3-106.2	30%	137.8-162.9	17%	261.8-306.6	8%
	116.4-139.8	29%	177.1-209.4	18%	359.1	12%
	554.8-666.7	29%	735.3-799.5	16%	420.6-576.9	17%
	730.8-801.1	12%	869.3	19%	2042.5	8%
	-	-	945.2-1117.5	30%	2392.1	16%
	-	-	-	-	2801.6	21%
			-	-	3281.3-3843.0	18%
90 min	21.3-26.0	2%	155.2-180.0	16%	228.9-253.1	12%
	86.8-106.2	20%	193.8-224.8	24%	279.9-342.4	20%
	117.4-129.8	12%	735.1-791.6	23%	1711.6-1892.7	20%
	175.4-237.0	52%	852.4	19%	2093.0	21%
	262.0-289.7	14%	917.9-988.5	18%	2314.5	17%
	-	-	-	-	2559.5-2830.3	10%
120 min	99.0-113.4	37%	100.3-139.9	22%	224.9-302.4	17%
	121.3-129.8	19%	486.9-529.1	19%	350.5-471.2	23%
	438.7-502.2	33%	574.9	23%	1538.4-1783.6	14%
	537.4-575.0	11%	624.8	21%	2068.0	17%
	-	-	678.9-737.8	15%	2397.6	17%
	-	-	-	-	2779.8-3222.8	12%

Table 3.50. Comparison of intensity-weighted HDS values of $(HA\text{-}TiO_2)_{,as\text{-}is}$, $(HA\text{-}TiO_2)_{,dark}$, $(HA\text{-}TiO_2)_{,photocat}$ and $(HA_{,pho}\text{-}TiO_2)$.

	$(HA\text{-}TiO_2)_{,as\text{-}is}$		$(HA\text{-}TiO_2)_{,dark}$		$(HA\text{-}TiO_2)_{,photocat}$		$(HA_{,pho}\text{-}TiO_2)$		
	HDS, nm	CR, %	HDS, nm	CR, %	HDS, nm	CR, %	HDS, nm	CR, %	
Initial	156.1-184.7	9%	Dark Mixing		Solar Irradiation and Mixing		60 min Solar Irradiation onto HA and 5 min Mixing with TiO_2		
	200.9-237.3	16%							
	840.8	9%							
	914.7	18%							
	995.1	25%							
	1082.5-1177.6	23%							
30 min	157.0-172.2	8%							
	188.9-227.3	21%							
	911.1-999.5	21%							
	1096.4	22%							
	1202.7-1447.3	28%							
60 min	193.0-208.8	15%	104.3-319.9	13%	253.2-286.5	8%	148.5-175.3	14%	Initial
	225.8-264.3	16%	362.3	14%	324.1-414.8	18%	190.5-207.0	8%	
	1005.2	13%	410.3-464.7	16%	1822.5	7%	783.0	11%	
	1087.4	18%	980.9-1110.9	20%	2061.8	15%	850.9	19%	
	1176.3	21%	1258.2	17%	2332.4	21%	924.6	25%	
	1272.5-1376.5	17%	1425.0	13%	2638.7	19%	1004.8-1091.9	23%	
	-	-	1613.9-1827.9	7%	2985.1-3376.9	13%	-	-	
90 min	164.6-192.0	18%	209.4-230.0	12%	218.5-242.3	10%	165.4-188.9	14%	30 min
	207.3-223.9	9%	252.6-304.7	10%	268.6-330.2	17%	201.9-230.5	9%	
	766.9-828.2	18%	1364.5-1498.6	16%	1721.5-1908.6	19%	623.1-665.8	12%	
	894.5	21%	1645.8	20%	2116.2	22%	711.5	19%	
	966.0	20%	1807.5	18%	2346.2	19%	760.2	22%	
	1043.3-1126.7	14%	1985.1-2180.1	14%	2603.1-2884.1	13%	812.3-868.0	18%	

Table 3.51. Comparison of intensity-weighted HDS values of $(HA\text{-}TiO_2)_{,as\text{-}is}$, $(HA\text{-}TiO_2)_{,dark}$, $(HA\text{-}TiO_2)_{,photocat}$ and $(HA_{,pho}\text{-}TiO_2)$ (Continue).

120 min	143.8-156.6	9%	212.8-291.0	18%	261.8-306.6	8%	113.4-154.9	20%	60 min
	170.5-202.2	15%	340.2	14%	359.1	12%	538.2-581.8	22%	
	789.6	8%	397.8-465.2	15%	420.6-576.9	17%	628.9	23%	
	859.8	16%	1390.4-1625.8	20%	2042.5	8%	679.9	21%	
	936.2	25%	1901.1	18%	2392.1	16%	734.9-794.4	13%	
	1019.4	17%	2229.9-2599.3	15%	2801.6	21%	-	-	
	1110.0-1208.7	10%	-	-	3281.3-3843.0	18%	-	-	
150 min	138.7-164.4	14%	155.0-186.5	15%	228.9-253.1	12%	204.4-234.5	19%	90 min
	179.0-194.9	11%	204.6-246.2	14%	279.9-342.4	20%	251.2-288.1	22%	
	761.3-829.0	25%	1082.6	11%	1711.6-1892.7	20%	753.8-807.2	20%	
	902.7	24%	1187.6	17%	2093.0	21%	864.5	19%	
	982.9	17%	1302.8	23%	2314.5	17%	926.0	13%	
	1070.2-1165.4	9%	1429.1-1567.7	22%	2559.5-2830.3	10%	991.8-1062.3	7%	
180 min	39.8-175.3	12%	172.5-207.6	11%	224.9-302.4	17%	225.9-239.9	13%	120 min
	200.6-262.6	20%	227.8-274.1	21%	350.5-471.2	23%	254.7	15%	
	674.9-772.4	18%	1098.7	9%	1538.4-1783.6	14%	270.5-304.9	20%	
	883.9	20%	1205.2	17%	2068.0	17%	749.8-796.1	14%	
	1011.5	17%	1322.1	22%	2397.6	17%	845.4	15%	
	1157.5-1324.5	13%	1450.3-1590.9	20%	2779.8-3222.8	12%	897.6-1012.0	23%	

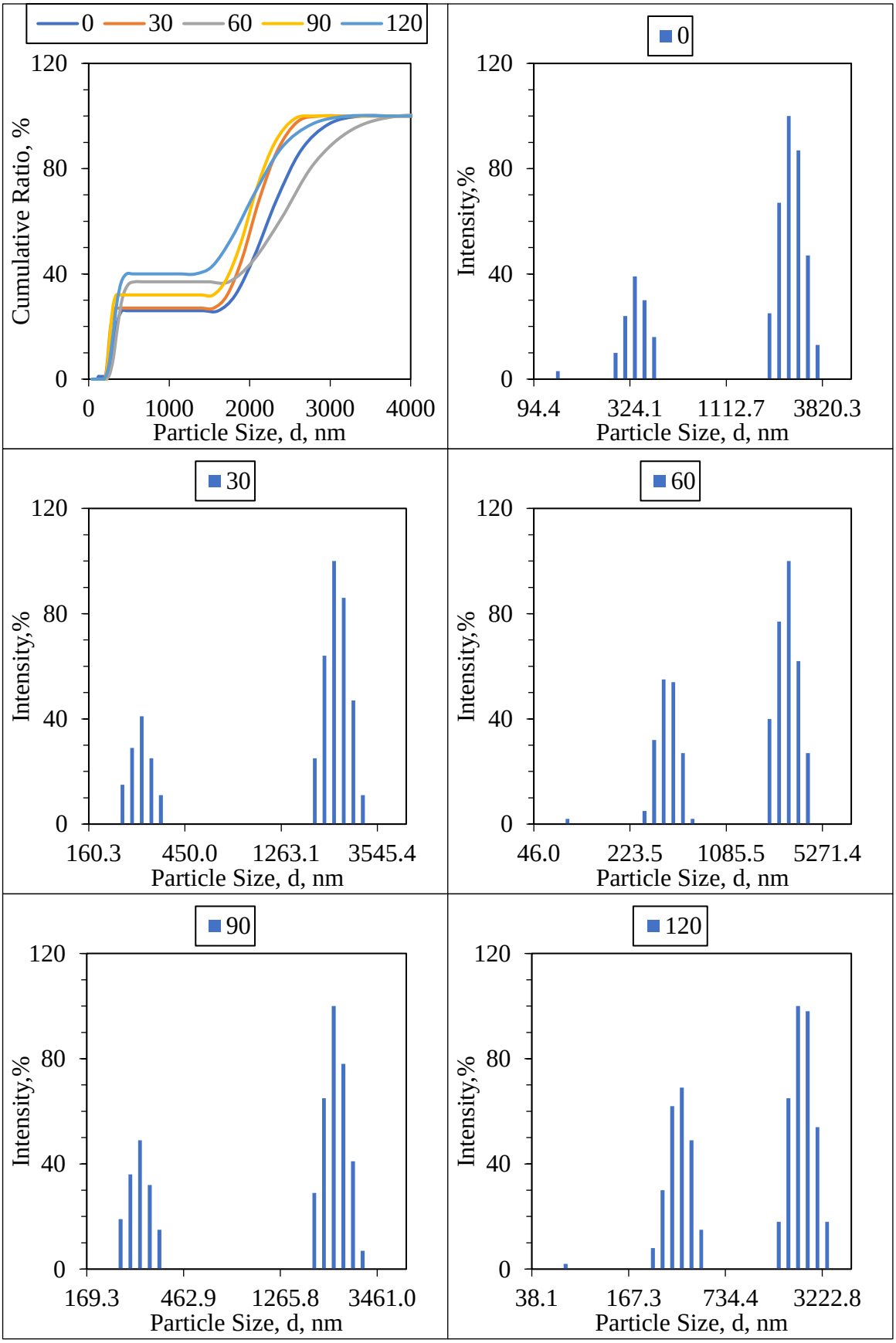


Figure 3.77. The cumulative ratio comparison and hydrodynamic size of $(HA\text{-}TiO_2)_{,photocat}$ as intensity-weighted HDS in 30 min intervals.

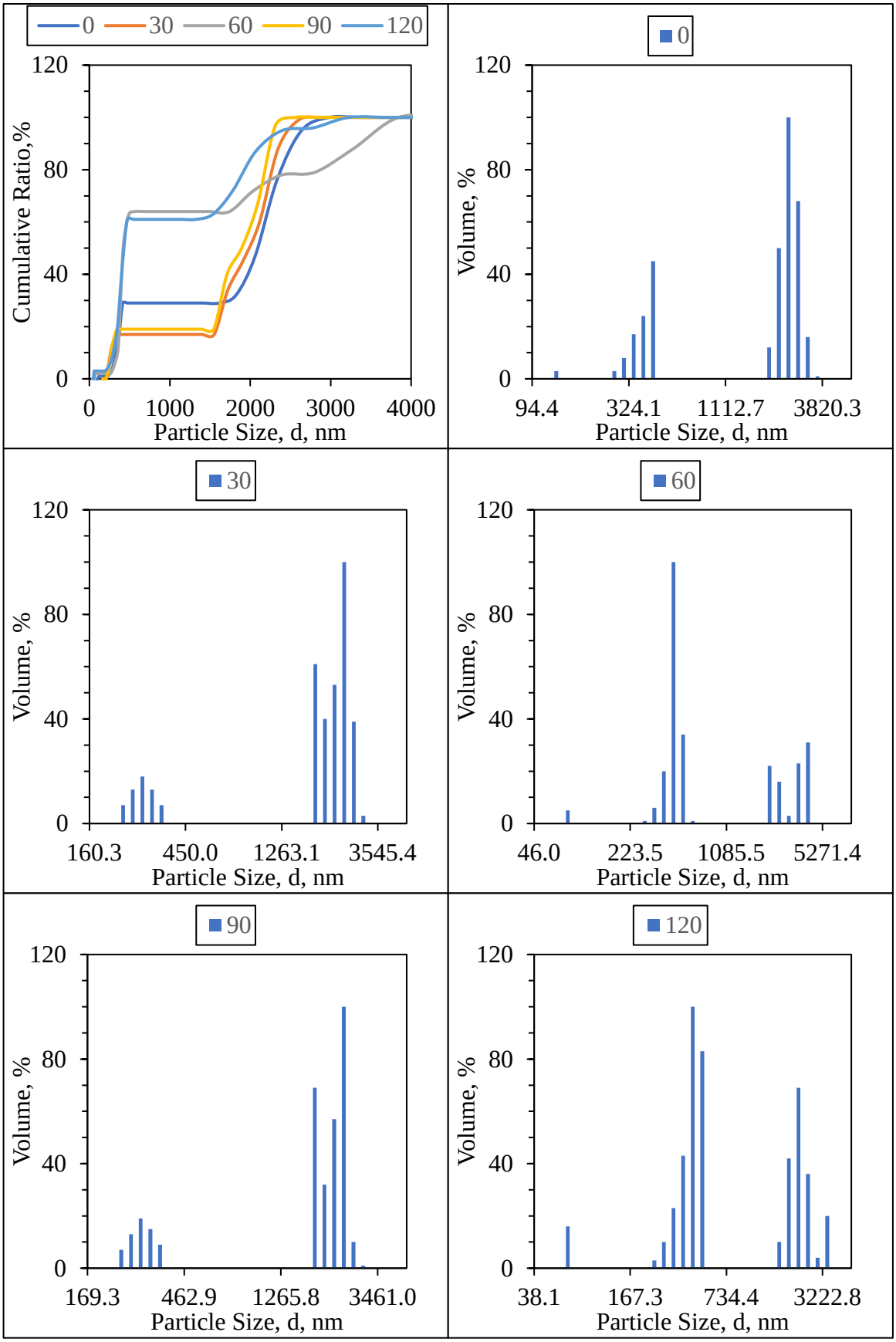


Figure 3.78. The cumulative ratio comparison and hydrodynamic size of $(HA\text{-}TiO_2)_{,photocat}$ as volume-weighted HDS in 30 min intervals.

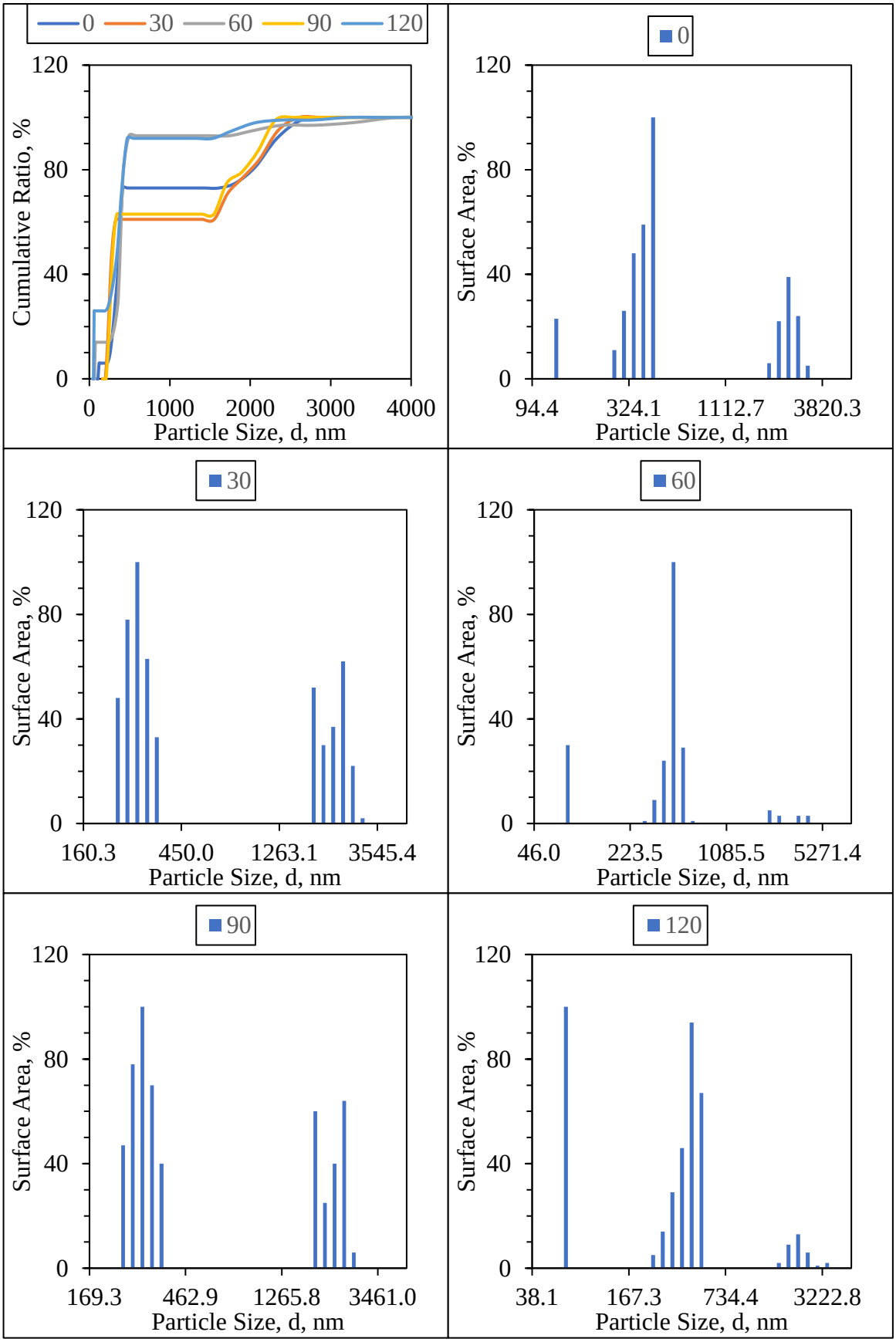


Figure 3.79. The cumulative ratio comparison and hydrodynamic size of $(HA\text{-}TiO_2)_{,photocat}$ as surface area-weighted HDS in 30 min intervals.

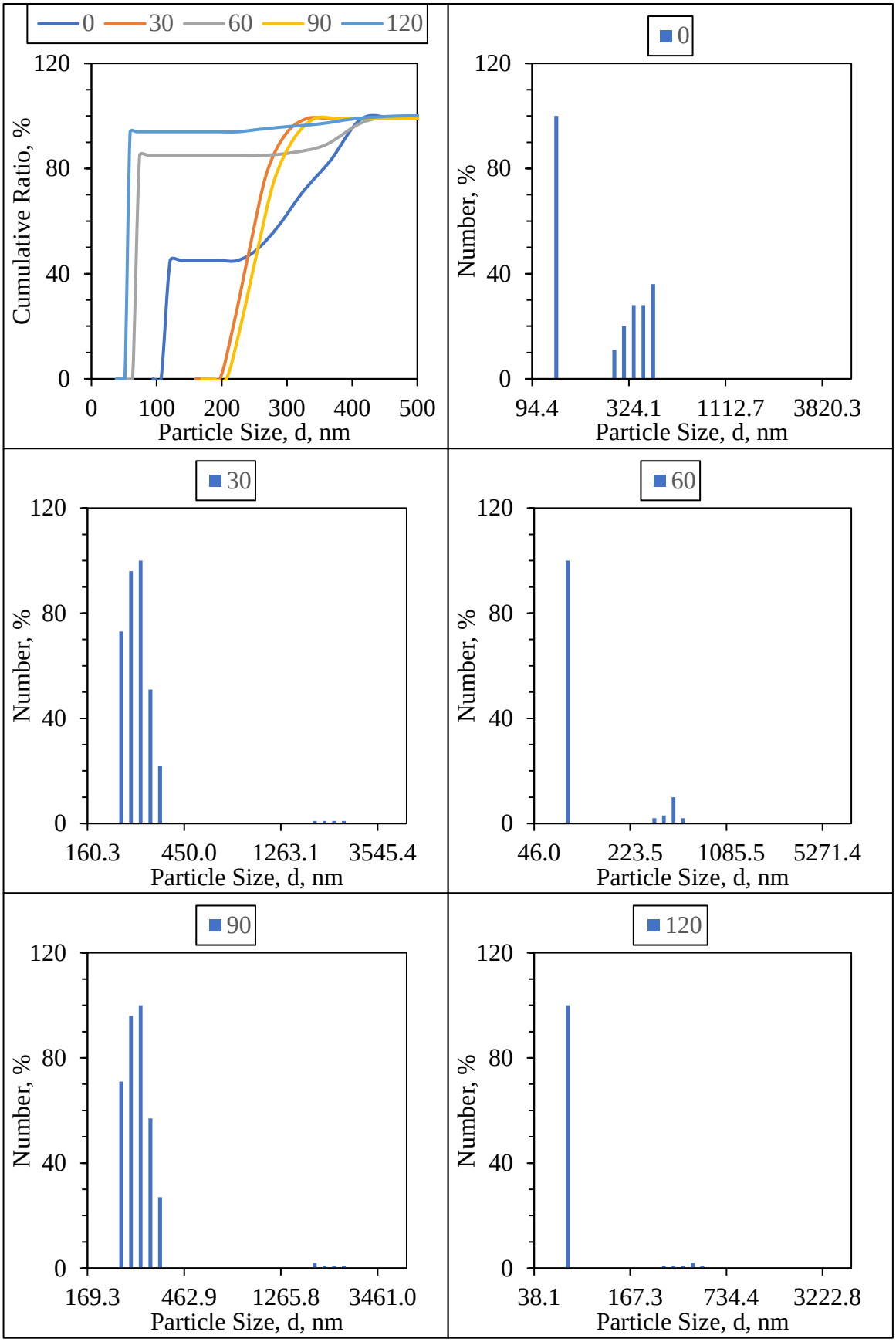


Figure 3.80. The cumulative ratio comparison and hydrodynamic size of $(HA\text{-}TiO_2)_{,photocat}$ as number-weighted HDS in 30 min intervals.

3.5.5. Hydrodynamic Size Assessment of (HA-Fe-TiO_2)$_{as-is}$

Hetero-aggregation and hetero-agglomeration of HA and Fe doped TiO_2 was investigated by suspending Fe-TiO_2 into HA (DOC: 4.80 mgL^{-1}) to achieve 0.25 mgL^{-1} Fe-TiO_2 concentration. The detailed preparation methodology was mentioned in the materials and methods section. As indicated in (HA-TiO_2)$_{as-is}$ same methodology was used to prepare (HA-Fe-TiO_2)$_{as-is}$. Fe-TiO_2 was weighted and added into HA and magnetically stirred for 30 min and 4 mL of prepared suspension was directly transferred to polystyrene cuvette for DLS measurement.

The obtained HDS results were compiled in the Table 3.51 and Table 3.52 as intensity-, volume-, surface area-, and number-weighted HDS and their corresponding CR% and a more detailed Table was constructed by giving the HDS range, min-max of the HDS range and maxima of CR% as intensity-weighted HDS. The graphical representation of the data represented in Table 3.51 and Table 3.52 has been shown in Figure 3.81, Figure 3.82, Figure 3.83 and Figure 3.84 as intensity-, volume, surface area-, and number-weighted HDS.

The initial HDS of (HA-Fe-TiO_2)$_{as-is}$ showed three maxima around 203.7 nm, 227.0 nm and 1192.2 nm. The maxima around 1192.2 nm might be related to the agglomeration formation, however the CR% of number-weighted HDS was very low so existence of this bigger cluster almost negligible (Table 3.52). Because the (HA-Fe-TiO_2)$_{as-is}$ was a complex media structures cannot be addressed as aggregates and agglomerates by only evaluating CR% of HDS. The system could be defined by comparing HA$_{as-is}$, Fe-$TiO_{2,as-is}$ and (HA-Fe-TiO_2)$_{as-is}$, which was represented in Table 3.53. However, the (HA-Fe-TiO_2)$_{as-is}$ system not only contained HA adsorbed onto Fe-TiO_2 hetero-aggregates/hetero-agglomerates but also HA hetero-aggregates, TiO_2 homo-aggregates, and HA chelated with Fe(II) ions. Even the substitutional doping was achieved for Fe-TiO_2, some of the Fe stays in the surface of TiO_2 which was beneficial for photocatalytic efficiency of Fe-TiO_2 under visible light (Teoh et al., 2007; Adán et al., 2014). The dopant Fe was in form of Fe(II) and can form chelates with the carboxylic acid (Arana et al., 2003; Adán et al., 2009), and could form HA-Fe-TiO_2 hetero-aggregation. Since HA resumed a supramolecular structure at neutral pH and low IS, hetero-aggregates formed by HA-Fe-TiO_2 might be comprised of aggregate structure Fe-TiO_2 as core and HA covering the core as attached -COOH sites to surface Fe(II). This hetero-aggregate forms a nearly spherical structure and increases the colloidal stability of Fe-TiO_2 aggregates in the media. The initial leaching amount of Fe-TiO_2 (1 wt%) prepared by in situ solgel method was reported as 0.054 mgL^{-1} (5.4%) by Türkten and Uyguner-Demirel (Türkten and Uyguner-Demirel, 2020). Adan and colleagues reported the leaching amount of Fe (from 1 wt% Fe doped TiO_2) was 4.7% (Adán et al.,

2014). As mentioned before (in section 3.5.1) in $HA_{,as\text{-}is}$ could tend to form physical hydrogel structure above 2000 nm, the cluster observed around 2220.7 nm-2475.4 nm might corresponding HA hetero-agglomeration. These physical hydrogels disappear with the settlement of the solution, so the presence of these structures was evidenced with the disappearance of hydrodynamic structures above 2000 nm at 30 min (Gilli and Gilli, 2013; Wells and Stretz, 2019). On the other hand, when the HDS of $HA_{,as\text{-}is}$, $Fe\text{-}TiO_{2,as\text{-}is}$, and $(HA\text{-}Fe\text{-}TiO_2)_{,as\text{-}is}$ compared the clusters above 1000 nm were mostly similar with the $Fe\text{-}TiO_{2,as\text{-}is}$ rather than $HA_{,as\text{-}is}$ (Table 3.53). For instance, the intensity-weighted HDSs of $Fe\text{-}TiO_{2,as\text{-}is}$ and respective CR% were 1416.8-1566.7 nm (10%), 1732.5 nm (16%), 1915.9 nm (21%) and 2118.6-2342.8 nm (17%) and the intensity-weighted HDSs of $(HA\text{-}Fe\text{-}TiO_2)_{,as\text{-}is}$ with the CR% were 1438.3-1603.2 nm (11%), 1787.2 nm (17%), 1991.2 nm (21%), and 2220.7-2475.4 nm (20%) (Table 3.53). The removal ratio could be decisive as deciding whether these bigger cluster corresponding mono system or binary system. The removal ratio of $Fe\text{-}TiO_{2,as\text{-}is}$ was approximately 35% and the removal efficiency of $(HA\text{-}Fe\text{-}TiO_2)_{,as\text{-}is}$ was approximately 20% at the end of 30 min (for the same wavelength). Hence the HDS of mono ($Fe\text{-}TiO_2$) and binary system ($HA\text{-}Fe\text{-}TiO_2$) might be similar but definitely not analogous to each other. The precipitated amount was related with the $Fe\text{-}TiO_2$ homo-aggregates, and dissaglomeration of physical hydrogel of HA and remaining part was the heteroaggregates formed by HA adsorbed onto $Fe\text{-}TiO_2$. Because the percentage of removal efficiency was not comparable with the CR% of HDS, the exact ratio of these structures cannot be reported. However, the 15% removal efficiency might be related to the colloidal stabilization effect of HA over $Fe\text{-}TiO_2$. Adan and colleagues were reported that short chain organic acids were more prone to interact with Fe ions so, $Fe\text{-}TiO_2$ aggregates might be covered with <100 kDa molecular size fraction of HA (Adan et al., 2014). Because of the thin layer formed by HA on the surface of $Fe\text{-}TiO_2$ aggregates, the HDS of binary system might be almost similar with the HDS of $Fe\text{-}TiO_2$ aggregate. This trend also explains the same size and colloidally more stable structures in $(HA\text{-}Fe\text{-}TiO_2)_{,as\text{-}is}$ system. The middle-sized cluster around 500-800 nm could be visualized after the dissaglomeration of the physical hydrogel above 2000 nm by removal of the masking effect (Table 3.51, Table 3.52). These middle-sized clusters might be mostly formed by $HA\text{-}Fe\text{-}TiO_2$ heteroaggregates by considering the colloidally stable appearance during 180 min. The comparison of the CR% of volume-, and surface area-weighted HDS also showed that the middle size cluster was mostly formed by spherical structures.

The intensity-weighted HDS of $(HA\text{-}TiO_2)_{,as\text{-}is}$ and $(HA\text{-}Fe\text{-}TiO_2)_{,as\text{-}is}$ was compared in Table 3.54. The HDS of $(HA\text{-}Fe\text{-}TiO_2)_{,as\text{-}is}$ binary system showed approximately two times bigger clusters around 2220.7-2475.4 nm in comparison to $(HA\text{-}TiO_2)_{,as\text{-}is}$ at initial time (Table 3.54). This clusters might be related with the formation of bigger $Fe\text{-}TiO_2$ aggregates as core in the $HA\text{-}Fe\text{-}TiO_2$

agglomerates. As indicated in the previous paragraph the hetero-agglomerates of $(HA\text{-}Fe\text{-}TiO_2)_{,as\text{-}is}$ above 1000 nm might be composed of physical hydrogel structures of HA and/or HA-Fe-TiO_2 agglomerates. However, after 30 min this bigger cluster disappeared via precipitation of HA-Fe-TiO_2 agglomerates and dissaglomeration of metachemical hydrogel structures of HA. The disappearance of the bigger cluster showed the even the small clusters around 100-200 nm were approximately similar in both $(HA\text{-}TiO_2)_{,as\text{-}is}$ and $(HA\text{-}Fe\text{-}TiO_2)_{,as\text{-}is}$ binary systems, the bigger clusters of $(HA\text{-}Fe\text{-}TiO_2)_{,as\text{-}is}$ were slightly smaller than $(HA\text{-}TiO_2)_{,as\text{-}is}$. This trend might be related to the complexation of carboxylic sites of HA with the Fe remained onto the surface of Fe-TiO_2. Because Fe-TiO_2 had more adsorption sites than TiO_2, the HA adsorbed onto Fe-TiO_2 could form a thinner layer which might cause smaller hydrodynamic size. As evidenced by the findings of Birben and colleagues, the initial surface adsorption rate of HA onto both TiO_2 and Fe-TiO_2 was 33% and 45.6%, respectively (Birben et al., 2017). Even though the initial surface adsorption rate of HA was higher for Fe-TiO_2 the HDS range of $(HA\text{-}Fe\text{-}TiO_2)_{,as\text{-}is}$ was narrower in comparison to the $(HA\text{-}TiO_2)_{,as\text{-}is}$ so, “tail, train, loop” formation with a short layer thickness was proper to visualize HA-Fe-TiO_2 heteroaggregates (Figure 3.63). Also, during 180 min the intensity-weighted CR% of the structures around 100-200 nm in $(HA\text{-}Fe\text{-}TiO_2)_{,as\text{-}is}$ binary system was higher than $(HA\text{-}TiO_2)_{,as\text{-}is}$. This phenomenon showed that affection of smaller size fractions of HA formed HA-Fe-TiO_2 hetero-agglomerates even in smaller size and prohibit the further homo-agglomeration of Fe-TiO_2 structures. Hence the smaller clusters of $(HA\text{-}Fe\text{-}TiO_2)_{,as\text{-}is}$ were colloidally more stable than $(HA\text{-}TiO_2)_{,as\text{-}is}$.

Table 3.52. Intensity-weighted HDS profile of $(HA\text{-}Fe\text{-}TiO_2)_{,as\text{-}is}$. Time dependent HDS cluster maximas, HDS range and min-max diameter difference with respect to multi-size distribution.

	Cluster				
Time, min	Max 1, nm	Max 2, nm	Max 3, nm	Range, nm	Difference, nm
Initial	203.7	227.0	1992.2	118.3-3822.0	3703.7
30	168.8	936.0		114.4-1381.5	1267.1
60	204.7	931.4	-	130.0-1467.4	1337.4
90	241.2	903.0	964.6	173.4-1433.3	1259.9
120	134.9	490.5	-	97.7-770.8	673.1
150	187.6	658.0	-	115.2-1071.8	956.6
180	260.7	675.1	791.1	62.6-10000.0	9937.4

Table 3.53. Intensity-, volume-, surface area- and number-weighted HDS and cumulative ratios of $(HA\text{-}Fe\text{-}TiO_2)_{,as\text{-}is}$.

	HDS, nm	Cumulative Ratio, %			
		Intensity	Volume	Surface Area	Number
Initial	163.9-203.7	15%	10%	41%	72%
	227.0-282.1	16%	8%	25%	27%
	1438.3-1603.2	11%	12%	6%	1%
	1787.2	17%	17%	7%	-
	1992.2	21%	46%	19%	-
	2220.7-2475.4	20%	7%	2%	-
30 min	144.4-168.8	20%	10%	35%	76%
	182.5-197.2	12%	4%	13%	21%
	801.0-865.9	25%	34%	23%	1%
	936.0	23%	14%	9%	1%
	1011.8-1093.7	20%	38%	20%	1%
60 min	175.9-189.8	13%	6%	17%	41%
	204.7	16%	5%	15%	30%
	220.8-238.2	18%	6%	14%	23%
	742.1-800.5	12%	37%	26%	4%
	863.5	14%	12%	8%	-
	931.4	16%	10%	6%	1%
	1004.7-1083.8	11%	24%	13%	1%
90 min	211.4-225.8	19%	9%	21%	43%
	241.2	19%	7%	18%	29%
	257.7-275.3	19%	9%	17%	23%
	791.3-903.0	19%	32%	21%	3%
	964.6-1100.7	22%	43%	23%	2%
120 min	118.5-134.9	14%	4%	14%	55%
	143.9-153.4	11%	3%	7%	21%
	431.1-459.8	25%	63%	56%	18%
	490.5	23%	21%	17%	5%
	523.2	17%	7%	4%	1%
	558.1-595.3	10%	2%	2%	-
150 min	152.2-175.0	18%	9%	24%	54%
	187.6	13%	5%	13%	24%
	201.2-215.7	12%	5%	10%	15%
	572.3-613.7	18%	11%	8%	1%
	658.0	19%	14%	10%	2%
	705.5-811.0	20%	56%	35%	4%
180 min	162.0-189.9	13%	7%	17%	43%
	222.5	18%	7%	15%	25%
	260.7	20%	7%	13%	15%
	305.5-358.0	17%	9%	13%	11%
	576.1-675.1	17%	15%	11%	2%
	791.1-1086.3	15%	55%	31%	4%

Table 3.54. Comparison of intensity-weighted HDS values of $HA_{,as\text{-}is}$, $Fe\text{-}TiO_{2,as\text{-}is}$ and $(HA\text{-}Fe\text{-}TiO_2)_{,as\text{-}is}$.

	$HA_{,as\text{-}is}$		$Fe\text{-}TiO_{2,as\text{-}is}$		$(HA\text{-}Fe\text{-}TiO_2)_{,as\text{-}is}$	
Initial	106.5-197.8	73%	155.0-189.5	16%	163.9-203.7	15%
	243.2-299.0	25%	209.5-256.2	20%	227.0-282.1	16%
	3561.7	1%	1416.8-1566.7	10%	1438.3-1603.2	11%
	6617.0	1%	1732.5	16%	1787.2	17%
	-	-	1915.9	21%	1992.2	21%
	-	-	2118.6-2342.8	17%	2220.7-2475.4	20%
60 min	155.4-182.0	72%	144.5-165.5	21%	175.9-189.8	13%
	185.3-188.5	28%	177.2	14%	204.7	16%
	-	-	189.6-203.0	12%	220.8-238.2	18%
	-	-	562.3-601.8	21%	742.1-800.5	12%
	-	-	644.1	18%	863.5	14%
	-	-	689.4-737.8	15%	931.4	16%
					1004.7-1083.8	11%
90 min	47.7-61.1	4%	158.1-170.3	11%	211.4-225.8	19%
	164.4-186.3	62%	183.3	15%	241.2	19%
	198.2-224.3	34%	197.4-228.9	25%	257.7-275.3	19%
	-	-	644.7-694.2	12%	791.3-903.0	19%
	-	-	747.5	13%	964.6-1100.7	22%
	-	-	804.9	15%	-	-
	-	-	866.7-933.3	9%	-	-
120 min	167.8-169.9	62%	128.5-147.0	17%	118.5-134.9	14%
	171.0-173.2	38%	157.1-179.6	19%	143.9-153.4	11%
	-	-	524.3-560.6	22%	431.1-459.8	25%
	-	-	599.4	21%	490.5	23%
	-	-	640.9-685.3	21%	523.2	17%
	-	-	-	-	558.1-595.3	10%

Table 3.55. Comparison of intensity-weighted HDS values of $(HA\text{-}TiO_2)_{,as\text{-}is}$ and $(HA\text{-}Fe\text{-}TiO_2)_{,as\text{-}is}$.

	$(HA\text{-}TiO_2)_{,as\text{-}is}$		$(HA\text{-}Fe\text{-}TiO_2)_{,as\text{-}is}$	
	HDS, nm	CR, %	HDS, nm	CR, %
Initial	156.1-184.7	9%	163.9-203.7	15%
	200.9-237.3	16%	227.0-282.1	16%
	840.8	9%	1438.3-1603.2	11%
	914.7	18%	1787.2	17%
	995.1	25%	1992.2	21%
	1082.5-1177.6	23%	2220.7-2475.4	20%
30 min	157.0-172.2	8%	144.4-168.8	20%
	188.9-227.3	21%	182.5-197.2	12%
	911.1-999.5	21%	801.0-865.9	25%
	1096.4	22%	936.0	23%
	1202.7-1447.3	28%	1011.8-1093.7	20%
60 min	193.0-208.8	15%	175.9-189.8	13%
	225.8-264.3	16%	204.7	16%
	1005.2	13%	220.8-238.2	18%
	1087.4	18%	742.1-800.5	12%
	1176.3	21%	863.5	14%
	1272.5-1376.5	17%	931.4	16%
	-	-	1004.7-1083.8	11%
90 min	164.6-192.0	18%	211.4-225.8	19%
	207.3-223.9	9%	241.2	19%
	766.9-828.2	18%	257.7-275.3	19%
	894.5	21%	791.3-903.0	19%
	966.0	20%	964.6-1100.7	22%
	1043.3-1126.7	14%	-	-
120 min	143.8-156.6	9%	118.5-134.9	14%
	170.5-202.2	15%	143.9-153.4	11%
	789.6	8%	431.1-459.8	25%
	859.8	16%	490.5	23%
	936.2	25%	523.2	17%
	1019.4	17%	558.1-595.3	10%
	1110.0-1208.7	10%	-	-
150 min	138.7-164.4	14%	152.2-175.0	18%
	179.0-194.9	11%	187.6	13%
	761.3-829.0	25%	201.2-215.7	12%
	902.7	24%	572.3-613.7	18%
	982.9	17%	658.0	19%
	1070.2-1165.4	9%	705.5-811.0	20%
180 min	39.8-175.3	12%	162.0-189.9	13%
	200.6-262.6	20%	222.5	18%
	674.9-772.4	18%	260.7	20%
	883.9	20%	305.5-358.0	17%
	1011.5	17%	576.1-675.1	17%
	1157.5-1324.5	13%	791.1-1086.3	15%

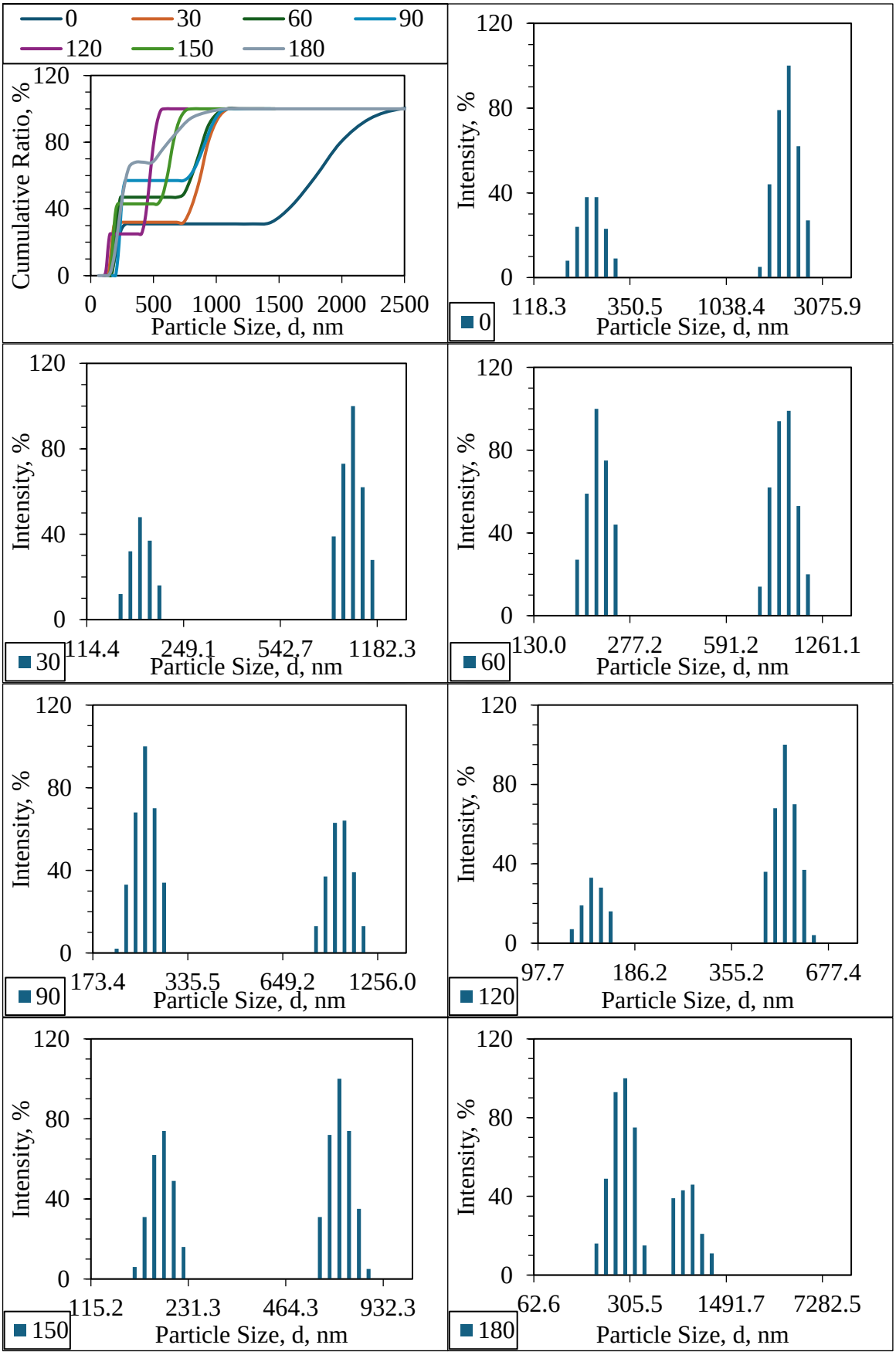


Figure 3.81. The cumulative ratio comparison and hydrodynamic size of $(HA\text{-}Fe\text{-}TiO_2)_{as\text{-}is}$ as intensity-weighted HDS in 30 min intervals.

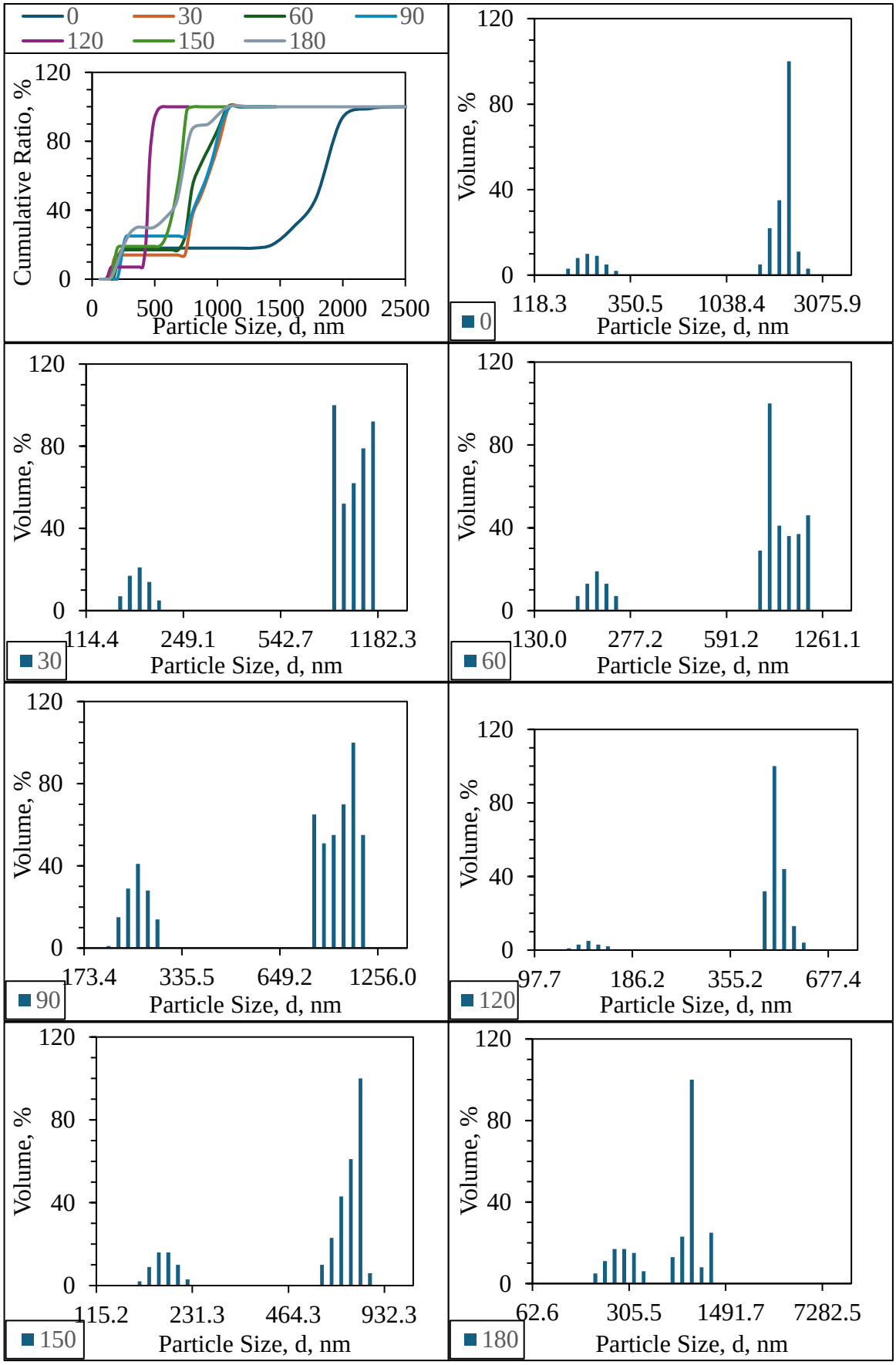


Figure 3.82. The cumulative ratio comparison and hydrodynamic size of $(HA\text{-}Fe\text{-}TiO_2)_{as\text{-}is}$ as volume-weighted HDS in 30 min intervals.

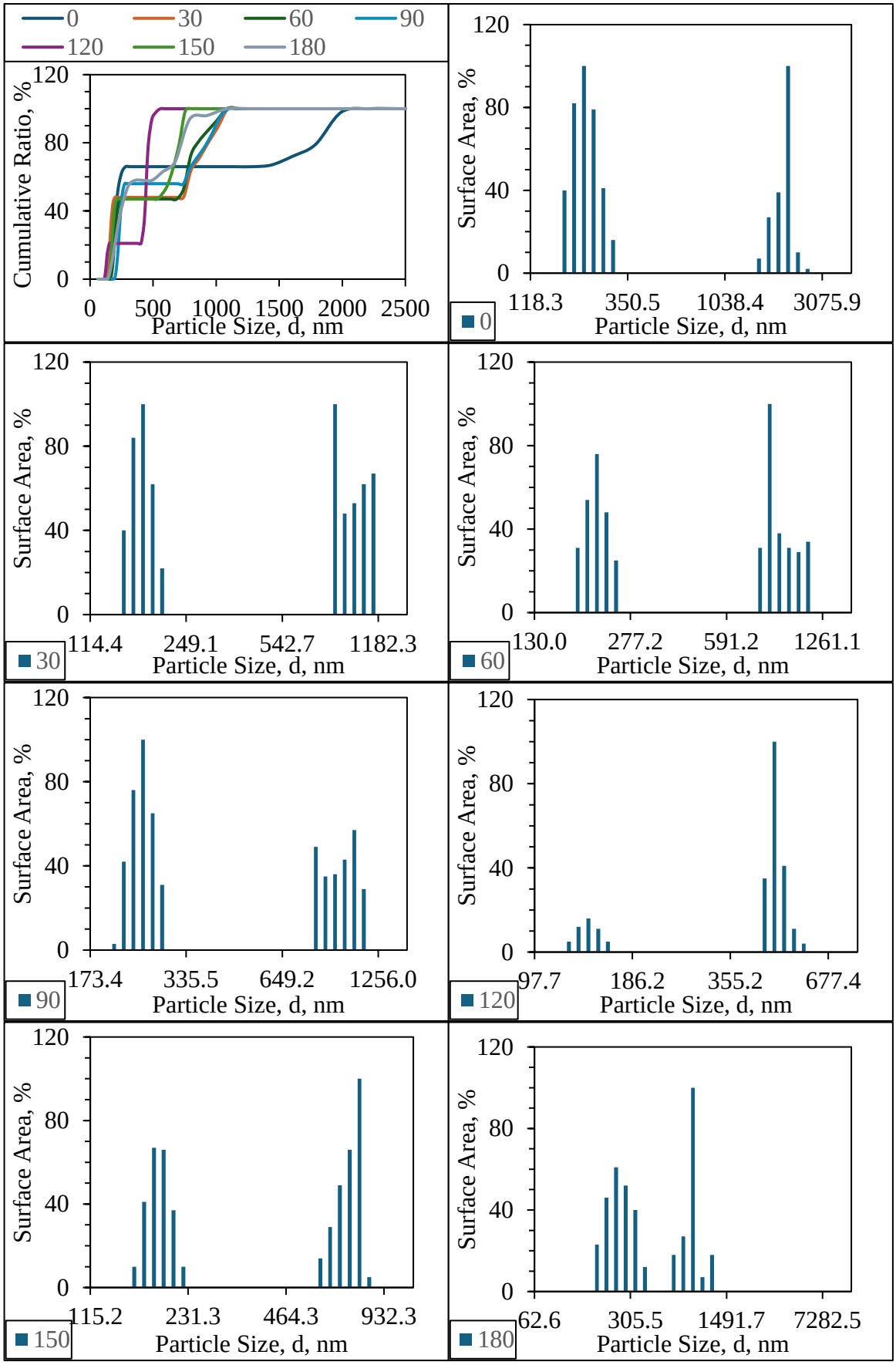


Figure 3.83. The cumulative ratio comparison and hydrodynamic size of $(HA\text{-}Fe\text{-}TiO_2)_{,as\text{-}is}$ as surface area-weighted HDS in 30 min intervals.

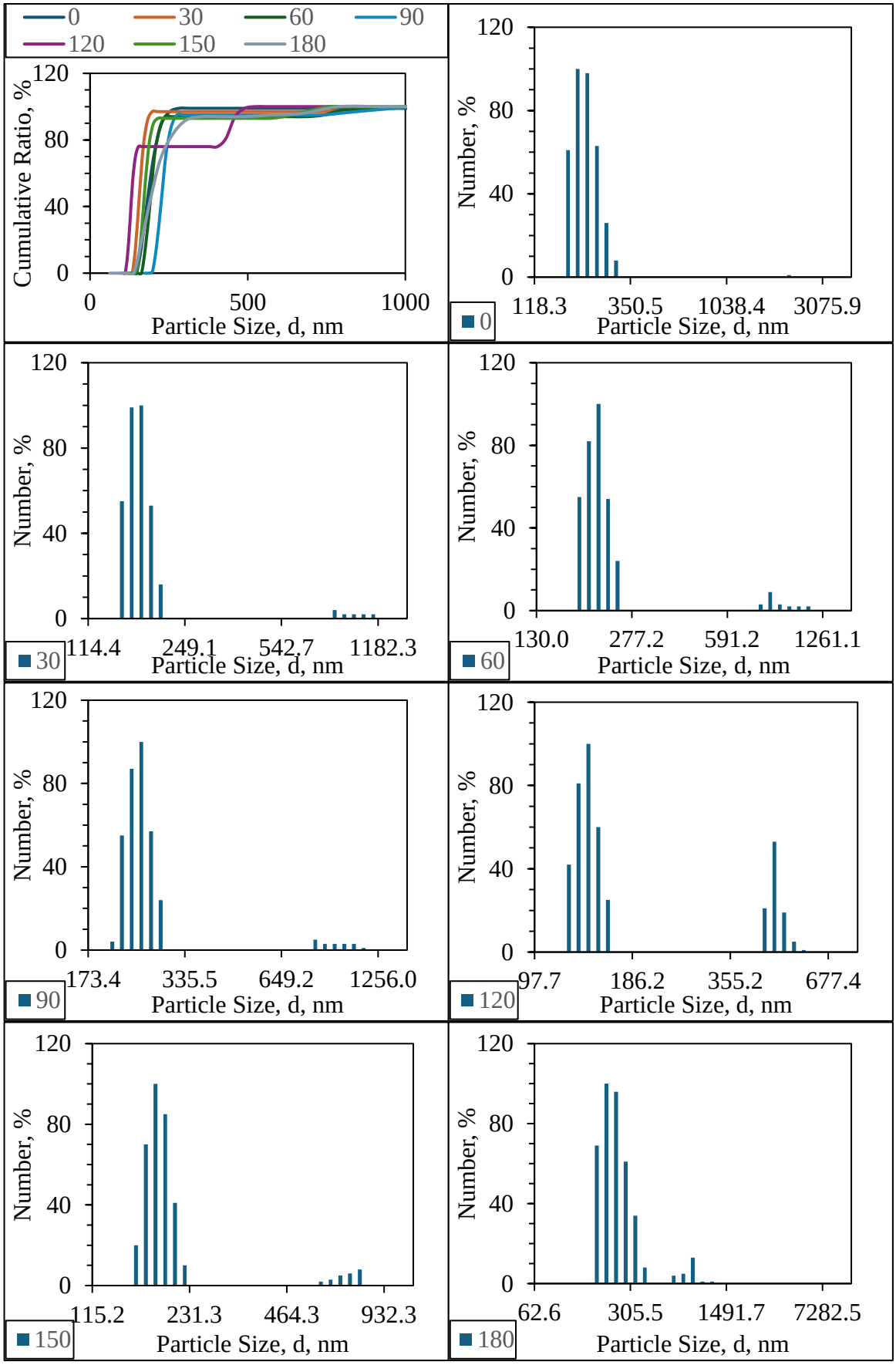


Figure 3.84. The cumulative ratio comparison and hydrodynamic size of $(HA\text{-}Fe\text{-}TiO_2)_{,as\text{-}is}$ as number-weighted HDS in 30 min intervals.

3.5.6. Hydrodynamic Size Assessment of (HA-Fe-TiO_2)$_{,dark}$

The effect of mixing on the aggregation/agglomeration behavior of the HA-Fe-TiO_2 binary system was investigated by following the HDS of HA-Fe-TiO_2 that mixed 60 min under dark conditions. 0.25 mgL^{-1} of Fe-TiO_2 was suspended in HA by magnetically stirring 30 min in room conditions then the solution was moved in the solar light simulator and continuously mixed for 60 min with magnetic stirrer under dark conditions. After 60 min, the obtained solution was named (HA-Fe-TiO_2)$_{,dark}$ and objected to DLS measurement.

HDS data (HA-Fe-TiO_2)$_{,dark}$ was compiled in Table 3.55 as intensity-, volume-, surface area, and number-weighted HDS with respective CR%. The graphical abstracts of intensity-, volume-, surface area, and number-weighted HDS were illustrated in Figure 3.85, Figure 3.86, Figure 3.87, and Figure 3.88, respectively. The HDS ranges, maxima and difference of maxima were gathered in Table 3.56. Finally, the intensity-weighted HDS of (HA-Fe-TiO_2)$_{,as-is}$ and (HA-Fe-TiO_2)$_{,dark}$, Table 3.57, and (HA-TiO_2)$_{,dark}$ and (HA-Fe-TiO_2)$_{,dark}$, Table 3.58, were gathered for comparative purposes.

The initial HDS of (HA-TiO_2)$_{,dark}$ showed a range of 1.8-177.8 nm with a 100% CR% of volume-, surface area-, and number-weighted HDS. The structures smaller than the crystalline size (16.4 nm) of Fe-TiO_2 were not expected to be detected, however Teoh and colleagues reported that the Fe leaching from Fe doped TiO_2 was higher in dark mixing conditions (Teoh et al., 2007). They reported that the highest Fe leaching amount was achieved in the presence of organic matter in dark conditions due to the chelation of Fe with OM. Hence the structures detected under 16.4 nm might be related with the leached Fe(II) ions and their chelate with HA structure < 3 kDa molecular size fractions. The intensity-weighted HDS of (HA-TiO_2)$_{,dark}$, on the other hand, showed a range of 1.0-10000.0 nm (Table 3.56) and the 1.8-3162.3 was the most visible structures with the highest CR%. The structures above 3000 nm might be the physico hydrogel structures formed by HA agglomerates due to the mixing and the structures > 1000 nm might be the Fe-TiO_2 homo-agglomerates and HA-Fe-TiO_2 hetero-agglomerates. Disappearance of the structures above 3000 nm after 30 min proves the existence of HA agglomerates in the form of physical hydrogel. Also, the structures smaller than 100 nm were not detectable after 30 min. It has been stated that smaller size fractions of HA (as OM) were more prone to Fe chelating so the leached Fe(II) ions might be bonded by HA hetero-aggregates (Teoh et al., 2007; Adán et al., 2014). The CR% of volume- and surface area-weighted HDS comparison implied that the agglomerated structure was mostly spherical. The middle size clusters around 500-800 nm were stable during 120 min so these structures might be the HA-Fe-TiO_2 hetero-agglomerates that colloidally stabilized by the surface adsorbed HA. These middle size agglomerates

also continued to grow during 120 min and formed the agglomerates around 1000 nm. These slightly bigger structures later precipitated, for instance the structure around 1080.5-1173.9 nm with a CR% of 1% as number-weighted HDS at 30 min measurement was not visible in 60 min (Table3.55, and Table 3.56). However, at 90 min structures around 1029.0-1099.2 nm were formed with a 2% CR% as number-weighted HDS and continued to growth as 1049.9-1121.5 nm with a 3% CR% as number-weighted HDS. This trend showed that agglomeration continued due to the charge localization formed by Fe leaching and chelating with HA. The removal ratio of $(HA\text{-}Fe\text{-}TiO_2)_{,dark}$ was 10-15% emphasizing that HA-Fe-TiO_2 agglomerates were colloidally stable on the contrary Fe-TiO_2 homo-agglomerates were more prone to the precipitate. The leached Fe also possibly created charge localization by leaving a hole on the surface of the Fe-TiO_2 structure which was attracting the both HA and other Fe-TiO_2 aggregates.

Table 3.57 compiles the comparison of $(HA\text{-}Fe\text{-}TiO_2)_{,as\text{-}is}$ and $(HA\text{-}Fe\text{-}TiO_2)_{,dark}$. The smaller clusters detected above 100 nm for $(HA\text{-}Fe\text{-}TiO_2)_{,dark}$ was not visible for $(HA\text{-}Fe\text{-}TiO_2)_{,as\text{-}is}$, which could be concluded as the Fe leaching was not effective for $(HA\text{-}Fe\text{-}TiO_2)_{,as\text{-}is}$. Also, 60 min dark mixing as pre-treatment of $(HA\text{-}Fe\text{-}TiO_2)_{,dark}$ supplied enough time for combination of leached Fe(II) and HA structures so agglomerates around 1778.3-3162.3 nm could be detected at initial time. Because leached Fe(II) was covering some of the active sites of HA, HA-Fe-TiO_2 hetero-aggregation formation was inhibited in comparison to the $(HA\text{-}Fe\text{-}TiO_2)_{,as\text{-}is}$ during 180 nm. The structures above 1000 nm were mostly colloidally stable in $(HA\text{-}Fe\text{-}TiO_2)_{,dark}$ in comparison to $(HA\text{-}Fe\text{-}TiO_2)_{,as\text{-}is}$. This might show that formation of HA-Fe-TiO_2 hetero-aggregation/agglomeration formation was more favorable in $(HA\text{-}Fe\text{-}TiO_2)_{,as\text{-}is}$. Because the structures above 1000 nm more tend to precipitate, colloidally stable structures above 1000 nm could be the HA hetero-aggregates/agglomerates.

The comparison of intensity-weighted HDS of $(HA\text{-}TiO_2)_{,dark}$ and $(HA\text{-}Fe\text{-}TiO_2)_{,dark}$ supported the findings mentioned above (Table 3.58). The HDS of $(HA\text{-}Fe\text{-}TiO_2)_{,dark}$ ranged between 1.8 nm to 3162.3 nm, and the HDS range of $(HA\text{-}TiO_2)_{,dark}$ was 92.1-1827.9 nm as intensity-weighted definition. Similar with the $(HA\text{-}Fe\text{-}TiO_2)_{,dark}$, $(HA\text{-}TiO_2)_{,dark}$ showed the hetero-agglomerated (physical hydrogel formation) HA structures above 1000 nm. On the other hand, $(HA\text{-}TiO_2)_{,dark}$ system might comprise more HA-TiO_2-HA bridge formation so these structures above 1000 nm not only comprising hetero-agglomerates of HA but also complex agglomerated structures of HA-TiO_2. Because the active sites of HA were occupied by leached Fe(II) formation of bridged agglomerates of $(HA\text{-}Fe\text{-}TiO_2)_{,dark}$ was less favorable.

Table 3.56. Intensity-, volume-, surface area- and number-weighted HDS and cumulative ratios of $(HA\text{-}Fe\text{-}TiO_2)_{,dark}$.

	HDS, nm	Cumulative Ratio, %			
		Intensity	Volume	Surface Area	Number
Initial	1.8-177.8	16%	100%	100%	100%
	237.1	14%	-	-	-
	316.2	13%	-	-	-
	421.7-1000.0	19%	-	-	-
	1333.5	16%	-	-	-
	1778.3-3162.3	22%	-	-	-
30 min	160.6-174.5	14%	5%	20%	51%
	189.6	12%	5%	13%	28%
	205.9-223.7	12%	3%	9%	16%
	775.6-842.7	17%	32%	25%	3%
	915.5	19%	10%	7%	-
	994.6	15%	14%	8%	1%
	1080.5-1173.9	11%	31%	18%	1%
60 min	170.0-180.2	14%	7%	19%	41%
	191.1	14%	7%	15%	30%
	202.5-214.7	15%	5%	13%	21%
	578.6-613.4	15%	11%	8%	2%
	650.2	18%	14%	10%	1%
	689.3-774.6	24%	56%	35%	5%
90 min	197.6-211.1	10%	5%	13%	27%
	225.5	16%	7%	17%	29%
	240.9	17%	7%	16%	24%
	257.3-274.9	14%	6%	13%	16%
	844.2-901.8	15%	16%	10%	1%
	963.3	14%	16%	9%	1%
	1029.0-1099.2	14%	43%	22%	2%
120 min	215.4-230.1	19%	7%	20%	41%
	245.8	20%	8%	17%	30%
	262.5-280.5	20%	7%	17%	25%
	861.3-920.1	9%	8%	6%	-
	982.8	12%	14%	8%	1%
	1049.9-1121.5	20%	56%	32%	3%

Table 3.57. Intensity-weighted HDS profile of $(HA\text{-}Fe\text{-}TiO_2)_{,dark}$. Time dependent HDS cluster maximas, HDS range and min-max diameter difference with respect to multi-size distribution.

	Cluster				
Time, min	Max 1, nm	Max 2, nm	Max 3, nm	Range, nm	Difference, nm
Initial	2.4	237.1	1333.5	1.0-10000.0	9999.0
30	189.6	915.5		115.3-1653.5	1520.0
60	191.1	650.2		142.7-922.7	780.0
90	240.9	963.3		173.2-1431.3	1258.1
120	245.8	982.8	1049.9	176.7-1460.4	1283.7

Table 3.58. Comparison of intensity-weighted HDS values of $(HA\text{-}Fe\text{-}TiO_2)_{,as\text{-}is}$ and $(HA\text{-}Fe\text{-}TiO_2)_{,dark}$.

	$(HA\text{-}Fe\text{-}TiO_2)_{,as\text{-}is}$		$(HA\text{-}Fe\text{-}TiO_2)_{,dark}$		
	HDS, nm	CR, %	HDS, nm	CR, %	
Initial	163.9-203.7	15%	Dark Mixing		
	227.0-282.1	16%			
	1438.3-1603.2	11%			
	1787.2	17%			
	1992.2	21%			
	2220.7-2475.4	20%			
30 min	144.4-168.8	20%			
	182.5-197.2	12%			
	801.0-865.9	25%			
	936.0	23%			
	1011.8-1093.7	20%			
60 min	175.9-189.8	13%	1.8-177.8	16%	Initial
	204.7	16%	237.1	14%	
	220.8-238.2	18%	316.2	13%	
	742.1-800.5	12%	421.7-1000.0	19%	
	863.5	14%	1333.5	16%	
	931.4	16%	1778.3-3162.3	22%	
	1004.7-1083.8	11%			
90 min	211.4-225.8	19%	160.6-174.5	14%	30 min
	241.2	19%	189.6	12%	
	257.7-275.3	19%	205.9-223.7	12%	
	791.3-903.0	19%	775.6-842.7	17%	
	964.6-1100.7	22%	915.5	19%	
	-	-	994.6	15%	
			1080.5-1173.9	11%	
120 min	118.5-134.9	14%	170.0-180.2	14%	60 min
	143.9-153.4	11%	191.1	14%	
	431.1-459.8	25%	202.5-214.7	15%	
	490.5	23%	578.6-613.4	15%	
	523.2	17%	650.2	18%	
	558.1-595.3	10%	689.3-774.6	24%	
150 min	152.2-175.0	18%	197.6-211.1	10%	90 min
	187.6	13%	225.5	16%	
	201.2-215.7	12%	240.9	17%	
	572.3-613.7	18%	257.3-274.9	14%	
	658.0	19%	844.2-901.8	15%	
	705.5-811.0	20%	963.3	14%	
	-	-	1029.0-1099.2	14%	
180 min	162.0-189.9	13%	215.4-230.1	19%	120 min
	222.5	18%	245.8	20%	
	260.7	20%	262.5-280.5	20%	
	305.5-358.0	17%	861.3-920.1	9%	
	576.1-675.1	17%	982.8	12%	
	791.1-1086.3	15%	1049.9-1121.5	20%	

Table 3.59. Comparison of intensity-weighted HDS values of $(HA\text{-}TiO_2)_{,dark}$ and $(HA\text{-}Fe\text{-}TiO_2)_{,dark}$.

	$(HA\text{-}TiO_2)_{,dark}$		$(HA\text{-}Fe\text{-}TiO_2)_{,dark}$	
	HDS, nm	CR, %	HDS, nm	CR, %
Initial	92.1-319.9	13%	1.8-177.8	16%
	362.3	14%	237.1	14%
	410.3-464.7	16%	316.2	13%
	980.9-1110.9	20%	421.7-1000.0	19%
	1258.2	17%	1333.5	16%
	1425.0	13%	1778.3-3162.3	22%
	1613.9-1827.9	7%	-	-
30 min	209.4-230.0	12%	160.6-174.5	14%
	252.6-304.7	10%	189.6	12%
	1364.5-1498.6	16%	205.9-223.7	12%
	1645.8	20%	775.6-842.7	17%
	1807.5	18%	915.5	19%
	1985.1-2180.1	14%	994.6	15%
	-	-	1080.5-1173.9	11%
60 min	212.8-291.0	18%	170.0-180.2	14%
	340.2	14%	191.1	14%
	397.8-465.2	15%	202.5-214.7	15%
	1390.4-1625.8	20%	578.6-613.4	15%
	1901.1	18%	650.2	18%
	2229.9-2599.3	15%	689.3-774.6	24%
90 min	155.0-186.5	15%	197.6-211.1	10%
	204.6-246.2	14%	225.5	16%
	1082.6	11%	240.9	17%
	1187.6	17%	257.3-274.9	14%
	1302.8	23%	844.2-901.8	15%
	1429.1-1567.7	22%	963.3	14%
	-	-	1029.0-1099.2	14%
120 min	172.5-207.6	11%	215.4-230.1	19%
	227.8-274.1	21%	245.8	20%
	1098.7	9%	262.5-280.5	20%
	1205.2	17%	861.3-920.1	9%
	1322.1	22%	982.8	12%
	1450.3-1590.9	20%	1049.9-1121.5	20%

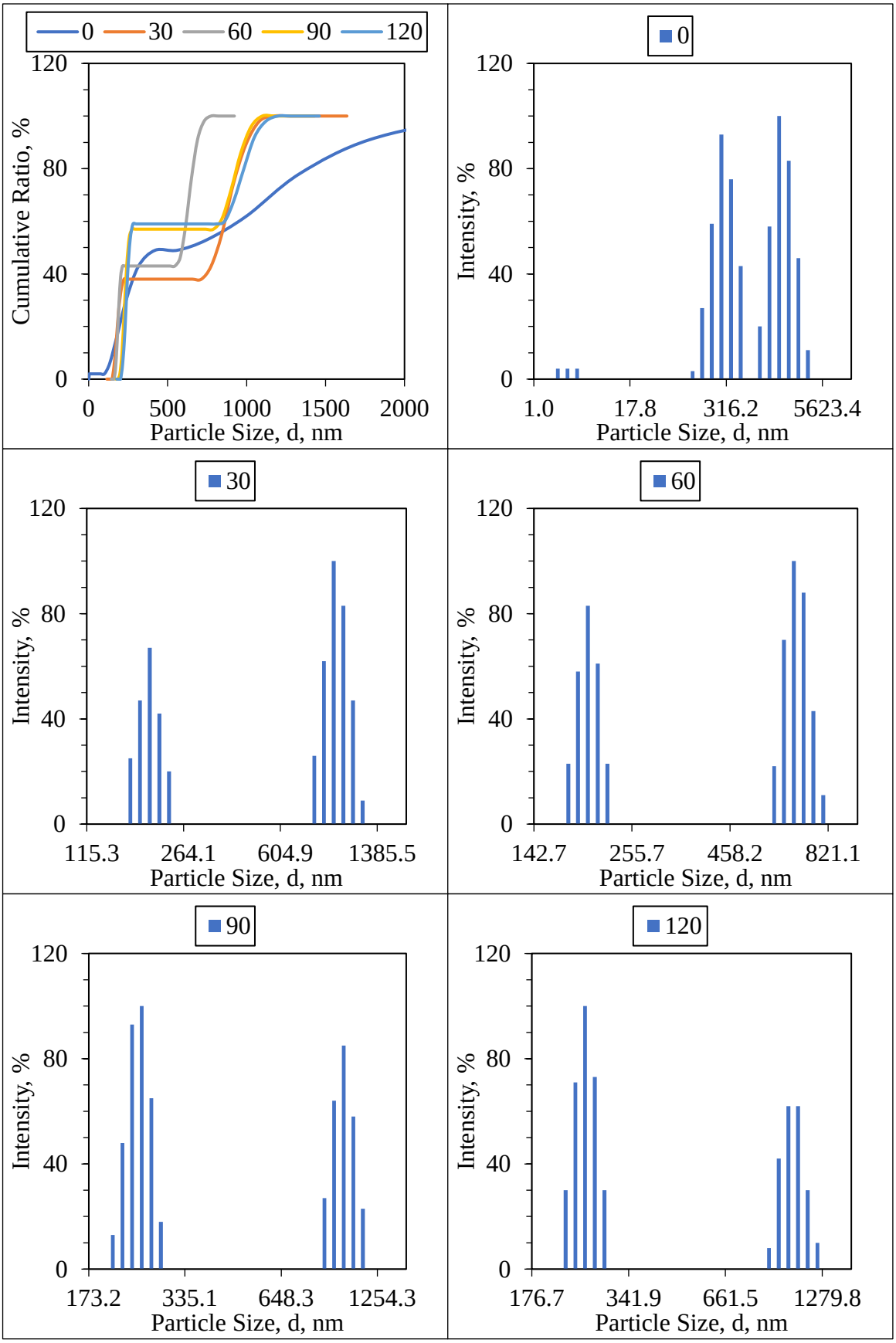


Figure 3.85. The cumulative ratio comparison and hydrodynamic size of $(HA\text{-}Fe\text{-}TiO_2)_{,dark}$ as intensity-weighted HDS in 30 min intervals.

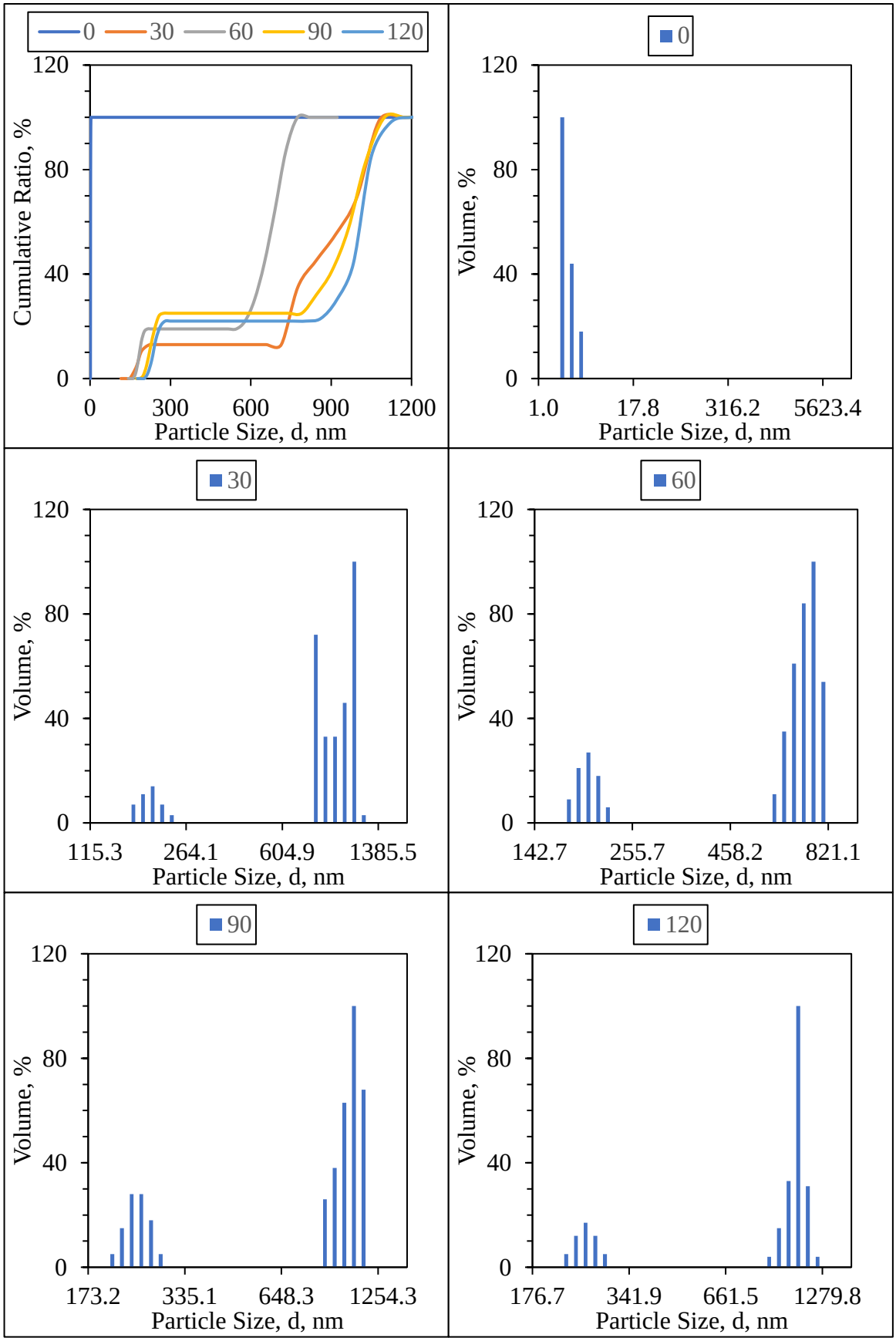


Figure 3.86. The cumulative ratio comparison and hydrodynamic size of $(HA\text{-}Fe\text{-}TiO_2)_{,dark}$ as volume-weighted HDS in 30 min intervals.

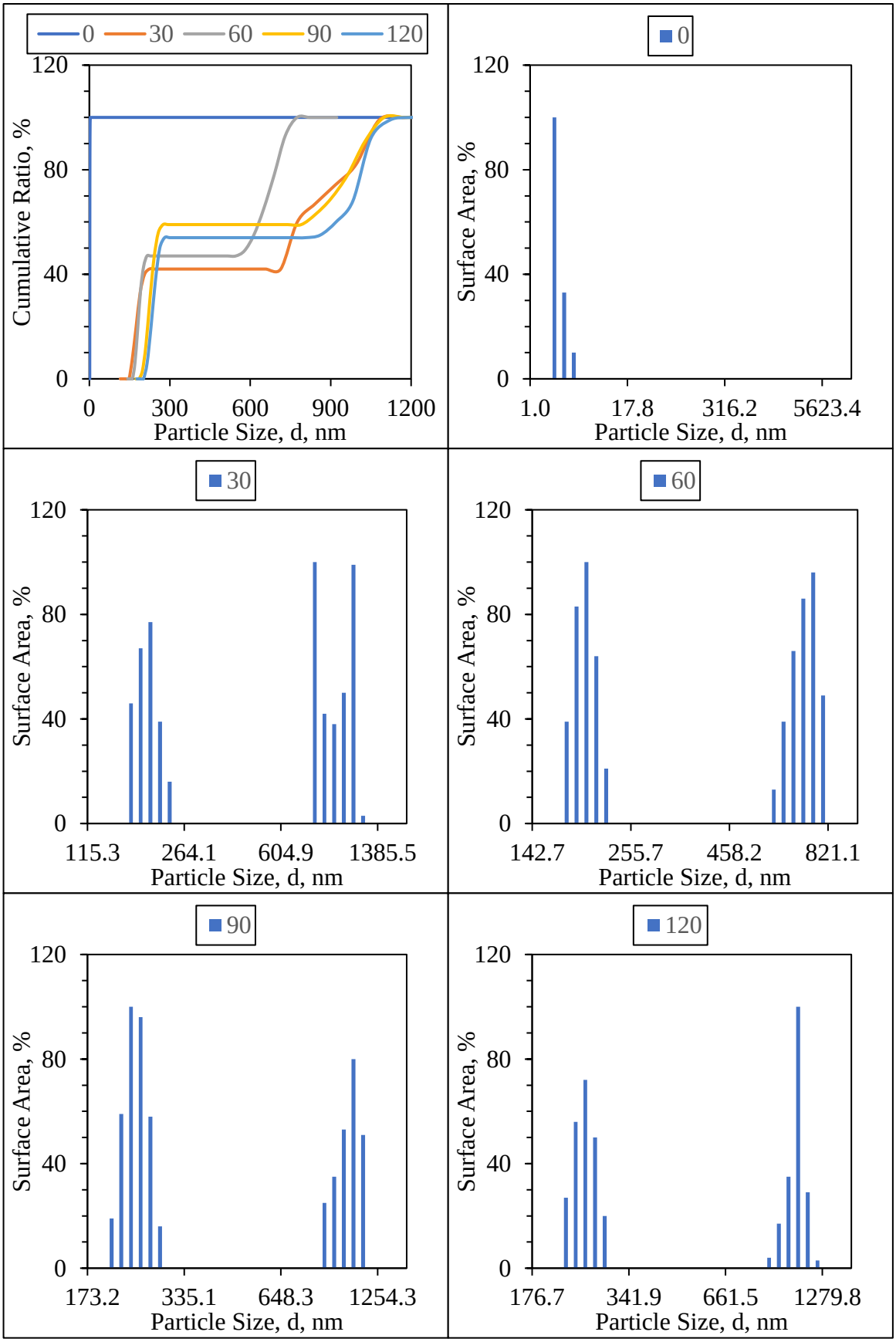


Figure 3.87. The cumulative ratio comparison and hydrodynamic size of $(HA\text{-}Fe\text{-}TiO_2)_{,dark}$ as surface area-weighted HDS in 30 min intervals.

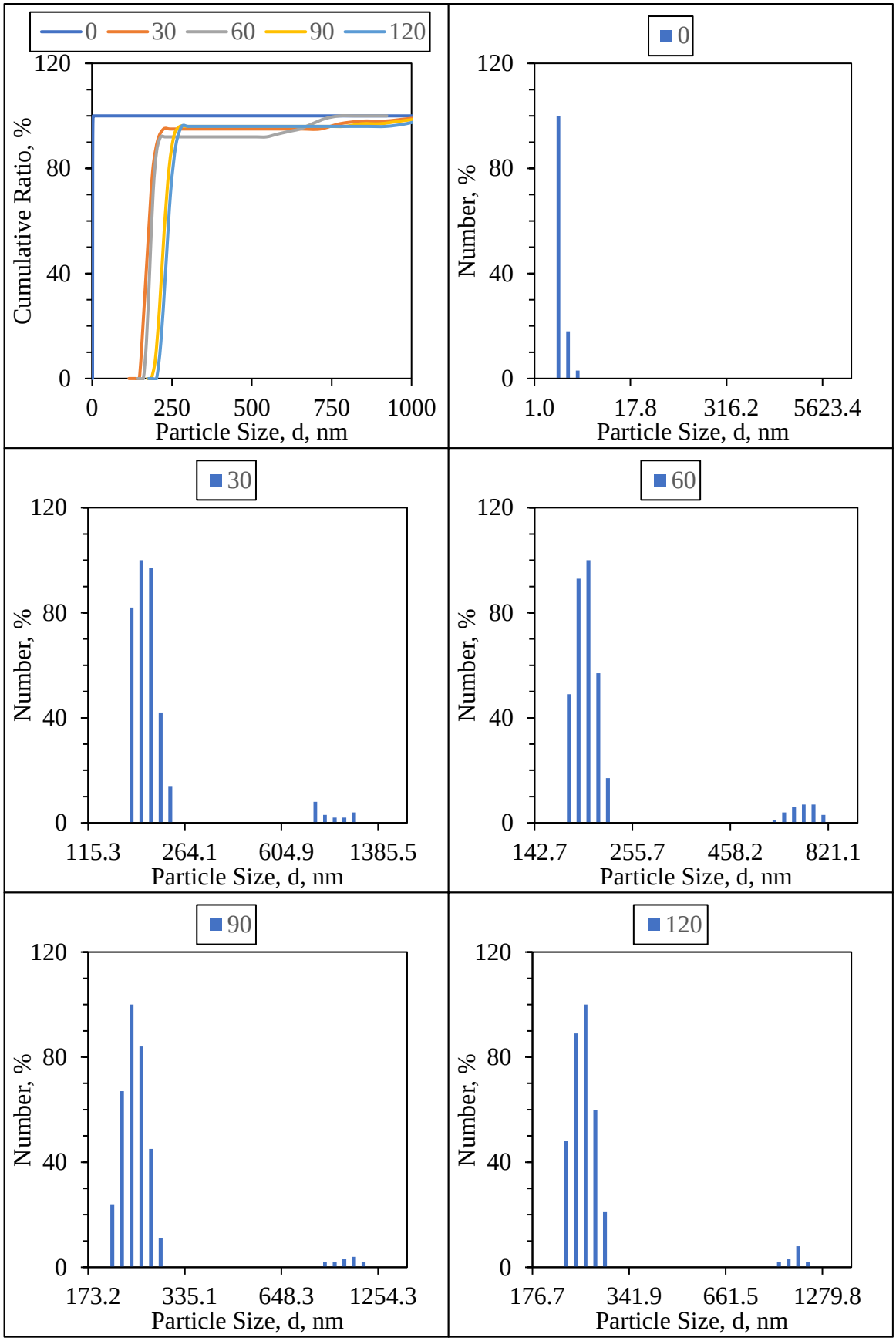


Figure 3.88. The cumulative ratio comparison and hydrodynamic size of $(HA\text{-}Fe\text{-}TiO_2)_{,dark}$ as number-weighted HDS in 30 min intervals.

3.5.7. Hydrodynamic Size Assessment of ($HA_{,pho}$-Fe-TiO_2

The change of aggregation/agglomeration behavior of Fe-TiO_2 in the presence of HA previously exposed to solar light was investigated by suspending 0.25 mgL^{-1} Fe-TiO_2 into photolytically treated HA. 50 mgL^{-1} HA solution (DOC: 4.80 mgL^{-1}) was placed in solar light simulator and photolytically treated for 60 min under continuously mixing condition and named $HA_{,pho}$. Fe-TiO_2 was suspended in this pre-treated HA solution by mixing with a magnetic stirrer for 30 min. Thus prepared Fe-TiO_2 and HA_{pho} binary system was referred as ($HA_{,pho}$-Fe-TiO_2). Detailed procedure had also been introduced in section 2.3. The initial DOC of HA was decreased to 4.53 mgL^{-1} after photolytic treatment due to the self-degradation of HA under solar irradiation. Also, structural changes occurred by the charge formation during solar irradiation and HA formed a more self-assembled aggregates (von Wandruszka et al., 1997; Uyguner-Demirel and Bekbolet, 2011; Vione et al, 2014). The pertaining solar light initiated reactions were presented in Section xx.

The polydispersity index of ($HA_{,pho}$-Fe-TiO_2) was found as 0.336, 0.310, 0.307, 0.284, 0.286 for initial, 30 min, 60 min, 90 min and 120 min, respectively. The average PDI of the system was calculated as 0.304 which was corresponding to nearly monodispersed structure during 120 min, therefore, MSD approximation was used to evaluate HDS of ($HA_{,pho}$-Fe-TiO_2).

The time depended HDS of ($HA_{,pho}$-Fe-TiO_2) was compiled in Table 3.59 as intensity-,volume-,surface area-, and number-weighted HDS and the graphical abstract of the presented data were illustrated at Figure 3.89, Figure 3.90, Figure 3.91 and Figure 3.92. Table 3.60 showed a more detailed information about the HDS range, maxima and difference of min-max values of ($HA_{,pho}$-Fe-TiO_2). The comparative HDS data of $HA_{,pho}$, Fe-$TiO_{2,as\text{-}is}$ and ($HA_{,pho}$-Fe-TiO_2) were gathered in Table 3.61 with the corresponding CR% as intensity-weighted. Finally, Table 3.62 compared the HDS results of ($HA_{,pho}$-Fe-TiO_2) and ($HA_{,pho}$-Fe-TiO_2).

The HDS of ($HA_{,pho}$-Fe-TiO_2) showed two maxima at 202.8 nm and 1983.4 nm (Table 3.60). The cluster related to the first maxima ranged from 163.2-280.9 nm that was mostly comprised of homo-aggregates of Fe-TiO_2 and hetero-aggregates of $HA_{,pho}$. The larger maxima region was in a range of 1596.2-2747.2 nm corresponding to both homo- and hetero-agglomerated structures. The self-assembly structure of $HA_{,pho}$ might increase the formation of Fe chelates due to the deformation of π bonds which could create more active sites. Hence the structures around 1000-2800 nm could possibly be related to the flocs formed by humic structures. These flocs however disagglomerated by settlement of the system after 30 min. Disappearance of these bigger structures revealed a middle

sized cluster around 600-900 nm that might be the hetero-agglomerated $HA_{,pho}$-Fe-TiO_2, due to the colloidally stabilized behavior during 120 min. It must be noted that this cluster also covered the disagglomerated aggregates of $HA_{,pho}$ structures. For instance, the structures around 793.9 nm at 30 min might be a hetero-agglomerate of $HA_{,pho}$ or hetero-agglomerate of $HA_{,pho}$-Fe-TiO_2, on the contrary the structure around 860.7 nm could probably be the homo-agglomeration of Fe-TiO_2. The theory was evidenced by comparing the CR% values of volume- and surface area-weighted HDS. Because the hetero-agglomerates of $HA_{,pho}$ and $HA_{,pho}$-Fe-TiO_2 tend to form less spherical structures they occupy higher volume and higher surface area, as in the examples of 793.9 nm. The volume-weighted CR% of 793.9 nm was 42% and the surface area-weighted CR% was 27% (Table 3.59). On the other hand, the structures around 860.7 nm were less in volume (CR%: 11%) and less in surface area (CR%: 7%) even their number weighted CR% (13%) was higher than the number weighted CR% of the 793.9 nm (5%) sized structures. A similar trend was observed at 90 min with the structures sizing 704.7 nm and 757.3 nm. The structures around 704.7 were covering less volume (CR%: 13%) and less surface area (CR%: 10%) while the structures around 757.3 showed higher volume (CR%: 57%) and higher surface area (CR%: 39%) with the same number-weighted CR% (1%) (Table 3.59). The agglomeration of structures around 704.7 nm and 757.3 nm were continued at the 120 min measurements and their HDS increased to 724.4 nm and 775.9 nm, respectively. These structures might also be slightly distorted forms of previous ones due to the electrostatic forces.

The comparison of HDS of $HA_{,pho}$, Fe-$TiO_{2,as\text{-}is}$, and ($HA_{,pho}$-Fe-TiO_2) evidenced that hetero-agglomeration of ($HA_{,pho}$-Fe-TiO_2) was not favorable. However, HA interaction with leached Fe added another dimension to formation of aggregates and agglomerates. Both $HA_{,pho}$ and Fe-TiO_2 did not display structures above 1000 nm during 120 min (Table 3.60). On the other hand, structures above 1000 nm were covering 7% of the system as number-weighted HDS in ($HA_{,pho}$-Fe-TiO_2) binary system. These structures were probably formed by the deformation of the scaffold structure $HA_{,pho}$ by the electrostatic interaction of leached Fe(II) (Arana et al., 2003; Adán et al., 2009). However, these agglomerates around 1500-2800 nm were not stable and disagglomerated after 30 min (Table 3.59, Table 3.61). After the disagglomeration of $HA_{,pho}$ hetero-agglomerates, ($HA_{,pho}$-Fe-TiO_2) showed similar properties with $HA_{,pho}$ hetero-aggregates and Fe-TiO_2 homo-aggregates.

Similar behavior was observed with the comparative results of ($HA_{,pho}$-TiO_2) and ($HA_{,pho}$-TiO_2) (Table 3.62) as indicated in the previous paragraph. The ($HA_{,pho}$-TiO_2) binary system was mostly comprised of $HA_{,pho}$ hetero-aggregates, $HA_{,pho}$ hetero-agglomerates and Fe-TiO_2 homo-agglomerates so structures above 1000 nm were not detected during 120 min. On the contrary, HA-Fe chelates formed hetero-agglomerates by the effect of mixing then disagglomerated when the suspension was

settled. Additionally, the Fe-TiO_2 homo-agglomerates more tend to precipitate in comparison to TiO_2 homo-aggregates so, the ($HA_{,pho}$-Fe-TiO_2) binary system was mostly comprised of aggregated structures around 100-300 nm while the ($HA_{,pho}$-TiO_2) binary system was comprised of structures around 700-900 nm.

Table 3.60. Intensity-, volume-, surface area- and number-weighted HDS and cumulative ratios of ($HA_{,pho}$-Fe-TiO_2).

	HDS, nm	Cumulative Ratio, %			
		Intensity	Volume	Surface Area	Number
Initial	163.2-202.8	17%	12%	46%	45%
	226.0-280.9	14%	9%	25%	46%
	1596.2-1779.3	20%	23%	9%	6%
	1983.4	22%	46%	17%	1%
	2210.9	17%	7%	2%	1%
	2464.5-2747.2	10%	3%	1%	1%
30 min	145.5-171.0	25%	10%	31%	69%
	185.4-201.0	17%	5%	14%	9%
	675.4-732.2	13%	24%	17%	1%
	793.9	15%	42%	27%	5%
	860.7	18%	11%	7%	13%
	933.1-1011.7	12%	8%	4%	3%
60 min	158.8-184.2	23%	9%	25%	71%
	198.3	16%	4%	12%	16%
	213.5-229.9	14%	4%	9%	9%
	697.4-750.9	15%	45%	30%	1%
	808.5	15%	28%	18%	1%
	870.6-1009.4	17%	10%	6%	2%
90 min	144.5-155.3	14%	5%	16%	23%
	166.9	14%	4%	13%	25%
	179.4-192.8	15%	3%	10%	33%
	610.2-655.7	7%	3%	2%	17%
	704.7	15%	13%	10%	1%
	757.3	19%	57%	39%	1%
	813.8-874.6	16%	15%	10%	-
120 min	1171.1-183.2	20%	6%	18%	74%
	196.3	16%	4%	12%	9%
	210.2-225.2	13%	3%	7%	2%
	631.3-676.3	13%	8%	6%	13%
	724.4	16%	24%	19%	1%
	775.9	12%	47%	33%	1%
	831.1-890.2	10%	8%	5%	-

Table 3.61. Intensity-weighted HDS profile of ($HA_{,pho}$-Fe-TiO_2). Time dependent HDS cluster maximas, HDS range and min-max diameter difference with respect to multi-size distribution.

	Cluster			
Time, min	Max 1, nm	Max 2, nm	Range, nm	Difference, nm
Initial	202.8	1983.4	117.8-3805.2	3687.4
30	171.0	860.7	105.3-1397.7	1292.4
60	198.3	808.5	118.2-1260.3	1142.1
90	166.9	757.3	108.4-1085.5	977.1
120	196.3	724.4	121.3-1094.0	972.7

Table 3.62. Comparison of intensity-weighted HDS values of $HA_{,pho}$, Fe-$TiO_{2,as-is}$, and ($HA_{,pho}$-Fe-TiO_2).

	$HA_{,pho}$		Fe-$TiO_{2,as-is}$		($HA_{,pho}$-Fe-TiO_2)	
	HDS, nm	CR, %	HDS, nm	CR, %	HDS, nm	CR, %
Initial	121.8-139.5	25%	144.5-165.5	21%	163.2-202.8	17%
	149.3-170.9	29%	177.2	14%	226.0-280.9	14%
	539.8-757.1	46%	189.6-203.0	12%	1596.2-1779.3	20%
	-	-	562.3-601.8	21%	1983.4	22%
	-	-	644.1	18%	2210.9	17%
	-	-	689.4-737.8	15%	2464.5-2747.2	10%
30 min	133.8-142.6	22%	158.1-170.3	11%	145.5-171.0	25%
	152.1	21%	183.3	15%	185.4-201.0	17%
	162.2-173.0	19%	197.4-228.9	25%	675.4-732.2	13%
	483.9-667.3	38%	644.7-694.2	12%	793.9	15%
	-	-	747.5	13%	860.7	18%
	-	-	804.9	15%	933.1-1011.7	12%
	-	-	866.7-933.3	9%	-	-
60 min	100.0-177.8	45%	128.5-147.0	17%	158.8-184.2	23%
	237.1	28%	157.1-179.6	19%	198.3	16%
	316.2-421.7	27%	524.3-560.6	22%	213.5-229.9	14%
			599.4	21%	697.4-750.9	15%
	-	-	640.9-685.3	21%	808.5	15%
	-	-	-	-	870.6-1009.4	17%
90 min	135.0-150.4	27%	165.9-175.5	13%	144.5-155.3	14%
	158.8	19%	185.6	17%	166.9	14%
	167.6-177.0	16%	196.3-207.7	21%	179.4-192.8	15%
	398.8-444.4	13%	570.4-603.4	19%	610.2-655.7	7%
	469.1-522.8	25%	638.2	16%	704.7	15%
	-	-	675.1-714.0	14%	757.3	19%
	-	-	-	-	813.8-874.6	16%
120 min	131.1-151.3	27%	126.6-146.1	19%	171.1-183.2	20%
	162.5	24%	156.9-181.1	21%	196.3	16%
	174.5-187.5	22%	492.0-528.4	16%	210.2-225.2	13%
	633.2-843.2	27%	567.5	16%	631.3-676.3	13%
	-	-	609.6	17%	724.4	16%
	-	-	654.7-703.2	11%	775.9	12%
	-	-	-	-	831.1-890.2	10%

Table 3.63. Comparison of intensity-weighted HDS values of ($HA_{,pho}$-TiO_2) and ($HA_{,pho}$-Fe-TiO_2).

	($HA_{,pho}$-TiO_2)		($HA_{,pho}$-Fe-TiO_2)	
	HDS, nm	CR, %	HDS, nm	CR, %
Initial	148.5-175.3	14%	163.2-202.8	17%
	190.5-207.0	8%	226.0-280.9	14%
	783.0	11%	1596.2-1779.3	20%
	850.9	19%	1983.4	22%
	924.6	25%	2210.9	17%
	1004.8-1091.9	23%	2464.5-2747.2	10%
30 min	165.4-188.9	14%	145.5-171.0	25%
	201.9-230.5	9%	185.4-201.0	17%
	623.1-665.8	12%	675.4-732.2	13%
	711.5	19%	793.9	15%
	760.2	22%	860.7	18%
	812.3-868.0	18%	933.1-1011.7	12%
60 min	113.4-154.9	20%	158.8-184.2	23%
	538.2-581.8	22%	198.3	16%
	628.9	23%	213.5-229.9	14%
	679.9	21%	697.4-750.9	15%
	734.9-794.4	13%	808.5	15%
	-	-	870.6-1009.4	17%
90 min	204.4-234.5	19%	144.5-155.3	14%
	251.2-288.1	22%	166.9	14%
	753.8-807.2	20%	179.4-192.8	15%
	864.5	19%	610.2-655.7	7%
	926.0	13%	704.7	15%
	991.8-1062.3	7%	757.3	19%
	-	-	813.8-874.6	16%
	-	-	1171.1-183.2	20%
120 min	225.9-239.9	13%	196.3	16%
	254.7	15%	210.2-225.2	13%
	270.5-304.9	20%	631.3-676.3	13%
	749.8-796.1	14%	724.4	16%
	845.4	15%	775.9	12%
	897.6-1012.0	23%	831.1-890.2	10%

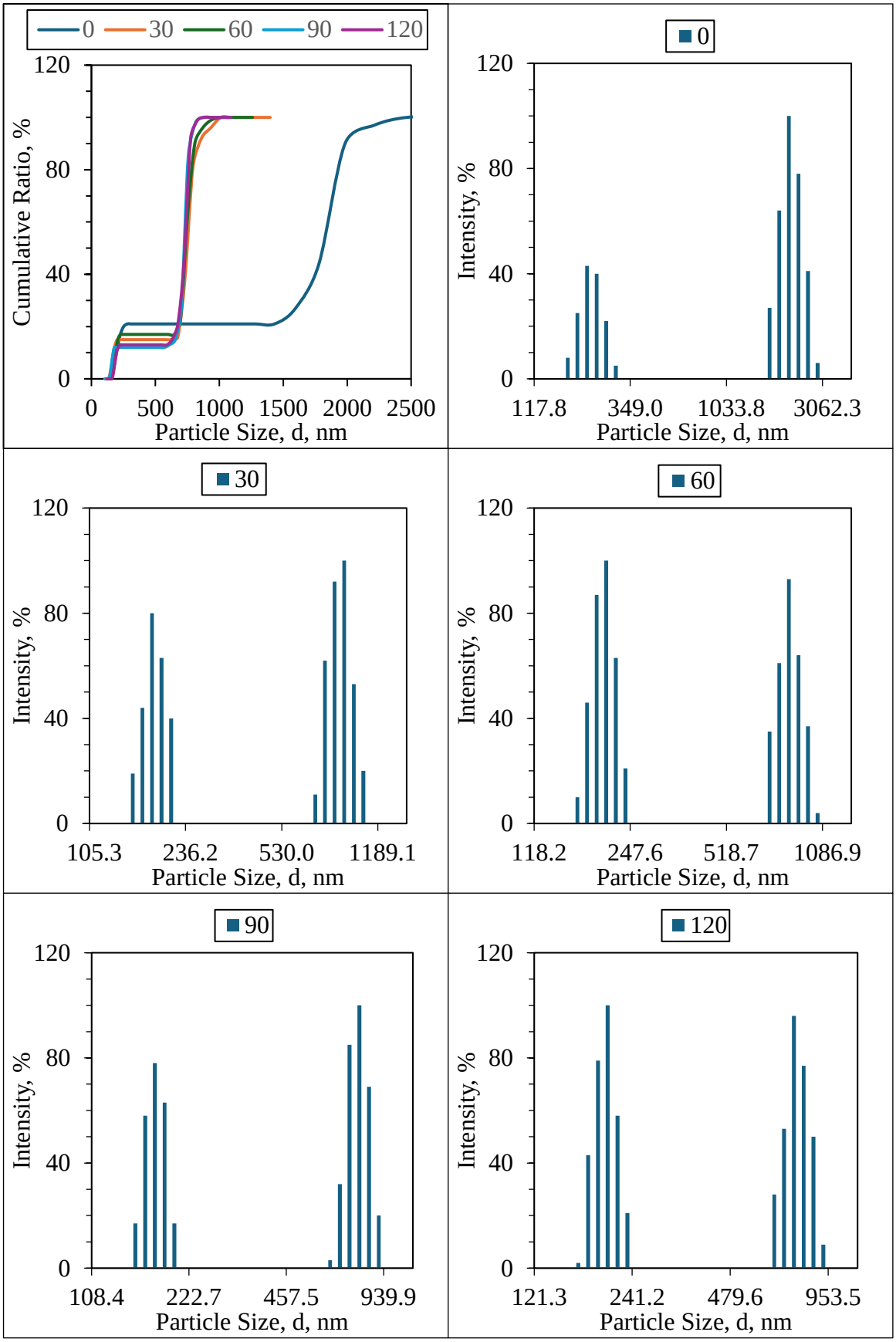


Figure 3.89. The cumulative ratio comparison and hydrodynamic size of ($HA_{,pho}$-Fe-TiO_2) as intensity-weighted HDS in 30 min intervals.

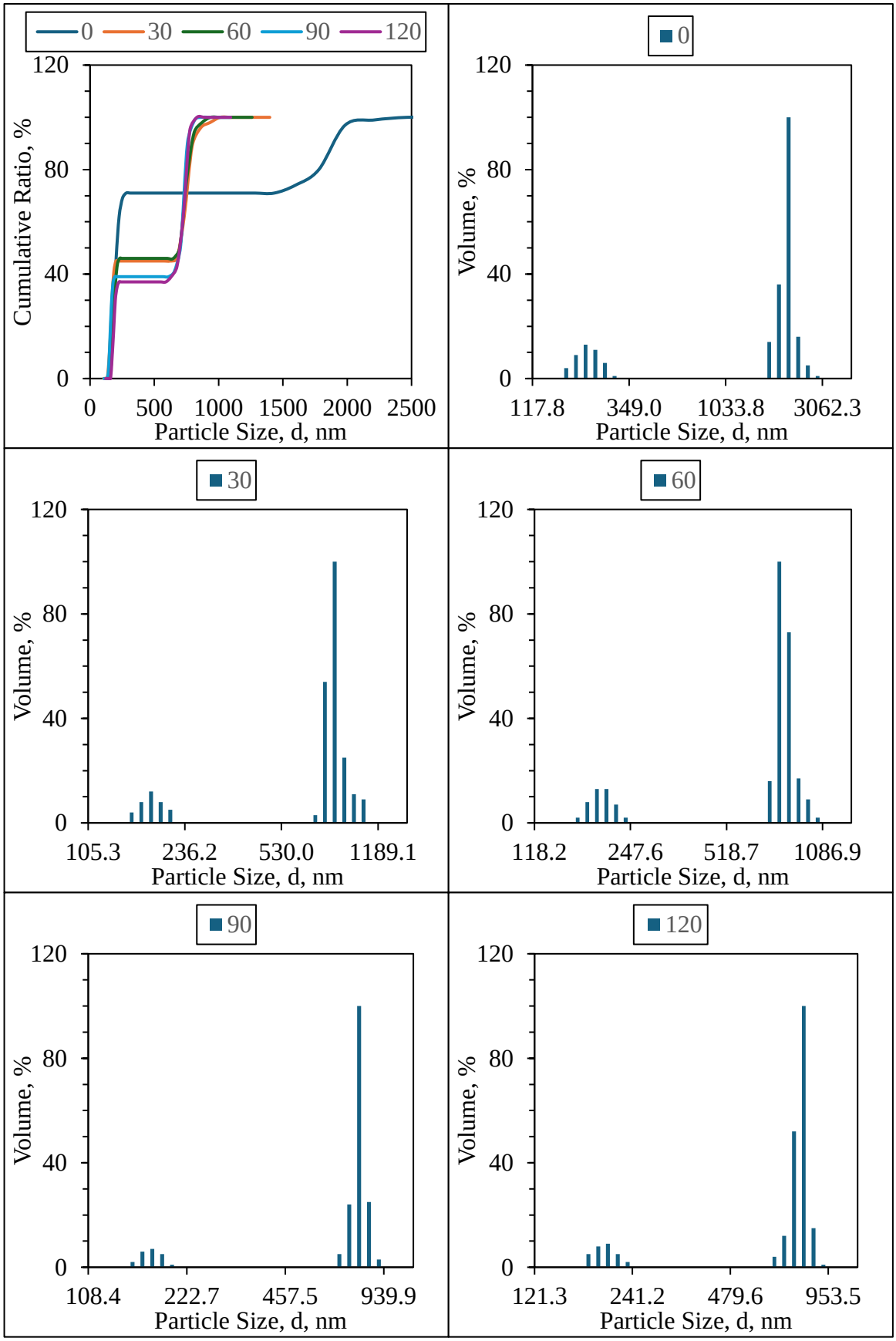


Figure 3.90. The cumulative ratio comparison and hydrodynamic size of ($HA_{,pho}$-Fe-TiO_2) as volume-weighted HDS in 30 min intervals.

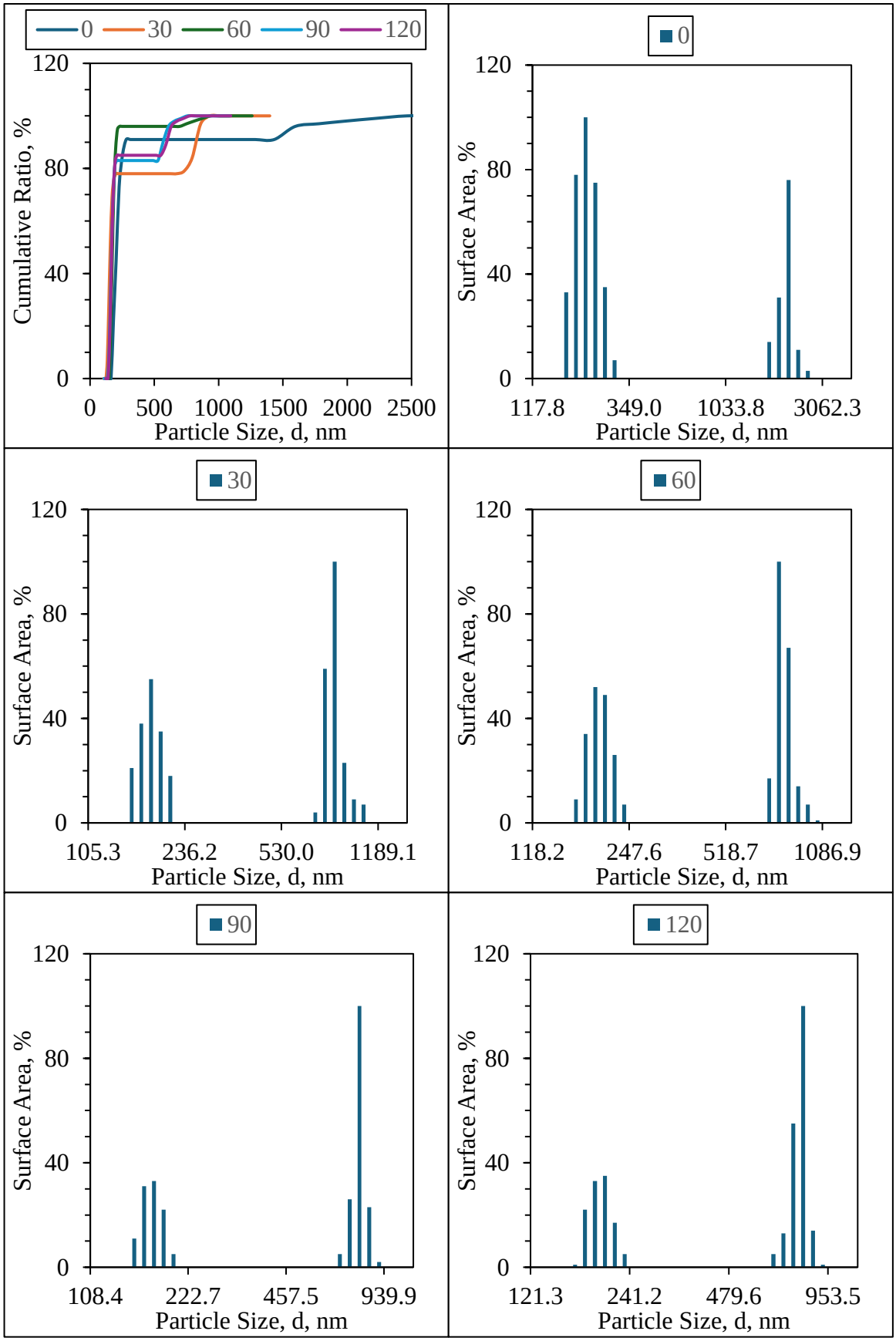


Figure 3.91. The cumulative ratio comparison and hydrodynamic size of ($HA_{,pho}$-Fe-TiO_2) as surface area-weighted HDS in 30 min intervals.

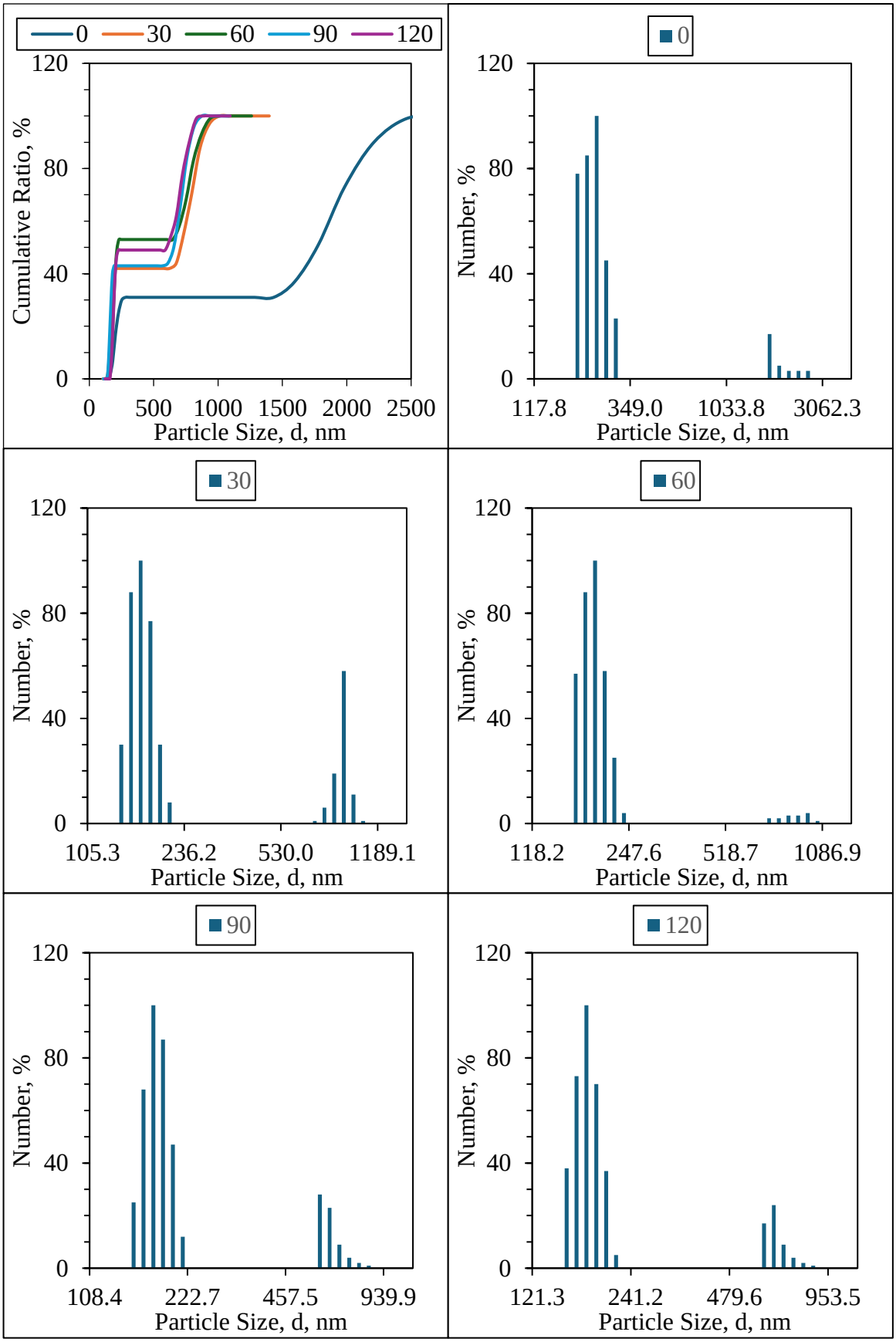


Figure 3.92. The cumulative ratio comparison and hydrodynamic size of ($HA_{,pho}$-Fe-TiO_2) as number-weighted HDS in 30 min intervals.

3.5.8. Hydrodynamic Size Assessment of (HA-Fe-TiO_2)$_{,photocat}$

The aggregation/agglomeration behavior of HA-Fe-TiO_2 binary system under solar irradiance was investigated via suspending Fe-TiO_2 in HA solution followed by exposure to solar irradiance (Section 3.2.3). Following photocatalysis, the binary solution named as (HA-Fe-TiO_2)$_{,photocat}$ was directly subjected to DLS measurements.

HDS data of (HA-Fe-TiO_2)$_{,photocat}$ were compiled in Table 3.63 as intensity-, volume-, surface area-, and number-weighted HDS with their corresponding CR%. Detailed information on maxima, min-max difference and HDS range was reported in Table 3.64. The graphical abstract of Table 1 and Table 2 was presented in Figure 3.93, Figure 3.94, Figure 3.95, and Figure 3.96 as intensity-, volume-, surface area-, and number-weighted HDS, respectively. Comparison of intensity-weighted HDS data of HA$_{,photocat}$, Fe-$TiO_{2,irr}$ and (HA-Fe-TiO_2)$_{,photocat}$ were gathered in Table 3.65 as. Also, intensity-weighted HDS results were compared with (HA-Fe-TiO_2)$_{,as\text{-}is}$, (HA-Fe-TiO_2)$_{,dark}$, and (HA$_{,pho}$-Fe-TiO_2) in Table 3.66 and with (HA-TiO_2)$_{,photocat}$ in Table 3.67.

The PDI of (HA-Fe-TiO_2)$_{,photocat}$ was found as 0.386, 0.345, 0.313, 0.281 and 0.245 for initial, 30 min, 60 min, 90 min and 120 min, respectively. The average of the PDIs was calculated as 0.314 which was an indicator of a nearly monodispersed system. Hence MSD approximation was used to explain HDS of (HA-Fe-TiO_2)$_{,photocat}$.

The HDS of (HA-Fe-TiO_2)$_{,photocat}$ system ranges between 225.2 nm to 3078.6 nm (Table 3.63) and giving two maxima around 275.4 nm and 2517.6 nm that were the most probable representative of the clusters as intensity-, volume-, and surface area-weighted HDS. On the other hand, the CR% of the cluster around 2517.6 nm was zero, which showed that these structures were very less in number. Because these structures around 2517.6 nm were just a few in number this cluster might be comprised of hetero-aggregates of photocatalytically degraded and re-aggregated/agglomerated HA structures. However, the 1000 nm – 1800 nm part of the cluster was more stable than the structures > 1800 nm during 60 min. Hence, the structures ranging between 1000 nm – 1800 nm were the hetero-agglomerates of photocatalytically treated HA and Fe-TiO_2. It might be concluded that structures above 1800 nm were disagglomerated after 30 min. However, Teoh and colleagues reported that the Fe on the TiO_2 surface might leach in dark conditions. Although Fe could leach, if there were organic matter in the media and system subjected to visible light irradiation, the leached Fe(III) could easily reduce to Fe(II) via reduction and re-adsorbed onto TiO_2 surface (Equations 3.48) (Teoh et al., 2007). This trend increased the photocatalytic efficiency of Fe-TiO_2, which was evidenced by the

physicochemical characterization of HA that was reported by Birben and colleagues (Table .3.1) (Birben et al., 2017). They stated that more surface coverage was achieved with Fe-TiO_2 (>45%) in comparison to TiO_2 (33%). Additionally, formation of smaller molecular size fractions (<10 kDa) was attained by Fe-TiO_2 more than TiO_2. Even the colloidally more stable cluster around 1000-1800 nm was mostly composed of hetero-aggregates, this cluster disappear at the end of 60 min. The removal efficiency at the end of 60 min was 35% which could be related to the precipitation of hetero-agglomerates structures. The remaining colloidal structures around the 700-1000 nm were mostly composed of spherical structures by comparing volume- and surface area weighted HDS. Because solar irradiation in the presence of Fe-TiO_2 degrade HA into smaller size fractions that were in form of more elongated structures they can adsorbed onto Fe-TiO_2 aggregates as brush-like structures (Figure 3.63) and create colloidally stable structures. Removal efficiency at the end of 120 min was 40 % that was supporting the theory that remaining structures were colloidally more stable.

The intensity-weighted HDS of $HA_{,photocat}$, Fe-$TiO_{2,irr}$ and (HA-Fe-TiO_2)$_{,photocat}$ were compared to understand the effect co-existence of HA and Fe-TiO_2 to aggregation/agglomeration behavior under solar irradiation (Table 3). After photocatalytic degradation of HA (>10 kDa), newly formed smaller molecular size fractions (<10 kDa) tend to self-oxidize or form higher molecular size fractions via hetero-aggregation (Birben et al., 2017), so the structures detected in $HA_{,photocat}$ around 7000 nm to 10000 nm were the hetero-aggregates of these smaller molecular size fractions. These structures were not formed in (HA-Fe-TiO_2)$_{,photocat}$ due to instantaneous HA adsorption onto Fe-TiO_2 aggregates. Because these photocatalytically degraded form of HA structures were rich in adsorption sites and chelating with Fe located on the surface of the Fe-TiO_2 were more favorable for smaller molecular size fractions (Teoh et al., 2007; Adán et al., 2014) “train, tail, loop” model structure was found to be more suitable to explain the extent of surface adsorption. The thin coverage created by HA adsorption onto surface led to slight increase of HDS of (HA-Fe-TiO_2)$_{,photocat}$ in comparison to Fe-$TiO_{2,irr}$. The intensity-weighted HDS of (HA-Fe-TiO_2)$_{,photocat}$ was more resembling to Fe-$TiO_{2,irr}$ during 120 min, however due to the HA sub fractions absorbed onto surface Fe-TiO_2 aggregates were more stable than Fe-TiO_2 mono system. The comparison results of intensity-weighted HDS of (HA-Fe-TiO_2)$_{,as\text{-}is}$, (HA-Fe-TiO_2)$_{,dark}$, ($HA_{,pho}$-Fe-TiO_2) and (HA-Fe-TiO_2)$_{,photocat}$ were compiled in Table 4. Results showed that the highest HDS achieved in (HA-Fe-TiO_2)$_{,photocat}$. The overall size comparison could be listed as (HA-Fe-TiO_2)$_{,photocat}$>($HA_{,pho}$-Fe-TiO_2)>(HA-Fe-TiO_2)$_{,dark}$>(HA-Fe-TiO_2)$_{,as\text{-}is}$. It might be concluded as;

i. The surface adsorption of the smaller HA subfractions onto Fe-TiO_2 aggregates were created more stable and colloidally stable hetero-aggregates.

ii. The photolytically treated HA sub fractions could tend to form HA-HA hetero-agglomerates, however Fe leaching from the Fe-TiO_2 disrupted the coiled HA-HA hetero-aggregates and disaggregated the HA structures than HA-Fe-TiO_2 hetero-agglomerates were formed. Even the adsorption of HA onto Fe-TiO_2 surface was achieved because HA adsorbed onto Fe-TiO_2, these structures were less stable due to the heavy Fe-TiO_2 hetero-agglomerate core.

iii. Magnetically mixing in the dark conditions could enhance the Fe leaching from the Fe-TiO_2 and those leached Fe(III) ions could directly form chelates with HA sub-fractions, therefore, HA-Fe-TiO_2 hetero-aggregate/agglomerate formation was unlikely to form under the specified conditions of $(HA\text{-}Fe\text{-}TiO_2)_{,dark}$. However, formation of Fe-TiO_2 homo-agglomerates and HA-HA hetero-agglomerates could lead to the formation of bigger structures in comparison to $(HA\text{-}Fe\text{-}TiO_2)_{,as\text{-}is}$. Since HA hetero-agglomerates were colloidally more stable than the Fe-TiO_2 homo-agglomerates, structures around 600-800 nm were possibly representing the hetero-agglomerates of HA during 120 min.

iv. Because there were no external forces as in the $(HA\text{-}Fe\text{-}TiO_2)_{,dark}$, $(HA_{,pho}\text{-}Fe\text{-}TiO_2)$ and $(HA\text{-}Fe\text{-}TiO_2)_{,photocat}$, the HDS of $(HA\text{-}Fe\text{-}TiO_2)_{,as\text{-}is}$ was the smallest in general. Similar with the $(HA\text{-}Fe\text{-}TiO_2)_{,dark}$, leached Fe(II) was interacted with HA, however the pre-treatment duration was only 30 min for $(HA\text{-}Fe\text{-}TiO_2)$, leached Fe(II) amount were less than $(HA\text{-}Fe\text{-}TiO_2)_{,dark}$ (pretreatment duration:60 min). Consequently, formation of bigger HA-HA hetero-agglomerates could probably not achieve as much as achieved in $(HA\text{-}Fe\text{-}TiO_2)_{,dark}$, so the agglomerate size of $(HA\text{-}Fe\text{-}TiO_2)_{,as\text{-}is}$ were less than other binary systems ($(HA\text{-}Fe\text{-}TiO_2)_{,dark}$, $(HA_{,pho}\text{-}Fe\text{-}TiO_2)$ and $(HA\text{-}Fe\text{-}TiO_2)_{,photocat}$).

Finally, the intensity-weighted HDS of $(HA\text{-}TiO_2)_{,photocat}$ and $(HA\text{-}Fe\text{-}TiO_2)_{,photocat}$ were compared to understand effect of Fe doping on aggregation/agglomeration of the binary system under visible light irradiation. As mentioned before, HA adsorption ratio onto Fe-TiO_2 (>45%) surface was higher TiO_2 (33%) (Birben et al., 2017). Also, formation of superhydrophilic surface could be achieved more easily on Fe-TiO_2 thereby the hydration layer would be covered with smaller aggregates of Fe-TiO_2 in comparison to TiO_2. This phenomenon could increase the possibility of Fe-TiO_2 homo-agglomerate formation, and bigger homo-agglomerates could precipitate easily. Also, not only TiO_2 homo-agglomerates after solar irradiation were more stable than Fe-TiO_2 homo-agglomerates, but also due to Fe doping increased the weight of TiO_2 aggregates therefore these structures were more prone to precipitate.

Table 3.64. Intensity-, volume-, surface area- and number-weighted HDS and cumulative ratios of $(HA\text{-}Fe\text{-}TiO_2)_{,photocat}$.

	HDS, nm	Cumulative Ratio, %			
		Intensity	Volume	Surface Area	Number
Initial	225.2-275.4	20%	20%	50%	70%
	304.5-336.7	13%	17%	32%	30%
	2058.8-2276.6	24%	50%	15%	-
	2517.6	23%	9%	2%	-
	2784.0-3078.6	20%	4%	1%	-
30 min	194.1-230.2	18%	6%	25%	60%
	250.7-297.4	20%	6%	21%	37%
	1166.3-1270.3	13%	10%	7%	-
	1383.5	18%	55%	34%	2%
	1506.9	17%	11%	6%	1%
	1641.2-1787.5	14%	12%	7%	-
60 min	147.5-171.8	18%	6%	22%	75%
	185.4-200.1	8%	2%	6%	15%
	678.9-732.8	17%	31%	21%	3%
	790.9	21%	49%	39%	6%
	853.6	21%	11%	8%	1%
	921.4-994.4	15%	7%	4%	-
90 min	182.0-195.4	12%	3%	11%	37%
	209.9	12%	4%	9%	27%
	225.4-242.1	15%	3%	3%	22%
	707.0-759.3	16%	51%	42%	9%
	815.5	17%	23%	18%	3%
	875.9	16%	9%	6%	1%
	940.8-1010.5	12%	7%	5%	1%
120 min	199.7-213.4	15%	8%	19%	35%
	227.9	19%	9%	20%	31%
	243.5	16%	8%	15%	20%
	260.1-277.8	10%	4%	8%	10%
	798.7-853.2	11%	25%	15%	2%
	911.4	14%	14%	7%	1%
	973.6-1040.0	15%	32%	16%	1%

Table 3.65. Intensity-weighted HDS profile of $(HA\text{-}Fe\text{-}TiO_2)_{,photocat}$. Time dependent HDS cluster maximas, HDS range and min-max diameter difference with respect to multi-size distribution.

	Cluster			
Time, min	Max 1, nm	Max 2, nm	Range, nm	Difference, nm
Initial	275.4	2517.6	184.1-4603.6	4419.5
30	250.7	1506.9	150.2-2309.5	2159.3
60	171.8	790.9	117.3-1349.6	1232.3
90	209.9	815.5	136.7-1344.7	1208.0
120	227.9	911.4	163.9-1354.2	1190.3

Table 3.66. Comparison of intensity-weighted HDS values of $HA_{,photocat}$, $TiO_{2,irr}$, and $(HA\text{-}TiO_2)_{,photocat}$.

	$HA_{,photocat}$		$Fe\text{-}TiO_{2,irr}$		$(HA\text{-}Fe\text{-}TiO_2)_{,photocat}$	
	HDS, nm	CR, %	HDS, nm	CR, %	HDS, nm	CR, %
Initial	52.3-62.7	24%	153.4-197.9	17%	225.2-275.4	20%
	75.2-90.1	19%	224.8-255.3	10%	304.5-336.7	13%
	6961.0-10000	57%	2225.5	7%	2058.8-2276.6	24%
	-	-	2527.8	17%	2517.6	23%
	-	-	2871.2	25%	2784.0-3078.6	20%
	-	-	3261.2-3704.2	24%	-	-
			-	-	-	-
30 min	45.8-51.7	9%	148.5-176.0	16%	194.1-230.2	18%
	155.0-175.1	50%	191.6	10%	250.7-297.4	20%
	186.1-210.2	41%	208.6-227.1	9%	1166.3-1270.3	13%
	-	-	811.1-882.9	11%	1383.5	18%
	-	-	961.1	16%	1506.9	17%
			1046.2	19%	1641.2-1787.5	14%
			1138.9-1239.8	17%		
60 min	88.3-106.2	30%	134.9-145.1	13%	147.5-171.8	18%
	116.4-139.8	29%	156.1	13%	185.4-200.1	8%
	554.8-666.7	29%	168.0-180.7	13%	678.9-732.8	17%
	730.8-801.1	12%	582.1-626.2	18%	790.9	21%
	-	-	673.7	19%	853.6	21%
	-	-	724.8	15%	921.4-994.4	15%
			779.8-838.9	9%	-	-
90 min	21.3-26.0	2%	132.1-150.1	17%	182.0-195.4	12%
	86.8-106.2	20%	160.0	12%	209.9	12%
	117.4-129.8	12%	170.5-181.7	11%	225.4-242.1	15%
	175.4-237.0	52%	504.1-537.3	22%	707.0-759.3	16%
	262.0-289.7	14%	572.7	20%	815.5	17%
	-	-	610.4-650.6	18%	875.9	16%
					940.8-1010.5	12%
120 min	99.0-113.4	37%	142.5-164.5	20%	199.7-213.4	15%
	121.3-129.8	19%	176.8	13%	227.9	19%
	438.7-502.2	33%	190.0-204.2	10%	243.5	16%
	537.4-575.0	11%	601.4-646.3	15%	260.1-277.8	10%
	-	-	694.5	16%	798.7-853.2	11%
	-	-	746.4	15%	911.4	14%
			802.1-862.0	11%	973.6-1040.0	15%

Table 3.67. Comparison of intensity-weighted HDS values of $(HA\text{-}Fe\text{-}TiO_2)_{,as\text{-}is}$, $(HA\text{-}Fe\text{-}TiO_2)_{,dark}$, $(HA_{,pho}\text{-}Fe\text{-}TiO_2)$ and $(HA\text{-}Fe\text{-}TiO_2)_{,photocat}$.

	$(HA\text{-}Fe\text{-}TiO_2)_{,as\text{-}is}$		$(HA\text{-}Fe\text{-}TiO_2)_{,dark}$		$(HA_{,pho}\text{-}Fe\text{-}TiO_2)$		$(HA\text{-}Fe\text{-}TiO_2)_{,photocat}$		
	HDS, nm	CR, %	HDS, nm	CR, %	HDS, nm	CR, %	HDS, nm	CR, %	
Initial	163.9-203.7	15%	Dark Mixing		60 min Solar Irradiation onto HA then TiO_2 suspended in $HA_{,pho}$		60 min Solar Irradiation and Mixing		
	227.0-282.1	16%							
	1438.3-1603.2	11%							
	1787.2	17%							
	1992.2	21%							
	2220.7-2475.4	20%							
30 min	144.4-168.8	20%							
	182.5-197.2	12%							
	801.0-865.9	25%							
	936.0	23%							
	1011.8-1093.7	20%							
60 min	175.9-189.8	13%	148.6-177.8	22%	163.2-202.8	17%	225.2-275.4	20%	Initial
	204.7	16%	194.5-212.7	15%	226.0-280.9	14%	304.5-336.7	13%	
	220.8-238.2	18%	522.0-624.6	19%	1596.2-1779.3	20%	2058.8-2276.6	24%	
	742.1-800.5	12%	683.3-747.4	12%	1983.4	22%	2517.6	23%	
	863.5	14%	978.4-1280.7	17%	2210.9	17%	2784.0-3078.6	20%	
	931.4	16%	1401.0-1676.5	15%	2464.5-2747.2	10%	-	-	
	1004.7-1083.8	11%	-	-	-	-	-	-	
90 min	211.4-225.8	19%	144.8-166.5	18%	145.5-171.0	25%	194.1-230.2	18%	30 min
	241.2	19%	178.5	13%	185.4-201.0	17%	250.7-297.4	20%	
	257.7-275.3	19%	191.4-205.2	12%	675.4-732.2	13%	1166.3-1270.3	13%	
	791.3-903.0	19%	544.5-583.9	16%	793.9	15%	1383.5	18%	
	964.6-1100.7	22%	626.0	16%	860.7	18%	1506.9	17%	
	-	-	671.2-771.6	9%	933.1-1011.7	12%	1641.2-1787.5	14%	

Table 3.68. Comparison of intensity-weighted HDS values of (HA-Fe-TiO_2)$_{,as\text{-}is}$, (HA-Fe-TiO_2)$_{,dark}$, (HA$_{,pho}$-Fe-TiO_2) and (HA-Fe-TiO_2)$_{,photocat}$ (Continue).

120 min	118.5-134.9	14%	170.0-180.2	14%	158.8-184.2	23%	147.5-171.8	18%	60 min
	143.9-153.4	11%	191.1	14%	198.3	16%	185.4-200.1	8%	
	431.1-459.8	25%	202.5-214.7	15%	213.5-229.9	14%	678.9-732.8	17%	
	490.5	23%	578.6-613.4	15%	697.4-750.9	15%	790.9	21%	
	523.2	17%	650.2	18%	808.5	15%	853.6	21%	
	558.1-595.3	10%	689.3-774.6	24%	870.6-1009.4	17%	921.4-994.4	15%	
150 min	152.2-175.0	18%	161.5-171.8	14%	144.5-155.3	14%	182.0-195.4	12%	90 min
	187.6	13%	182.8	16%	166.9	14%	209.9	12%	
	201.2-215.7	12%	194.6-207.1	19%	179.4-192.8	15%	225.4-242.1	15%	
	572.3-613.7	18%	559.9-595.8	16%	610.2-655.7	7%	707.0-759.3	16%	
	658.0	19%	634.0	16%	704.7	15%	815.5	17%	
	705.5-811.0	20%	674.7	12%	757.3	19%	875.9	16%	
	-	-	718.0-764.0	7%	813.8-874.6	16%	940.8-1010.5	12%	
180 min	162.0-189.9	13%	179.0-190.2	16%	171.1-183.2	20%	199.7-213.4	15%	120 min
	222.5	18%	202.1	18%	196.3	16%	227.9	19%	
	260.7	20%	214.8-228.3	20%	210.2-225.2	13%	243.5	16%	
	305.5-358.0	17%	604.6-642.5	10%	631.3-676.3	13%	260.1-277.8	10%	
	576.1-675.1	17%	682.9	13%	724.4	16%	798.7-853.2	11%	
	791.1-1086.3	15%	725.7	13%	775.9	12%	911.4	14%	
	-	-	771.3-819.7	10%	831.1-890.2	10%	973.6-1040.0	15%	

Table 3.69. Comparison of intensity-weighted HDS values of $(HA\text{-}TiO_2)_{,photocat}$ and $(HA\text{-}Fe\text{-}TiO_2)_{,photocat}$.

	$(HA\text{-}TiO_2)_{,photocat}$		$(HA\text{-}Fe\text{-}TiO_2)_{,photocat}$	
	HDS, nm	CR, %	HDS, nm	CR, %
Initial	253.2-286.5	8%	225.2-275.4	20%
	324.1-414.8	18%	304.5-336.7	13%
	1822.5	7%	2058.8-2276.6	24%
	2061.8	15%	2517.6	23%
	2332.4	21%	2784.0-3078.6	20%
	2638.7	19%	-	-
	2985.1-3376.9	13%	-	-
30 min	218.5-242.3	10%	194.1-230.2	18%
	268.6-330.2	17%	250.7-297.4	20%
	1721.5-1908.6	19%	1166.3-1270.3	13%
	2116.2	22%	1383.5	18%
	2346.2	19%	1506.9	17%
	2603.1-2884.1	13%	1641.2-1787.5	14%
60 min	261.8-306.6	8%	147.5-171.8	18%
	359.1	12%	185.4-200.1	8%
	420.6-576.9	17%	678.9-732.8	17%
	2042.5	8%	790.9	21%
	2392.1	16%	853.6	21%
	2801.6	21%	921.4-994.4	15%
	3281.3-3843.0	18%	-	-
90 min	228.9-253.1	12%	182.0-195.4	12%
	279.9-342.4	20%	209.9	12%
	1711.6-1892.7	20%	225.4-242.1	15%
	2093.0	21%	707.0-759.3	16%
	2314.5	17%	815.5	17%
	2559.5-2830.3	10%	875.9	16%
	-	-	940.8-1010.5	12%
120 min	224.9-302.4	17%	199.7-213.4	15%
	350.5-471.2	23%	227.9	19%
	1538.4-1783.6	14%	243.5	16%
	2068.0	17%	260.1-277.8	10%
	2397.6	17%	798.7-853.2	11%
	2779.8-3222.8	12%	911.4	14%
	-	-	973.6-1040.0	15%

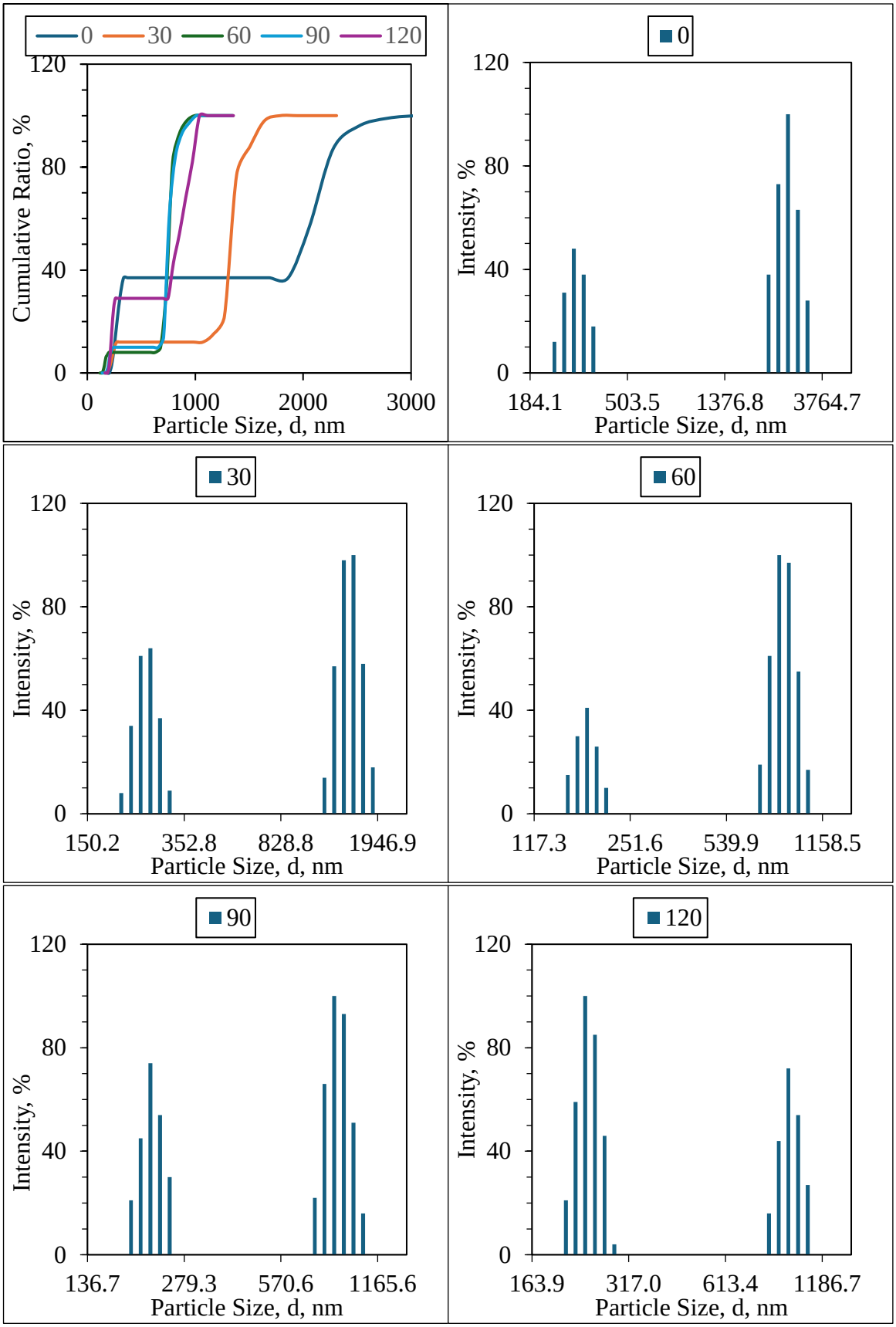


Figure 3.93. The cumulative ratio comparison and hydrodynamic size of (HA-Fe-TiO_2)$_{,photocat}$ as intensity-weighted HDS in 30 min intervals.

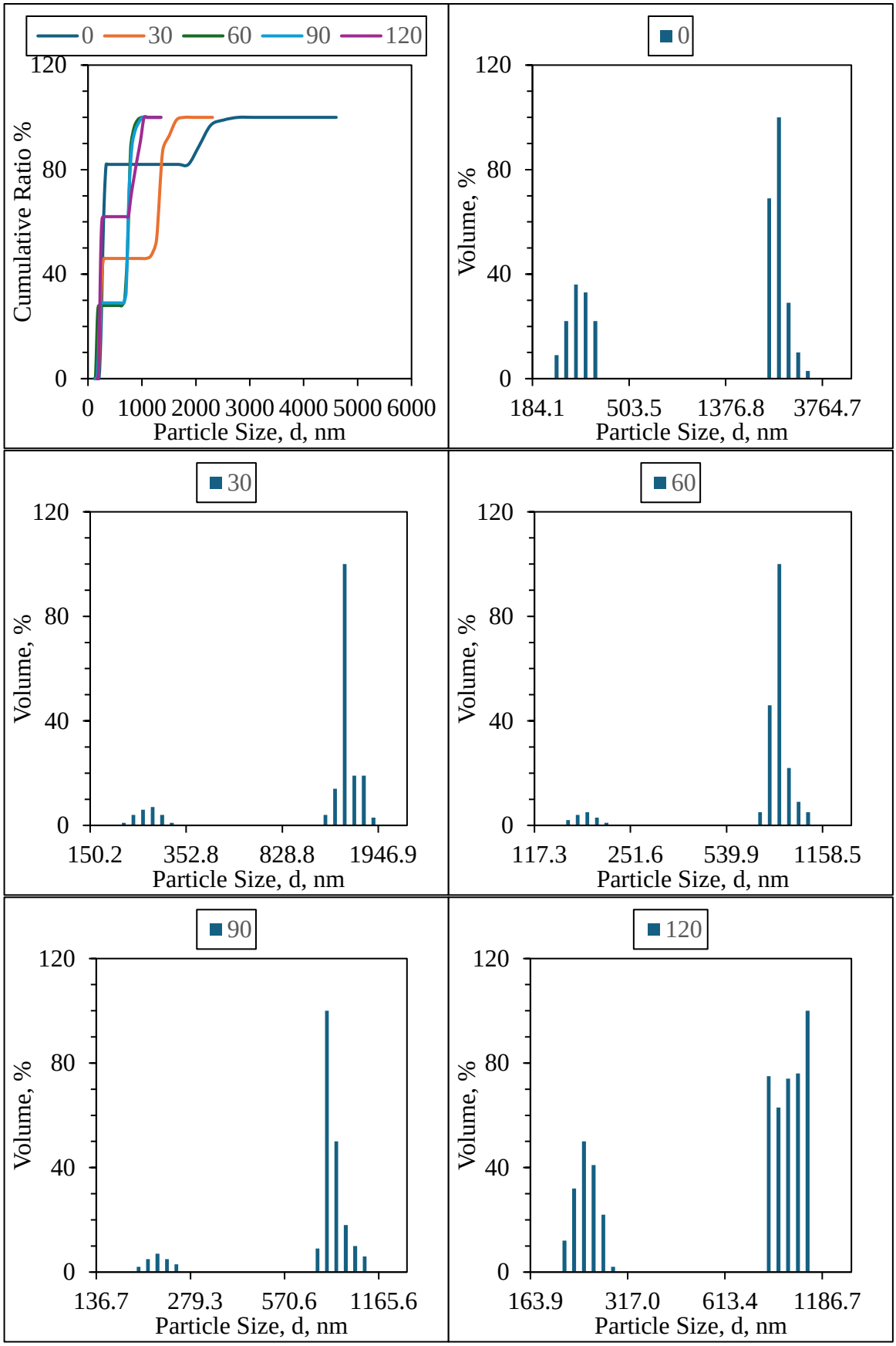


Figure 3.94. The cumulative ratio comparison and hydrodynamic size of $(HA\text{-}Fe\text{-}TiO_2)_{,photocat}$ as volume-weighted HDS in 30 min intervals.

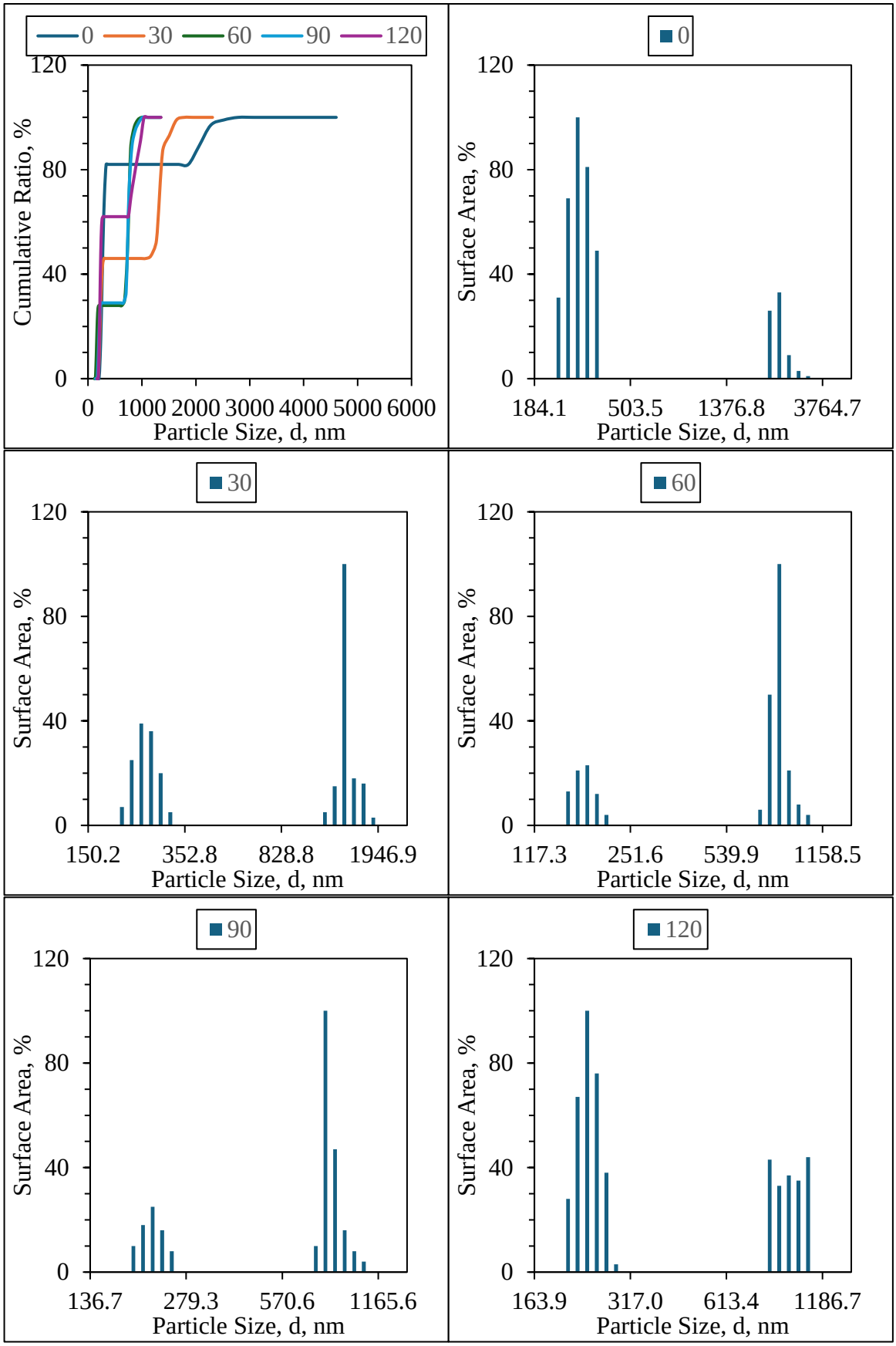


Figure 3.95. The cumulative ratio comparison and hydrodynamic size of $(HA\text{-}Fe\text{-}TiO_2)_{,photocat}$ as surface area-weighted HDS in 30 min intervals.

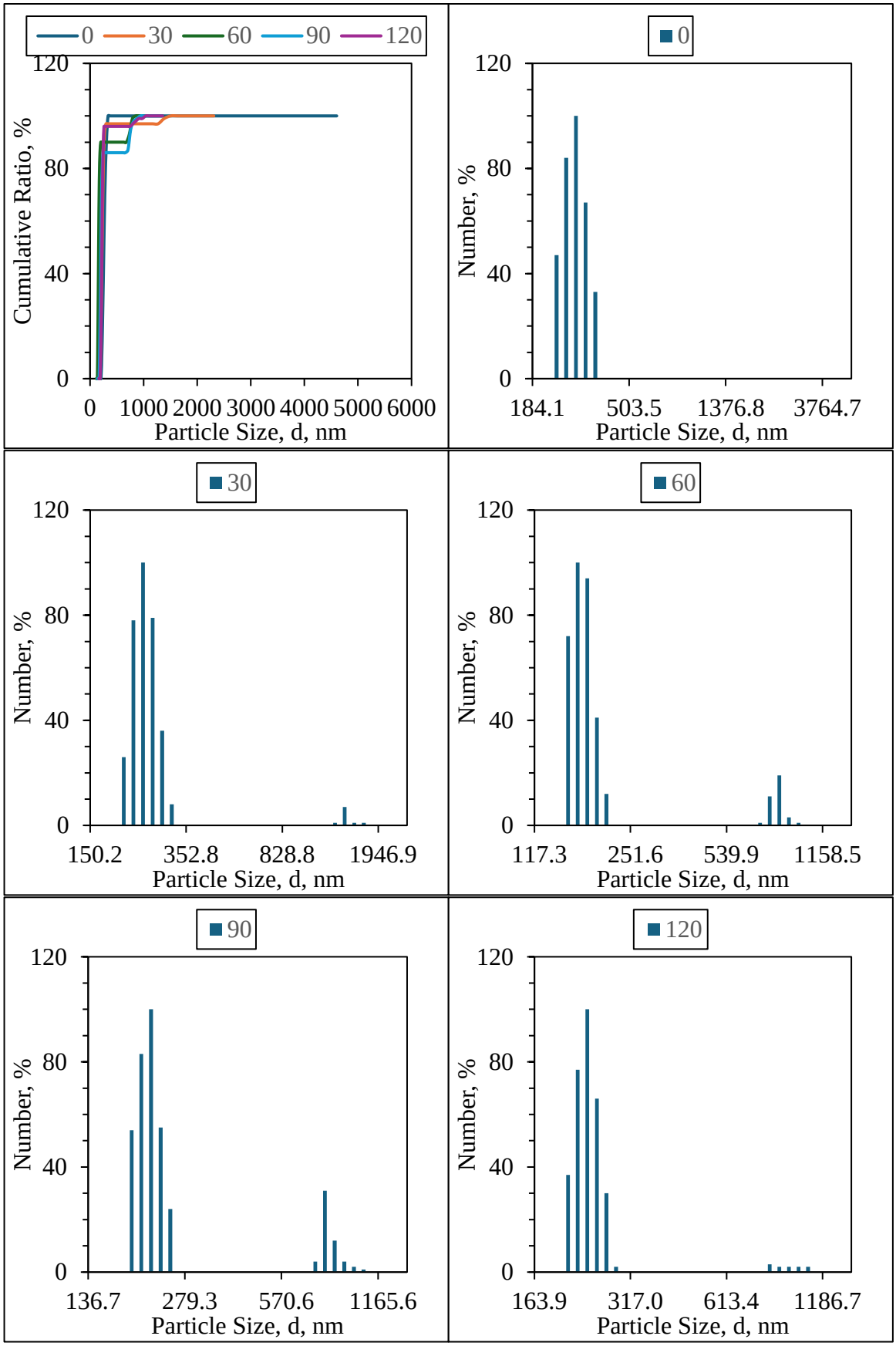


Figure 3.96. The cumulative ratio comparison and hydrodynamic size of $(HA\text{-}Fe\text{-}TiO_2)_{,photocat}$ as volume-weighted HDS in 30 min intervals.

3.5.9. Hydrodynamic Size Assessment of (HA-N-TiO_2)$_{as-is}$

The effect of anion doping on TiO_2 hetero-aggregation/agglomeration behavior in the presence of HA was investigated by suspending N-TiO_2 in HA solution. Appropriate amount of N-TiO_2 was weighted and added into 100 mL HA solution to achieve 0.25 mgL^{-1} N-TiO_2 concentration as final solution. Obtained N-TiO_2-HA mixture was mixed with a magnetic stirrer for 30 min to obtain proper suspension of N-TiO_2 and named as (HA-N-TiO_2)$_{,as-is}$. The 4 mL of the prepared suspension was directly subjected to DLS measurements after preparation for 180 min without removing the cuvette. The HDS results were compiled in Table 3.68 as intensity-, volume-, surface area-, and number-weighted HDS with their corresponding CR%. Also, the maxima, range and min max differences were compiled in Table 3.69. The graphical abstracts of Table 3.68 and Table 3.69 were illustrated in Figure 3.97, Figure 3.98, Figure 3.99 and Figure 3.100 and intensity-, volume-, surface area-, and number-weighted HDS, respectively. The PDI values of the (HA-N-TiO_2)$_{,as-is}$ system was found for initial, 30 min, 60 min, 90 min, 120 min, 150 min and 180 min measurements as 0.374, 0.322, 0.269, 0.286, 0.285, 0.226 and 0.283, respectively. The average PDI for the (HA-N-TiO_2)$_{,as-is}$ binary system was calculated as 0.292 that was an indicator of nearly monodispersed composition, therefore MSD approximation was applied to explain HDS of (HA-N-TiO_2)$_{,as-is}$ binary system.

The initial HDS profile of (HA-N-TiO_2)$_{,as-is}$ comprised of two main clusters around 175.1-261.8 nm and 1600.7-2646.9 nm (Table 3.68) with the peak points of 214.1 nm and 1957.4 nm, respectively. The number-weighted CR% of the 175.1-261.8 nm cluster was approximately 100% that implied the system mostly composed of aggregated structures and the larger cluster around 1600.7-2646.9 nm was only few in number. Birben and colleagues reported that the instantaneous adsorption extent of HA onto N-TiO_2 was 41.3% of the initial DOC whereas, HA adsorption onto TiO_2 surface was determined as (47.6% DOC) (Birben et al., 2015). Hence the bigger cluster ranging between 1600.7-2646.9 nm were mostly comprised of HA hetero-agglomerates or in another word physical hydrogel formation. The volume- (15%) and surface area-weighted (4%) CR% of these structures showed that these structures were mostly spherical supramolecular agglomerates with a high volume and smaller surface area. As mentioned before physical hydrogel formation was depending on mixing and when the solution settled down these structures disagglomerated as evidenced in the 30 min results (Table 3.68). This trend also showed that the structures around 1070.5-1275.7 nm might be mostly formed by HA-N-TiO_2 hetero-aggregates. The removal efficiency of the (HA-N-TiO_2)$_{,as-is}$ was 30% at the end of 30 min. This ratio covered both disagglomeration of HA hetero-agglomerates and small amount of precipitated HA-N-TiO_2 hetero-aggregates. At the end of 90 min, the removal ratio increased to 40%. The 10% difference might be related to the HA-N-TiO_2 hetero-aggregate

precipitation. The HDS profile of $(HA\text{-}N\text{-}TiO_2)_{,as\text{-}is}$ was sporting this theory by disappearance of the structures > 1000 nm in 90 min. After the disappearance of the structures above 1000 nm, the visibility of a middle size cluster around 500-900 nm increased with a CR% of approximately 10% as number-weighted HDS. These structures mostly comprised of $HA\text{-}N\text{-}TiO_2$ hetero-aggregates with a smaller $N\text{-}TiO_2$ aggregate core, so the surface adsorbed HA could increase the colloidal stability, hence these structures were colloidally stable in the $(HA\text{-}N\text{-}TiO_2)_{,as\text{-}is}$ system during 180 min (Table 3.68).

The HA adsorption onto $N\text{-}TiO_2$ aggregates was evidenced by the comparison of intensity-weighted HDS of $HA_{,as\text{-}is}$, $N\text{-}TiO_{2,as\text{-}is}$ and $(HA\text{-}N\text{-}TiO_2)_{,as\text{-}is}$ in Table 3.70. Both HA and $N\text{-}TiO_2$ were composed of aggregates around 100-300 nm, however the physical hydrogel formation was observed around 3165.7-6617.0 nm for HA and $N\text{-}TiO_2$ hetero-agglomerates were around 1269.9-2099.9 nm in mono system as-is conditions. The $(HA\text{-}N\text{-}TiO_2)_{,as\text{-}is}$ binary system resembling mostly to $N\text{-}TiO_{2,as\text{-}is}$. Because of the HA structures adsorbed onto $N\text{-}TiO_2$ in the binary system, the physical hydrogel around 3000-6000 nm were not observed however, smaller hetero-agglomerates of HA were observed as mentioned in previous paragraph. The intensity-weighted HDS of the structures observed in $(HA\text{-}N\text{-}TiO_2)_{,as\text{-}is}$ was slightly higher than the $N\text{-}TiO_{2,as\text{-}is}$. This trend might be related with the HA adsorption onto $N\text{-}TiO_2$ aggregates and HA hetero-agglomerates in the media. Also, the CR% of the bigger clusters were higher in $(HA\text{-}N\text{-}TiO_2)_{,as\text{-}is}$ in comparison to $N\text{-}TiO_2$ that could be concluded as the HA adsorption onto $N\text{-}TiO_2$ surface created colloidally more stable structures. Table 3.71 compared the intensity-weighted HDS results of $(HA\text{-}TiO_2)_{,as\text{-}is}$, $(HA\text{-}Fe\text{-}TiO_2)_{,as\text{-}is}$ and $(HA\text{-}N\text{-}TiO_2)_{,as\text{-}is}$ to understand effect of anion and cation doping on the aggregation/agglomeration behavior of $HA\text{-}TiO_2$ binary system. In all three systems HA showed different affinities toward non doped and doped TiO_2 which was mainly affecting the hetero-aggregate formation. The hetero-aggregate formation order of binary systems was $HA\text{-}Fe\text{-}TiO_2 > HA\text{-}TiO_2 > HA\text{-}N\text{-}TiO_2$ in as-is conditions. Even the surface adsorption was higher in $(HA\text{-}Fe\text{-}TiO_2)_{,as\text{-}is}$ due to the chelate formation between Fe and HA, $HA\text{-}Fe\text{-}TiO_2$ hetero-aggregates were not colloidally stable due to the increased weight of $Fe\text{-}TiO_2$ after Fe doping, so the HDS order at the end of 180 min was listed as $HA\text{-}TiO_2 > HA\text{-}Fe\text{-}TiO_2 > HA\text{-}N\text{-}TiO_2$ in as-is conditions. It must be also noted that $N\text{-}TiO_2$ precipitation of homo-agglomerate formation was slightly less than $Fe\text{-}TiO_2$ and TiO_2 due to the electrostatic effect created by the hetero-agglomerated HA structures in the media. Consequently, it could be concluded as doping directly affected the HDS of colloidally stable structures while more stabilized hetero-aggregates were achieved with anion (N) doped TiO_2 in comparison to cation (Fe) doped TiO_2. The main reason of the HDS difference was the additional forces created by Fe ions, such as magnetic forces, and increased hydrogen bonding capacity by N doping.

Table 3.70. Intensity-, volume-, surface area- and number-weighted HDS and cumulative ratios of $(HA\text{-}N\text{-}TiO_2)_{,as\text{-}is}$.

	HDS, nm	Cumulative Ratio, %			
		Intensity	Volume	Surface Area	Number
Initial	175.1-214.1	19%	14%	48%	75%
	236.7-261.8	14%	9%	25%	25%
	1600.7-1770.1	22%	31%	12%	-
	1957.4	21%	31%	11%	-
	2164.5	16%	8%	2%	-
	2393.6-2646.9	8%	7%	2%	-
30 min	185.3-202.3	11%	4%	16%	36%
	220.3	14%	5%	16%	29%
	241.1	14%	5%	14%	21%
	263.2-287.3	11%	3%	8%	12%
	1070.5-1275.7	19%	18%	13%	1%
	1392.6	16%	52%	27%	1%
	1520.3-1659.6	15%	13%	6%	-
60 min	167.9-192.3	23%	10%	26%	53%
	205.7	16%	6%	15%	26%
	220.1-235.6	16%	5%	12%	16%
	744.1-796.2	13%	49%	31%	4%
	851.9	14%	14%	8%	-
	911.6-1043.7	18%	16%	8%	1%
90 min	139.6-161.0	17%	8%	24%	59%
	172.9-199.5	21%	6%	19%	35%
	582.5-625.6	17%	8%	6%	-
	671.9	19%	13%	9%	2%
	721.7	15%	26%	17%	2%
	775.1-832.5	11%	39%	15%	2%
120 min	151.2-174.6	22%	7%	23%	63%
	187.6-216.7	23%	5%	15%	29%
	638.1-685.7	14%	9%	7%	1%
	736.9	17%	37%	27%	4%
	791.9	15%	38%	24%	3%
	791.9-914.6	11%	6%	4%	-
150 min	181.7-192.9	12%	4%	12%	30%
	204.8	15%	5%	12%	27%
	217.5	15%	5%	11%	20%
	230.9-245.2	12%	4%	8%	13%
	602.7-639.9	13%	40%	6%	1%
	679.5	13%	13%	9%	2%
	721.5-813.4	20%	62%	42%	7%
180 min	139.1-149.4	12%	8%	23%	48%
	160.6	12%	7%	17%	29%
	172.6-185.5	12%	5%	13%	17%
	546.9-587.7	15%	10%	6%	1%
	631.6	19%	12%	8%	1%
	678.8	17%	17%	11%	1%
	729.6-784.1	13%	41%	22%	2%

Table 3.71. Intensity-weighted HDS profile of $(HA\text{-}N\text{-}TiO_2)_{,as\text{-}is}$. Time dependent HDS cluster maximas, HDS range and min-max diameter difference with respect to multi-size distribution.

	Cluster				
Time, min	Max 1, nm	Max 2, nm	Max 3, nm	Range, nm	Difference, nm
Initial	214.1	1957.4	-	3579.3-143.2	3436.1
30	220.8	241.1	1392.6	130.5-2159.0	2028.5
60	192.3	205.7	851.9	146.7-1278.5	1131.8
90	172.9	671.9	-	112.6-1107.9	995.3
120	174.6	187.6	736.9	113.3-1135.1	1021.8
150	204.8	217.5	679.5	151.8-1033.9	882.1
180	160.6	631.6	678.8	104.2-1046.1	941.9

Table 3.72. Comparison of intensity-weighted HDS values of $HA_{,as\text{-}is}$, $N\text{-}TiO_{2,as\text{-}is}$ and $(HA\text{-}N\text{-}TiO_2)_{,as\text{-}is}$.

	$HA_{,as\text{-}is}$		$N\text{-}TiO_{2,as\text{-}is}$		$(HA\text{-}N\text{-}TiO_2)_{,as\text{-}is}$	
Initial	106.5-197.8	73%	153.6-187.8	23%	175.1-214.1	19%
	243.2-299.0	25%	207.7-229.7	15%	236.7-261.8	14%
	3561.7	1%	1269.9-1404.3	10%	1600.7-1770.1	22%
	6617.0	1%	1552.9	17%	1957.4	21%
	-	-	1717.2	19%	2164.5	16%
	-	-	1898.9-2099.9	17%	2393.6-2646.9	8%
60 min	155.4-182.0	72%	148.6-159.4	13%	167.9-192.3	23%
	185.3-188.5	28%	171.0	14%	205.7	16%
	-	-	183.5-196.9	17%	220.1-235.6	16%
	-	-	607.2-651.5	15%	744.1-796.2	13%
	-	-	699.0	17%	851.9	14%
	-	-	749.9	14%	911.6-1043.7	18%
	-	-	804.6-863.6	10%	-	-
90 min	47.7-61.1	4%	151.6-175.7	22%	139.6-161.0	17%
	164.4-186.3	62%	189.2	16%	172.9-199.5	21%
	198.2-224.3	34%	203.7-219.4	14%	582.5-625.6	17%
	-	-	665.4-716.5	20%	671.9	19%
	-	-	771.5	15%	721.7	15%
	-	-	830.7-894.5	13%	775.1-832.5	11%
120 min	167.8-169.9	62%	180.4-190.3	13%	151.2-174.6	22%
	171.0-173.2	38%	200.8	17%	187.6-216.7	23%
	-	-	211.8	16%	638.1-685.7	14%
	-	-	223.4-235.7	14%	736.9	17%
	-	-	525.4-554.3	14%	791.9	15%
	-	-	584.7	12%	791.9-914.6	11%
	-	-	616.8-686.4	14%	-	-

Table 3.73. Comparison of intensity-weighted HDS values of $(HA\text{-}TiO_2)_{,as\text{-}is}$, $(HA\text{-}Fe\text{-}TiO_2)_{,as\text{-}is}$ and $(HA\text{-}N\text{-}TiO_2)_{,as\text{-}is}$.

	$(HA\text{-}TiO_2)_{,as\text{-}is}$		$(HA\text{-}Fe\text{-}TiO_2)_{,as\text{-}is}$		$(HA\text{-}N\text{-}TiO_2)_{,as\text{-}is}$	
	HDS, nm	CR, %	HDS, nm	CR, %	HDS, nm	CR, %
Initial	156.1-184.7	9%	163.9-203.7	15%	175.1-214.1	19%
	200.9-237.3	16%	227.0-282.1	16%	236.7-261.8	14%
	840.8	9%	1438.3-1603.2	11%	1600.7-1770.1	22%
	914.7	18%	1787.2	17%	1957.4	21%
	995.1	25%	1992.2	21%	2164.5	16%
	1082.5-1177.6	23%	2220.7-2475.4	20%	2393.6-2646.9	8%
30 min	157.0-172.2	8%	144.4-168.8	20%	185.3-202.3	11%
	188.9-227.3	21%	182.5-197.2	12%	220.3	14%
	911.1-999.5	21%	801.0-865.9	25%	241.1	14%
	1096.4	22%	936.0	23%	263.2-287.3	11%
	1202.7-1447.3	28%	1011.8-1093.7	20%	1070.5-1275.7	19%
	-	-	-	-	1392.6	16%
	-	-	-	-	1520.3-1659.6	15%
60 min	193.0-208.8	15%	175.9-189.8	13%	167.9-192.3	23%
	225.8-264.3	16%	204.7	16%	205.7	16%
	1005.2	13%	220.8-238.2	18%	220.1-235.6	16%
	1087.4	18%	742.1-800.5	12%	744.1-796.2	13%
	1176.3	21%	863.5	14%	851.9	14%
	1272.5-1376.5	17%	931.4	16%	911.6-1043.7	18%
	-	-	1004.7-1083.8	11%	-	-
90 min	164.6-192.0	18%	211.4-225.8	19%	139.6-161.0	17%
	207.3-223.9	9%	241.2	19%	172.9-199.5	21%
	766.9-828.2	18%	257.7-275.3	19%	582.5-625.6	17%
	894.5	21%	791.3-903.0	19%	671.9	19%
	966.0	20%	964.6-1100.7	22%	721.7	15%
	1043.3-1126.7	14%	-	-	775.1-832.5	11%
120 min	143.8-156.6	9%	118.5-134.9	14%	151.2-174.6	22%
	170.5-202.2	15%	143.9-153.4	11%	187.6-216.7	23%
	789.6	8%	431.1-459.8	25%	638.1-685.7	14%
	859.8	16%	490.5	23%	736.9	17%
	936.2	25%	523.2	17%	791.9	15%
	1019.4	17%	558.1-595.3	10%	791.9-914.6	11%
	1110.0-1208.7	10%	-	-	-	-
150 min	138.7-164.4	14%	152.2-175.0	18%	181.7-192.9	12%
	179.0-194.9	11%	187.6	13%	204.8	15%
	761.3-829.0	25%	201.2-215.7	12%	217.5	15%
	902.7	24%	572.3-613.7	18%	230.9-245.2	12%
	982.9	17%	658.0	19%	602.7-639.9	13%
	1070.2-1165.4	9%	705.5-811.0	20%	679.5	13%
	-	-	-	-	721.5-813.4	20%
180 min	39.8-175.3	12%	162.0-189.9	13%	139.1-149.4	12%
	200.6-262.6	20%	222.5	18%	160.6	12%
	674.9-772.4	18%	260.7	20%	172.6-185.5	12%
	883.9	20%	305.5-358.0	17%	546.9-587.7	15%
	1011.5	17%	576.1-675.1	17%	631.6	19%
	1157.5-1324.5	13%	791.1-1086.3	15%	678.8	17%
	-	-	-	-	729.6-784.1	13%

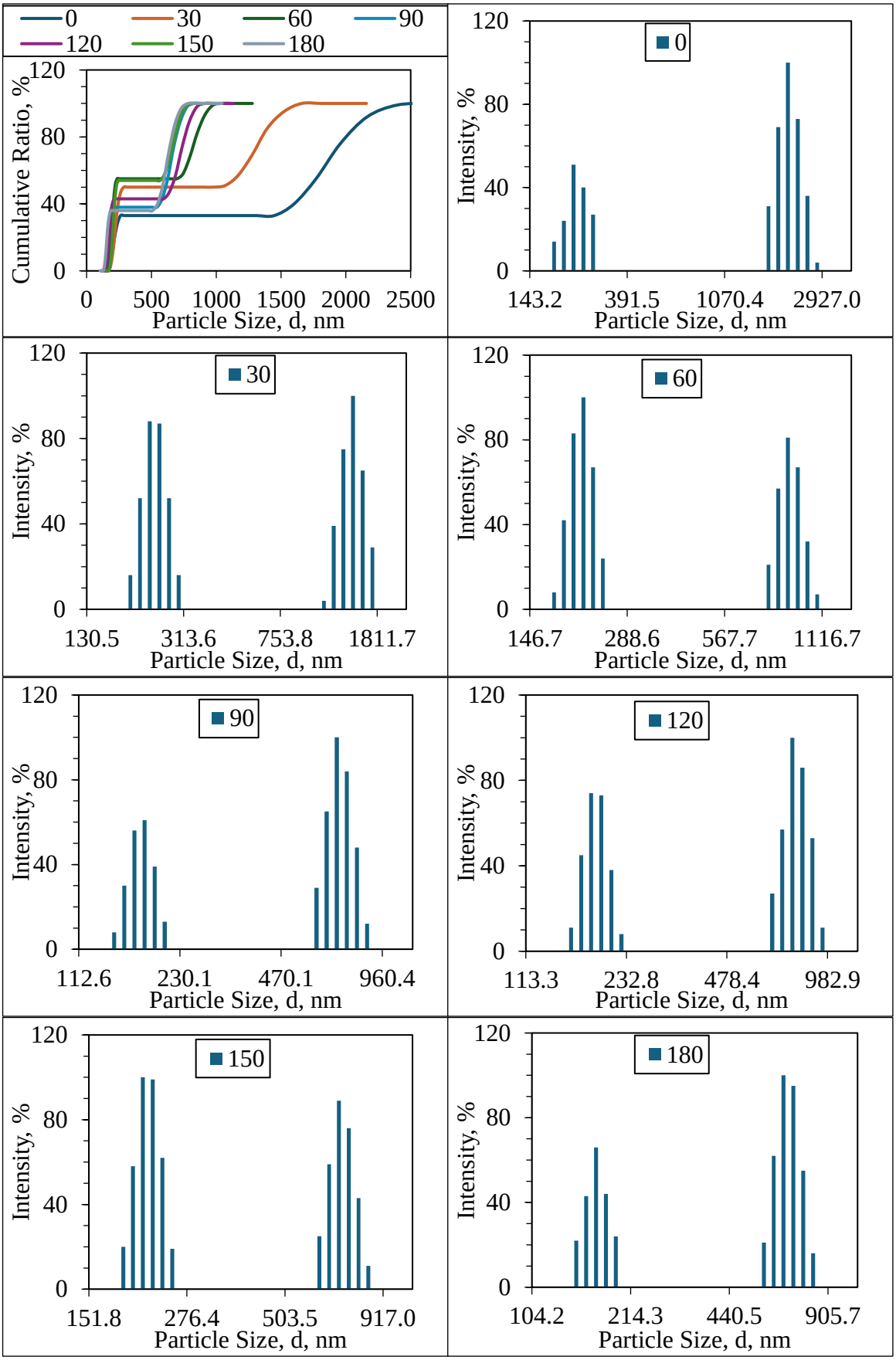


Figure 3.97. The cumulative ratio comparison and hydrodynamic size of $(HA\text{-}N\text{-}TiO_2)_{,as\text{-}is}$ as intensity-weighted HDS in 30 min intervals.

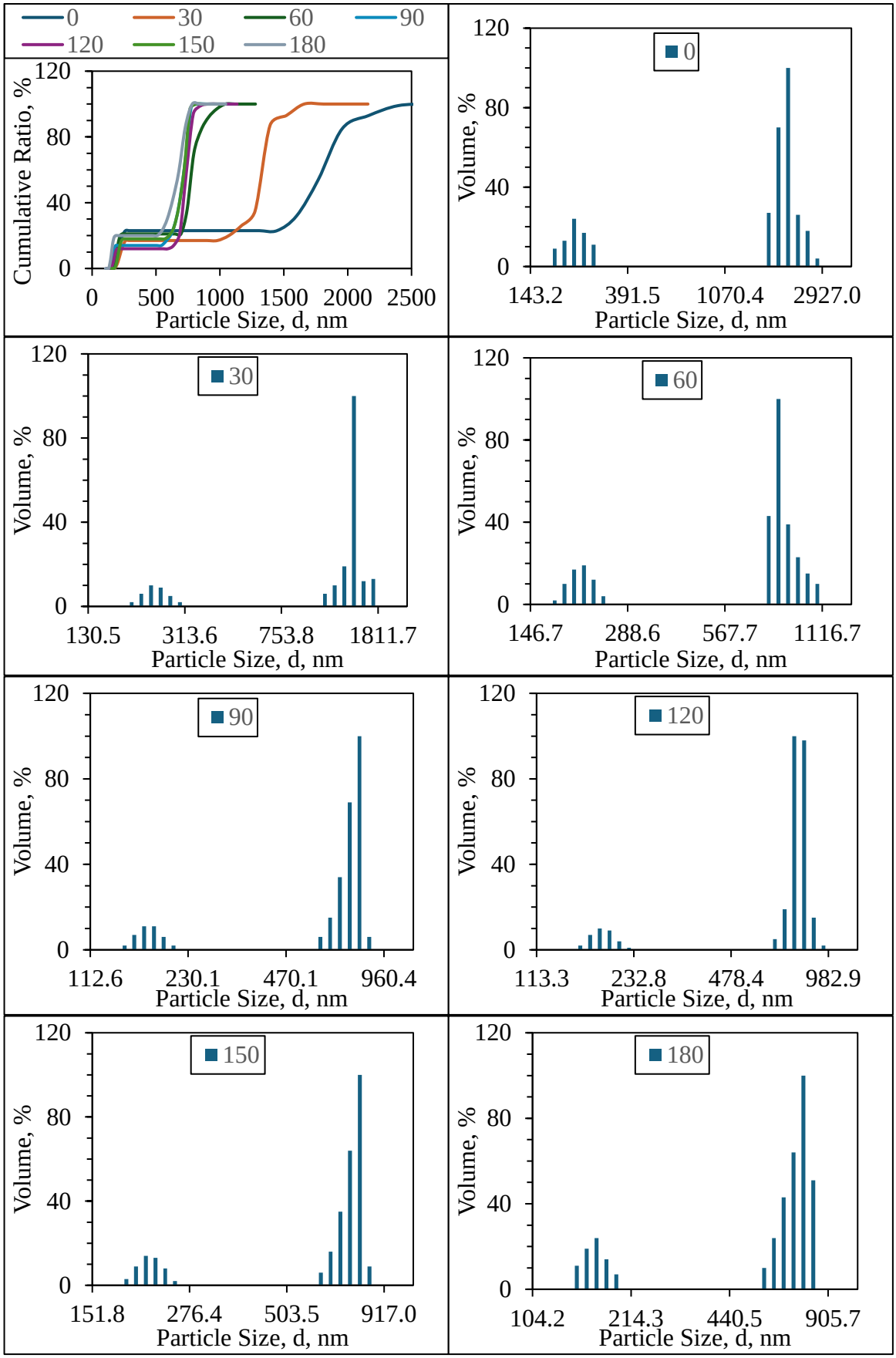


Figure 3.98. The cumulative ratio comparison and hydrodynamic size of $(HA\text{-}N\text{-}TiO_2)_{,as\text{-}is}$ as volume-weighted HDS in 30 min intervals.

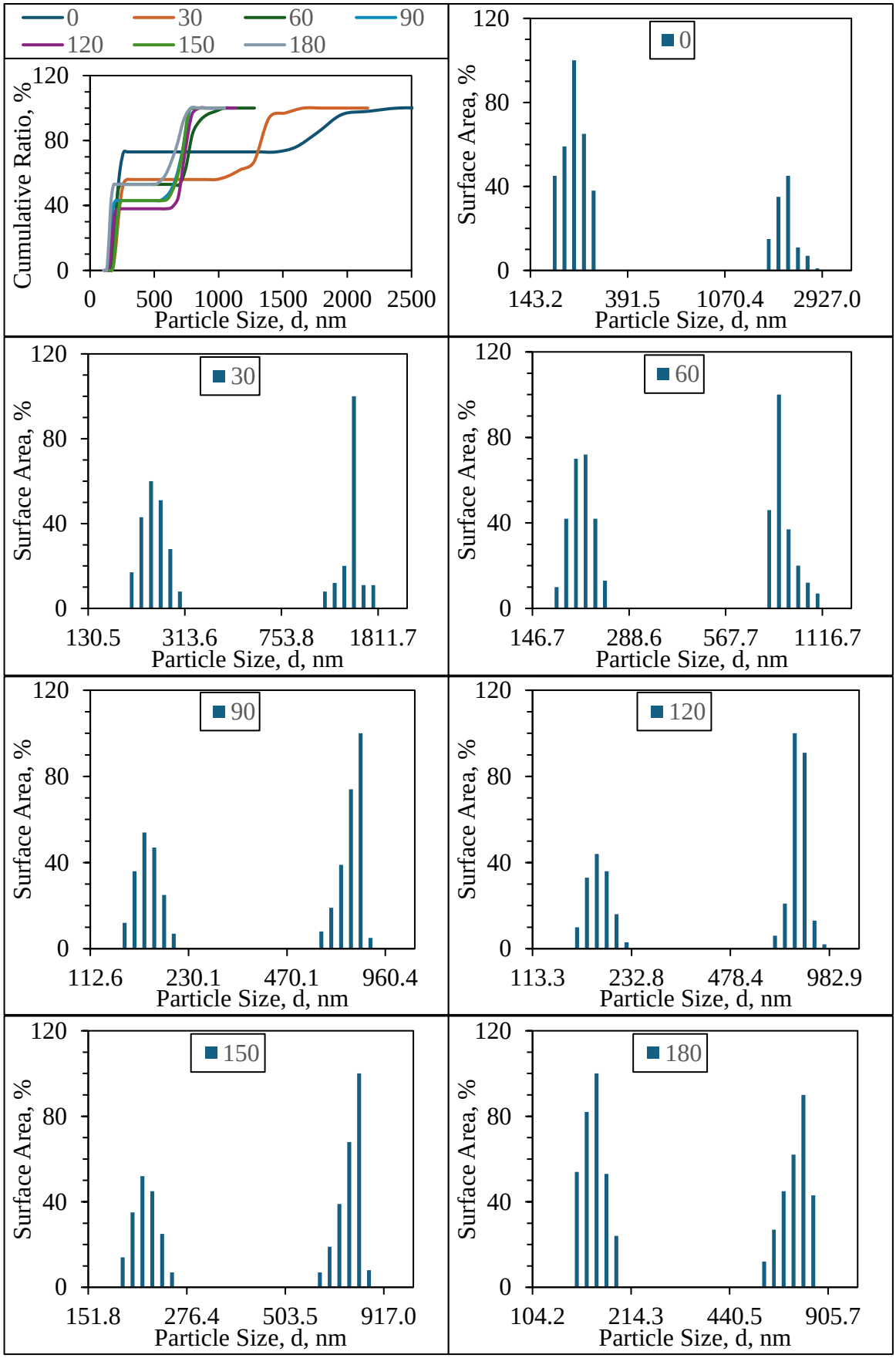


Figure 3.99. The cumulative ratio comparison and hydrodynamic size of $(HA\text{-}N\text{-}TiO_2)_{,as\text{-}is}$ as surface area-weighted HDS in 30 min intervals.

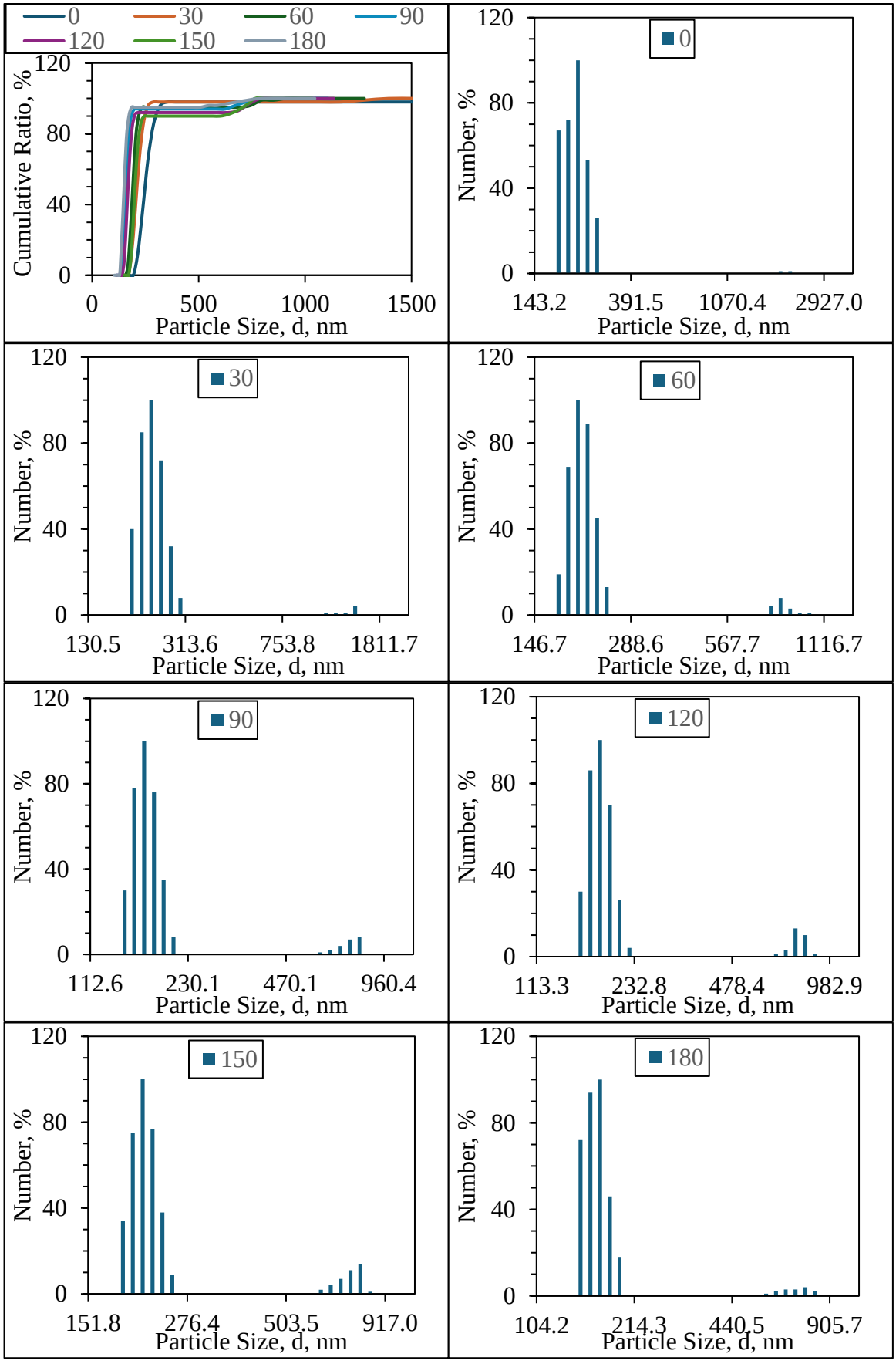


Figure 3.100. The cumulative ratio comparison and hydrodynamic size of $(HA\text{-}N\text{-}TiO_2)_{,as\text{-}is}$ as number-weighted HDS in 30 min intervals.

3.5.10. Hydrodynamic Size Assessment of (HA-N-TiO_2)$_{,dark}$

The aggregation and agglomeration behavior of HA-N-TiO_2 binary system under dark mixing conditions was investigated by suspending N-TiO_2 onto HA solution to achieve a final N-TiO_2 concentration of 0.25 mgL^{-1}. N-TiO_2 was suspended into HA by mixing with magnetic stirrer then the solution was moved to solar light simulator without opening the light and solution was continued mixing during 60 min. The obtained solution was named as (HA-N-TiO_2)$_{,dark}$ and directly subjected to HDS measurement by transferring the 4 mL of the solution into a polystyrene cuvette for 120 min without removing the cuvette.

Table 3.72 compiled the HDS results as intensity- volume-, surface area-, and number-weighted HDS with their corresponding CR%. Table 3.73 showed the min-max values, HDS range and min-max differences of the data presented in Table 1. The graphical abstracts of the Table 3.72 and Table 3.73 were illustrated in Figure 3.101, Figure 3.102, Figure 3.103, and Figure 3.104 as intensity-, volume-, surface area-, and number-weighted HDS, respectively. The PDI of the (HA-N-TiO_2)$_{,dark}$ binary system was found as 0.368 for initial, 0.303 for 30 min, 0.264 for 60 min, 0.290 for 90 min, and 0.226 for 120 min. The average PDI of the (HA-N-TiO_2)$_{,dark}$ binary system during 120 min was calculated as 0.290 showing a nearly monodispersed composition. Hence the MSD approximation was applied to investigate the HDS profiles of (HA-N-TiO_2)$_{,dark}$.

The HDS data of (HA-N-TiO_2)$_{,dark}$ showed that the binary system in dark conditions was comprised of two clusters around 144.3-230.5 nm and 1133.6-1649.1 nm at the initial time. The smaller clusters gave two maxima at 174.1 nm and 191.1 nm. These smaller clusters might be the N-TiO_2 aggregates that were formed by 10 or 11 particles of N-TiO_2 as the primary crystalline size of N-TiO_2 was 16.4 nm (Table 3.7). The bigger cluster around 1133.6-1649.1 nm might be related to both HA-N-TiO_2 hetero-agglomerates and/or HA-HA hetero-agglomerates. The removal efficiency achieved at the end of 30 min was less than 10% and this bigger cluster was still visible with slight size change as 1006.2-1300.6 nm. Hence the removed amount (< 10%) might be related to disagglomerated HA physical hydrogel structures. These bigger structures mostly have high volume-weighted CR% (75%) and smaller surface area-weighted CR% (41%) which implied that HA-N-TiO_2 hetero-aggregates mostly formed spherical structures (Table 3.72). This bigger cluster continued to agglomerate until 60 min and reached a range of 1390.4-2599.3 nm which was almost two times bigger structures in comparison to initial time. However, these biggest hetero-aggregates precipitated after 60 min, and they were not visible at 90 min. The remaining small and middle clusters continued to form bigger structures following the increase of number-weighted CR%. For instance, the number-

weighted CR% of structures around 700-800 nm was approximately 5% at 90 min, however their number-weighted CR% increased to 8% at the end of 120 min. Due to the extended mixing as pre-treatment, the smaller N-TiO_2 aggregates, and HA structures were collided and before N-TiO_2 formed homo-agglomerates HA covered the N-TiO_2 surface. The HA adsorbed onto N-TiO_2 was colloidally more stable than N-TiO_2 homo-agglomerates, but the surface adsorbed HA structures could form bridges between two HA-N-TiO_2 hetero-aggregates, so the bigger cluster continued to expand rather than precipitate. This was also an indicator of "train, tail, loop" formation on the N-TiO_2 surface. While the "trains" neutralized the surface charge of N-TiO_2 and stabilize the aggregates into the aqueous media, "loops and tails" tangled another "loops and tails" located on another N-TiO_2 aggregate to form bridges. This trend might be evidenced by comparing $(HA\text{-}N\text{-}TiO_2)_{,as\text{-}is}$ and $(HA\text{-}N\text{-}TiO_2)_{,dark}$. While the $(HA\text{-}N\text{-}TiO_2)_{,as\text{-}is}$ binary system was stable, after the precipitation of bigger structures, for both smaller and bigger clusters, $(HA\text{-}N\text{-}TiO_2)_{,dark}$ binary system showed increased HDS until 90 min later these bigger structures precipitated and remining smaller and middle size clusters continued to agglomerate (Table 3.74).

Table 3.75 compiled comparative data of the intensity-weighted HDS and their corresponding CR% of $(HA\text{-}TiO_2)_{,dark,}$ $(HA\text{-}Fe\text{-}TiO_2)_{,dark}$ and $(HA\text{-}N\text{-}TiO_2)_{,dark}$. The HDS order of the binary systems mixed in the dark was $(HA\text{-}Fe\text{-}TiO_2)_{,dark} > (HA\text{-}TiO_2)_{,dark,} > (HA\text{-}N\text{-}TiO_2)_{,dark}$ at initial time. At the end of the 120 min the order was changed as $(HA\text{-}TiO_2)_{,dark} > (HA\text{-}TiO_2)_{,dark} > (HA\text{-}N\text{-}TiO_2)_{,dark}$. The only difference between these three systems was the different affinity towards the metal oxide surface. Since, Fe leached from the Fe-TiO_2 in the dark condition HA-Fe-TiO_2 hetero-aggregate formation was inhibited by the chelated Fe-HA formation. Hence, colloidally less stable Fe-TiO_2 homo-agglomerates formed and these structures mostly precipitated at the end of 120 min. Birben and colleagues reported that no N leaching was observed from N-TiO_2 suspension (Birben et al., 2015), however Yalçın and colleagues stated that doping with N could increase the negative charge onto the TiO_2 surface (Yalçın et al., 2010) therefore HA-N-TiO_2 hetero-agglomerate formation probability would be less than HA-TiO_2 but higher than HA-Fe-TiO_2. Also, HA structural model during surface adsorption held great importance in binary systems. According to HA positioning on the metal oxide surface, volume- and surface area-weighted CR% were altered. For instance, the HA positioning on the hetero-agglomerates formed in the $(HA\text{-}TiO_2)_{,dark}$ and $(HA\text{-}N\text{-}TiO_2)_{,dark}$ binary systems probably resembling "train, tail, loop" structures. However, HA hetero-aggregates/agglomerates formed in $(HA\text{-}Fe\text{-}TiO_2)_{,dark}$ might resemble supramolecular assemblies. While the "train, tail, loop" structure increasing the CR% of surface area-weighted HDS, formation of supramolecular assemblies increases the CR% volume-weighted HDS. Hence system definition had great importance while evaluating binary system in dark conditions.

Table 3.74. Intensity-, volume-, surface area- and number-weighted HDS and cumulative ratios of $(HA\text{-}N\text{-}TiO_2)_{,dark}$.

	HDS, nm	Cumulative Ratio, %			
		Intensity	Volume	Surface Area	Number
Initial	144.3-174.0	16%	7%	32%	68%
	191.1-230.5	17%	6%	21%	30%
	1133.6	9%	13%	9%	1%
	1245.0	18%	10%	5%	-
	1367.3	21%	51%	27%	1%
	1501.6-1649.1	19%	13%	6%	-
30 min	166.9-181.8	14%	6%	20%	44%
	198.0	16%	6%	18%	30%
	215.7-235.0	20%	6%	17%	23%
	848.0-923.7	11%	7%	4%	1%
	1006.2	13%	17%	10%	-
	1096.1	15%	50%	27%	2%
	1194.0-1300.6	11%	8%	4%	-
60 min	212.8-291.0	18%	9%	40%	98%
	340.2	14%	6%	8%	-
	397.8-465.2	15%	45%	42%	2%
	1390.4-1625.8	20%	29%	8%	-
	1901.1	18%	6%	1%	-
	2222.9-2599.3	15%	5%	1%	-
90 min	153.3-178.4	20%	9%	25%	58%
	192.5	15%	5%	14%	24%
	207.6-223.9	11%	3%	8%	12%
	697.6-752.5	10%	35%	24%	3%
	811.7	15%	27%	17%	2%
	875.6	15%	10%	6%	1%
	944.5-1018.8	14%	11%	6%	-
120 min	182.1-193.5	15%	5%	13%	36%
	205.6	19%	5%	13%	29%
	218.5-232.3	21%	5%	13%	25%
	615.1-694.7	20%	17%	13%	2%
	738.3	13%	34%	25%	4%
	784.7-833.9	12%	34%	23%	4%

Table 3.75. Intensity-weighted HDS profile of $(HA\text{-}N\text{-}TiO_2)_{,dark}$. Time dependent HDS cluster maximas, HDS range and min-max diameter difference with respect to multi-size distribution.

	Cluster					
Time, min	Max 1, nm	Max 2, nm	Max 3, nm	Max 4, nm	Range, nm	Difference, nm
Initial	174.0	191.1	1367.3		108.9-2184.4	2075.5
30	198.0	1006.2	1096.1		118.5-1831.4	1712.9
60	52.1	340.2	1901.1		23.8-3553.9	3530.1
90	178.4	192.5	811.7	875.6	122.2-1379.4	1257.2
120	205.6	738.3			151.7-1063.8	912.1

Table 3.76. Comparison of intensity-weighted HDS values of $(HA\text{-}N\text{-}TiO_2)_{,as\text{-}is}$ and $(HA\text{-}N\text{-}TiO_2)_{,dark}$.

	$(HA\text{-}N\text{-}TiO_2)_{,as\text{-}is}$		$(HA\text{-}N\text{-}TiO_2)_{,dark}$		
	HDS, nm	CR, %	HDS, nm	CR, %	
Initial	175.1-214.1	19%	Dark Mixing		
	236.7-261.8	14%			
	1600.7-1770.1	22%			
	1957.4	21%			
	2164.5	16%			
	2393.6-2646.9	8%			
30 min	185.3-202.3	11%			
	220.3	14%			
	241.1	14%			
	263.2-287.3	11%			
	1070.5-1275.7	19%			
	1392.6	16%			
	1520.3-1659.6	15%			
60 min	167.9-192.3	23%	144.3-174.0	16%	Initial
	205.7	16%	191.1-230.5	17%	
	220.1-235.6	16%	1133.6	9%	
	744.1-796.2	13%	1245.0	18%	
	851.9	14%	1367.3	21%	
	911.6-1043.7	18%	1501.6-1649.1	19%	
90 min	139.6-161.0	17%	166.9-181.8	14%	30 min
	172.9-199.5	21%	198.0	16%	
	582.5-625.6	17%	215.7-235.0	20%	
	671.9	19%	848.0-923.7	11%	
	721.7	15%	1006.2	13%	
	775.1-832.5	11%	1096.1	15%	
	-	-	1194.0-1300.6	11%	
120 min	151.2-174.6	22%	212.8-291.0	18%	60 min
	187.6-216.7	23%	340.2	14%	
	638.1-685.7	14%	397.8-465.2	15%	
	736.9	17%	1390.4-1625.8	20%	
	791.9	15%	1901.1	18%	
	791.9-914.6	11%	2222.9-2599.3	15%	
150 min	181.7-192.9	12%	153.3-178.4	20%	90 min
	204.8	15%	192.5	15%	
	217.5	15%	207.6-223.9	11%	
	230.9-245.2	12%	697.6-752.5	10%	
	602.7-639.9	13%	811.7	15%	
	679.5	13%	875.6	15%	
	721.5-813.4	20%	944.5-1018.8	14%	
180 min	139.1-149.4	12%	182.1-193.5	15%	120 min
	160.6	12%	205.6	19%	
	172.6-185.5	12%	218.5-232.3	21%	
	546.9-587.7	15%	615.1-694.7	20%	
	631.6	19%	738.3	13%	
	678.8	17%	784.7-833.9	12%	
	729.6-784.1	13%	-	-	

Table 3.77. Comparison of intensity-weighted HDS values of $(HA\text{-}TiO_2)_{,dark,}$ $(HA\text{-}Fe\text{-}TiO_2)_{,dark}$ and $(HA\text{-}N\text{-}TiO_2)_{,dark}$.

	$(HA\text{-}TiO_2)_{,dark}$		$(HA\text{-}Fe\text{-}TiO_2)_{,dark}$		$(HA\text{-}N\text{-}TiO_2)_{,dark}$	
	HDS, nm	CR, %	HDS, nm	CR, %	HDS, nm	CR, %
Initial	92.1-319.9	13%	1.8-177.8	16%	144.3-174.0	16%
	362.3	14%	237.1	14%	191.1-230.5	17%
	410.3-464.7	16%	316.2	13%	1133.6	9%
	980.9-1110.9	20%	421.7-1000.0	19%	1245.0	18%
	1258.2	17%	1333.5	16%	1367.3	21%
	1425.0	13%	1778.3-3162.3	22%	1501.6-1649.1	19%
	1613.9-1827.9	7%	-	-	-	-
30 min	209.4-230.0	12%	160.6-174.5	14%	166.9-181.8	14%
	252.6-304.7	10%	189.6	12%	198.0	16%
	1364.5-1498.6	16%	205.9-223.7	12%	215.7-235.0	20%
	1645.8	20%	775.6-842.7	17%	848.0-923.7	11%
	1807.5	18%	915.5	19%	1006.2	13%
	1985.1-2180.1	14%	994.6	15%	1096.1	15%
	-	-	1080.5-1173.9	11%	1194.0-1300.6	11%
60 min	212.8-291.0	18%	170.0-180.2	14%	212.8-291.0	18%
	340.2	14%	191.1	14%	340.2	14%
	397.8-465.2	15%	202.5-214.7	15%	397.8-465.2	15%
	1390.4-1625.8	20%	578.6-613.4	15%	1390.4-1625.8	20%
	1901.1	18%	650.2	18%	1901.1	18%
	2229.9-2599.3	15%	689.3-774.6	24%	2222.9-2599.3	15%
90 min	155.0-186.5	15%	197.6-211.1	10%	153.3-178.4	20%
	204.6-246.2	14%	225.5	16%	192.5	15%
	1082.6	11%	240.9	17%	207.6-223.9	11%
	1187.6	17%	257.3-274.9	14%	697.6-752.5	10%
	1302.8	23%	844.2-901.8	15%	811.7	15%
	1429.1-1567.7	22%	963.3	14%	875.6	15%
	-	-	1029.0-1099.2	14%	944.5-1018.8	14%
120 min	172.5-207.6	11%	215.4-230.1	19%	182.1-193.5	15%
	227.8-274.1	21%	245.8	20%	205.6	19%
	1098.7	9%	262.5-280.5	20%	218.5-232.3	21%
	1205.2	17%	861.3-920.1	9%	615.1-694.7	20%
	1322.1	22%	982.8	12%	738.3	13%
	1450.3-1590.9	20%	1049.9-1121.5	20%	784.7-833.9	12%

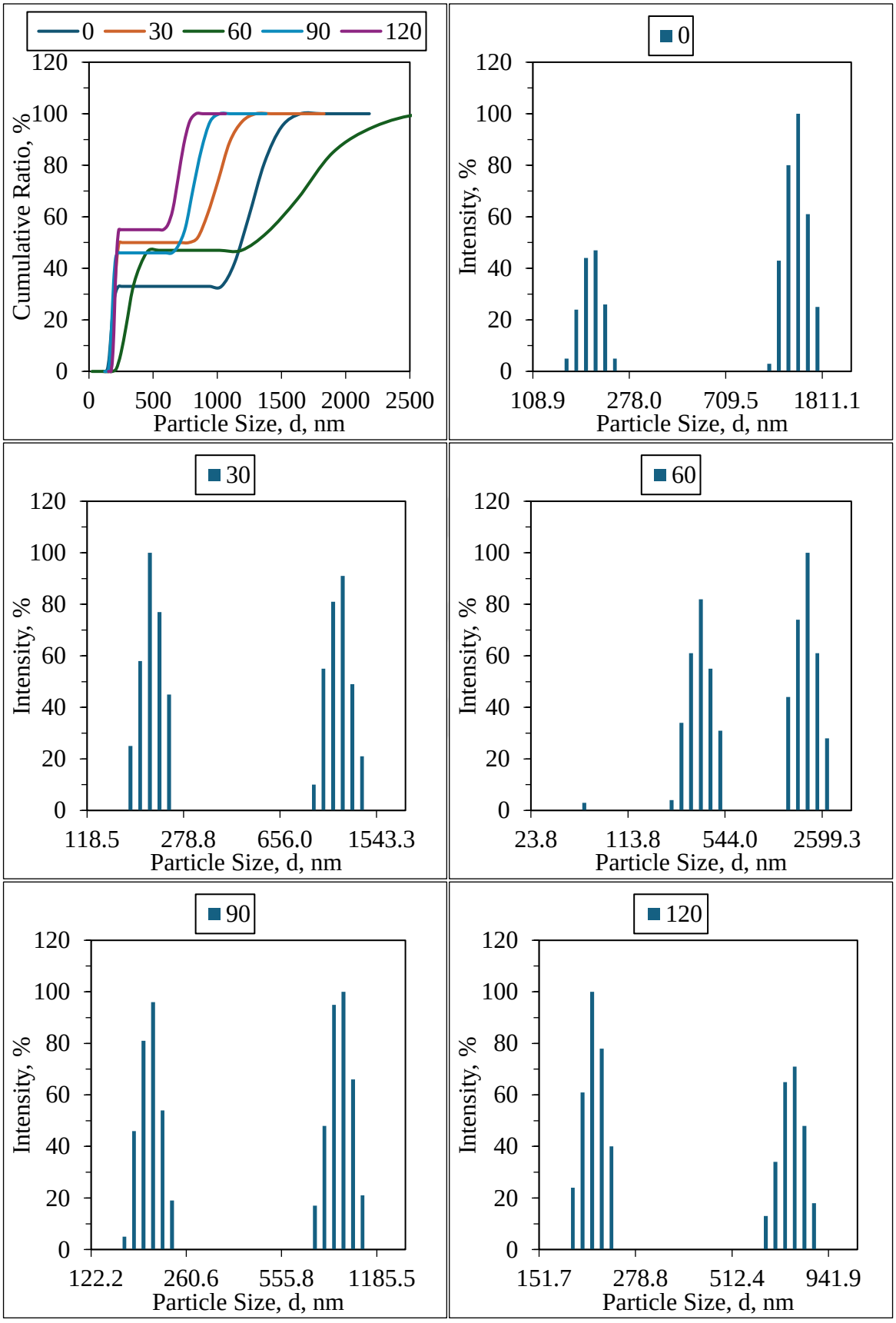


Figure 3.101. The cumulative ratio comparison and hydrodynamic size of $(HA\text{-}N\text{-}TiO_2)_{,dark}$ as intensity-weighted HDS in 30 min intervals.

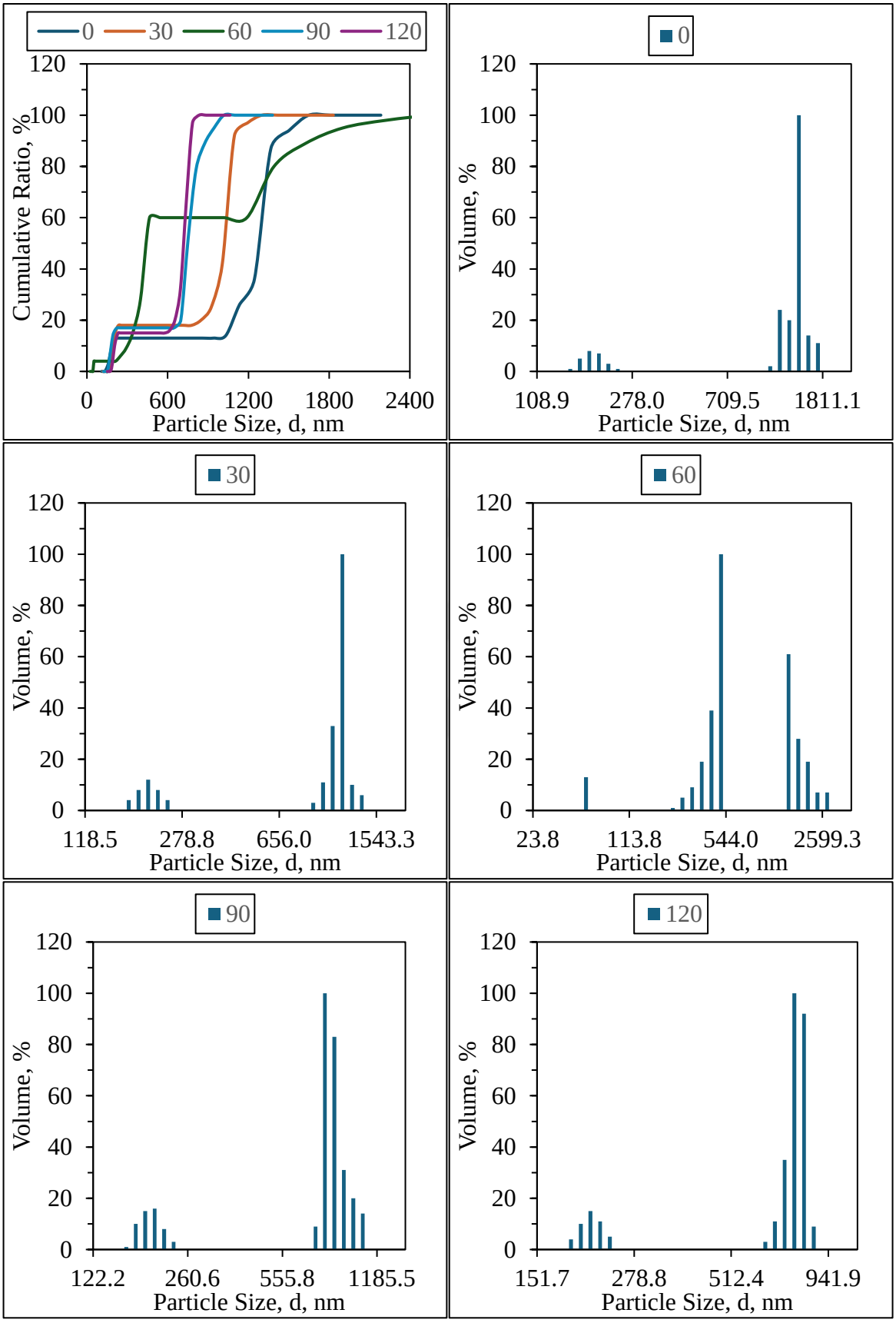


Figure 3.102. The cumulative ratio comparison and hydrodynamic size of $(HA\text{-}N\text{-}TiO_2)_{,dark}$ as volume-weighted HDS in 30 min intervals.

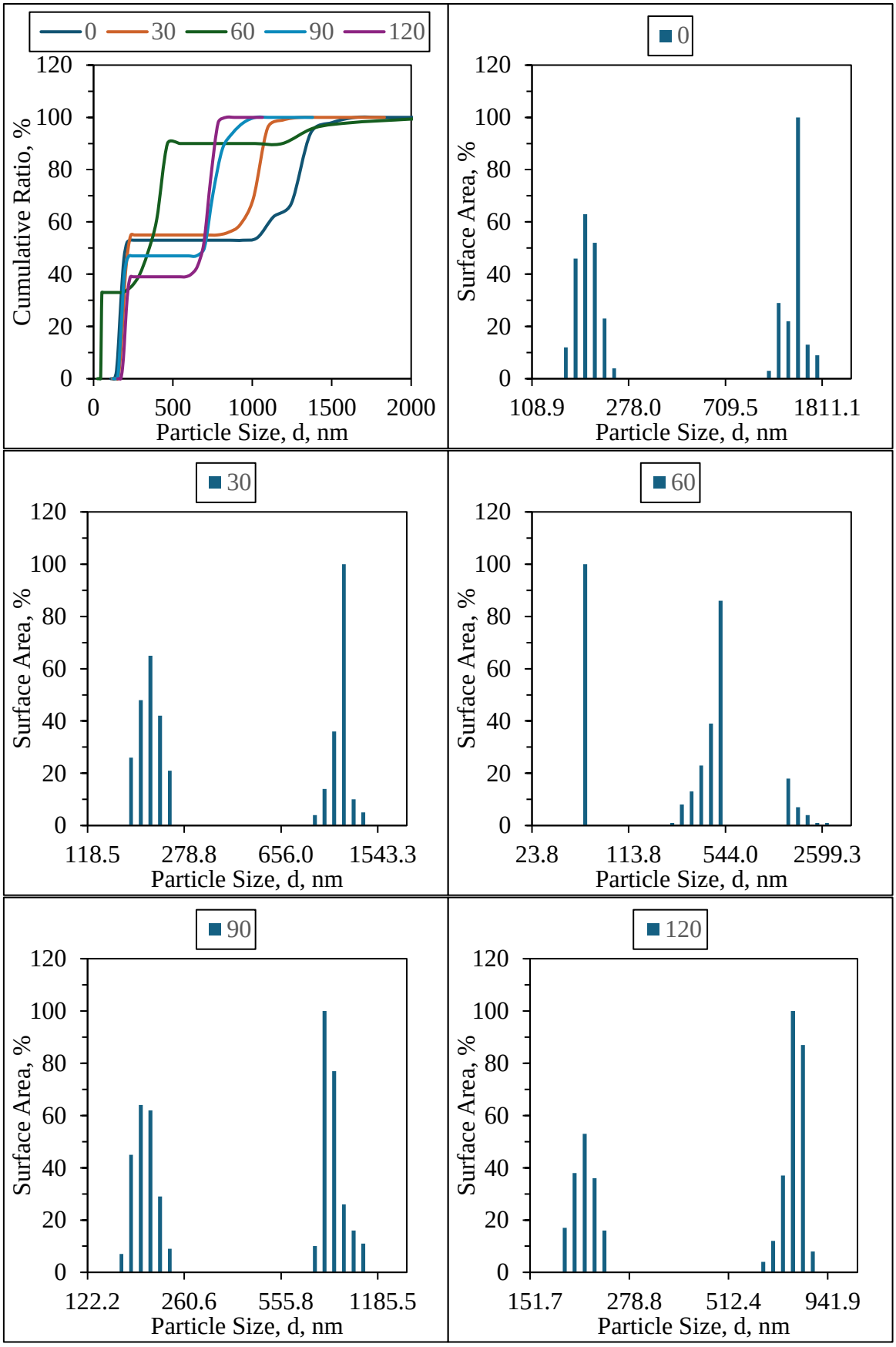


Figure 3.103. The cumulative ratio comparison and hydrodynamic size of $(HA\text{-}N\text{-}TiO_2)_{,dark}$ as surface area-weighted HDS in 30 min intervals.

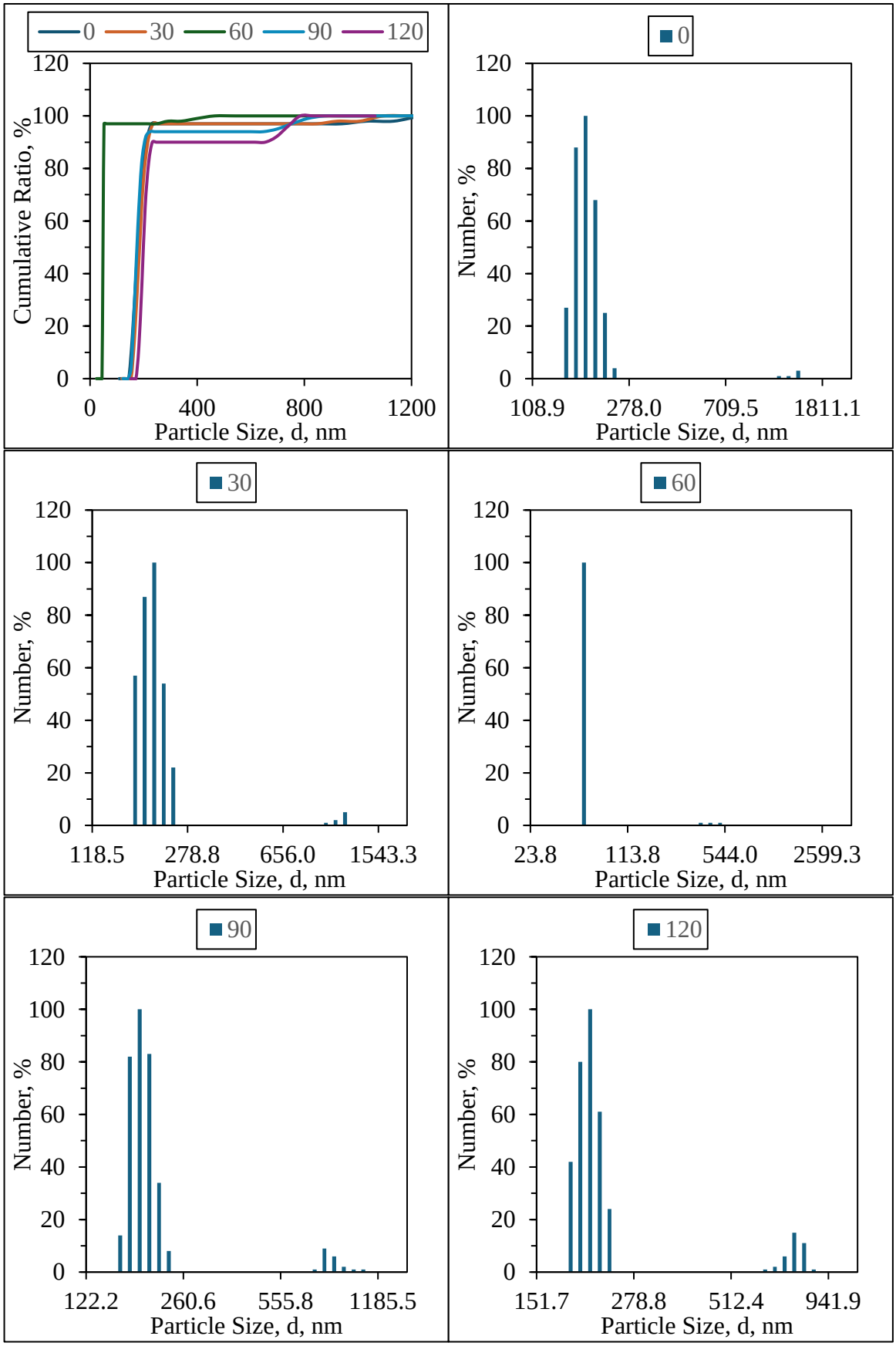


Figure 3.104. The cumulative ratio comparison and hydrodynamic size of $(HA\text{-}N\text{-}TiO_2)_{,dark}$ as number-weighted HDS in 30 min intervals.

3.5.11. Hydrodynamic Size Assessment of ($HA_{,pho}$-N-TiO_2)

The effect of photolytically treated HA on HDS of HA-N-TiO_2 binary system was investigated. HA solution was photolytically treated in solar light simulator for 60 min and named $HA_{,pho}$. Following photolytic treatment $HA_{,pho}$ was subjected to physico chemical characterization. The initial DOC was decreased to 4.53 mgL^{-1} due to the self-degradation of HA (Table 3.1). The detailed reactions under solar light irradiation and explanations were reported in section 3.2.2 (Uyguner-Demirel et al., 2023). Solar photolytic treatment led to charge transitions in the HA structure that ended up with the increase in aromaticity and hydrophobic behavior (Bekbolet et al., 2002). Consequently, a supramolecular formation of HA was observed tending to form self-assembled (aggregated) structures (von Wandruszka et al., 1997; Uyguner-Demirel and Bekbolet, 2011; Vione et al, 2014). These outcomes were detailly explained in section 3.1.1. After photolytic treatment N-TiO_2 in the powder form was weighted and suspended in $HA_{,pho}$ to achieve 0.25 mgL^{-1} N-TiO_2 concentration and mixed with a magnetic stirrer for 30 min to maintain a dispersion of N-TiO_2.

The PDI of the ($HA_{,pho}$-N-TiO_2) binary system was 0.357 at initial time, 0.331 at 30 min, 0.301 at 60 min, 0.280 at 90 min, and 0.287 at 120 min. The average PDI of the binary system was calculated as 0.311 indicating a nearly mono dispersed composition therefore, MSD approximation was used to explain the HDS of the ($HA_{,pho}$-N-TiO_2) binary system.

The HDS data of ($HA_{,pho}$-N-TiO_2) as MSD were compiled in Table 3.77 as intensity-, volume-, surface area-, and number weighted HDS with their corresponding CR%. Table 3.76 showed the min-max values, range and difference data derived from the Table 3.77 and the graphical abstracts of the Table 3.76 and Table 3.77 was showed in Figure 3.105, Figure 3.106, Figure 3.107, and Figure 3.108 as intensity-, volume-, surface area-, and number-weighted HDS, respectively. Comparative results were gathered in Table 3.78 and Table 3.79 as intensity-weighted HDS. Table 3.78 showed the comparison of $HA_{,pho}$, Fe-$TiO_{2,as\text{-}is}$, and ($HA_{,pho}$-Fe-TiO_2). Table 3.79 gathered the comparative results of ($HA_{,pho}$-TiO_2), ($HA_{,pho}$-Fe-TiO_2) and ($HA_{,pho}$-N-TiO_2).

The HDS of the ($HA_{,pho}$-N-TiO_2) showed three main clusters maximizing around 140.5 nm, 446.6 nm, and 2530.3 nm at initial time (Table 3.76 and Table 3.77). The smaller cluster ranging between 105.2-386.5 nm which was mostly comprised of N-TiO_2 aggregates and $HA_{,pho}$ aggregates/agglomerates of smaller size fractions <30 kDa. The middle cluster ranging between 446.6-596.3 nm might be composed of aggregates/agglomerates of relatively bigger molecular size fractions >30 kDa of $HA_{,pho}$ due to the high number-weighted CR% (15%) however this range also

covered homo-agglomerates of N-TiO_2 structures. This middle size cluster might be composed of HA,pho aggregates/agglomerates due to the high volume-weighted CR% (66%). The supramolecular structure of $HA_{,pho}$ was high in volume and surface area (Figure 1.14) so this cluster might be related with these structures. Because these structures were mostly stable and hydrophobic in nature they did not interact with N-TiO_2 and stayed in the media by themselves. Even though their visibility decreased after initial measurements they were still in range for 120 min. The formation of bigger agglomerated structures might be masking the visibility of these structures. Finally, the largest cluster observed in initial measurement were the hetero-agglomerates of $HA_{,pho}$ structures. These structures were formed during the mixing and disappeared after the settlement of the ($HA_{,pho}$-N-TiO_2) system. The removal efficiency of the ($HA_{,pho}$-N-TiO_2) was supporting the theory. The removal efficiency of the binary system was approximately 10% at the end of 30 min by disagglomeration of the structures > 1000 nm that mostly composed by $HA_{,pho}$ hetero-agglomerates. After the disagglomeration of $HA_{,pho}$ structures, HDS of the ($HA_{,pho}$-N-TiO_2) was mostly stable and no significant change was observed. The smallest cluster around 100-200 nm and middle size cluster around 500-700 nm showed similar number-weighted CR% which could be concluded as no further agglomeration was observed. Similarly, the removal efficiency of ($HA_{,pho}$-N-TiO_2) binary system was approximately 15%. The 5% difference between the 30 min (10%) and 120 min (15%) might be the result of the slight precipitation of hetero-agglomerates of N-TiO_2.

The comparative data presented in Table 3.78 that compiled the intensity-weighted HDS of $HA_{,pho}$, Fe-$TiO_{2,as\text{-}is}$, and ($HA_{,pho}$-Fe-TiO_2) with the corresponding CR% was supported the theories stated in previous paragraph. The $HA_{,pho}$ mono system was composed of stable structures ranging between 100-800 nm. The HDS range of $HA_{,pho}$ showed slight changes during 120 min which might be related to the laser shut position of molecular structure. Since HA was not a uniform floc, hydrodynamic rotation might cause slight size changes. The intensity-weighted HDS profile of ($HA_{,pho}$-N-TiO_2) binary system mostly resembling the intensity-weighted HDS of N-$TiO_{2,as\text{-}is}$ mono system. However, the presence of $HA_{,pho}$ in the binary system directly affected the agglomerate formation and precipitation behavior of N-TiO_2. Even the formation of $HA_{,pho}$-N-TiO_2 hetero-aggregates were not favorable, presence of $HA_{,pho}$ structures prevented the formation of bigger N-TiO_2 homo-agglomerates and precipitation of them. This relation was evidenced by the comparison of the removal efficiencies. The removal efficiency of the N-$TiO_{2,as\text{-}is}$ mono system was approximately 35% at the end of experiment, however the removal efficiency of the ($HA_{,pho}$-N-TiO_2) system was ~15%. Hence it could be concluded that the decrease in removal efficiency was related to the electrostatic interactions caused by $HA_{,pho}$ structures.

The effect of doping in the presence of photolytically treated HA was investigated by comparing the intensity-weighted HDS of ($HA_{,pho}$-TiO_2), ($HA_{,pho}$-Fe-TiO_2) and ($HA_{,pho}$-N-TiO_2) in Table 3.79. The intensity-weighted HDS order of the binary systems was ($HA_{,pho}$-N-TiO_2)>($HA_{,pho}$-Fe-TiO_2)> ($HA_{,pho}$-TiO_2) at initial time. However, at the end of 120 min this order changed as ($HA_{,pho}$-TiO_2)> ($HA_{,pho}$-Fe-TiO_2)≥ ($HA_{,pho}$-N-TiO_2). This difference was related to surface interaction between photolytically treated HA and non-doped or doped-TiO_2. The N doping created a more negative surface on the TiO_2 structures which prohibited the possible formation of $HA_{,pho}$-N-TiO_2 hetero-agglomeration formation. The intensity-weighted HDS profile of ($HA_{,pho}$-Fe-TiO_2) was slightly similar ($HA_{,pho}$-N-TiO_2) on the other side the formation of hydrodynamic structures was totally different. The Fe(II) leached from the surface of Fe-TiO_2 disturbed the stable structure of $HA_{,pho}$ and enabled the formation of HA-Fe-TiO_2 hetero-agglomerates. Because the HA-Fe-TiO_2 hetero-agglomerates more tend to precipitate in comparison to TiO_2 and N-TiO_2, even the intensity-weighted HDS range of ($HA_{,pho}$-Fe-TiO_2) was higher than ($HA_{,pho}$-N-TiO_2) binary system, the CR% of the bigger structures were lower than ($HA_{,pho}$-N-TiO_2). This trend could be evidenced by the removal efficiency order of the binary system which was ($HA_{,pho}$-Fe-TiO_2) (30%)>($HA_{,pho}$-N-TiO_2) (15%) ≈ ($HA_{,pho}$-TiO_2) (15%).

Table 3.78. Intensity-weighted HDS profile of ($HA_{,pho}$-N-TiO_2). Time dependent HDS cluster maximas, HDS range and min-max diameter difference with respect to multi-size distribution.

	Cluster				
Time, min	Max 1, nm	Max 2, nm	Max 3, nm	Range, nm	Difference, nm
Initial	140.5	446.6	2530.3	68.2-6959.6	6891.4
30	177.2	1066.9	-	103.4-1828.2	1724.8
60	175.3	839.3	-	120.8-1312.9	1192.1
90	158.0	667.1	-	102.6-1027.5	924.9
120	155.1	647.3	-	101.0-993.7	892.7

Table 3.79. Intensity-, volume-, surface area- and number-weighted HDS and cumulative ratios of ($HA_{,pho}$-N-TiO_2).

	HDS, nm	Cumulative Ratio, %			
		Intensity	Volume	Surface Area	Number
Initial	105.2-187.6	17%	10%	29%	82%
	334.5-386.5	12%	9%	9%	3%
	446.6-596.3	14%	66%	60%	15%
	1895.1-2189.8	20%	5%	1%	-
	2530.3	18%	2%	-	-
	2923.8-3378.5	19%	8%	1%	-
30 min	135.4-162.0	18%	9%	30%	61%
	177.2	14%	5%	16%	24%
	193.9-212.1	13%	3%	11%	13%
	891.6-975.3	20%	15%	8%	1%
	1066.9	18%	57%	30%	1%
	1167.1-1276.7	17%	11%	5%	-
60 min	140.2-162.7	22%	9%	28%	62%
	175.3	14%	5%	13%	23%
	188.9-203.5	11%	2%	7%	11%
	723.1-779.0	20%	62%	40%	3%
	839.3	17%	14%	8%	1%
	904.3-974.3	16%	8%	4%	-
90 min	136.8-147.1	12%	7%	20%	42%
	158.0	14%	6%	17%	31%
	169.8-182.5	16%	6%	15%	23%
	577.6-620.7	18%	9%	6%	-
	667.1	18%	13%	8%	1%
	716.9	13%	21%	13%	1%
	770.4-827.9	9%	38%	21%	2%
120 min	134.5-144.4	14%	10%	26%	49%
	155.1	13%	8%	20%	29%
	166.6-178.9	14%	7%	14%	19%
	561.1-602.7	18%	11%	7%	1%
	647.3	20%	14%	8%	-
	695.2	14%	18%	9%	1%
	746.7	7%	32%	16%	1%

Table 3.80. Comparison of intensity-weighted HDS values of $HA_{,pho}$, Fe-$TiO_{2,as-is}$, and ($HA_{,pho}$-Fe-TiO_2).

	$HA_{,pho}$		N-$TiO_{2,as-is}$		($HA_{,pho}$-N-TiO_2)	
	HDS, nm	CR, %	HDS, nm	CR, %	HDS, nm	CR, %
Initial	121.8-139.5	25%	153.6-187.8	23%	105.2-187.6	17%
	149.3-170.9	29%	207.7-229.7	15%	334.5-386.5	12%
	539.8-757.1	46%	1269.9-1404.3	10%	446.6-596.3	14%
	-	-	1552.9	17%	1895.1-2189.8	20%
	-	-	1717.2	19%	2530.3	18%
	-	-	1898.9-2099.9	17%	2923.8-3378.5	19%
30 min	133.8-142.6	22%	184.8-200.4	13%	135.4-162.0	18%
	152.1	21%	217.4	17%	177.2	14%
	162.2-173.0	19%	235.7	18%	193.9-212.1	13%
	483.9-667.3	38%	255.6-277.2	14%	891.6-975.3	20%
	-	-	935.9-1015.0	12%	1066.9	18%
	-	-	1100.8	12%	1167.1-1276.7	17%
			1193.8-1294.6	14%	-	-
60 min	100.0-177.8	45%	148.6-159.4	13%	140.2-162.7	22%
	237.1	28%	171.0	14%	175.3	14%
	316.2-421.7	27%	183.5-196.9	17%	188.9-203.5	11%
			607.2-651.5	15%	723.1-779.0	20%
	-	-	699.0	17%	839.3	17%
	-	-	749.9	14%	904.3-974.3	16%
	-	-	804.6-863.6	10%	-	-
90 min	135.0-150.4	27%	151.6-175.7	22%	136.8-147.1	12%
	158.8	19%	189.2	16%	158.0	14%
	167.6-177.0	16%	203.7-219.4	14%	169.8-182.5	16%
	398.8-444.4	13%	665.4-716.5	20%	577.6-620.7	18%
	469.1-522.8	25%	771.5	15%	667.1	18%
	-	-	830.7-894.5	13%	716.9	13%
	-	-			770.4-827.9	9%
120 min	131.1-151.3	27%	180.4-190.3	13%	134.5-144.4	14%
	162.5	24%	200.8	17%	155.1	13%
	174.5-187.5	22%	211.8	16%	166.6-178.9	14%
	633.2-843.2	27%	223.4-235.7	14%	561.1-602.7	18%
	-	-	525.4-554.3	14%	647.3	20%
	-	-	584.7	12%	695.2	14%
	-	-	616.8-686.4	14%	746.7	7%

Table 3.81. Comparison of intensity-weighted HDS values of ($HA_{,pho}$-TiO_2), ($HA_{,pho}$-Fe-TiO_2) and ($HA_{,pho}$-N-TiO_2).

	($HA_{,pho}$-TiO_2)		($HA_{,pho}$-Fe-TiO_2)		($HA_{,pho}$-N-TiO_2)	
	HDS, nm	CR, %	HDS, nm	CR, %	HDS, nm	CR, %
Initial	148.5-175.3	14%	163.2-202.8	17%	105.2-187.6	17%
	190.5-207.0	8%	226.0-280.9	14%	334.5-386.5	12%
	783.0	11%	1596.2-1779.3	20%	446.6-596.3	14%
	850.9	19%	1983.4	22%	1895.1-2189.8	20%
	924.6	25%	2210.9	17%	2530.3	18%
	1004.8-1091.9	23%	2464.5-2747.2	10%	2923.8-3378.5	19%
30 min	165.4-188.9	14%	145.5-171.0	25%	135.4-162.0	18%
	201.9-230.5	9%	185.4-201.0	17%	177.2	14%
	623.1-665.8	12%	675.4-732.2	13%	193.9-212.1	13%
	711.5	19%	793.9	15%	891.6-975.3	20%
	760.2	22%	860.7	18%	1066.9	18%
	812.3-868.0	18%	933.1-1011.7	12%	1167.1-1276.7	17%
60 min	113.4-154.9	20%	158.8-184.2	23%	140.2-162.7	22%
	538.2-581.8	22%	198.3	16%	175.3	14%
	628.9	23%	213.5-229.9	14%	188.9-203.5	11%
	679.9	21%	697.4-750.9	15%	723.1-779.0	20%
	734.9-794.4	13%	808.5	15%	839.3	17%
	-	-	870.6-1009.4	17%	904.3-974.3	16%
90 min	204.4-234.5	19%	144.5-155.3	14%	136.8-147.1	12%
	251.2-288.1	22%	166.9	14%	158.0	14%
	753.8-807.2	20%	179.4-192.8	15%	169.8-182.5	16%
	864.5	19%	610.2-655.7	7%	577.6-620.7	18%
	926.0	13%	704.7	15%	667.1	18%
	991.8-1062.3	7%	757.3	19%	716.9	13%
	-	-	813.8-874.6	16%	770.4-827.9	9%
	-	-	1171.1-183.2	20%	-	-
120 min	225.9-239.9	13%	196.3	16%	134.5-144.4	14%
	254.7	15%	210.2-225.2	13%	155.1	13%
	270.5-304.9	20%	631.3-676.3	13%	166.6-178.9	14%
	749.8-796.1	14%	724.4	16%	561.1-602.7	18%
	845.4	15%	775.9	12%	647.3	20%
	897.6-1012.0	23%	831.1-890.2	10%	695.2	14%
	-	-	-	-	746.7	7%

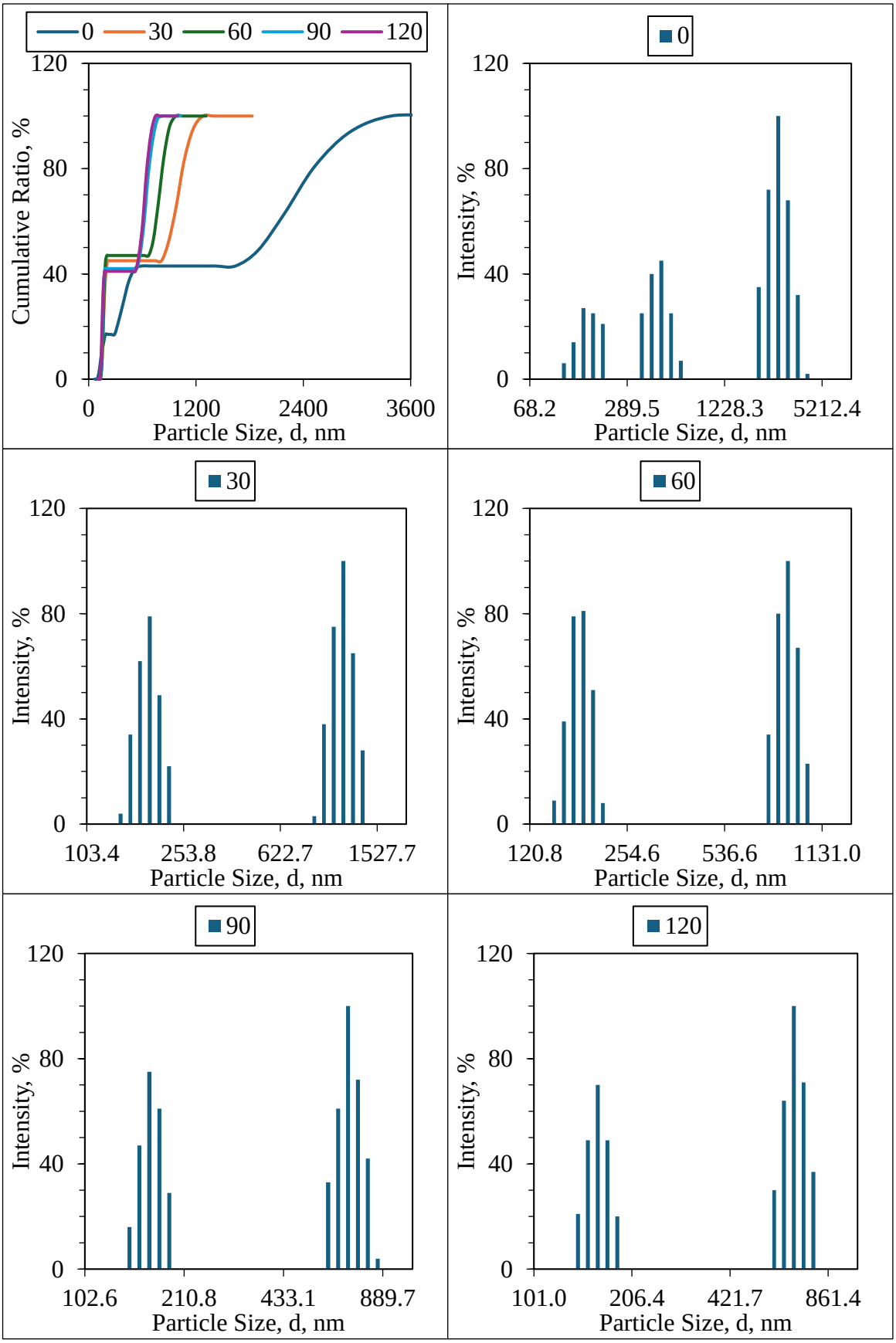


Figure 3.105. The cumulative ratio comparison and hydrodynamic size of ($HA_{,pho}$-N-TiO_2) as intensity-weighted HDS in 30 min intervals.

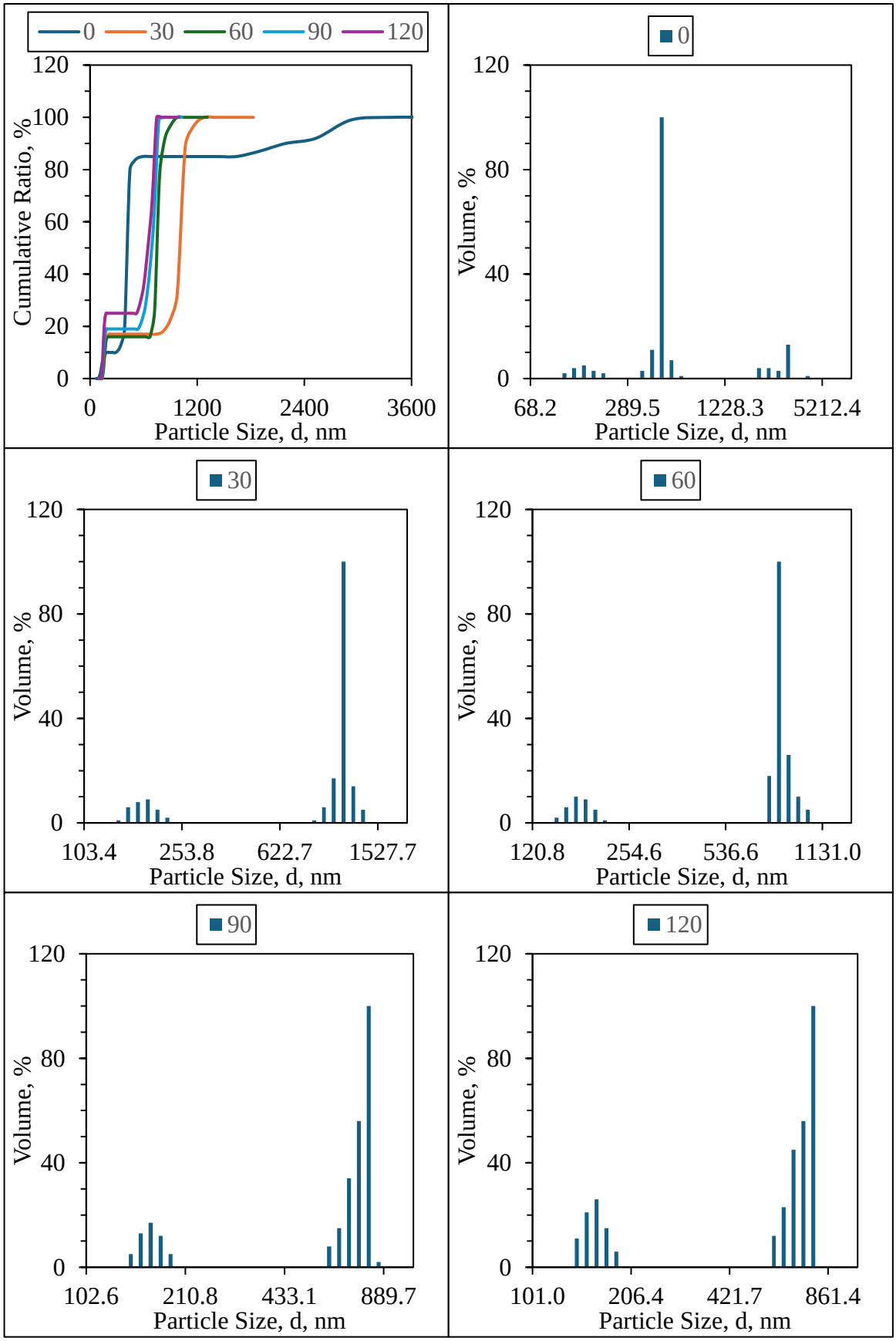


Figure 3.106. The cumulative ratio comparison and hydrodynamic size of ($HA_{,pho}$-N-TiO_2) as volume-weighted HDS in 30 min intervals.

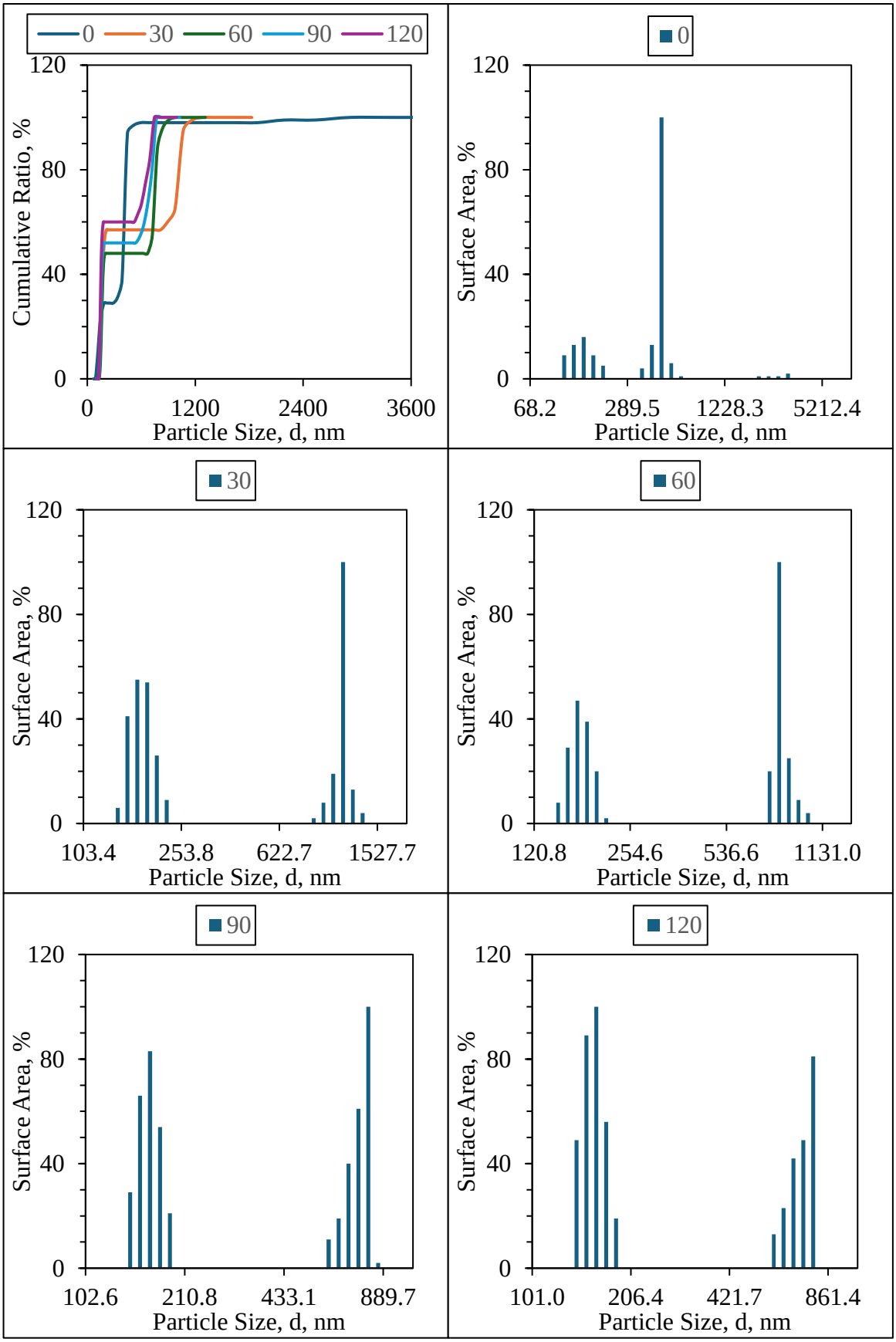


Figure 3.107. The cumulative ratio comparison and hydrodynamic size of ($HA_{,pho}$-N-TiO_2) as surface area-weighted HDS in 30 min intervals.

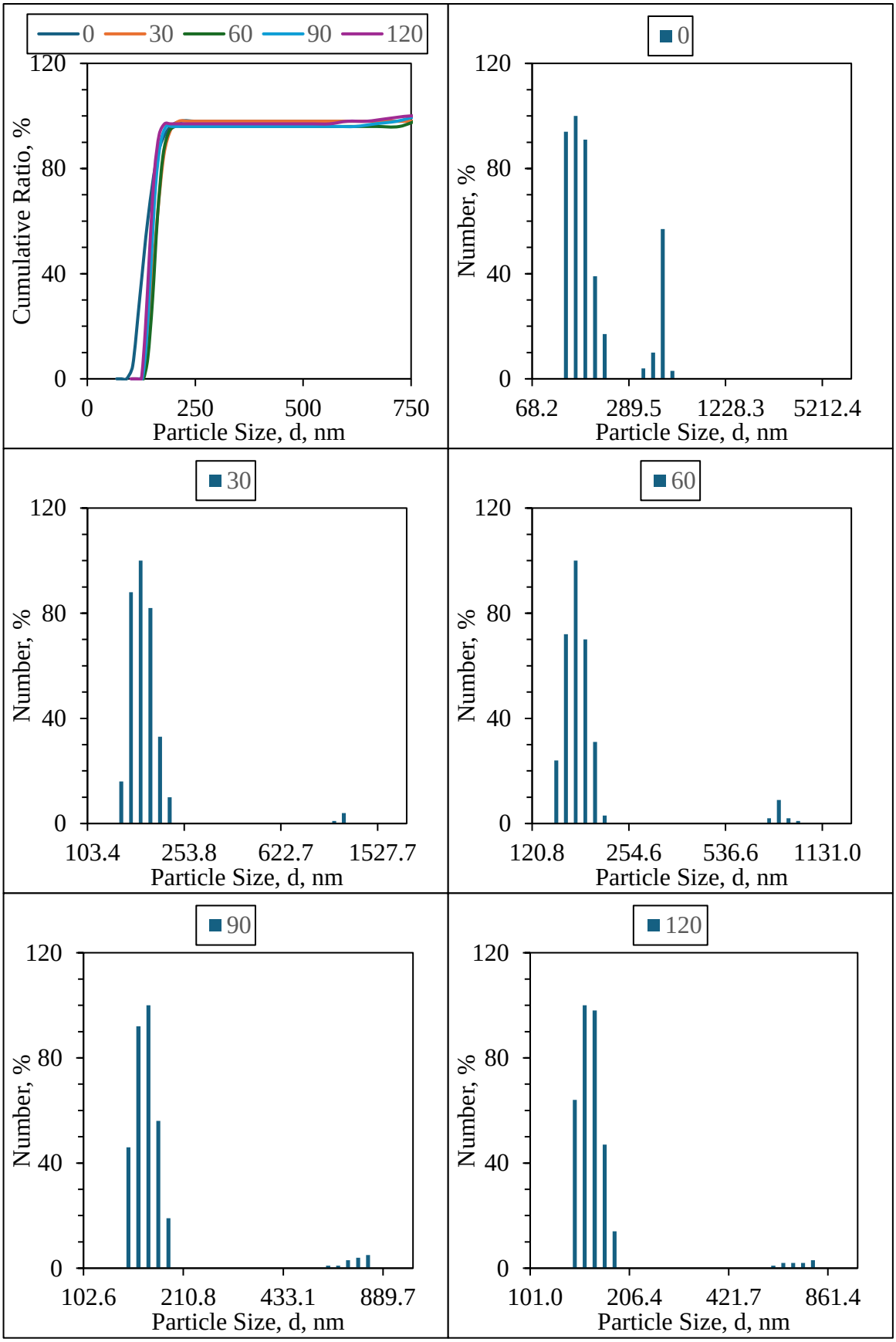


Figure 3.108. The cumulative ratio comparison and hydrodynamic size of ($HA_{,pho}$-N-TiO_2) as number-weighted HDS in 30 min intervals.

3.5.12. Hydrodynamic Size Assessment of $(HA\text{-}N\text{-}TiO_2)_{,photocat}$

The aggregation/agglomeration behavior of the N-TiO_2 and HA following photocatalytically treatment was investigated and the system was named as $(HA\text{-}N\text{-}TiO_2)_{,photocat}$. The N-$TiO_2$ was suspended in HA solution to achieve 0.25 mgL^{-1} N-TiO_2 concentration and mixed under solar irradiation in a solar light simulator for 60 min. After 60 min, the obtained system was directly transferred to the DLS polystyrene cuvette and subjected to HDS measurements for 120 min without removing the cuvette. The photocatalytic treatment with N-TiO_2 decreased the molecular size fractions of HA and increased the presence of structures < 30 kDa. These smaller molecular size fractions were mostly composed of aliphatic structures that tend to form "train, tail, loop" model surface adsorption onto N-TiO_2 surface and "tails" of the surface adsorbed HA structures might form bridges between other tails that located another N-TiO_2.

Results of the DLS data were compiled in Table 3.80 as intensity-, volume-, surface area-, and number weighted HDS with their corresponding CR%. Table 3.81 was formed by using the data obtained from Table 3.80 to show maximas of the clusters, range and the range differences. The graphical abstract of Table 3.80 and Table 3.81 was showed in Figure 3.109, Figure 3.110, Figure 3.111, and Figure 3.112 as intensity-, volume-, surface area-, and number-weighted HDS. To simplify the complex system comparative tables were prepared to evaluate HDS of the $(HA\text{-}N\text{-}TiO_2)_{,photocat}$ binary system. Table 3.82 compared the intensity-weighted HDS values of $HA_{,photocat}$, $N\text{-}TiO_{2,irr}$ and $(HA\text{-}N\text{-}TiO_2)_{,photocat}$. Table 3.83 compiled the intensity-weighted HDS values of $(HA\text{-}N\text{-}TiO_2)_{,as\text{-}is}$, $(HA\text{-}N\text{-}TiO_2)_{,dark}$, $(HA_{,pho}\text{-}N\text{-}TiO_2)$ and $(HA\text{-}TiO_2)_{,photocat}$ to see the effect of the HA composition change. The comparison of three binary systems, $(HA\text{-}TiO_2)_{,photocat}$, $(HA\text{-}Fe\text{-}TiO_2)_{,photocat}$, and $(HA\text{-}N\text{-}TiO_2)_{,photocat}$, were gathered in Table 3.84 to evaluate the effect of doping on aggregation/agglomeration in the presence of photocatalytically degraded HA structures.

The PDI of the $(HA\text{-}N\text{-}TiO_2)_{,photocat}$ binary system was found as 0.377, 0.343, 0.319, 0.293, and 0.278 for initial, 30 min, 60 min, 90 min and 120 min measurements. The average PDI of the $(HA\text{-}N\text{-}TiO_2)_{,photocat}$ during 120 min was calculated as 0.322 which was an indicator of a nearly monodispersed structure, therefore the MSD approximation was used to evaluate the HDS of the system.

MSD of the $(HA\text{-}N\text{-}TiO_2)_{,photocat}$ expressed four main clusters as 276.8 nm, 314.5 nm, 2759.8 nm, and 3135.9 nm at intensity-, volume- and surface area-weighted HDS data exhibiting different CR% under initial conditions. The two smaller clusters around 276.8 nm and 314.5 nm were mostly

comprising the system with a 100% number-weighted CR%, which means the bigger structures were very few in number in the system (Table 3.80 and Table 3.82). These bigger structures bigger than 2000 nm might be the HA-N-TiO_2 hetero-agglomerates that connected with each other with HA bridges and forming a bigger agglomerate. These bridged agglomerates were disagglomerated and formed the structures between 1087.7-1662.7 nm. The removal efficiency results supported the phenomena. At the end of 30 min 15% removal was achieved by the disagglomeration of HA-N-TiO_2-HA-N-TiO_2 structures. These structures continued to disagglomerate during 120 min. The trend was evidenced with the decrease of number weighted CR% of bigger structures with a decrease of HDS and increase of the number-weighted CR% of smaller structures. The overall removal efficiency at the end of 120 min was approximately 22%. All the agglomerated structures above 1000 nm showed spherical shapes by comparing volume- and surface area-weighted CR% with a big volume and smaller surface area.

The comparison result showed in Table 3.83 implied that HA sub structures were mostly composed of 50-90 nm sized structures. Because the photocatalytically treated HA structures tend to form bigger aggregates, in photocatalytically treated HA mono system, structures around 7000-10000 nm were also observed. These structures later disagglomerated to smaller structures around 200 nm (Table 3.83). Formation of these bigger HA hetero-agglomerates were not observed in (HA-N-TiO_2)$_{,photocat}$ binary system because adsorption onto N-TiO_2 aggregates were more favorable for photocatalytically degraded HA structures rather than formation of HA hetero-agglomerates. Also, the solar light irradiated N-TiO_2 (N-$TiO_{2,irr}$) formed bigger homo-agglomerates approximately 4000-9000 nm in its mono system due to the formation of superhydrophilic surface after solar irradiation. These bigger structures were also not observed in (HA-N-TiO_2)$_{,photocat}$ system due to the prohibition of homo-agglomerate formation after HA adsorption onto N-TiO_2 surface. However, the cluster ranging between approximately 2000-4000 nm might cover N-TiO_2 homo-agglomerates. Even the bigger homo-agglomerates of N-TiO_2 were not present in the (HA-N-TiO_2)$_{,photocat}$ binary system, the stable clusters above 1000 nm showed that N-TiO_2 aggregates were colloidally stabilized by surface adsorbed HA.

The intensity-weighted HDS comparison of (HA-N-TiO_2)$_{,as-is}$, (HA-N-TiO_2)$_{,dark}$, (HA$_{,pho}$-N-TiO_2) and (HA-TiO_2)$_{,photocat}$ showed that biggest hetero-agglomerates were achieved in the (HA-TiO_2)$_{,photocat}$ (Table 3.84). The HDS order of the N doped TiO_2 in the presence of HA was (HA-TiO_2)$_{,photocat}$>(HA$_{,pho}$-N-TiO_2)> (HA-N-TiO_2)$_{,dark}$>(HA-N-TiO_2)$_{,as-is}$ at initial time. This order was altered to (HA-TiO_2)$_{,photocat}$>(HA-N-TiO_2)$_{,dark}$>(HA-N-TiO_2)$_{,as-is}$>(HA$_{,pho}$-N-TiO_2). It must be noted that the lowest HA-N-TiO_2 hetero-agglomerate formation was observed in (HA$_{,pho}$-N-TiO_2) binary

system so the precipitation of N-TiO_2 agglomerates decreased the HDS of ($HA_{,pho}$-N-TiO_2) binary system. The removal efficiency order of the HA-N-TiO_2 binary systems was ($HA_{,pho}$-N-TiO_2)≥(HA-N-TiO_2)$_{,as\text{-}is}$>(HA-N-TiO_2)$_{,photocat}$>(HA-N-TiO_2)$_{,dark}$ at the end of 30 min and this order altered to ($HA_{,pho}$-N-TiO_2)>(HA-N-TiO_2)$_{,as\text{-}is}$>(HA-N-TiO_2)$_{,photocat}$≈(HA-N-TiO_2)$_{,dark}$ at the end of the experiment. The removal ratio of (HA-N-TiO_2)$_{,photocat}$ was mostly related with the disagglomeration of colloidal structures rather than precipitation. However, the removal ratios of the other binary systems, (HA-N-TiO_2)$_{,as\text{-}is}$, (HA-N-TiO_2)$_{,dark}$, and ($HA_{,pho}$-N-TiO_2), were mostly related with the precipitated N-TiO_2 mono agglomerates.

The effect of doping on aggregation/agglomeration profile of binary systems after solar irradiation were evaluated by comparing the intensity-weighted HDS of (HA-TiO_2)$_{,photocat}$, (HA-Fe-TiO_2)$_{,photocat}$, and (HA-N-TiO_2)$_{,photocat}$ with their corresponding CR%. The HDS order of the systems was (HA-N-TiO_2)$_{,photocat}$>(HA-TiO_2)$_{,photocat}$>(HA-Fe-TiO_2)$_{,photocat}$ at initial time and this order altered to (HA-TiO_2)$_{,photocat}$>(HA-Fe-TiO_2)$_{,photocat}$>(HA-N-TiO_2)$_{,photocat}$ at the end of DLS experiments. Because the Fe easily formed chelates with smaller size HA structures before the formation of homo-agglomeration of Fe-TiO_2, HA-Fe-TiO_2 hetero-aggregates were formed that led to formation of smaller structures in comparison to other binary systems. Also, the surface adsorption ratio of HA was slightly higher in undoped TiO_2 in comparison to the N-TiO_2, therefore the core TiO_2 aggregate size was smaller than in N-TiO_2. Hence the (HA-N-TiO_2)$_{,photocat}$ formed the bigger structures in comparison to the other two binary system at initial time. At the end of DLS experiments the removal efficiencies were determined the difference between the HDS order. The removal efficiencies derived from sedimentation profiles of (HA-TiO_2)$_{,photocat}$, (HA-Fe-TiO_2)$_{,photocat}$, and (HA-N-TiO_2)$_{,photocat}$ were 25%, 35% and 22%, respectively at the end of DLS measurements. The higher removal efficiency of the (HA-Fe-TiO_2)$_{,photocat}$ showed the remaining structures at the end of experiments were mostly composed of homo-agglomerates of Fe-TiO_2 and hetero-aggregates of photocatalytically degraded HA structures. The removal ratios of (HA-TiO_2)$_{,photocat}$ and (HA-N-TiO_2)$_{,photocat}$ binary systems were almost similar. However, while the biggest cluster remained in the (HA-TiO_2)$_{,photocat}$ was ranging between 1538.4-3222.8 nm, the biggest cluster endured in the (HA-N-TiO_2)$_{,photocat}$ binary system was ranging between 608.6-869.8 nm. The size difference of the clusters might be the result of the HA-TiO_2-HA-TiO_2 bridged hetero-agglomerate formation rather than individual HA-N-TiO_2 hetero-agglomerate formation. Because N doping altered the surface charge of TiO_2 surface, after the surface adsorption of photocatalytically degraded HA structures electric double layer formation might be thinner on the surface of HA-N-TiO_2 hetero-agglomerates in comparison to HA-TiO_2. Hence two different HA-N-TiO_2 hetero-agglomerates might not affected with each other as much as two different HA-TiO_2 hetero-agglomerates.

Table 3.82. Intensity-, volume-, surface area- and number-weighted HDS and cumulative ratios of $(HA\text{-}N\text{-}TiO_2)_{,photocat}$.

	HDS, nm	Cumulative Ratio, %			
		Intensity	Volume	Surface Area	Number
Initial	146.1-276.8	21%	10%	45%	79%
	314.5-357.4	16%	9%	30%	21%
	2137.6-2428.9	14%	5%	2%	-
	2759.4	18%	2%	1%	-
	3135.9	18%	2%	1%	-
	3563.3-4048.9	13%	72%	21%	-
30 min	168.1-199.2	14%	5%	21%	54%
	216.9-257.0	22%	7%	24%	43%
	1087.7-1184.1	18%	25%	18%	1%
	1289.0	19%	15%	9%	1%
	1403.2	16%	41%	24%	1%
	1527.4-1662.7	11%	7%	4%	-
60 min	166.0-180.2	15%	6%	21%	50%
	195.5	14%	5%	15%	28%
	212.1-230.1	14%	4%	12%	19%
	848.9-921.0	16%	10%	7%	-
	999.3	18%	19%	12%	1%
	1084.2-1276.4	23%	56%	33%	1%
90 min	187.2-203.3	15%	6%	19%	43%
	220.7	17%	6%	17%	30%
	239.7-260.3	20%	6%	15%	23%
	896.5-973.6	14%	12%	8%	1%
	1057.3	14%	49%	30%	2%
	1148.1-1353.9	20%	21%	11%	1%
120 min	156.6-180.7	25%	7%	23%	68%
	194.1-208.4	15%	4%	10%	22%
	608.6-653.7	12%	5%	4%	-
	702.1	16%	14%	11%	2%
	754.0	18%	55%	42%	7%
	809.9-869.8	14%	15%	10%	1%

Table 3.83. Intensity-weighted HDS profile of $(HA\text{-}N\text{-}TiO_2)_{,photocat}$. Time dependent HDS cluster maximas, HDS range and min-max diameter difference with respect to multi-size distribution.

	Cluster					
Time, min	Max 1, nm	Max 2, nm	Max 3, nm	Max 4, nm	Range, nm	Difference, nm
Initial	276.8	314.5	2759.8	3135.9	113.2-6749.4	6636.2
30	216.9	1289.0			141.9-2144.9	2003.0
60	195.5	999.3			119.8-1630.4	1510.6
90	220.7	1057.3			134.6-1882.8	1748.2
120	180.7	702.1	754.0		117.7-1157.5	1039.8

Table 3.84. Comparison of intensity-weighted HDS values of $HA_{,photocat}$, $N\text{-}TiO_{2,irr}$ and $(HA\text{-}N\text{-}TiO_2)_{,photocat}$.

	$HA_{,photocat}$		$N\text{-}TiO_{2,irr}$		$(HA\text{-}N\text{-}TiO_2)_{,photocat}$	
	HDS, nm	CR, %	HDS, nm	CR, %	HDS, nm	CR, %
Initial	52.3-62.7	24%	134.2-209.6	19%	146.1-276.8	21%
	75.2-90.1	19%	243.1-511.3	18%	314.5-357.4	16%
	6961.0-10000	57%	593.3-4098.3	11%	2137.6-2428.9	14%
	-	-	4755.2	12%	2759.4	18%
	-	-	5517.4	16%	3135.9	18%
	-	-	6401.8	14%	3563.3-4048.9	13%
	-	-	7427.9-8618.9	10%	-	-
30 min	45.8-51.7	9%	89.5-173.1	21%	168.1-199.2	14%
	155.0-175.1	50%	334.7-394.6	12%	216.9-257.0	22%
	186.1-210.2	41%	465.3	16%	1087.7-1184.1	18%
	-	-	548.7	20%	1289.0	19%
	-	-	647.1	16%	1403.2	16%
			763.0-4676.9	15%	1527.4-1662.7	11%
60 min	88.3-106.2	30%	115.7-132.4	19%	166.0-180.2	15%
	116.4-139.8	29%	141.7-151.6	14%	195.5	14%
	554.8-666.7	29%	511.5	7%	212.1-230.1	14%
	730.8-801.1	12%	547.2	16%	848.9-921.0	16%
	-	-	585.5	23%	999.3	18%
	-	-	626.4-670.2	21%	1084.2-1276.4	23%
	-	-	-	-	187.2-203.3	15%
90 min	21.3-26.0	2%	49.1-210.5	18%	220.7	17%
	86.8-106.2	20%	240.3	21%	239.7-260.3	20%
	117.4-129.8	12%	274.3	17%	896.5-973.6	14%
	175.4-237.0	52%	313.1-790.6	17%	1057.3	14%
	262.0-289.7	14%	902.5-1030.2	18%	1148.1-1353.9	20%
	-	-	1175.9-1342.2	8%		
120 min	99.0-113.4	37%	144.9-155.2	10%	156.6-180.7	25%
	121.3-129.8	19%	166.3	14%	194.1-208.4	15%
	438.7-502.2	33%	178.1-190.7	17%	608.6-653.7	12%
	537.4-575.0	11%	534.3-572.3	18%	702.1	16%
	-	-	613.0	18%	754.0	18%
	-	-	656.5-753.2	23%	809.9-869.8	14%

Table 3.85. Comparison of intensity-weighted HDS values of $(HA\text{-}N\text{-}TiO_2)_{,as\text{-}is}$, $(HA\text{-}N\text{-}TiO_2)_{,dark}$, $(HA_{,pho}\text{-}N\text{-}TiO_2)$ and $(HA\text{-}TiO_2)_{,photocat}$.

	$(HA\text{-}N\text{-}TiO_2)_{,as\text{-}is}$		$(HA\text{-}N\text{-}TiO_2)_{,dark}$		$(HA_{,pho}\text{-}N\text{-}TiO_2)$		$(HA\text{-}N\text{-}TiO_2)_{,photocat}$		
	HDS, nm	CR, %	HDS, nm	CR, %	HDS, nm	CR, %	HDS, nm	CR, %	
Initial	175.1-214.1	19%	Dark Mixing		60 min Solar Irradiation onto HA then TiO_2 suspended in $HA_{,pho}$		60 min Solar Irradiation and Mixing		
	236.7-261.8	14%							
	1600.7-1770.1	22%							
	1957.4	21%							
	2164.5	16%							
	2393.6-2646.9	8%							
30 min	185.3-202.3	11%							
	220.3	14%							
	241.1	14%							
	263.2-287.3	11%							
	1070.5-1275.7	19%							
	1392.6	16%							
	1520.3-1659.6	15%							
60 min	167.9-192.3	23%	144.3-174.0	16%	105.2-187.6	17%	146.1-276.8	21%	Initial
	205.7	16%	191.1-230.5	17%	334.5-386.5	12%	314.5-357.4	16%	
	220.1-235.6	16%	1133.6	9%	446.6-596.3	14%	2137.6-2428.9	14%	
	744.1-796.2	13%	1245.0	18%	1895.1-2189.8	20%	2759.4	18%	
	851.9	14%	1367.3	21%	2530.3	18%	3135.9	18%	
	911.6-1043.7	18%	1501.6-1649.1	19%	2923.8-3378.5	19%	3563.3-4048.9	13%	
90 min	139.6-161.0	17%	166.9-181.8	14%	135.4-162.0	18%	168.1-199.2	14%	30 min
	172.9-199.5	21%	198.0	16%	177.2	14%	216.9-257.0	22%	
	582.5-625.6	17%	215.7-235.0	20%	193.9-212.1	13%	1087.7-1184.1	18%	
	671.9	19%	848.0-923.7	11%	891.6-975.3	20%	1289.0	19%	
	721.7	15%	1006.2	13%	1066.9	18%	1403.2	16%	
	775.1-832.5	11%	1096.1	15%	1167.1-1276.7	17%	1527.4-1662.7	11%	
	-	-	1194.0-1300.6	11%	-	-	-	-	

Table 3.86. Comparison of intensity-weighted HDS values of $(HA\text{-}N\text{-}TiO_2)_{,as\text{-}is}$, $(HA\text{-}N\text{-}TiO_2)_{,dark}$, $(HA_{,pho}\text{-}N\text{-}TiO_2)$ and $(HA\text{-}TiO_2)_{,photocat}$ (Continue).

120 min	151.2-174.6	22%	212.8-291.0	18%	140.2-162.7	22%	166.0-180.2	15%	60 min
	187.6-216.7	23%	340.2	14%	175.3	14%	195.5	14%	
	638.1-685.7	14%	397.8-465.2	15%	188.9-203.5	11%	212.1-230.1	14%	
	736.9	17%	1390.4-1625.8	20%	723.1-779.0	20%	848.9-921.0	16%	
	791.9	15%	1901.1	18%	839.3	17%	999.3	18%	
	791.9-914.6	11%	2222.9-2599.3	15%	904.3-974.3	16%	1084.2-1276.4	23%	
150 min	181.7-192.9	12%	153.3-178.4	20%	136.8-147.1	12%	187.2-203.3	15%	90 min
	204.8	15%	192.5	15%	158.0	14%	220.7	17%	
	217.5	15%	207.6-223.9	11%	169.8-182.5	16%	239.7-260.3	20%	
	230.9-245.2	12%	697.6-752.5	10%	577.6-620.7	18%	896.5-973.6	14%	
	602.7-639.9	13%	811.7	15%	667.1	18%	1057.3	14%	
	679.5	13%	875.6	15%	716.9	13%	1148.1-1353.9	20%	
	721.5-813.4	20%	944.5-1018.8	14%	770.4-827.9	9%	-	-	
180 min	139.1-149.4	12%	182.1-193.5	15%	134.5-144.4	14%	156.6-180.7	25%	120 min
	160.6	12%	205.6	19%	155.1	13%	194.1-208.4	15%	
	172.6-185.5	12%	218.5-232.3	21%	166.6-178.9	14%	608.6-653.7	12%	
	546.9-587.7	15%	615.1-694.7	20%	561.1-602.7	18%	702.1	16%	
	631.6	19%	738.3	13%	647.3	20%	754.0	18%	
	678.8	17%	784.7-833.9	12%	695.2	14%	809.9-869.8	14%	
	729.6-784.1	13%			746.7	7%	-	-	

Table 3.87. Comparison of intensity-weighted HDS values of $(HA\text{-}TiO_2)_{,photocat}$, $(HA\text{-}Fe\text{-}TiO_2)_{,photocat}$, and $(HA\text{-}N\text{-}TiO_2)_{,photocat}$.

	$(HA\text{-}TiO_2)_{,photocat}$		$(HA\text{-}Fe\text{-}TiO_2)_{,photocat}$		$(HA\text{-}N\text{-}TiO_2)_{,photocat}$	
	HDS, nm	CR, %	HDS, nm	CR, %	HDS, nm	CR, %
Initial	253.2-286.5	8%	225.2-275.4	20%	146.1-276.8	21%
	324.1-414.8	18%	304.5-336.7	13%	314.5-357.4	16%
	1822.5	7%	2058.8-2276.6	24%	2137.6-2428.9	14%
	2061.8	15%	2517.6	23%	2759.4	18%
	2332.4	21%	2784.0-3078.6	20%	3135.9	18%
	2638.7	19%	-	-	3563.3-4048.9	13%
	2985.1-3376.9	13%	-	-	-	-
30 min	218.5-242.3	10%	194.1-230.2	18%	168.1-199.2	14%
	268.6-330.2	17%	250.7-297.4	20%	216.9-257.0	22%
	1721.5-1908.6	19%	1166.3-1270.3	13%	1087.7-1184.1	18%
	2116.2	22%	1383.5	18%	1289.0	19%
	2346.2	19%	1506.9	17%	1403.2	16%
	2603.1-2884.1	13%	1641.2-1787.5	14%	1527.4-1662.7	11%
60 min	261.8-306.6	8%	147.5-171.8	18%	166.0-180.2	15%
	359.1	12%	185.4-200.1	8%	195.5	14%
	420.6-576.9	17%	678.9-732.8	17%	212.1-230.1	14%
	2042.5	8%	790.9	21%	848.9-921.0	16%
	2392.1	16%	853.6	21%	999.3	18%
	2801.6	21%	921.4-994.4	15%	1084.2-1276.4	23%
	3281.3-3843.0	18%	-	-	-	-
90 min	228.9-253.1	12%	182.0-195.4	12%	187.2-203.3	15%
	279.9-342.4	20%	209.9	12%	220.7	17%
	1711.6-1892.7	20%	225.4-242.1	15%	239.7-260.3	20%
	2093.0	21%	707.0-759.3	16%	896.5-973.6	14%
	2314.5	17%	815.5	17%	1057.3	14%
	2559.5-2830.3	10%	875.9	16%	1148.1-1353.9	20%
	-	-	940.8-1010.5	12%	-	-
120 min	224.9-302.4	17%	199.7-213.4	15%	156.6-180.7	25%
	350.5-471.2	23%	227.9	19%	194.1-208.4	15%
	1538.4-1783.6	14%	243.5	16%	608.6-653.7	12%
	2068.0	17%	260.1-277.8	10%	702.1	16%
	2397.6	17%	798.7-853.2	11%	754.0	18%
	2779.8-3222.8	12%	911.4	14%	809.9-869.8	14%
	-	-	973.6-1040.0	15%	-	-

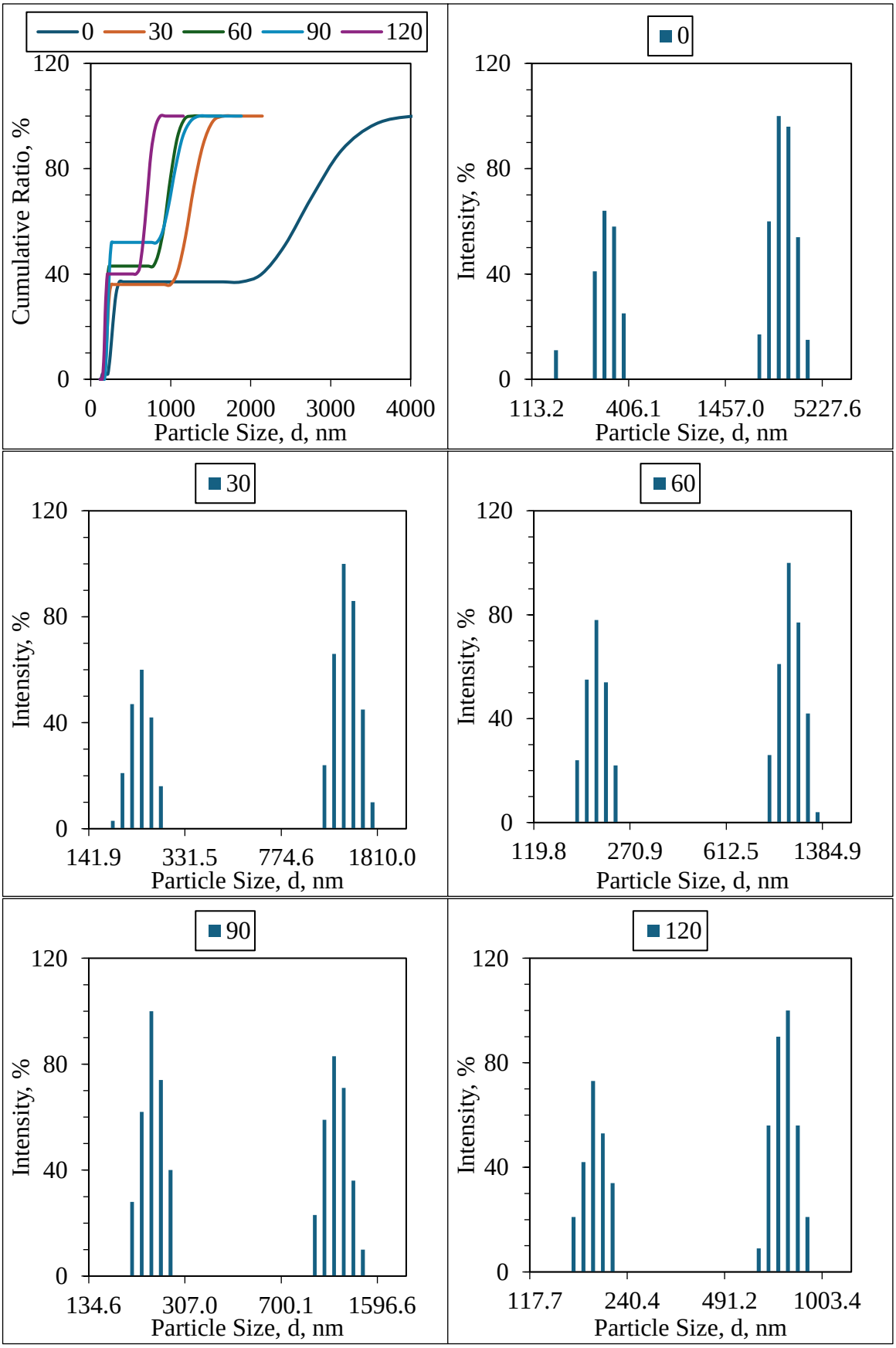


Figure 3.109. The cumulative ratio comparison and hydrodynamic size of $(HA\text{-}N\text{-}TiO_2)_{,photocat}$ as intensity-weighted HDS in 30 min intervals.

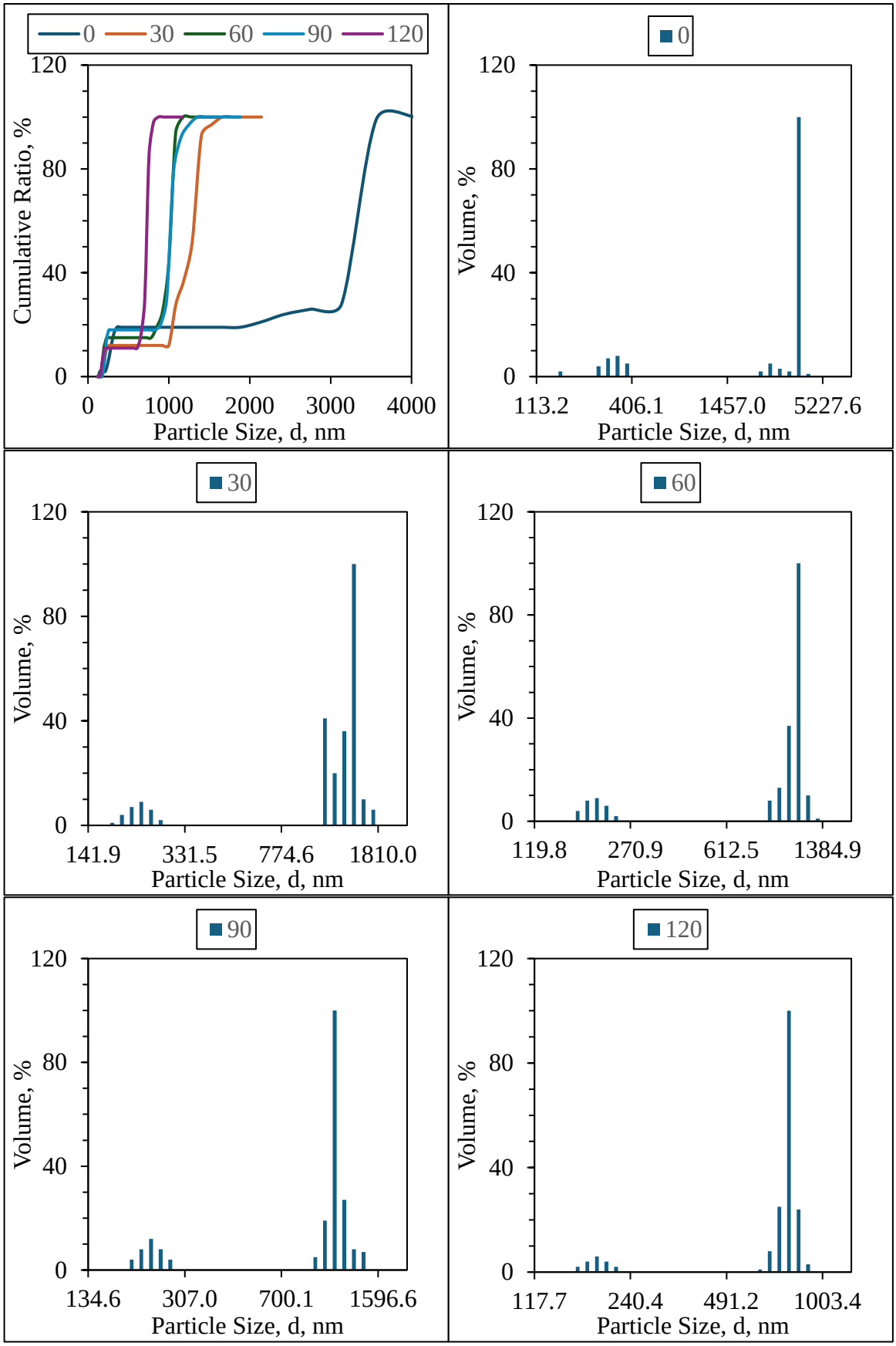


Figure 3.110. The cumulative ratio comparison and hydrodynamic size of $(HA\text{-}N\text{-}TiO_2)_{,photocat}$ as volume-weighted HDS in 30 min intervals.

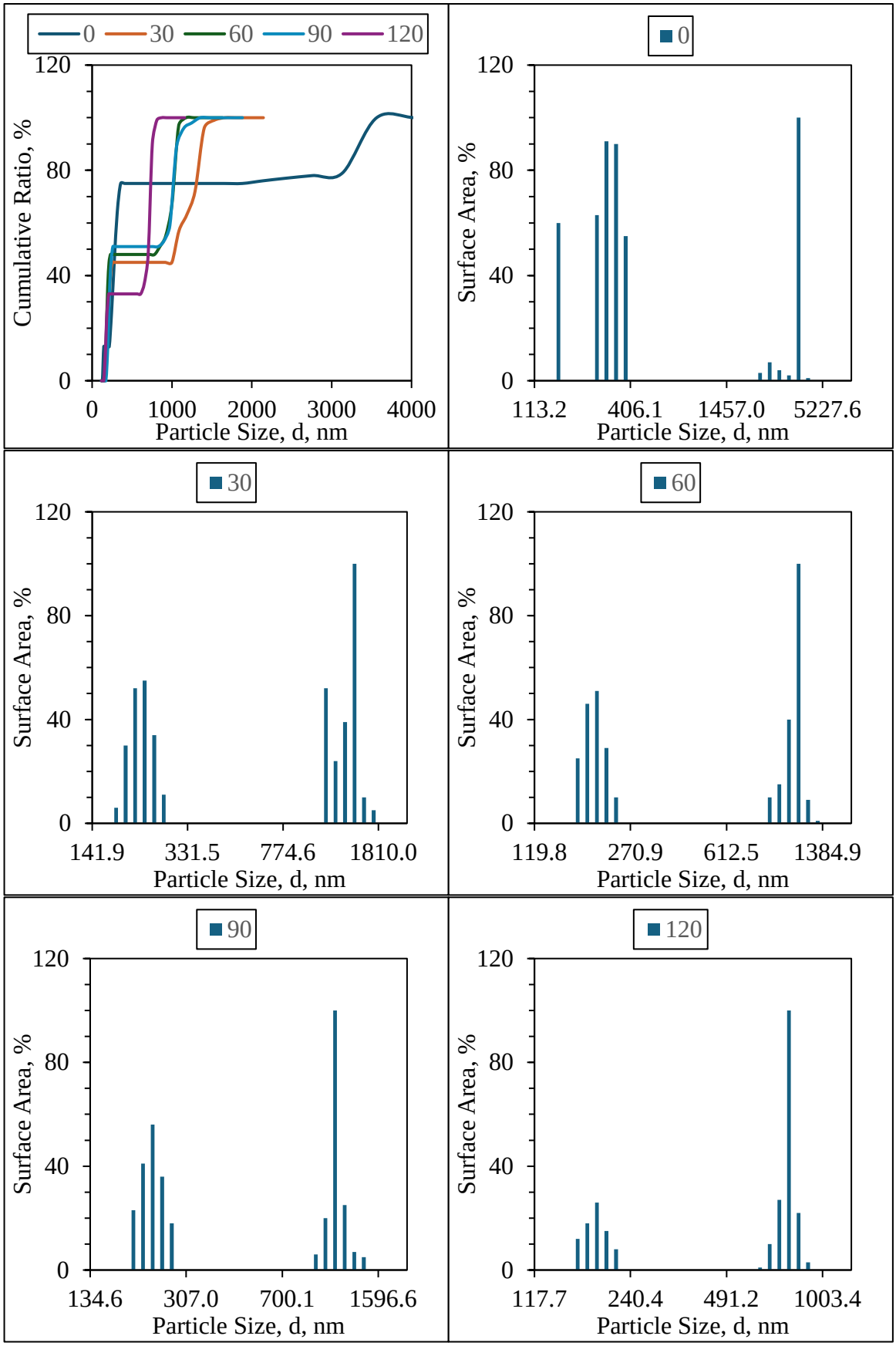


Figure 3.111. The cumulative ratio comparison and hydrodynamic size of $(HA\text{-}N\text{-}TiO_2)_{,photocat}$ as surface area-weighted HDS in 30 min intervals.

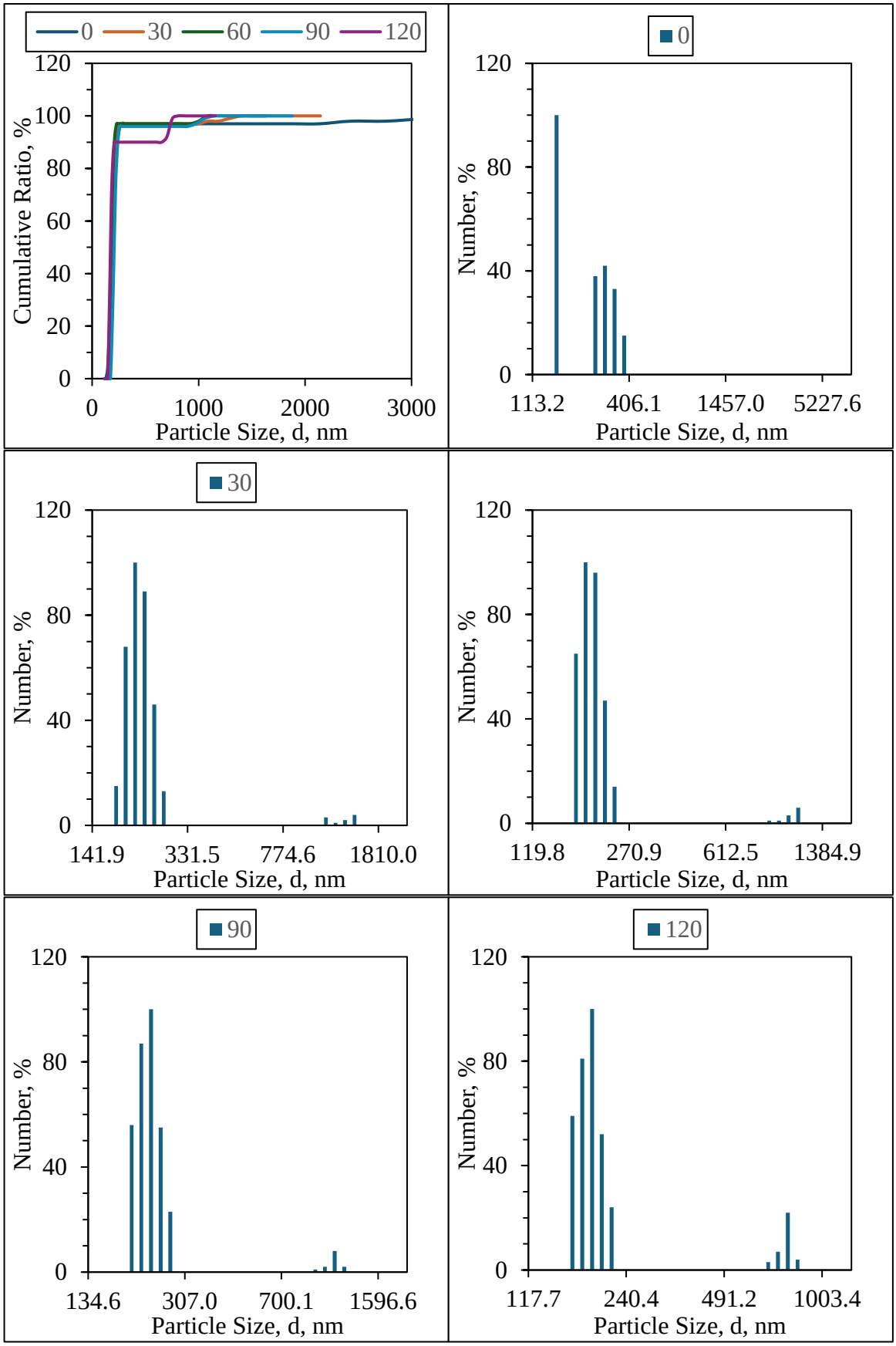


Figure 3.112. The cumulative ratio comparison and hydrodynamic size of $(HA\text{-}N\text{-}TiO_2)_{,photocat}$ as number-weighted HDS in 30 min intervals.

4. CONCLUSION AND RECOMMENDATIONS

This study covered information on the aggregation/agglomeration behavior of selected NPs in aqueous medium. NPs were chosen as TiO_2 and visible-light active versions as Fe doped and N doped TiO_2 specimens. In order to address the natural water conditions, the role of natural organic matter modeled by humic acids (HA) and solar irradiation effects were considered. Aggregation/agglomeration behavior of NPs as mono- and binary systems were assessed by hydrodynamic size measurements achieved through dynamic light scattering technique. Descriptors were intensity-, number-, surface area and volume-weighted HDS size and these parameters were evaluated with respect to the expected changes in components depending on the applied conditions.

TiO_2 as the most widely consumed oxide material as well as a semiconductor displayed aggregate sizes beyond nano-particle ranges both in the absence and presence of HA. Time dependent variations of HDS data revealed disaggregation of bigger structures to smaller ones as expressed by multi-size distribution profiles. The presence of HA significantly altered the aggregate/ agglomerate size especially under irradiation. Furthermore, "TiO_2 and HA" binary system upon irradiation was simply photocatalysis resulting in multi-site variation of HDS due to substantial changes in HA structure due to operational conditions. Since HA is composed of diverse and discrete molecular size fractions, polydispersity of HA is quite different than the polydispersity (PDI) of the system therefore the system properties should be cautiously evaluated.

Doping TiO_2 with either Fe or N was introduced to enhance the photocatalytic properties of TiO_2 through beneficial light harvesting capacity under solar irradiation. Both oxide specimens displayed similar tendency of HDS variations under all conditions. However, the role of Fe as a surface-oriented chelating agent was more pronounced with respect to N as a hydrogen bonding promotor during particle interactions.

All HDS descriptive parameters *i.e.,* intensity-, number-, surface area and volume-weighted HDS size were evaluated with respect to their definitions. Generally, intensity-based data was selected as a comparison basis to literature findings. However, number-weighted data along with cumulative ratios were found to be more important in assessment of aggregate/agglomerate sizes verified by HDS data.

In sun-lit waters and in the presence of humic matter, aggregate/agglomerate behavior of NPs should not be attributed to a single entity as a particle. NPs would behave as a “binary inorganic and organic colloidal system” through all interactions resulting in homo- and/or hetero aggregate formations accompanied by simultaneously functioning disaggregation during prolonged time periods. HDS variations over time were correlated with sedimentation kinetics resulting in system dependent inconsistencies. As sedimentation data were dependent on absorbance recordings, slight variations in absorbance with respect to large multi-size variations of HDS data could only reveal an indication of settlement tendency related to instability of the system under consideration.

Based on the literature survey on aggregation/agglomeration behavior of NPs, this study is a unique example of a systematic approach using DLS derived HDS data. The conditions were selected in a sequential order of exposure *i.e.,* as-is, dark, irradiation in the absence and presence of organic matter reaching real photocatalytic conditions under solar irradiation. Therefore, the outcome of this study addressing both NPs in the environment issue as well as photocatalysis holds prime importance and will constitute a basis for further studies.

This study revealed the significance of binary system considerations. Since natural waters also contain various colloidal particles *e.g.* clays, bio-molecules *etc.*, their respective roles deserve to be investigated. Therefore, eco-nano-toxicological studies depending on sole NP’s should be extended to real conditions of aquatic systems prior to be found eligible for regulations suitable for human health. Moreover, naturally occurring photocatalysis due to semiconductor properties of NPs should be strictly considered in relation to their compartmentalization through biological systems.

REFERENCES

Abbas, Q., Yousaf, B., Ali, M. U., Munir, M. A. M., El-Naggar, A., Rinklebe, J., & Naushad, M. (2020). Transformation pathways and fate of engineered nanoparticles (ENPs) in distinct interactive environmental compartments: A review. *Environment International, 138*, 105646.

Adán, C., Martínez-Arias, A., Malato, S., & Bahamonde, A. (2009). New insights on solar photocatalytic degradation of phenol over Fe-TiO_2 catalysts: Photo-complex mechanism of iron lixiviates. *Applied Catalysis B: Environmental, 93*(1-2), 96-105.

Aguer, J.-P., & Richard, C. (1996). Reactive species produced on irradiation at 365 nm of aqueous solutions of humic acids. *Journal of Photochemistry and Photobiology A: Chemistry, 93*(2), 193-198.
Akhtar, K., Khan, S. A., Khan, S. B., & Asiri, A. M. (2018). Scanning electron microscopy: Principle and applications in nanomaterials characterization. In *Handbook of Materials Characterization* (pp. 1-20). Springer.

Alexander, C. M., Dabrowiak, J. C., & Goodisman, J. (2013). Gravitational sedimentation of gold nanoparticles. *Journal of Colloid and Interface Science, 396*, 53-62.

Allahbakhsh, A., & Bahramian, A. R. (2018). Self-assembly of graphene quantum dots into hydrogels and cryogels: Dynamic light scattering, UV-vis spectroscopy and structural investigations. *Journal of Molecular Liquids, 265*, 172-180.

Allen, G. (1997). *Protein: A Comprehensive Treatise*. Jai Press, Inc.

Allouni, Z. E., Cimpan, M. R., Høl, P. J., Skodvin, T., & Gjerdet, N. R. (2009). Agglomeration and sedimentation of TiO_2 nanoparticles in cell culture medium. *Colloids and Surfaces B: Biointerfaces, 68*(1), 83-87.

Ambati, R., & Gogate, P. R. (2018). Ultrasound assisted synthesis of iron doped TiO_2 catalyst. *Ultrasonics Sonochemistry, 40*, 91-100.

Arana, J., Díaz, O. G., Rodríguez, J. D., Melián, J. H., i Cabo, C. G., Peña, J. P., Hidalgo, M. C., & Navío-Santos, J. A. (2003). Role of Fe^{3+}/Fe^{2+} as TiO_2 dopant ions in photocatalytic degradation of carboxylic acids. *Journal of Molecular Catalysis A: Chemical, 197*, 157-171.

Aranson, I. S. (2013). Active colloids. *Physics-Uspekhi, 56*(1), 79-92.

Armaković, S. J., Savanović, M. M., & Armaković, S. (2023). Titanium dioxide as the most used photocatalyst for water purification: An overview. *Catalysts, 13*(1), 26-39.

AZoNano. (2016). Classification, definitions, properties, hazards, risks and toxicology of nanoparticles and nanotechnology. Retrieved June 2024, from

Bahnemann, D. W. (1991). Mechanism of organic transformations on semiconductor particles. In E. Pelizzetti & M. Schiavello (Eds.), *Photochemical conversion and storage of solar energy* (pp. 251-276). Kluwer Academic Publishers.

Barnett, C. E. (1942). Some applications of wave-length turbidimetry in the infrared. *The Journal of Physical Chemistry, 46*(1), 69-75.

Bekbolet, M., & Balcioglu, I. A. (1996). Photocatalytic degradation kinetics of humic acid in aqueous TiO_2 dispersions: The influence of hydrogen peroxide and bicarbonate ion. *Water Science and Technology, 34*(1), 73-80.

Bekbolet, M., & Özkösemen, G. (1996). A preliminary investigation on the photocatalytic degradation of a model humic acid. *Water Science and Technology, 33*(6), 189-194.

Bekbolet, M., & Sen-Kavurmaci, S. (2015). The effect of photocatalytic oxidation on molecular size distribution profiles of humic acid. *Photochemical & Photobiological Sciences, 14*(4), 576-582.

Bekbolet, M., Suphandag, A. S., & Uyguner, C. S. (2002). An investigation of the photocatalytic efficiencies of TiO_2 powders on the decolorisation of humic acids. *Journal of Photochemistry and Photobiology A: Chemistry, 148*(1), 121-128.

Berne, B. J., & Pecora, R. (1976). *Dynamic light scattering: With applications to chemistry, biology, and physics*. John Wiley & Sons, Inc.

Bhatia, S. (2016). *Natural polymer drug delivery systems: Nanoparticles, plants, and algae*. Springer International Publishing.

Bhattacharjee, S. (2016). DLS and zeta potential—What they are and what they are not? *Journal of Controlled Release, 235*, 337-351.

Birben, N. C., Uyguner-Demirel, C. S., Kavurmaci, S. S., Gürkan, Y. Y., Türkten, N., Çınar, Z., & Bekbolet, M. (2017). Application of Fe-doped TiO_2 specimens for the solar photocatalytic degradation of humic acid. *Catalysis Today, 281*, 78-84.

Birben, N. C., Uyguner-Demirel, C. S., Sen-Kavurmaci, S., Gürkan, Y. Y., Türkten, N., Çınar, Z., & Bekbolet, M. (2015). Comparative evaluation of anion doped photocatalysts on the mineralization and decolorization of natural organic matter. *Catalysis Today, 240*, 125-131.

Bittelli, M., Pellegrini, S., Olmi, R., Andrenelli, M. C., Simonetti, G., Borrelli, E., & Morari, F. (2022). Experimental evidence of laser diffraction accuracy for particle size analysis. *Geoderma, 409*, 115627.

Blough, N. V., & Zepp, R. G. (1995). Reactive oxygen species in natural waters. In C. S. Foote, J. S. Valentine, A. Greenberg, & J. F. Liebman (Eds.), *Active oxygen in chemistry* (Vol. 2, pp. 280-333). Blackie Academic & Professional.

Bolton, J. R., & Cater, S. R. (1994). In *Surface and aquatic environmental photochemistry*. CRC Press.

Bolton, J. R., Bircher, K. G., Tumas, W., & Tolman, C. A. (2001). Figures-of-merit for the technical development and application of advanced oxidation technologies for both electric-and solar-driven systems (IUPAC Technical Report). *Pure and Applied Chemistry, 73*(4), 627-637.

Bond, T., Henriet, D., Goslan, H., Parsons, S. A., & Jefferson, B. (2009). Disinfection byproduct formation and fractionation behavior of natural organic matter surrogates. *Environmental Science & Technology, 43*(15), 5982-5989.

Bordi, F., Paradossi, G., Rinaldi, C., & Ruzicka, B. (2002). Chemical and physical hydrogels: Two case systems studied by quasi elastic light scattering. *Physica A: Statistical Mechanics and Its Applications, 304*(1-2), 119-128.

Brunelli, A., Foscari, A., Basei, G., Lusvardi, G., Bettiol, C., Semenzin, E., Marcomini, A., & Badetti, E. (2022). Colloidal stability classification of TiO_2 nanoparticles in artificial and natural waters by cluster analysis and a global stability index: Influence of standard and natural colloidal particles. *Science of the Total Environment, 829*, 154658.

Budarz, J. F., Turolla, A., Piasecki, A. F., Bottero, J. Y., Antonelli, M., & Wiesner, M. R. (2017). Influence of aqueous inorganic anions on the reactivity of nanoparticles in TiO_2 photocatalysis. *Langmuir, 33*(11), 2770-2779.

Burchard, W. (1983). Static and dynamic light scattering from branched polymers and biopolymers. In *Light Scattering From Polymers* (pp. 81-104). Springer.

Buxton, G. V., Greenstock, C. L., Helman, W. P., & Ross, A. (1988). Critical review of rate constants for reactions of hydrated electrons, hydrogen atoms, and hydroxyl radicals in aqueous solution. *Journal of Physical and Chemical Reference Data, 17*(2), 513-886.

Buzzaccaro, S., Tripodi, A., Rusconi, R., Vigolo, D., & Piazza, R. (2008). Kinetics of sedimentation in colloidal suspensions. *Journal of Physics: Condensed Matter, 20*(49), 494219.

Cabaniss, S. E., Zhou, Q., Maurice, P. A., Chin, Y. P., & Aiken, G. R. (2000). A log-normal distribution model for the molecular weight of aquatic fulvic acids. *Environmental Science & Technology, 34*(6), 1103-1109.

Cabannes, J., & Rocard, Y. (1929). *La diffusion moléculaire de la lumière*. Les Presses Universitaires de France.

Caputo, F., Vogel, R., Savage, J., Vella, G., Law, A., Della Camera, G., Hannon, G., Peacock, B., Mehn, D., Ponti, J., Geiss, O., Aubert, D., Prina-Mello, A., & Calzolai, L. (2021). Measuring particle size distribution and mass concentration of nanoplastics and microplastics: Addressing some analytical challenges in the sub-micron size range. *Journal of Colloid and Interface Science, 588*, 401-417.

Carbajo, J., Tolosana-Moranchel, A., Casas, J. A., Faraldos, M., & Bahamonde, A. (2018). Analysis of photoefficiency in TiO_2 aqueous suspensions: Effect of titania hydrodynamic particle size and catalyst loading on their optical properties. *Applied Catalysis B: Environmental, 221*, 1-8.

Cardot, P. J., Rasouli, S., & Blanchart, P. (2001). TiO_2 colloidal suspension polydispersity analyzed with sedimentation field flow fractionation and electron microscopy. *Journal of Chromatography A, 905*(1), 163-173.

Chang, Q. (2016). *Sedimentation in colloid and interface chemistry for water quality control*. Academic Press.

Chen, K. L., & Elimelech, M. (2007). Influence of humic acid on the aggregation kinetics of fullerene (C_{60}) nanoparticles in monovalent and divalent electrolyte solutions. *Journal of Colloid and Interface Science, 309*(1), 126-134.

Cheung, H. M., Bhatnagar, A., & Jansen, G. (1991). Sonochemical destruction of chlorinated hydrocarbons in dilute aqueous solution. *Environmental Science & Technology, 25*(9), 1510-1512.

Chin, Y. P., Alken, G., & O'Loughlin, E. (1994). Molecular weight, polydispersity, and spectroscopic properties of aquatic humic substances. *Environmental Science & Technology, 28*(10), 1853-1858.

Christian, P., von der Kammer, F., Baalousha, M., & Hoffmann, T. (2008). Nanoparticles: Structure, properties, preparation, and behavior in environmental media. *Ecotoxicology, 17*(4), 326-343.

Cooper, W. J., Curry, R. D., & O'Shea, K. E. (1998). *Environmental applications of ionizing radiation*. Wiley.

Dahal, A., & Dohnálek, Z. (2017). Formation of metastable water chains on anatase TiO_2 (101). *The Journal of Physical Chemistry C, 121*(36), 20413-20418.

Dahneke, B. E. (1983). *Measurement of Suspended Particles by Quasi-Elastic Light Scattering*. Wiley.

Dale, A. L., Casman, E. A., Lowry, G. V., Lead, J. R., Viparelli, E., & Baalousha, M. (2015). Modeling nanomaterial environmental fate in aquatic systems. *Environmental Science & Technology, 49*(4), 2587-2593.

Danovaro, R., Bongiorni, L., Corinaldesi, C., Giovannelli, D., Damiani, E., Astolfi, P., Greci, L., & Pusceddu, A. (2008). Sunscreens cause coral bleaching by promoting viral infections. *Environmental Health Perspectives, 116*(4), 441-447.

de Aguiar, T. C., de Oliveira Torchia, D. F., de Castro, T. A. V. T., Tavares, O. C. H., de Abreu Lopes, S., da Silva, L. D. S., Castro, R. N., Berbara, R. L. L., Pereira, M. G., & García, A. C. (2022). Spectroscopic–chemometric modeling of 80 humic acids confirms the structural pattern identity of humified organic matter despite different formation environments. *Science of the Total Environment, 833*, 155133.

Derjaguin, B. V., & Landau, L. D. (1941). Theory of the stability of strongly charged lyophobic sols and of the adhesion of strongly charged particles in solutions of electrolytes. *Acta Physicochimica URSS, 14*, 733–762.

Dette, C., Pérez-Osorio, M. A., Mangel, S., Giustino, F., Jung, S. J., & Kern, K. (2018). Atomic structure of water monolayer on anatase TiO_2 (101) surface. *The Journal of Physical Chemistry C, 122*(22), 11954-11960.

Domingos, R. F., Baalousha, M. A., Ju-Nam, Y., Reid, M. M., Tufenkji, N., Lead, J. R., Leppard, G. G., & Wilkinson, K. J. (2009). Characterizing manufactured nanoparticles in the environment: Multimethod determination of particle sizes. *Environmental Science & Technology, 43*(19), 7277-7284.

Dordevic, V., Milicevic, B., & Dramicanin, M. D. (2017). Rare earth-doped anatase TiO_2 nanoparticles. In *IntechOpen*.

Dunphy Guzman, K. A., Finnegan, M. P., & Banfield, J. F. (2006). Influence of surface potential on aggregation and transport of titania nanoparticles. *Environmental Science & Technology, 40*(24), 7688-7693.

Dwivedi, A. D., Dubey, S. P., Silanpaa, M., Kwon, Y. N., Lee, C., & Varma, R. S. (2015). Fate of engineered nanoparticles: Implications in the environment. *Coordination Chemistry Reviews, 287*, 64-78.

e Silva, W. A. P. M., & Pathiratne, A. (2023). Nano-titanium dioxide induced genotoxicity and histological lesions in a tropical fish model, Nile tilapia (Oreochromis niloticus). *Environmental Toxicology and Pharmacology, 98*, 104043-104052.

Einstein, A. (1906). Zur Theorie der Brownschen Bewegung. *Annalen der Physik, 324*(2), 371-381.
Einstein, A. (1910). Theory of opalescence of homogeneous liquids and liquid mixtures near critical conditions. *Annalen der Physik, 33*(7), 1275-1298.

Engebretson, R. R., & Von Wandruszka, R. (1997). The effect of molecular size on humic acid associations. *Organic Geochemistry, 26*(9-10), 759-767.

Erhayem, M., & Sohn, M. (2014). Effect of humic acid source on humic acid adsorption onto titanium dioxide nanoparticles. *Science of the Total Environment, 470-471*, 92-98.

Erickson, H. P. (2009). Size and shape of protein molecules at the nanometer level determined by sedimentation, gel filtration, and electron microscopy. *Biological Procedures Online, 11*(1), 32-51.

Esfahani, M. R., Stretz, H. A., & Wells, M. J. M. (2015). Abiotic reversible self-assembly of fulvic and humic acid aggregates in low electrolytic conductivity solutions by dynamic light scattering and zeta potential investigation. *Science of the Total Environment, 537*, 81-92.

Espinoza, T. L. A., & Frimmel, F. H. (2009). A simple simulation of the degradation of natural organic matter in homogeneous and heterogeneous advanced oxidation processes. *Water Research, 43*(15), 3902-3909.

European Commission Scientific Committee on Consumer Safety. (2012). Opinion on zinc oxide (nano form).

Fairbairn, E. A., Keller, A. A., Madler, L., Zhou, D., Pokhrel, S., & Cherr, G. N. (2011). Metal oxide nanomaterials in seawater: Linking physicochemical characteristics with biological response in sea urchin development. *Journal of Hazardous Materials, 192*(2), 1565-1571.

Fisher, P., Aumann, C., Chia, K., O'Halloran, N., & Chandra, S. (2017). Adequacy of laser diffraction for soil particle size analysis. *PLOS ONE, 12*(1), 1-20.

Foord, R., Jakeman, E., Oliver, C. J., Pike, E. R., Blagrove, R. J., Wood, E., & Peacocke, A. R. (1970). Determination of diffusion coefficients of haemocyanin at low concentration by intensity fluctuation spectroscopy of scattered laser light. *Nature, 227*(5259), 242-245.

Frazier, E. A., Patil, R. P., Mane, C. B., Sanaei, D., Asiri, F., Seo, S. S., & Sharifan, H. (2023). Environmental exposure and nanotoxicity of titanium dioxide nanoparticles in irrigation water with the flavonoid luteolin. *RSC Advances, 13*(13), 14110-14118.

French, R. A., Jacobson, A. R., Kim, B., Isley, S. L., Penn, L., & Baveye, P. C. (2009). Influence of ionic strength, pH, and cation valence on aggregation kinetics of titanium dioxide nanoparticles. *Environmental Science & Technology, 43*(4), 1354-1359.

Frimmel, F. H., & Christman, R. F. (1988). *Humic substances and their role in the environment*. John Wiley & Sons.

Frimmel, F. H., Abbt-Braun, G., Heumann, K. G., Hock, B., Lüdemann, H.-D., & Spiteller, M. (2008). *Refractory organic substances in the environment*. Wiley-VCH.

Fujishima, A., Zhang, X., & Tryk, D. A. (2008). TiO_2 photocatalysis and related surface phenomena. *Surface Science Reports, 63*(12), 515-582.

Gans, R. (1921). Asymmetry of gas molecules - an article to determine the molecular form. *Annalen der Physik, 65*(2), 97-123.

Gans, R. (1923). The Tyndall effect in liquids. *Zeitschrift für Physik, 17*(8), 353-397.

Gao, X., & Lowry, G. V. (2018). Progress towards standardized and validated characterizations for measuring physicochemical properties of manufactured nanomaterials relevant to nano health and safety risks. *NanoImpact, 9*, 14-30.

Garner, K. L., & Keller, A. A. (2014). Emerging patterns for engineered nanomaterials in the environment: A review of fate and toxicity studies. *Journal of Nanoparticle Research, 16*(8), 2503.

Garner, K. L., Suh, S., & Keller, A. A. (2017). Assessing the risk of engineered nanomaterials in the environment: Development and application of the nanoFate model. *Environmental Science & Technology, 51*(10), 5541-5551.

Gensdarmes, F. (2015). Methods of detection and characterization. In P. I. Dolez (Ed.), *Nanoengineering: Global approaches to health and safety issues* (pp. 31-50). Springer.

Ghosh, K., & Schnitzer, M. (1980). Effects of pH and neutral electrolyte concentration on free radicals in humic substances. *Soil Microbiology and Biochemistry, 44*(5), 975-978.

Gilli, G., & Gilli, P. (2013). *The nature of the hydrogen bond: Outline of a comprehensive hydrogen bond theory*. Oxford University Press.

Goldstein, J. I., Newbury, D. E., Michael, J. R., Ritchie, N. W. M., Scott, J. H. J., & Joy, D. C. (2017). *Scanning electron microscopy and X-ray microanalysis* (4th ed.). Springer.

Guo, Q., Ma, Z., Zhou, C., Ren, Z., & Yang, X. (2019). Single molecule photocatalysis on TiO_2 surfaces: Focus review. *Chemical Reviews, 119*(12), 11020-11041.

Guo, Q., Zhou, C., Ma, Z., & Yang, X. (2019). Fundamentals of TiO_2 photocatalysis: Concepts, mechanisms, and challenges. *Advanced Materials, 31*(19), 1901997.

Gupta, N., Bansal, P., & Pal, B. (2015). Metal ion-TiO_2 nanocomposites for the selective photooxidation of benzene to phenol and cycloalkanol to cycloalkanone. *Journal of Experimental Nanoscience, 10*(2), 148-160.

Gupta, S. M., & Tripathi, M. (2011). A review of TiO_2 nanoparticles. *Chinese Science Bulletin, 56*(17), 1639-1657.

Haag, W. R., & Hoigné, J. (1986). Singlet oxygen in surface waters: 3. Photochemical formation and steady-state concentrations in various types of waters. *Environmental Science & Technology, 20*(4), 341-348.

Haiss, W., Thanh, N. T. K., Aveyard, J., & Fernig, D. G. (2007). Determination of size and concentration of gold nanoparticles from UV-vis spectra. *Analytical Chemistry, 79*(11), 4215-4221.

Hajdú, A., Illés, E., Tombácz, E., & Borbáth, I. (2009). Surface charging, polyanionic coating, and colloid stability of magnetite nanoparticles. *Colloids and Surfaces A: Physicochemical and Engineering Aspects, 347*(1-3), 104-108.

Han, J., Liu, Y., Singhal, N., Wang, L., & Gao, W. (2012). Comparative photolytic degradation of estrone in water by ZnO and TiO_2 under artificial UVA and solar irradiation. *Chemical Engineering Journal, 213*, 150-162.

Harding, S. E. (1999). Protein hydrodynamics. In G. Allen (Ed.), *Protein: A comprehensive treatise* (Vol. 2, pp. 1-24). JAI Press.

Harding, S. E., & Jumel, K. (1998). Light scattering. In J. E. Coligan, B. M. Dunn, H. L. Ploegh, D. W. Speicher, & P. T. Wingfield (Eds.), *Current protocols in protein science* (pp. 1.6.1-1.6.16). John Wiley & Sons.

Hartland, A., Lead, J. R., Slaveykova, V. I., O'Carroll, D., & Valsami-Jones, E. (2013). The environmental significance of natural nanoparticles. *Nature Education Knowledge, 4*(1), 7-21.

Hassan, P. A., & Kulshreshtha, S. K. (2006). Modification to the cumulant analysis of polydispersity in quasielastic light scattering data. *Journal of Colloid and Interface Science, 300*(2), 744-748.

He, H., Cheng, Y., Yang, C., Zeng, G., Zhu, C., & Yan, Z. (2017). Influences of anion concentration and valence on dispersion and aggregation of titanium dioxide nanoparticles in aqueous solutions. *Journal of Environmental Sciences, 54*, 135-141.

Heine, M. C., & Pratsinis, S. E. (2007). Agglomerate TiO_2 aerosol dynamics at high concentrations. *Particle & Particle Systems Characterization, 24*(1), 56-65.

Hendren, C. O., Mesnard, X., Dröge, J., & Wiesner, M. R. (2011). Estimating production data for five engineered nanomaterials as a basis for exposure assessment. *Environmental Science & Technology, 45*(8), 2562-2569.

Hendricks, D. (2006). *Water treatment unit processes: Physical and chemical*. CRC Press.

Hinderliter, P. M., Minard, K. R., Orr, G., Chrisler, W. B., Thrall, B. D., Pounds, J. G., & Teeguarden, J. G. (2010). ISDD: A computational model of particle sedimentation, diffusion, and target cell dosimetry for in vitro toxicity studies. *Particle and Fibre Toxicology, 7*, 1-20.

Hoffmann, M. R., Martin, S. T., Choi, W., & Bahnemann, D. W. (1995). Environmental applications of semiconductor photocatalysis. *Chemical Reviews, 95*(1), 69-96.

Hsiung, C. E., Lien, H. L., Galliano, A. E., Yeh, C. S., & Shih, Y. H. (2016). Effects of water chemistry on the destabilization and sedimentation of commercial TiO_2 charge neutralization. *Chemosphere, 151*, 145-151.

Hur, J., Jung, K. Y., & Jung, Y. M. (2011). Characterization of spectral responses of humic substances upon UV irradiation using two-dimensional correlation spectroscopy. *Water Research, 45*(9), 2965-2974.

Hussainova, I. (2012). *Nanomaterials: Fundamentals of nanomaterials, Lecture 5*. Retrieved from https://www.ttu.ee/public/m/Mehaanikateaduskond/Instituudid/Materjalitehnika_instituut/MTX9100/Lecture5_NanomatFundamentals.pdf. Accessed January 2024.

Hyung, H., Fortner, J. D., Hughes, J. B., & Kim, J. H. (2007). Natural organic matter stabilizes carbon nanotubes in the aqueous phase. *Environmental Science & Technology, 41*(1), 179-184.

International Organization for Standardization (ISO). (1998). *ISO 9276-1:1998 - Representation of results of particle size analysis - Part 1: Graphical representation*. Geneva: ISO.

International Organization for Standardization (ISO). (2017). *ISO/DIS 22412 - Particle size analysis - Dynamic light scattering (DLS)*. Draft International Standard. Geneva: ISO.

Jackman, A. P., & Powell, R. L. (Eds.). (1990). *Proceedings of the Symposium on Advanced Oxidation Processes for the Treatment of Contaminated Water and Air*. Toronto, Canada: June 1990.
Jaffrezic-Renault, N., Pichat, P., Foissy, A., & Mercier, R. (1986). Effect of deposited Pt-particles on the surface charge of TiO_2 aqueous solutions by potentiometry, electrophoresis, and labeled ion adsorption. *Journal of Physical Chemistry, 90*(11), 2733-2738.

Järvinen, A., Heikkilä, P., Keskinen, J., & Yli-Ojanperä, J. (2017). Particle charge-size distribution measurement using a differential mobility analyzer and an electrical low pressure impactor. *Aerosol Science & Technology, 51*(1), 20-29.

Jassby, D., Budarz, J. F., & Wiesner, M. (2012). Impact of aggregate size and structure on the photocatalytic properties of TiO_2 and ZnO nanoparticles. *Environmental Science & Technology, 46*(13), 6934-6941.

Jia, N., Su, M. X., & Cai, X. S. (2019). Particle size distribution measurement based on ultrasonic attenuation spectra using burst superposed wave. *Results in Physics, 13*, 102273.

Jia, Z., Li, J., Gao, L., Yang, D., & Kanaev, A. (2023). Dynamic light scattering: A powerful tool for in situ nanoparticle sizing. *Colloids and Interfaces, 7*(1), 15-33.

Jiang, J., Oberdörster, G., & Biswas, P. (2009). Characterization of size, surface charge, and agglomeration state of nanoparticle dispersions for toxicological studies. *Journal of Nanoparticle Research, 11*(1), 77-89.

Jones, R. G., Ober, C. K., Hodge, P., Kratochvíl, P., Moad, G., & Vert, M. (2012). Terminology for aggregation and self-assembly in polymer science (IUPAC Recommendations 2013). *Pure and Applied Chemistry, 85*(3), 463-492.

Jose, N., Deshmukh, G. P., & Ravindra, M. R. (2019). Dynamic light scattering: Advantages and applications. *Acta Scientific Nutritional Health, 3*(8), 50-52.

Kaegi, R., Ulrich, A., Sinnet, B., Vonbank, R., Wichser, A., Zuleeg, S., Simmler, H., Brunner, S., Vonmont, H., Burkhardt, M., & Boller, M. (2008). Synthetic TiO_2 nanoparticle emission from exterior facades into the aquatic environment. *Environmental Pollution, 156*(2), 233-239.

Kalan, R. E., Yaparatne, S., Amirbahman, A., & Tripp, C. P. (2016). P25 titanium dioxide coated magnetic particles: Preparation, characterization and photocatalytic activity. *Applied Catalysis B: Environmental, 187*, 249-258.

Kavurmaci, S. S., & Bekbolet, M. (2013). Photocatalytic degradation of humic acid in the presence of montmorillonite. *Applied Clay Science, 75*, 60-66.

Kavurmaci, S. S., & Bekbolet, M. (2014). Tracing TiO_2 photocatalytic degradation of humic acid in the presence of clay particles by excitation–emission matrix (EEM) fluorescence spectra. *Journal of Photochemistry and Photobiology A: Chemistry, 282*, 53-61.

Keller, A. A., McFerran, S., Lazareva, A., & Suh, S. (2013). Global life cycle releases of engineered nanomaterials. *Journal of Nanoparticle Research, 15*(11), 1692.

Keller, A. A., Wang, H., Zhou, D., Lenihan, H. S., Cherr, G., Cardinale, B. J., Miller, R., & Ji, Z. (2010). Stability and aggregation of metal oxide nanoparticles in natural aqueous matrices. *Environmental Science & Technology, 44*(7), 1962-1967.

Keller, F., Feist, M., Nirschl, H., & Dörfler, W. (2010). Investigation of the nonlinear effects during the sedimentation process of a charged colloidal particle by direct numerical simulation. *Journal of Colloid and Interface Science, 344*(1), 228-236.

Khan, I., Saeed, K., & Khan, I. (2017). Nanoparticles: Properties, applications, and toxicities. *Arabian Journal of Chemistry*. Advance online publication.

Kignelman, G., Eyley, S., Zhou, C., Tunca, B., Gonon, M., Lahem, D., Seo, W. J., & Thielemans, W. (2021). Colloidal stability and aggregation mechanism in aqueous suspensions of TiO_2 nanoparticles prepared by sol–gel synthesis. *Langmuir, 37*(49), 14846-14855.

Klucakova, M., & Veznikova, K. (2017). Micro-organization of humic acids in aqueous solutions. *Journal of Molecular Structure, 1144*, 33-40.

Koparde, V. N., & Cummings, P. T. (2007). Molecular dynamics study of water adsorption on TiO_2 nanoparticles. *The Journal of Physical Chemistry C, 111*(18), 6920-6926.

Koppel, D. E. (1972). Analysis of macromolecular polydispersity in intensity correlation spectroscopy: The method of cumulants. *The Journal of Chemical Physics, 57*(11), 4814-4820.

Kosmulski, M. (2002). The significance of the difference in the point of zero charge between rutile and anatase. Advances in Colloid and Interface Science, 99, 255-264.

Koudriachova, M. V., de Leeuw, S. W., & Harrison, N. M. (2004). First-principles study of H intercalation in rutile TiO_2. *Physical Review B, 70*, 165421-165432.

Kulkarni, V. S., & Shaw, C. (2016). *Essential chemistry for formulators of semisolids and liquid dosages: Microscopy techniques*. Springer.

Laube, J., Dörrmann, M., Schmid, H. J., Mädler, L., & Colombi Ciacchi, L. (2017). Dependencies of the adhesion forces between TiO_2 nanoparticles on size and ambient humidity. *The Journal of Physical Chemistry C, 121*, 15294-15303.

Lefebvre, A. H. (1989). *Atomization and sprays*. Hemisphere Pub. Corp.

Legrini, O., Oliveros, E., & Braun, A. M. (1993). Photochemical processes for water treatment. *Chemical Reviews, 93*, 671-698.

Li, Y., Yang, C., Guo, X., Dang, Z., Li, X., & Zhang, Q. (2015). Effects of humic acids on the aggregation and sorption of nano-TiO_2. *Chemosphere, 119*, 171-176.

Li, Z., Shakiba, S., Deng, N., Chen, J., Louie, S. M., & Hu, Y. (2020). Natural organic matter (NOM) imparts molecular-weight-dependent steric stabilization or electrostatic destabilization to ferrihydrite nanoparticles. *Environmental Science & Technology, 54*, 6761-6770.

Lin, H., Huang, C. P., Li, W., Ni, C., Shah, S. I., & Tseng, Y. H. (2006). Size dependency of nanocrystalline TiO_2 on its optical property and photocatalytic reactivity exemplified by 2-chlorophenol. *Applied Catalysis B: Environmental, 68*, 1-11.

Lin, S., Wang, H., & Yu, T. (2017). A promising trend for nano-EHS research-integrating fate and transport analysis with safety assessment using model organisms. *NanoImpact, 7*, 1-6.

Liu, S., Lim, M., Fabris, R., Chow, C., Chiang, K., Drikas, M., & Amal, R. (2008). Removal of humic acid using TiO_2 photocatalytic process–fractionation and molecular weight characterisation studies. *Chemosphere, 72*, 263-271.

Liu, Y., Tian, Q., & Guan, X. (2021). Grain size estimation using phased array ultrasound attenuation. *NDT & E International, 122*, 102479-102488.

Liu, Y., Wang, X., Shang, J., Xu, W., Sheng, M., & Ye, C. (2022). The positive effect of formaldehyde on the photocatalytic renoxification of nitrate on TiO_2 particles. *Atmospheric Chemistry and Physics, 22*, 11347-11358.

Liu, Z., Wang, C., Hou, J., Wang, P., Miao, L., Lv, B., Yang, Y., You, G., Xu, Y., Zhang, M., & Ci, H. (2018). Aggregation, sedimentation, and dissolution of CuO and ZnO nanoparticles in five waters. *Environmental Science and Pollution Research, 25*, 31240-31249.

Lowry, G. V., Gregory, K. B., Apte, S. C., & Lead, J. R. (2012). Transformations of nanomaterials in the environment. *Environmental Science & Technology, 46*, 6893-6899.

Maira, A. J., Yeung, K. L., Lee, C. Y., Yue, P. L., & Chan, C. K. (2000). Size effects in gas-phase photo-oxidation of trichloroethylene using nanometer-sized TiO_2 catalysts. *Journal of Catalysis, 192*, 185-196.

Manahan, S. E. (2022). *Environmental chemistry* (11th ed.). CRC Press.

Matilainen, A., & Sillanpää, M. (2010). Removal of natural organic matter from drinking water by advanced oxidation processes. *Chemosphere, 80*, 351-365.

Matsoukas, T., Desai, T., & Lee, K. (2015). Engineered nanoparticles and their applications. *Journal of Nanomaterials, 2015*, 1-2.

McGlade, J. (2017). Nanomaterials: Applying the precautionary principle. In *Frontiers 2017: Emerging issues of environmental concern* (pp. 24-35).

McNaught, A. D., & Wilkinson, A. (1997). *IUPAC compendium of chemical terminology* (2nd ed.). Blackwell Science.

Mie, G. (1908). Beiträge zur Optik trüber Medien, speziell kolloidaler Metallösungen. *Annalen der Physik, 330*, 377-445.

Minassian-Saraga, L. T. (1994). Thin films including layers: Terminology in relation to their preparation and characterization (IUPAC Recommendations 1994). *Pure and Applied Chemistry, 66*, 1667-1738.

Morrison, I. D., & Ross, S. (2002). *Colloidal dispersions: Suspensions, emulsions, and foams*. Wiley-Interscience.

Morrison, I. D., Grabowski, E. F., & Herb, C. A. (1985). Improved techniques for particle size determination by quasi-elastic light scattering. *Langmuir, 1*, 496-501.

Mueller, N. C., & Nowack, B. (2008). Exposure modeling of engineered nanoparticles in the environment. *Environmental Science & Technology, 42*, 4447-4453.

Naasz, S., Altenburger, R., & Kühnel, D. (2018). Environmental mixtures of nanomaterials and chemicals: The Trojan-horse phenomenon and its relevance for ecotoxicity. *Science of the Total Environment, 635*, 1170-1181.

Nakata, K., & Fujishima, A. (2012). TiO_2 photocatalysis: Design and applications. *Journal of Photochemistry and Photobiology C: Photochemistry Reviews, 13*, 169-189.

Nic, M., Hovorka, L., Jirat, J., Kosata, B., & Znamenacek, J. (2005). *IUPAC compendium of chemical terminology-the gold book* (3rd ed.). International Union of Pure and Applied Chemistry.

Nickel, C., Angelstorf, J., Bienert, R., Burkart, C., Gabsch, S., Giebner, S., Haase, A., Hellack, B., Hollert, H., Hund-Rinke, K., Jungmann, D., Kaminski, H., Luch, A., Maes, H. M., Nogowski, A., Oetken, M., Schaeffer, A., Schiwy, A., Schlich, K., Stintz, M., von der Kammer, F., & Kuhlbusch, T. A. (2014). Dynamic light-scattering measurement comparability of nanomaterial suspensions. *Journal of Nanoparticle Research, 16*, 1-12.

Nobbmann, U. (2015). A basic guide to particle characterization. Retrieved from https://www.malvernpanalytical.com/en/learn/knowledge-center/whitepapers/WP120620BasicGuidePartChar

Nobbmann, U. (2017). Polydispersity - What does it mean for DLS and chromatography? Retrieved from https://www.materials-talks.com/polydispersity-what-does-it-mean-for-dls-and-chromatography/

O'Shea, K. E., & Cardona, C. (1995). The reactivity of phenol in irradiated aqueous suspensions of TiO_2: Mechanistic changes as a function of solution pH. *Journal of Photochemistry and Photobiology A: Chemistry, 91*, 67-72.

Okouchi, S., Nojima, O., & Arai, T. (1992). Cavitation-induced degradation of phenol by ultrasound. *Water Science and Technology, 26*(7), 2053-2056.

Olatunji, O. N., Du, J., Hintz, W., & Tomas, J. (2016). Application of particle sedimentation analysis in sterically-stabilized TiO_2 particles stability assessment. *Advanced Powder Technology, 27*(4), 1325-1336.

Paramo, L., Jiménez-Chávez, A., Medina-Ramirez, I. E., Böhnel, H. N., Escobar-Alarcón, L., & Esquivel, K. (2023). Biocompatibility evaluation of TiO_2, Fe_3O_4, and TiO_2/Fe_3O_4 nanomaterials: Insights into potential toxic effects in erythrocytes and HepG2 cells. *Nanomaterials, 13*(12), 2824.

Park, H. G., & Yeo, M. K. (2016). Nanomaterial regulatory policy for human health and environment. *Molecular and Cellular Toxicology, 12*(2), 223-236.

Pate, K., & Safier, P. (Eds.). (2016). *Chemical methodology methods for CMP quality*. In S. Babu (Ed.), *Advances in chemical mechanical planarization* (pp. 1-20). Elsevier.

Pecora, R. D. (1964). Doppler shifts in light scattering from pure liquids and polymer solutions. *The Journal of Chemical Physics, 40*(5), 1604-1614.

Pecora, R. D. (1974). *Photon correlation and light beating spectroscopy*. Plenum Press.

Peng, H., Li, J., Li, S., & Xia, J. (2008). First-principles study of the electronic structures and magnetic properties of 3d transition metal-doped anatase TiO_2. *Journal of Physics: Condensed Matter, 20*(7), 1-6.

Petrucci, R. H., Herring, F. G., Madura, J. D., & Bissonnette, C. (2017). *General chemistry: Principles and modern applications* (11th ed.). Pearson Education.

Piccino, F., Gottschalk, F., Seeger, S., & Nowack, B. (2012). Industrial production quantities and uses of ten engineered nanomaterials in Europe and the world. *Journal of Nanoparticle Research, 14*(6), 1109-1120.

Polewski, K., Slawinska, D., Slawinski, J., & Pawlak, A. (2005). The effect of UV and visible light radiation on natural humic acid EPR spectral and kinetic studies. *Geoderma, 126*(3-4), 291-299.
Pusey, P. N. (1974). *Photon correlation and light beating spectroscopy*. Plenum Press.

Quik, J. T. K., Vonk, J. A., Hansen, S. F., Baun, A., & Meent, D. V. D. (2011). How to assess exposure of aquatic organisms to manufactured nanoparticles? *Environmental International, 37*(4), 1068-1077.

Quik, J. T., Velzeboer, I., Wouterse, M., Koelmans, A. A., & Van de Meent, D. (2014). Heteroaggregation and sedimentation rates for nanomaterials in natural waters. *Water Research, 48*(1), 269-279.

Ragheb, R., & Nobbmann, U. (2020). Multiple scattering effects on intercept, size, polydispersity index, and intensity for parallel (VV) and perpendicular (VH) polarization detection in photon correlation spectroscopy. *Scientific Reports, 10*(1), 21768-21777.

Romanias, M. N., Zein, A. E., & Bedjanian, Y. (2012). Heterogeneous interaction of H_2O_2 with TiO_2 surface under dark and UV light irradiation conditions. *The Journal of Physical Chemistry A, 116*(41), 8191-8200.

Rook, J. J. (1976). Haloforms in drinking water. *Journal of the American Water Works Association, 68*(3), 168-172.

Sağlık, D. (2021). *Aggregation of natural colloidal particles under solar irradiation* (Master's thesis). Boğaziçi University.

Satoh, A., Chantrell, R. W., & Coverdale, G. N. (1999). Brownian dynamics simulations of ferromagnetic colloidal dispersions in a simple shear flow. *Journal of Colloid and Interface Science, 209*(1), 44-59.

Sauter, J. (1928). Untersuchung der von spritzvergasern gelieten zerstäubung. *Forschungsarbeiten auf dem Gebiete des Ingenieurwesens, 312*, 29-37.

Scala, F. (2013). Fluidized bed technologies for near-zero emission combustion and gasification. Woodhead Publishing Limited, UK.

SCENIHR. (2005). *Request for a scientific opinion on the appropriateness of existing methodologies to assess the potential risks associated with engineered and adventitious nanotechnologies* (SCENIHR/002/05). European Commission

Scherrer, P. (1918). Estimation of the size and internal structure of colloidal particles by means of röntgen. *Nachrichten von der Gesellschaft der Wissenschaften zu Göttingen, 2*, 96-100.

Schneider, J., Matsuoka, M., Takeuchi, M., Zhang, J., Horiuchi, Y., Anpo, M., & Bahnemann, D. W. (2014). Understanding TiO_2 photocatalysis: Mechanisms and materials. *Chemical Reviews, 114*(3), 9919-9986.

Schwarzenbach, R. P., Gschwend, P. M., & Imboden, D. M. (2017). *Environmental organic chemistry*. John Wiley & Sons, Inc.

Selcuk, H., & Bekbolet, M. (2008). Photocatalytic and photoelectrocatalytic humic acid removal and selectivity of TiO_2 coated photoanode. *Chemosphere*, *73*(6), 854-858.

Sharma, G., Dhawan, S., Reed, N., Chakrabarty, R., & Biswas, P. (2019). Collisional growth rate and correction factor for TiO_2 nanoparticles at high temperatures in free molecular regime. *Journal of Aerosol Science, 127*, 27-37.

Sharma, V. K., Filip, J., Zboril, R., & Varma, S. (2015). Natural inorganic nanoparticles—Formation, fate, and toxicity in the environment. *The Royal Society of Chemistry: Review, 44*(24), 8410-8423.

Shuaibu, A. D., Rubab, R., Ali, S., Umoh, G. V., Shaikh, A. J., Khan, S. A., & Khan, A. M. (2024). Synthesis and stabilities of Fe, Ni, and Zn oxide incorporated colloidal TiO_2. *Colloids and Surfaces A: Physicochemical and Engineering Aspects, 691*, 133955-133964.

Siedl, N., Elser, M. J., Bernardi, J., & Diwald, O. (2009). Functional interfaces in pure and blended oxide nanoparticle networks: Recombination versus separation of photogenerated charges. *The Journal of Physical Chemistry C, 113*(37), 15792-15795.

Smoluchowski, M. (1908). Molekular-kinetische theorie der opaleszenz von gasen im kritischen zustande, sowie einiger verwandter erscheinungen. *Annalen der Physik, 330*(3), 205-226.

Song, D., Hatami, M., Wang, Y., Jing, D., & Yang, Y. (2016). Prediction of hydrodynamic and optical properties of TiO_2/water suspension considering particle size distribution. *International Journal of Heat and Mass Transfer, 92*, 864-876.

Spurr, R. A., & Myers, H. (1957). Quantitative analysis of anatase-rutile mixtures with an X-ray diffractometer. *Analytical Chemistry, 29*(5), 760-762.

Starchevskii, V. L., Kislenko, V. M., Maksymiv, N. L., & Koval, I. Z. (2009). Variation kinetics of chemical and bacterial contaminations of water containing yeast cells. *Journal of Water Chemistry and Technology, 31*(5), 269-273.

Stepto, R. F. T. (2009). Dispersity in polymer science (IUPAC Recommendations 2009). *Pure and Applied Chemistry, 81*(2), 351-353.

Stetefeld, J., McKenna, S. A., & Patel, T. R. (2016). Dynamic light scattering: A practical guide and applications in biomedical sciences. *Biophysical Reviews, 8*(4), 409-427.

Stolpe, B., & Hassellöv, M. (2007). Changes in size distribution of fresh water nanoscale colloidal matter and associated elements on mixing with seawater. *Geochimica et Cosmochimica Acta, 71*(14), 3291-3310.

Stumm, W., & Morgan, J. J. (1996). *Aquatic chemistry*. Wiley-Interscience.

Sun, J., Guo, L. H., Zhang, H., & Zhao, L. (2014). UV irradiation induced transformation of TiO_2 nanoparticles in water: Aggregation and photoreactivity. *Environmental Science & Technology, 48*(20), 11962-11968.

Sun, Y., Yu, Y., Li, D., Zhai, J., & Zheng, H. (2021). Enhanced coagulation for TiO_2-NPs removal by using a hybrid flocculant. *Separation and Purification Technology, 277*, 119480-119493.

Suresh, V., Liu, Z., Perry, Z., & Gopalakrishnan, R. (2022). Modeling particle-particle binary coagulation rate constants for spherical aerosol particles at high volume fractions using Langevin dynamics simulations. *Journal of Aerosol Science, 164*, 106001-106018.

Suttiponparnit, K., Jiang, J., Sahu, M., Suvachittanont, S., Charinpanitkul, T., & Biswas, P. (2011). Role of surface area, primary particle size, and crystal phase on titanium dioxide nanoparticle dispersion properties. *Nanoscale Research Letters, 6*(1), 1-8.

Tan, L., Liu, Z., Zhou, C., & Ding, L. (2021). Combined factors influencing the surface charge and aggregation behaviors of TiO_2 nanoparticles in the presence of humic acid and UV irradiation. *Journal of Nanoparticle Research, 23*(1), 191-203.

Tantra, R., Sikora, A., Hartmann, N. B., Sintes, J. R., & Robinson, K. N. (2015). Comparison of the effects of different protocols on the particle size distribution of TiO_2 dispersions. *Particuology, 19*, 35-44.

Tester, J. W., Holgate, H. R., Armellini, F. J., Webley, P. A., Killilea, W. R., Hong, G. T., & Barner, H. E. (1993). Supercritical water oxidation: Technology process development and fundamental research. In *Emerging technologies in hazardous waste management III* (Vol. 518, pp. 35-76). ACS Symposium Series.

Tester, J. W., Holgate, H. R., Armellini, F. J., Webley, P. A., Killilea, W. R., Hong, G. T., & Barner, H. E. (1993). Supercritical water oxidation: Technology process development and fundamental research. In *Emerging technologies in hazardous waste management III* (Vol. 518, pp. 35-76). ACS Symposium Series.

Teulon, J. M., Godon, C., Chantalat, L., Moriscot, C., Cambedouzou, J., Odorico, M., Ravaux, J., Podor, R., Gerdil, A., Habert, A., Herlin-Boime, N., Chen, S. W., & Pellequer, J. L. (2018). On the operational aspects of measuring nanoparticle sizes. *Nanomaterials, 9*(1), 18-47.

Thio, B. J. R., Zhou, D., & Keller, A. A. (2011). Influence of natural organic matter on the aggregation and deposition of titanium dioxide nanoparticles. *Journal of Hazardous Materials, 189*(1-2), 556-563.

Tolosana-Moranchel, A., Pecharromán, C., Faraldos, M., & Bahamonde, A. (2021). Strong effect of light scattering by distribution of TiO_2 particle aggregates on photocatalytic efficiency in aqueous suspensions. *Chemical Engineering Journal, 403*, 126186-126197.

Tomaszewska, E., Soliwoda, K., Kadziola, K., Tkacz-Szczesna, B., Celichowski, G., Cichomski, M., Szmaja, W., & Grobelny, J. (2013). Detection limits of DLS and UV-Vis spectroscopy in characterization of polydisperse nanoparticles colloids. *Journal of Nanomaterials, 2013*, 60-70.

Tomchuk, O. V., Avdeev, M. V., & Bulavin, L. A. (2020). Modeling fractal aggregates of polydisperse particles with tunable dimension. *Colloids and Surfaces A: Physicochemical and Engineering Aspects, 605*, 125331-125339.

Trickler, W. J., Lantz, S. M., Murdock, R. C., Schrand, A. M., Robinson, B. L., Newport, G. D., Schlager, J. J., Oldenburg, S. J., Paule, M. G., Slikker, W., Jr., Hussain, S. M., & Ali, S. F. (2010). Silver nanoparticle induced blood-brain barrier inflammation and increased permeability in primary rat brain microvessel endothelial cells. *Toxicological Sciences, 118*(1), 160-170.

Tseng, Y. H., Lin, H. Y., Kuo, C. S., Li, Y. Y., & Huang, C. P. (2006). Thermostability of nano-TiO_2 and its photocatalytic activity. *Reaction Kinetics and Catalysis Letters, 89*(1), 63-69.

Turkten, N., & Bekbolet, M. (2020). Photocatalytic performance of titanium dioxide and zinc oxide binary system on degradation of humic matter. *Journal of Photochemistry and Photobiology A: Chemistry, 401*, 112748-112758.

Turkten, N., Karatas, Y., Uyguner-Demirel, C. S., & Bekbolet, M. (2023). Preparation of PANI-modified TiO_2 and characterization under pre- and post-photocatalytic conditions. *Environmental Science and Pollution Research, 30*(1), 1-26.

Turley, R. S., Benavides, R., Hernández-Viezcas, J. Á., & Gardea-Torresdey, J. L. (2018). Insights on ligand interactions with titanium dioxide nanoparticles via dynamic light scattering and electrophoretic light scattering. *Microchemical Journal, 139*, 333-338.

Turolla, A., Piazzoli, A., Budarz, J. F., Wiesner, M. R., & Antonelli, M. (2015). Experimental measurement and modeling of reactive species generation in TiO_2 nanoparticle photocatalysis. *Chemical Engineering Journal, 271*, 260-268.

Tyndall, J. (1868). On the blue colour of the sky, the polarization of skylight, and on the polarization of light by cloudy matter generally. *Proceedings of the Royal Society of London, 17*, 223-233.

Usenko, E., Glamazda, A., Svidzerska, A., Valeev, V., Laguta, A., Petrushenko, S., & Karachevtsev, V. (2023). DNA: TiO_2 nanoparticle nanoassemblies: Effect of temperature and nanoparticle concentration on aggregation. *Journal of Nanoparticle Research, 25*(1), 113-124.

Uyguner, C. S., & Bekbolet, M. (2004). Evaluation of humic acid, chromium (VI), and TiO_2 ternary system in relation to adsorptive interactions. *Applied Catalysis B: Environmental, 49*(3), 267-275.

Uyguner, C. S., & Bekbolet, M. (2005a). A comparative study on the photocatalytic degradation of humic substances of various origins. *Desalination, 176*(1-3), 167-176.

Uyguner, C. S., & Bekbolet, M. (2009). Application of photocatalysis for the removal of natural organic matter in simulated surface and ground waters. *Journal of Advanced Oxidation Technologies, 12*(1), 87-92.

Uyguner, C. S., & Bekbolet, M. (2010). TiO_2-assisted photocatalytic degradation of humic acids: Effect of copper ions. *Water Science and Technology, 61*(10), 2581-2590.

Uyguner-Demirel, C. S., & Bekbolet, M. (2011). Significance of analytical parameters for the understanding of natural organic matter in relation to photocatalytic oxidation. *Chemosphere, 84*(7), 1009-1031.

Uyguner-Demirel, C. S., Birben, C., & Bekbolet, M. (2013). Key role of common anions on the photocatalytic degradation profiles of the molecular size fractions of humic acids. *Catalysis Today, 209*, 122-126.

Uyguner-Demirel, C. S., Turkten, N., Karatas, Y., & Bekbolet, M. (2023). Photocatalytic performance of PANI-modified TiO_2: Degradation of refractory organic matter. *Environmental Science and Pollution Research, 30*(48), 85626-85638.

Uyguner-Demirel, C. S., Turkten, N., Kaya, D., & Bekbolet, M. (2022). Effect of oxidative and non-oxidative conditions on molecular size fractionation of humic acids: TiO_2 and Cu-doped TiO_2 photocatalysis. *Environmental Science and Pollution Research, 29*(63), 85413-85432.

Van Saarloos, W. (1987). On the hydrodynamic radius of fractal aggregates. *Physica A: Statistical Mechanics and Its Applications, 147*(2), 280-296.

Vance, M. E., Kuiken, T., Vejerano, E. P., McGinnis, S. P., Hochella, M. F., Rejeski, D., & Hull, M. S. (2015). Nanotechnology in the real world: Redeveloping the nanomaterial consumer products inventory. *Beilstein Journal of Nanotechnology, 6*, 1769-1780.

Vert, M., Doi, Y., Hellwich, K. H., Hess, M., Hodge, P., Kubisa, P., Rinaudo, M., & Schué, F. (2012). *Recommendations, I.U.P.A.C. Terminology for biorelated polymers and applications*. RSC Publishing.

Verwey, E. J. W., & Overbeek, J. T. (1948). *Theory of the stability of lyophobic colloids*. Elsevier.

Vione, D., Minella, M., Maurino, V., & Minero, C. (2014). Indirect photochemistry in sunlit surface waters: Photoinduced production of reactive transient species. *Chemistry-A European Journal, 20*(36), 10590-10606.

Von Wandruszka, R., Ragle, C., & Engebretson, R. (1997). The role of selected cations in the formation of pseudomicelles in aqueous humic acid. *Talanta, 44*(5), 805-809.

Wang, C., Cai, X., Chen, Y., Cheng, Z., Luo, X., Mo, S., Jia, L., Lin, P., & Yang, Z. (2017). Improved hydrogen production from glycerol photo-forming over sol-gel derived TiO_2 coupled with metal oxides. *Chemical Engineering Journal, 317*, 522-532.

Wang, G. S., Hsieh, S. T., & Hong, C. S. (2000). Destruction of humic acid in water by UV light-catalyzed oxidation with hydrogen peroxide. *Water Research, 34*(15), 3882-3887.

Wang, P., Qi, N., Ao, Y., Hou, J., Wang, C., & Qian, J. (2016). Effect of UV irradiation on the aggregation of TiO_2 in an aquatic environment: Influence of humic acid and pH. *Environmental Pollution, 212*, 178-187.

Wang, R., Hashimoto, K., Fujishima, A., Chikuni, M., Kojima, E., Kitamura, A., Shimohigoshi, M., & Watanabe, T. (1997). Light-induced amphiphilic surfaces. *Nature, 388*(6642), 431-432.

Wang, W., Wang, W., Fan, Q., Wang, Y., Qiao, Z., & Wang, X. (2014). Effects of UV radiation on humic acid coagulation characteristics in drinking water treatment processes. *Chemical Engineering Journal, 256,* 137-143.

Wells, M. J., & Stretz, H. A. (2019). Supramolecular architectures of natural organic matter. *Science of the Total Environment, 671,* 1125-1133.

Wenzel, A., Gahr, A., and Niessner, R. (1999). TOC-removal and degradation of pollutants in leachate using a thin-film photoreactor. Water Research, 33, 937-946.

Wershaw, R. L. (1986). A new model for humic materials and their interactions with hydrophobic organic chemicals in soil-water or sediment-water systems. *Journal of Contaminant Hydrology, 1*(1), 29-45.

Widegren, J., & Bergström, L. (2002). Electrostatic stabilization of ultrafine titania in ethanol. *Journal of the American Ceramic Society, 85*(3), 523-528.

Wu, S., & Choi, H. (2016). Interpreting unique colloidal response of TiO_2 nanomaterials to controlled sonication for understanding their assembly configuration in water. *Water Science and Technology: Water Supply, 16*(6), 1768-1775.

Wyrwoll, A. J., Lautenschläger, P., Bach, A., Hellack, B., Dybowska, A., Kuhlbusch, T. A., Hollert, H., Schaffer, A., & Maes, H. M. (2016). Size matters—the phototoxicity of TiO_2 nanomaterials. *Environmental Pollution, 208*, 859-867.

Xu, F. (2018). Review of analytical studies on TiO_2 nanoparticles and particle aggregation, coagulation, flocculation, sedimentation, stabilization. *Chemosphere, 212*, 662-677.

Yalçın, Y., Kılıç, M., & Çınar, Z. (2010). The role of non-metal doping in TiO_2 photocatalysis. *Journal of Advanced Oxidation Technologies, 13*(2), 281-296.

Yalçın, Y., Kılıç, M., & Çınar, Z. (2010b). Fe^{+3}-doped TiO_2: A combined experimental and computational approach to the evaluation of visible light activity. *Applied Catalysis B: Environmental, 99*(1-2), 469-477.

You, Z., Zhuang, C., Sun, Y., Zhang, S., & Zheng, H. (2019). Efficient removal of TiO_2 nanoparticles by enhanced flocculation-coagulation. *Industrial & Engineering Chemistry Research, 58*(38), 14528-14537.

Yu, S., Liu, J., Yin, Y., & Shen, M. (2018). Interactions between engineered nanoparticles and dissolved organic matter: A review on mechanisms and environmental effects. *Journal of Environmental Sciences, 63*, 198-217.

Zavarzina, A. G., Danchenko, N. N., Demin, V. V., Artemyeva, Z. S., & Kogut, B. M. (2021). Humic substances: Hypotheses and reality (a review). *Eurasian Soil Science, 54*(12), 1826-1854.

Zepp, R. G., Schlotzhauer, P. F., & Sink, R. M. (1985). Photosensitized transformations involving electronic energy transfer in natural waters: Role of humic substances. *Environmental Science & Technology, 19*(1), 74-81.

Zhang, C., Lohwacharin, J., & Takizawa, S. (2017). Properties of residual titanium dioxide nanoparticles after extended periods of mixing and settling in synthetic and natural waters. *Scientific Reports, 7*, 9943-9954.

Zhang, Q., Gao, L., & Guo, J. (2000). Effects of calcination on the photocatalytic properties of nanosized TiO_2 powders prepared by TiCl4 hydrolysis. *Applied Catalysis B: Environmental, 26*(4), 338-389.

Zhang, Y., Chen, Y., Westerhoff, P., & Crittenden, J. (2009). Impact of natural organic matter and divalent cations on the stability of aqueous nanoparticles. *Water Research, 43*(16), 4249-4257.

Zhao, T., Fang, M., Tang, Z., Zhao, X., Wu, F., & Giesy, J. P. (2019). Adsorption, aggregation, and sedimentation of titanium dioxide nanoparticles and nanotubes in the presence of different sources of humic acids. *Science of The Total Environment, 692*, 660-668.

Zheng, X., Li, Y., Chen, D., Zheng, A., & Que, Q. (2019). Study on analysis and sedimentation of alumina nanoparticles. *International Journal of Environmental Research and Public Health, 16*(3), 510-521.

Zhou, D., & Keller, A. A. (2010). Role of morphology in the aggregation kinetics of ZnO nanoparticles. *Water Research, 44*(10), 2948-2956.

Ziepke, A., Maryshev, I., Aranson, I. S., & Frey, E. (2022). Multi-scale organization in communicating active matter. *Nature Communications, 13*, 6727-6737.

Zuber, A., Purdey, M., Schartner, E., Forbes, C., Van der Hoek, B., Giles, D., Abell, A., Monro, T., & Ebendorff-Heidepriem, H. (2016). Detection of gold nanoparticles with different sizes using absorption and fluorescence based method. *Sensors and Actuators B: Chemical, 227*, 117-127.

APPENDIX A: SEDIMENTATION PROFILES AND HDS CORRELATION

In aquatic systems nanoparticles would undergo several processes such as dispersion, transportation, aggregation/agglomeration, and sedimentation depending on physicochemical properties, viscosity, temperature, *etc*., of media. Experimental exploration of the sedimentation profiles could be attained by applying UV-visible absorption spectra over time (Starchevskii et al., 2009; Keller et al., 2010; Alexander et al., 2013; Quik et al., 2014; Liu et al., 2018; Zheng et al., 2019). Basically, UV-visible spectroscopy as a potent technique could be primarily employed for analyzing the colloidal stability of nanoparticles in aqueous suspensions. The absorbance peak of UV spectrum could correlate with the concentration of monodisperse particles in the solution thereby determination of the sedimentation profiles could be a useful tool in providing supplementary information of DLS measurements in order to assess the HDS of the particles.

Sedimentation profiles were attained by recording the absorbance changes with respect to a specific wavelength using a UV-vis spectrophotometer instrument. The absorbance, A, is defined as;

$$A = \varepsilon C l \qquad (0.1)$$

where ε is the molar absorption coefficient, C is the concentration and *l* are the optical path length. Therefore, absorbance would be directly proportional with the concentration and the concentration change could be followed by the normalization factor of A/A_0, where A is the absorbance in time and A_o is the initial absorbance. The normalization factor can be used to formulate sedimentation rate (Keller et al., 2010).

At a characteristic wavelength, both exponential and linear models could be used to explain sedimentation kinetics of TiO_2.

A.1. Relationship Between Sedimentation Profiles and HDS Variations Over Time:

The relationship between sedimentation profiles and HDS variations of all systems was investigated. Sedimentation data were compiled from an accompanying work performed by Sağlık (Sağlık, 2021). Both experiments were performed simultaneously under similar laboratory conditions.

Incremental change in absorbance with respect to time (DA/Dt) was correlated with HDS expressed as size diameter (D) change (DD/Dt) determined under the same time duration.

A.1.1. TiO_2 Mono and Binary Systems:

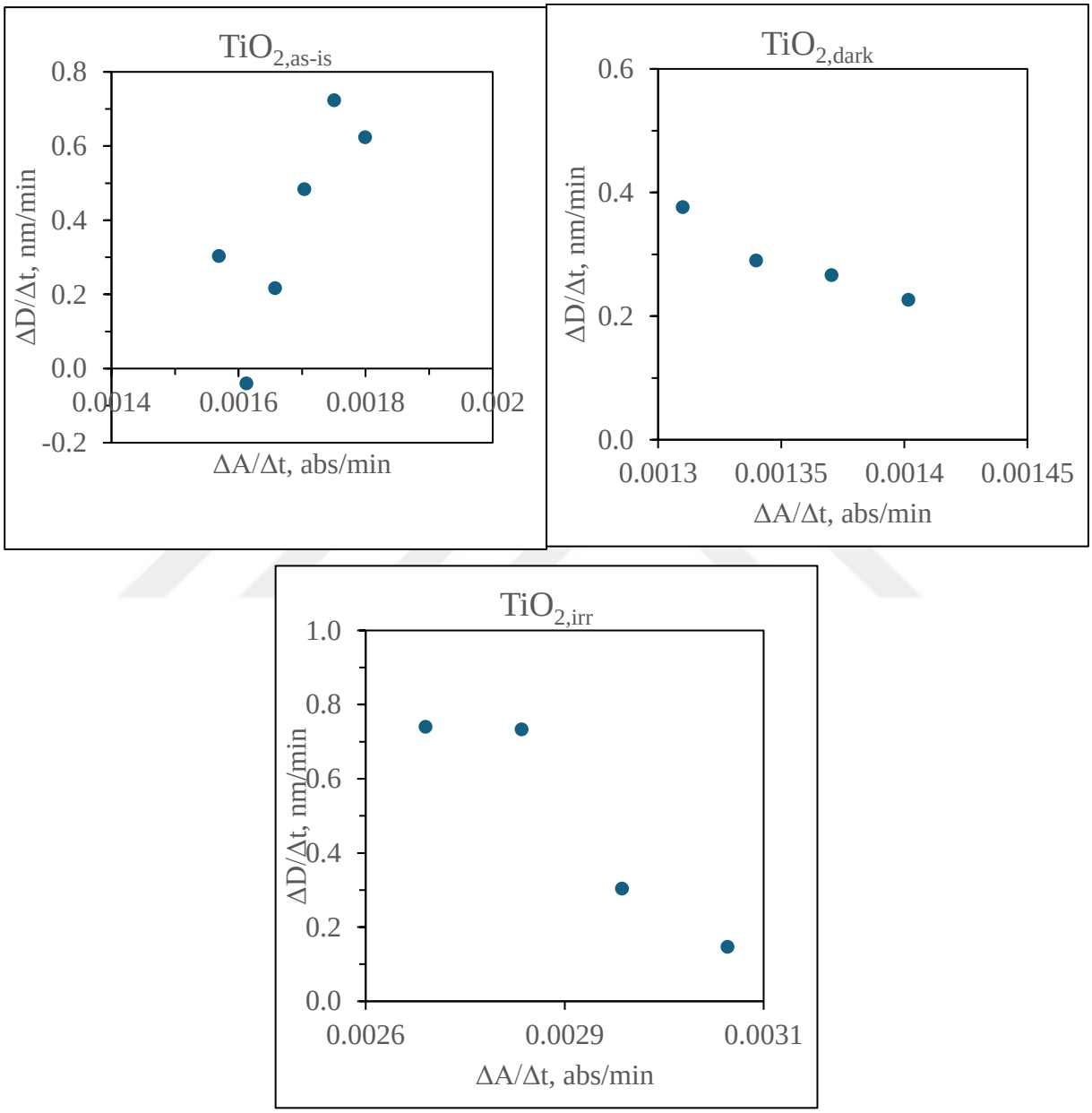


Figure A.1. Time dependent HDS variation in relation to absorbance changes during sedimentation of TiO_2 under as-is, dark and irradiation conditions.

Under as-is conditions TiO_2 expressed a direct relationship between sedimentation performance and time dependent HDS variations (R^2=0.63). However, under dark conditions, an

inverse relationship (R^2=0.92) was attained indicating complete dispersion of particles displaying narrow range of both variables. Upon irradiation, although a wider range of DD/Dt was attained, an inverse relationship was still evident (R^2=0.90).

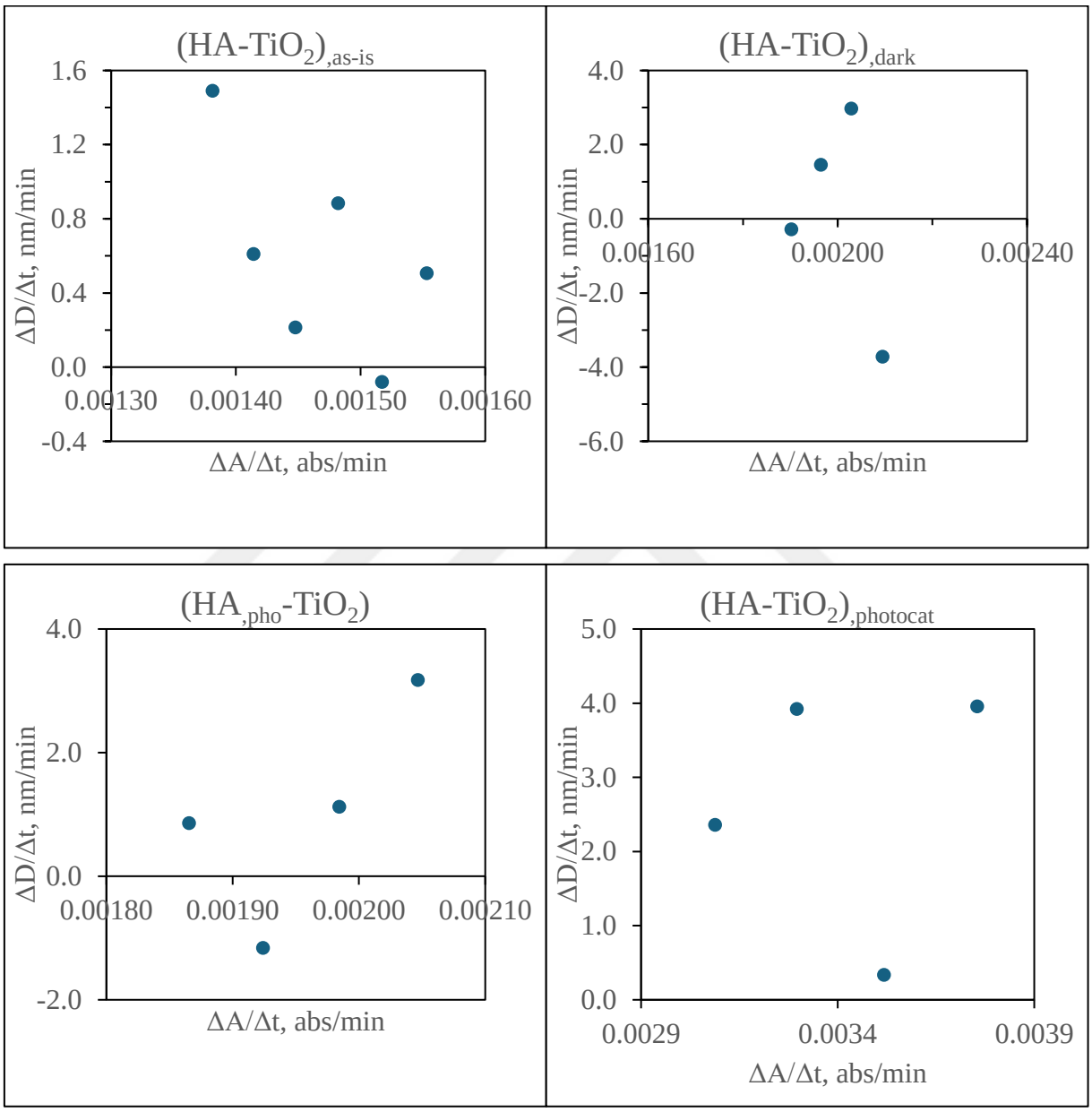


Figure A.2. Time dependent HDS variation in relation to absorbance changes during sedimentation of HA-TiO_2 under as-is, dark and irradiation conditions.

In the presence of HA, insignificant correlation could be visualized through Figure 0.2. The effect of humic sub-fractions affected TiO_2 stabilization resistant to sedimentation although variations in HDS were determined.

A.1.2. Fe-TiO_2 Mono and Binary Systems:

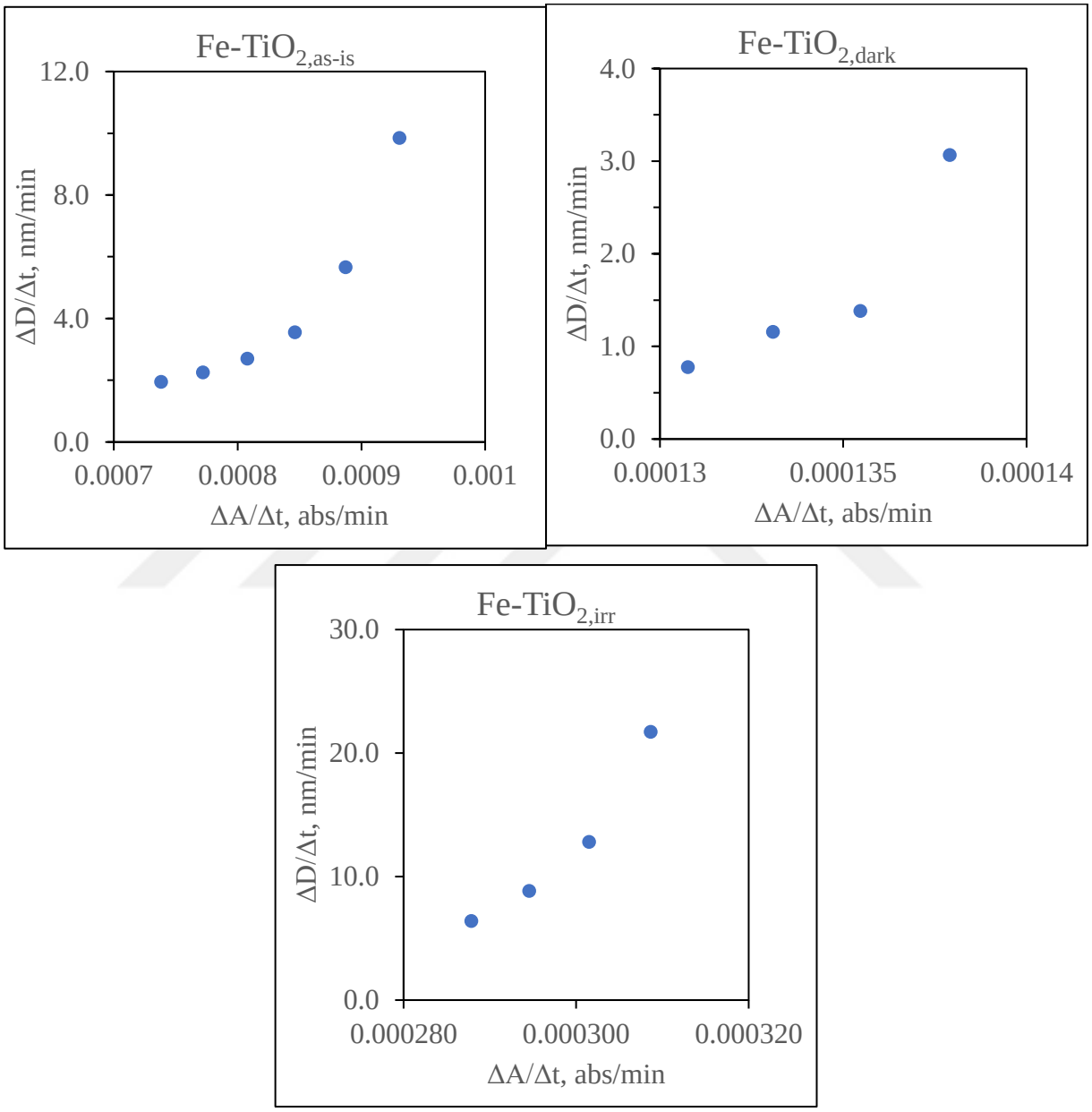


Figure A.3. Time dependent HDS variation in relation to absorbance changes during sedimentation of Fe-TiO_2 under as-is, dark and irradiation conditions.

A linear relationship (R^2 > 0.80) could be established in between time dependent sedimentation and HDS variations of Fe-TiO_2 under as-is, dark and irradiation conditions. However, this direct proportionality was completely disturbed in the presence of HA as HA-Fe-TiO_2 binary system. HA-Fe-TiO_2 binary system expressed a non-significant trend under as-is and dark conditions. Upon exposure to irradiation *i.e.*, ($HA_{,pho}$-Fe-TiO_2) and under photocatalytic conditions (HA-Fe-TiO_2)$_{,photocat}$, a linear correlation (R^2 > 0.64) could be assessed. The reason could be attributed to the light-induced structural and conformational changes of humic sub-fractions that would induce sedimentation and HDS variations through interaction with Fe-TiO_2.

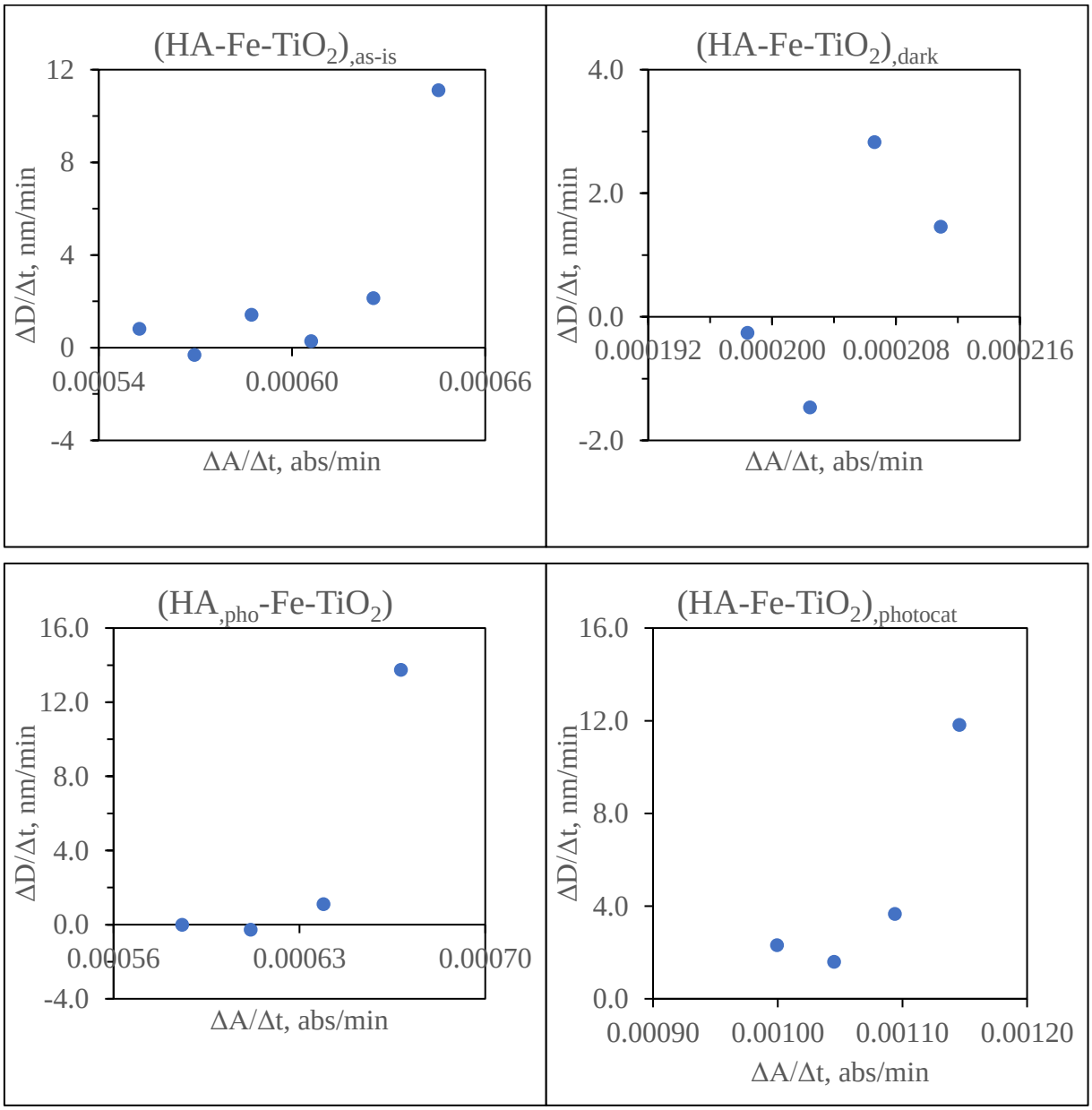


Figure A.4. Time dependent HDS variation in relation to absorbance changes during sedimentation of HA-Fe-TiO_2 under as-is, dark and irradiation conditions.

A.1.3. N-TiO_2 Mono and Binary Systems

In a similar fashion to Fe-TiO_2, a linear relationship ($R^2 > 0.84$) could be established in between time dependent sedimentation and HDS variations of N-TiO_2 under as-is, dark and irradiation conditions. HA-Fe-TiO_2 binary system expressed a rather insignificant trend under as-is and dark conditions ($R^2 > 0.60$). Upon exposure to irradiation *i.e.*, ($HA_{,pho}$-N-TiO_2) and under photocatalytic conditions (HA-N-TiO_2)$_{,photocat}$, the expected relationship improved, and a linear correlation ($R^2 > 0.70$) could be assessed. The reason could also be attributed to the light-induced structural and conformational changes of humic sub-fractions that would induce sedimentation and HDS variations through interactions with N-TiO_2. The role of dopant type could be visualized under both cases especially in terms of humic interactions leading to variations in time dependent aggregation/agglomeration tendencies.

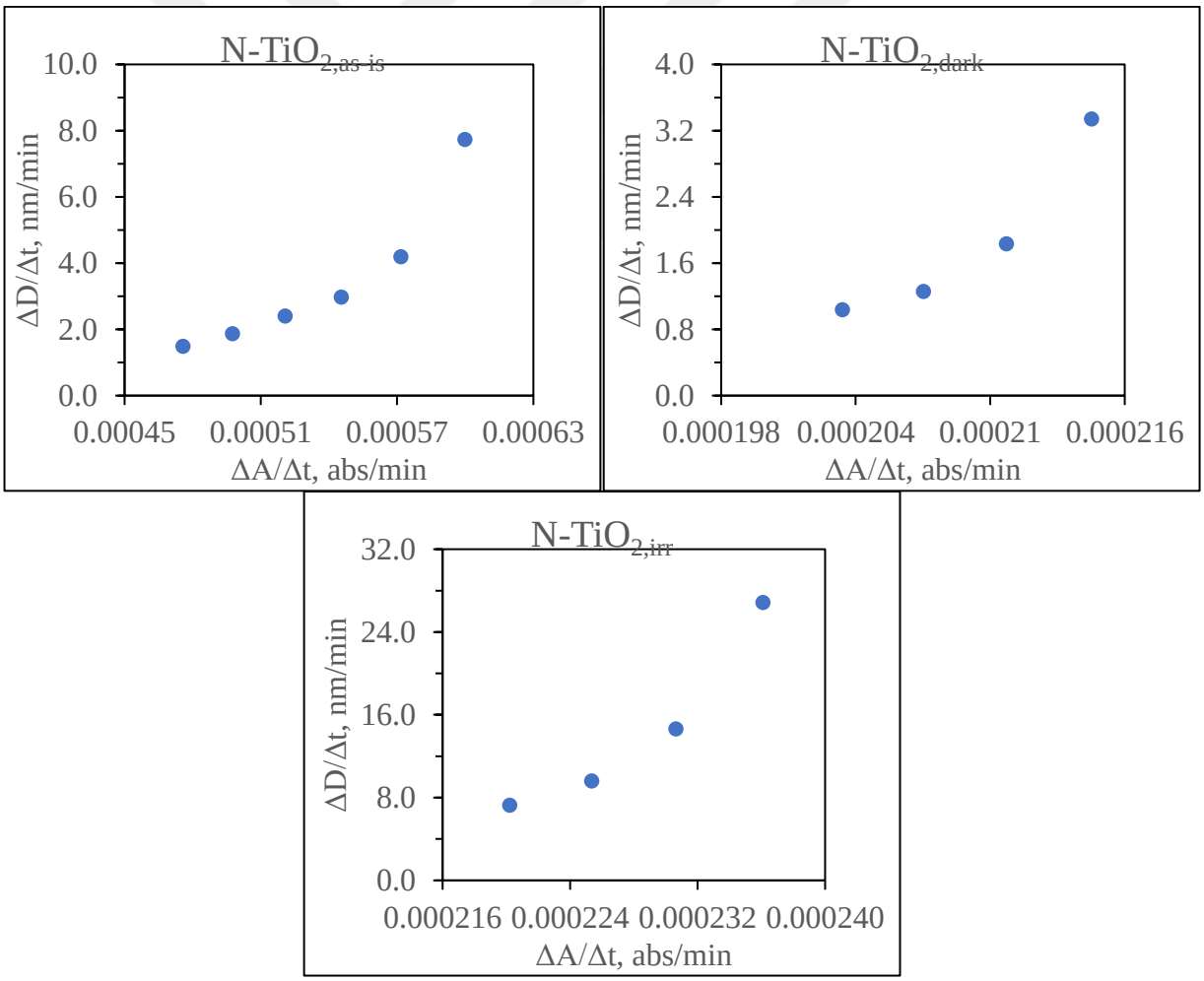


Figure A.5. Time dependent HDS variation in relation to absorbance changes during sedimentation of N-TiO_2 under as-is, dark and irradiation conditions.

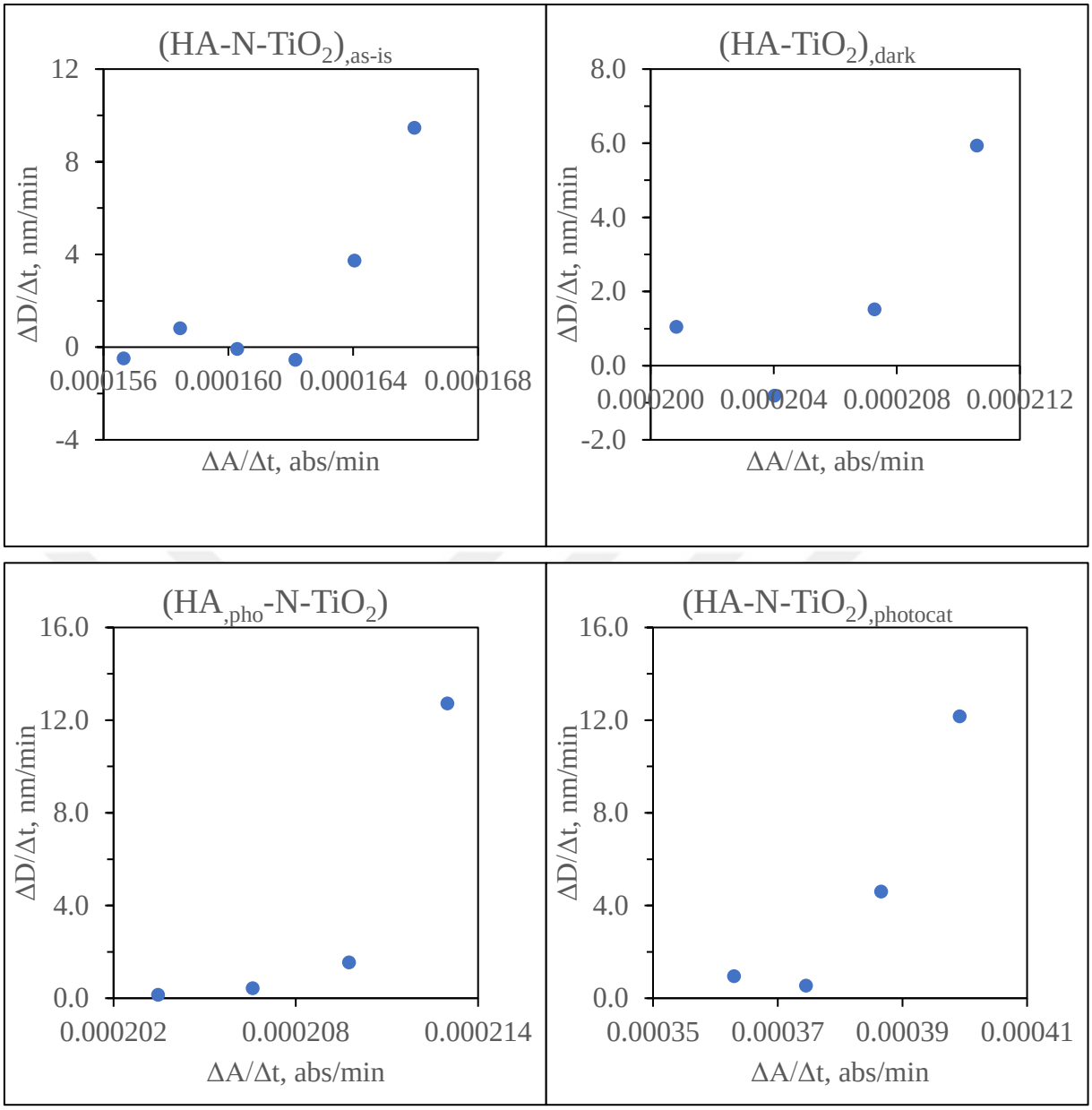


Figure A.6. Time dependent HDS variation in relation to absorbance changes during sedimentation of HA-N-TiO_2 under as-is, dark and irradiation conditions.

APPENDIX B: DEFINITIONS

Advanced oxidation process/technologies: Advanced oxidation technologies (AOTs), which involve the in situ generation of highly potent chemical oxidants, such as the hydroxyl radical (•OH), have emerged (Jackman and Powell, 1991) as an important class of technologies for accelerating the oxidation (and hence contaminant removal) of a wide range of organic contaminants in polluted water and air (Bolton e al., 2001). A partial list of these technologies includes: homogeneous ultraviolet irradiation (Bolton and Cater, 1994) (either direct irradiation of the contaminant or photolytic oxidation mediated by hydrogen peroxide (UV/H_2O_2), and/or ozone ($UV/H_2O_2/O_3$ or UV/O_3), heterogeneous photocatalysis using semiconductor catalysts (e.g., UV/TiO_2) (Legrini et al., 1993; Hoffman et al., 1995), electron-beam irradiation (Cooper et al., 1995), X-ray or gamma-ray radiolysis, nonthermal electric discharge (Donaldson et al., 1991; Rosocha et al., 1992), supercritical water oxidation (Tester et al., 1993) and ultrasonic irradiation (sonolysis) (Cheung et al., 1991; Okouchi et al., 1992) or electrohydraulic cavitation.

Aggregate: Irregular cluster of otherwise individual molecules or particles (Jones et al., 2012).

Aggregation: The aggregation of oppositely charged free ions into ion pairs or larger, and not necessarily well-defined, clusters of ions held together by electrostatic attraction (Jones et al., 2012).

Agglomerate: Cluster of molecules or particles that results from agglomeration (Nic et al., 2005).

Agglomeration: Process of contact and adhesion whereby dispersed particles are held together by weak physical interactions ultimately leading to phase separation by the formation of precipitates of larger than colloidal size (Nic et al., 2005).

Bandgap Energy: The energy difference between the bottom of the conduction band and the top of the valence band in a semiconductor or an insulator (Nic et al., 2005).

Conduction band: A vacant or only partially occupied set of many closely spaced electronic levels resulting from an array of a large number of atoms forming a system in which the electrons can

move freely or nearly so. This term is usually used to describe the properties of metals and semiconductors (Nic et al., 2005).

Dissolved organic carbon: Concentration of organic carbon remaining in solution after filtration and/or centrifugation under defined conditions (ISO 11074:2015).

Electric double layer: The Coulombic interaction of interfacial charges (e.g. ions) and the magnetic or electrostatic interaction of interfacial molecules lead to particularly complex interfacial structures. Complex interfacial profiles that can be approximated by two distinct sub-layers with different physical properties (e.g. structure and/or nature and/or composition), are referred to as interfacial double-layers. Examples of such approximated complex profiles are: the electrical double-layer consisting of a surface charge layer (i.e. a two dimensional distribution of one type of ions) and a diffuse charge layer (counter-ions distributed over the space region next to the surface); the approximated profile of the orientation angle of anisotropic liquid molecules within a 'double-layer' consisting of a distribution of so-called anchored molecules which are perturbed (strongly bound and orientated) by the surface, and the adjacent, so-called, transition layer, i.e. the region where the surface perturbation is damped (Minassian-Saraga, 1994).

Homogeneity: The degree to which a property or a constituent is uniformly distributed throughout a quantity of material. A material may be homogeneous with respect to one analyte or property but heterogeneous with respect to another. The degree of heterogeneity (the opposite of homogeneity) is the determining factor of sampling error (Nic et al., 2015).

Hydrodynamic Volume: The volume of a hydrodynamically equivalent sphere (Nic et al., 2015).

Hydrodynamic Diameter: The diameter of systems are moving via Brownian motion in liquid phase individually or in aggregate/agglomerate form and including their outer shell, *i.e.*, electric double layer (ISO 9276).

Light Scattering: The redirection of a light beam due to interactions with molecules (Rayleigh and Raman scattering) and aerosols (Mie scattering) (Nic et al., 2005).

Mie Theory: Theory of light scattering by isotropic, homogeneous spheres (Nic et al., 2005).

Monodisperse medium: A colloidal system in which all particles are of (nearly) the same size (Nic et al., 2005).

Monodispersed Polymer: Uniform polymer. A polymer composed of molecules uniform with respect to relative molecular mass and constitution (Nic et al., 2005).

Notes

1. A polymer comprising a mixture of linear and branched chains, all of uniform relative molecular mass, is not uniform. 2. A copolymer comprising linear molecules of uniform relative molecular mass and uniform elemental composition but different sequential arrangements of the various types of monomeric units, is not uniform (e.g. a copolymer comprising molecules with a random arrangement as well as a block arrangement of monomeric units).

3. A polymer uniform with respect only to either relative molecular mass or constitution may be termed 'uniform', provided a suitable qualifier is used (e.g. 'a polymer uniform with respect to relative molecular mass').

4. The adjectives 'monodisperse' and 'polydisperse' are deeply rooted in the literature, despite the former being non-descriptive and self-contradictory. They are in common usage, and it is recognized that they will continue to be used for some time; nevertheless, more satisfactory terms are clearly desirable. After an extensive search for possible replacements, the terms 'uniform' and 'non-uniform' have been selected and they are now the preferred adjectives.

Nanoparticle: a particle of any shape with dimensions in the 1×10^{-9} and 1×10^{-7} m range (Vert et al., 2012).

Particle: Minute piece of matter with defined physical boundaries (ISO 22412).

Particle Size: To describe the size of liquid or solid particles (aerosol) the average or equivalent diameter is used. For non-spherical particles collected in an impactor, for example, the aerodynamic diameter of a particle of arbitrary shape and density refers to the size of a spherical particle of unit density that would deposit on a given impactor surface (Nic et al., 2005).

Particle size distribution: The size of the liquid or solid particles in the atmosphere usually extends from >0.01 to <100 μm in diameter. In the earth's atmosphere the distribution function which describes the number of particles as a function of diameter, mass or surface area of the aerosol can be determined reasonably well with modern instrumentation (Nic et al., 2005).

Photon: Particle of zero charge, zero rest mass, spin quantum number 1, energy hν and momentum hν/c (h is the Planck constant, ν the frequency of radiation and c the speed of light), carrier of electromagnetic force (Nic et al., 2005).

Polydisperse medium: A colloidal system in which many particle sizes occur (Nic et al., 2005).

Polydisperse polymer: Non-uniform polymer. A polymer comprising molecules non-uniform with respect to relative molecular mass or constitution or both (Nic et al., 2005).

Polydispersity Index: 1. A dimensionless ratio of two average values of a property is widely used in polymer science as a characteristic of the dispersion, or spread, of the distribution of values of that property in a sample of polymer. In particular, the ratios M_w/M_n and X_w/X_n are quantities commonly used to characterize the dispersions of distributions of molar masses and degrees of polymerization, respectively. However, they do not have satisfactory names and the present recommendation seeks to rectify this situation (Stepto, 2009).

2. dimensionless measure of the broadness of the size distribution (ISO 22412).

Radiation: A term embracing electromagnetic waves as well as fast moving particles (Nic et al., 2005).

Radius of gyration: A parameter characterizing the size of a particle of any shape. For a rigid particle consisting of mass elements of mass m_i, each located at a distance r_i from the center of mass, the radius of gyration, s, is defined as the square root of the mass-average of r^2_i for all the mass elements, i.e.

$$s = \sqrt{\frac{\sum_i m_i r_i^2}{\sum_i m_i}}$$

For a non-rigid particle, an average over all conformations is considered, i.e.

$$\sqrt{\langle s^2 \rangle} = \frac{\sqrt{\langle \sum_i m_i r_i^2 \rangle}}{\sqrt{\sum_i m_i}}$$

The subscript zero is used to indicate unperturbed dimensions, as in $\langle s^2 \rangle_0^{1/2}$ (Nic et al., 2005).

Rayleigh Scattering: The scattering of light by particles and molecules which are much smaller than the wavelength of the light. In the ideal case, the process is one of pure dipole and induced dipole

interactions with the electric field of the light wave. The scattering cross section for light of wavelength λ is proportional to λ^{-4} (Nic et al., 2005).

Scattering: A process in which a change in direction or energy of an incident radiation is caused by interaction with a particle, a system of particles, or a photon (Nic et al., 2005).

Scattering angle: The angle between the forward direction of the incident beam and a straight line connecting the scattering point and the detector. Synonymous with angle of observation (Nic et al., 2005).

Stern layer: Counter and co-ions in immediate contact with a surface are said to be located in the Stern layer, and form with the fixed charge a molecular capacitor (Nic et al., 2005).

Valance Band: The valence band is lower in energy than the conduction band and is generally completely full in semiconductors. When heated, electrons from the valence band jump out of the band across the band gap and into the conduction band, making the material conductive (Nic et al., 2005).

Zeta potential: Electrokinetic potential. Potential drop across the mobile part of the double layer, that is responsible for electrokinetic phenomena. ζ (zeta) is positive if the potential increases from the bulk of the liquid phase towards the interface. In calculating the electrokinetic potential from electrokinetic phenomena, it is often assumed that the liquid adhering to the solid wall and the mobile liquid are separated by a sharp shear plane. As long as there is no reliable information on the values of the permittivity and the viscosity in the electrical double layer close to the interface, the calculation of the electrokinetic potential from electrokinetic experiments remains open to criticism. It is therefore essential to indicate in all cases which equations have been used in the calculation of ζ. It can be shown, however, that for the same assumptions about the permittivity and viscosity all electrokinetic phenomena must give the same value for the electrokinetic potential (Nic et al., 2005).

Z-average: The cumulants method yields a scattered light intensity-weighted harmonic mean particle diameter, which is sometimes also referred to as the "z-average diameter." (ISO 22412).